frontiers | Research Topics

Advanced oral disease therapy: Approaches, biotechnology, and bioactive materials

Edited by
Xing Wang, Hai Zhang, Xianqi Li, Jianyun Zhang and Yuan Yin

Published in
Frontiers in Bioengineering and Biotechnology

ISSN 1664-8714
ISBN 978-2-8325-2643-9
DOI 10.3389/978-2-8325-2643-9

About Frontiers

Frontiers is more than just an open access publisher of scholarly articles: it is a pioneering approach to the world of academia, radically improving the way scholarly research is managed. The grand vision of Frontiers is a world where all people have an equal opportunity to seek, share and generate knowledge. Frontiers provides immediate and permanent online open access to all its publications, but this alone is not enough to realize our grand goals.

Frontiers journal series

The Frontiers journal series is a multi-tier and interdisciplinary set of open-access, online journals, promising a paradigm shift from the current review, selection and dissemination processes in academic publishing. All Frontiers journals are driven by researchers for researchers; therefore, they constitute a service to the scholarly community. At the same time, the *Frontiers journal series* operates on a revolutionary invention, the tiered publishing system, initially addressing specific communities of scholars, and gradually climbing up to broader public understanding, thus serving the interests of the lay society, too.

Dedication to quality

Each Frontiers article is a landmark of the highest quality, thanks to genuinely collaborative interactions between authors and review editors, who include some of the world's best academicians. Research must be certified by peers before entering a stream of knowledge that may eventually reach the public - and shape society; therefore, Frontiers only applies the most rigorous and unbiased reviews. Frontiers revolutionizes research publishing by freely delivering the most outstanding research, evaluated with no bias from both the academic and social point of view. By applying the most advanced information technologies, Frontiers is catapulting scholarly publishing into a new generation.

What are Frontiers Research Topics?

Frontiers Research Topics are very popular trademarks of the *Frontiers journals series*: they are collections of at least ten articles, all centered on a particular subject. With their unique mix of varied contributions from Original Research to Review Articles, Frontiers Research Topics unify the most influential researchers, the latest key findings and historical advances in a hot research area.

Find out more on how to host your own Frontiers Research Topic or contribute to one as an author by contacting the Frontiers editorial office: frontiersin.org/about/contact

Advanced oral disease therapy: Approaches, biotechnology, and bioactive materials

Topic editors

Xing Wang — Shanxi Medical University, China
Hai Zhang — University of Washington, United States
Xianqi Li — Matsumoto Dental University, Japan
Jianyun Zhang — Peking University Hospital of Stomatology, China
Yuan Yin — Fourth Military Medical University, China

Citation

Wang, X., Zhang, H., Li, X., Zhang, J., Yin, Y., eds. (2023). *Advanced oral disease therapy: Approaches, biotechnology, and bioactive materials*. Lausanne: Frontiers Media SA. doi: 10.3389/978-2-8325-2643-9

Table of contents

frontiers | Frontiers in Bioengineering and Biotechnology

TYPE Editorial
PUBLISHED 24 May 2023
DOI 10.3389/fbioe.2023.1211443

OPEN ACCESS

EDITED AND REVIEWED BY
Hasan Uludag,
University of Alberta, Canada

*CORRESPONDENCE
Hai Zhang,
haizhang@uw.edu
Xing Wang,
kqwx100@163.com

†These authors share first authorship

RECEIVED 24 April 2023
ACCEPTED 10 May 2023
PUBLISHED 24 May 2023

CITATION
Zhang H, Wang X, Li X, Yin Y, Zhang J and Zhang X (2023), Editorial: Advanced oral disease therapy: approaches, biotechnology, and bioactive materials. *Front. Bioeng. Biotechnol.* 11:1211443. doi: 10.3389/fbioe.2023.1211443

Editorial: Advanced oral disease therapy: approaches, biotechnology, and bioactive materials

Hai Zhang[1*†], Xing Wang[2*†], Xianqi Li[3], Yuan Yin[4], Jianyun Zhang[5] and Xiaoxuan Zhang[2]

[1]Department of Restorative Dentistry, University of Washington, Seattle, WA, United States, [2]Shanxi Medical University School and Hospital of Stomatology, Taiyuan, China, [3]Department of Oral and Maxillofacial Surgery, Matsumoto Dental University, Shiojiri, Japan, [4]State Key Laboratory of Military Stomatology, Department of Periodontology, Fourth Military Medical University, Xi'an, China, [5]Department of Oral Pathology, Peking University School and Hospital of Stomatology, Beijing, China

KEYWORDS

biomaterial, bioengineering, biomimetic, regeneration, biotechnology

Editorial on the Research Topic
Advanced oral disease therapy: approaches, biotechnology, and bioactive materials

In recent years, the advancement in biotechnology has enabled much improvement in quality and outcomes of medicine. These innovations have also drawn great attention in dental research fields. Regenerative medicine such as tissue (bone and tooth) engineering has been a hot topic in oral and craniofacial research for a few decades. Cells, signaling molecules and scaffold materials are three key components of tissue engineering approaches. Almost everyday new bioengineering approaches are proposed and tested for various diseases and treatment in dentistry.

Stem cells such as mesenchymal stem cells (MSCs) are multipotent and may differentiate into different cell types for tissue repair and regeneration. However technical issues including phenotype consistency, host immune response and potential tumorigenicity are still not completely resolved. Extracellular vesicles (EVs) originate from cellular endosomes and contain bioactive molecules to target cells by paracrine. It is known that these EVs are one of the major mediators of stem cells leading to their biological effects. MSC-derived EVs (MSC-EVs), instead of MSCs, may be potentially used in tissue repair and regeneration. The current status and future therapeutic applications of MCS-EVs in oral and craniofacial tissue regeneration are discussed in a review (Liu et al.). EVs secreted by human gingival MSCs (hGMSC-derived EVs) were shown to promote osteogenesis and neovascularization *in vitro* and *in vivo* (Wang et al.). The roles of stem cell-derived EVs and non-stem cell-derived EVs in bone tissue regeneration (critical-size defect model) are reviewed (Liu et al.). Engineering modified EVs may play important roles in future cell free EV-based bone tissue engineering therapies.

A new generation of scaffold materials has been developed for tissue engineering. A multifunctional structurally optimized hydrogel scaffold was designed by integrating polyvinyl alcohol, gelatin, and sodium alginate with aspirin and nano-hydroxyapatite (nHAP). The osteogenic of nHAP and anti-inflammatory function of aspirin were

successfully synergized (Li et al.). Similarly, nanofibrous scaffold material can be modified to provide better coordinated regenerative endodontic treatment when pulp connective-tissue, dentin formation, revascularization and reinnervation need to be well orchestrated (Huang et al.). Silk fibroin nanoparticles were coated with genetically engineered cell membrane overexpressing toll-like receptor 4 and loaded with minocycline hydrochloride. These biomimetic nanoparticles demonstrated excellent targeted antibacterial and immunoregulatory effects *in vitro* and *in vivo* (ligature-induced periodontitis mouse model) (Deng et al.).

Other advancements in oral disease therapies are also made in recent years. Eldecalcitol, a novel active vitamin D3 analog, was shown to be effective on preventing alveolar bone loss in diabetes-associated periodontitis (Gao et al.). Targeted delivery of antitumor drugs has been recognized as a promising therapeutic modality to improve treatment efficacy, reduce toxic side effects and inhibit tumor recurrence. A controlled-release of an anti-tumor drug (apatinib) from supramolecular nanovalve-modified mesoporous silica was designed for targeted inhibition of osteosarcoma (Wang et al.). This *in vitro* study showed efficient release of antitumor drug and promising results for future osteosarcoma treatment. Enamel white spot lesions do not have effective yet conservative treatment methods. Synergistic remineralization of enamel white spot lesions was achieved by using mesoporous bioactive glasses loaded with amorphous calcium phosphate, which implies great potential for clinical application (Ren et al.).

The microbial composition and structural diversity of supragingival plaque on the surface of fixed prostheses were found to differ from that of normal natural crowns, with relatively high levels of periodontally related pathogens and higher microbial metabolism. The microflora on the surface of all-ceramic crowns was more similar to that of natural crowns than to that of porcelain-fused-to-metal crowns (Li et al.). Understanding the composition and differences between supragingival plaque biofilm microbes on the surface of fixed prostheses and natural crowns can provide patients with targeted guidance to focus on oral hygiene habits, reduce the risk of periodontal diseases and improve the success rate of fixed prostheses.

In addition to biotechnology, digital technology has also been applied in oral disease treatment, such as implant therapy. Additive manufacturing (AM) can enable the direct fabrication of customized physical objects with complex shapes, based on computer-aided designs. The applications of AM technologies in oral implantology, including implant surgery and restorative products, was reviewed (Huang et al.). Through the use of AM technology, personalized implant treatment for individual patients can be achieved.

With the quick advancement of therapeutic approaches, biotechnology, and bioactive materials, it will not be too long before precision and personalized dentistry become reality.

Author contributions

HZ and XW contributed to conception and design of this Editorial. HZ wrote the first draft of the manuscript. All authors contributed to the article and approved the submitted version.

Conflict of interest

The authors declare that the research was conducted in the absence of any commercial or financial relationships that could be construed as a potential conflict of interest.

Publisher's note

frontiers | Frontiers in Bioengineering and Biotechnology

TYPE Review
PUBLISHED 29 November 2022
DOI 10.3389/fbioe.2022.1054370

OPEN ACCESS

EDITED BY
Xing Wang,
Shanxi Medical University, China

REVIEWED BY
Xiangxiang Hu,
University of North Carolina at Chapel Hill, United States
YIng Chen,
Zhejiang University, China
Solen Novello,
University of Rennes 1, France

*CORRESPONDENCE
Kun Xuan,
xuankun@fmmu.edu.cn
Xinyu Qiu,
qxyturbo911@163.com

†These authors contributed equally to this work and share first authorship

‡These authors contributed equally to this work and share last authorship

SPECIALTY SECTION
This article was submitted to Biomaterials, a section of the journal Frontiers in Bioengineering and Biotechnology

RECEIVED 26 September 2022
ACCEPTED 03 November 2022
PUBLISHED 29 November 2022

CITATION
Liu M, Liu X, Su Y, Li S, Chen Y, Liu A, Guo J, Xuan K and Qiu X (2022), Emerging role of mesenchymal stem cell-derived extracellular vesicles in oral and craniomaxillofacial tissue regenerative medicine. *Front. Bioeng. Biotechnol.* 10:1054370. doi: 10.3389/fbioe.2022.1054370

Emerging role of mesenchymal stem cell-derived extracellular vesicles in oral and craniomaxillofacial tissue regenerative medicine

Meng Liu[1†], Xin Liu[2†], Yuting Su[3], Shijie Li[1], Yuan Chen[1], Anqi Liu[1], Jing Guo[1], Kun Xuan[1*‡] and Xinyu Qiu[1*‡]

[1]State Key Laboratory of Military Stomatology and National Clinical Research Center for Oral Diseases and Shaanxi International Joint Research Center for Oral Diseases, Department of Preventive Dentistry, School of Stomatology, Fourth Military Medical University, Xi'an, Shaanxi, China, [2]Department of Orthodontics, School of Stomatology, Fourth Military Medical University, Xi'an, Shaanxi, China, [3]Center of Clinical Aerospace Medicine, School of Aerospace Medicine, Fourth Military Medical University, Xi'an, Shaanxi, China

Mesenchymal stem cells (MSCs) are multipotent stem cells with differentiation potential and paracrine properties, drawing significant attention in the field of regenerative medicine. Extracellular vesicles (EVs), mainly including exosomes, microvesicles and apoptotic bodies (ABs), are predominantly endosomal in origin and contain bioactive molecules, such as miRNAs, mRNAs, and proteins, which are transferred from their original cells to target cells. Recently it has emerged that MSC-derived EVs (MSC-EVs) combine the advantages of MSCs and EVs, which may be used as a promising MSC-based therapy in tissue repair and regeneration. Oral and craniomaxillofacial diseases are clinically complications containing the soft and hard tissues in craniofacial and dental arches. These diseases are often induced by various factors, such as chemical, microbiological, physical factors, and systemic disorders. For decades, tissue repair and regeneration in oral and craniomaxillofacial regions provide substantial improvements in the prevention and treatment of some severe diseases. In this review we discuss MSC-EVs and their therapeutic potential in oral and craniomaxillofacial tissue regenerative medicine.

KEYWORDS

mesenchymal stem cells, extracellular vesicles, regenerative medicine, tissue engineering, oral and craniomaxillofacial tissue

1 Introduction

Oral and craniomaxillofacial regions consist of soft and hard tissues like muscles, bone, cartilage and skin, which brings great obstacles for therapies in oral and craniomaxillofacial diseases, including infectious disease such as caries and periodontitis, function disorders like temporomandibular joint (TMJ) disorders, and maxillofacial tissue defects caused by tumors, trauma and deformities (Ding et al., 2020). To deal with different diseases, multiple treatments have been developed, among which the requirements for tissue reconstruction arises because of congenital deformities, trauma through sports and other accidents in oral and craniomaxillofacial regions (Gaihre et al., 2017). However, conventional tissue reconstruction with designed biomaterials encounters different limitations such as confined biocompatibility, frequent skin or mucosa irritations. These limitations have brought out urgent demands for new remedies in this field.

Mesenchymal stem cells (MSCs) have been isolated from various tissues, such as bone marrow, adipose tissue, umbilical cord, and dental pulp (Keshtkar et al., 2018). Due to its low immunogenicity, great self-renewal potential and multidirectional differentiation, MSCs have been widely used in the field of tissue engineering and regenerative medicine (Keshtkar et al., 2018; Chen et al., 2020), which exhibited remarkable capacity on promoting tissue repair in oral and craniomaxillofacial diseases. However, it has been observed that exogenous MSCs only survived a short time after transplantation, failing to proliferate and differentiate in quantity, which impacts the therapeutic effects (Hoogduijn and Lombardo, 2019), leading to further investigation and modification of MSCs. In the beginning, researchers found that MSCs interact with recipient cells through differentiation and paracrine signaling pathway, while recent studies reveal that MSCs play a vital role in treatments of various diseases mainly by secreting extracellular vesicles (EVs) as well as soluble paracrine factors (Sigmarsdottir et al., 2020). EVs contain various bioactive molecules for communication and interaction between donor and recipient cells, which maintain life function and normal development of cells.

This finding provides opportunities to develop novel cell-free therapeutic strategies in oral and craniomaxillofacial diseases. At present, MSCs-based therapy still suffers from considerable limitations in the following aspects: i) difficult to determine best culture conditions and proper administration mode, ii) hard to detect and quantitate in real-time due to individual differences after MSCs transplantation, iii) adverse reactions to MSCs injection, such as venous thrombosis (Furlani et al., 2009), iv) low survival rate of MSCs after transplantation (Warrier et al., 2022). Inspiringly, since EVs are cell-free, MSC-derived EVs (MSC-EVs) are safer and more stable than MSCs. The application of MSC-EVs has covered these disadvantages to some extent. The application of MSC-EVs makes it possible for quantitative index and quality control in tissue regenerative medicine. Therefore, research of therapy based on MSC-EVs has attracted more and more attention in the field of oral and craniomaxillofacial tissue regenerative medicine.

2 Extracellular vesicles

2.1 Characteristics and isolation of EVs

EVs are nano-vesicles with lipid bilayers secreted by almost all cell types. Based on the vital role MSCs played in tissue repair and its strong connection with EVs *via* paracrine signaling pathways, MSC-EVs have gradually entered the scene in tissue engineering and regenerative medicine (Keshtkar et al., 2018). Researchers have found that various peptides and glycoproteins exist on the membrane of EVs, which is crucial for intercellular recognition and adhesion. EVs are relatively stable in circulation, and these distinct membrane landmarks can influence their tropism to specific organs. It is reported that different integrins on membrane enable EVs to accumulate in brain, liver or lungs, depending on the particular integrin type (Hoshino et al., 2015). What's more, bioactive molecules EVs contained during their formation are in plenty, such as lipids, proteins, and nucleic acids (van Niel et al., 2018). Once released into the extracellular space, EVs can reach recipient cells and deliver their contents to elicit the corresponding functional responses (Figure 1). Through these molecules, also called EV cargoes, EVs participate in intercellular communication and interaction frequently, acting like loaded vehicles, shuttling between cells to realize molecular information transferring (Panda et al., 2021). However, the mode of vesicle interaction with the cell surface and the mechanisms that mediate the transfer of EV cargoes are not completely unraveled until nowadays. These procedures are complex and relate to the origins of EVs and the recipient cells, linking to the downstream effects and processes (van Niel et al., 2018).

Current studies focus on utilizing EVs as candidates for cell-free therapy or targeted drug delivery system due to its ability of loading biological macromolecules (Sun et al., 2021), while the role of EVs played in the regenerative medicine is still under investigation. Compared with exogenous MSCs transplantation in regenerative medicine, MSC-EVs show greater advantages because of its lower immunoreactivity and biological stability. Since MSC-EVs have no potential to differentiate, they are also more controllable and possess higher biosecurity. The studies have reported that MSCs were rapidly removed within 48 h after administration, which restricted its direct effects on tissue repair (Liu et al., 2020). On the contrary, EVs are characterized with extended half-life and excellent penetration in drug delivery (Kunter et al., 2007; Lai et al., 2013). The cell-free conditioned medium of MSCs demonstrates similar therapeutic effects on tissue repair (Gnecchi et al., 2005). Therefore, EVs based cell-free

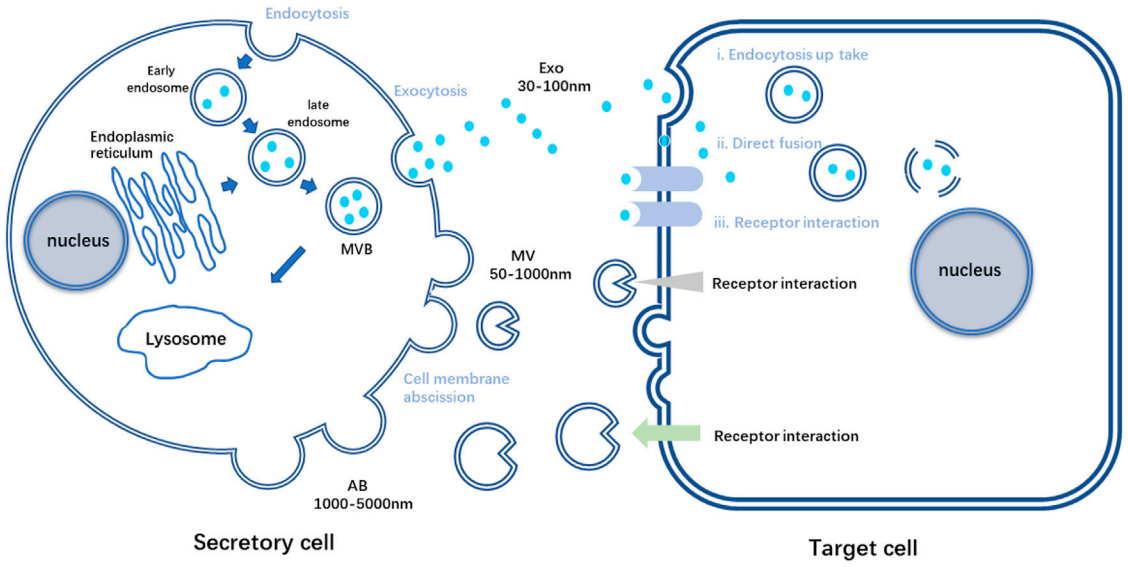

FIGURE 1
Schematic diagram of the process of secretory cells secreting three kinds of EVs and the process of target cells receiving three kinds of vesicles. AB, apoptotic bodies; Exo, exosome; MV, Microvesicles; MVB, multivesicular bodies.

therapy has become an emerging hot spot and may gradually replace MSC-based therapy.

In view of the promising prospect of MSC-EVs in regenerative medicine, it is important to isolate and apply EVs in tissue repair. There are various methods to isolate EVs, which demonstrate different advantages and disadvantages in terms of purity, time, and cost (Crescitelli et al., 2021). Among all these methods, ultracentrifugation is one of the most common and convenient. Firstly, cells and debris are deposited and removed by centrifugation. Then the supernatant containing biological macromolecules undergoes further ultra-centrifugation to concentrate EVs in the pellet. Specifically, to isolate ABs, inducing cell apoptosis is necessary before centrifugation (Liu et al., 2018). Even though it is easy to implement, this method costs a long time. In addition, aggregation of different types of EVs during ultracentrifugation largely affect the purity, it is impossible to specifically separate each type of EVs only by centrifugation. As for therapy or experiment, EVs need to be isolated and concentrated while MSCs are strictly removed. Hence, many studies have utilized size-exclusion chromatography to isolate EVs, through which particles not in the required size range are excluded. However, passing through the filters by force may lead to the deformation and rupture of large vesicles and platelets, resulting in a loss of purity. Moreover, it costs lots of time to pass through multiple filters with different sizes (György et al., 2011). Due to the immunoaffinity of specific proteins on surfaces of EVs, immunoaffinity separation have been utilized (Clayton et al., 2001). Nevertheless, for each specific type of EVs, the specific antibody should be selected, which leads to low universality and inefficiency (Théry et al., 2006). There are several methods available for combined application, including polymerization precipitation, microfluidics, and so on (Chen et al., 2010; Yamada et al., 2012; Witwer et al., 2013). After isolation, identification of the acquired "EVs" is necessary. The common methods include observing morphological characteristics of "EVs" by electron microscopy, measuring particle size distribution by dynamic light scattering (DLS) analysis, and detecting molecular markers by western blot or immunofluorescence.

2.2 Main classes of EVs

Since there is no consensus emerged on specific markers of EVs subtypes so far, some measurable and operational terms are used to classify EVs. For example, size was referred to define EV subtype as "small EV" (sEVs, < 100 nm or < 200 nm) and "medium/large EVs" (m/lEVs, > 200 nm). Biochemical composition, condition description or origin of cells were also recommended to distinguish different EVs (Théry et al., 2018). However, it is still wide accepted that EVs are divided into the following three categories according to biogenesis, particle size and surface markers (Table 1).

2.2.1 Exosomes

Exosomes were first discovered and named when researchers were investigating reticulocytes transformation (Johnstone et al., 1987). As the smallest kind of EVs, exosomes are formed by

TABLE 1 Comparison of basic physiological characteristics of three kinds of EVs.

Characteristics	Exosome	Microvesicles	Apoptotic bodies
General characteristics	Almost all cells can secrete Presented in body fluids Rich in protein, lipid and genetic material		
Biogenesis mechanism	Endocytosis and exocytosis, Generated by multi vesicle system	Cell membrane budding	Release during apoptosis
Diameter	30-150 nm	50-1000 nm	1000-5000 nm
Main markers	Transmembrane protein (CD9, CD63, CD81) TSG101, Lactadherin, LAMP1	CD40 Phosphatidylserine Cell surface antigen	Phosphatidylserine

exocytosis, ranging in diameters from 30 nm to 150 nm. Exosomes, also referred as intraluminal vesicles (ILVs), originate from early endosomes and are produced by inward budding of the endosomal membrane. With the participation of Golgi apparatus, ILVs mature into multivesicular bodies (MVBs), which either undergo metabolization and excretion in lysosomes, or fuse to plasma membrane and eventually release its contents, including exosomes, to the extracellular space (Pant et al., 2012). The biogenesis of exosomes requires the participation of both complex proteins and enzymes, which constitute endosomal sorting complexes required for transport (ESCRT) pathway. With the development of electron microscope, the structure of exosomes has been observed, which are constrained by lipid bilayers, with different markers on the membrane. CD9, CD63, and CD81are discovered to be located on the outer membrane and they are the most common surface markers for exosomes sorting, both of which contain four transmembrane domains (Jansen et al., 2009; Kosaka et al., 2010; Salunkhe et al., 2020). Previous studies have found that major histocompatibility complexes I and II (MHC-I and MHC-II) exist on the membrane of exosomes, indicating the important role exosomes playing in regulating immune responses, like presenting antigens, activating macrophages and T cells with recognition and elimination (Wolfers et al., 2001; Blanchard et al., 2002; Segura et al., 2005). This feature of exosomes has two sides, it boosted the interest in further exploration of immune dysregulation in tumors by modifying the tumor immunity of exosomes while compromised their therapeutic use in transplantation with potential risk of immunological rejection. However, exosomes derived from MSCs can avoid immune rejection comfortingly, which can compensate for exosomes. Besides, exosomes are reported to be enriched in glycoproteins, proteins related to phosphorylation and so on (Doyle and Wang, 2019). As a result, to improve the sorting accuracy, it is necessary to explore more sensitive and specific molecular markers for composite screening.

Existing in various body fluids and secretions, exosomes reflect the physiological and pathological state of human body. For example, exosomes isolated from alveolar lavage fluid of asthmatic patients contain unique miRNAs, which can be used as the prospective indicators for asthmatic (Levänen et al., 2013). In terms of treatment, it has been found that MSC-derived exosomes reduced monocytes infiltration and thus inhibited inflammation by downregulating MCP-1, an attractant of monocytes (Yu et al., 2016). Despite this, the important role of exosomes in regenerative medicine has been explored. Recent studies confirmed that MSC-derived exosomes enhance the wound healing of skin burn injury by delivering several proteins (Wu et al., 2018). Some studies also verified that noncoding RNAs in exosomes play a crucial role in bone regeneration (Yin et al., 2021). What's more, the possible future potential for microRNA-containing exosomes to treat peripheral nerve injuries are also recognized (Qing et al., 2018).

2.2.2 Microvesicles

Microvesicles (MVs) are formed by the shedding of plasma membrane, ranging in diameters from 150 nm to 1,000 nm. MVs were initially considered as secretions of cells for removing wastes, while the procoagulant property of MVs has been found in the subsequent studies (Loyer et al., 2014; Desrochers et al., 2016; Xie et al., 2019). MVs are formed by the budding of and pinching of the plasma membrane, which is the result of the dynamic interaction between phospholipid redistribution and cytoskeletal protein contraction. Actin myosin is involved in the budding process, so it depends on intracellular calcium ions. The membrane of MVs is rich in lipids such as cholesterol, sphingomyelin and ceramide, and the specific surface marker is like CD40 (Phelps et al., 2018). It is reported that MVs are responsible for the transport of genetic regulatory molecules like mRNAs and miRNAs, which are effective by the interaction of specific receptors and ligands after contacting with the target cells (Keshtkar et al., 2018). Meanwhile, MVs protect the genetic regulatory molecules from degradation by RNA enzymes in the blood.

Recently, the significant roles of MSC-derived MVs (MSC-MVs) in anti-inflammatory regulation and tissue repair have been demonstrated. It has been reported that MSC-MVs improved repair upon lung injury *via* transferring mRNA for angiopoietin1 (Ang1) to endothelial cells, which increased the expression of connexin (Hu et al., 2018). The study has shown

that MVs act as intercellular messengers in cutaneous wound healing (Laberge et al., 2018), which has brilliant future in tissue repair. With further investigation, the researchers discovered that the therapeutic effect of transplanted cells may be associated with their ability to release MVs. These may because that MVs take part in intercellular communication, transferring bioactive molecules like DNAs, mRNAs and miRNAs. Because of their nanoscale size and unique subcellular structures, MVs can be applied as physiological mediators in tissue regeneration (Agrahari et al., 2019).

2.2.3 Apoptotic bodies

As the largest type of EVs, apoptotic bodies (ABs) are released by apoptotic cells, ranging in diameters from 1,000 nm to 5,000 nm, and expressing cell death markers like Caspase-3 and Annexin V (Akers et al., 2013). In fact, apoptotic cells also release vesicles with the similar particle size of exosomes and MVs, which are described as the apoptotic microvesicles (Akers et al., 2013; Poon et al., 2014; Atkin-Smith et al., 2015). As a programmed cell death manner, apoptosis plays an important role in tissue development, cell renewal and homeostasis maintenance, during which molecular signals are released to induce tissue regeneration. Studies have shown that ABs are involved in the regulation of bone homeostasis, metabolic homeostasis, and vascularization during tissue regeneration (Liu et al., 2018; Liu et al., 2020; Zheng et al., 2021). Meanwhile, like their parental cells, ABs are responsible for wastes disposure. Thus, it is reasonable to speculate that there is signal transmission between ABs and macrophages, the professional phagocytes closely related to inflammation and metabolism (Zheng et al., 2021).

Macrophages are the major cell type responsible for clearing apoptotic cells by efferocytosis, through which inhibiting inflammatory responses (Perry et al., 2019; Boada-Romero et al., 2020). It has been found that cadherin anchored on the surface of ABs, mediating the uptake of ABs by macrophages, and reducing the infiltration and activation of macrophages in the sick liver (Zheng et al., 2021). To our knowledge, M2 macrophages play an important role in suppressing inflammation and promoting tissue repair (Smith et al., 2017). It has been observed that proteins able to induce macrophage polarization to M2 phenotype existed on the surface of ABs, which made the ABs beneficial to bone homeostasis and metabolic homeostasis. Moreover, in type II diabetic (T2D) mice, it has been demonstrated that MSC-derived ABs are targeted to macrophages and played vital roles in immunological regulation of macrophages, with remarkable improvements in lowering the chronic inflammation induced by diabetes (Castegna et al., 2020; Zheng et al., 2021). Therefore, there is a close relationship between ABs and macrophages, which may lead to future application of ABs in tissue repair and regenerative medicine. As a kind of underestimated EVs, the functions of ABs need to be further explored.

3 Functions of EVs

3.1 Intercellular communication

Intercellular interactions mainly rely on the molecular signal transmission and modification of target genes, which regulates biological functions of cells (Zhang et al., 2021). Through direct contact and fusion with the plasma membrane, molecular signals are transferred to the target cells by endocytosis of EVs. For example, exosomes have been found in the intracellular space of the marginal region of the heart membrane in myocardial ischemia mice, which has been proved to be linked with intercellular interaction (Sahoo and Losordo, 2014). Except for regulating inflammation and oxidative stress to protect cells from hypoxia and ischemia-reperfusion, the therapeutic effects of exosomes depend on angiogenesis to resist tissue ischemia, which requires communication among endothelial cells, stromal cells, and stem cells. Moreover, it has been discovered that endothelial cell-derived exosomes stimulate endothelial cell migration and angiogenesis through the miR-214 dependent pathway (van Balkom et al., 2013). The EVs isolated from the conditioned medium cultured with $CD34^+$ stem cells promote angiogenesis both *in vivo* and *in vitro* (Sahoo et al., 2011). It has also been reported that $CD34^+$ stem cells transported Shh protein into other cells partially through exosomes with beneficial effects, while injecting Shh protein directly into the heart showed no therapeutic effects. Thus, the protective effects of exosomes on Shh protein degradation by protease have been indirectly proved, which prolonged the half-life of Shh (Mackie et al., 2012). Similarly, EVs isolated from the blood of patients with glioblastoma contain specific mRNAs, which not only shows the protective effects, but also indicates EVs as biomarkers for diseases like glioblastoma (Skog et al., 2008). All the evidence demonstrated that EVs play a crucial role in intercellular communication, accelerating signal transmission between cells.

3.2 Immunomodulation

A remarkable feature of MSCs is immunomodulation. Besides inherited genes, MSCs are affected by surrounding cytokines and receptors on plasma membrane, such as toll like receptors (TLRs) (Costa et al., 2021). Thereby, MSCs tend to exhibit more than one phenotype. Many studies have shown that TLR4 and LPS activated the MSC1 phenotype expressing pro-inflammatory mediators, while interferon-y (INF-y) and tumor necrosis factor α (TNF-α) activated TLR3 and promoted the differentiation towards MSC2 phenotype, which regulated peripheral immune cells (Naftali-Shani et al., 2017; Ferreira et al., 2018; Almeria et al., 2019; Ananthakrishnan et al., 2020). However, the functions of MSCs cannot be controlled after transplantation, and the secretion of immunomodulating factors from MSCs cannot be activated by chronic or minor

inflammation (Gonzalez-Pujana et al., 2020). As a kind of secretion, the cargos of EVs are determined by the parental cells (Liang et al., 2019). Therefore, isolating EVs from cultured MSCs has attracted more attention. After culturing MSCs in specific environment and inducing MSCs to express corresponding phenotype, MSC-derived EVs then extracted may be a more controllable and safer therapeutic tool. The recent study has shown that TNF-α pretreated MSCs produced exosomes containing miR-146a, which inhibited the activation of fibroblasts and inflammatory responses in the model of urethral fibrosis (Liang et al., 2019). Additionally, EVs derived from IL-1β-pretreated MSCs contained more miR-146a, which were transferred into macrophages to induce M2 polarization and thus inhibit inflammation (Song et al., 2017).

3.3 Targeted delivery system

It is acknowledged that paracrine factors, like vascular endothelial growth factors (VEGF), transforming growth factors (TGF), interleukin-1 receptor antagonists (IL-1RA), are imperative in mediating biological functions of MSCs, including immunomodulation, and promoting tissue repair (Christodoulou et al., 2018). However, the soluble factors have no ability to target cells and exist only a short time, which hinders the clinical transformation. Transportation through EVs not only protect soluble factors from degradation, but also position them to target cells through the receptor-ligand system on the membranes (Li et al., 2017). Thus, EVs have become a promising candidate for targeted drug delivery. Once used for drug delivery, the requirements on safety, yield and targeting must be met. It can be considered to increase the number of MSCs and stimulate the secretion ability of MSCs to expand the production of EVs. Although MSCs possess strong ability of self-renewal, the unlimited proliferation is unrealistic. It is far from enough to depend on ligand-receptor system for positioning the target cells, as a result, modifying surface markers of EVs has been considered. Certainly, appropriate targeted peptides and approaches should be selected according to the specific target region (Tian et al., 2018). At present, the common modification methods include genetic engineering, covalent modification, and non-covalent modification (Salunkhe et al., 2020). For example, to improve the distribution level of exosomes in brain and weaken the metabolism, targeting effect on glioma have been achieved by binding nerve targeting peptides to the outer membrane of exosomes (Jia et al., 2018). According to recent studies, the distribution of iron oxide nanoparticles (IPON) after intravenous injection can be controlled by external magnetic field. Thus, IPON has been loaded into MSC-EVs, and the modified EVs have been found guided to the target area by the external magnetic field. Moreover, it can also be used to detect the distribution of EVs both qualitatively and quantitatively (Kim et al., 2020).

4 MSC-EVs in tissue repair and regeneration in oral and craniomaxillofacial regions

Different soft and hard tissues co-exist in oral and craniomaxillofacial regions, such as muscle, bone, cartilage, skin and dental pulp tissue. MSC-EVs derived from different types of mesenchymal stem cells can response or react through different biomolecules or signaling pathways in tissue repair and regeneration, which is a new research hotspot in regenerative medicine (Figure 2).

4.1 Muscle

Normal healing process of muscle injuries depends on the differentiation of endogenous stem cells, while excessive disordered growth often leads to scar formation, due to inflammation and other factors (Sharma and Maffulli, 2006). It is the endogenous stem cells which largely determine the self-healing capability, the functional signalling pathways and regulatory molecules vary from tissue to tissue. In young xenopus laevis model, the role of Ca^{2+} signalling pathway and extracellular signal regulated kinase 1/2 (ERK1/2) in regeneration of spinal cord and muscle have been investigated. It has been proved that ERK1/2 was activated in stem cells of the damaged area. In skeletal muscle associated tissues, the activation of ERK1/2 was necessary for an injury-induced increase in intracellular store-dependent Ca^{2+} dynamics, but in spinal cord, injury increases Ca^{2+} influx-dependent Ca^{2+} activity independent of ERK1/2 signalling (Levin and Borodinsky, 2022). It is obvious to see the vital role of stem cells in muscle repair, and the purpose is to regulate the inflammatory environment by stimulating transformation of stem cells. Thus, the infiltration of inflammatory cells is reduced, and extracellular matrix (ECM) is deposited orderly (Sousa-Victor et al., 2022). Additionally, in a muscle injury mouse model, local application of MSC-EVs at the wound site reduced the formation of fibrotic tissue and promoted angiogenesis, and then improved muscle regeneration (Nakamura et al., 2015). Pretreating MSCs with specific conditions may induce the secretion of EVs with specific functions. In the acute myocardial infarction model, MSC cultured under hypoxia for 72 h significantly released EVs which promoted blood flow recovery, reduced the infarct area, and improved cardiac function (Bian et al., 2014). Therefore, stem cells and stem cell secretions are required for muscle regeneration, which stimulating the proliferation and differentiation of the remaining stem cells, reducing the impact of inflammation on the damaged environment.

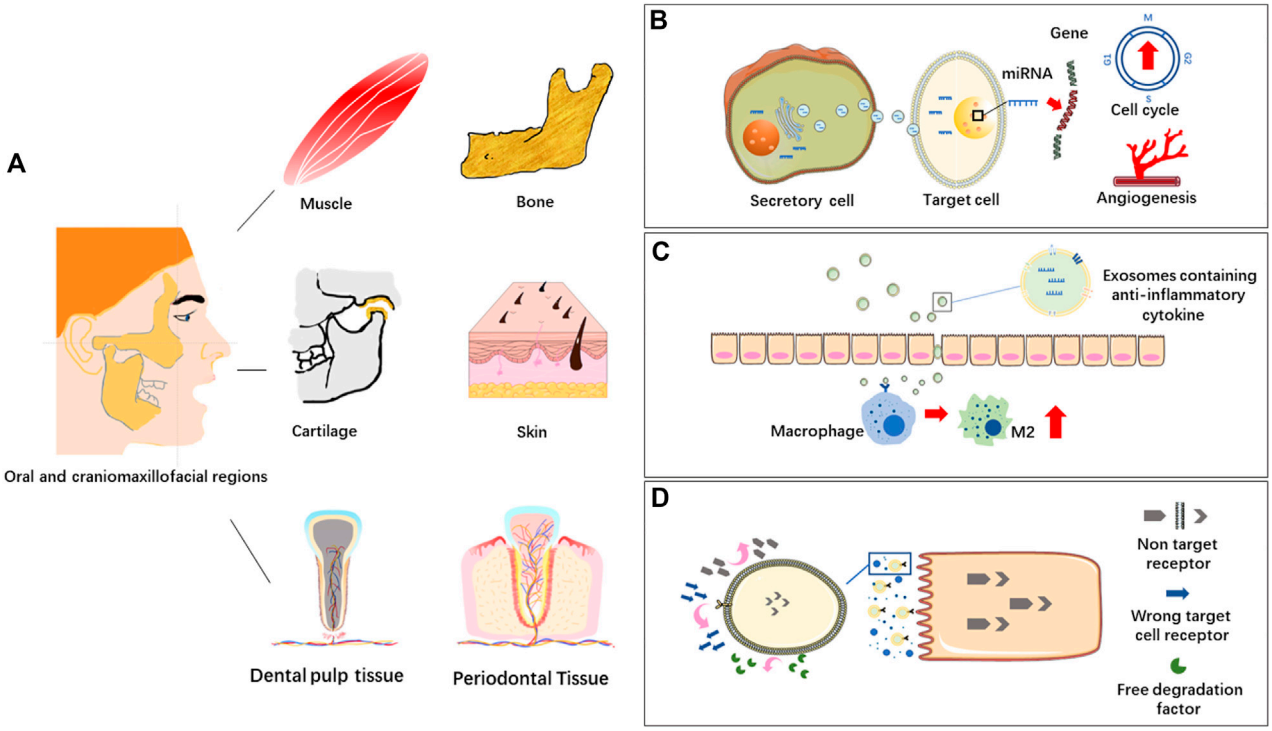

FIGURE 2
(A) Oral and craniomaxillofacial tissues. **(B)** EVs in intercellular communication. Extracellular vesicles (EVs) transport bioactive molecules like miRNAs to regulate gene expression of target cells, affecting cell life activities, such as angiogenesis and cell cycle. **(C)** EVs in immunomodulation. EVs containing immunomodulating factors are transferred into macrophages to induce M2 polarization and thus inhibit inflammation. **(D)** EVs in targeted delivery system. EVs bind to target cells through the receptor-ligand system on the membranes.

4.2 Bone

The bone tissue in craniomaxillofacial region is mostly irregular with rich blood supply, which not only means the strong anti-infection ability, but also indicates more chances of injury-caused severe inflammation. The bone density varies slightly according to the site, and the craniomaxillofacial bone tissue contains more pores, manifesting a high possibility of fracture. Moreover, bone defect induced by tumors and infections severely impact the function and aesthetics of the craniomaxillofacial region, thus the repair and regeneration of craniomaxillofacial bone tissue has always been a complicated clinical problem. The difficulty is that the immune responses and immunological rejection result in the rejection of implanted biomaterials, no matter autogenous bone tissue or biosynthetic materials. Meanwhile, hypoxia, lack of cells and blood vessels in the damaged area led to nonhealing wound and even bone necrosis (Marx, 1983). Hence, angiogenesis is of great importance for bone regeneration. It has been pointed that MSC-EVs activated various signaling pathways in endothelial cells to stimulate sprouting and capillaries formation *via* transferring abundant contents. Besides, MSC-EVs transported Wnt3 protein into endothelial cells to enhance angiogenesis (McBride et al., 2017). Immunomodulation is one of the important functions of EVs, which making differences in solving the inflammation in radiation-induced osteonecrosis (ORN) (Pu et al., 2020). The major goal in immunomodulation is to transform macrophage phenotype from pro-inflammatory M1 to anti-inflammatory M2 by regulating the microenvironment, such as miR-146 and miR-34 (Jiang et al., 2012; Domenis et al., 2018). Wnt/β-catenin signaling pathway is closely involved in macrophage polarization towards M2 phenotype. EVs loaded with activate Wnt/β-catenin signaling pathway and alleviate radiation induced bone loss (Zuo et al., 2019). In addition, EVs transport metallothionein-2, which promote the anti-inflammatory effects of macrophages, and participate in NO mediated osteogenesis (Li et al., 2020). Dental pulp stem cells (DPSCs) also play an important role in the treatment of bone defects, it has been reported that co-culture of DPSCs and ADSCs significantly enhanced the osteogenic ability, compared to culture alone. DPSC-derived EVs promote osteogenic differentiation of ADSCs by enhancing the phosphorylation of ERK1/2 and JNK, and thus activating MAPK signaling pathway. The similar co-culture systems are effective approaches, less expensive than adding specific growth factors (Jin et al.,

2020). Currently, there are various kinds of seed cells, the combining application of which show excellent therapeutic potential. EVs derived from MSCs which pretreated by TNF-α can change the composition of miRNAs, thereby controlling macrophage phenotype to control inflammation balance, create a good environment, and promote osteogenesis process (Kang et al., 2022). Meanwhile, it has been found that MSC-EVs promoted osteoblast proliferation and differentiation through miR-122-5p and MAPK signaling pathway (Zhao et al., 2018).

4.3 Cartilage

Unlike limbs, bone tissue in craniomaxillofacial region is mostly hard bone with limited mobility. It is only TMJ that moves in craniomaxillofacial region, in which functions of articular cartilage play important roles. Articular cartilage is the elastic tissue covered the end of the joint with no blood supply nor nerves. It is surrounded by ECM rich in collagen and proteoglycan, which supports and buffers the joint (Carballo et al., 2017). Therefore, regulation on surrounding environment of articular cartilage is key to its repair and regeneration. Based on the outstanding performance of MSCs in tissue engineering, many studies have shown that MSCs from synovial joint tissue had better cartilage forming ability than that from non-joint tissues (Huang et al., 2017). Moreover, with science and technology advanced, the focus of studies gradually shifted to EV-based therapy (Ruiz et al., 2016). It has been reported that EVs derived from MSCs not only promoted cartilage regeneration, but also downregulated TNF-α mediated COX-2 and pro-inflammatory interleukins, inhibiting collagenase activity. Adding MSC-EVs to chondrocytes isolated from osteoarthritis patients also promoted the secretion of proteoglycan and cartilage regeneration (Vonk et al., 2018). Moreover, these secretions were encapsulated in EVs, and these EVs fused with target cells to release the contents (Yin et al., 2016; Tao et al., 2017a). A recent study showed that activated platelet-rich plasma (PRP) upregulated platelet-derived growth factor AB (PDGF-AB), transforming growth factor-β (TGF-β) and VEGF, which were secreted through EVs. These factors were secreted in PRP-derived EVs (PRP-EVs) to promote cell proliferation (with reduced apoptosis) and cartilaginous matrix secretion *via* suppressing the Wnt/β-catenin signal pathway in interleukin-1β (IL-1β)-stimulated chondrocytes, which were harvested from the terminal of tibia and femur of rabbits (Liu et al., 2019). The study has shown that injection of infrapatellar fat pad derived EVs (IPFP-EVs) inhibited apoptosis, enhanced matrix synthesis, and reduced the production of catabolic cytokines like MMP-13 (Wu et al., 2019). In addition to the bioactive molecules secreted under physiological condition, it is also effective to modify stem cells to obtain desired abilities. Wnt5a and Wnt5b carried by exosomes activate yes associated protein (YAP) through Wnt signaling pathway, which enhances the proliferation and migration of chondrocytes while significantly reduces the secretion of ECM. However, the high expression of miR-140-5p block it through RalA. Therefore, gene modification of EVs avoid the side effects, and enhance the proliferation and migration of articular chondrocytes (Tao et al., 2017b). Thus, modifying cells to acquire specific EVs can be used as a potential treatment, beneficial to tissue repair and regeneration in cartilage.

4.4 Skin

Skin injuries are common disease caused by trauma and resection of large tumor. However, long healing time often leads to excessive scar formation, which bring burden to patients psychologically and physiologically (Frykberg and Banks, 2015). With further research on MSCs, it has been widely used in cutaneous wound healing, which opened a new situation for tissue engineering and regenerative medicine (Marofi et al., 2019). It has been found that MSCs transported hepatocyte growth factor (HGF) through EVs and promoted the proliferation of a variety of cells (Yang et al., 2021). HGF stimulates the activation of MMP-2 and MMP-9, participating in angiogenesis, cell migration and fiber remodeling, and supporting cutaneous wound healing with reduced scar formation (Yoshida et al., 2004). It has been found that EVs secreted by induced pluripotent stem cells (iPSCs) derived MSCs (iMSCs) activated ERK-1/2 signal pathway and promoted the growth of human keratinocytes and human dermal fibroblasts. Moreover, epidermal growth factor (EGF) and epidermal growth factor receptor (EGFR) are very important for the stability of the environment in the epidermis and hair follicles. Therefore, it can be inferred that EVs may induce ERK1/2 by activating EGFR-Ras-Raf signaling pathway, to stimulate skin growth (Okamoto, 2010; Kim et al., 2018). In recent years, the important role of EVs in wound healing has become more and more obvious. Exosomes derived from MSCs stimulated re-epithelialization, increased expression of cytokeratin 19 (CK19), promoted synthesis of type I collagen and improved cutaneous regeneration. In the rat burn model, EVs induced Akt signaling pathway and reduced apoptosis caused by heat stress (Zhang et al., 2015). Umbilical cord mesenchymal stem cells (UCMSC) derived EVs promoted transformation of dermal fibroblasts into myofibroblasts through TGF-β1/Smad2/3 signaling pathway and improved the cutaneous wound healing by promoting epithelialization and angiogenesis (Hu et al., 2020; Zhao et al., 2020). Even in systemic sclerosis (SSC), a rare disease characterized by the development of skin fibrosis, MSC-EVs slow down the disease process and make differences (Rozier et al., 2021). In general, EVs are widely used in cutaneous wound healing and the beneficial effects have been showed both in preclinical and clinical research.

4.5 Dental pulp tissue

Dental pulp is neurovascular tissue surrounded by hard tissues, which is prone to inflammation. The common risk factors are caries, trauma, and retrograde infection of periodontitis, which lead to serious infection and necrosis on dental pulp and periapical tissues (Mu et al., 2020). To cure diseases in dental pulp tissue, drug therapy and root canal therapy are used as common treatments. However, after the pulp is damaged or extracted, the teeth cannot get nutrition, increasing the fragility and decreasing the resistance of hard tissues, resulting in elevated risk of fracture. Therefore, it is of great significance to protect and restore dental pulp tissue. The researchers attempted to regenerate dental pulp tissue by introducing blood into the root canal from the tissue around the root tip, promoting tissue growth with instruments (Ostby, 1961; Nygaard-Ostby and Hjortdal, 1971). The potential of DPSC-derived EVs in inducing odontogenic differentiation has been explored. It has been found that the combination of exosomes and matrix proteins leaded to the adhesion of biomaterials and endocytosis of DPSCs, to triggering p38/MAPK signaling pathway and promote odontogenic differentiation and tissue regeneration (Huang et al., 2016). DPSC-derived EVs isolated from both normal conditions and odontogenic conditions have been detected to confirm the miRNA sequences. The results showed that EVs isolated from odontogenic conditioned medium up-regulated DSP, dmp-1, ALP, and Runx2 proteins to induce odontogenic differentiation of DPSCs. At the same time, miRNAs in exosomes down-regulated recessive TGF-β binding protein 1 (LTBP1), promoting odontogenic differentiation mediated by TGF-β1/Smad signaling pathway (Hu et al., 2019). Moreover, deciduous autologous tooth stem cells have been implanted into necrotic immature permanent anterior teeth to produce pulp dentin complex, including functional dental pulp tissue regeneration with vasculature, innervation, and the lining odontoblast layer. Furthermore, the regenerated pulp tissues functionally promoted root elongation and apical hole closure. Thus, the physiological function of regenerated dental pulp has been proved, which is of great significance in promoting the development of immature permanent teeth (Xuan et al., 2018). Subsequently, mechanisms under-lying the bioengineering teeth constructed by polymer combined with acellular dental matrix in whole tooth regeneration have been explored. Increased EVs produced by the co-culture of human exfoliated deciduous teeth (SHED) aggregate and acellular dental matrix were found, indicating that the microenvironment provided by acellular dental matrix promoted the odontogenic differentiation. It is an important step in the treatment to accomplish teeth regeneration after complete dislocation (Guo et al., 2021). Therefore, regeneration of dental pulp tissue is continually moving forward.

4.6 Periodontal tissue

Teeth are surrounded by periodontal tissue, which participates in supporting and stabilizing the teeth. Once the periodontal tissue is destroyed, alveolar bone resorption and loss of periodontal attachment will happen. Periodontitis is a kind of infectious disease with microorganism as the main pathogenic factor. Prevention is most important for treating periodontitis, accompanied with treatment for infection. If periodontitis develops to the late stage, it should be treated with certain regenerative therapy (Zijnge et al., 2012). Periodontal ligament stem cells (PDLSC) derived EVs contain miR-155-5p, which regulates the balance between Th17 and Tregs by targeting sirtuin-1 in periodontitis (Zheng et al., 2019). The phenotypic transformation of macrophages also plays an important role in the regulation of local immune environment. Bacteria activate macrophages to release pro-inflammatory factors, such as IL-1β and TNF-α, inducing inflammatory cells infiltration, destroying soft tissue and leading to alveolar bone resorption (Spiller and Koh, 2017). Destruction of alveolar bone by T cells and neutrophils is stimulated, which leads to the differentiation of osteoclasts in periodontal cells and the gradual loss of alveolar bone by increasing the local expression of Receptor Activator of Nuclear Factor-κ B Ligand (RANKL) (Darveau, 2010; Hienz et al., 2015). Interestingly, periodontitis compromised dental pulp stem cells secrete EVs carrying miR-378 to promote local angiogenesis to activate the Hedgehog/Gli1 signaling pathway (Zhou et al., 2021). Therefore, the stem cells in the damaged area have certain application ability. It has been reported that EVs derived from SHED were injected into the bone defective area in periodontitis model. The results revealed that EVs had therapeutic effects on bone defects to the same extent as the parental stem cells, and specifically promoted the osteogenesis and inhibited adipogenesis (Wei et al., 2020). Meanwhile, human MSC-EVs loaded on collagen sponge was applied in rat models of alveolar bone defect, and the regeneration of alveolar bone and functional periodontal ligament fibers were observed. Further study proved that MSC-EVs promoted the proliferation and migration of periodontal ligament cells and realized the regeneration of defective periodontal tissue by activating Akt/ERK signaling pathways (Chew et al., 2019). In conclusion, MSCs and MSC-EVs are widely used in tissue repair and regeneration in periodontitis (Table 2).

5 Conclusions and future perspectives

The application and mechanism of EVs are one of the hot spots of current research. Because EVs can be produced by

TABLE 2 Effects of MSC-EVs in various tissue repair and regeneration relevant to oral and craniomaxillofacial regions.

	Stem cell type of MSC-EVs	Type of EVs	Target tissue	Biomolecules/ Signaling pathways	Mechanism of treatment effect	References
1	MSC	EVs	Muscle	Ca^{2+}, ERK 1/2	ERK1/2 in muscle tissue is necessary for calcium signaling, but not in the spinal cord	Levin and Borodinsky, (2022)
2	ADSC	EVs	Skin	ADSC-EVs, MMP-9	ADSC-EVs inhibit downregulating MMP-9 and improve collagen deposition	Wang et al. (2022)
3	ADSC	Exos	Nerve	ADSC-Exos	Enhance the expression and differentiation of PC12 cells into neurons	Shariati Najafabadi et al. (2021)
4	BMMSC	Exos	Vessel	Wnt3a	BMMSC-Exos transport Wnt3a exteriorly and enhance dermal fibroblast proliferation, migration, and angiogenesis *in vitro*	McBride et al. (2017)
5	BMMSC	Exos	Bone	Wnt/β-catenin signaling pathway, Exos	BMMSC-Exo loaded with Wnt can activate Wnt/β-Catenin signal transduction and alleviate bone loss caused by radiation	Zuo et al. (2019)
6	BMMSC	EVs	Bone	Cordycepin	Cordycepin promotes osteogenesis of BMMSCs and accelerates fracture healing *via* hypoxia	Li et al. (2020)
7	DPSC ADSC	EVs	Bone	ERK1/2, JNK, MAPK signaling pathway	When DPSC is co cultured with ADSC, the osteogenic ability is significantly enhanced. DPSC-EV can promote the osteogenic differentiation of ADSC through MAPK pathway by enhancing the phosphorylation of ERK1/2 and JNK	Jin et al. (2020)
8	MSC	Exos	Bone	miRNA	MSC-EVs pretreated with TNF-α can change miRNA composition, thereby controlling macrophage phenotype to control inflammatory balance and promote osteogenesis	Kang et al. (2022)
9	MSC	Exos	Bone	MAPK signaling pathway	MSC-Exo could promote the proliferation of hFOB 1.19 through MAPK signaling pathway, thus alleviating the progression of osteoporosis	Zhao et al. (2018)
10	BMMSC	EVs	Cartilage	TNF-α, COX-2, collagenase	BMMSC-EV can down regulate TNF-α mediated COX-2 and pro-inflammatory interleukin levels inhibit collagenase activity and promote cartilage regeneration	Vonk et al. (2018)
11	MSC	Exos	Cartilage	Akt/Bad/Bcl-2 signaling pathway	PRP-Exos have the capability to prevent GC-induced apoptosis in a rat model of ONFH by promoting Bcl-2 expression *via* the Akt/Bad/Bcl-2 signal pathway under ER stress	Tao et al. (2017a)
12	hUCMSC	Exos	Skin	Wnt4	hUCMSC-Exo contributes to skin wound healing by transmitting Wnt4	Zhang et al. (2015)
13	hUCMSC	Exos	Skin	TGF-β1/Smad 2/3 signaling pathway	hUCMSC-Exo suppress dermal fbroblasts-myofbroblats transition *via* inhibiting the TGF-β1/Smad 2/3 signaling pathway	Hu et al. (2020)
14	MSC	EVs	Skin	miR-29a-3p	MSC-EVs alleviate systemic sclerosis *via* miR-29a-3p	Rozier et al. (2021)
15	DPSC	Exos	Tooth	miRNAs, TGF-β1/smads signaling pathway	Lineage specific exosomes can transfer miRNA in TGFbeta1/ smads signaling pathway to induce odontogenic differentiation of human dental pulp stem cells	Hu et al. (2019)
16	PDLSC	Exos	Periodontal	miRNA-155-5p, Th17 Treg	In chronic periodontitis, exosomal microRNA-155-5p in PDLSCs can be used to regulate sirtuin-1 to achieve Th17/Treg balance	Zheng et al. (2019)
17	DPSC	EVs	Periodontal	miRNA-378a, Hedgehog/ Gli1 signaling pathway	Periodontitis-compromised DPSCs secrete EVs carrying miRNA-378a promote local angiogenesis by targeting Sufu to activate the Hedgehog/Gli1 signaling	Zhou et al. (2021)
18	SHED BMMSC	Exos	Periodontal	Runx2, p-Smad5	SHED-Exo directly promoted BMMSC osteogenesis, differentiation and bone formation	Wei et al. (2020)
19	BMMSC	Exos	Periodontal	Akt/ERK signaling pathway	MSC exosomes can increase PDL cell migration and proliferation through CD73 mediated adenosine receptor activation of survival promoting Akt and ERK signaling	Chew et al. (2019)

Note: Biomolecules/Signaling pathways refers to the biomolecules or signaling pathways through which MSC-EVs, work out in target tissue.

almost all types of MSCs, MSC-EVs take part in different intercellular communication in different tissues. Based on the immunoregulatory function and regenerative ability, MSC-EVs are widely used as a specific biological macromolecule in the paracrine signalling pathway (Kordelas et al., 2019). Using MSC-EVs not only avoids the difficulty of obtaining and culturing MSCs, but also can quantitatively and qualitatively modify the desired substances to act on directly. The advantages of MSC-

EVs therapy are: (a) The source of MSC-EVs is plentiful and the collection method is relatively simple (Ragni et al., 2020), (b) MSC-EVs have good biocompatibility and stability (Papait et al., 2022), (c) The molecular structure of MSC-EVs is small and can pass through the blood-brain barrier (Ophelders et al., 2016), (d) MSC-EVs can avoid some risks associated to MSC-based therapy like venous thrombosis. Therefore, cell-free therapy based on MSC-EVs is quietly emerging.

Oral and craniomaxillofacial regions contain various tissues, such as muscle, bone and cartilage, which are targets for extensive infections and pathological conditions. Complex composition and complicated environment in oral and craniomaxillofacial regions bring out some situations which cannot be cured by drugs and surgeries, for instance, large bone defects and skin injuries. Current therapeutic strategies, such as bone regenerative growth factors and allografts, have inevitable limitations such as lower osteogenic capacity, immunological rejection, and morbidity at the donor site, when tissue repair and regeneration are needed (Dimitriou et al., 2011). Owing to this increasing demand, there is a rapid development in regenerative medicine mediated by MSC-EVs, satisfying the needs of remedies like bone reconstruction in areas of large defects (Lakshmi et al., 2020).

As illustrated above, MSC-EVs can be produced by different types of MSCs, which helps to fulfill complicated tissue repair needs in oral and craniomaxillofacial regions, such as muscle, bone, cartilage, skin, dental pulp tissue and periodontal tissue. Plentiful treatments are developed with participation of MSC-EVs due to their low immunogenicity and multidirectional function. However, until nowadays, the application of EVs is not unlimited. There is no consensus met on measurement standards and industry regulations for the concentration and dose of specific treatment by using EVs (Théry et al., 2018). Meanwhile, the specific working mechanism of different EVs is not clear. Moreover, the safety of the modified EVs cannot be fully guaranteed. With the rapid development of science and technology, it is believed that through continuous exploration, application of MSC-EVs in tissue repair and regenerative medicine will embrace a brighter future, not only in the field of oral and craniomaxillofacial regions.

Author contributions

ML, XL, YS, SL, YC, and AL collected the references and wrote the manuscript. JG, KX and XQ revised the manuscript. All authors read and approved the final manuscript as submitted.

Funding

This work is supported by the National Natural Science Foundation of China (32101096 to XQ, 32100953 to YS and 82100992 to AL), the Youth Talent Training Project for School of Stomatology in Fourth Military Medical University (2020QNYC01 to XQ), the Shaanxi Provincial Key Research and Development Plan Project (2021SF-051 to KX and 2021SF-263 to JG).

Conflict of interest

The authors declare that the research was conducted in the absence of any commercial or financial relationships that could be construed as a potential conflict of interest.

Acknowledgments

We thanked for the valuable suggestions provided by Professor YJ of Fourth Military Medical University.

Publisher's note

All claims expressed in this article are solely those of the authors and do not necessarily represent those of their affiliated organizations, or those of the publisher, the editors and the reviewers. Any product that may be evaluated in this article, or claim that may be made by its manufacturer, is not guaranteed or endorsed by the publisher.

References

Agrahari, V., Agrahari, V., Burnouf, P.-A., Chew, C. H., and Burnouf, T. (2019). Extracellular microvesicles as new industrial therapeutic frontiers. *Trends Biotechnol.* 37 (7), 707–729. doi:10.1016/j.tibtech.2018.11.012

Akers, J. C., Gonda, D., Kim, R., Carter, B. S., and Chen, C. C. (2013). Biogenesis of extracellular vesicles (EV): Exosomes, microvesicles, retrovirus-like vesicles, and apoptotic bodies. *J. Neurooncol.* 113 (1), 1–11. doi:10.1007/s11060-013-1084-8

Almeria, C., Weiss, R., Roy, M., Tripisciano, C., Kasper, C., Weber, V., et al. (2019). Hypoxia conditioned mesenchymal stem cell-derived extracellular vesicles induce increased vascular tube formation *in vitro*. *Front. Bioeng. Biotechnol.* 7, 292. doi:10.3389/fbioe.2019.00292

Ananthakrishnan, A. N., Kaplan, G. G., and Ng, S. C. (2020). Changing global epidemiology of inflammatory bowel diseases: Sustaining health care delivery into the 21st century. *Clin. Gastroenterology Hepatology* 18 (6), 1252–1260. doi:10.1016/j.cgh.2020.01.028

Atkin-Smith, G. K., Tixeira, R., Paone, S., Mathivanan, S., Collins, C., Liem, M., et al. (2015). A novel mechanism of generating extracellular vesicles during apoptosis via a beads-on-a-string membrane structure. *Nat. Commun.* 6, 7439. doi:10.1038/ncomms8439

Bian, S., Zhang, L., Duan, L., Wang, X., Min, Y., and Yu, H. (2014). Extracellular vesicles derived from human bone marrow mesenchymal stem cells promote angiogenesis in a rat myocardial infarction model. *J. Mol. Med.* 92 (4), 387–397. doi:10.1007/s00109-013-1110-5

Blanchard, N., Lankar, D., Faure, F., Regnault, A., Dumont, C., Raposo, G., et al. (2002). TCR activation of human T cells induces the production of exosomes bearing the TCR/CD3/ζ complex. *J. Immunol.* 168 (7), 3235–3241. doi:10.4049/jimmunol.168.7.3235

Boada-Romero, E., Martinez, J., Heckmann, B. L., and Green, D. R. (2020). The clearance of dead cells by efferocytosis. *Nat. Rev. Mol. Cell Biol.* 21 (7), 398–414. doi:10.1038/s41580-020-0232-1

Carballo, C. B., Nakagawa, Y., Sekiya, I., and Rodeo, S. A. (2017). Basic science of articular cartilage. *Clin. Sports Med.* 36 (3), 413–425. doi:10.1016/j.csm.2017.02.001

Castegna, A., Gissi, R., Menga, A., Montopoli, M., Favia, M., Viola, A., et al. (2020). Pharmacological targets of metabolism in disease: Opportunities from macrophages. *Pharmacol. Ther.* 210, 107521. doi:10.1016/j.pharmthera.2020.107521

Chen, C., Skog, J., Hsu, C.-H., Lessard, R. T., Balaj, L., Wurdinger, T., et al. (2010). Microfluidic isolation and transcriptome analysis of serum microvesicles. *Lab. Chip* 10 (4), 505–511. doi:10.1039/b916199f

Chen, Y. S., Lin, E. Y., Chiou, T. W., and Harn, H. J. (2020). Exosomes in clinical trial and their production in compliance with good manufacturing practice. *Tzu Chi Med. J.* 32 (2), 113–120. doi:10.4103/tcmj.tcmj_182_19

Chew, J. R. J., Chuah, S. J., Teo, K. Y. W., Zhang, S., Lai, R. C., Fu, J. H., et al. (2019). Mesenchymal stem cell exosomes enhance periodontal ligament cell functions and promote periodontal regeneration. *Acta Biomater.* 89, 252–264. doi:10.1016/j.actbio.2019.03.021

Christodoulou, I., Goulielmaki, M., Devetzi, M., Panagiotidis, M., Koliakos, G., and Zoumpourlis, V. (2018). Mesenchymal stem cells in preclinical cancer cytotherapy: A systematic review. *Stem Cell Res. Ther.* 9 (1), 336. doi:10.1186/s13287-018-1078-8

Clayton, A., Court, J., Navabi, H., Adams, M., Mason, M., Hobot, J., et al. (2001). Analysis of antigen presenting cell derived exosomes, based on immuno-magnetic isolation and flow cytometry. *J. Immunol. Methods* 247, 163–174. doi:10.1016/s0022-1759(00)00321-5

Costa, L. A., Eiro, N., Fraile, M., Gonzalez, L. O., Saá, J., Garcia-Portabella, P., et al. (2021). Functional heterogeneity of mesenchymal stem cells from natural niches to culture conditions: Implications for further clinical uses. *Cell. Mol. Life Sci.* 78 (2), 447–467. doi:10.1007/s00018-020-03600-0

Crescitelli, R., Lässer, C., and Lötvall, J. (2021). Isolation and characterization of extracellular vesicle subpopulations from tissues. *Nat. Protoc.* 16 (3), 1548–1580. doi:10.1038/s41596-020-00466-1

Darveau, R. P. (2010). Periodontitis: A polymicrobial disruption of host homeostasis. *Nat. Rev. Microbiol.* 8 (7), 481–490. doi:10.1038/nrmicro2337

Desrochers, L. M., Bordeleau, F., Reinhart-King, C. A., Cerione, R. A., and Antonyak, M. A. (2016). Microvesicles provide a mechanism for intercellular communication by embryonic stem cells during embryo implantation. *Nat. Commun.* 7, 11958. doi:10.1038/ncomms11958

Dimitriou, R., Jones, E., McGonagle, D., and Giannoudis, P. V. (2011). Bone regeneration: Current concepts and future directions. *BMC Med.* 9, 66. doi:10.1186/1741-7015-9-66

Ding, Q., Cui, J., Shen, H., He, C., Wang, X., Shen, S. G. F., et al. (2020). Advances of nanomaterial applications in oral and maxillofacial tissue regeneration and disease treatment. *Wiley Interdiscip. Rev. Nanomed. Nanobiotechnol.* 13, e1669. doi:10.1002/wnan.1669

Domenis, R., Cifù, A., Quaglia, S., Pistis, C., Moretti, M., Vicario, A., et al. (2018). Pro inflammatory stimuli enhance the immunosuppressive functions of adipose mesenchymal stem cells-derived exosomes. *Sci. Rep.* 8 (1), 13325. doi:10.1038/s41598-018-31707-9

Doyle, L. M., and Wang, M. Z. (2019). Overview of extracellular vesicles, their origin, composition, purpose, and methods for exosome isolation and analysis. *Cells* 8 (7), 727. doi:10.3390/cells8070727

Ferreira, J. R., Teixeira, G. Q., Santos, S. G., Barbosa, M. A., Almeida-Porada, G., and Gonçalves, R. M. (2018). Mesenchymal stromal cell secretome: Influencing therapeutic potential by cellular pre-conditioning. *Front. Immunol.* 9, 2837. doi:10.3389/fimmu.2018.02837

Frykberg, R. G., and Banks, J. (2015). Challenges in the treatment of chronic wounds. *Adv. Wound Care (New. Rochelle.* 4 (9), 560–582. doi:10.1089/wound.2015.0635

Furlani, D., Ugurlucan, M., Ong, L., Bieback, K., Pittermann, E., Westien, I., et al. (2009). Is the intravascular administration of mesenchymal stem cells safe? Mesenchymal stem cells and intravital microscopy. *Microvasc. Res.* 77 (3), 370–376. doi:10.1016/j.mvr.2009.02.001

Gaihre, B., Uswatta, S., and Jayasuriya, A. C. (2017). Reconstruction of craniomaxillofacial bone defects using tissue-engineering strategies with injectable and non-injectable scaffolds. *J. Funct. Biomater.* 8 (4), 49. doi:10.3390/jfb8040049

Gnecchi, M., He, H., Liang, O., Melo, L., Morello, F., Mu, H., et al. (2005). Paracrine action accounts for marked protection of ischemic heart by Akt-modified mesenchymal stem cells. *Nat. Med.* 11 (4), 367–368. doi:10.1038/nm0405-367

Gonzalez-Pujana, A., Igartua, M., Santos-Vizcaino, E., and Hernandez, R. M. (2020). Mesenchymal stromal cell based therapies for the treatment of immune disorders: Recent milestones and future challenges. *Expert Opin. Drug Deliv.* 17 (2), 189–200. doi:10.1080/17425247.2020.1714587

Guo, H., Li, B., Wu, M., Zhao, W., He, X., Sui, B., et al. (2021). Odontogenesis-related developmental microenvironment facilitates deciduous dental pulp stem cell aggregates to revitalize an avulsed tooth. *Biomaterials* 279, 121223. doi:10.1016/j.biomaterials.2021.121223

György, B., Módos, K., Pállinger, E., Pálóczi, K., Pásztói, M., Misják, P., et al. (2011). Detection and isolation of cell-derived microparticles are compromised by protein complexes resulting from shared biophysical parameters. , 117(4), e39-e48. doi:10.1182/blood-2010-09-307595

Hienz, S. A., Paliwal, S., and Ivanovski, S. (2015). Mechanisms of bone resorption in periodontitis. *J. Immunol. Res.* 2015, 1–10. doi:10.1155/2015/615486

Hoogduijn, M. J., and Lombardo, E. (2019). Mesenchymal stromal cells anno 2019: Dawn of the therapeutic era? Concise review. *Stem Cells Transl. Med.* 8 (11), 1126–1134. doi:10.1002/sctm.19-0073

Hoshino, A., Costa-Silva, B., Shen, T.-L., Rodrigues, G., Hashimoto, A., Tesic Mark, M., et al. (2015). Tumour exosome integrins determine organotropic metastasis. *Nature* 527 (7578), 329–335. doi:10.1038/nature15756

Hu, J., Chen, Y., Huang, Y., and Su, Y. (2020). Human umbilical cord mesenchymal stem cell-derived exosomes suppress dermal fibroblasts-myofibroblats transition via inhibiting the TGF-β1/Smad 2/3 signaling pathway. *Exp. Mol. Pathology* 115, 104468. doi:10.1016/j.yexmp.2020.104468

Hu, S., Park, J., Liu, A., Lee, J., Zhang, X., Hao, Q., et al. (2018). Mesenchymal stem cell microvesicles restore protein permeability across primary cultures of injured human lung microvascular endothelial cells. *Stem Cells Transl. Med.* 7 (8), 615–624. doi:10.1002/sctm.17-0278

Hu, X., Zhong, Y., Kong, Y., Chen, Y., Feng, J., and Zheng, J. (2019). Lineage-specific exosomes promote the odontogenic differentiation of human dental pulp stem cells (DPSCs) through TGFβ1/smads signaling pathway via transfer of microRNAs. *Stem Cell Res. Ther.* 10 (1), 170. doi:10.1186/s13287-019-1278-x

Huang, C.-C., Narayanan, R., Alapati, S., and Ravindran, S. (2016). Exosomes as biomimetic tools for stem cell differentiation: Applications in dental pulp tissue regeneration. *Biomaterials* 111, 103–115. doi:10.1016/j.biomaterials.2016.09.029

Huang, Y.-Z., Xie, H.-Q., Silini, A., Parolini, O., Zhang, Y., Deng, L., et al. (2017). Mesenchymal stem/progenitor cells derived from articular cartilage, synovial membrane and synovial fluid for cartilage regeneration: Current status and future perspectives. *Stem Cell Rev. Rep.* 13 (5), 575–586. doi:10.1007/s12015-017-9753-1

Jansen, F. H., Krijgsveld, J., van Rijswijk, A., van den Bemd, G.-J., van den Berg, M. S., van Weerden, W. M., et al. (2009). Exosomal secretion of cytoplasmic prostate cancer xenograft-derived proteins. *Mol. Cell. Proteomics* 8 (6), 1192–1205. doi:10.1074/mcp.M800443-MCP200

Jia, G., Han, Y., An, Y., Ding, Y., He, C., Wang, X., et al. (2018). NRP-1 targeted and cargo-loaded exosomes facilitate simultaneous imaging and therapy of glioma *in vitro* and *in vivo*. *Biomaterials* 178, 302–316. doi:10.1016/j.biomaterials.2018.06.029

Jiang, P., Liu, R., Zheng, Y., Liu, X., Chang, L., Xiong, S., et al. (2012). MiR-34a inhibits lipopolysaccharide-induced inflammatory response through targeting Notch1 in murine macrophages. *Exp. Cell Res.* 318 (10), 1175–1184. doi:10.1016/j.yexcr.2012.03.018

Jin, Q., Li, P., Yuan, K., Zhao, F., Zhu, X., Zhang, P., et al. (2020). Extracellular vesicles derived from human dental pulp stem cells promote osteogenesis of adipose-derived stem cells via the MAPK pathway. *J. Tissue Eng.* 11, 204173142097556. doi:10.1177/2041731420975569

Johnstone, R. M., Adam, M., Hammond, J. R., Orr, L., and Turbide, C. (1987). Vesicle formation during reticulocyte maturation. Association of plasma membrane activities with released vesicles (exosomes). *J. Biol. Chem.* 262 (19), 9412–9420. doi:10.1016/s0021-9258(18)48095-7

Kang, M., Huang, C.-C., Gajendrareddy, P., Lu, Y., Shirazi, S., Ravindran, S., et al. (2022). Extracellular vesicles from TNFα preconditioned MSCs: Effects on immunomodulation and bone regeneration. *Front. Immunol.* 13, 878194. doi:10.3389/fimmu.2022.878194

Keshtkar, S., Azarpira, N., and Ghahremani, M. H. (2018). Mesenchymal stem cell-derived extracellular vesicles: Novel frontiers in regenerative medicine. *Stem Cell Res. Ther.* 9 (1), 63. doi:10.1186/s13287-018-0791-7

Kim, H. Y., Kim, T. J., Kang, L., Kim, Y.-J., Kang, M. K., Kim, J., et al. (2020). Mesenchymal stem cell-derived magnetic extracellular nanovesicles for targeting and treatment of ischemic stroke. *Biomaterials* 243, 119942. doi:10.1016/j.biomaterials.2020.119942

Kim, S., Lee, S. K., Kim, H., and Kim, T. M. (2018). Exosomes secreted from induced pluripotent stem cell-derived mesenchymal stem cells accelerate skin cell proliferation. *Int. J. Mol. Sci.* 19 (10), 3119. doi:10.3390/ijms19103119

Kordelas, L., Schwich, E., Dittrich, R., Horn, P. A., Beelen, D. W., Börger, V., et al. (2019). Individual immune-modulatory capabilities of MSC-derived extracellular vesicle (EV) preparations and recipient-dependent responsiveness. *Int. J. Mol. Sci.* 20 (7), 1642. doi:10.3390/ijms20071642

Kosaka, N., Iguchi, H., Yoshioka, Y., Takeshita, F., Matsuki, Y., and Ochiya, T. (2010). Secretory mechanisms and intercellular transfer of microRNAs in living cells. *J. Biol. Chem.* 285 (23), 17442–17452. doi:10.1074/jbc.M110.107821

Kunter, U., Rong, S., Boor, P., Eitner, F., Muller-Newen, G., Djuric, Z., et al. (2007). Mesenchymal stem cells prevent progressive experimental renal failure but maldifferentiate into glomerular adipocytes. *J. Am. Soc. Nephrol.* 18 (6), 1754–1764. doi:10.1681/ASN.2007010044

Laberge, A., Arif, S., and Moulin, V. J. (2018). Microvesicles: Intercellular messengers in cutaneous wound healing. *J. Cell. Physiol.* 233 (8), 5550–5563. doi:10.1002/jcp.26426

Lai, R. C., Yeo, R. W., Tan, K. H., and Lim, S. K. (2013). Exosomes for drug delivery - a novel application for the mesenchymal stem cell. *Biotechnol. Adv.* 31 (5), 543–551. doi:10.1016/j.biotechadv.2012.08.008

Lakshmi, J. S. J., Nallusamy, J., Manivasagam, G., Ramalingam, M., Sunil, P. M., and Tom, A. (2020). Exosomes in the oral and maxillofacial region. *J. Pharm. Bioall. Sci.* 12, S43–S48. doi:10.4103/jpbs.JPBS_144_20

Levänen, B., Bhakta, N. R., Torregrosa Paredes, P., Barbeau, R., Hiltbrunner, S., Pollack, J. L., et al. (2013). Altered microRNA profiles in bronchoalveolar lavage fluid exosomes in asthmatic patients. *J. Allergy Clin. Immunol.* 131 (3), 894–903.e8. doi:10.1016/j.jaci.2012.11.039

Levin, J. B., and Borodinsky, L. N. (2022). Injury-induced Erk1/2 signaling tissue-specifically interacts with Ca2+ activity and is necessary for regeneration of spinal cord and skeletal muscle. *Cell Calcium* 102, 102540. doi:10.1016/j.ceca.2022.102540

Li, J., Chen, Y., Guo, X., Zhou, L., Jia, Z., Peng, Z., et al. (2017). GPC1 exosome and its regulatory miRNAs are specific markers for the detection and target therapy of colorectal cancer. *J. Cell. Mol. Med.* 21 (5), 838–847. doi:10.1111/jcmm.12941

Li, Z., Gu, Y., Lin, Z., Ma, H., and Zhang, S. (2020). Cordycepin promotes osteogenesis of bone marrow-derived mesenchymal stem cells and accelerates fracture healing via hypoxia in a rat model of closed femur fracture. *Biomed. Pharmacother.* 125, 109991. doi:10.1016/j.biopha.2020.109991

Liang, Y.-C., Wu, Y.-P., Li, X.-D., Chen, S.-H., Ye, X.-J., Xue, X.-Y., et al. (2019). TNF-α-induced exosomal miR-146a mediates mesenchymal stem cell-dependent suppression of urethral stricture. *J. Cell. Physiol.* 234 (12), 23243–23255. doi:10.1002/jcp.28891

Liu, D., Kou, X., Chen, C., Liu, S., Liu, Y., Yu, W., et al. (2018). Circulating apoptotic bodies maintain mesenchymal stem cell homeostasis and ameliorate osteopenia via transferring multiple cellular factors. *Cell Res.* 28 (9), 918–933. doi:10.1038/s41422-018-0070-2

Liu, H., Liu, S., Qiu, X., Yang, X., Bao, L., Pu, F., et al. (2020). Donor MSCs release apoptotic bodies to improve myocardial infarction via autophagy regulation in recipient cells. *Autophagy* 16 (12), 2140–2155. doi:10.1080/15548627.2020.1717128

Liu, X., Wang, L., Ma, C., Wang, G., Zhang, Y., and Sun, S. (2019). Exosomes derived from platelet-rich plasma present a novel potential in alleviating knee osteoarthritis by promoting proliferation and inhibiting apoptosis of chondrocyte via Wnt/β-catenin signaling pathway. *J. Orthop. Surg. Res.* 14 (1), 470. doi:10.1186/s13018-019-1529-7

Loyer, X., Vion, A.-C., Tedgui, A., and Boulanger, C. M. (2014). Microvesicles as cell-cell messengers in cardiovascular diseases. *Circ. Res.* 114 (2), 345–353. doi:10.1161/CIRCRESAHA.113.300858

Mackie, A. R., Klyachko, E., Thorne, T., Schultz, K. M., Millay, M., Ito, A., et al. (2012). Sonic hedgehog-modified human CD34+ cells preserve cardiac function after acute myocardial infarction. *Circ. Res.* 111 (3), 312–321. doi:10.1161/CIRCRESAHA.112.266015

Marofi, F., Hassanzadeh, A., Solali, S., Vahedi, G., Mousavi Ardehaie, R., Salarinasab, S., et al. (2019). Epigenetic mechanisms are behind the regulation of the key genes associated with the osteoblastic differentiation of the mesenchymal stem cells: The role of zoledronic acid on tuning the epigenetic changes. *J. Cell. Physiol.* 234, 15108–15122. doi:10.1002/jcp.28152

Marx, R. E. (1983). Osteoradionecrosis: A new concept of its pathophysiology. *J. Oral Maxillofac. Surg.* 41 (5), 283–288. doi:10.1016/0278-2391(83)90294-x

McBride, J. D., Rodriguez-Menocal, L., Guzman, W., Candanedo, A., Garcia-Contreras, M., and Badiavas, E. V. (2017). Bone marrow mesenchymal stem cell-derived CD63$^+$ exosomes transport Wnt3a exteriorly and enhance dermal fibroblast proliferation, migration, and angiogenesis *in vitro*. *Stem Cells Dev.* 26 (19), 1384–1398. doi:10.1089/scd.2017.0087

Mu, X., Shi, L., Pan, S., He, L., Niu, Y., and Wang, X. (2020). A customized self-assembling peptide hydrogel-wrapped stem cell factor targeting pulp regeneration rich in vascular-like structures. *ACS Omega* 5 (27), 16568–16574. doi:10.1021/acsomega.0c01266

Naftali-Shani, N., Levin-Kotler, L.-P., Palevski, D., Amit, U., Kain, D., Landa, N., et al. (2017). Left ventricular dysfunction switches mesenchymal stromal cells toward an inflammatory phenotype and impairs their reparative properties via toll-like receptor-4. *Circulation* 135 (23), 2271–2287. doi:10.1161/CIRCULATIONAHA.116.023527

Nakamura, Y., Miyaki, S., Ishitobi, H., Matsuyama, S., Nakasa, T., Kamei, N., et al. (2015). Mesenchymal-stem-cell-derived exosomes accelerate skeletal muscle regeneration. *FEBS Lett.* 589 (11), 1257–1265. doi:10.1016/j.febslet.2015.03.031

Nygaard-Ostby, B., and Hjortdal, O. (1971). Tissue formation in the root canal following pulp removal. *Eur. J. Oral Sci.* 79 (5), 333–349. doi:10.1111/j.1600-0722.1971.tb02019.x

Okamoto, I. (2010). Epidermal growth factor receptor in relation to tumor development: EGFR-targeted anticancer therapy. *FEBS J.* 277 (2), 309–315. doi:10.1111/j.1742-4658.2009.07449.x

Ophelders, D. R. M. G., Wolfs, T. G. A. M., Jellema, R. K., Zwanenburg, A., Andriessen, P., Delhaas, T., et al. (2016). Mesenchymal stromal cell-derived extracellular vesicles protect the fetal brain after hypoxia-ischemia. *Stem Cells Transl. Med.* 5 (6), 754–763. doi:10.5966/sctm.2015-0197

Ostby, B. N. (1961). The role of the blood clot in endodontic therapy. An experimental histologic study. *Acta Odontol. Scand.* 19, 323–353. doi:10.3109/00016356109043395

Panda, B., Sharma, Y., Gupta, S., and Mohanty, S. (2021). Mesenchymal stem cell-derived exosomes as an emerging paradigm for regenerative therapy and nano-medicine: A comprehensive review. *Life (Basel, Switz.* 11 (8), 784. doi:10.3390/life11080784

Pant, S., Hilton, H., and Burczynski, M. E. (2012). The multifaceted exosome: Biogenesis, role in normal and aberrant cellular function, and frontiers for pharmacological and biomarker opportunities. *Biochem. Pharmacol.* 83 (11), 1484–1494. doi:10.1016/j.bcp.2011.12.037

Papait, A., Ragni, E., Cargnoni, A., Vertua, E., Romele, P., Masserdotti, A., et al. (2022). Comparison of EV-free fraction, EVs, and total secretome of amniotic mesenchymal stromal cells for their immunomodulatory potential: A translational perspective. *Front. Immunol.* 13, 960909. doi:10.3389/fimmu.2022.960909

Perry, J. S. A., Morioka, S., Medina, C. B., Iker Etchegaray, J., Barron, B., Raymond, M. H., et al. (2019). Interpreting an apoptotic corpse as anti-inflammatory involves a chloride sensing pathway. *Nat. Cell Biol.* 21 (12), 1532–1543. doi:10.1038/s41556-019-0431-1

Phelps, J., Sanati-Nezhad, A., Ungrin, M., Duncan, N. A., and Sen, A. (2018). Bioprocessing of mesenchymal stem cells and their derivatives: Toward cell-free therapeutics. *Stem Cells Int.* 2018, 1–23. doi:10.1155/2018/9415367

Poon, I. K. H., Chiu, Y.-H., Armstrong, A. J., Kinchen, J. M., Juncadella, I. J., Bayliss, D. A., et al. (2014). Unexpected link between an antibiotic, pannexin channels and apoptosis. *Nature* 507 (7492), 329–334. doi:10.1038/nature13147

Pu, X., Ma, S., Gao, Y., Xu, T., Chang, P., and Dong, L. (2020). Mesenchymal stem cell-derived exosomes: Biological function and their therapeutic potential in radiation damage. *Cells* 10 (1), 42. doi:10.3390/cells10010042

Qing, L., Chen, H., Tang, J., and Jia, X. (2018). Exosomes and their MicroRNA cargo: New players in peripheral nerve regeneration. *Neurorehabil. Neural Repair* 32 (9), 765–776. doi:10.1177/1545968318798955

Ragni, E., Perucca Orfei, C., De Luca, P., Mondadori, C., Viganò, M., Colombini, A., et al. (2020). Inflammatory priming enhances mesenchymal stromal cell secretome potential as a clinical product for regenerative medicine approaches through secreted factors and EV-miRNAs: The example of joint disease. *Stem Cell Res. Ther.* 11 (1), 165. doi:10.1186/s13287-020-01677-9

Rozier, P., Maumus, M., Maria, A. T. J., Toupet, K., Lai-Kee-Him, J., Jorgensen, C., et al. (2021). Mesenchymal stromal cells-derived extracellular vesicles alleviate systemic sclerosis via miR-29a-3p. *J. Autoimmun.* 121, 102660. doi:10.1016/j.jaut.2021.102660

Ruiz, M., Cosenza, S., Maumus, M., Jorgensen, C., and Noël, D. (2016). Therapeutic application of mesenchymal stem cells in osteoarthritis. *Expert Opin. Biol. Ther.* 16 (1), 33–42. doi:10.1517/14712598.2016.1093108

Sahoo, S., Klychko, E., Thorne, T., Misener, S., Schultz, K. M., Millay, M., et al. (2011). Exosomes from human CD34(+) stem cells mediate their proangiogenic

paracrine activity. *Circ. Res.* 109 (7), 724–728. doi:10.1161/CIRCRESAHA.111.253286

Sahoo, S., and Losordo, D. W. (2014). Exosomes and cardiac repair after myocardial infarction. *Circ. Res.* 114 (2), 333–344. doi:10.1161/CIRCRESAHA.114.300639

Salunkhe, S., DheerajBasak, M., Chitkara, D., and Mittal, A. (2020). Surface functionalization of exosomes for target-specific delivery and *in vivo* imaging & tracking: Strategies and significance. *J. Control. Release* 326, 599–614. doi:10.1016/j.jconrel.2020.07.042

Segura, E., Amigorena, S., and Théry, C. (2005). Mature dendritic cells secrete exosomes with strong ability to induce antigen-specific effector immune responses. *Blood Cells Mol. Dis.* 35 (2), 89–93. doi:10.1016/j.bcmd.2005.05.003

Shariati Najafabadi, S., Amirpour, N., Amini, S., Zare, N., Kazemi, M., and Salehi, H. (2021). Human adipose derived stem cell exosomes enhance the neural differentiation of PC12 cells. *Mol. Biol. Rep.* 48 (6), 5033–5043. doi:10.1007/s11033-021-06497-5

Sharma, P., and Maffulli, N. (2006). Biology of tendon injury: Healing, modeling and remodeling. *J. Musculoskelet. Neuronal Interact.* 6 (2), 181–190.

Sigmarsdottir, T., McGarrity, S., Rolfsson, O., Yurkovich, J. T., and Sigurjonsson, O. E. (2020). Current status and future prospects of genome-scale metabolic modeling to optimize the use of mesenchymal stem cells in regenerative medicine. *Front. Bioeng. Biotechnol.* 8, 239. doi:10.3389/fbioe.2020.00239

Skog, J., Würdinger, T., van Rijn, S., Meijer, D. H., Gainche, L., Sena-Esteves, M., et al. (2008). Glioblastoma microvesicles transport RNA and proteins that promote tumour growth and provide diagnostic biomarkers. *Nat. Cell Biol.* 10 (12), 1470–1476. doi:10.1038/ncb1800

Smith, T. D., Nagalla, R. R., Chen, E. Y., and Liu, W. F. (2017). Harnessing macrophage plasticity for tissue regeneration. *Adv. Drug Deliv. Rev.* 114, 193–205. doi:10.1016/j.addr.2017.04.012

Song, Y., Dou, H., Li, X., Zhao, X., Li, Y., Liu, D., et al. (2017). Exosomal miR-146a contributes to the enhanced therapeutic efficacy of interleukin-1β-primed mesenchymal stem cells against sepsis. *Stem Cells Dayt. Ohio)* 35 (5), 1208–1221. doi:10.1002/stem.2564

Sousa-Victor, P., García-Prat, L., and Muñoz-Cánoves, P. (2022). Control of satellite cell function in muscle regeneration and its disruption in ageing. *Nat. Rev. Mol. Cell Biol.* 23 (3), 204–226. doi:10.1038/s41580-021-00421-2

Spiller, K. L., and Koh, T. J. (2017). Macrophage-based therapeutic strategies in regenerative medicine. *Adv. Drug Deliv. Rev.* 122, 74–83. doi:10.1016/j.addr.2017.05.010

Sun, Y., Liu, G., Zhang, K., Cao, Q., Liu, T., and Li, J. (2021). Mesenchymal stem cells-derived exosomes for drug delivery. *Stem Cell Res. Ther.* 12 (1), 561. doi:10.1186/s13287-021-02629-7

Tao, S.-C., Yuan, T., Rui, B.-Y., Zhu, Z.-Z., Guo, S.-C., and Zhang, C.-Q. (2017a). Exosomes derived from human platelet-rich plasma prevent apoptosis induced by glucocorticoid-associated endoplasmic reticulum stress in rat osteonecrosis of the femoral head via the Akt/Bad/Bcl-2 signal pathway. *Theranostics* 7 (3), 733–750. doi:10.7150/thno.17450

Tao, S.-C., Yuan, T., Zhang, Y.-L., Yin, W.-J., Guo, S.-C., and Zhang, C.-Q. (2017b). Exosomes derived from miR-140-5p-overexpressing human synovial mesenchymal stem cells enhance cartilage tissue regeneration and prevent osteoarthritis of the knee in a rat model. *Theranostics* 7 (1), 180–195. doi:10.7150/thno.17133

Théry, C., Amigorena, S., Raposo, G., and Clayton, A. (2006). Isolation and characterization of exosomes from cell culture supernatants and biological fluids. *Curr. Protoc. Cell Biol.* 3, 3.22. doi:10.1002/0471143030.cb0322s30

Théry, C., Witwer, K. W., Aikawa, E., Alcaraz, M. J., Anderson, J. D., Andriantsitohaina, R., et al. (2018). Minimal information for studies of extracellular vesicles 2018 (MISEV2018): A position statement of the international society for extracellular vesicles and update of the MISEV2014 guidelines. *J. Extracell. Vesicles* 7 (1), 1535750. doi:10.1080/20013078.2018.1535750

Tian, T., Zhang, H.-X., He, C.-P., Fan, S., Zhu, Y.-L., Qi, C., et al. (2018). Surface functionalized exosomes as targeted drug delivery vehicles for cerebral ischemia therapy. *Biomaterials* 150, 137–149. doi:10.1016/j.biomaterials.2017.10.012

van Balkom, B. W. M., de Jong, O. G., Smits, M., Brummelman, J., den Ouden, K., de Bree, P. M., et al. (2013). Endothelial cells require miR-214 to secrete exosomes that suppress senescence and induce angiogenesis in human and mouse endothelial cells. *Blood* 121 (19), 3997–4006. doi:10.1182/blood-2013-02-478925

van Niel, G., D'Angelo, G., and Raposo, G. (2018). Shedding light on the cell biology of extracellular vesicles. *Nat. Rev. Mol. Cell Biol.* 19 (4), 213–228. doi:10.1038/nrm.2017.125

Vonk, L. A., van Dooremalen, S. F. J., Liv, N., Klumperman, J., Coffer, P. J., Saris, D. B. F., et al. (2018). Mesenchymal stromal/stem cell-derived extracellular vesicles promote human cartilage regeneration *in vitro*. *Theranostics* 8 (4), 906–920. doi:10.7150/thno.20746

Wang, J.-W., Zhu, Y.-Z., Hu, X., Nie, J.-Y., Wang, Z.-H., Wu, S., et al. (2022). Extracellular vesicles derived from adipose-derived stem cells accelerate diabetic wound healing by suppressing the expression of matrix metalloproteinase-9. *Curr. Pharm. Biotechnol.* 23 (6), 894–901. doi:10.2174/1389201022666210719154009

Warrier, S., Mohana Sundaram, S., Varier, L., and Balasubramanian, A. (2022). Stalling SARS-CoV2 infection with stem cells: Can regenerating perinatal tissue mesenchymal stem cells offer a multi-tiered therapeutic approach to COVID-19? *Placenta* 117, 161–168. doi:10.1016/j.placenta.2021.12.005

Wei, J., Song, Y., Du, Z., Yu, F., Zhang, Y., Jiang, N., et al. (2020). Exosomes derived from human exfoliated deciduous teeth ameliorate adult bone loss in mice through promoting osteogenesis. *J. Mol. Hist.* 51 (4), 455–466. doi:10.1007/s10735-020-09896-3

Witwer, K. W., Buzás, E. I., Bemis, L. T., Bora, A., Lässer, C., Lötvall, J., et al. (2013). Standardization of sample collection, isolation and analysis methods in extracellular vesicle research. *J. Extracell. Vesicles* 2, 20360. doi:10.3402/jev.v2i0.20360

Wolfers, J., Lozier, A., Raposo, G., Regnault, A., Théry, C., Masurier, C., et al. (2001). Tumor-derived exosomes are a source of shared tumor rejection antigens for CTL cross-priming. *Nat. Med.* 7 (3), 297–303. doi:10.1038/85438

Wu, J., Kuang, L., Chen, C., Yang, J., Zeng, W.-N., Li, T., et al. (2019). miR-100-5p-abundant exosomes derived from infrapatellar fat pad MSCs protect articular cartilage and ameliorate gait abnormalities via inhibition of mTOR in osteoarthritis. *Biomaterials* 206, 87–100. doi:10.1016/j.biomaterials.2019.03.022

Wu, P., Zhang, B., Shi, H., Qian, H., and Xu, W. (2018). MSC-exosome: A novel cell-free therapy for cutaneous regeneration. *Cytotherapy* 20 (3), 291–301. doi:10.1016/j.jcyt.2017.11.002

Xie, C., Ji, N., Tang, Z., Li, J., and Chen, Q. (2019). The role of extracellular vesicles from different origin in the microenvironment of head and neck cancers. *Mol. Cancer* 18 (1), 83. doi:10.1186/s12943-019-0985-3

Xuan, K., Li, B., Guo, H., Sun, W., Kou, X., He, X., et al. (2018). Deciduous autologous tooth stem cells regenerate dental pulp after implantation into injured teeth. *Sci. Transl. Med.* 10 (455), eaaf3227. doi:10.1126/scitranslmed.aaf3227

Yamada, T., Inoshima, Y., Matsuda, T., and Ishiguro, N. (2012). Comparison of methods for isolating exosomes from bovine milk. *J. Veterinary Med. Sci.* 74 (11), 1523–1525. doi:10.1292/jvms.12-0032

Yang, Y., Zhao, Y., Zhang, L., Zhang, F., and Li, L. (2021). The application of mesenchymal stem cells in the treatment of liver diseases: Mechanism, efficacy, and safety issues. *Front. Med.* 8, 655268. doi:10.3389/fmed.2021.655268

Yin, B., Ma, Q., Song, C., Zhao, L., Yu, F., Wang, C., et al. (2021). Exosome-derived noncoding RNAs as a promising treatment of bone regeneration. *Stem Cells Int.* 2021, 1–8. doi:10.1155/2021/6696894

Yin, W.-J., Xu, H.-T., Sheng, J.-G., An, Z.-Q., Guo, S.-C., Xie, X.-T., et al. (2016). Advantages of pure platelet-rich plasma compared with leukocyte- and platelet-rich plasma in treating rabbit knee osteoarthritis. *Med. Sci. Monit.* 22, 1280–1290. doi:10.12659/msm.898218

Yoshida, S., Matsumoto, K., Tomioka, D., Bessho, K., Itami, S., Yoshikawa, K., et al. (2004). Recombinant hepatocyte growth factor accelerates cutaneous wound healing in a diabetic mouse model. *Growth Factors (Chur, Switz.* 22 (2), 111–119. doi:10.1080/08977190410001701005

Yu, B., Shao, H., Su, C., Jiang, Y., Chen, X., Bai, L., et al. (2016). Exosomes derived from MSCs ameliorate retinal laser injury partially by inhibition of MCP-1. *Sci. Rep.* 6, 34562. doi:10.1038/srep34562

Zhang, B., Wang, M., Gong, A., Zhang, X., Wu, X., Zhu, Y., et al. (2015). HucMSC-exosome mediated-wnt4 signaling is required for cutaneous wound healing. *Stem Cells Dayt. Ohio)* 33 (7), 2158–2168. doi:10.1002/stem.1771

Zhang, Y., Liu, T., Hu, X., Wang, M., Wang, J., Zou, B., et al. (2021). CellCall: Integrating paired ligand-receptor and transcription factor activities for cell-cell communication. *Nucleic Acids Res.* 49 (15), 8520–8534. doi:10.1093/nar/gkab638

Zhao, G., Liu, F., Liu, Z., Zuo, K., Wang, B., Zhang, Y., et al. (2020). MSC-derived exosomes attenuate cell death through suppressing AIF nucleus translocation and enhance cutaneous wound healing. *Stem Cell Res. Ther.* 11 (1), 174. doi:10.1186/s13287-020-01616-8

Zhao, P., Xiao, L., Peng, J., Qian, Y. Q., and Huang, C. C. (2018). Exosomes derived from bone marrow mesenchymal stem cells improve osteoporosis through promoting osteoblast proliferation via MAPK pathway. *Eur. Rev. Med. Pharmacol. Sci.* 22 (12), 3962–3970. doi:10.26355/eurrev_201806_15280

Zheng, C., Sui, B., Zhang, X., Hu, J., Chen, J., Liu, J., et al. (2021). Apoptotic vesicles restore liver macrophage homeostasis to counteract type 2 diabetes. *J. Extracell. Vesicles* 10 (7), e12109. doi:10.1002/jev2.12109

Zheng, Y., Dong, C., Yang, J., Jin, Y., Zheng, W., Zhou, Q., et al. (2019). Exosomal microRNA-155-5p from PDLSCs regulated Th17/Treg balance by targeting sirtuin-1 in chronic periodontitis. *J. Cell. Physiology* 234 (11), 20662–20674. doi:10.1002/jcp.28671

Zhou, H., Li, X., Wu, R.-X., He, X.-T., An, Y., Xu, X.-Y., et al. (2021). Periodontitis-compromised dental pulp stem cells secrete extracellular vesicles carrying miRNA-378a promote local angiogenesis by targeting Sufu to activate the Hedgehog/Gli1 signalling. *Cell Prolif.* 54 (5), e13026. doi:10.1111/cpr.13026

Zijnge, V., Ammann, T., Thurnheer, T., and Gmür, R. (2012). Subgingival biofilm structure. *Front. Oral Biol.* 15, 1–16. doi:10.1159/000329667

Zuo, R., Liu, M., Wang, Y., Li, J., Wang, W., Wu, J., et al. (2019). BM-MSC-derived exosomes alleviate radiation-induced bone loss by restoring the function of recipient BM-MSCs and activating Wnt/β-catenin signaling. *Stem Cell Res. Ther.* 10 (1), 30. doi:10.1186/s13287-018-1121-9

frontiers | Frontiers in Bioengineering and Biotechnology

TYPE Review
PUBLISHED 12 December 2022
DOI 10.3389/fbioe.2022.1078453

OPEN ACCESS

EDITED BY
Hai Zhang,
University of Washington, United States

REVIEWED BY
Yongxi Liang,
Boston University, United States
Maobin Yang,
Temple University Health System, Inc., United States

*CORRESPONDENCE
Jiyao Li,
jiyaoliscu@163.com
Biao Ren,
renbiao@scu.edu.cn

SPECIALTY SECTION
This article was submitted to Biomaterials, a section of the journal Frontiers in Bioengineering and Biotechnology

RECEIVED 24 October 2022
ACCEPTED 30 November 2022
PUBLISHED 12 December 2022

CITATION
Huang F, Cheng L, Li J and Ren B (2022), Nanofibrous scaffolds for regenerative endodontics treatment.
Front. Bioeng. Biotechnol. 10:1078453.
doi: 10.3389/fbioe.2022.1078453

Nanofibrous scaffolds for regenerative endodontics treatment

Fangting Huang[1,2], Lei Cheng[1,3], Jiyao Li[1,3]* and Biao Ren[1]*

[1]State Key Laboratory of Oral Diseases & National Clinical Research Center for Oral Diseases, Sichuan University, Chengdu, Sichuan, China, [2]Department of Preventive Dentistry, Guanghua School of Stomatology, Sun Yat-sen University, Guangzhou, Guangdong, China, [3]Department of Operative Dentistry and Endodontics, West China School of Stomatology, Sichuan University, Chengdu, Sichuan, China

Untreated dental caries, tooth trauma and dental anatomical variations such as dens invaginatus can result in pulpitis. However, standard root canal therapy cannot treat immature permanent teeth due to an open apical foramen and thin dentinal walls. Thus, regenerative endodontics treatment (RET) following a disinfection step with pulp regeneration has been developed. Pulp connective-tissue, dentin formation, revascularization and reinnervation can occur in this procedure which should be supplemented with intelligent biomaterials to improve repeatability and support well-coordinated regeneration. Furthermore, nanofibrous scaffolds, as one of the most commonly used materials, show promise. The purpose of this article is to highlight the advantages of nanofibrous scaffolds and discuss the future modification and application of them.

KEYWORDS

regenerative endodontics treatment, RET, nanofiber, scaffolds, nanomateials

1 Introduction

Untreated dental caries, tooth trauma, and dental anatomical variations such as dens invaginatus can result in endodontic infections and inflammatory pulpal reactions, a highly prevalent inflammatory condition worldwide (Bletsa et al., 2006; Agnihotry et al., 2016; Estefan et al., 2016). This kind of inflammation can be reversed with appropriate treatment at an early stage (Bjørndal et al., 2014). However, as inflammation progresses, irreversible pulpitis, which manifests as violently acute pain in the tooth, occurs frequently (Lin et al., 2020). If the irreversible pulpits are not treated promptly, it can induce the dental necrosis, apical periodontitis, abscess, and eventual tooth loss (Bjørndal et al., 2019). Current endodontic treatment concepts for fully developed necrotic permanent teeth include removing inflammatory or necrotic pulp tissue and replacing it with biomaterials (Jung et al., 2019). Nowadays, the most popular therapeutic strategy is root canal therapy (RCT), which includes debridement, instrumentation, and obturation of the pulp canal space (Ma et al., 2016; Manfredi et al., 2016). However, the traditional RCT is not recommended for the immature permanent teeth in children due to their thinner dentinal walls and unclosed apical foramen compared to mature permanent teeth

(Mc et al., 2019). The apexogenesis/apexification (Figure 1) is an alternative method to solve this challenge. It entails removing all necrotic pulp tissues and utilizing biomaterials such as mineral trioxide aggregate (MTA) or calcium hydroxide (Ca(OH)2) to create an artificial barrier or stimulate the creation of a mineralized barrier in the root apex after enough debridement (Frank, 1966; Heithersay, 1975; Rafter, 2005). However, apexogenesis does not restore the pulp's vitality and immunocompetence and cannot promote the root maturation (the closure of the apical foramen as mature permanent teeth and/or the thickening of the root canal walls), which may compromise tooth and root wall stability and eventually increase the likelihood of dental secondary trauma, even tooth loss (Andreasen et al., 2002; Kim et al., 2018; Mc et al., 2019). Likewise, apexification cannot ensure the root maturation completely and it need repeated return visits over a long period to determine the final effect for every patient (Rafter, 2005).

Pulp regeneration (Figure 1) is another approach for immature permanent teeth necrosis. A healthy and alive pulp is required for long-term tooth survival and preservation (Schmalz et al., 2020). In 2001, Iwaya et al. (Iwaya et al., 2001) established a novel treatment technique to address a young permanent tooth which was immature and suffered from apical periodontitis and then named it as "revascularization". In 2007, "regenerative endodontics", which is based on a tissue engineering notion, was coined by the American Association of Endodontists, indicating this kind of regeneration included both soft and hard tissues rather than vessels (Murray et al., 2007).

Regenerative endodontics treatment (RET) refers to biologically based procedures to replace damaged tooth tissues with newborn tissues (Schmalz et al., 2020). Following a disinfecting phase, RET induces bleeding by periapical tissue tearing. Blood clot can act as a natural scaffold which provide a platform for stem cells to grow into. Various endodontic studies have shown that RET could improve root maturation and reinforce thin and weak young roots (Kahler and Rossi-Fedele, 2016; Chan et al., 2017). RET also led to comparable survival and success rates compared to apexification (Ribeiro et al., 2020). However, this treatment needs the supplement of innovative biomaterials to improve repeatability and encourage a well-orchestrated regeneration (Keller et al., 2015).

RET includes three crucial parts in regeneration engineering: stem cells, bioactive molecules, and scaffolds. Stem cells can serve as a source to differentiate into different cells and form new regeneration-related tissues. Bioactive molecules can promote the cell migration, growth. The scaffold is considered an essential

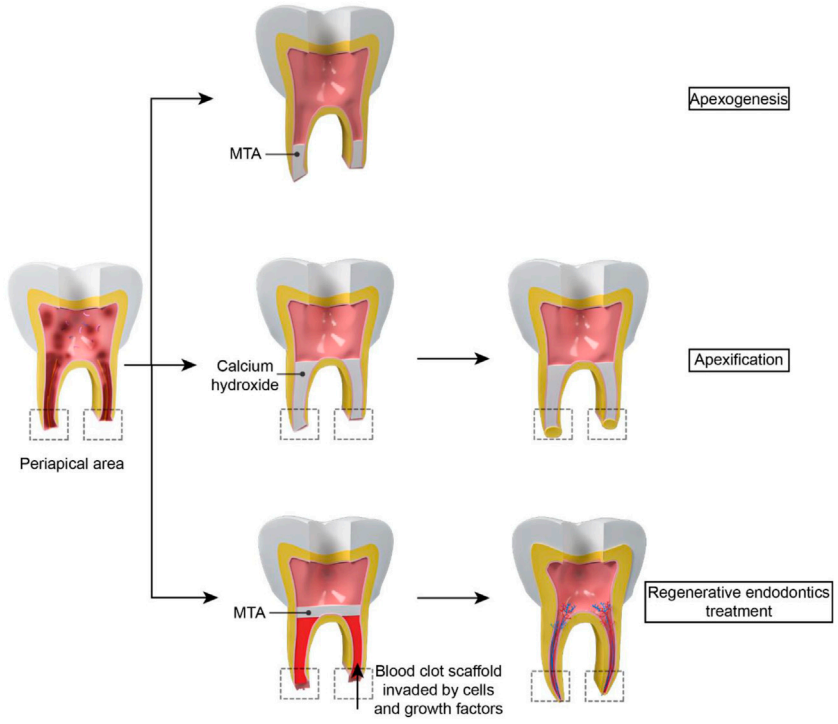

FIGURE 1
The difference between apexogenesis, apexification and RET: For apexogenesis, MTA is placed in the apical 1/3 of the root canal to form an unnatural barrier. For apexification, biomaterials such as calcium hydroxide is put in the root to stimulate the creation of a mineralized barrier in the root apex. However, vessels cannot regenerate in the pulp cavity. For RET, periapical tissue tearing results in a blood clot which acts as a natural scaffold for stem cells and growth factor to grow into. Then the closure of the apical foramen and/or the thickening of the root canal walls can be observed in the treatment.

factor in the RET to coordinate drug delivery of active biomolecules or antibiotics and offers a surface for cells to communicate, migrate, proliferate, and spatially organize (Nakashima and Akamine, 2005; Galler et al., 2011).

With the development of pulp regeneration, the scaffolds become one of the key factors to improve the RET's success rate. Here we summarized the research and development of nanofibrous scaffolds in RET to highlight the advantages of nanofibrous and discuss the future modification and application of nanofibrous.

2 Nanofibrous scaffolds

An essential process of the RET is placing a scaffold to generate a three-dimensional (3D) microenvironment for supporting cells, resulting in better outcomes of restoring tissue function (Gupte and Ma, 2012). A variety of materials can be utilized to construct scaffolds in regeneration engineering (Galler et al., 2011). Synthetic polymers [such as polymers of glycolic acid (PGA), polymers of lactic acid (PLA)], and biological matrices (such as reconstituted collagen and fibrin) are two principal alternatives (Galler et al., 2011; Zein et al., 2019). A suitable scaffold should closely be similar to the natural extracellular matrix (ECM), which is the physiological microenvironment of the cells (Gupte and Ma, 2012). ECM is the cell-environmental nanofibrous protein network in all tissues and consists of various nano-scale proteins, such as fibronectin, vitronectin and collagen (Kwon et al., 2005). This matrix can serve as structural support for cell adhesion and ingrowth and give cells chemical signals to govern their activity and reinforce a specific phenotypic (Galler et al., 2011).

Recent breakthroughs in nanotechnology have tremendously aided in creating innovative ECM-mimicking materials. Nanofibrous scaffolds which are becoming increasingly common in the RET can improve adhesion, allow cells to manifest more normal 3D morphologies when compared with smooth materials, solid films, and tissue culture polymers (Gupte and Ma, 2012; Mc et al., 2019). A nanofibrous scaffold is characterized by the diameter ranging from 1 nm to 100 nm, similar to the size of collagen (Sheikh et al., 2015). And it has a large surface area inversely linked to diameter, facilitating cellular adhesion and migration. Furthermore, the pores of nanofibers are suitable for the cell adhesion and penetration. Cells grown on very porous nanofibrous meshes have been proved to increase cellular adhesion and multiply (Kwon et al., 2005). Thus, nanofibrous scaffolds become an ideal material for RET due to nano-scale fibre, large surface area, and interconnected porosity similar to the ECM.

Biodegradability is also an important character for tissue regeneration. Most nanofibrous scaffolds are biodegradable and can be chemically destroyed in the biological environment by enzymes such as lysozyme (Sheikh et al., 2015). The degradability of the nanofibers is determined by two significant factors: the chemical composition of the fibres and hydrophilicity. Therefore, by adjusting these two factors, the biodegradation speed of scaffolds can be controlled in line with the rate of tissue regeneration for better regeneration. The biocompatibility of scaffolds' broken down chemical compounds matters as well. To better pulp regeneration, the material of the nanofibrous scaffold should be taken into consideration.

Acting as the reservoirs for stem cells, antimicrobial, anti-inflammatory molecules, and growth factors is a considerable advantage for nanofibrous scaffolds (Albuquerque et al., 2015; Keller et al., 2015). Thus, by providing physical and chemical stimulation, nanofibrous scaffolds have been shown to drive positive cell interactions, stimulate cell growth, preserve cell phenotypics, assist stem cell development, and activate cell-signaling pathways (Sun et al., 2010; Gupte and Ma, 2012; Li et al., 2020).

Currently, several materials processing techniques, including electrospinning, molecular self-assembly, and thermally induced phase separation, have also been developed for the production of nanofibrous scaffolds (Gupte and Ma, 2012; Albuquerque et al., 2014).

Electrospinning is extensively employed to make natural and synthetic polymer fibres because of its ease of usage and compatibility with practically any dissolvable polymer. A strong electric field is applied to control the deposition of polymer fibres with diameters ranging from nanometers to micrometers. Fibre morphology, pore size, and fibre alignment may be altered by adjusting electrospinning parameters as well (Yang et al., 2005; Gupte and Ma, 2012). However, it is frequently unable to make real nanofibers at 100 nm or less using commonly used biodegradable polymers. In addition to low production efficiency, factors such as air humidity, temperature, and air velocity in the spinning environment are difficult to control which affect the physical properties of nanofibrous scaffold can also be its shortcomings to achieve industrial production (Sill and von Recum, 2008).

Molecular self-assembly is a bottom-up technique that has been utilized to create nanofibres as small as 10 nm by using spontaneous molecular organization *via* weak non-covalent interactions (Dahlin et al., 2011). Molecular self-assembly nanofibers for RET benefit from being built into solutions and producing gels utilized for stem cell encapsulation (Rosa et al., 2013). Besides, the fluid may be administered *via* a minimally invasive technique, resulting in an in-suit nanofibrous structure. However, this method has limitations in controlling pore size/shape inside the hydrogel scaffold (Gupte and Ma, 2012) and poor mechanical properties in general (Zhang et al., 2012).

Thermally-induced phase separation (TIPS) involves drastically quenching a single-phase homogenous polymer solution, inducing separation into a solvent-rich phase and a polymer-rich phase and with fiber diameters between 50 and 500 nm. It is a technique that has been utilized for a long time to make membranes and scaffolds. This method is common to create nanofibrous scaffolds. TIPS can also be used with other approaches to create macro/micropore/channel networks within 3D nanofibrous scaffolds (Gupte and Ma, 2012).

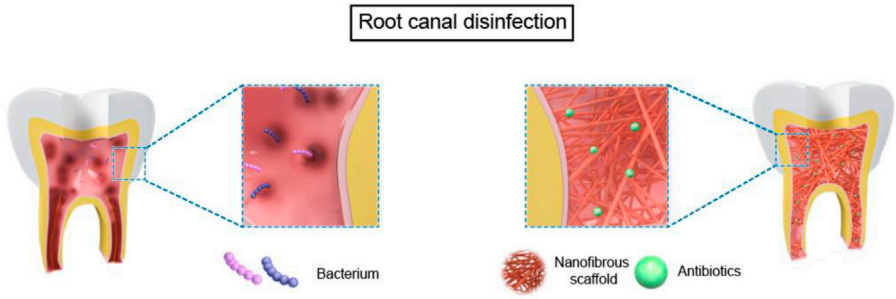

FIGURE 2
The use of nanofibrous scaffolds in root cannal disinfection.

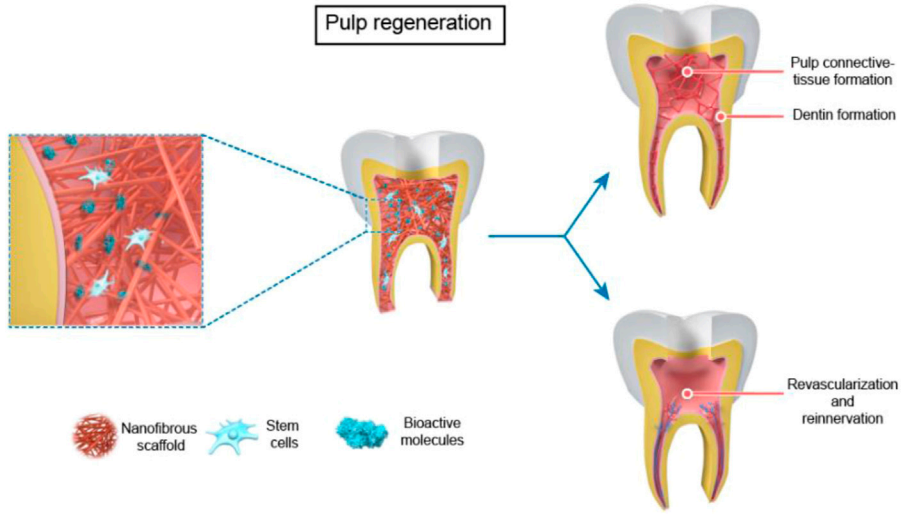

FIGURE 3
The use of nanofibrous scaffolds in pulp regeneration --- Pulp Connective -Tissue and Dentin Formation, Revascularization and Reinnervation.

The application of nanofiber scaffolds in RET can be devived into two parts in immature teeth based on tissue-engineering-techniques (Gupte and Ma, 2012): 1) bioactive nanofibrous scaffold with antibiotics for root canal disinfection. 2) nanofibrous scaffolds with stem cells and/or biomolecules for dental regeneration in a broad sense, which contains four parts: pulp connective-tissue formation; dentin formation; revascularization; reinnervation (Figure 2, Figure 3).

3 Nanofibrous scaffolds for root canal disinfection

Pulp regeneration processes can be quite complex (Schmalz et al., 2020), and bacteria in the root canal further complicates the RET (Kim et al., 2018). Over 600 bacterial species have been identified as potentially involved with pulp infections (Sampaio-Maia et al., 2016). The microbial ecology in the pulp canals of infected young permanent teeth was comparable to that of mature permanen teeth (Nagata et al., 2014). *Enterococcus faecalis* (*E. faecalis*) is commonly isolated from early-root canal infections. *Prophyromonas*, *Treponema*, *Bacteroides*, *Fusobacterium*, *Prevotella*, *Peptostreptococcos*, *Eubacterium*, and *Campylobacter* species are the most commonly found endodontic bacteria in primary endodontic infections (Neelakantan et al., 2017). Bacteria can not only enter the dentinal canal tubules of infected teeth but form biofilms on the radicular canal walls (Lin et al., 2014). Previously, the most commonly used drug in clinical practice for successful disinfection is triple antibiotic paste (TAP), which is made up

10.3389/fbioe.2022.1078453

TABLE 1 Nanofibrous scaffolds for root canal disinfection.

Scaffolds	Processing technique	Model	Involved antibiotic	Biocompatiblility		Biodegradability		Results	Reference
				Cells	Cytotoxics	Yes	No		
PSD	electrospinning	*in vitro*: antibacterial experiment, cell cultivation	MET or CIP	hDPSCs	all scaffolds, except 25 wt% CIP group, were considered biologically safe compared with non-antibiotic scaffolds	√		• scaffolds released MET/CIP gradually • electrospinning process did not affect antimicrobial properties • antimicrobial activities against *E. faecalis*, *P.gingivalis*	Bottino et al. (2013)
PSD	electrospinning	*in vitro*: antibacterial experiment, cell cultivation	MET and CIP in different proportion	hDPSCs	antibiotic-containing scaffolds had slight toxicity (60%–90% cell viability) or non-cytotoxicity (>90% cell viability)	√		• antimicrobial activities against *E. faecalis*, *P.gingivalis*, *F. nucleatum*	Palasuk et al. (2014)
PSD	electrospinning	*in vitro*: cell cultivation	MET or/and CIP in different proportion	hDPSCs	significantly lower effects on cell proliferation and survival compared with the saturated CIP/MET solution	√		• a burst release of antibiotic within the first 24 h, a sustained maintenance of the drug(s) concentration for 14 days • significantly lower effects on cell proliferation and survival compared with the saturated CIP/MET solution	Kamocki et al. (2015)
PSD	electrospinning	*in vitro*	MINO, CIP and MET	hDPSCs	enhanced adhesion/spreading on dentin specimens treated with antibiotic-containing nanofibers when compared with its TAP counterparts	√		• antimicrobial activities against *A. naeslundii*, *P.gingivalis* dual-species biofilm whereas not affect *DPSC* attachment and proliferation on dentin	Pankajakshan et al. (2016)
PSD	electrospinning	*in vitro*	MET, CIP and CLIN	hDPSCs	CLIN-containning nanofibers scaffolds showed cell viability above 50%	√		• antimicrobial activities against *A. naeslundii, A. actinomycetemcomitans, E. faecalis* • CLIN-containning nanofibers resulted in a slight decrease in hDPSCs viability • no discernibledentin discoloration for the CLIN-containing groups	Karczewski et al. (2018)
PSD	electrospinning	*in vivo* and vitro	MINO, CIP and MET	hDPSCs	histological data showed the scaffolds are biocompatible	√		• antimicrobial activities against *A. naeslundii* • apical foramen closure and the formation of a thin layer of osteodentin-like tissue	Mc et al. (2019)

PSD, polydioxanone; MET, Metronidazol; CIP, Ciprofloxacin; hDPSCs, human dental pulp stem cells; CLIN, clindamycin; PCL, poly(e-caprolactone); nHA, nano-hydroxyapatite; MgP, magnesium phosphate; ECM, extracellular matrix; BGNs, bioactive glass nanoparticles; hDPCs, human dental pulp cells; BMP, bone morphogenetic protein; SHED, stem cells from human exfoliated deciduous teeth; hAPCs, human apical papilla cells; PLLA, poly(L-lactic acid); BMP-7, bone morphogenetic protein 7; DXM, dexamethasone; DEX, dexamethasone; PCL-PEG-PCL, poly-caprolactone-poly-ethylene glycol-poly caprolactone; NaF, sodium fluoride; MSH, melanocyte-stimulating hormone; SIM, simvastatin; TGF-β1, transforming growth factor b1; FGF2, fibroblast growth factor basic; VEGF, vascular endothelial growth factor; GFs, the growth factors; HUVECs, human umbilical vein endothelial cells; PLLA, poly(L-lactic acid).

of equivalent doses of metronidazole (MET), ciprofloxacin (CIP) and minocycline (MINO) (Arruda et al., 2018). The antibacterial effects of this drug are widely recognized in the therapeutic setting, but it has garnered numerous complaints (Kim et al., 2018). One of the most crucial issues reported at TAP was dentin discolouration induced by the presence of MINO (Porter et al., 2016). Therefore, the double antibiotic paste (DAP) combining MET and CIP or the incorporation of ampicillin (AMP) into a new TAP formulation were used (Arslan et al., 2015). However, antibiotic pastes at therapeutically recommended doses will impair the viability of human apical papilla stem cells (SCAPs) (Ruparel et al., 2012). In view of the above disadvantages, Ca $(OH)_2$ is commonly used in RET currently. However, it also has several disadvantages. For example, it can form a calcified barrier in the root canal, hindering the growth of pulp tissue (Song et al., 2017; Almutairi et al., 2022). And because of its high pH, it may destroy cells from the apical papilla and periapical tissue as well (Banchs and Trope, 2004; Jadhav et al., 2012).

Thus, it is crucial to employ biomaterials that reduce germs in the root canal while remaining non-cytotoxic and encouraging the creation of new tissues (Murray, 2018). New nano-scaffolds which are capable of serving as drug delivery vehicles in a regulated manner depending on therapeutic use are developed (Sundararaj et al., 2014). Compared to propylene glycol, which is the most often utilized carrier for delivering antimicrobial pastes to the root canal, nanofibers have the potential benefit of increasing the surface area and, presumably, allowing for controllable drug release over a more extended period (Bottino et al., 2013; Palasuk et al., 2014). Figure 2 and Table 1 summarized the use of nanofibrous scaffolds in root canal disinfection.

In 2013, Bottino et al. (Bottino et al., 2013) mixed polydioxanone monofilament solution material (PDS-II) with MET or CIP in different concentrations (5% or 25%), and typical electrospinning procedures were applied. Almost all scaffolds demonstrated an early burst followed by a general linear continuous drug release. Within the first 48 h, all nanofibrous scaffolds only release a portion of the medication from 22.4% to 51.4% indicated the sustained drug release from the scaffolds. All CIP-containing scaffolds strongly reduced the growth of *Porphyromonas gingivalis* (*P.gingivalis*) and *E. faecalis*. However, MET-containing's have no *E. faecalis* resistance. Although they all have good antibacterial properties, only the 25% wt CIP-containing extract had a substantial adverse effect on Human dental pulp stem cells (hDPSCs).

A nanofibrous scaffold by combining MET and CIP in different ratios and using PDS as a drug carrier is created in another study (Palasuk et al., 2014). All scaffolds containing antibiotics suppressed the growth of *P. gingivalis*, *E. faecalis*, and *Fusobacterium nucleatum* (*F. nucleatum*), except for the MET-containing scaffold. When compared to scaffolds integrated with individual antimicrobials, scaffolds with two antibiotics did not increase their antimicrobial abilities. Moreover, antibiotic-containing aliquots slightly reduced cell viability to hDPSC.

To further determine the drug release abilities of the new dual-mix antibacterial scaffolds and their effect on the proliferation and activity of hDPSCs. Kamocki et al. (Kamocki et al., 2015) uses electrospinning to create PDS-based nanofibrous scaffolds containing MET and CIP. Pure PDS scaffolds are utilized as the negative (non-toxic) controls, while saturated CIP/MET solution scaffolds are treated as the positive (toxic) groups. The results show no differences in cell proliferation in the pure PDS or MET scaffold groups. For pure CIP-containing scaffolds, increasing drug concentration led to decreased cell viability. However, no cells could be observed after exposing to the saturated CIP/MET solution after 3 days, indicating that antibiotic-containing nanofibrous scaffolds had considerably reduced impacts on hDPSC proliferation. Pankajakshan et al. (Pankajakshan et al., 2016) discovered a similar experimental phenomenon: antibiotic–containing (MINO, CIP, MET) polymer nanofibers resulted in numerous bacterial killing but had no effect on hDPSC adhesion and growth on dentin when compared to a saturated TAP solution. These studies suggest that nanofibrous scaffolds are more biologically friendly to cells when compared with antibiotic paste.

Karczewski et al. (Karczewski et al., 2018) changed the formula of triple antibiotics, including MET, CIP, and clindamycin (CLIN). Hydrated triple antibiotic-containing nanofibrous scaffolds showed pronounced antimicrobial activity against *Actinomyces* naeslundii (A. naeslundii), Aggregatibacter actinomycetemcomitans (A. actinomycetemcomitans), and *E. faecalis*, but with no cytotoxic effects on hDPSC indicating that this kind of triple antibiotic-containing scaffolds might be a feasible option in the RET. Bottino et al. (Mc et al., 2019) optimized electrospinning parameters and created a 3D tubular triple antibiotic-eluting construct to increase the antibacterial activity and the ability to remove bacterial biofilm. The 3D nanofibrous scaffold created an optimal environment with apical foramen closure and a thin layer of osteodentin-like *tissue* within the root canal.

In general, compared with antibiotic pastes, utilizing nanofibrous scaffolds as drug-carrying carriers is more conducive to drug release and increase the capacity of pathogen clearance in the first stage of pulp regeneration. Moreover, it has no toxic effects on stem cells during regeneration. However, there are also some limitations in these researches. The main problem is the lack of *in vivo* studies including antibacterial, degradability and compatibility. Only one article established a canine model of periapical disease. The rest of the studies were still limited to *in vitro* experiments which lack of enough reliability. At the same time, as drug-loaded scaffolds, they also lack the exploration of the best speed for drug release as well as the best degradation rate of the scaffolds which determine the long-term bactericidal ability.

10.3389/fbioe.2022.1078453

TABLE 2 Nanofibrous scaffolds for pulp connective-tissue and dentin formation.

Scaffolds	Processing technique	Model	Asscociated tissue engineering strategy		Biocompatibility		Degradability		Results	Reference
			Biomolecules	Cells	Yes	No	Yes	No		
PCL, gelatin and nHA	electrospinning	*in vitro*: cell cultivation *in vivo*: mice subcutaneous transplantation		hDPSCs	√		√		• the scaffolds supported hDPSC adhesion, proliferation, and odontoblastic differentiation • *in vivo* implants were enveloped by a thin fibrous tissue capsule with no negative impacts and increased odontogenic differentiation of stem cells	Yang et al. (2010)
gelatin and silica bioactive glass	thermally induced phase separation	*in vitro*: cell cultivation		hDPSCs	√		√		• compared to nanofibrous gelatin scaffolds, the scaffolds promoted greater cell differentiation and biomineralization	Qu and Liu, (2013)
Gelatin	thermally induced phase separation	*in vitro*: cell cultivation *in vivo*: mice subcutaneous transplantation	MgP	hDPSCs	√		√		• the nanofibrous gelatin/MgP8 above scaffolds produced greater ECM[9] deposition, hard tissue formation, and odontogenic differentiation protein compared to the nanofibrousgelatin scaffolds	Qu et al. (2014)
PCL	Electrospinning	*in vitro*: cell cultivation		hDPSCs[4]	√		√		• cell growth, mineralization and odontoblastic differetiation on the scaffolds' surface • the mineralized scaffolds promoting growth and odontogenic differentiation through the integrin-mediated signaling pathway	Kim et al. (2014)
PCL, gelatin, BGNs	electrospinning	*in vitro*: cell cultivation		hDPCs	√		—		• the scaffolds promoted odontogenic differentiation through the integrin, BMP, and mitogen-activated protein kinases signaling path-way	Kim et al. (2015)
Collagen	electrospinning	*in vitro*: cell cultivation		hDPCs	√		√		• scaffolds promoted cell migration, viability, proliferation, adhesion and spreading, as well as collagen production and gene expression	Zhang et al. (2019)
Hydrogel	self-assembling	*in vitro*:cell cultivation	b-glycerophosphate, dexamethasone, KH2PO4	SHED and hDPSCs	√		√		• SHED resulted in soft tissue formation • hDPSCs expressed osteoblast marker genes, and deposited minerals	Galler et al. (2008)
PCL	electrospinning	*in vitro*: cell cultivation	fibronectin	hAPCs	√		—		• The fibronectin added to the scaffolds increase the cell viability, migration, adhesion, growth, and gene expression (ITGA5, ITGAV, COL1A1, COL3A1) at a dose dependent manner	Leite et al. (2021)

(Continued on following page)

TABLE 2 (*Continued*) Nanofibrous scaffolds for pulp connective-tissue and dentin formation.

Scaffolds	Processing technique	Model	Asscociated tissue engineering strategy		Biocompatibility		Degradability		Results	Reference
			Biomolecules	Cells	Yes	No	Yes	No		
PLLA	thermally induced phase separation	*in vitro*: cell cultivation *in vivo*: mice subcutaneous transplantation	BMP-7, DXM	hDPSCs	√		√		• both "DXM" group and "BMP-7 + DXM" group induced the hDPSCs to odontoblast-like cells • "BMP-7 + DXM" group presented more ECM and hard tissue formation than "DXM" group	Wang et al. (2010)
BGNs	electrospinning	*in vitro*: cell cultivation	DEX	hDPSCs	√		√		• The release of DEX showed a slow releasing profile, lasting a month • The scaffolds were demonstrated to promote odontogenesis, and the integrins, bone morphogenetic protein, and mTOR signaling pathways are proposed to be the possible mechanisms	Lim et al. (2016)
PCL-PEG-PCL	electrospinning	*in vitro*: cell cultivation	NaF, MSH, and SIM	hDPSCs	√		—		• significant higher adhesive behavior, viability, alizarin red activity, and dentin specific gene expression in MSH - and SIM - treated cells	Zijah et al. (2017b)

PSD, polydioxanone; MET, Metronidazol; CIP, Ciprofloxacin; hDPSCs, human dental pulp stem cells; CLIN, clindamycin; PCL, poly(e-caprolactone); nHA, nano-hydroxyapatite; MgP, magnesium phosphate; ECM, extracellular matrix; BGNs, bioactive glass nanoparticles; hDPCs, human dental pulp cells; BMP, bone morphogenetic protein; SHED, stem cells from human exfoliated deciduous teeth; hAPCs, human apical papilla cells; PLLA, poly(L-lactic acid); BMP-7, bone morphogenetic protein 7; DXM, dexamethasone; DEX, dexamethasone; PCL-PEG-PCL, poly-caprolactone-poly-ethylene glycol-poly caprolactone; NaF, sodium fluoride; MSH, melanocyte-stimulating hormone; SIM, simvastatin; TGF-β1, transforming growth factor b1; FGF2, fibroblast growth factor basic; VEGF, vascular endothelial growth factor; GFs, the growth factors; HUVECs, human umbilical vein endothelial cells; PLLA, poly(L-lactic acid).

10.3389/fbioe.2022.1078453

4 Nanofibers for dental pulp regeneration in the broad sense

4.1 Nanofibrous scaffolds for pulp connective-tissue and dentin formation

Potential cell sources for the RET include hDPSCs, stem cells from human exfoliated deciduous teeth (SHED) and stem cells of the apical papilla (Huang et al., 2008; Morsczeck and Reichert, 2018). These stem cells were incubated with different materials to explore their ability in the RET. Table 2 summarized all the nanofibrous scaffolds used in Pulp Connective-Tissue and Dentin Formation.

Yang et al. (Yang et al., 2010) seeded hDPSCs on electrospun polycaprolactone (PCL) and gelatin scaffolds with or without nano-hydroxyapatite (nHA). The cells showed the growth and mineralization properties on both the scaffolds. Moreover, a thin fibrous tissue capsule enveloped all implants and osteocyte-like cells and osteoblast-like cells orderly arranged at the scaffolds' surface in mice subcutaneous transplantation model. And, the incorporation of nHA into scaffolds could increase the expression of specific odontogenic genes.

(Qu and Liu, 2013) created 3D nanofibrous gelatin andsilica bioactive glass (NF-gelatin/SBG) hybrid scaffolds. The hDPSCs proliferated significantly faster on NF-gelatin/SBG scaffolds which promoted better cell differentiation and biomineralization compared to NF-gelatin scaffolds. And the same research group found the 3D NF-gelatin andmagnesium phosphate hybrid scaffolds had a similar effect on hDPSCs which was proved in animal experiments as well (Qu et al., 2014).

(Kim et al., 2014) utilized apatite to deal with the scaffolds' surface and created mineralized PCL nanofibrous scaffolds. They tested their ability to induce odontogenic differentiation of human dental pulp cells (hDPCs) and the situation of cell adhesion, growth on the scaffolds' suface. Mineralized PCL scaffold showed better capability in cell growth, mineralized nodule formation, and expression of odontoblastic marker genes compared with the pure PCL scaffolds. And these mineralized scaffolds were appealing for regenerating dentin tissue because they promoted odontogenic differentiation and growth of hDPCs *via* the integrin-mediated signaling pathway. And the same group proved that the bioactive glass nanoparticles - biopolymer blend PCL-gelatin composite nano matrix could promote the odontogenic differentiation of HDPCs by activating the BMP, integrin, and mitogen-activated protein kinase signaling pathway (Kim et al., 2015). Moreover, better ability of promoting cell adhesion, growth and odontoblastic differentiation of hDPCs on collagen nanofibrous matrix (Col_NFM) *versus* collagen flat film (Col-FF) were also observed by Zhang's group (Zhang et al., 2019).

In addition to using different nanofibrous scaffolds, active biomolecules are also combined with scaffolds to enhance the ability of dental pulp regeneration.

Galler et al. (Galler et al., 2008) combined SHED and hDPSCs with peptide-amphiphile (PA) hydrogel scaffolds which could form 3D nanofibrous networks by self-assemble method. After 4 weeks of cultivating stem cells with different osteogenic supplements, SHED and hDPSCs could proliferate and differentiate within the scaffolds. *In vitro* experiment showed that SHED led to collagen production, while hDPSCs could expressed osteoblast marker genes, manifested an osteoblast-like phenotype, and deposited minerals.

Leite et al. (Leite et al., 2021) developed and evaluated fibronectin (FN)-loaded PCL nanofiber scaffolds of PCL on human apical papilla cells (hAPCs). FN has been postulated as a chemotactic agent that promotes cell migration, adhesion, growth, and differentiation (Grigoriou et al., 2017). The FN added to the scaffolds increase the cell viability, migration, adhesion, growth, and gene expression (ITGA5, ITGAV, COL1A1, COL3A1) at a dose dependent manner.

In order to examine the odontogenic development of hDPSCs, Wang et al. (Wang et al., 2010) fabricated highly porous nanofibrous PLLA scaffolds that resembled the structure of collagen type I fibres. Stem cells were sown onto the scaffolds and grown in various conditions to induce odontogenic differentiation. Both the "DXM" medium (medium containing dexamethasone (DXM)) and "BMP-7+DXM" medium [medium containing DXM, ascorbic acid, β-glycerophosphate plus bone morphogenetic protein 7 (BMP-7)] promoted DPSCs to odontoblast-like cells. After ectopic implantation in nude mice, the "BMP-7 + DXM" group showed greater ECM and complicated tissue development.

The dexamethasone (DEX) - releasing nanofiber matrices with bioactive glass nanoparticles (BGNs) scaffolds were considered a promising therapeutic nano matrix for RET by Lim's group (Lim et al., 2016). These scaffolds were shown to enhance the odontogenic ability of hDPCs. Bone morphogenetic protein, the integrins, and mTOR signaling pathways were involved in this process (Lim et al., 2016). (Zijah et al., 2017a) aimed to assess and compare the effect of poly-caprolactone-poly-ethylene glycol-poly caprolactone (PCL-PEG-PCL) nanofibrous scaffold containing 3 different biofactors, including sodium fluoride (NaF), melanocyte-stimulating hormone (MSH), and simvastatin (SIM). They found that MSH- and SIM-treated cells had greater adhesive behavior, vitality, dentin-specific gene expression and alizarin red activity.

In terms of nanofibrous scaffolds promoting pulp connective-tissue and dentin formation, we can find scaffolds promoted better cell adhesion, growth, differentiation and biomineralization or high expression of odontoblastic marker genes *in vitro* experiments or mice subcutaneous transplantation model. However, we can't clearly find the closure of the apical foramen and/or the thickening of the root canal walls in animal experiments. Thus, we need to complete more animal experiments to perfect this defect before clinical trials.

TABLE 3 Nanofibrous scaffolds for revascularization and reinnervation.

Scaffolds	Processing technique	Model	Asscociated tissue engineering strategy		Biocompatibility		Biodegradability		Results	Reference
			Biomolecules	Cells	Yes	No	Yes	No		
Peptide	self-assembling	*in vitro*:cell cultivation *in vivo*: mice subcutaneous transplantation	TGF-β1, FGF2, and VEGF	hDPSCs	√		√		• cell culture with GFs release from scaffolds showed better cell morphology and proliferation rates • *in vivo* experiment showed the development of a vascularized soft connective tissue	Galler et al. (2012)
peptide hydrogel: PuraMatrix™		*in vitro*: cell cultivation *in vivo*: mice subcutaneous transplantation		HUVECs, hDPSCs	√		√		• co-culturing hDPSCs and HUVECs in PuraMatrix promoted HUVEC survival and induced vessel-like structure formation • *in vivo* experiment showed developed early vascular networks	Dissanayaka et al. (2015)
PLLA	self-assembling	*in vitro*: cell cultivation *in vivo*: mice subcutaneous transplantation	VEGF	hDPSCs	—	√			• hDPSC could attach and proliferate on the scaffolds • *in vivo* experiment showed regenerated pulp-like tissue fulfilled the whole apical	Li et al. (2016)
PCL	electrospinning	*in vitro*: cell cultivation		hDPCs, HUVECs	√		√		• increased cell viability and odontogenic differentiation of HDPCs • increased capillary-like tube formation of HUVECs	Yun et al. (2016)
PLLA	phase-separation	*in vitro*: cell cultivation *in vivo*: subcutaneous implantation mouse model	simvastatin	hDPCs, HUVECs	—	—			• *in vivo* experiment showed formed vessel-like structures • simvastatin could up-regulate odontoblastic markers, exert a pro-angiogenic effect on endothelial cells, resulting in enhanced vascularization and mineralized dentin tissue regeneration	Soares et al. (2018)

PSD, polydioxanone; MET, Metronidazol; CIP, Ciprofloxacin; hDPSCs, human dental pulp stem cells; CLIN, clindamycin; PCL, poly(e-caprolactone); nHA, nano-hydroxyapatite; MgP, magnesium phosphate; ECM, extracellular matrix; BGNs, bioactive glass nanoparticles; hDPCs, human dental pulp cells; BMP, bone morphogenetic protein; SHED, stem cells from human exfoliated deciduous teeth; hAPCs, human apical papilla cells; PLLA, poly(L-lactic acid); BMP-7, bone morphogenetic protein 7; DXM, dexamethasone; DEX, dexamethasone; PCL-PEG-PCL, poly-caprolactone-poly-ethylene glycol-poly caprolactone; NaF, sodium fluoride; MSH, melanocyte-stimulating hormone; SIM, simvastatin; TGF-β1, transforming growth factor b1; FGF2, fibroblast growth factor basic; VEGF, vascular endothelial growth factor; GFs, the growth factors; HUVECs, human umbilical vein endothelial cells; PLLA, poly(L-lactic acid).

10.3389/fbioe.2022.1078453

4.2 Nanofibrous scaffolds for revascularization and reinnervation

In addition to promoting cell growth, differentiate, nanofibrous scaffolds can also promote angiogenesis and reinnervation in pulp regeneration. The vascularization and reinnervation capabilities of a scaffold are crucial for RET. Table 3 summarized the scaffolds used in revascularization and reinnervation.

Dissanayaka et al. (Dissanayaka et al., 2015) utilized the peptide hydrogel PuraMatrix to test its vascularization ability. In 3D PuraMatrix, they enclosed Human umbilical vein endothelial cells (HUVECs), hDPSCs, or cocultures of these 2 cells and found that hDPSCs aided in developing early vascular networks by promoting the migration of HUVECs and boosting vascular endothelial growth factor (VEGF) expression. Both the hDPSC-only and coculture groups showed vascularized pulp-like tissue with patches of osteodentin in mice subcutaneous transplantation model. Also, Galler et al. (Galler et al., 2012) encapsulated hDPSCs in a self-assembling hydrogel integrated VEGF, fibroblast growth factor primary and transforming growth factor b1. A vascularized soft connective tissue compared to the tooth pulp generated after subcutaneous transplantation within dentin cylinders into mice. Likewise, Li et al. (Li et al., 2016) manufactured a novel hierarchical growth factor-loaded nanofibrous scaffold to solve the vascularization problem. Heparin-binding VEGF was encased in heparin-conjugated gelatin nanospheres, which were subsequently confined in the nanofibers of an injectable PLLA microsphere. This structure shielded the VEGF against degradation and denaturation, and also showed a precise control over its long-term release. After implantation of tooth loaded with nanofibrous scaffolds into immunocompromised nude, the pulp-like tissues filled the whole apical and 2/3 of the root canal, and reached the coronal third. The blood vessels could also be found in the canal.

Yun et al. (Yun et al., 2016) tested the impact of magnetic nanofibrous scaffolds (MNS) on the behaviors of hDPCs. The results indicated that the magnetic scaffolds increased hDPCs development and also promoted the hDPCs-induced angiogenesis of endothelial cells. Soares et al. (Soares et al., 2018) investigated the NF-PLLA scaffolds in mouse model and demonstrated that the addition of simvastatin to a hDPCs/NF-PLLA scaffold might dramatically suppress the production of pro-inflammatory mediators. The detrimental effects of LPS on odontoblastic marker expression might be reversed. Meanwhile, the NF-PLLA nanofibrous scaffolds allowed the HUVECs to form vessel-like structures inside.

For reinnervation, Yoo et al. (Yoo et al., 2018) seeded the hDPCs onto PCLF and PCLF/DMOG dentin slices before transplanting them into mice. The PCLF/DMOG scaffolds increased the expression of VEGF, dentin sialoprotein, bone sialoprotein in the hDPCs, mouse VEGF, mouse neurofilament light polypeptide and mouse platelet endothelial cell adhesion molecule one in the surrounding host cells. These data indicated that pulp-dentin complex regenerated by increasing odontoblastic differentiation of hDPCs, host cell recruitment, neurogenesis and angiogenesis was potentially promoted by PCLF/DMOG.

In conclusion, nanofibrous scaffolds with stem cells and/or active biomolecules promote stem cell-mediated pulp regeneration of pulp connective-tissue formation, dentin formation, revascularization, reinnervation. Currently, nanofibrous scaffolds used for vascular and nerve regeneration are relatively small, and all *in vivo* experiments were still limited to subcutaneous implantation in mice, not in either human or animal pulpless tooth roots. Though, their studies positively showed their regenerative potential to develop early pulp-like tissues by promoting the migration of stem cells and forming vascularized soft connective tissue. However, we still have a long way to go: Does bioparticle-loaded nanofibrous scaffolds have the same effect in immature pulpless teeth? What is the best apical opening size for the scaffolds? What is the optimal degradation rate of the scaffolds for pulp regeneration? In order to avoid cell damage while maintaining the support force of the scaffolds, how much hardness should be selected?

5 Conclusion

Currently, there are two significant challenges in the pulp regeneration, including the disinfection of the pulp and the regeneration of tooth-related issues. Regarding pulp disinfection, antibiotic pastes at therapeutically recommended doses impaired the viability of stem cells. And pastes cannot be released at a steady and lasting pace as well. As for the regeneration of tooth-related issues, RET has to be supplemented with scaffolds to improve repeatability and encourage a well-orchestrated regeneration. To address the challenges, nanofibrous scaffolds mimicking extra-cellular matrix (ECM) have been developed. They can act as antibacterial molecule reservoirs and provide growth factors, stem cells to guide the various cells' migration, growth, and differentiation. However, most of the application of nanofibrous scaffolds is still at the laboratory research stage and lack of the *in vivo* and clinical investigation and evaluation. Meanwhile, we still have a lot of details to work out, including: the optimal degradation rate and drug release rate, the best hardness, suitable physical properties etc. Moreover, no single material can perfectly combine the antibacterial characteristics and stimulate regeneration of connective-tissue, dentin, nerves, and blood vessels simultaneously. New materials are still needed to construct the composite nanofibrous scaffolds for all needs in RET. Furthermore, the *in vivo* and clinical

evaluation are also critical for the development of new nanofibrous scaffolds.

Author contributions

FH and BR conceived the layout of this manuscript. FH wrote the first draft of the manuscript that was iteratively improved by LC, JL, and BR.

Funding

This research was funded by National Natural Science Foundation of China, grant number: 81870778, 81870759, 82071106, 81991500, 81991501, Applied Basic Research Programs of Sichuan Province, grant number: 2020YJ0227, Technology Innovation R&D Project of Chengdu, grant number: 2022-YF05-01401-SN, and by Science & Technology Department of Sichuan Province, grant number: 2021YFQ0064.

Acknowledgments

Our special thanks go to Jiaojiao Yang and Fangjie Zhou for their help in suggesting the general direction of this manuscript.

Conflict of interest

The authors declare that the research was conducted in the absence of any commercial or financial relationships that could be construed as a potential conflict of interest.

Publisher's note

References

Agnihotry, A., Fedorowicz, Z., van Zuuren, E. J., Farman, A. G., and Al-Langawi, J. H. (2016). Antibiotic use for irreversible pulpitis. *Cochrane Database Syst. Rev.* 2, CD004969. doi:10.1002/14651858.CD004969.pub4

Albuquerque, M. T. P., Ryan, S. J., Münchow, E. A., Kamocka, M. M., Gregory, R. L., Valera, M. C., et al. (2015). Antimicrobial effects of novel triple antibiotic paste-mimic scaffolds on Actinomyces naeslundii biofilm. *J. Endod.* 41, 1337–1343. doi:10.1016/j.joen.2015.03.005

Albuquerque, M. T. P., Valera, M. C., Nakashima, M., Nör, J. E., and Bottino, M. C. (2014). Tissue-engineering-based strategies for regenerative endodontics. *J. Dent. Res.* 93, 1222–1231. doi:10.1177/0022034514549809

Almutairi, W., Al-Dahman, Y., Alnassar, F., and Albalawi, O. (2022). Intracanal calcification following regenerative endodontic treatment: A systematic review and meta-analysis. *Clin. Oral Investig.* 26, 3333–3342. doi:10.1007/s00784-021-04333-5

Andreasen, J. O., Farik, B., and Munksgaard, E. C. (2002). Long-term calcium hydroxide as a root canal dressing may increase risk of root fracture. *Dent. Traumatol.* 18, 134–137. doi:10.1034/j.1600-9657.2002.00097.x

Arruda, M. E. F., Neves, M. A. S., Diogenes, A., Mdala, I., Guilherme, B. P. S., Siqueira, J. F., et al. (2018). Infection control in teeth with apical periodontitis using a triple antibiotic solution or calcium hydroxide with chlorhexidine: A randomized clinical trial. *J. Endod.* 44, 1474–1479. doi:10.1016/j.joen.2018.07.001

Arslan, Hakan, Akcay, Merve, Çakir, Mustafa, Gok, Adem, Yasa, B., and Dalli, M. (2015). Comparison of bond strength of self-etch adhesive to pulp chamber dentin after placement of calcium hydroxide and various antibiotic pastes. *Acta odontol. Scand.* 73, 226–231. doi:10.3109/00016357.2014.992811

Banchs, F., and Trope, M. (2004). Revascularization of immature permanent teeth with apical periodontitis: New treatment protocol? *J. Endod.* 30, 196–200. doi:10.1097/00004770-200404000-00003

Bjørndal, L., Demant, S., and Dabelsteen, S. (2014). Depth and activity of carious lesions as indicators for the regenerative potential of dental pulp after intervention. *J. Endod.* 40, S76–S81. doi:10.1016/j.joen.2014.01.016

Bjørndal, L., Simon, S., Tomson, P. L., and Duncan, H. F. (2019). Management of deep caries and the exposed pulp. *Int. Endod. J.* 52, 949–973. doi:10.1111/iej.13128

Bletsa, A., Berggreen, E., Fristad, I., Tenstad, O., and Wiig, H. (2006). Cytokine signalling in rat pulp interstitial fluid and transcapillary fluid exchange during lipopolysaccharide-induced acute inflammation. *J. Physiol.* 573, 225–236. doi:10.1113/jphysiol.2006.104711

Bottino, M. C., Kamocki, K., Yassen, G. H., Platt, J. A., Vail, M. M., Ehrlich, Y., et al. (2013). Bioactive nanofibrous scaffolds for regenerative endodontics. *J. Dent. Res.* 92, 963–969. doi:10.1177/0022034513505770

Chan, E. K. M., Desmeules, M., Cielecki, M., Dabbagh, B., and Ferraz Dos Santos, B. (2017). Longitudinal cohort study of regenerative endodontic treatment for immature necrotic permanent teeth. *J. Endod.* 43, 395–400. doi:10.1016/j.joen.2016.10.035

Dahlin, R. L., Kasper, F. K., and Mikos, A. G. (2011). Polymeric nanofibers in tissue engineering. *Tissue Eng. Part B Rev.* 17, 349–364. doi:10.1089/ten.TEB.2011.0238

Dissanayaka, W. L., Hargreaves, K. M., Jin, L., Samaranayake, L. P., and Zhang, C. (2015). The interplay of dental pulp stem cells and endothelial cells in an injectable peptide hydrogel on angiogenesis and pulp regeneration *in vivo*. *Tissue Eng. Part A* 21, 550–563. doi:10.1089/ten.TEA.2014.0154

Estefan, B. S., El Batouty, K. M., Nagy, M. M., and Diogenes, A. (2016). Influence of age and apical diameter on the success of endodontic regeneration procedures. *J. Endod.* 42, 1620–1625. doi:10.1016/j.joen.2016.06.020

Frank, A. L. (1966). Therapy for the divergent pulpless tooth by continued apical formation. *J. Am. Dent. Assoc.* 72, 87–93. doi:10.14219/jada.archive.1966.0017

Galler, K. M., Cavender, A., Yuwono, V., Dong, H., Shi, S., Schmalz, G., et al. (2008). Self-assembling peptide amphiphile nanofibers as a scaffold for dental stem cells. *Tissue Eng. Part A* 14, 2051–2058. –2058. doi:10.1089/ten.tea.2007.0413

Galler, K. M., D'Souza, R. N., Hartgerink, J. D., and Schmalz, G. (2011). Scaffolds for dental pulp tissue engineering. *Adv. Dent. Res.* 23, 333–339. doi:10.1177/0022034511405326

Galler, K. M., Hartgerink, J. D., Cavender, A. C., Schmalz, G., and D'Souza, R. N. (2012). A customized self-assembling peptide hydrogel for dental pulp tissue engineering. *Tissue Eng. Part A* 18, 176–184. doi:10.1089/ten.TEA.2011.0222

Grigoriou, E., Cantini, M., Dalby, M. J., Petersen, A., and Salmeron-Sanchez, M. (2017). Cell migration on material-driven fibronectin microenvironments. *Biomater. Sci.* 5, 1326–1333. doi:10.1039/c7bm00333a

Gupte, M. J., and Ma, P. X. (2012). Nanofibrous scaffolds for dental and craniofacial applications. *J. Dent. Res.* 91, 227–234. doi:10.1177/0022034511417441

Heithersay, G. S. (1975). Calcium hydroxide in the treatment of pulpless teeth with associated pathology. *Int. Endod. J.* 8, 74–93. doi:10.1111/j.1365-2591.1975.tb01000.x

Huang, G. T.-J., and Lin, L. M. (2008). Letter to the editor: Comments on the use of the term "revascularization" to describe. *J. Endod.* 34, 511. author reply 511-512. doi:10.1016/j.joen.2008.02.009

Huang, G. T.-J., Sonoyama, W., Liu, Y., Liu, H., Wang, S., and Shi, S. (2008). The hidden treasure in apical papilla: The potential role in pulp/dentin regeneration and bioroot engineering. *J. Endod.* 34, 645–651. doi:10.1016/j.joen.2008.03.001

Iwaya, S. I., Ikawa, M., and Kubota, M. (2001). Revascularization of an immature permanent tooth with apical periodontitis and sinus tract. *Dent. Traumatol.* 17, 185–187. doi:10.1034/j.1600-9657.2001.017004185.x

Jadhav, G., Shah, N., and Logani, A. (2012). Revascularization with and without platelet-rich plasma in nonvital, immature, anterior teeth: A pilot clinical study. *J. Endod.* 38, 1581–1587. doi:10.1016/j.joen.2012.09.010

Jung, C., Kim, S., Sun, T., Cho, Y.-B., and Song, M. (2019). Pulp-dentin regeneration: Current approaches and challenges. *J. Tissue Eng.* 10, 204173141881926. doi:10.1177/2041731418819263

Kahler, B., and Rossi-Fedele, G. (2016). A review of tooth discoloration after regenerative endodontic therapy. *J. Endod.* 42, 563–569. doi:10.1016/j.joen.2015.12.022

Kamocki, K., Nör, J. E., and Bottino, M. C. (2015). Dental pulp stem cell responses to novel antibiotic-containing scaffolds for regenerative endodontics. *Int. Endod. J.* 48, 1147–1156. doi:10.1111/iej.12414

Karczewski, A., Feitosa, S. A., Hamer, E. I., Pankajakshan, D., Gregory, R. L., Spolnik, K. J., et al. (2018). Clindamycin-modified triple antibiotic nanofibers: A stain-free antimicrobial intracanal drug delivery system. *J. Endod.* 44, 155–162. doi:10.1016/j.joen.2017.08.024

Keller, L., Offner, D., Schwinté, P., Morand, D., Wagner, Q., Gros, C., et al. (2015). Active nanomaterials to meet the challenge of dental pulp regeneration. *Mater. (Basel)* 8, 7461–7471. doi:10.3390/ma8115387

Kim, G.-H., Park, Y.-D., Lee, S.-Y., El-Fiqi, A., Kim, J.-J., Lee, E.-J., et al. (2015). Odontogenic stimulation of human dental pulp cells with bioactive nanocomposite fiber. *J. Biomater. Appl.* 29, 854–866. doi:10.1177/0885328214546884

Kim, J.-J., Bae, W.-J., Kim, J.-M., Kim, J.-J., Lee, E.-J., Kim, H.-W., et al. (2014). Mineralized polycaprolactone nanofibrous matrix for odontogenesis of human dental pulp cells. *J. Biomater. Appl.* 28, 1069–1078. doi:10.1177/0885328213495903

Kim, S. G., Malek, M., Sigurdsson, A., Lin, L. M., and Kahler, B. (2018). Regenerative endodontics: A comprehensive review. *Int. Endod. J.* 51, 1367–1388. doi:10.1111/iej.12954

Kwon, I. K., Kidoaki, S., and Matsuda, T. (2005). Electrospun nano- to microfiber fabrics made of biodegradable copolyesters: Structural characteristics, mechanical properties and cell adhesion potential. *Biomaterials* 26, 3929–3939. doi:10.1016/j.biomaterials.2004.10.007

Leite, M. L., Soares, D. G., Anovazzi, G., Mendes Soares, I. P., Hebling, J., and de Souza Costa, C. A. (2021). Development of fibronectin-loaded nanofiber scaffolds for guided pulp tissue regeneration. *J. Biomed. Mat. Res.* 109, 1244–1258. doi:10.1002/jbm.b.34785

Li, Q.-M., Li, J.-L., Feng, Z.-H., Lin, H.-C., and Xu, Q. (2020). Effect of histone demethylase KDM5A on the odontogenic differentiation of human dental pulp cells. *Bioengineered* 11, 449–462. doi:10.1080/21655979.2020.1743536

Li, X., Ma, C., Xie, X., Sun, H., and Liu, X. (2016). Pulp regeneration in a full-length human tooth root using a hierarchical nanofibrous microsphere system. *Acta Biomater.* 35, 57–67. doi:10.1016/j.actbio.2016.02.040

Lim, H.-C., Nam, O. H., Kim, M.-J., El-Fiqi, A., Yun, H.-M., Lee, Y.-M., et al. (2016). Delivery of dexamethasone from bioactive nanofiber matrices stimulates odontogenesis of human dental pulp cells through integrin/BMP/mTOR signaling pathways. *Int. J. Nanomedicine* 11, 2557–2567. doi:10.2147/IJN.S97846

Lin, L. M., Ricucci, D., Saoud, T. M., Sigurdsson, A., and Kahler, B. (2020). Vital pulp therapy of mature permanent teeth with irreversible pulpitis from the perspective of pulp biology. *Aust. Endod. J.* 46, 154–166. doi:10.1111/aej.12392

Lin, L. M., Shimizu, E., Gibbs, J. L., Loghin, S., and Ricucci, D. (2014). Histologic and histobacteriologic observations of failed revascularization/revitalization therapy: A case report. *J. Endod.* 40, 291–295. doi:10.1016/j.joen.2013.08.024

Ma, X., Li, C., Jia, L., Wang, Y., Liu, W., Zhou, X., et al. (2016). Materials for retrograde filling in root canal therapy. *Cochrane Database Syst. Rev.* 12, CD005517. doi:10.1002/14651858.CD005517.pub2

Manfredi, M., Figini, L., Gagliani, M., and Lodi, G. (2016). Single versus multiple visits for endodontic treatment of permanent teeth. *Cochrane Database Syst. Rev.* 12, CD005296. doi:10.1002/14651858.CD005296.pub3

Mc, B., Mtp, A., A, A., Ea, M., Kj, S., Je, N., et al. (2019). A novel patient-specific three-dimensional drug delivery construct for regenerative endodontics. *J. Biomed. Mat. Res.* 107, 1576–1586. doi:10.1002/jbm.b.34250

Morsczeck, C., and Reichert, T. E. (2018). Dental stem cells in tooth regeneration and repair in the future. *Expert Opin. Biol. Ther.* 18, 187–196. doi:10.1080/14712598.2018.1402004

Murray, P. E., Garcia-Godoy, F., and Hargreaves, K. M. (2007). Regenerative endodontics: A review of current status and a call for action. *J. Endod.* 33, 377–390. doi:10.1016/j.joen.2006.09.013

Murray, P. E. (2018). Platelet-rich plasma and platelet-rich fibrin can induce apical closure more frequently than blood-clot revascularization for the regeneration of immature permanent teeth: A meta-analysis of clinical efficacy. *Front. Bioeng. Biotechnol.* 6, 139. doi:10.3389/fbioe.2018.00139

Nagata, J. Y., Soares, A. J., Souza-Filho, F. J., Zaia, A. A., Ferraz, C. C. R., Almeida, J. F. A., et al. (2014). Microbial evaluation of traumatized teeth treated with triple antibiotic paste or calcium hydroxide with 2% chlorhexidine gel in pulp revascularization. *J. Endod.* 40, 778–783. doi:10.1016/j.joen.2014.01.038

Nakashima, M., and Akamine, A. (2005). The application of tissue engineering to regeneration of pulp and dentin in endodontics. *J. Endod.* 31, 711–718. doi:10.1097/01.don.0000164138.49923.e5

Neelakantan, P., Romero, M., Vera, J., Daood, U., Khan, A. U., Yan, A., et al. (2017). Biofilms in endodontics-current status and future directions. *Int. J. Mol. Sci.* 18, E1748. doi:10.3390/ijms18081748

Palasuk, J., Kamocki, K., Hippenmeyer, L., Platt, J. A., Spolnik, K. J., Gregory, R. L., et al. (2014). Bimix antimicrobial scaffolds for regenerative endodontics. *J. Endod.* 40, 1879–1884. doi:10.1016/j.joen.2014.07.017

Pankajakshan, D., Albuquerque, M. T. P., Evans, J. D., Kamocka, M. M., Gregory, R. L., and Bottino, M. C. (2016). Triple antibiotic polymer nanofibers for intracanal drug delivery: Effects on dual species biofilm and cell function. *J. Endod.* 42, 1490–1495. doi:10.1016/j.joen.2016.07.019

Porter, M. L. A., Münchow, E. A., Albuquerque, M. T. P., Spolnik, K. J., Hara, A. T., and Bottino, M. C. (2016). Effects of novel 3-dimensional antibiotic-containing electrospun scaffolds on dentin discoloration. *J. Endod.* 42, 106–112. doi:10.1016/j.joen.2015.09.013

Qu, T., Jing, J., Jiang, Y., Taylor, R. J., Feng, J. Q., Geiger, B., et al. (2014). Magnesium-containing nanostructured hybrid scaffolds for enhanced dentin regeneration. *Tissue Eng. Part A* 20, 2422–2433. doi:10.1089/ten.TEA.2013.0741

Qu, T., and Liu, X. (2013). Nano-structured gelatin/bioactive glass hybrid scaffolds for the enhancement of odontogenic differentiation of human dental pulp stem cells. *J. Mat. Chem. B* 1, 4764–4772. doi:10.1039/C3TB21002B

Rafter, M. (2005). Apexification: A review. *Dent. Traumatol.* 21, 1–8. doi:10.1111/j.1600-9657.2004.00284.x

Ribeiro, J. S., Münchow, E. A., Ferreira Bordini, E. A., de Oliveira da Rosa, W. L., and Bottino, M. C. (2020). Antimicrobial therapeutics in regenerative endodontics: A scoping review. *J. Endod.* 46, S115–S127. doi:10.1016/j.joen.2020.06.032

Rosa, V., Zhang, Z., Grande, R. H. M., and Nör, J. E. (2013). Dental pulp tissue engineering in full-length human root canals. *J. Dent. Res.* 92, 970–975. doi:10.1177/0022034513505772

Ruparel, N. B., Teixeira, F. B., Ferraz, C. C. R., and Diogenes, A. (2012). Direct effect of intracanal medicaments on survival of stem cells of the apical papilla. *J. Endod.* 38, 1372–1375. doi:10.1016/j.joen.2012.06.018

Sampaio-Maia, B., Caldas, I. M., Pereira, M. L., Pérez-Mongiovi, D., and Araujo, R. (2016). The oral microbiome in Health and its implication in oral and systemic diseases. *Adv. Appl. Microbiol.* 97, 171–210. doi:10.1016/bs.aambs.2016.08.002

Schmalz, G., Widbiller, M., and Galler, K. M. (2020). Clinical perspectives of pulp regeneration. *J. Endod.* 46, S161–S174. doi:10.1016/j.joen.2020.06.037

Sheikh, Z., Najeeb, S., Khurshid, Z., Verma, V., Rashid, H., and Glogauer, M. (2015). Biodegradable materials for bone repair and tissue engineering applications. *Mater. (Basel)* 8, 5744–5794. doi:10.3390/ma8095273

Sill, T. J., and von Recum, H. A. (2008). Electrospinning: Applications in drug delivery and tissue engineering. *Biomaterials* 29, 1989–2006. doi:10.1016/j.biomaterials.2008.01.011

Soares, D. G., Zhang, Z., Mohamed, F., Eyster, T. W., de Souza Costa, C. A., and Ma, P. X. (2018). Simvastatin and nanofibrous poly(l-lactic acid) scaffolds to promote the odontogenic potential of dental pulp cells in an inflammatory environment. *Acta Biomater.* 68, 190–203. doi:10.1016/j.actbio.2017.12.037

Song, M., Cao, Y., Shin, S.-J., Shon, W.-J., Chugal, N., Kim, R. H., et al. (2017). Revascularization-associated intracanal calcification: Assessment of prevalence and contributing factors. *J. Endod.* 43, 2025–2033. doi:10.1016/j.joen.2017.06.018

Sun, H., Feng, K., Hu, J., Soker, S., Atala, A., and Ma, P. X. (2010). Osteogenic differentiation of human amniotic fluid-derived stem cells induced by bone morphogenetic protein-7 and enhanced by nanofibrous scaffolds. *Biomaterials* 31, 1133–1139. doi:10.1016/j.biomaterials.2009.10.030

Sundararaj, S. C., Thomas, M. V., Dziubla, T. D., and Puleo, D. A. (2014). Bioerodible system for sequential release of multiple drugs. *Acta Biomater.* 10, 115–125. doi:10.1016/j.actbio.2013.09.031

Wang, J., Liu, X., Jin, X., Ma, H., Hu, J., Ni, L., et al. (2010). The odontogenic differentiation of human dental pulp stem cells on nanofibrous poly(L-lactic acid) scaffolds *in vitro* and *in vivo*. *Acta Biomater.* 6, 3856–3863. doi:10.1016/j.actbio.2010.04.009

Yang, F., Murugan, R., Wang, S., and Ramakrishna, S. (2005). Electrospinning of nano/micro scale poly(L-lactic acid) aligned fibers and their potential in neural tissue engineering. *Biomaterials* 26, 2603–2610. doi:10.1016/j.biomaterials.2004.06.051

Yang, X., Yang, F., Walboomers, X. F., Bian, Z., Fan, M., and Jansen, J. A. (2010). The performance of dental pulp stem cells on nanofibrous PCL/gelatin/nHA scaffolds. *J. Biomed. Mat. Res. A* 93, 247–257. doi:10.1002/jbm.a.32535

Yoo, Y.-J., Oh, J.-H., Zhang, Q., Lee, W., and Woo, K. M. (2018). Dimethyloxalylglycine-embedded poly(ε-caprolactone) fiber meshes promote odontoblastic differentiation of human dental pulp-derived cells. *J. Endod.* 44, 98–103.e1. doi:10.1016/j.joen.2017.09.002

Yun, H.-M., Kang, S.-K., Singh, R. K., Lee, J.-H., Lee, H.-H., Park, K.-R., et al. (2016). Magnetic nanofiber scaffold-induced stimulation of odontogenesis and pro-angiogenesis of human dental pulp cells through Wnt/MAPK/NF-κB pathways. *Dent. Mat.* 32, 1301–1311. doi:10.1016/j.dental.2016.06.016

Zein, N., Harmouch, E., Lutz, J.-C., Fernandez De Grado, G., Kuchler-Bopp, S., Clauss, F., et al. (2019). Polymer-based instructive scaffolds for endodontic regeneration. *Mater. (Basel)* 12, E2347. doi:10.3390/ma12152347

Zhang, H., Liu, S., Zhou, Y., Tan, J., Che, H., Ning, F., et al. (2012). Natural mineralized scaffolds promote the dentinogenic potential of dental pulp stem cells via the mitogen-activated protein kinase signaling pathway. *Tissue Eng. Part A* 18, 677–691. doi:10.1089/ten.TEA.2011.0269

Zhang, Q. L., Dong, C. Y., Liu, L., Wen, S. P., and Wang, X. Y. (2019). Effects of electrospun collagen nanofibrous matrix on the biological behavior of human dental pulp cells. *Beijing Da Xue Xue Bao Yi Xue Ban.* 51, 28–34. doi:10.19723/j.issn.1671-167X.2019.01.006

Zijah, Vahid, Salehi, Roya, Aghazadeh, Marziyeh, Samiei, Mohammad, Alizadeh, Effat, and Davaran, S. (2017a). Towards optimization of odonto/osteogenic bioengineering: *In vitro* comparison of simvastatin, sodium fluoride, melanocyte-stimulating hormone. *Vitro Cell. Dev. Biol. -Animal.* 53, 502–512. doi:10.1007/s11626-017-0141-6

Zijah, V., Salehi, R., Aghazadeh, M., Samiei, M., Alizadeh, E., and Davaran, S. (2017b). Towards optimization of odonto/osteogenic bioengineering: *In vitro* comparison of simvastatin, sodium fluoride, melanocyte-stimulating hormone. *Vitro Cell. Dev. Biol. -Animal.* 53, 502–512. doi:10.1007/s11626-017-0141-6

frontiers | Frontiers in Bioengineering and Biotechnology

TYPE Review
PUBLISHED 17 January 2023
DOI 10.3389/fbioe.2023.1050916

OPEN ACCESS

EDITED BY
Xing Wang,
Shanxi Medical University, China

REVIEWED BY
Dehao Fu,
Shanghai General Hospital, China
Lu Wang,
Shanxi Medical University, China

*CORRESPONDENCE
Fengqing Shang,
shangfengqing1988@163.com
Zhifei Zhou,
geoffrey2002@sina.com

†These authors have contributed equally to this work and share first authorship

SPECIALTY SECTION
This article was submitted to Biomaterials, a section of the journal Frontiers in Bioengineering and Biotechnology

RECEIVED 18 October 2022
ACCEPTED 02 January 2023
PUBLISHED 17 January 2023

CITATION
Liu F, Sun T, An Y, Ming L, Li Y, Zhou Z and Shang F (2023), The potential therapeutic role of extracellular vesicles in critical-size bone defects: Spring of cell-free regenerative medicine is coming. *Front. Bioeng. Biotechnol.* 11:1050916. doi: 10.3389/fbioe.2023.1050916

The potential therapeutic role of extracellular vesicles in critical-size bone defects: Spring of cell-free regenerative medicine is coming

Fen Liu[1†], Tianyu Sun[2†], Ying An[3], Leiguo Ming[4], Yinghui Li[5], Zhifei Zhou[6*] and Fengqing Shang[7*†]

[1]Department of Periodontology, Shenzhen Stomatological Hospital (Pingshan), Southern Medical University, Shenzhen, Guangdong, China, [2]Department of Periodontology, Stomatological Hospital, Southern Medical University, Guangzhou, Guangdong, China, [3]State Key Laboratory of Military Stomatology and National Clinical Research Center for Oral Diseases and Shaanxi Engineering Research Center for Dental Materials and Advanced Manufacture and Department of Periodontology, School of Stomatology, Fourth Military Medical University, Xi'an, Shaanxi, China, [4]Department of Research and Development, Shaanxi Zhonghong Institute of Regenerative Medicine, Xi'an, Shaanxi, China, [5]Department of Orthodontics, Stomatological Hospital, Hebei Medical University, Shijiazhuang, Hebei, China, [6]Department of Stomatology, General Hospital of Tibetan Military Command, Lhasa, Tibet, China, [7]Department of Stomatology, Air Force Medical Center, Fourth Military Medical University, Beijing, China

In recent years, the incidence of critical-size bone defects has significantly increased. Critical-size bone defects seriously affect patients' motor functions and quality of life and increase the need for additional clinical treatments. Bone tissue engineering (BTE) has made great progress in repairing critical-size bone defects. As one of the main components of bone tissue engineering, stem cell-based therapy is considered a potential effective strategy to regenerate bone tissues. However, there are some disadvantages including phenotypic changes, immune rejection, potential tumorigenicity, low homing efficiency and cell survival rate that restrict its wider clinical applications. Evidence has shown that the positive biological effects of stem cells on tissue repair are largely mediated through paracrine action by nanostructured extracellular vesicles (EVs), which may overcome the limitations of traditional stem cell-based treatments. In addition to stem cell-derived extracellular vesicles, the potential therapeutic roles of nonstem cell-derived extracellular vesicles in critical-size bone defect repair have also attracted attention from scholars in recent years. Currently, the development of extracellular vesicles-mediated cell-free regenerative medicine is still in the preliminary stage, and the specific mechanisms remain elusive. Herein, the authors first review the research progress and possible mechanisms of extracellular vesicles combined with bone tissue engineering scaffolds to promote bone regeneration *via* bioactive molecules. Engineering modified extracellular vesicles is an emerging component of bone tissue engineering and its main progression and clinical

Abbreviations: ADSCs, adipose-derived stem cells; ALP, alkaline phosphatase; BMMSCs, bone marrow mesenchymal stem cells; BMP2, bone morphogenetic protein 2; BTE, bone tissue engineering; DC, dendritic cell; EVs, extracellular vesicles; HIF-1α, hypoxia inducible factor-1α; IL, interleukin; iPS-MSCs, MSCs derived from induced pluripotent stem cells; MAPK, mitogen-activated protein kinase; MSCs, mesenchymal stem cells; NF-κB, nuclear factor-κB; OCN, osteocalcin; PI3K, phosphoinositide 3-kinase; PLGA, polylactic-co-glycolic acid; RANKL, receptor activator of nuclear factor-κB ligand; Runx2, runt-related transcription factor 2; SHEDs, stem cells from human exfoliated deciduous teeth; Smad4, mothers against decapentaplegic homologue 4; TCP, tricalcium phosphate; TGF, transforming growth factor; UCMSCs, umbilical cord mesenchymal stem cells; UVECs, umbilical vein endothelial cells; VEGF, vascular endothelial growth factor.

applications will be discussed. Finally, future perspectives and challenges of developing extracellular vesicle-based regenerative medicine will be given. This review may provide a theoretical basis for the future development of extracellular vesicle-based biomedicine and provide clinical references for promoting the repair of critical-size bone defects.

KEYWORDS

extracellular vesicles, critical-size bone defects, cell-free therapy, bioactive scaffold, bone tissue regeneration, engineering modification

1 Introduction

Critical-size bone defects refer to the smallest intraosseous wound that cannot heal spontaneously (Falacho et al., 2021). The aetiologies include trauma, tumour and infection (Shang et al., 2020). In today's rapidly ageing global population, the incidence of this disease has significantly increased. Critical-size bone defects considerably affect patients' motor function and quality of life and increase the need for additional clinical treatments (Nauth et al., 2018). Currently, the clinical strategies for repairing critical-size bone defects mainly include autologous or allogeneic bone transplantation and synthetic biomaterial transplantation (Yu et al., 2022). Autologous bone transplantation is generally considered the gold standard for repairing critical-size bone defects; however, there are many limitations, including injury to the donor site, limited source, and unpredicted spontaneous resorption and disease transmission risk (Stahl and Yang, 2021). The clinical application of pure allogeneic bone transplantation also has some disadvantages, manifested by immune rejection (Behrend et al., 2016) or unwanted disease transmission (Baldwin et al., 2019).

Bone tissue engineering (BTE), which uses biomaterials with sophisticated biophysical or biochemical features to circumvent the constraints described above, has made great progress in repairing critical-size bone defects. BTE includes three basic components: biological scaffolds, seed cells and bone inductive factors (Roseti et al., 2017). Biological scaffolds are commonly referred to as bioactive materials, which can be combined with mesenchymal stem cells (MSCs) and their secreted cytokines to repair critical-size bone defects (Wu et al., 2021). MSCs are a heterogeneous mesenchymal stem cell subpopulation with the potential for multidirectional differentiation into mesoderm, ectoderm and endoderm lineages (Bianco and Gehron Robey, 2000). Therefore, stem cell therapy is considered to be a potential effective strategy to regenerate bone tissues (Silva et al., 2021). However, stem cell therapy also has some disadvantages that restrict its wider clinical applications, including phenotypic changes, immune rejection, potential tumorigenicity, low homing efficiency and cell survival rate (Sissung and Figg, 2020). These concerns, together with problems caused by storage and transport, further limit the application of MSCs in repairing critical-size bone defects (Nagelkerke et al., 2021). In addition, even after successful transplantation, factors such as donor age, passage times of *in vitro* expansion, culture conditions, cell transplantation procedures and recipient pathological microenvironments also have adverse effects on the survival and biological characteristics of cells (Rezaie et al., 2018). Many studies have attempted to overcome these shortcomings by genetically modifying MSCs and optimizing their culture conditions (García-Sánchez et al., 2019), but key limitations on the biological safety of MSCs still exist.

In recent years, cell-free regenerative medicine for critical-size bone defects has received extensive attention (Kang et al., 2022). Evidence has shown that the positive biological effects of MSCs on tissue repair are largely mediated through paracrine action by extracellular vesicles (EVs) rather than direct differentiation into parenchymal cells to repair or replace damaged tissues (Zhang J. et al., 2016). EVs are double phospholipid bilayer vesicles with nanostructures that bud from the membrane of their parent cells and play vital roles in cell-to-cell communications (Vizoso et al., 2017). Based on different diameters, compositions and sources, EVs mainly include exosomes, microvesicles and apoptotic bodies (Figure 1) (Zhou et al., 2022). Previously, the effects of EVs were mistaken for removing the generated waste of parent cells. Currently, EVs are reputed to be typical representatives of nanotherapeutics carrying abundant nucleic acids, proteins, lipid substances and bioactive small molecules derived from parent cells (Puddu et al., 2010). They transfer internal cargoes to target cells through ligand–receptor interactions, endocytosis or direct membrane fusion to exert regulatory effects (Li Q. C. et al., 2022). Studies have shown that EVs obtained from MSCs have more ideal biocompatibility, effective cell interaction characteristics, exogenous cargo delivery and the ability to target specific tissues (van der Koog et al., 2022), and most importantly, they overcome the limitations of traditional MSC treatment (Malekpour et al., 2022). In recent years, in studies of bone regeneration and homeostasis, EVs have also become remarkable hotspots (Zara et al., 2011). EVs loaded with bioactive materials can significantly promote osteogenesis, angiogenesis and inflammation regulation, thus effectively repairing critical-size bone defects (Liang et al., 2022). Because EV subtypes do not have well-recognized specific markers, the International Society for Extracellular Vesicles recommends using "small EVs" for EV subtypes (Théry et al., 2018). However, most studies used the term "exosomes" in their experiments. In this review, to respect the cited literature, we reserve to use the term "exosomes" when the author gave a specific definition in the article. We use the generic term "EVs" when they were not clearly noted.

Although considerable research on EVs has focused on promoting the repair of critical-size bone defects, their development is still in the preliminary stage, and the specific mechanisms remain elusive. What is more, for critical-size bone defects, application of EVs alone could not fill defect spaces and guide bioactive molecules to repair and reconstruct the bone defect. Thus, some bioactive scaffolds are needed in EVs-based BTE application. Herein, the authors first review the research progress and possible mechanisms of EVs combined with BTE scaffolds to promote bone regeneration *via* bioactive molecules. Engineering modified EVs is an emerging component of BTE. Their main progress and opportunities will then be discussed. Finally, future perspectives and challenges of the developing EV-based regenerative

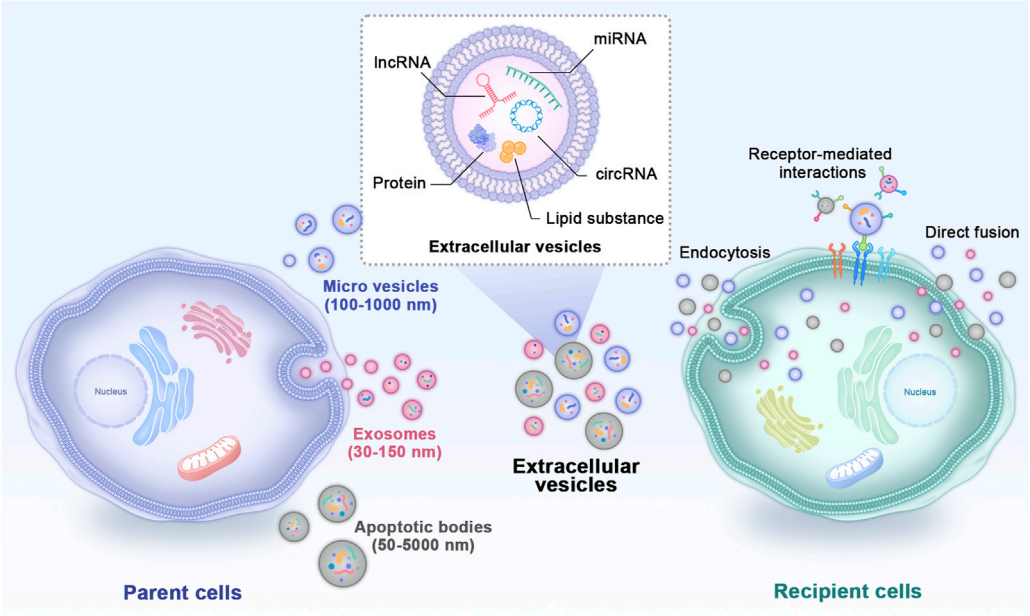

FIGURE 1
Types and internal cargoes of EVs and the way they act on target cells. EVs mainly include exosomes, microvesicles and apoptotic bodies. EVs carry abundant amounts of proteins, miRNAs, mRNAs, circRNAs and other biological molecules derived from parent cells. They transfer internal cargoes to target cells through ligand–receptor interactions, endocytosis or direct membrane fusion. EVs: extracellular vesicles.

medicine are given. Thus, this review may provide a theoretical basis for the future development of the EV-based biomedicine and provide clinical references for promoting the repair of critical-size bone defects.

2 Potential therapeutic applications of extracellular vesicles in bone repair

Tissue regenerative medicine aims to enhance the positive effects of stem cells delivered *in vivo*. To date, multiple studies have demonstrated that very few transplanted cells can be tracked *in vivo* after 4–8 weeks, suggesting that their regenerative ability is more likely to be associated with the indirect mechanisms of seed cells, including cytokine paracrine, immunoregulation, and signal transduction (Caplan, 2019). Based on that, researchers used cell aggregates with abundant extracellular matrix to replace dispersed stem cells, and the obtained results showed promising new bone formation in critical-size bone defects in osteoporosis rats (Shang et al., 2014). Although cell aggregates showed better results in preclinical experiments, limitations of cell-based therapy still rendered it taking a step from the research stage to clinical applications. Stem cell-based regenerative medicine has some disadvantages. These limitations, together with problems caused by storage and transport, further limit the application of MSCs in repairing critical-size bone defects (Sissung and Figg, 2020). EVs could overcome these shortages of stem cells while maintain similar functions in regenerating critical-size bone defects. Besides, effects of stem cells in BTE largely dependent on their paracrine action. Direct use of EVs may lead to more stable and predicable results. These are all reasons for applying EVs in cell-free regenerative medicine. In a femur fracture animal model without EV secretion, delayed bone healing was observed, while the healing situation was improved by injecting additional EVs (Furuta et al., 2016). Moreover, the application of MSC-derived EVs also shortened the recovery time, suggesting that EVs promote bone tissue regeneration. This finding highlighted the perspective of EV-mediated bone regenerative medicine (Gunawardena et al., 2019). Although the study of MSC-derived EVs in regenerative medicine is just at the outset, preclinical tests have shown more positive results and fewer adverse effects compared to applications of MSCs.

2.1 Parent cells of extracellular vesicles

EVs were originally observed in reticulocytes during their maturation and were treated as a way to remove waste transferrin receptors (Harding et al., 1983). Afterwards, the phenomenon of EV secretion was found not only in most human fluids but also in a variety of cell types (Johnstone et al., 1987). EVs take chemical or genetic materials to pass messages for cell–cell communication. Thus, their function is more than that of superfluous membrane vesicles. The possible therapeutic roles of takeover stem cells are being further explored. Mounting evidence indicates that EVs can facilitate cell differentiation and viability and are actively involved in bone homeostasis through cargoes containing microRNAs (miRNAs), proteins and so on.

2.1.1 Mesenchymal stem cells-derived extracellular vesicles

During bone remodelling, the interaction between osteoblasts and osteoclasts is necessary to replace mechanically weak fibrous bone with

mechanically strong lamellar bone. Takeuchi et al. (2019) confirmed that MSC-derived EVs manifested the same effects in critical-size bone defect repair with a complete MSC secretome, and both groups had almost half of the defect site covered with new bone tissues after 4 weeks of treatment by promoting angiogenesis and osteogenesis. MSC-derived exosomes, which are the most active vesicles from MSCs (Phan et al., 2018), have been identified as important messengers (Lai et al., 2010) and play a more vital immunoregulatory role than the parent cells (Del Fattore et al., 2015). It has been demonstrated that MSC-derived EVs can accelerate every step of bone defect repair, contributing to bone rehabilitation through immunoregulation. In the regenerative treatment of critical-size bone defects, MSC-derived EVs can stimulate the proliferation and angiogenesis of osteoblasts by delivering endogenous cargoes and inhibit osteoclast maturation (Qin et al., 2016a). Recent studies supported the view that MSC-derived EVs had comparable therapeutic properties compared with their parent cells (Kou et al., 2018). The expression of the protein spectrum showed that 1,927 of a total of 6,342 proteins were expressed in both MSCs and MSC-derived EVs (Anderson et al., 2016). Hence, EVs secreted by different MSCs may inherit matrilineal characteristics in bone regeneration and repair *via* similar mechanisms to parent cells (Tan et al., 2021). Therefore, selecting an applicable source of parent cells is extremely important for ideal applications of EVs in hard tissue regeneration for critical-size bone defects (Behera and Tyagi, 2018). The commonly applied parent MSCs of EVs mainly include bone marrow mesenchymal stem cells (BMMSCs) (Qin et al., 2016b), adipose-derived stem cells (ADSCs) (Li et al., 2018), umbilical cord mesenchymal stem cells (UCMSCs) (Zhang Y. et al., 2021), MSCs derived from induced pluripotent stem cells (iPS-MSCs) (Fu et al., 2012) and stem cells from human exfoliated deciduous teeth (SHEDs) (Wang M. et al., 2020).

BMMSCs are a major type of MSCs. Their bioactive molecules are now extensively investigated for better applications. Proteomic analyses indicated that as many as 1,533 proteins were involved in various biological actions (Baberg et al., 2019). Preclinical studies have also shown that BMMSC-derived EVs exerted favourable effects in promoting osteogenesis and angiogenesis of osteoblast precursor cells at the injury sites in a critical-size bone defect model, thus forming ideal bone mineralization (Zhang et al., 2022). Martins et al. (2016) discovered that hBMMSC-derived exosomes could promote osteogenic differentiation, as verified by early alkaline phosphatase (ALP) activation and bone morphogenetic protein 2 (BMP2) upregulation.

ADSCs are regarded as one of the most applicable cell sources for EVs because they can be more easily obtained and are widely distributed in the human body (Parker and Katz, 2006). In addition, these cells rapidly proliferate *in vitro* and retain stem cell phenotypes together with less susceptibility to ageing (Mirsaidi et al., 2012). These advantages make them favourable parent cells for increasing EV isolation (McIntosh et al., 2006). Although the osteogenic capacity of ADSCs is still controversial compared with BMMSCs, hADSC-derived exosomes have been proven to exhibit the capabilities of enhancing the proliferation, migration and osteogenic differentiation of hBMMSCs *ex vivo* and accelerating bone regeneration at critical-size bone defect sites *in vivo* (Liu A. et al., 2021).

UCMSCs Umbilical cords are cheap and exhaustless stem cell sources (Wang et al., 2004). hUCMSCs are primitive MSC subpopulations obtained from human postnatal waste tissues (Hendijani et al., 2014). Their collection process requires no invasive operation and has no ethical or moral issues like human embryonic stem cells (Zhao et al., 2010). Compared with other MSCs, hUCMSCs exhibit higher pluripotency (Wang et al., 2015), less immunorejection *in vivo* and no tumorigenic risk peculiarities (Can and Karahuseyinoglu, 2007). Instead of directly inducing osteogenic and chondrogenic differentiation, hUCMSCs improved bone regeneration by indirectly inducing angiogenesis. To date, hUCMSCs have shown significant clinical potential and have also attracted extensive attention from scholars in the bone regeneration field (Wang L. et al., 2020). In an animal model of critical-size bone defects of rat femurs, exosomes derived from hUCMSCs promoted angiogenesis at the injury site through hypoxia inducible factor-1α (HIF-1α) to achieve bone repair (Zhang et al., 2019).

iPS-MSCs Similar to hUCMSCs, there are neither immunorejection nor ethical problems in the clinical applications of iPSCs. However, some scholars have pointed out that using iPSCs may bring about tumorigenic risks (Jiang et al., 2016). Compared with iPSCs, iPS-MSCs can maintain their self-renewal capacity even after forty passages and have no tumorigenic risk (Lian et al., 2010). In treating bone defects, applications of iPS-MSCs have shown promising prospects in promoting bone repair and regeneration due to their strong proliferation and immunoregulation abilities (Fu et al., 2012). Because EVs from iPS-MSCs have nearly the same biological characteristics as the parent cell, iPS-MSCs have attracted increasing attention as a cell source to promote bone regeneration by using EVs (Zhang J. et al., 2016). *In vivo* studies reported that hiPS-MSC-derived exosomes enhanced osteogenesis in ovariectomized rats with critical-size calvarial defects (Qi et al., 2016). Moreover, iPS-MSC-derived exosomes may play a certain role in bone defect repair by promoting angiogenesis, as previous research has already demonstrated that they have significant therapeutic effects in treating ischaemic diseases (Hu et al., 2015).

SHEDs Deciduous teeth are the only organ that are replaceable and exfoliate naturally from the human body. Additionally, there are no ethical issues when harvesting stem cells from them, which makes these cells attractive for clinical therapy. SHEDs are not mature MSCs and have multidirectional differentiation potentials (Martinez Saez et al., 2016). Compared with BMMSCs, SHEDs showed increased proliferation ability because they secreted more growth factors, including fibroblast growth factor 2 and transforming growth factor-β2 (TGF-β2) (Nakamura et al., 2009). Studies have also demonstrated that SHED-derived exosomes combined with tricalcium phosphate (TCP) could improve alveolar bone repair by inducing angiogenesis and osteogenesis (Wu et al., 2019).

2.1.2 Non-mesenchymal stem cells-derived extracellular vesicles

MSCs differentiating into osteoblasts participate not only in endochondral ossification but also in the formation of intramembranous bones. These two procedures are essential for bone formation. In addition to the participation of MSCs, new bone formation and regeneration also require the functions of osteoblasts, osteoclasts, and chondrocytes. In particular, endothelial cells play a part in osteoblast maturation and angiogenesis (Qin et al., 2016a). A favourable microenvironment is essential for ideal osteogenesis and angiogenesis. It is well-known that immunoregulatory-related cells are of critical importance in maintaining an appropriate microenvironment for new bone and

vascular formation. Thus, the potential therapeutic roles of non-MSC-derived EVs in critical-size bone defect repair have also attracted attention from scholars in recent years.

Osteoblasts are differentiated from BMMSCs. They synthesize and mineralize the bone matrix by releasing collagen and glycoprotein. Osteoblast-derived exosomes were confirmed to regulate Wnt and calcium signalling pathways and miRNAs to induce osteogenic differentiation of BMMSCs (Cui et al., 2016). Osteo-related miRNAs (miR-1192, miR-680 and miR-302a) were expressed in preosteoblast MC3T3-E1-derived exosomes, and the miRNAs in the target cells were also altered to promote their differentiation into osteoblasts (Cui et al., 2016). The effects of these exosomes have even been demonstrated to surpass the original extracellular matrix of parent cells in inducing the directional differentiation of stromal cells (Narayanan et al., 2018). In one study, the comprehensive analysis of EVs showed that the proteome profile changed continuously at different stages of osteoblast mineralization. At the later stage of mineralization, proteins with specific functions in promoting angiogenesis and bone development are enriched in EVs (Davies et al., 2019). A previous study confirmed that osteoblast-derived EVs could regulate osteoclast differentiation through the receptor activator of nuclear factor-κB ligand (RANKL)-RANK signalling pathway. Live cell imaging in the transgenic zebrafish fracture healing model also found internalization of osteoblast-derived EVs within osteoclasts (Kobayashi-Sun et al., 2020).

Osteocytes are terminally differentiated cells, occupying the largest proportion of cells that constitute bone tissues. Although soluble factors and signalling molecules secreted from osteocytes are considered to play key roles in the maintenance of bone homeostasis, current studies on EVs derived from osteocytes are very limited. It was confirmed that osteocyte-derived exosomes contained miRNAs that contributed to bone remodelling (Sato et al., 2017). Osteocytes are sensitive to mechanical stress and respond to external stimuli by regulating the internal cargoes of their exosomes. EVs derived from osteocytes can promote osteogenic differentiation when exposed to mechanical stress. RNA sequencing results suggested that the possible mechanisms were to upregulate miR-181b-5p, thereby inhibiting phosphatase and tensin homologue and thus activating the protein kinase B signalling pathway (Lv et al., 2020). In another similar study, osteocytes subjected to fluid shear stress were able to recruit more stromal progenitor cells through specific EVs, thus promoting local bone remodelling (Eichholz et al., 2020). Of note, the processes of repairing critical-size bone defects by osteocyte-derived EVs are negatively regulated by muscle. Myostatin secreted by muscle can upregulate the expression of miR-218 in exosomes derived from osteocytes, thereby blocking runt-related transcription factor 2 (Runx2) and Wnt signalling pathways and ultimately inhibiting the osteogenic differentiation of BMMSCs (Qin et al., 2017).

Endothelial cells Angiogenesis plays a key role in bone metabolism, in which endothelial cells comprise a single layer of the inner wall of blood vessels. The endothelial cells carry circulating blood macromolecules for the surrounding cells to guarantee their metabolism. Exosomes derived from endothelial cells highly directionally target bone tissues, inhibiting the development and activity of osteoclasts (Li X. et al., 2016). In a study of distraction osteogenesis, endothelial progenitor cell-derived exosomes promoted angiogenesis by upregulating miR-126, thereby accelerating the formation of new bones at the defect site (Jia et al., 2019). Another study also found that endothelial progenitor cell-derived EVs could directly act on BMMSCs to promote their osteogenic differentiation *in vitro* (Qin and Zhang, 2017).

Immune cells in the microenvironment of critical-size bone defects specifically activate osteoblasts or inhibit osteoclasts through paracrine action. EVs derived from immune cells trigger an immune response by presenting certain antigens. Dendritic cell (DC)-derived EVs were demonstrated to have a good osteogenic inductive effect (Cao et al., 2021), and the possible mechanisms were to regulate the Hippo signalling pathway and induce bone regeneration through exosomal miR-335 *via* LATS1 signalling (Cao et al., 2021). DC-derived exosomes also contain immunoregulatory cargoes TGF-β1 and interleukin (IL)-10, which enhance the recruitment of regulatory T-cell in inflammatory responses and ultimately inhibit bone loss caused by osteoclasts (Elashiry et al., 2020). Active DC-derived EVs may bring about the activation of humoral immune responses and $CD4^+/CD8^+$ T-cell, while immature DC-derived EVs were more likely to decrease systematic inflammation (Lindenbergh and Stoorvogel, 2018). In addition to DCs, exosomes from non-polarized M0, polarized M1 (proinflammatory phenotype) and M2 (anti-inflammatory phenotype) macrophages could specifically target BMMSCs to promote their directional osteogenic differentiation (Xia et al., 2020). Macrophage-derived exosomes can also regulate the gene expression of salt-inducible kinase 2/3 through miR-5106, thereby inducing osteoblast differentiation (Xiong et al., 2020). Effective regulation of the cargoes of EVs derived from immune cells will help scholars better understand the crosstalk between different cells in the microenvironment of critical-size bone defects in the future.

2.2 Applications of extracellular vesicles-loaded bioactive materials in bone tissue engineering

EV-mediated bone regeneration strategies have attracted increasing attention in the treatment of critical-size bone defects in recent years (Fernandez-Yague et al., 2015). Accumulating studies have shown that EVs alone or loaded in different scaffolds, such as hydrogels, can significantly promote local bone regeneration. Scaffold materials are required to fill defect spaces and guide bioactive molecules, such as EVs, to exert certain effects on bone defect repair and reconstruction, especially critical-size bone defects. EV-loaded scaffold materials have already achieved gratifying results in repairing animal models of critical-size bone defects. It effectively stimulates bone regeneration in critical-size skull defects (Qin et al., 2016b), promotes cartilage repair and subchondral bone regeneration in osteochondral defects (Zhang S. et al., 2016), and enhances angiogenesis in repairing femoral defects (Liu et al., 2017). In mouse animal models, EV-loaded scaffolds also showed a more ideal ability to promote bone regeneration and angiogenesis compared with the application of scaffold materials alone, suggesting that scaffolds rich in EVs are an attractive treatment alternative for repairing critical-size bone defects (Xie et al., 2017). Applications of different types of bioactive materials loaded with EVs in BTE are summarized in Table 1.

TABLE 1 Applications and possible mechanisms of different EVs-loaded bioactive scaffold materials in BTE.

Bioactive scaffold materials	Parent cells of loaded EVs	Nanovesicles	Applications and possible mechanisms	References
Hydrogels				
Hydrogel	BMMSCs	EVs	Stimulating bone growth in critical-sized calvarial bone defects through miR-196a by regulating osteoblastic differentiation	Qin et al. (2016b)
Hydrogel	hADSCs	Exosomes	Enhancing the bone regenerative capacity in calvarial defect by miR-375	Chen et al. (2017)
Injectable hydrogel	hUVECs	Exosomes	Promoting callus formation and fracture healing at the early over-active inflammation phase through inhibiting T-cell	Lin et al. (2021)
Alginate-Arg-Gly-Asp modified hydrogels	hMSCs	EVs	Sustained delivery of osteoinductive functional engineered EVs in calvarial defects	Huang et al. (2021)
Sulfur alcohol modified hyaluronic acid-heparin hydrogel	BMMSCs	EVs	Improving bone formation in the critical-size calvarial defects by regulating multiple signaling pathways through miRNA-196a	Qin et al. (2016b)
Extracellular matrix-mimic hydrogel	BMMSCs	Exosomes	Promoting the anabolism of chondrocytes by inhibiting inflammation and promoting growth plate injury repair through extracellular matrix remodeling	Guan et al. (2021)
Chitosan/β-glycerophosphate hydrogel	BMMSCs	EVs	Promoting angiogenesis in critical-sized rat calvarial defects by miR-21 targeting sprouty homolog 2	Wu et al. (2022)
Hyaluronic acid hydrogel	hUCMSCs	Secretion factors	Initiating osteogenesis of BMMSCs and promoting calvarial bone defect repair	Wang et al. (2015)
Hyaluronic acid-alginate hydrogel	hUCMSCs	Exosomes	Enhancing bone regeneration through promoting angiogenesis in critical-sized calvarial defects	Yang et al. (2020b)
Polyethylene glycol/DNA hybrid hydrogel	Stem cells from apical papilla	Exosomes	Promoting vascularized bone regeneration in the mandibular bone defect through highly expressed miRNA-126-5p and miRNA-150-5p	Jing et al. (2022)
Bioceramics				
β-TCP	hBMMSCs	Secretome	Improving MSCs differentiation capacity and reducing cell senescence by miR-10a	Katagiri et al. (2017)
β-TCP	hiPS-MSCs	Exosomes	Promoting bone regeneration in critical-sized calvarial defects by enhancing angiogenesis and the osteoinductivity of β-TCP through activating the PI3K/Akt signaling pathway	Qi et al. (2016) Zhang et al. (2016a)
β-TCP	SHEDs	Exosomes	Promoting neovascularization and new bone formation, through the adenosine 5′-monophosphate-activated protein kinase signaling pathway	Wu et al. (2019)
Mesoporous bioactive glass scaffold	rBMMSCs, rADSCs	Exosomes	Enhancing bone forming and inducing rapid initiation of bone regeneration by let-7a-5p, let-7c-5p, miR-328a-5p and miR-31a-5p targeting activin A receptor 1/2b and regulating Smad1/5/9 phosphorylation in cranial defect	Liu et al. (2021a)
Polylactic acid-calcium silicates-dicalcium phosphate dihydrate	ADSCs	EVs	Enhancing regenerative bone healing by stimulating the osteogenic commitment of hADSCs	Gandolfi et al. (2020)
Metals				
Ti6Al4V scaffolds	Schwann cells	Exosomes	Promoting the migration, proliferation and differentiation of BMMSCs in bone repair	Wu et al. (2020)
Titanium nanotubes	Macrophages	Exosomes	Activating autophagy during osteogenic differentiation	Wei et al. (2019a)
3D-printed titanium alloy scaffolds	hMSCs	Exosomes	Inducing osteogenic differentiation by up-regulating osteogenic miRNAs or down-regulating anti-osteogenic miRNAs to activate the PI3K and MAPK signaling pathways	Zhai et al. (2020)
Zinc	Nitric oxide synthase-1 positive cells	Matrix vesicles	Increasing the ALP activity of osteoblasts	Kawakubo et al. (2011)

(Continued on following page)

TABLE 1 (*Continued*) Applications and possible mechanisms of different EVs-loaded bioactive scaffold materials in BTE.

Bioactive scaffold materials	Parent cells of loaded EVs	Nanovesicles	Applications and possible mechanisms	References
Strontium-substituted calcium silicate	BMMSCs	Exosomes	Promoting angiogenesis of hUVECs through elevating miR-146a and inhibiting Smad4 proteins to accelerate developmental vascularization along with the neovascularization and bone regeneration in distal femur defects	Liu et al. (2021b)
Polymers				
Polycaprolactone scaffold	MSCs	Exosomes	Reducing the inflammation stimulated by inflammatory macrophages and further accelerating osteogenic differentiation of MSCs	Wang et al. (2020d)
Tannic acid modified sulfonated polyetheretherketone	BMMSCs	Exosomes	Exerting osteoimmunomodulation effect to promote osteogenesis through promoting macrophage M2 polarization *via* the NF-κB pathway	Fan et al. (2021)
Polydopamine-coating PLGA scaffolds	hADSCs	Exosomes	Promoting bone regeneration in critical-sized calvarial defects	Li et al. (2018)
PLGA-polyethyleneglycol-PLGA	human dental pulp stem cells	Exosomes	Providing pro-mineralization cues to drive local stem/progenitor cells towards osteogenic differentiation in critical-size calvarial bone defect	Swanson et al. (2020)
Others				
Hyaluronic acid	hMSCs	Exosomes	Promoting functional cartilage and subchondral bone repair	Zhang et al. (2022)
Type I collagen, fibronectin	MSCs	Exosomes	Promoting differentiation of MSCs	Narayanan et al. (2016)
Decalcified bone matrix	MSCs	EVs	Enhancing bone regeneration though promoting vascularization	Xie et al. (2017)

ADSCs: adipose derived stem cells; ALP: alkaline phosphatase; BMMSCs: bone marrow mesenchymal stem cells; β-TCP: β-tricalcium phosphate; BTE: bone tissue engineering; EVs: extracellular vesicles; iPS-MSCs: MSCs, derive from induced pluripotent stem cells; MAPK: mitogen-activated protein kinase; MSCs: mesenchymal stem cells; NF-κB: nuclear factor-κB; PI3K: phosphoinositide 3-kinase; PLGA: poly lactic-co-glycolic acid; SHEDs: stem cells from human exfoliated deciduous teeth; Smad: mothers against decapentaplegic homolog; UCMSCs: umbilical cord mesenchymal stem cells; UVECs: umbilical vein endothelial cells.

2.2.1 Applications of extracellular vesicles-loaded hydrogels

As mentioned above, EVs are an ideal seed cell substitute in BTE. In preclinical or clinical applications, it can avert the safety and ethical problems caused by cell-based therapy, and it is also an effective bone inductive substance. However, there are also many limitations in the application of EVs alone in critical-size bone defect repair. The typical one is that due to the clearance of the reticuloendothelial system, EVs are quickly lost *in vivo,* and therefore, it is difficult to reach an effective therapeutic concentration locally. Thus, clinical applications require appropriate scaffold materials to ensure sustained release of EVs and maintain a local effective concentration of EVs (Riau et al., 2019).

Hydrogels with suitable biocompatibility and controlled release kinetics have been regarded as a preferred carrier material for delivering EVs to bone defect sites (Yan et al., 2020). Subcutaneous implantation of type I collagen hydrogel loaded with hBMMSC-derived exosomes showed better regenerative potential through the upregulation of Runx2 and osterix (Narayanan et al., 2016). EVs loaded in the hydrogel could also improve the bioactivity of this material, leading to the acceleration of human umbilical vein endothelial cell (UVEC) growth and differentiation and finally promoting bone regeneration at critical-size bone defect sites. Therapeutic applications of MSC-derived EVs loaded in hydrogels for treating critical-size calvarial defects have shown significant increases in bone volume, bone mineral density, and newly formed bone area (Qi et al., 2016). It was demonstrated that after being loaded into the hydrogels, EVs could be slowly released in a controlled manner. In addition, hydrogel biomaterials can be fully absorbed at defect sites while promoting osteogenic induction and enhancing bone remodelling (Yang S. et al., 2020). Recently, scholars have focused on constructing novel synthetic hydrogel composites to enhance their function as EV carriers to promote bone regeneration. Adding hydroxyapatite to hyaluronic acid and alginate, Yang S. et al. (2020) produced an injectable hydrogel, which could effectively promote osteoblast differentiation at the critical-size bone defect site after loading MSC exosomes. Another hotspot is how to optimize the controlled release of EVs loaded into hydrogels. Huang et al. (2021) generated engineered modified EVs and loaded them into photocrosslinked sodium alginate hydrogels. It was found that the release process of EVs could be sustained for as long as 7 days, and the biological functions of the loaded EVs did not change during the whole research period. Significant bone regeneration could be observed when applying this system to repair critical-size skull defects.

2.2.2 Applications of extracellular vesicles-loaded bioceramics

In the traditional MSC-based BTE used to treat bone defects, cells need to be directly injected into the target sites. After injection, the

multidirectional differentiation potential of MSCs helps to regenerate bone tissues. However, because the injected MSCs lack mechanical support and cannot withstand local pressure, this method is generally not applicable, especially for critical-size bone defect repair (Korhonen and Jurvelin, 2010). To overcome this limitation, bioceramics have become a preferred scaffold material for transplanting cells or cytokines. Porous bioceramics have ideal mechanical strength, biocompatibility and biodegradability (Huang X. et al., 2020). Currently, there are absorbable bioceramics, such as β-TCP, and non-absorbable bioceramics, such as zirconia and alumina, applied in the clinic. Some bioceramics even have biological activities, such as hydroxyapatite glass ceramics. EVs derived from MSCs have similar biological characteristics to MSCs. Therefore, many scholars have loaded them into bioceramic scaffolds to improve the bioactivities of this material. It was found that loading EVs from BMMSCs into hydroxyapatite/TCP bioceramics could better induce new bone formation (Wang et al., 2015). Osteoconductive β-TCP could release hiPSC-MSC-derived exosomes in a controlled manner *in vitro*, thus stimulating the proliferation, migration and osteogenic differentiation of homing hBMMSCs in the injury sites to promote new bone formation. Application of this delivery system loaded with EVs in critical-size calvaria defects showed increased new bone formation through upregulating the expression of osteocalcin (OCN) and osteopontin along with increased levels of the vascular marker CD31 both in healthy (Zhang J. et al., 2016) and osteoporotic rats (Qi et al., 2016). Currently, scholars are also trying to better improve the survival microenvironment of EVs by adding minerals that can enhance the bioactivity of bioceramic materials so that EVs released from them can maintain favourable biological functions to play a bridge role in intercellular communications and promote osteogenic differentiation of stromal cells (Gandolfi et al., 2020). In a recent study, scholars used strontium to replace calcium silicate in the original scaffold materials and found that EVs loaded into new bioceramics could better exert osteogenic differentiation and angiogenesis potentials in zebrafish and rat femoral bone defect models, resulting in ideal regeneration of bone tissues and blood vessels at the defect sites. The possible mechanisms may be that composition changes upregulate the expression of miR-146a in EVs, which in turn inhibits the protein expression of mothers against decapentaplegic homologue (Smad) 4 and NF2 (Liu L. et al., 2021). In addition to modifying the compositions of bioceramics, decreasing the porous diameters would also create a better survival microenvironment for EVs. Micrometer-scale porous (.5–2 μm) graded mesoporous bioactive glass with osteogenesis, angiogenesis, and antimicrobial activities may provide BMMSC-derived exosomes with a larger surface area to meet the bone regeneration demand (Liu A. et al., 2021). In addition to optimizing the composition and construction of bioceramic materials, similar to hydrogels, scholars are also further exploring and improving the release kinetics of EVs loaded into them *in vivo*.

2.2.3 Applications of extracellular vesicles-loaded polymers

Synthetic biodegradable polymers are considered effective delivery carriers of EVs because of their unique advantages, such as adjustable release kinetics. Exosomes from ADSCs were loaded into polylactic-co-glycolic acid (PLGA) scaffolds with a polydopamine coating. *In vitro*, the sustained release of exosomes could be observed, while *in vivo*, it would promote bone regeneration of critical-size bone defects by enhancing homing of BMMSCs to the defect sites (Li et al., 2018). Scholars have also explored copolymer systems, such as PLGA-polyethylene glycol triblock, as a loading platform for the controlled release of EVs and found that its ability to induce osteogenesis is superior to that of exogenous direct delivery of EVs (Swanson et al., 2020). Polycaprolactone is another biomaterial with specificity for inducing bone regeneration. It has a degradable property. Loaded with EVs derived from BMMSCs, polycaprolactone could effectively repair bone defects *in vivo* (Wang X. et al., 2020). Polymer composites have the same elastic modulus as bone tissues, but their biological activity is weak compared with certain types of hydrogels or bioceramics. Therefore, the ability to repair critical-size bone defects *in vivo* could be further improved after loading with EVs.

2.2.4 Applications of extracellular vesicles-loaded metals

As the most traditional bone repair material, metal has good mechanical properties (Zhao et al., 2021). Titanium and its alloys are the most widely used metals in BTE. They have ideal biocompatibility, including non-toxicity, optimal porosity suitable for cell migration and proliferation, high mechanical strength and corrosion resistance. In addition, they are the only metals that have been proven to have osseointegration characteristics (Briguglio et al., 2019). Similar to polymers, many studies that used metals as scaffold materials for EVs have focused on improving their biological functions. Some scholars generated titanium scaffolds by selective laser sintering and 3D printing and then decorated them with EVs derived from hMSCs with preosteogenic differentiation for 4–20 days (Liang et al., 2020). Meanwhile, the adsorption of EVs on the scaffold material was enhanced by coating the scaffold surface with positively charged polylysine to mediate charge interaction. RNA sequencing results suggested that these treatments could simultaneously upregulate specific osteogenic miRNAs and downregulate anti-osteogenic miRNAs of loaded EVs to activate mitogen-activated protein kinase (MAPK) and phosphoinositide 3-kinase (PI3K)/Akt signals and finally obtained good bone induction effects in a rat radial bone defect model (Zhai et al., 2020). In addition, researchers have also tried to produce titanium alloys with porous properties and matching the elastic modulus of bone by 3D printing. After loading Schwann cell-derived exosomes, it was found that the modified titanium alloy had a better ability to repair critical-size bone defects (Wu et al., 2020). In another attempt to improve the function of implanted titanium, researchers loaded BMP2 prestimulated macrophage-derived exosomes into titanium nanotubes and found that surrounding BMMSCs had significantly enhanced osteogenic differentiation ability compared with applying scaffold materials alone (Wei F. et al., 2019). Polyetheretherketone, which has solid mechanical strength and favourable biocompatibility, such as transmissivity and anti-chemical corrosion, is now regarded as an alternative metal scaffold in BTE. After etching with concentrated sulfuric acid, the surface of polyethe retherketone showed a 3D porous structure, which was ideal for the loading and distribution of exosomes. Thus, this system was better at promoting osseointegration by regulating inflammatory responses. Detailed mechanisms include blocking nuclear factor-κB (NF-κB) signalling and enhancing macrophage M2 polarization, and these two

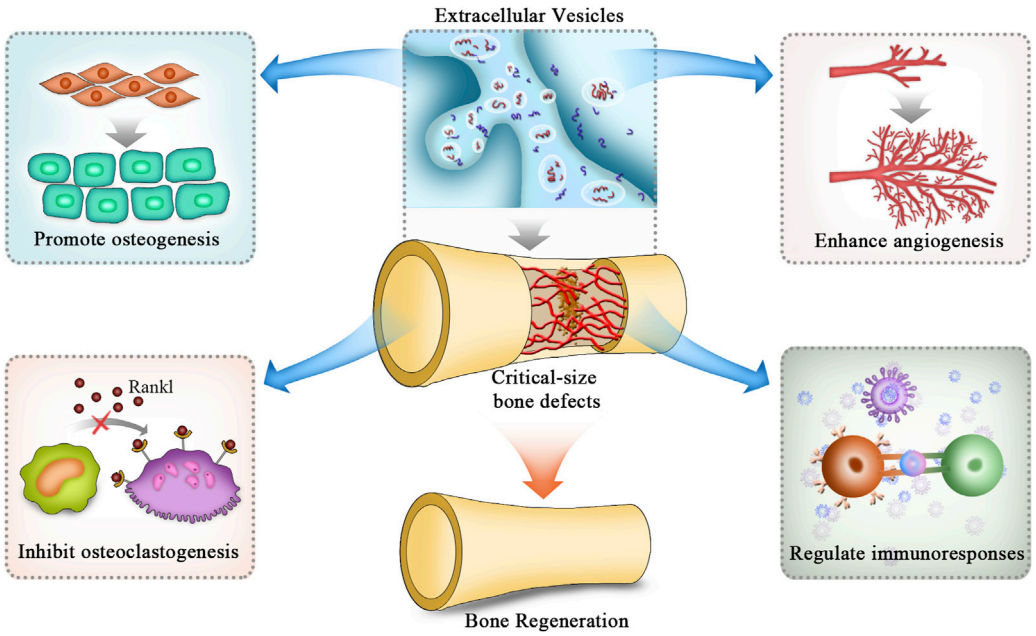

FIGURE 2
Mechanisms of EVs applied in BTE to repair critical-size bone defects. The mechanisms of EVs in repairing critical-size bone defects are mainly attributed to the promotion of osteogenic differentiation of stromal cells while inhibiting the differentiation of osteoclasts. In addition, they also promote angiogenesis and modulate inflammatory responses to provide a suitable environment for bone regeneration. EVs: extracellular vesicles.

processes are reversible (Wei R. et al., 2019). Moreover, tannic acid coated with polyphenol systems has been developed to form reversible hydrogen connections between EVs and scaffold materials, allowing the long-term release of EVs to be realized. The sustained release of exosomes would formulate an immune microenvironment ideal for bone regeneration (Liu and Xiong, 2021c).

In summary, EVs-based cell free regenerative medicine is playing a more and more important role in critical-size bone defect repair. MSC-derived EVs have similar effects to their parental cells while non-MSC-derived EVs have their own advantages in regulating microenvironment. In repairing critical-size bone defects, both MSC and non-MSC-derived EVs need the support of bioactive scaffold materials. These scaffold materials would not only maintain the shape of critical-size bone defect, but also help EVs to better exert their effects through different mechanisms. In future, according to different characteristics of diverse bioactive scaffold materials, more studies are needed to provide references for choosing more favorable EVs under different pathological or regenerative regulatory microenvironments.

3 Mechanisms of extracellular vesicles on critical-size bone defect repair

In treating bone defects, EVs can regulate osteogenesis, angiogenesis, and immune responses, inhibit osteoclast activity, and finally promote repair processes by transporting their internal cargoes to target cells *via* downstream signalling pathways (Figure 2) (Gao et al., 2018). A large number of bioactive substances are contained in EVs, such as nucleic acids, proteins and lipids. Among these bioactive molecules, miRNAs are the most common cargoes (Toh et al., 2017). MiRNAs exert critical effects in cell-to-cell crosstalk and regulate bone tissue repair and regeneration by posttranscriptional modification. In addition to promoting osteogenesis and angiogenesis, EVs take part in regulating immune responses through their cargoes to suppress the activities of osteoclasts during the repair of critical-size bone defects (Li R. et al., 2022). Nevertheless, because EVs contain many miRNAs, these miRNAs may interact with each other to form a complex network. In addition to miRNAs, EVs also contain many proteins, lipids and other types of nucleic acids, such as long non-coding RNAs, circular RNAs and mRNAs. Thus, elucidating the intrinsic molecular mechanisms of EVs in regenerating bone tissues is necessary.

3.1 Extracellular vesicles promote critical-size bone defect repair by enhancing osteogenesis

The crux to repair critical-size bone defects is to enhance the activities of osteoblasts while inhibiting those of osteoclasts in the local microenvironment. Researchers have already confirmed that EVs can enhance the homing of endogenous stromal cells to defect sites, thereby shortening the time of bone formation and mineralization (Chew et al., 2019). In addition, EVs can bind matrix proteins, such as type I collagen and fibronectin, to induce the development and maturation of osteoblasts both *ex vivo* and *in vivo* (Narayanan et al., 2016). Some scholars used EVs derived from hBMMSCs with preosteogenic induction for RNA sequencing. The obtained results

indicated that these EVs contained miR-196a, miR-27a and miR-206, which are important for osteogenic differentiation. Among those miRNAs, miR-196a has the potential to induce the expression of ALP, OCN, osteopontin and Runx2, leading to the formation of more bone tissues in critical-size calvarial defects (Qin et al., 2016b). Moreover, the expression of osteogenic-related miRNAs, such as miR-146a-5p, miR-503-5p, miR-483-3p and miR-129-5p, were upregulated, and the expression of anti-osteogenic-related miRNAs, such as miR-32-5p, miR-133a-3p and miR-204-5p, were downregulated. These miRNAs could activate the PI3K/Akt and MAPK signalling pathways to exert the biological effects of promoting bone mineralization in the local microenvironment (Zhai et al., 2020).

EVs promoting osteogenesis also involve several other signalling pathways, including BMP/Smad, Wnt/β-Catenin, tensin homologue/PI3K/Akt and HIPPO. These signalling pathways have been confirmed by many studies to play active roles in promoting the repair of critical-size bone defects (Cao et al., 2021). In addition to miRNAs, EVs can transport long non-coding RNAs to stromal cells at bone defect sites and indirectly promote bone mineralization by downregulating genes that inhibit osteogenesis (Yang et al., 2019). In addition to MSC-derived EVs, Qi et al. (2016) also demonstrated that human iPS-MSC-derived exosomes significantly promoted osteogenesis and angiogenesis through their internal miRNAs. The application of iPSC-MSC-derived exosomes together with β-TCP scaffolds promoted bone regeneration in critical-sized calvarial defects in an ovariectomized rat model. The results of Li et al. (2018) showed that in the critical-size bone defect microenvironment, in addition to activating the extracellular regulated protein kinase 1/2 pathways, hADSC-derived exosomes could also promote the expression of vascular endothelial growth factor (VEGF) in MSCs through various miRNAs, thus indirectly creating a good microenvironment for bone tissue regeneration by promoting angiogenesis.

Other researchers analysed the proteomics of osteoblast-derived EVs. The obtained results showed that up to 786 proteins in EVs were involved in osteogenic-related signalling pathways, such as mammalian target of rapamycin and eukaryotic initiation factor-2 (Ge et al., 2015). Similar studies have focused on EVs derived from mouse MC3T3 cells. Proteomic analysis found that among the 1,536 proteins, 172 were closely related to bone development and functions (Ge et al., 2017). Therefore, EVs may improve the differentiation ability of stromal cells or osteoblast precursor cells by transporting cargoes such as miRNAs and proteins in the bone defect microenvironment and enhancing the repair of critical-size bone defects.

3.2 Extracellular vesicles promote critical-size bone defect repair by suppressing osteoclastogenesis

Under normal circumstances, the regeneration processes of critical-size bone defects involve the imbalance of bone resorption and bone formation; that is, the activity of osteoblasts needs to be more dynamic than that of osteoclasts (Wu et al., 2010). Therefore, understanding the mechanisms by which EVs regulate osteoclast differentiation and formation will also provide new concepts for treating critical-size bone defects. EVs in the BTE can regulate the bone marrow microenvironment and inhibit osteoclast activities through their internal proteins and miRNAs. Prostate cancer cell-derived exosomes could downregulate miR-214 in osteoclasts and block NF-κB signalling, therefore inhibiting osteoclast differentiation (Duan et al., 2019). In addition, these exosomes could also inhibit osteoclast proliferation and differentiation by reducing the expression of osteoclast markers such as tartrate-resistant acid phosphatase, cathepsin K and matrix metalloproteinase-9, ultimately regulating bone formation (Karlsson et al., 2016). ADSC-derived exosomes not only reduce the mRNA and protein expression of RANKL but also reduce the ratio of RANKL/osteoprotegerin, thereby inhibiting RANKL-involved osteoclast maturation (Ren et al., 2019). EVs derived from endothelial cells could effectively inhibit bone resorption at bone defect sites by reducing osteoclast activities (Song et al., 2019). In addition, osteoclast-derived EVs could act as mediators between osteoclasts and osteoblasts, regulating the osteogenic function of osteoblasts. Osteoclast exosomes are rich in miRNAs, which inhibit osteoblast activity. MiR-214-3p in osteoclast-derived exosomes could target osteoblasts, inhibiting osteoblast activities *ex vivo* and deteriorating bone formation *in vivo*, while *in vivo* injection of antagomir-214-3p could effectively reverse these negative effects (Li D. et al., 2016). Therefore, miR-214 or miR-214-3p in EVs not only serve as biological tags of bone mass reduction but also as therapeutic targets to promote bone regeneration. Researchers also found that RANKL could induce the expression of miR-23a-5p in osteoclast-derived exosomes. Because miR-23a-5p suppresses the expression of Runx2 and promotes Yes-associated protein-1-mediated anti-osteogenic signalling, RANKL may be a target protein that regulates EV-mediated osteoclastogenesis differentiation (Yang J. X. et al., 2020). In conclusion, EVs may regulate osteoclast activities, thus mediating the development of bone regeneration; and some specific miRNAs can be used as therapeutic targets for bone defect repair. However, compared with the functional study of EVs promoting osteogenesis, there are currently fewer studies on the effects of EVs on osteoclast differentiation. Therefore, it is necessary to conduct more in-depth and comprehensive research in the future.

3.3 Extracellular vesicles promote critical-size bone defect repair by enhancing angiogenesis

Bone contains a high density of vasculature. Numerous bone cells participate in maintaining normal functions of bone, while the biological activities of these bone cells rely on the ambient vasculature. There is increasing evidence that maintaining adequate local blood supply or maintaining continuously increased angiogenesis plays an important role in critical-size bone defect regeneration (Wang et al., 2017). Therefore, one of the basic strategies for promoting the repair of critical-size bone defects is to promote angiogenesis (Jia et al., 2016). Various studies have demonstrated that EVs enhance angiogenesis near tendon-bone junctions *in vivo* (Vizoso et al., 2017), which is shown by promoting the expression of angiogenic factors and tube formation and stimulating the proliferation and migration of endothelial cells (Zhang B. et al., 2021). It was also confirmed that endothelial progenitor cell-derived exosomes enhanced the proliferation, migration and angiogenesis of endothelial cells by delivering miR-126. Transduced miR-126 improved the vascular areas and thicknesses

around the shin bones of rats and finally accelerated the bone repair process in the defect sites (Jia et al., 2019). Scholars also found that miR-21 in MSC-derived exosomes downregulates the expression of sprouty homologue 2 and promotes angiogenesis (Wu et al., 2022). It was reported that BMMSC-derived exosomes may independently activate the VEGF or Hippo signalling pathway by regulating cell-to-cell contact and activating cytoskeleton dynamics (Wang Z. et al., 2021). Another study performed by Takeuchi et al. (2019) showed that MSC-derived EVs enhanced tissue and vascular development in parietal bone defects in Wistar rats by upregulating the mRNA expression of VEGF, angiopoietin 1 and 2 together with osteogenesis-related collagen I, ALP, OCN and osteopontin. Zhang et al. (2015) found that hiPSC-derived exosomes could directly promote angiogenesis and collagen synthesis. Similar studies have also demonstrated that EVs derived from MSCs could upregulate the expression of functional angiogenesis molecules and enhance the migration of hUVECs, exhibiting a larger area of angiogenic tube formation (Zhang et al., 2020). A rat model of femoral fracture demonstrated that transplanting MSC-derived EVs to the defect sites could significantly enhance angiogenesis and osteogenesis, leading to better bone tissue regeneration. Other researchers found that exosomes from apical papilla stem cells promoted angiogenesis through miR-126-5p, which was indirectly manifested by increased expression of VEGF and angiopoietin-1 (Jing et al., 2022). Scholars have also demonstrated that hypoxia pretreatment can regulate the expression of bioactive substances in exosomes, thus promoting angiogenesis in different microenvironments. After hypoxia preconditioning, the expression of miR-126 in MSC-derived exosomes was upregulated, which further promoted angiogenesis, proliferation and migration of stromal cells, thus enhancing the process of fracture healing (Liu et al., 2020). In addition to hypoxia, the proangiogenic ability of exosome components is also enhanced by certain biomaterials. A biomaterial containing lithium induced miR-130a expression in exosomes, activated tensin homologue/Akt signalling pathways, and finally promoted angiogenesis in the bone defect microenvironment (Liu et al., 2019). In conclusion, by selecting appropriate EVs and regulating the expression of bioactive substances within them, EVs may be promising candidates for treating critical-size bone defects as proangiogenic vesicles.

3.4 Extracellular vesicles promote critical-size bone defect repair by regulating immune responses

The healing processes of bone defects are often accompanied by local inflammatory responses and imbalanced immune reactions. These changes will always result in unsuccessful scaffold implantation in bone defect treatments (Guder et al., 2020). Large numbers of inflammatory and immune cells are present in the microenvironment of bone defect sites. Mild inflammation-related responses are critical for bone defect regeneration (Lin et al., 2021). The functions of EVs in immune response regulation are diverse. EVs not only participate in the processes of anti-inflammatory responses, such as in collagen-induced arthritis mice (Cosenza et al., 2018) and antigen-induced synovitis pigs (Casado et al., 2017) but also modulate beneficial regenerative immune phenotypes, which are important in tissue repair as well as calcification (Lindenbergh and Stoorvogel, 2018). In addition, EVs can regulate the functions of T-cell, B cells, macrophages and other immune cells directly by membrane fusion or indirectly by transporting bioactive cargoes (Qian et al., 2021). It has already been demonstrated that MSC-derived exosomes are effective in suppressing immune responses by attenuating the proliferation of T-cell and B cells. Moreover, MSC-derived exosomes can also suppress the secretion of the proinflammatory cytokines tumour necrosis factor-α and IL-1β, together with increasing the excretion of the anti-inflammatory cytokine TGF-β *in vitro* (Chen et al., 2016), thus maintaining a favourable immune balance that was crucial for bone healing. Macrophages are part of innate immunity. They participate in removing pathogens and modulating inflammatory responses in the human body (Bozec and Soulat, 2017). Macrophage M2 polarization can enhance angiogenesis and bone tissue regeneration (Wasnik et al., 2018). EVs loaded into scaffolds could promote macrophage M2 polarization and suppress the inflammatory responses in the local microenvironment, as manifested by decreased mRNA and protein expression of the proinflammatory factors IL-6 and tumour necrosis factor-α (Guan et al., 2021). The inhibited inflammatory responses would indirectly boost vascularization, therefore facilitating osteoblast function and bone tissue mineralization and finally leading to favourable new bone tissue formation (Kim et al., 2021). This EV-mediated transplantation system has been recognized as a novel alternative for treating bone defects. Further mechanistic studies showed that the NF-κB pathway may play an important role in this process (Fan et al., 2021). To further confirm whether the bioactive molecules of MSC-derived exosomes play a key role in regulating immune responses, Li R. et al. (2022) analysed the role of miR-451a, which is highly expressed in ADSC-derived exosomes, in repairing rat skull defects. By transfecting miR-451a analogues and inhibitors into macrophages, it was found that miR-451a could directly regulate the mRNA expression of macrophage migration inhibitory factor by specifically binding to its 3′UTR, thereby promoting the polarization of the macrophage phenotype from M1 to M2. Moreover, the results of other studies also found that UVEC-derived exosomes, in which programmed cell death ligand 1 was overexpressed, could bind to programmed cell death-1 on the surface of T-cell, thereby inhibiting its activation. As a result, the osteogenic differentiation of MSCs was significantly enhanced after inhibiting the local hyperactivated inflammatory responses (Lin et al., 2021). Therefore, EVs are critical modulators of immune responses for regenerating new bone tissues.

In summary, the roles of EVs in repairing critical-size bone defects are attributed to 1) promoting osteogenic differentiation of stromal cells while inhibiting the differentiation of osteoclasts; 2) enhancing angiogenesis to provide a suitable environment for bone regeneration; and 3) modulating inflammatory responses to maintain a favourable immune microenvironment (Figure 2). Thus, EVs would be an ideal cell-free therapeutic component to treat critical-size bone defects. As we have reviewed, mechanistic studies of EV application in BTE are mainly performed from the aspect of internal cargoes of miRNAs and proteins. More studies focused on these are summarized in Table 2.

4 Application of engineering modified extracellular vesicles in bone tissue engineering

Although natural EVs exert diverse functions in regenerative medicine through multiple biological mechanisms, their limitations

TABLE 2 Therapeutic roles and possible mechanisms of certain miRNAs and proteins of EVs in critical-size bone defects repair.

Cargoes of EVs	Parent cells	Nanovesicles	Therapeutic roles and possible mechanisms	References
miR-196a	BMMSCs	EVs	Stimulating bone growth in critical-sized calvarial bone defects through enhancing osteoblast activity and the expression of osteogenic genes	Qin et al. (2016b)
miR-218, miR-92a, miR-199b	BMMSCs	Exosomes	Promoting osteogenic differentiation of BMMSCs	Xu et al. (2014)
miR-26a-5p	BMMSCs	Exosomes	Inhibiting the damage of synovial fibroblasts by targeting prostaglandin-endoperoxide synthase 2	Jin et al. (2020)
miR-192-5p	BMMSCs	Exosomes	Inhibiting local inflammatory responses by regulating the expression of proinflammatory factors	Zheng et al. (2020)
miR-328-3p	BMMSCs	Apoptotic bodies	Maintaing MSCs homeostasis and ameliorating osteopenia through inhibiting Axin1 and thereby activate the Wnt/β-catenin pathway	Liu et al. (2018)
miR-34	BMMSCs, ADSCs	Exosomes	Promoting proliferation and osteogenic differentiation of BMMSCs	Baglio et al. (2015)
miR-375	ADSCs	Exosomes	Promoting bone regeneration by binding to insulin growth factor binding protein-3	Chen et al. (2019)
miR-451a	ADSCs	Exosomes	Regulating bone immune metabolism and further promoting bone healing through targeting macrophage migration inhibitory factor	Li et al. (2022b)
miR-503-3p	Osteoblast	Exosomes	Inhibiting the osteoclast differentiation through downregulating the expression of heparanase	Wang et al. (2021a)
miR-1192, miR-680, miR-302a	Pre-osteoblast Osteoblast	Exosomes	Promoting osteoblastic differentiation by inhibiting Axin1 expression and increasing β-catenin expression to activate the Wnt signaling	Cui et al. (2016)
miR-8485	Chondrocyte	Exosomes	Regulating the Wnt/β-catenin pathways to promote chondrogenic differentiation of BMMSCs	Li et al. (2020c)
miR-221-3p	Chondrogenic progenitor cells	EVs	Stimulating chondrocyte proliferation and migration	Wang et al. (2020c)
miR-214	Endothelial cells	Exosomes	Stimulating angiogenesis through silencing the ataxia telangiectasia mutated gene in neighboring target cells	van Balkom et al. (2013) Duan et al. (2019)
	Prostate cancer cell		Inhibiting osteoclast differentiation by blocking the NF-κB signaling pathway	
miR-155	Endothelial cells	Exosomes	Indirectly inhibiting osteoclast activity by interacting with macrophages	Song et al. (2019)
miR-126	Endothelial progenitor cell	Exosomes	Promoting angiogenesis *via* Raf/ERK signaling pathway	Jia et al. (2019)
miR-335	DC	Exosomes	Enhancing bone regeneration by promoting the proliferation and osteogenic differentiation of BMMSCs through inhibiting Hippo signaling targeting large tongue suppressor kinase 1	Cao et al. (2021)
miR-5106	M2 macrophages	Exosomes	Inducing osteoblast differentiation by regulating the expression of salt-inducible kinase 2/3	Xiong et al. (2020)
miR-23a	Nasopharyngeal carcinoma cells	Exosomes	Mediating angiogenesis by targeting The testis- specific protein 10	Bao et al. (2018)

(Continued on following page)

TABLE 2 (*Continued*) Therapeutic roles and possible mechanisms of certain miRNAs and proteins of EVs in critical-size bone defects repair.

Cargoes of EVs	Parent cells	Nanovesicles	Therapeutic roles and possible mechanisms	References
miR-135b	hypoxia-resistant multiple myeloma cells	Exosomes	Enhancing endothelial tube formation under hypoxia *via* the HIF signaling pathway	Umezu et al. (2014)
Ring finger protein 146	BMMSCs	Apoptotic bodies	Maintaing MSCs homeostasis and ameliorating osteopenia through inhibiting Axin1 and activating the Wnt/β-catenin pathway	Liu et al. (2018)
Membrane cofactor protein-1/3, Stromal cell derived factor-1	BMMSCs	Exosomes	Promoting cell proliferation and MSCs recruitment to injury sites	Furuta et al. (2016) Ando et al. (2014)
BMP2	BMMSCs	Exosomes	Enhancing fracture healing by promoting osteogenesis and angiogenesis through activating BMP-2/Smad1/Runx2 and the HIF-1α/VEGF signaling pathways	Zhang et al. (2020)
HIF-1α, VEGF	hUCMSCs	Exosomes	Enhancing angiogenesis and bone healing processes by promoting vascular endothelial proliferation, migration and tube formation	Zhang et al. (2019)
C-Type lectin domain family 11-Member A	hUCMSCs	EVs	Preventing bone loss and maintaining bone strength by enhancing bone formation, reducing marrow fat accumulation and decreasing bone resorption through shifting from adipogenic to osteogenic differentiation of BMMSCs and inhibiting osteoclast formation	Hu et al. (2020)
Matrix metalloproteinase 2	Osteoblasts	Exosomes	Promoting the angiogenesis of endothelial cells through VEGF signaling pathway	Tang et al. (2019)
Annexin	Osteoblasts	EVs	Inducing osteogenesis, calcium channeling by activating Wnt proteins	Xiao et al. (2007)
Platelet derived growth factor	Osteoclasts	Apoptotic bodies	Inducing endothelial progenitor cell Differentiation in a bone defect model	Ma et al. (2021)
TGF-β1, IL-10	DC	Exosomes	Enhancing the recruitment of regulatory T-cell in inflammatory responses and inhibiting bone loss caused by osteoclasts	Elashiry et al. (2020)
Insulin growth factor-1	Macrophages	Microvesicles	Redirecting epithelial cells towards internalizing microvesicles	Blander (2017)

ADSCs: adipose derived stem cells; BMMSCs: bone marrow mesenchymal stem cells; BMP2: bone morphogenetic protein 2; DC: dendritic cell; EVs: extracellular vesicles; HIF-1α: hypoxia inducible factor-1α; IL: interleukin; MSCs: mesenchymal stem cells; NF-κB: nuclear factor-κB; Runx2: runt-related transcription factor 2; Smad: mothers against decapentaplegic homolog; TGF: transforming growth factor; UCMSCs: umbilical cord mesenchymal stem cells; VEGF: vascular endothelial growth factor.

in repairing critical-size bone defects have gradually been recognized. Specifically, the targeting effect of natural EVs is poor. Most of the mature EVs delivered to bone defect sites will enter the circulatory system and cannot all accurately act on the target cells. In addition, not all EVs isolated from parent cells have therapeutic effects; thus, the number of effective natural EVs is far from sufficient. As a result, the bioactive molecules that are needed in different pathological circumstances cannot reach a therapeutic concentration. Although EVs are processed and assembled in parent cells and inherit similar biological characteristics to them, the bioactive molecules in natural EVs vary greatly, which will bring unstable efficacy in repairing critical-size bone defects. Therefore, engineering-modified EVs have been investigated to accelerate the bone regeneration process by applying multiple techniques that fall into two main categories in most circumstances: endogenous engineering strategies and exogenous engineering strategies. Advantages and disadvantages of some commonly used techniques are summarized in Table 3. Applications of engineered modified EVs can enhance therapeutic efficiency and more accurate targeting effects over natural EVs (Arenaccio et al., 2019).

4.1 Endogenous engineering modified extracellular vesicles

In the previous sections, the authors summarized the biological characteristics of EVs derived from different parent cells and their applications in BTE to repair critical-size bone defects. Studies have shown that except for selecting appropriate types of parent cells, modification of the parent cells before EV isolation through genetic strategies, preconditioning treatment and physical manipulations could also modify the biological characteristics of EVs (Jafari et al., 2020). These approaches are categorized as endogenous engineering modifications.

TABLE 3 Commonly applied techniques for engineering modified EVs preparation.

Techniques	Operation approaches	Advantages	Disadvantages	References
Genetic engineering	Transfecting parent cells by plasmid or virus carrying target genes	Significantly increase the therapeutic effects of EVs through modifying their loading cargoes	High technical request and long preparation time	Stickney et al. (2016)
Preconditioning	Co-incubating parent cells or EVs with drugs or reagents	Easy to operate and the membranes of parent cells or EVs keep intact	Cargoes loading efficiency is relatively low and the drugs or reagents may have toxicity to parent cells or EVs	Pascucci et al. (2014)
Electroporation	Exerting electric field to parent cells or EVs suspended in conducting solution, exogenous siRNA or miRNA would be easy to load through the perforated membrane	Both exogenous macromoleculars and hydrophilic small molecular compounds could be loaded	The integrity of the membrane is destroyed, leading to unstable biological characteristics of parent cells or EVs	Johnsen et al. (2016)
Mechanical extrusion	Mixing parent cells or EVs with drugs or reagents and then process by extrusion	Easy to operate and more exogenous substances could be loaded	The integrity of the membrane is destroyed, leading to unstable biological characteristics of parent cells or EVs	Fuhrmann et al. (2015) Wan et al. (2018)
Sonication	Mixing EVs with drugs or reagents and then process by sonication treatment	More exogenous substances could be loaded with higher loading efficiency	The integrity of the EVs membrane is destroyed with uncontrollable loading capacity of target drugs	Kim et al. (2016)
Freezing/thawing	Rapid freezing mixed EVs and drugs or reagents and then thaw at room temperature	Easy to operate and the membrane of EVs keeps intact	Cargoes loading efficiency is relatively low and the biological activities of EVs or drugs might change	Sato et al. (2016)
Chemical conjugation	Conjugating target moleculars to the surface of EVs directly through covalent bond	Increasing the EVs targeting characteristic while keeping the morphology and structure of the membrane intact	Difficult to operate and only molecular with specific functional group could be loaded	Tian et al. (2018) Zhao et al. (2019)

EV: extracellular vesicle.

4.1.1 Genetic engineering strategies

Genetically modifying the natural procedures of protein synthesis of parent cells can endow the modified EVs with membrane modification and more desirable functions, such as precise targeting and individualized therapeutic performance, by regulating some targeted biomolecules. Compared with natural EVs, specific ligands can be added to the EV membrane to improve its targeting effects through genetic engineering (Hu et al., 2021). After transfection with the *RUNX2* gene, the osteogenic differentiation of hBMMSCs was potentiated. Meanwhile, the differentiation induction capabilities of EVs derived from this gene-transfected cell were also enhanced *in vitro* (Martins et al., 2016). In a similar study, the expression of HIF-1α in parental MSCs was upregulated. The EVs derived from these cells exhibited better regenerative characteristics. The *in vitro* results indicated that EVs from HIF-1α-upregulated MSCs could better enhance matrix mineralization, ALP activity and osteogenesis-related gene expression in BMMSCs and promote the migration, proliferation and tube formation of HUVECs. Meanwhile, *in vivo* results indicated better bone tissue regeneration and neovascularization; therefore, the trabecula bone healing time was significantly shortened in rabbit necrotic femoral heads (Li et al., 2017). Another study also upregulated HIF-1α expression in BMMSCs. Their derived exosomes were loaded into a β-TCP scaffold to repair critical-size bone defects in rats. The obtained results also confirmed that compared with applying normal BMMSC-derived exosomes, exosomes derived from HIF-1α-upregulated BMMSCs considerably accelerated the regeneration of new bone tissues with favourable stromal cell neovascularization differentiation (Ying et al., 2020). Other researchers have tried to activate the endogenous BMP signalling pathway by downregulating the natural BMP antagonist noggin in the parent cells of EVs (Fan et al., 2016). They observed EVs obtained from noggin knockdown MSCs and found that a large number of endogenous aggregations of osteogenic-related molecules appeared in EVs. When these modified EVs were loaded into injectable ethylene glycol methacrylate chitosan hydrogels and transplanted into mouse critical-size calvarial defects, more desired bone regeneration could be observed (Fan et al., 2020).

4.1.2 Preconditioning treatment of parent cells

Preconditioning treatment of parent cells through conditioned culturing medium could improve the biological activities of EVs derived from them. It is an effective strategy to boost EV-mediated BTE in regenerating bone tissues. Preconditioning treatment can directly modify the DNA or RNA of the parent cells to obtain needed EVs rich in target cargoes. Narayanan et al. (2018) found that exosomes derived from MSCs that were precultured in osteogenic induction medium showed better capabilities of inducing osteogenic differentiation of other MSCs *in vitro* and of promoting neovascularization in 3D cultures *in vivo*. Liu A. et al. (2021) compared EVs derived from different types of stem cell sources and culturing media. The obtained results suggested that exosomes from rBMMSCs preconditioned with osteogenic induction medium exhibited the most desirable osteogenesis characteristics, and the ALP activity increased by more than 2 times compared with the blank control. In-depth bioinformatics analysis further confirmed that preconditioning rBMMSCs with osteogenic induction medium could upregulate the expression of multiple osteogenic-related miRNAs in their derived EVs such as let-7a-5p, let-7c-5p, miR-328a-5p and miR-31a-59. Mesoporous bioactive glass scaffold materials loaded with these modified exosomes could effectively repair rat skull defects *in vivo*. Another study found that exosomes derived from hBMMSCs

preconditioned with dimethyloxaloylglycine, which stabilizes HIF-1α at a low concentration, could improve bone healing by boosting angiogenesis in critical-sized calvarial defects in rats (Liang et al., 2019). Moreover, Huang C. C. et al. (2020) demonstrated that in a rat skull critical-size defect model, compared with natural hBMMSC-derived EVs, BMP2 preconditioned hBMMSC-derived EVs had significantly enhanced bone regeneration ability. Other scholars used BMP2 to precondition mouse macrophages (RAW 264.7) and observed the osteogenic potential of their exosomes in bone regeneration applications (Wei F. et al., 2019). The obtained results showed that the preconditioned macrophage-derived EVs enhanced the osteogenic differentiation of BMMSCs. These results demonstrated that preconditioned parent cell-derived EVs could be better applied in bone regeneration.

Another widely applied preconditioning treatment of parent cells is a hypoxic environment. MSCs, which were preconditioned in a hypoxic environment, promoted angiogenesis capability. In addition, EVs derived from these cells also had better angiogenic characteristics and led to enhanced osteogenic capability. The *in vitro* experiments showed that these modified EVs could promote the proliferation and migration of HUVECs and tube formation. Due to the favourable angiogenic microenvironment, osteogenic differentiation of BMMSCs at the bone defect site was also enhanced, which was manifested by increased gene expression of serum OCN and ALP (Li et al., 2017). The *in vivo* experiments were performed using the steroid-induced avascular necrosis model in the femoral head. The obtained results indicated that the femoral head transplanted into EVs derived from hypoxia-preconditioned cells had higher vascular density and denser trabecular bone tissue formation (Li et al., 2017). The results of Sakaguchi et al. (2017) were similar. Researchers also found that exosomes derived from BMMSCs in a hypoxic environment could enhance the formation of tubular structures by HUVECs. Compared with natural exosomes, *in vivo* applications of modified EVs showed more favourable new bone formation.

4.1.3 Physical manipulation approaches

Physical manipulation could change the amount of EVs released from parent cells together with the type and amount of therapeutic cargoes in EVs. Generally, physical manipulation is performed by directly exerting physical forces on the parent cells by electroporation and extrusion (Richter et al., 2021), thereby optimizing EVs derived from them. Cui et al. (2022) reported bioinspired nanovesicles prepared from human iPSC-derived endothelial cells under hypoxia culture through an extrusion approach. Abundant membrane C-X-C motif chemokine receptor 4 conferred these nanovesicles bone-targeting ability and the endothelial homology facilitated the bone marrow endothelial cells tropism. Due to their unique endogenous miRNA cargoes, these nanovesicles re-educated bone marrow endothelial cells to secret cytokines favoring osteogenesis and anti-inflammation, leading to a better bone homeostasis. Researchers also used hydroxyapatite ceramics containing magnetic nanoparticles as a scaffold material to simultaneously load osteoblasts and osteoclasts. They found that magnetic nanoparticles could change the internal cargoes of osteoclast-derived exosomes, resulting in a decreased amount of osteoclast-derived exosomes absorbed by osteoblasts, thus weakening the negative regulatory effect of osteoclasts on osteoblasts. Osteoblasts showed enhanced proliferation and differentiation capabilities (Zhu et al., 2020). Further studies found that changes in the cargoes of exosomes derived from osteoclasts were mainly reflected in the magnetic nanoparticle-mediated upregulation of Rho kinase and the downregulation of ubiquitination and reactive oxygen species.

4.2 Exogenous engineering modified extracellular vesicles

To summarize briefly, exogenous engineering of EVs involves functional modification after their isolation, directly loading specific external cargoes into nanoscale EVs to deliver bioactive molecules with therapeutic effects to the local microenvironment, thereby promoting critical-size bone defect repair (Zha et al., 2021). Currently, engineered EVs can be prepared by incubation, electroporation, sonication, mechanical extrusion, recurrent freezing and thawing, and direct EV surface modification by applying covalent or non-covalent interactions (Liao et al., 2019). Using these techniques, the modified EVs would load a desired amount of therapeutic biomolecules, including small molecular drugs, nucleic acids, and proteins either inside or on the surface. In addition, these modified EVs specifically bind antibodies through covalent bonds on lipid membranes and ligands.

Liang et al. (2020) added a plasmid encoding BMP2 to EVs derived from rat MSCs to potentiate the bone inducibility of demineralized bone matrix. The specific method was to coat the membrane of EVs with polyethyleneimine, a cationic polymer usually applied to coat negatively charged DNA, and then add the plasmid BMP2 through a layer-by-layer self-assembly method. This easy technique constructed 100–1,000 nm diameter EV-polyethyleneimine/plasmid BMP2 complexes. Compared with the control group, EV complexes showed upregulated BMP2 gene transfection efficiency and lower toxicity to target cells *in vitro*. In addition, demineralized bone matrix loaded with these novel complexes exhibited increased bone regeneration induction capability after being implanted subcutaneously in rat and rabbit femoral head bone defect models.

VEGF plays a critical role in angiogenesis and BTE for bone tissue regeneration (Grosso et al., 2017). However, as a protein, VEGF has many problems in its direct delivery, including rapid degradation, uncontrolled release and unstable biological activities (Hu and Olsen, 2016). Zha et al. (2020) designed a matrix that could locally release VEGF plasmids for bone defect repair. They used EVs derived from rBMMSCs to transport the plasmid VEGF, which was equivalent to providing a protective layer for VEGF, thus avoiding the problems mentioned above, such as rapid degradation. Researchers first used the electroporation technique to temporarily create holes on the surface of EVs by an electric pulse to increase membrane permeability. After that, VEGF plasmids were loaded into EVs. The modified EVs successfully promoted vascularization and osteogenesis in rat skull defects. In addition, it could also effectively achieve vascularized bone regeneration in segmental bone defects (Zha et al., 2021).

Cui et al. (2021) developed an exosome delivery system based on exosomes secreted by iPSC-MSC. The engineered exosomes collaborated with the loaded siRNA of the *SHN3* gene to enhance their therapeutic effects. Modification of a bone-targeting peptide endowed the engineered exosomes an ability to deliver siRNA to osteoblasts specifically. Silencing of the osteoblastic *SHN3* gene enhanced osteogenic differentiation, and inhibited osteoclast formation. Furthermore, *SHN3* gene silencing could facilitated vascularization, especially formation of type H vessels. This study

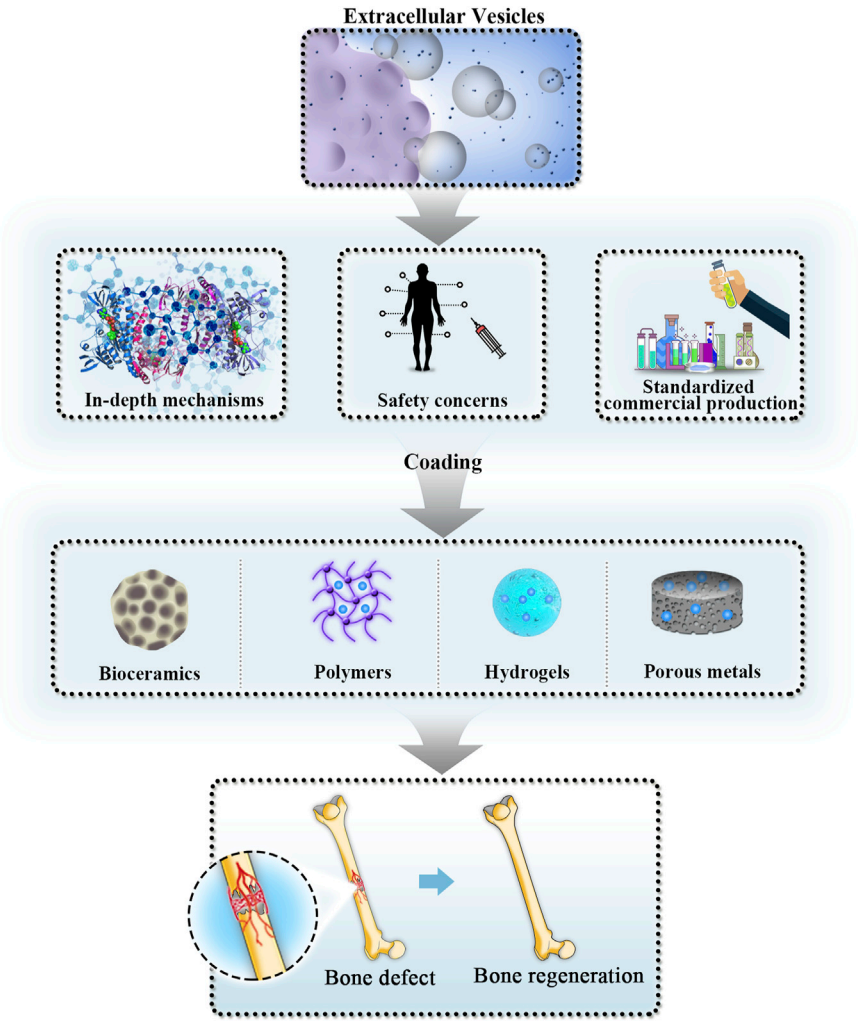

FIGURE 3
Future perspectives and challenges of EV clinical application in BTE. EVs have shown exciting application prospects in repairing critical-size bone defects. In the near future, scholars will focus on studying in-depth mechanisms, solving safety concerns and promoting standardized commercial production of EVs applied in BTE. With further development of bioactive scaffold materials, cell-free regenerative medicine in BTE will soon be widely used. BTE: bone tissue engineering; EVs: extracellular vesicles.

demonstrated that exogenous engineered exosomes could serve as a promising therapy vesicle to kill three birds with one stone. Luo et al. (2019) also provided a promising method to enhance the ability of exosomes to target specific tissues. In their study, the surface of exosomes from bone marrow stromal cell was conjugated with a BMSC-specific aptamer, which delivers exosomes into BMSCs within bone marrow. Intravenous injection of the exosome-aptamer complex enhances bone mass in osteoporosis mice and accelerates bone regeneration in a femur fracture mouse model.

5 Future perspectives and challenges

With meticulous and thorough research exploring the biogenesis and biofunctions of EVs, natural and engineered modified EVs that possess various promising advantages, such as biological functions similar to those of parent cells, low immunorejection, desirable biocompatibility, and the capability to deliver individualized drugs, have shown exciting application prospects in diagnosing and treating diverse pathological conditions (Nagelkerke et al., 2021). The first phase I clinical trial on EVs derived from DCs was conducted for patients with malignant melanoma, and the obtained results indicated that their clinical application was safe (Escudier et al., 2005). Although this clinical safety evaluation trial started as early as 2005, further clinical studies focusing on the evaluation of the safety and effectiveness of EVs applied in tissue repair and regeneration are still in progress mainly in phases I and II. As an important part of BTE development, the progress of EVs in the future will largely determine the progress of BTE-led critical-size bone defect repair and regeneration. Certain achievements have been made in preclinical trials of EV-mediated nanotherapies, and the obtained results showed ideal effects in bone fracture healing (Zhang et al., 2019). However, scholars believe that there are still some unsolved theoretical challenges and important practical problems that should be addressed during future and wider clinical utilization (Figure 3). Nevertheless, challenges and difficulties could not hinder EVs from being a promising alternative for MSC-based therapy in bone regenerative medicine.

5.1 More in-depth mechanisms of extracellular vesicle-mediated bone defect regeneration

Although extensive studies have focused on various therapeutic mechanisms of natural or engineered modified EVs for different diseases, such as cancer and inflammatory diseases (Karlsson et al., 2016; Cosenza et al., 2018), the potential roles of specific functional units from EVs in bone defect regeneration have not been completely explained. In this review, the authors summarized some of the most widely raised clinical mechanisms of EVs as regenerative agents, such as immune regulation, as well as regulation of cell osteogenesis or angiogenesis. However, the detailed therapeutic mechanisms or related downstream targeted signalling cascades largely remain unclear and need to be further explored. These studies are of basic critical importance for scholars to comprehend the therapeutic effects of EVs in regenerative medicine and the biomedical applications of EVs.

Future studies at this stage will mainly focus on exploring the mechanisms of inducing bone regeneration and manufacturing more ideal scaffold materials. Theoretically, EVs regulate bone defect repair and regeneration through the interaction of their multiple internal cargoes (Arenaccio et al., 2019). However, most of the currently available studies focused on the roles of miRNAs in EVs, which indicated that the mechanisms of EVs in bone regeneration are far from being fully explored. It is also necessary to further elucidate the different types of effective active factors of EVs that promote osteogenic differentiation, angiogenesis, inflammation regulation and osteoclast inhibition. In addition, as previously mentioned, the *in vivo* application of EVs cannot be separated from the scaffold materials. In current studies, based on the combined applications of different scaffold materials, scholars have developed a variety of innovative methods to improve the delivery efficiency of EVs (Liao et al., 2019). However, problems such as ineffective delivery and lack of long-term retention of EVs still exist (Riau et al., 2019). In the future, with the development of innovative scaffold materials and standardization of the porosity value or size of biocompatible 3D porous scaffolds for bone defects, efficient transportation, sustained release and long-term storage of EVs will be achieved.

Furthermore, deeper investigations of *in vivo* bioeffects of EVs, such as distribution or bioelimination in blood circulation or in diverse pathological microenvironments, will also provide a deeper understanding of the pharmacokinetic and pharmacodynamic performances of EVs. This broader understanding will be beneficial to the proposal of EV-mediated targeted nanotherapeutic strategies.

5.2 Potential safety concerns of extracellular vesicles in clinical applications

As reviewed earlier, EVs have more favourable biocompatibility and enhanced biosafety over conventional stem cell therapy; however, the whole components of EVs, including some other unknown bioactive molecules, are still not completely clear (Phan et al., 2018). Although the Extracellular RNA Communication Consortium (Das et al., 2019) and the International Society for Extracellular Vesicles (Théry et al., 2018) have published guidelines to recommend researchers in standardizing the isolation and characterization procedures of EVs, the applications of EVs in the clinic would still lead to some unpredictable or undesirable biological effects. On the other hand, the heterogeneous constituents of EVs may lead to side effects that accumulate in non-target organs (Phan et al., 2018). Thus, more efforts to clarify the compositions of EVs are needed to avoid possible side effects during clinical applications in the human body.

Currently, the optimal therapeutic dose of EVs is still uncertain; thus, there would also be potential side effects after application. More preclinical studies are needed, especially on applying EVs in bone defect repair in large animals, to provide more safety references and a basis for the clinical promotion of EVs in later stages.

5.3 Standardized and commercialized production of extracellular vesicles

Effective isolation of EVs is the basis for their clinical application. From this point of view, standardized purification, preparation, production and preservation are essential. Increasing evidence indicates that EVs from different types of parent cells carry distinct bioactive molecules that play different biological functions in bone remodelling and regeneration (Tian et al., 2018). Even EVs derived from the same parent cell still have diverse sizes, component cargoes, proteins, and other biophysics or biochemical properties (Yan et al., 2020). Thus, only by solving the standardizing issues can we realize a safer clinical application of EVs.

Currently, differential ultracentrifugation and sequential ultrafiltration are the most commonly employed approaches to isolate EVs (Richter et al., 2021). However, these techniques have certain disadvantages, including being time-consuming, having low EV purity and output, and having unfavourable reproducibility (Théry et al., 2018). Commercialized isolation kits for EVs are now available but have not overcome the low efficiency limitation and are expensive. Therefore, the development of a standardized and time-saving isolation technique to harvest high-purity EVs at low costs would be a cornerstone to eventually achieve commercialized clinical application of EVs.

Accordingly, technology to accurately regulate the expression of bioactive molecules in EVs is crucial to achieve more desirable tissue repair. Therefore, we will further explore the engineering strategies of EVs through gene modification, specific preconditioning treatment, external gene/protein loading or combination to prepare EVs with enhanced bone induction ability. In addition to engineering modification of EVs, improving the loading efficiency of internal cargoes without interfering with the natural lipid and protein compositions of EVs is also an important issue that cannot be ignored.

6 Conclusion

Critical-size bone defects have become a serious threat to populations at both the individual and societal levels. The progress of stem cell therapy has led to promising results for remodelling and regeneration of bone tissues. However, stem cell therapy has some disadvantages that restrict its wider clinical applications. These disadvantages, together with

problems caused by storage and transport, further limit the application of MSCs in repairing critical-size bone defects. An increasing amount of convincing evidence has demonstrated that most beneficial functions of stem cells are attributed to EVs, which gives rise to a new paradigm in which EVs secreted from both stem cells and other cells promote bone regeneration by modulating crosstalk between EVs and resident bone cells or the surrounding microenvironment. Although the utilization of EVs as bioactive nanotherapeutics in regenerative medicine has just started from the preliminary stage, the results of preclinical tests showed that applications of EVs would overcome limitations of stem cell-based therapies and possible side effects associated with the administration of stem cells. In addition, some unique advantages of EVs, including low immune rejection, feasibility to modify membrane constituents, ability to pass the blood–brain barrier, convenient isolation, and lack of tumorigenicity, make the application of EVs a promising choice in biomedical treatment for critical-size bone defects.

Accumulated findings suggest that EV-mediated therapy may be an effective alternative to regulate the bone metabolism microenvironment. Here, the authors reviewed the molecular mechanisms of the effects of EVs on osteogenesis, osteoclast differentiation, angiogenesis, and immune reactions. It is well-recognized that EVs derived from different sources have different internal cargoes, such as inflammatory cytokines, signalling molecules, mRNAs, miRNAs and lncRNAs. The diverse capabilities of EVs come from different internal cargoes. Currently, scholars mainly focus on miRNAs, which play a critical role in EV-mediated critical-size bone defect regeneration. However, researchers had no information about critical proteins and other RNAs involved in the interactions between different EVs and EV-target cells, especially in distinct pathological circumstances. These problems must be of great interest to future preclinical and clinical studies aiming to explore the underlying therapeutic mechanisms of EVs. In addition to mechanistic studies, further functional studies of EV-mediated therapy are also needed, as EVs extracted *ex vivo* do not exactly mirror those extracted *in vivo* when parent cells are exposed to specific diseases or injury-related conditions.

Efficient delivery, bioactivity maintenance, and controlled/sustained release will become key factors for the safe and effective application of EVs in critical-size bone defect repair. Before resolving these issues, the isolation and characterization techniques need to be standardized first, but the field has yet to achieve consensus. Although scholars in EV-mediated BTE face numerous challenges, with continued advances in understanding EV biology and therapeutic mechanisms, together with the rapid development of related disciplines, such as bioengineering, chemistry, material science, and nanotechnology, it is believed that EVs will stimulate further explorations and inspirations for tissue engineering and efficient nanotherapeutics in the near future, eventually bringing the spring of cell-free regenerative medicine for critical-size bone defect repair.

Author contributions

All authors contributed to the review concept, design, manuscript preparation and writing. FL and TS conducted extensive literature searches, designed the figures and wrote the main part of the manuscript. YA and LM prepared the tables and edited the manuscript. YL contributed to the figure and table preparation. ZZ and FS both performed final revision of the manuscript.

Funding

This work was supported by the National Natural Science Foundation of China (No. 82201069), the Innovative Talent Promotion Plan of Shaanxi Province - Research Fund for Young Star of Science and Technology (No. 2021KJXX-24), the Postdoctoral Science Foundation of China (No. 2022M713578) and Guangdong Basic and Applied Basic Research Foundation (No. 2022A1515110175).

Conflict of interest

The authors declare that the research was conducted in the absence of any commercial or financial relationships that could be construed as a potential conflict of interest.

Publisher's note

All claims expressed in this article are solely those of the authors and do not necessarily represent those of their affiliated organizations, or those of the publisher, the editors and the reviewers. Any product that may be evaluated in this article, or claim that may be made by its manufacturer, is not guaranteed or endorsed by the publisher.

References

Anderson, J. D., Johansson, H. J., Graham, C. S., Vesterlund, M., Pham, M. T., Bramlett, C. S., et al. (2016). Comprehensive proteomic analysis of mesenchymal stem cell exosomes reveals modulation of angiogenesis via nuclear factor-KappaB signaling. *Stem. Cells* 34 (3), 601–613. doi:10.1002/stem.2298

Ando, Y., Matsubara, K., Ishikawa, J., Fujio, M., Shohara, R., Hibi, H., et al. (2014). Stem cell-conditioned medium accelerates distraction osteogenesis through multiple regenerative mechanisms. *Bone* 61, 82–90. doi:10.1016/j.bone.2013.12.029

Arenaccio, C., Chiozzini, C., Ferrantelli, F., Leone, P., Olivetta, E., and Federico, M. (2019). Exosomes in therapy: Engineering, pharmacokinetics and future applications. *Curr. Drug. Targets* 20 (1), 87–95. doi:10.2174/1389450119666180521100409

Baberg, F., Geyh, S., Waldera-Lupa, D., Stefanski, A., Zilkens, C., Haas, R., et al. (2019). Secretome analysis of human bone marrow derived mesenchymal stromal cells. *Biochim. Biophys. Acta. Proteins. Proteom.* 1867 (4), 434–441. doi:10.1016/j.bbapap.2019.01.013

Baglio, S. R., Rooijers, K., Koppers-Lalic, D., Verweij, F. J., Pérez Lanzón, M., Zini, N., et al. (2015). Human bone marrow- and adipose-mesenchymal stem cells secrete exosomes enriched in distinctive miRNA and tRNA species. *Stem. Cell. Res. Ther.* 6 (1), 127. doi:10.1186/s13287-015-0116-z

Baldwin, P., Li, D. J., Auston, D. A., Mir, H. S., Yoon, R. S., and Koval, K. J. (2019). Autograft, allograft, and bone graft substitutes: Clinical evidence and indications for use in the setting of orthopaedic trauma surgery. *J. Orthop. Trauma.* 33 (4), 203–213. doi:10.1097/BOT.0000000000001420

Bao, L., You, B., Shi, S., Shan, Y., Zhang, Q., Yue, H., et al. (2018). Metastasis-associated MiR-23a from nasopharyngeal carcinoma-derived exosomes mediates angiogenesis by repressing A novel target gene TSGA10. *Oncogene* 37 (21), 2873–2889. doi:10.1038/s41388-018-0183-6

Behera, J., and Tyagi, N. (2018). Exosomes: Mediators of bone diseases, protection, and therapeutics potential. *Oncoscience* 5 (5-6), 181–195. doi:10.18632/oncoscience.421

Behrend, C., Carmouche, J., Millhouse, P. W., Ritter, L., Moskal, J., Rubery, P., et al. (2016). Allogeneic and autogenous bone grafts are affected by historical donor environmental exposure. *Clin. Orthop. Relat. Res.* 474 (6), 1405–1409. doi:10.1007/s11999-015-4572-7

Bianco, P., and Gehron Robey, P. (2000). Marrow stromal stem cells. *J. Clin. Investig.* 105 (12), 1663–1668. doi:10.1172/JCI10413

Blander, J. M. (2017). The many ways tissue phagocytes respond to dying cells. *Immunol. Rev.* 277 (1), 158–173. doi:10.1111/imr.12537

Bozec, A., and Soulat, D. (2017). Latest perspectives on macrophages in bone homeostasis. *Pflugers. Arch.* 469 (3-4), 517–525. doi:10.1007/s00424-017-1952-8

Briguglio, F., Falcomatà, D., Marconcini, S., Fiorillo, L., Briguglio, R., and Farronato, D. (2019). The use of titanium mesh in guided bone regeneration: A systematic review. *Int. J. Dent.* 2019, 1–8. doi:10.1155/2019/9065423

Can, A., and Karahuseyinoglu, S. (2007). Concise review: Human umbilical cord stroma with regard to the source of fetus-derived stem cells. *Stem Cells* 25 (11), 2886–2895. doi:10.1634/stemcells.2007-0417

Cao, Z., Wu, Y., Yu, L., Zou, L., Yang, L., Lin, S., et al. (2021). Exosomal MiR-335 derived from mature dendritic cells enhanced mesenchymal stem cell-mediated bone regeneration of bone defects in athymic rats. *Mol. Med.* 27 (1), 20. doi:10.1186/s10020-021-00268-5

Caplan, A. I. (2019). There is No "stem cell mess. *Tissue. Eng. Part b. Rev.* 25 (4), 291–293. doi:10.1089/ten.TEB.2019.0049

Casado, J. G., Blázquez, R., Vela, F. J., Álvarez, V., Tarazona, R., and Sánchez-Margallo, F. M. (2017). Mesenchymal stem cell-derived exosomes: Immunomodulatory evaluation in an antigen-induced synovitis porcine model. *Front. Vet. Sci.* 4, 39. doi:10.3389/fvets.2017.00039

Chen, S., Tang, Y., Liu, Y., Zhang, P., Lv, L., Zhang, X., et al. (2019). Exosomes derived from miR-375-overexpressing human adipose mesenchymal stem cells promote bone regeneration. *Cell. Prolif.* 52 (5), e12669. doi:10.1111/cpr.12669

Chen, S., Zheng, Y., Zhang, S., Jia, L., and Zhou, Y. (2017). Promotion effects of miR-375 on the osteogenic differentiation of human adipose-derived mesenchymal stem cells. *Stem. Cell. Rep.* 8 (3), 773–786. doi:10.1016/j.stemcr.2017.01.028

Chen, W., Huang, Y., Han, J., Yu, L., Li, Y., Lu, Z., et al. (2016). Immunomodulatory effects of mesenchymal stromal cells-derived exosome. *Immunol. Res.* 64 (4), 831–840. doi:10.1007/s12026-016-8798-6

Chew, J., Chuah, S. J., Teo, K., Zhang, S., Lai, R. C., Fu, J. H., et al. (2019). Mesenchymal stem cell exosomes enhance periodontal ligament cell functions and promote periodontal regeneration. *Acta. Biomater.* 89, 252–264. doi:10.1016/j.actbio.2019.03.021

Cosenza, S., Toupet, K., Maumus, M., Luz-Crawford, P., Blanc-Brude, O., Jorgensen, C., et al. (2018). Mesenchymal stem cells-derived exosomes are more immunosuppressive than microparticles in inflammatory arthritis. *Theranostics* 8 (5), 1399–1410. doi:10.7150/thno.21072

Cui, Y., Guo, Y., Kong, L., Shi, J., Liu, P., Li, R., et al. (2021). A bone-targeted engineered exosome platform delivering siRNA to treat osteoporosis. *Bioact. Mat.* 10, 207–221. doi:10.1016/j.bioactmat.2021.09.015

Cui, Y., Li, Z., Guo, Y., Qi, X., Yang, Y., Jia, X., et al. (2022). Bioinspired nanovesicles convert the skeletal endothelium-associated secretory phenotype to treat osteoporosis. *Acs. Nano.* 16 (7), 11076–11091. doi:10.1021/acsnano.2c03781

Cui, Y., Luan, J., Li, H., Zhou, X., and Han, J. (2016). Exosomes derived from mineralizing osteoblasts promote ST2 cell osteogenic differentiation by alteration of MicroRNA expression. *Febs. Lett.* 590 (1), 185–192. doi:10.1002/1873-3468.12024

Das, S., Galas, D. J., Ansel, K. M., Bitzer, M., Breakefield, X. O., Charest, A., et al. (2019). Extracellular RNA communication ConsortiumThe extracellular RNA communication Consortium: Establishing foundational knowledge and technologies for extracellular RNA research. *Cell.* 177 (2), 231–242. doi:10.1016/j.cell.2019.03.023

Davies, O. G., Cox, S. C., Azoidis, I., McGuinness, A., Cooke, M., Heaney, L. M., et al. (2019). Osteoblast-derived vesicle protein content is temporally regulated during osteogenesis: Implications for regenerative therapies. *Front. Bioeng. Biotechnol.* 7, 92. doi:10.3389/fbioe.2019.00092

Del Fattore, A., Luciano, R., Pascucci, L., Goffredo, B. M., Giorda, E., Scapaticci, M., et al. (2015). Immunoregulatory effects of mesenchymal stem cell-derived extracellular vesicles on T lymphocytes. *Cell. Transpl.* 24 (12), 2615–2627. doi:10.3727/096368915X687543

Duan, Y., Tan, Z., Yang, M., Li, J., Liu, C., Wang, C., et al. (2019). PC-3-Derived exosomes inhibit osteoclast differentiation by downregulating miR-214 and blocking NF-κB signaling pathway. *Biomed. Res. Int.* 2019, 1–8. doi:10.1155/2019/8650846

Eichholz, K. F., Woods, I., Riffault, M., Johnson, G. P., Corrigan, M., Lowry, M. C., et al. (2020). Human bone marrow stem/stromal cell osteogenesis is regulated via mechanically activated osteocyte-derived extracellular vesicles. *Stem. Cells. Transl. Med.* 9 (11), 1431–1447. doi:10.1002/sctm.19-0405

Elashiry, M., Elashiry, M. M., Elsayed, R., Rajendran, M., Auersvald, C., Zeitoun, R., et al. (2020). Dendritic cell derived exosomes loaded with immunoregulatory cargo reprogram local immune responses and inhibit degenerative bone disease *in vivo*. *J. Extracell. Vesicles.* 9 (1), 1795362. doi:10.1080/20013078.2020.1795362

Escudier, B., Dorval, T., Chaput, N., André, F., Caby, M. P., Novault, S., et al. (2005). Vaccination of metastatic melanoma patients with autologous dendritic cell (DC) derived-exosomes: Results of the first phase I clinical trial. *J. Transl. Med.* 3 (1), 10. doi:10.1186/1479-5876-3-10

Falacho, R. I., Palma, P. J., Marques, J. A., Figueiredo, M. H., Caramelo, F., Dias, I., et al. (2021). Collagenated porcine heterologous bone grafts: Histomorphometric evaluation of bone formation using different physical forms in a rabbit cancellous bone model. *Molecules* 26 (5), 1339. doi:10.3390/molecules26051339

Fan, J., Im, C. S., Guo, M., Cui, Z. K., Fartash, A., Kim, S., et al. (2016). Enhanced osteogenesis of adipose-derived stem cells by regulating bone morphogenetic protein signaling antagonists and agonists. *Stem. Cells. Transl. Med.* 5 (4), 539–551. doi:10.5966/sctm.2015-0249

Fan, J., Lee, C. S., Kim, S., Chen, C., Aghaloo, T., and Lee, M. (2020). Generation of small RNA-modulated exosome mimetics for bone regeneration. *Acs. Nano.* 14 (9), 11973–11984. doi:10.1021/acsnano.0c05122

Fan, L., Guan, P., Xiao, C., Wen, H., Wang, Q., Liu, C., et al. (2021). Exosome-functionalized polyetheretherketone-based implant with immunomodulatory property for enhancing osseointegration. *Bioact. Mat.* 6 (9), 2754–2766. doi:10.1016/j.bioactmat.2021.02.005

Fernandez-Yague, M. A., Abbah, S. A., McNamara, L., Zeugolis, D. I., Pandit, A., and Biggs, M. J. (2015). Biomimetic approaches in bone tissue engineering: Integrating biological and physicomechanical strategies. *Adv. Drug. Deliv. Rev.* 84, 1–29. doi:10.1016/j.addr.2014.09.005

Fu, Q. L., Chow, Y. Y., Sun, S. J., Zeng, Q. X., Li, H. B., Shi, J. B., et al. (2012). Mesenchymal stem cells derived from human induced pluripotent stem cells modulate T-cell phenotypes in allergic rhinitis. *Allergy* 67 (10), 1215–1222. doi:10.1111/j.1398-9995.2012.02875.x

Fuhrmann, G., Serio, A., Mazo, M., Nair, R., and Stevens, M. M. (2015). Active loading into extracellular vesicles significantly improves the cellular uptake and photodynamic effect of porphyrins. *J. Control. Release.* 205, 35–44. doi:10.1016/j.jconrel.2014.11.029

Furuta, T., Miyaki, S., Ishitobi, H., Ogura, T., Kato, Y., Kamei, N., et al. (2016). Mesenchymal stem cell-derived exosomes promote fracture healing in a mouse model. *Stem. Cells. Transl. Med.* 5 (12), 1620–1630. doi:10.5966/sctm.2015-0285

Gandolfi, M. G., Gardin, C., Zamparini, F., Ferroni, L., Esposti, M. D., Parchi, G., et al. (2020). Mineral-doped poly(L-lactide) acid scaffolds enriched with exosomes improve osteogenic commitment of human adipose-derived mesenchymal stem cells. *Nanomater. (Basel)* 10 (3), 432. doi:10.3390/nano10030432

Gao, M., Gao, W., Papadimitriou, J. M., Zhang, C., Gao, J., and Zheng, M. (2018). Exosomes-the enigmatic regulators of bone homeostasis. *Bone. Res.* 6, 36. doi:10.1038/s41413-018-0039-2

García-Sánchez, D., Fernández, D., Rodríguez-Rey, J. C., and Pérez-Campo, F. M. (2019). Enhancing survival, engraftment, and osteogenic potential of mesenchymal stem cells. *World. J. Stem. Cells* 11 (10), 748–763. doi:10.4252/wjsc.v11.i10.748

Ge, M., Ke, R., Cai, T., Yang, J., and Mu, X. (2015). Identification and proteomic analysis of osteoblast-derived exosomes. *Biochem. Biophys. Res. Commun.* 467 (1), 27–32. doi:10.1016/j.bbrc.2015.09.135

Ge, M., Wu, Y., Ke, R., Cai, T., Yang, J., and Mu, X. (2017). Value of osteoblast-derived exosomes in bone diseases. *J. Craniofac. Surg.* 28 (4), 866–870. doi:10.1097/SCS.0000000000003463

Grosso, A., Burger, M. G., Lunger, A., Schaefer, D. J., Banfi, A., and Di Maggio, N. (2017). It takes two to tango: Coupling of angiogenesis and osteogenesis for bone regeneration. *Front. Bioeng. Biotechnol.* 5, 68. doi:10.3389/fbioe.2017.00068

Guan, P., Liu, C., Xie, D., Mao, S., Ji, Y., Lin, Y., et al. (2021). Exosome-loaded extracellular matrix-mimic hydrogel with anti-inflammatory property facilitates/promotes growth plate injury repair. *Bioact. Mat.* 10, 145–158. doi:10.1016/j.bioactmat.2021.09.010

Guder, C., Gravius, S., Burger, C., Wirtz, D. C., and Schildberg, F. A. (2020). Osteoimmunology: A current update of the interplay between bone and the immune system. *Front. Immunol.* 11, 58. doi:10.3389/fimmu.2020.00058

Gunawardena, T., Rahman, M. T., Abdullah, B., and Abu Kasim, N. H. (2019). Conditioned media derived from mesenchymal stem cell cultures: The next generation for regenerative medicine. *J. Tissue. Eng. Regen. Med.* 13 (4), 569–586. doi:10.1002/term.2806

Harding, C., Heuser, J., and Stahl, P. (1983). Receptor-mediated endocytosis of transferrin and recycling of the transferrin receptor in rat reticulocytes. *J. Cell. Biol.* 97 (2), 329–339. doi:10.1083/jcb.97.2.329

Hendijani, F., Sadeghi-Aliabadi, H., and Haghjooy Javanmard, S. (2014). Comparison of human mesenchymal stem cells isolated by explant culture method from entire umbilical cord and wharton's jelly matrix. *Cell. Tissue. Bank.* 15 (4), 555–565. doi:10.1007/s10561-014-9425-1

Hu, G. W., Li, Q., Niu, X., Hu, B., Liu, J., Zhou, S. M., et al. (2015). Exosomes secreted by human-induced pluripotent stem cell-derived mesenchymal stem cells attenuate limb ischemia by promoting angiogenesis in mice. *Stem. Cell. Res. Ther.* 6 (1), 10. doi:10.1186/scrt546

Hu, K., and Olsen, B. R. (2016). The roles of vascular endothelial growth factor in bone repair and regeneration. *Bone* 91, 30–38. doi:10.1016/j.bone.2016.06.013

Hu, Y., Li, X., Zhang, Q., Gu, Z., Luo, Y., Guo, J., et al. (2021). Exosome-guided bone targeted delivery of antagomir-188 as an anabolic therapy for bone loss. *Bioact. Mater* 6 (9), 2905–2913. doi:10.1016/j.bioactmat.2021.02.014

Hu, Y., Zhang, Y., Ni, C. Y., Chen, C. Y., Rao, S. S., Yin, H., et al. (2020). Human umbilical cord mesenchymal stromal cells-derived extracellular vesicles exert potent bone protective effects by clec11a-mediated regulation of bone metabolism. *Theranostics* 10 (5), 2293–2308. doi:10.7150/thno.39238

Huang, C. C., Kang, M., Lu, Y., Shirazi, S., Diaz, J. I., Cooper, L. F., et al. (2020a). Functionally engineered extracellular vesicles improve bone regeneration. *Acta. Biomater.* 109, 182–194. doi:10.1016/j.actbio.2020.04.017

Huang, C. C., Kang, M., Shirazi, S., Lu, Y., Cooper, L. F., Gajendrareddy, P., et al. (2021). 3D encapsulation and tethering of functionally engineered extracellular vesicles to hydrogels. *Acta. Biomater.* 126, 199–210. doi:10.1016/j.actbio.2021.03.030

Huang, X., Chen, Z., Zhao, G., Shi, J., Huang, G., Chen, F., et al. (2020b). Combined culture experiment of mouse bone marrow mesenchymal stem cells and bioceramic scaffolds. *Exp. Ther. Med.* 20 (5), 1. doi:10.3892/etm.2020.9147

Jafari, D., Shajari, S., Jafari, R., Mardi, N., Gomari, H., Ganji, F., et al. (2020). Designer exosomes: A new platform for Biotechnology therapeutics. *BioDrugs* 34 (5), 567–586. doi:10.1007/s40259-020-00434-x

Jia, P., Chen, H., Kang, H., Qi, J., Zhao, P., Jiang, M., et al. (2016). Deferoxamine released from poly(lactic-co-glycolic acid) promotes healing of osteoporotic bone defect via enhanced angiogenesis and osteogenesis. *J. Biomed. Mat. Res. A* 104 (10), 2515–2527. doi:10.1002/jbm.a.35793

Jia, Y., Zhu, Y., Qiu, S., Xu, J., and Chai, Y. (2019). Exosomes secreted by endothelial progenitor cells accelerate bone regeneration during distraction osteogenesis by stimulating angiogenesis. *Stem. Cell. Res. Ther.* 10 (1), 12. doi:10.1186/s13287-018-1115-7

Jiang, Z. Z., Liu, Y. M., Niu, X., Yin, J. Y., Hu, B., Guo, S. C., et al. (2016). Exosomes secreted by human urine-derived stem cells could prevent kidney complications from type I diabetes in rats. *Stem. Cell. Res. Ther.* 7, 24. doi:10.1186/s13287-016-0287-2

Jin, Z., Ren, J., and Qi, S. (2020). Human bone mesenchymal stem cells-derived exosomes overexpressing MicroRNA-26a-5p alleviate osteoarthritis via down-regulation of PTGS2. *Int. Immunopharmacol.* 78, 105946. doi:10.1016/j.intimp.2019.105946

Jing, X., Wang, S., Tang, H., Li, D., Zhou, F., Xin, L., et al. (2022). Dynamically bioresponsive DNA hydrogel incorporated with dual-functional stem cells from apical papilla-derived exosomes promotes diabetic bone regeneration. *Acs. Appl. Mat. Interfaces.* 14 (14), 16082–16099. doi:10.1021/acsami.2c02278

Johnsen, K. B., Gudbergsson, J. M., Skov, M. N., Christiansen, G., Gurevich, L., Moos, T., et al. (2016). Evaluation of electroporation-induced adverse effects on adipose-derived stem cell exosomes. *Cytotechnology* 68 (5), 2125–2138. doi:10.1007/s10616-016-9952-7

Johnstone, R. M., Adam, M., Hammond, J. R., Orr, L., and Turbide, C. (1987). Vesicle Formation during reticulocyte maturation. Association of plasma membrane activities with released vesicles (exosomes). *J. Biol. Chem.* 262 (19), 9412–9420. doi:10.1016/s0021-9258(18)48095-7

Kang, Y., Xu, C., Meng, L., Dong, X., Qi, M., and Jiang, D. (2022). Exosome-functionalized magnesium-organic framework-based scaffolds with osteogenic, angiogenic and anti-inflammatory properties for accelerated bone regeneration. *Bioact. Mat.* 18, 26–41. doi:10.1016/j.bioactmat.2022.02.012

Karlsson, T., Lundholm, M., Widmark, A., and Persson, E. (2016). Tumor cell-derived exosomes from the prostate cancer cell line TRAMP-C1 impair osteoclast formation and differentiation. *PLoS One* 11 (11), e0166284. doi:10.1371/journal.pone.0166284

Katagiri, W., Watanabe, J., Toyama, N., Osugi, M., Sakaguchi, K., and Hibi, H. (2017). Clinical study of bone regeneration by conditioned medium from mesenchymal stem cells after maxillary sinus floor elevation. *Implant Dent.* 26 (4), 607–612. doi:10.1097/ID.0000000000000618

Kawakubo, A., Matsunaga, T., Ishizaki, H., Yamada, S., and Hayashi, Y. (2011). Zinc as an essential trace element in the acceleration of matrix vesicles-mediated mineral deposition. *Microsc. Res. Tech.* 74 (12), 1161–1165. doi:10.1002/jemt.21009

Kim, D. S., Lee, J. K., Kim, J. H., Lee, J., Kim, D. S., An, S., et al. (2021). Advanced PLGA hybrid scaffold with a bioactive PDRN/BMP2 nanocomplex for angiogenesis and bone regeneration using human fetal MSCs. *Sci. Adv.* 7 (50), eabj1083. doi:10.1126/sciadv.abj1083

Kim, M. S., Haney, M. J., Zhao, Y., Mahajan, V., Deygen, I., Klyachko, N. L., et al. (2016). Development of exosome-encapsulated paclitaxel to overcome MDR in cancer cells. *Nanomedicine* 12 (3), 655–664. doi:10.1016/j.nano.2015.10.012

Kobayashi-Sun, J., Yamamori, S., Kondo, M., Kuroda, J., Ikegame, M., Suzuki, N., et al. (2020). Uptake of osteoblast-derived extracellular vesicles promotes the differentiation of osteoclasts in the zebrafish scale. *Commun. Biol.* 3 (1), 190. doi:10.1038/s42003-020-0925-1

Korhonen, R. K., and Jurvelin, J. S. (2010). Compressive and tensile properties of articular cartilage in axial loading are modulated differently by osmotic environment. *Med. Eng. Phys.* 32 (2), 155–160. doi:10.1016/j.medengphy.2009.11.004

Kou, X., Xu, X., Chen, C., Sanmillan, M. L., Cai, T., Zhou, Y., et al. (2018). The fas/fap-1/cav-1 complex regulates IL-1RA secretion in mesenchymal stem cells to accelerate wound healing. *Sci. Transl. Med.* 10 (432), eaai8524. doi:10.1126/scitranslmed.aai8524

Lai, R. C., Arslan, F., Lee, M. M., Sze, N. S., Choo, A., Chen, T. S., et al. (2010). Exosome secreted by MSC reduces myocardial ischemia/reperfusion injury. *Stem. Cell. Res.* 4 (3), 214–222. doi:10.1016/j.scr.2009.12.003

Li, D., Liu, J., Guo, B., Liang, C., Dang, L., Lu, C., et al. (2016a). Osteoclast-derived exosomal miR-214-3p inhibits osteoblastic bone formation. *Nat. Commun.* 7, 10872. doi:10.1038/ncomms10872

Li, H., Liu, D., Li, C., Zhou, S., Tian, D., Xiao, D., et al. (2017). Exosomes secreted from mutant-HIF-1α-modified bone-marrow-derived mesenchymal stem cells attenuate early steroid-induced avascular necrosis of femoral head in rabbit. *Cell. Biol. Int.* 41 (12), 1379–1390. doi:10.1002/cbin.10869

Li, Q. C., Li, C., Zhang, W., Pi, W., and Han, N. (2022a). Potential effects of exosomes and their MicroRNA carrier on osteoporosis. *Curr. Pharm. Des.* 28 (11), 899–909. doi:10.2174/1381612828666220128104206

Li, R., Li, D., Wang, H., Chen, K., Wang, S., Xu, J., et al. (2022b). Exosomes from adipose-derived stem cells regulate M1/M2 macrophage phenotypic polarization to promote bone healing via MiR-451a/MIF. *Stem. Cell. Res. Ther.* 13 (1), 149. doi:10.1186/s13287-022-02823-1

Li, W., Liu, Y., Zhang, P., Tang, Y., Zhou, M., Jiang, W., et al. (2018). Tissue-engineered bone immobilized with human adipose stem cells-derived exosomes promotes bone regeneration. *Acs. Appl. Mat. Interfaces* 10 (6), 5240–5254. doi:10.1021/acsami.7b17620

Li, X., Chen, C., Wei, L., Li, Q., Niu, X., Xu, Y., et al. (2016b). Exosomes derived from endothelial progenitor cells attenuate vascular repair and accelerate reendothelialization by enhancing endothelial function. *Cytotherapy* 18 (2), 253–262. doi:10.1016/j.jcyt.2015.11.009

Li, Z., Wang, Y., Xiang, S., Zheng, Z., Bian, Y., Feng, B., et al. (2020c). Chondrocytes-derived exosomal MiR-8485 regulated the wnt/β-catenin pathways to promote chondrogenic differentiation of BMSCs. *Biochem. Biophys. Res. Commun.* 523 (2), 506–513. doi:10.1016/j.bbrc.2019.12.065

Lian, Q., Zhang, Y., Zhang, J., Zhang, H. K., Wu, X., Zhang, Y., et al. (2010). Functional mesenchymal stem cells derived from human induced pluripotent stem cells attenuate limb ischemia in mice. *Circulation* 121 (9), 1113–1123. doi:10.1161/CIRCULATIONAHA.109.898312

Liang, B., Liang, J. M., Ding, J. N., Xu, J., Xu, J. G., and Chai, Y. M. (2019). Dimethyloxaloylglycine-stimulated human bone marrow mesenchymal stem cell-derived exosomes enhance bone regeneration through angiogenesis by targeting the AKT/mTOR pathway. *Stem. Cell. Res. Ther.* 10 (1), 335. doi:10.1186/s13287-019-1410-y

Liang, W., Han, B., Hai, Y., Sun, D., and Yin, P. (2022). Mechanism of action of mesenchymal stem cell-derived exosomes in the intervertebral disc degeneration treatment and bone repair and regeneration. *Front. Cell. Dev. Biol.* 9, 833840. doi:10.3389/fcell.2021.833840

Liang, Z., Luo, Y., and Lv, Y. (2020). Mesenchymal stem cell-derived microvesicles mediate BMP2 gene delivery and enhance bone regeneration. *J. Mat. Chem. B* 8 (30), 6378–6389. doi:10.1039/d0tb00422g

Liao, W., Du, Y., Zhang, C., Pan, F., Yao, Y., Zhang, T., et al. (2019). Exosomes: The next generation of endogenous nanomaterials for advanced drug delivery and therapy. *Acta. Biomater.* 86, 1–14. doi:10.1016/j.actbio.2018.12.045

Lin, Z., Xiong, Y., Meng, W., Hu, Y., Chen, L., Chen, L., et al. (2021). Exosomal PD-L1 induces osteogenic differentiation and promotes fracture healing by acting as an immunosuppressant. *Bioact. Mat.* 13, 300–311. doi:10.1016/j.bioactmat.2021.10.042

Lindenbergh, M., and Stoorvogel, W. (2018). Antigen presentation by extracellular vesicles from professional antigen-presenting cells. *Annu. Rev. Immunol.* 36, 435–459. doi:10.1146/annurev-immunol-041015-055700

Liu, A., Lin, D., Zhao, H., Chen, L., Cai, B., Lin, K., et al. (2021a). Optimized BMSC-derived osteoinductive exosomes immobilized in hierarchical scaffold via lyophilization for bone repair through bmpr2/acvr2b competitive receptor-activated Smad pathway. *Biomaterials* 272, 120718. doi:10.1016/j.biomaterials.2021.120718

Liu, D., Kou, X., Chen, C., Liu, S., Liu, Y., Yu, W., et al. (2018). Circulating apoptotic bodies maintain mesenchymal stem cell homeostasis and ameliorate osteopenia via transferring multiple cellular factors. *Cell. Res.* 28 (9), 918–933. doi:10.1038/s41422-018-0070-2

Liu, L., Liu, Y., Feng, C., Chang, J., Fu, R., Wu, T., et al. (2019). Lithium-containing biomaterials stimulate bone marrow stromal cell-derived exosomal miR-130a secretion to promote angiogenesis. *Biomaterials* 192, 523–536. doi:10.1016/j.biomaterials.2018.11.007

Liu, L., Yu, F., Li, L., Zhou, L., Zhou, T., Xu, Y., et al. (2021b). Bone marrow stromal cells stimulated by strontium-substituted calcium silicate ceramics: Release of exosomal miR-146a regulates osteogenesis and angiogenesis. *Acta. Biomater.* 119, 444–457. doi:10.1016/j.actbio.2020.10.038

Liu, W., Li, L., Rong, Y., Qian, D., Chen, J., Zhou, Z., et al. (2020). Hypoxic mesenchymal stem cell-derived exosomes promote bone fracture healing by the transfer of MiR-126. *Acta. Biomater.* 103, 196–212. doi:10.1016/j.actbio.2019.12.020

Liu, X., Li, Q., Niu, X., Hu, B., Chen, S., Song, W., et al. (2017). Exosomes secreted from human-induced pluripotent stem cell-derived mesenchymal stem cells prevent osteonecrosis of the femoral head by promoting angiogenesis. *Int. J. Biol. Sci.* 13 (2), 232–244. doi:10.7150/ijbs.16951

Liu, Y., and Xiong, D. (2021c). A tannic acid-reinforced PEEK-hydrogel composite material with good biotribological and self-healing properties for artificial joints. *J. Mat. Chem. B* 9 (38), 8021–8030. doi:10.1039/d1tb01357b

Luo, Z. W., Li, F. X., Liu, Y. W., Rao, S. S., Yin, H., Huang, J., et al. (2019). Aptamer-functionalized exosomes from bone marrow stromal cells target bone to promote bone regeneration. *Nanoscale* 11 (43), 20884–20892. doi:10.1039/c9nr02791b

Lv, P. Y., Gao, P. F., Tian, G. J., Yang, Y. Y., Mo, F. F., Wang, Z. H., et al. (2020). Osteocyte-derived exosomes induced by mechanical strain promote human periodontal ligament stem cell proliferation and osteogenic differentiation via the MiR-181b-5p/PTEN/AKT signaling pathway. *Stem. Cell. Res. Ther.* 11 (1), 295. doi:10.1186/s13287-020-01815-3

Ma, Q., Liang, M., Wu, Y., Luo, F., Ma, Z., Dong, S., et al. (2021). Osteoclast-derived apoptotic bodies couple bone resorption and formation in bone remodeling. *Bone. Res.* 9 (1), 5. doi:10.1038/s41413-020-00121-1

Malekpour, K., Hazrati, A., Zahar, M., Markov, A., Zekiy, A. O., Navashenaq, J. G., et al. (2022). The potential use of mesenchymal stem cells and their derived exosomes for orthopedic diseases treatment. *Stem. Cell. Rev. Rep.* 18 (3), 933–951. doi:10.1007/s12015-021-10185-z

Martinez Saez, D., Sasaki, R. T., Neves, A. D., and da Silva, M. C. (2016). Stem cells from human exfoliated deciduous teeth: A growing literature. *Cells. Tissues. Organs* 202 (5-6), 269–280. doi:10.1159/000447055

Martins, M., Ribeiro, D., Martins, A., Reis, R. L., and Neves, N. M. (2016). Extracellular vesicles derived from osteogenically induced human bone marrow mesenchymal stem cells can modulate lineage commitment. *Stem. Cell. Rep.* 6 (3), 284–291. doi:10.1016/j.stemcr.2016.01.001

McIntosh, K., Zvonic, S., Garrett, S., Mitchell, J. B., Floyd, Z. E., Hammill, L., et al. (2006). The immunogenicity of human adipose-derived cells: Temporal changes *in vitro*. *Stem. Cells* 24 (5), 1246–1253. doi:10.1634/stemcells.2005-0235

Mirsaidi, A., Kleinhans, K. N., Rimann, M., Tiaden, A. N., Stauber, M., Rudolph, K. L., et al. (2012). Telomere length, telomerase activity and osteogenic differentiation are maintained in adipose-derived stromal cells from senile osteoporotic SAMP6 mice. *J. Tissue. Eng. Regen. Med.* 6 (5), 378–390. doi:10.1002/term.440

Nagelkerke, A., Ojansivu, M., van der Koog, L., Whittaker, T. E., Cunnane, E. M., Silva, A. M., et al. (2021). Extracellular vesicles for tissue repair and regeneration: Evidence, challenges and opportunities. *Adv. Drug. Deliv. Rev.* 175, 113775. doi:10.1016/j.addr.2021.04.013

Nakamura, S., Yamada, Y., Katagiri, W., Sugito, T., Ito, K., and Ueda, M. (2009). Stem cell proliferation pathways comparison between human exfoliated deciduous teeth and dental pulp stem cells by gene expression profile from promising dental pulp. *J. Endod.* 35 (11), 1536–1542. doi:10.1016/j.joen.2009.07.024

Narayanan, K., Kumar, S., Padmanabhan, P., Gulyas, B., Wan, A., and Rajendran, V. M. (2018). Lineage-specific exosomes could override extracellular matrix mediated human mesenchymal stem cell differentiation. *Biomaterials* 182, 312–322. doi:10.1016/j.biomaterials.2018.08.027

Narayanan, R., Huang, C. C., and Ravindran, S. (2016). Hijacking the cellular mail: Exosome mediated differentiation of mesenchymal stem cells. *Stem. Cells. Int.* 2016, 1–11. doi:10.1155/2016/3808674

Nauth, A., Schemitsch, E., Norris, B., Nollin, Z., and Watson, J. T. (2018). Critical-size bone defects: Is there a consensus for diagnosis and treatment? *J. Orthop. Trauma.* 32 (1), S7–S11. S7–S11. doi:10.1097/BOT.0000000000001115

Parker, A. M., and Katz, A. J. (2006). Adipose-derived stem cells for the regeneration of damaged tissues. *Expert. Opin. Biol. Ther.* 6 (6), 567–578. doi:10.1517/14712598.6.6.567

Pascucci, L., Coccè, V., Bonomi, A., Ami, D., Ceccarelli, P., Ciusani, E., et al. (2014). Paclitaxel is incorporated by mesenchymal stromal cells and released in exosomes that inhibit *in vitro* tumor growth: A new approach for drug delivery. *J. Control. Release* 192, 262–270. doi:10.1016/j.jconrel.2014.07.042

Phan, J., Kumar, P., Hao, D., Gao, K., Farmer, D., and Wang, A. (2018). Engineering mesenchymal stem cells to improve their exosome efficacy and yield for cell-free therapy. *J. Extracell. Vesicles.* 7 (1), 1522236. doi:10.1080/20013078.2018.1522236

Puddu, P., Puddu, G. M., Cravero, E., Muscari, S., and Muscari, A. (2010). The involvement of circulating microparticles in inflammation, coagulation and cardiovascular diseases. *Can. J. Cardiol.* 26 (4), 140–145. doi:10.1016/s0828-282x(10)70371-8

Qi, X., Zhang, J., Yuan, H., Xu, Z., Li, Q., Niu, X., et al. (2016). Exosomes secreted by human-induced pluripotent stem cell-derived mesenchymal stem cells repair critical-sized bone defects through enhanced angiogenesis and osteogenesis in osteoporotic rats. *Int. J. Biol. Sci.* 12 (7), 836–849. doi:10.7150/ijbs.14809

Qian, X., An, N., Ren, Y., Yang, C., Zhang, X., and Li, L. (2021). Immunosuppressive effects of mesenchymal stem cells-derived exosomes. *Stem. Cell. Rev. Rep.* 17 (2), 411–427. doi:10.1007/s12015-020-10040-7

Qin, Y., Peng, Y., Zhao, W., Pan, J., Ksiezak-Reding, H., Cardozo, C., et al. (2017). Myostatin inhibits osteoblastic differentiation by suppressing osteocyte-derived exosomal MicroRNA-218: A novel mechanism in muscle-bone communication. *J. Biol. Chem.* 292 (26), 11021–11033. doi:10.1074/jbc.M116.770941

Qin, Y., Sun, R., Wu, C., Wang, L., and Zhang, C. (2016a). Exosome: A novel approach to stimulate bone regeneration through regulation of osteogenesis and angiogenesis. *Int. J. Mol. Sci.* 17 (5), 712. doi:10.3390/ijms17050712

Qin, Y., Wang, L., Gao, Z., Chen, G., and Zhang, C. (2016b). Bone marrow stromal/stem cell-derived extracellular vesicles regulate osteoblast activity and differentiation *in vitro* and promote bone regeneration *in vivo*. *Sci. Rep.* 6, 21961. doi:10.1038/srep21961

Qin, Y., and Zhang, C. (2017). Endothelial progenitor cell-derived extracellular vesicle-meditated cell-to-cell communication regulates the proliferation and osteoblastic differentiation of bone mesenchymal stromal cells. *Mol. Med. Rep.* 16 (5), 7018–7024. doi:10.3892/mmr.2017.7403

Ren, L., Song, Z. J., Cai, Q. W., Chen, R. X., Zou, Y., Fu, Q., et al. (2019). Adipose mesenchymal stem cell-derived exosomes ameliorate hypoxia/serum deprivation-induced osteocyte apoptosis and osteocyte-mediated osteoclastogenesis *in vitro*. *Biochem. Biophys. Res. Commun.* 508 (1), 138–144. doi:10.1016/j.bbrc.2018.11.109

Rezaie, J., Mehranjani, M. S., Rahbarghazi, R., and Shariatzadeh, M. A. (2018). Angiogenic and restorative abilities of human mesenchymal stem cells were reduced following treatment with serum from diabetes mellitus type 2 patients. *J. Cell. Biochem.* 119 (1), 524–535. doi:10.1002/jcb.26211

Riau, A. K., Ong, H. S., Yam, G., and Mehta, J. S. (2019). Sustained delivery system for stem cell-derived exosomes. *Front. Pharmacol.* 10, 1368. doi:10.3389/fphar.2019.01368

Richter, M., Vader, P., and Fuhrmann, G. (2021). Approaches to surface engineering of extracellular vesicles. *Adv. Drug. Deliv. Rev.* 173, 416–426. doi:10.1016/j.addr.2021.03.020

Roseti, L., Parisi, V., Petretta, M., Cavallo, C., Desando, G., Bartolotti, I., et al. (2017). Scaffolds for bone tissue engineering: State of the art and new perspectives. *Mat. Sci. Eng. C. Mat. Biol. Appl.* 78, 1246–1262. doi:10.1016/j.msec.2017.05.017

Sakaguchi, K., Katagiri, W., Osugi, M., Kawai, T., Sugimura-Wakayama, Y., and Hibi, H. (2017). Periodontal tissue regeneration using the cytokine cocktail mimicking secretomes in the conditioned media from human mesenchymal stem cells. *Biochem. Biophys. Res. Commun.* 484 (1), 100–106. doi:10.1016/j.bbrc.2017.01.065

Sato, M., Suzuki, T., Kawano, M., and Tamura, M. (2017). Circulating osteocyte-derived exosomes contain miRNAs which are enriched in exosomes from MLO-Y4 cells. *Biomed. Rep.* 6 (2), 223–231. doi:10.3892/br.2016.824

Sato, Y. T., Umezaki, K., Sawada, S., Mukai, S. A., Sasaki, Y., Harada, N., et al. (2016). Engineering hybrid exosomes by membrane fusion with liposomes. *Sci. Rep.* 6, 21933. doi:10.1038/srep21933

Shang, F., Ming, L., Zhou, Z., Yu, Y., Sun, J., Ding, Y., et al. (2014). The effect of licochalcone A on cell-aggregates ecm secretion and osteogenic differentiation during bone formation in metaphyseal defects in ovariectomized rats. *Biomaterials* 35 (9), 2789–2797. doi:10.1016/j.biomaterials.2013.12.061

Shang, F., Yu, Y., Liu, S., Ming, L., Zhang, Y., Zhou, Z., et al. (2020). Advancing application of mesenchymal stem cell-based bone tissue regeneration. *Bioact. Mater.* 6 (3), 666–683. doi:10.1016/j.bioactmat.2020.08.014

Silva, D., Paz, A., Portinho, C. P., Lima, E., Kliemann, L. M., and Collares, M. (2021). Reconstruction of parietal bone defects with adiposederived mesenchymal stem cells. Experimental study. *Acta. Cir. Bras.* 35 (12), e351201. doi:10.1590/ACB351201

Sissung, T. M., and Figg, W. D. (2020). Stem cell clinics: Risk of proliferation. *Lancet. Oncol.* 21 (2), 205–206. doi:10.1016/S1470-2045(19)30787-9

Song, H., Li, X., Zhao, Z., Qian, J., Wang, Y., Cui, J., et al. (2019). Reversal of osteoporotic activity by endothelial cell-secreted bone targeting and biocompatible exosomes. *Nano. Lett.* 19 (5), 3040–3048. doi:10.1021/acs.nanolett.9b00287

Stahl, A., and Yang, Y. P. (2021). Regenerative approaches for the treatment of large bone defects. *Tissue. Eng. Part. b. Rev.* 27 (6), 539–547. doi:10.1089/ten.TEB.2020.0281

Stickney, Z., Losacco, J., McDevitt, S., Zhang, Z., and Lu, B. (2016). Development of exosome surface display technology in living human cells. *Biochem. Biophys. Res. Commun.* 472 (1), 53–59. doi:10.1016/j.bbrc.2016.02.058

Swanson, W. B., Zhang, Z., Xiu, K., Gong, T., Eberle, M., Wang, Z., et al. (2020). Scaffolds with controlled release of pro-mineralization exosomes to promote craniofacial bone healing without cell transplantation. *Acta. Biomater.* 118, 215–232. doi:10.1016/j.actbio.2020.09.052

Takeuchi, R., Katagiri, W., Endo, S., and Kobayashi, T. (2019). Exosomes from conditioned media of bone marrow-derived mesenchymal stem cells promote bone regeneration by enhancing angiogenesis. *PloS. One* 14 (11), e0225472. doi:10.1371/journal.pone.0225472

Tan, S., Tjio, C., Wong, J., Wong, K. L., Chew, J., Hui, J., et al. (2021). Mesenchymal stem cell exosomes for cartilage regeneration: A systematic review of preclinical *in vivo* studies. *Tissue. Eng. Part b. Rev.* 27 (1), 1–13. doi:10.1089/ten.TEB.2019.0326

Tang, H., He, Y., Li, L., Mao, W., Chen, X., Ni, H., et al. (2019). Exosomal MMP2 derived from mature osteoblasts promotes angiogenesis of endothelial cells via VEGF/Erk1/2 signaling pathway. *Exp. Cell. Res.* 383 (2), 111541. doi:10.1016/j.yexcr.2019.111541

Théry, C., Witwer, K. W., Aikawa, E., Alcaraz, M. J., Anderson, J. D., Andriantsitohaina, R., et al. (2018). Minimal information for studies of extracellular vesicles 2018 (MISEV2018): A position statement of the international society for extracellular vesicles and update of the MISEV2014 guidelines. *J. Extracell. Vesicles.* 7 (1), 1535750. doi:10.1080/20013078.2018.1535750

Tian, T., Zhang, H. X., He, C. P., Fan, S., Zhu, Y. L., Qi, C., et al. (2018). Surface functionalized exosomes as targeted drug delivery vehicles for cerebral ischemia therapy. *Biomaterials* 150, 137–149. doi:10.1016/j.biomaterials.2017.10.012

Toh, W. S., Lai, R. C., Hui, J., and Lim, S. K. (2017). MSC exosome as A cell-free MSC therapy for cartilage regeneration: Implications for osteoarthritis treatment. *Semin. Cell. Dev. Biol.* 67, 56–64. doi:10.1016/j.semcdb.2016.11.008

Umezu, T., Tadokoro, H., Azuma, K., Yoshizawa, S., Ohyashiki, K., and Ohyashiki, J. H. (2014). Exosomal MiR-135b shed from hypoxic multiple myeloma cells enhances angiogenesis by targeting factor-inhibiting HIF-1. *Blood* 124 (25), 3748–3757. doi:10.1182/blood-2014-05-576116

van Balkom, B. W., de Jong, O. G., Smits, M., Brummelman, J., den Ouden, K., de Bree, P. M., et al. (2013). Endothelial cells require MiR-214 to secrete exosomes that suppress senescence and induce angiogenesis in human and mouse endothelial cells. *Blood* 121 (19), 3997–4006. doi:10.1182/blood-2013-02-478925

van der Koog, L., Gandek, T. B., and Nagelkerke, A. (2022). Liposomes and extracellular vesicles as drug delivery systems: A comparison of composition, pharmacokinetics, and functionalization. *Adv. Healthc. Mat.* 11 (5), e2100639. doi:10.1002/adhm.202100639

Vizoso, F. J., Eiro, N., Cid, S., Schneider, J., and Perez-Fernandez, R. (2017). Mesenchymal stem cell secretome: Toward cell-free therapeutic strategies in regenerative medicine. *Int. J. Mol. Sci.* 18 (9), 1852. doi:10.3390/ijms18091852

Wan, Y., Wang, L., Zhu, C., Zheng, Q., Wang, G., Tong, J., et al. (2018). Aptamer-conjugated extracellular nanovesicles for targeted drug delivery. *Cancer. Res.* 78 (3), 798–808. doi:10.1158/0008-5472.CAN-17-2880

Wang, H. S., Hung, S. C., Peng, S. T., Huang, C. C., Wei, H. M., Guo, Y. J., et al. (2004). Mesenchymal stem cells in the wharton's jelly of the human umbilical cord. *Stem. Cells* 22 (7), 1330–1337. doi:10.1634/stemcells.2004-0013

Wang, K. X., Xu, L. L., Rui, Y. F., Huang, S., Lin, S. E., Xiong, J. H., et al. (2015). The effects of secretion factors from umbilical cord derived mesenchymal stem cells on osteogenic differentiation of mesenchymal stem cells. *PLoS. One.* 10 (3), e0120593. doi:10.1371/journal.pone.0120593

Wang, L., Jia, P., Shan, Y., Hao, Y., Wang, X., Jiang, Y., et al. (2017). Synergistic protection of bone vasculature and bone mass by desferrioxamine in osteoporotic mice. *Mol. Med. Rep.* 16 (5), 6642–6649. doi:10.3892/mmr.2017.7451

Wang, L., Wang, J., Zhou, X., Sun, J., Zhu, B., Duan, C., et al. (2020a). A new self-healing hydrogel containing hucMSC-derived exosomes promotes bone regeneration. *Front. Bioeng. Biotechnol.* 8, 564731. doi:10.3389/fbioe.2020.564731

Wang, M., Li, J., Ye, Y., He, S., and Song, J. (2020b). SHED-Derived conditioned exosomes enhance the osteogenic differentiation of PDLSCs via Wnt and BMP signaling *in vitro*. *Differentiation* 111, 1–11. doi:10.1016/j.diff.2019.10.003

Wang, Q., Shen, X., Chen, Y., Chen, J., and Li, Y. (2021a). Osteoblasts-derived exosomes regulate osteoclast differentiation through MiR-503-3p/hpse Axis. *Acta. Histochem.* 123 (7), 151790. doi:10.1016/j.acthis.2021.151790

Wang, R., Jiang, W., Zhang, L., Xie, S., Zhang, S., Yuan, S., et al. (2020c). Intra-articular delivery of extracellular vesicles secreted by chondrogenic progenitor cells from MRL/MpJ superhealer mice enhances articular cartilage repair in A mouse injury model. *Stem. Cell. Res. Ther.* 11 (1), 93. doi:10.1186/s13287-020-01594-x

Wang, X., Ao, J., Lu, H., Zhao, Q., Ma, Y., Zhang, J., et al. (2020d). Osteoimmune modulation and guided osteogenesis promoted by barrier membranes incorporated with S-nitrosoglutathione (GSNO) and mesenchymal stem cell-derived exosomes</p> Nitrosoglutathione (GSNO) and mesenchymal stem cell-derived exosomes. *Int. J. Nanomedicine.* 15, 3483–3496. doi:10.2147/IJN.S248741

Wang, Z., Yuan, Y., Ji, X., Xiao, X., Li, Z., Yi, X., et al. (2021b). The hippo-TAZ Axis mediates vascular endothelial growth factor C in glioblastoma-derived exosomes to promote angiogenesis. *Cancer. Lett.* 513, 1–13. doi:10.1016/j.canlet.2021.05.002

Wasnik, S., Rundle, C. H., Baylink, D. J., Yazdi, M. S., Carreon, E. E., Xu, Y., et al. (2018). 1, 25-dihydroxyvitamin D suppresses M1 macrophages and promotes M2 differentiation at bone injury sites. *JCI. Insight.* 3 (17), e98773. doi:10.1172/jci.insight.98773

Wei, F., Li, M., Crawford, R., Zhou, Y., and Xiao, Y. (2019a). Exosome-integrated titanium oxide nanotubes for targeted bone regeneration. *Acta. Biomater.* 86, 480–492. doi:10.1016/j.actbio.2019.01.006

Wei, R., Wu, J., and Li, Y. (2019b). Macrophage polarization following three-dimensional porous PEEK. *Mat. Sci. Eng. C. Mat. Biol. Appl.* 104, 109948. doi:10.1016/j.msec.2019.109948

Wu, D., Chang, X., Tian, J., Kang, L., Wu, Y., Liu, J., et al. (2021). Bone mesenchymal stem cells stimulation by magnetic nanoparticles and A static magnetic field: Release of exosomal miR-1260a improves osteogenesis and angiogenesis. *J. Nanobiotechnology.* 19 (1), 209. doi:10.1186/s12951-021-00958-6

Wu, D., Qin, H., Wang, Z., Yu, M., Liu, Z., Peng, H., et al. (2022). Bone mesenchymal stem cell-derived sEV-encapsulated thermosensitive hydrogels accelerate osteogenesis and angiogenesis by release of exosomal miR-21. *Front. Bioeng. Biotechnol.* 9, 829136. doi:10.3389/fbioe.2021.829136

Wu, J., Chen, L., Wang, R., Song, Z., Shen, Z., Zhao, Y., et al. (2019). Exosomes secreted by stem cells from human exfoliated deciduous teeth promote alveolar bone defect repair through the regulation of angiogenesis and osteogenesis. *Acs. Biomater. Sci. Eng.* 5 (7), 3561–3571. doi:10.1021/acsbiomaterials.9b00607

Wu, X., Pang, L., Lei, W., Lu, W., Li, J., Li, Z., et al. (2010). Inhibition of sca-1-positive skeletal stem cell recruitment by alendronate blunts the anabolic effects of parathyroid hormone on bone remodeling. *Cell. stem. Cell.* 7 (5), 571–580. doi:10.1016/j.stem.2010.09.012

Wu, Z., Pu, P., Su, Z., Zhang, X., Nie, L., and Chang, Y. (2020). Schwann cell-derived exosomes promote bone regeneration and repair by enhancing the biological activity of porous Ti6Al4V scaffolds. *Biochem. Biophys. Res. Commun.* 531 (4), 559–565. doi:10.1016/j.bbrc.2020.07.094

Xia, Y., He, X. T., Xu, X. Y., Tian, B. M., An, Y., and Chen, F. M. (2020). Exosomes derived from M0, M1 and M2 macrophages exert distinct influences on the proliferation and differentiation of mesenchymal stem cells. *PeerJ* 8, e8970. doi:10.7717/peerj.8970

Xiao, Z., Camalier, C. E., Nagashima, K., Chan, K. C., Lucas, D. A., de la Cruz, M. J., et al. (2007). Analysis of the extracellular matrix vesicle proteome in mineralizing osteoblasts. *J. Cell. Physiol.* 210 (2), 325–335. doi:10.1002/jcp.20826

Xie, H., Wang, Z., Zhang, L., Lei, Q., Zhao, A., Wang, H., et al. (2017). Extracellular vesicle-functionalized decalcified bone matrix scaffolds with enhanced pro-angiogenic and pro-bone regeneration activities. *Sci. Rep.* 7, 45622. doi:10.1038/srep45622

Xiong, Y., Chen, L., Yan, C., Zhou, W., Yu, T., Sun, Y., et al. (2020). M2 macrophagy-derived exosomal miRNA-5106 induces bone mesenchymal stem cells towards osteoblastic fate by targeting salt-inducible kinase 2 and 3. *J. Nanobiotechnology.* 18 (1), 66. doi:10.1186/s12951-020-00622-5

Xu, J. F., Yang, G. H., Pan, X. H., Zhang, S. J., Zhao, C., Qiu, B. S., et al. (2014). Altered MicroRNA expression profile in exosomes during osteogenic differentiation of human bone marrow-derived mesenchymal stem cells. *PLoS. One.* 9 (12), e114627. doi:10.1371/journal.pone.0114627

Yan, H. C., Yu, T. T., Li, J., Qiao, Y. Q., Wang, L. C., Zhang, T., et al. (2020). The delivery of extracellular vesicles loaded in biomaterial scaffolds for bone regeneration. *Front. Bioeng. Biotechnol.* 8, 1015. doi:10.3389/fbioe.2020.01015

Yang, J. X., Xie, P., Li, Y. S., Wen, T., and Yang, X. C. (2020a). Osteoclast-derived miR-23a-5p-containing exosomes inhibit osteogenic differentiation by regulating Runx2. *Cell. Signal.* 70, 109504. doi:10.1016/j.cellsig.2019.109504

Yang, S., Zhu, B., Yin, P., Zhao, L., Wang, Y., Fu, Z., et al. (2020b). Integration of human umbilical cord mesenchymal stem cells-derived exosomes with hydroxyapatite-embedded hyaluronic acid-alginate hydrogel for bone regeneration. *Acs. Biomater. Sci. Eng.* 6 (3), 1590–1602. doi:10.1021/acsbiomaterials.9b01363

Yang, X., Yang, J., Lei, P., and Wen, T. (2019). LncRNA MALAT1 shuttled by bone marrow-derived mesenchymal stem cells-secreted exosomes alleviates osteoporosis through mediating MicroRNA-34c/SATB2 Axis. *Aging* 11 (20), 8777–8791. doi:10.18632/aging.102264

Ying, C., Wang, R., Wang, Z., Tao, J., Yin, W., Zhang, J., et al. (2020). BMSC-exosomes carry mutant HIF-1α for improving angiogenesis and osteogenesis in critical-sized calvarial defects. *Front. Bioeng. Biotechnol.* 8, 565561. doi:10.3389/fbioe.2020.565561

Yu, W., Li, S., Guan, X., Zhang, N., Xie, X., Zhang, K., et al. (2022). Higher yield and enhanced therapeutic effects of exosomes derived from MSCs in hydrogel-assisted 3D culture system for bone regeneration. *Biomater. Adv.* 133, 112646. doi:10.1016/j.msec.2022.112646

Zara, J. N., Siu, R. K., Zhang, X., Shen, J., Ngo, R., Lee, M., et al. (2011). High doses of bone morphogenetic protein 2 induce structurally abnormal bone and inflammation *in vivo*. *Tissue. Eng. Part. a.* 17 (9-10), 1389–1399. doi:10.1089/ten.TEA.2010.0555

Zha, Y., Li, Y., Lin, T., Chen, J., Zhang, S., and Wang, J. (2021). Progenitor cell-derived exosomes endowed with VEGF plasmids enhance osteogenic induction and vascular remodeling in large segmental bone defects. *Theranostics* 11 (1), 397–409. doi:10.7150/thno.50741

Zha, Y., Lin, T., Li, Y., Zhang, X., Wang, Z., Li, Z., et al. (2020). Exosome-mimetics as an engineered gene-activated matrix induces *in-situ* vascularized osteogenesis. *Biomaterials* 247, 119985. doi:10.1016/j.biomaterials.2020.119985

Zhai, M., Zhu, Y., Yang, M., and Mao, C. (2020). Human mesenchymal stem cell derived exosomes enhance cell-free bone regeneration by altering their miRNAs profiles. *Adv. Sci. (Weinh).* 7 (19), 2001334. doi:10.1002/advs.202001334

Zhang, B., Huang, J., Liu, J., Lin, F., Ding, Z., and Xu, J. (2021a). Injectable composite hydrogel promotes osteogenesis and angiogenesis in spinal fusion by optimizing the bone marrow mesenchymal stem cell microenvironment and exosomes secretion. *Mat. Sci. Eng. C. Mat. Biol. Appl.* 123, 111782. doi:10.1016/j.msec.2020.111782

Zhang, J., Guan, J., Niu, X., Hu, G., Guo, S., Li, Q., et al. (2015). Exosomes released from human induced pluripotent stem cells-derived MSCs facilitate cutaneous wound healing by promoting collagen synthesis and angiogenesis. *J. Transl. Med.* 13, 49. doi:10.1186/s12967-015-0417-0

Zhang, J., Liu, X., Li, H., Chen, C., Hu, B., Niu, X., et al. (2016a). Exosomes/tricalcium phosphate combination scaffolds can enhance bone regeneration by activating the PI3K/akt signaling pathway. *Stem. Cell. Res. Ther.* 7 (1), 136. doi:10.1186/s13287-016-0391-3

Zhang, L., Jiao, G., Ren, S., Zhang, X., Li, C., Wu, W., et al. (2020). Exosomes from bone marrow mesenchymal stem cells enhance fracture healing through the promotion of osteogenesis and angiogenesis in a rat model of nonunion. *Stem. Cell. Res. Ther.* 11 (1), 38. doi:10.1186/s13287-020-1562-9

Zhang, S., Chu, W. C., Lai, R. C., Lim, S. K., Hui, J. H., and Toh, W. S. (2016b). Exosomes derived from human embryonic mesenchymal stem cells promote osteochondral regeneration. *Osteoarthr. Cartil.* 24 (12), 2135–2140. doi:10.1016/j.joca.2016.06.022

Zhang, S., Wong, K. L., Ren, X., Teo, K., Afizah, H., Choo, A., et al. (2022). Mesenchymal stem cell exosomes promote functional osteochondral repair in a clinically relevant porcine model. *Am. J. Sports. Med.* 50 (3), 788–800. doi:10.1177/03635465211068129

Zhang, Y., Hao, Z., Wang, P., Xia, Y., Wu, J., Xia, D., et al. (2019). Exosomes from human umbilical cord mesenchymal stem cells enhance fracture healing through HIF-1α-mediated promotion of angiogenesis in a rat model of stabilized fracture. *Cell. Prolif.* 52 (2), e12570. doi:10.1111/cpr.12570

Zhang, Y., Xie, Y., Hao, Z., Zhou, P., Wang, P., Fang, S., et al. (2021b). Umbilical mesenchymal stem cell-derived exosome-encapsulated hydrogels accelerate bone repair by enhancing angiogenesis. *Acs. Appl. Mat. Interfaces* 13 (16), 18472–18487. doi:10.1021/acsami.0c22671

Zhao, L., Burguera, E. F., Xu, H. H., Amin, N., Ryou, H., and Arola, D. D. (2010). Fatigue and human umbilical cord stem cell seeding characteristics of calcium phosphate-chitosan-biodegradable fiber scaffolds. *Biomaterials* 31 (5), 840–847. doi:10.1016/j.biomaterials.2009.09.106

Zhao, R., Yang, R., Cooper, P. R., Khurshid, Z., Shavandi, A., and Ratnayake, J. (2021). Bone grafts and substitutes in dentistry: A review of current trends and developments. *Molecules* 26 (10), 3007. doi:10.3390/molecules26103007

Zhao, Z., McGill, J., Gamero-Kubota, P., and He, M. (2019). Microfluidic on-demand engineering of exosomes towards cancer immunotherapy. *Lab. Chip* 19 (10), 1877–1886. doi:10.1039/c8lc01279b

Zheng, J., Zhu, L., Chen, Y., Jia, N., and Zhu, W. (2020). Iok InBone marrow-derived mesenchymal stem cells-secreted exosomal MicroRNA-192-5p delays inflammatory response in rheumatoid arthritis. *Int. Immunopharmacol* 78, 105985. doi:10.1016/j.intimp.2019.105985

Zhou, X., Cao, H., Guo, J., Yuan, Y., and Ni, G. (2022). Effects of BMSC-derived EVs on bone metabolism. *Pharmaceutics* 14 (5), 1012. doi:10.3390/pharmaceutics14051012

Zhu, Y., Li, Z., Zhang, Y., Lan, F., He, J., and Wu, Y. (2020). The essential role of osteoclast-derived exosomes in magnetic nanoparticle-infiltrated hydroxyapatite scaffold modulated osteoblast proliferation in an osteoporosis model. *Nanoscale* 12 (16), 8720–8726. doi:10.1039/d0nr00867b

frontiers | Frontiers in Bioengineering and Biotechnology

TYPE Original Research
PUBLISHED 19 January 2023
DOI 10.3389/fbioe.2023.1109195

OPEN ACCESS

EDITED BY
Lina Altomare,
Politecnico di Milano, Italy

REVIEWED BY
Chao Qi,
College of Bioengineering, Chongqing University, China
Junchao Wei,
Nanchang University, China

*CORRESPONDENCE
Wei Bian,
weibian@sxmu.edu.cn
Bin Zhao,
18636666068@163.com
Xing Wang,
kqwx100@163.com

†These authors have contributed equally to this work and share first authorship

SPECIALTY SECTION
This article was submitted to Biomaterials, a section of the journal Frontiers in Bioengineering and Biotechnology

RECEIVED 27 November 2022
ACCEPTED 09 January 2023
PUBLISHED 19 January 2023

CITATION
Ren J, Rao J, Wang H, He W, Feng J, Wei D, Zhao B, Wang X and Bian W (2023), Synergistic remineralization of enamel white spot lesions using mesoporous bioactive glasses loaded with amorphous calcium phosphate.
Front. Bioeng. Biotechnol. 11:1109195.
doi: 10.3389/fbioe.2023.1109195

Synergistic remineralization of enamel white spot lesions using mesoporous bioactive glasses loaded with amorphous calcium phosphate

Juan Ren[1,3†], Jianping Rao[1,3†], He Wang[1,3], Wenjing He[2], Jinnan Feng[1,3], Danni Wei[1,3], Bin Zhao[1,3*], Xing Wang[1,3*] and Wei Bian[2*]

[1]Shanxi Medical University School and Hospital of Stomatology, Taiyuan, China, [2]Department of Biochemistry and Molecular Biology, School of Basic Medical Science, Shanxi Medical University, Taiyuan, China, [3]Shanxi Province Key Laboratory of Oral Diseases Prevention and New Materials, Taiyuan, China

Objectives: The purpose of this study was to create a new delivery system that can synergistically remineralize enamel white spot lesions (WSLs).

Materials and methods: The delivery system (PAA-ACP@aMBG) was prepared by using aminated mesoporous bioactive glasses (aMBG) as the carrier loaded with polyacrylic-stabilized amorphous calcium phosphate (PAA-ACP). The materials were characterized by transmission electron microscopy (TEM), X-ray powder diffraction (XRD), inductively coupled plasma–optical emission spectrometry (ICP–OES), and so on. Forty-eight artificial WSLs enamel samples were randomized to four groups: artificial saliva (negative control, NC), casein phosphopeptide-amorphous calcium phosphate (CPP-ACP), PAA-ACP@aMBG, and MBG. The effects of demineralization and remineralization of the enamel surface were compared by means of surface microhardness (SMH) measurements, surface color change measurements, fluorescence microscopy (FM), X-ray diffraction (XRD) analysis and scanning electron microscopy (SEM).

Results: There was no significant difference in the surface microhardness recovery rate (SMHRR) or color recovery rate (CRR) among the CPP-ACP group, PAA-ACP@aMBG group and MBG group (P>0.05), but these values were significantly higher than those in the NC group ($p < 0.01$). FM demonstrated that the remineralization depth in the PAA-ACP@aMBG group was significantly greater than that of the remaining three groups ($p < 0.01$). SEM analysis indicated that the enamel demineralization marks in the PAA-ACP@aMBG group, CPP-ACP group, and MBG group were obscured by mineral deposition.

Conclusions: PAA-ACP@aMBG showed good mineralization properties, implying its great potential for clinical application.

KEYWORDS

fixed orthodontic, remineralization, white spot lesions, amorphous calcium phosphate, mesoporous bioactive glasses

1 Introduction

Orthodontic treatment can improve patient's quality of life through aesthetic and functional improvement, but it may also damage the dental tissue (Peng et al., 2022).

White spot lesions (WSLs) caused by early enamel demineralization are one of the most frequent complications of fixed orthodontic treatment, with the incidence of at least one WSLs ranging from 36% to 46% (Chapman et al., 2010). In severe cases, orthodontic brackets may even need to be removed. The main mechanism of WSLs demineralization is the acidic erosion of plaque biofilm, which dissolves the enamel hydroxyapatite minerals (Miller et al., 2016). Therefore, remineralization therapy with hydroxyapatite reformation has become a treatment option for WSLs. This method causes calcium and phosphorus from external sources to precipitate into the micropores at the end of the enamel prism, filling the gap between the prisms caused by demineralization and restoring the mineral content in the demineralized areas (Bansal et al., 2014). The latest systematic review and meta-analysis of studies indicated that the commonly used re-mineralization agents had an unsatisfactory micro-mineralization effect, and their prevention or treatment effects on WSLs were limited (Hu et al., 2020). Therefore, the prevention and treatment of enamel demineralization is still a major challenge for dentists (Mohabatpour et al., 2022).

In recent years, amorphous calcium phosphate (ACP) has emerged as a successful precursor for the biological mineralization of dentin and bone (Qi et al., 2018; Qi et al., 2019). In light of this, a new biomineralization theory that differs from the natural enamel crystallization pathway has been confirmed (Cölfen, 2010). This theory suggests that the solution-based biomimetic mineralization system has an outstanding effect on mineralization (Wang et al., 2016). In this biomimetic mineralization system, casein phosphopeptide (CPP), polyacrylic acid (PAA), polyamidoamine (PAMAM), L-glutamic acid (L-Glu), and seven other non-collagenous biomimetic analogs play important roles in inducing ACP to remineralize type I collagen (Thula et al., 2010). Studies have demonstrated that by employing biomimetic analogs as ACP precursor stabilizers, ACP can be maintained in a moldable and nanoparticulate state, known as the polymer-induced liquid precursor (PILP) phase, and then transformed into apatite microcrystals (Yan et al., 2022). *In vitro* and animal model studies have shown that stable amorphous calcium phosphate precursors with biomimetic analogs have great potential for remineralization therapy (Ye et al., 2016; Gonçalves et al., 2021).

However, it has been reported that the existing CPP-ACP product produces a small amount of dotted and blocky high-density mineralization with uneven distribution, and a large number of demineralized pores are still visible (Fernández-Ferrer et al., 2018). It has been suggested that this is due to the rapid and uneven release rate of ACP mineralization precursors from CPP-ACP, which is dissolved and transformed into apatite microcrystals before reaching the demineralized enamel surface (Höchli et al., 2017). To solve the above problems caused by the CPP-ACP material characteristics, we introduced a novel carrier that can directly deliver CPP-ACP to the enamel surface. This material is a special mesoporous bioactive Na_2O-CaO-SiO_2-P_2O_5 glass system with good biocompatibility and surface bioactivity and a higher calcium content than the general silica-based class materials (Chen et al., 2018). It was confirmed that hydroxyapatite mineral deposits formed on the enamel and dentin surfaces after treatment with this bioactive glass (Dai et al., 2019).

At present, there are a number of reports of the use of mesoporous bioactive glass to load various metal cations (Shuai et al., 2019; Vallet-Regi and Salinas, 2021). Fang Hua et al. used mesoporous silica loaded with amorphous calcium phosphate to deliver mineralized precursors (Hua et al., 2020), Jinhua Song et al. used carboxymethyl chitosan and lysozyme to wrap amorphous calcium phosphate to construct an amorphous enamel-like layer (Song et al., 2021), and Zuohui Xiao et al. used polypeptides to induce amorphous calcium phosphate remineralization and biomimetic remineralization of dental enamel (Xiao et al., 2017). Inspired by these studies, we used an ammoniated mesoporous bioactive glass carrier loaded with polyacrylic acid-stabilized amorphous calcium phosphate PAA-ACP@aMBG. The advantage of our material is that it can achieve uniform delivery and periodic replenishment of mineralized precursors, and fully remineralized to form hydroxyapatite crystals on the enamel surface under synergistic action.

This study's objective was to evaluate the ability of PAA-ACP@aMBG to remineralize WSLs and compare it with CPP-ACP, a commercially available remineralizer. This new material with synergistic remineralization effects is expected to be a new prospect for the treatment of early enamel caries.

2 Materials and methods

2.1 Materials

Cetyl trimethyl ammonium bromide (CTAB), calcium nitrate ($Ca(NO_3)_2{\cdot}4H_2O$), ethyl acetate, tetraethyl orthosilicate, anhydrous toluene, 3-aminopropyl triethoxysilane (APTES), polyacrylic acid (PAA), calcium chloride, disodium hydrogen phosphate, dipotassium hydrogen phosphate, glacial acetic acid, potassium hydroxide and fluoride (NaF) were all purchased from Sinopharm Chemical Reagent Co., Ltd. Artificial saliva was provided by Beijing Leigen Biotechnology Co., Ltd. All of the chemicals used in the experiments were of analytical grade. CPP-ACP dental protectors were purchased from GC Corporation Tokyo, Japan.

2.2 Preparation of PAA-ACP@aMBG

First, .56 g of cetyl trimethyl ammonium bromide (CTAB) was dissolved in 26 mL of deionized water and stirred vigorously at 40°C for 30 min, and then 8 mL of ethyl acetate was quickly added to the solution. Second, after adjusting the pH of the solution to 9 with ammonia, 6 mL of ethyl orthosilicate was slowly dropped into the mixture, and then 2.8 g of calcium nitrate tetrahydrate was added. Third, after stirring vigorously for 4h, the samples were centrifuged, washed three times and dried at 60°C overnight. The dried product was calcined at 700°C for 6 h to remove the structure template CTAB and obtain MBG. Finally, 100 mg MBG was dispersed in 80 mL of anhydrous toluene, and 1 mL of 3-aminopropyl triethoxysilane (APTES) was added. The mixture was condensed and refluxed for 24 h, washed three times, and then dried for 12 h at 80°C to obtain aminated mesoporous bioactive glasses (aMBG).

Add Polyacrylic acid (PAA) to a 9.0 mM $CaCl_2{\cdot}2H_2O$ solution to obtain a 1,000 μg/mL polyacrylic acid solution, and then 4.2 mM Na_2HPO_4 was added to synthesize the polyacrylate-stabilized amorphous calcium phosphate (PAA-ACP) solution. Finally, 200 mg of aMBG was added to 50 ml of PAA-ACP solution, and the mixture was

stirred at room temperature for 24 h, centrifuged and dried to obtain PAA-ACP@aMBG.

2.3 Material characterization

2.3.1 Characterization of MBG/aMBG/PAA-ACP@aMBG

X-ray powder diffraction (XRD; D8 ADVANCE A25, Germany) was used to analyze the MBG and PAA-ACP@aMBG powders. Scanning was repeated 4 times in the wide-angle diffraction range of 2θ to obtain the crystal structures of MBG and PAA-ACP@aMBG.

The chemical compositions of MBG, aMBG, and PAA-ACP@aMBG were analyzed by Fourier transform infrared spectroscopy (INVENIO, Germany). The zeta potentials of MBG, aMBG, and PAA-ACP@aMBG were measured with a zeta potential analyzer (Zeta sizer Nano, Malvern, UK). Thermogravimetric analysis (TGA) measured the load rate of aMBG from room temperature to 1,000°C under nitrogen protection at a rate of 10°C/min. The surface areas and pore sizes of MBG and aMBG were calculated using BET and BJH techniques (ASAP2020HD88 Micropore Physisorption Analyzer, United States).

2.3.2 TEM evaluation of PAA-ACP@aMBG

A proper amount of PAA-ACP@aMBG was dispersed in anhydrous ethanol, followed by ultrasonic oscillation for 30 min, and a drop of solution was added to the copper net of the transmission electron microscope. After drying, solution deposition was repeated twice. TEM (JEM-2100F, JEOL, Tokyo, Japan) was used for ultra structural observation.

2.3.3 ICP–OES evaluation of PAA-ACP@aMBG

To detect whether there is a difference in the amounts of calcium and phosphorus ions released by the PAA-ACP@aMBG group at different environmental pH values, this experiment utilized three groups of solutions with different pH values: pH = 4.0 (the minimum pH value of oral bacterial acid production), pH = 5.5 (the critical value of enamel demineralization) and pH = 7.0 (the normal oral pH value); 50 mmol/L lactic acid, 50 mmol/L acetic acid and 50 mmol/L HEPES solutions were used to prepare the solutions with the above pH values. One hundred milligrams of PAA-ACP@aMBG powder were immersed in the artificial saliva solutions with different pH values, and the solutions were placed in a 37°C constant temperature shaker. Centrifugation was performed at 0.5, 1, 3, 6, 12, 24, 48, 72, 96, and 120 h. Aspirate 1 mL of supernatant and add 1 mL of fresh solution. After a 10-fold dilution, the release of calcium and phosphorus ions in solution was detected by ICP-OES.

2.4 Preparation of enamel samples

Forty orthodontic premolars were collected with the approval of the Ethics Committee of The School of Stomatology of Shanxi Medical University (2022SLL016). After the removal of caries, restorations, fractured teeth and teeth with surface attachments, the samples were stored in 0.1% thymol at 4°C. Each collected premolar root was removed, and the crown was divided longitudinally into buccal and lingual enamel blocks. The smooth enamel surface was obtained by grinding and polishing the enamel surface with 800, 1,000, and 1,200 particle size silicon carbide sandpaper (Shenyang, China) in flowing deionized water. Finally, the samples were ultrasonically rinsed for 15 min in deionized water to remove residues. After the samples were dried, a blank window with a size of 1 mm × 3 mm was left on the enamel surface, and the other areas were painted with acid-resistant nail polish. Vickers micro hardness tester was used to evaluate the samples surface micro hardness (SMH). Vickers micro hardness values (VHNs) > 430 or <340 were excluded. Finally, 48 samples were reserved for further experiments.

Artificial WSLs was performed by soaking the enamel samples in demineralization solution (2.2 mM Ca $(NO_3)_2$, 2.2 mM KH_2PO_4, 50 mM glacial acetic acid, .1 mM NaF) and adjusting their pH value to 5. The samples were demineralized at 37°C for 4 days, after that they were washed with ultrasonication in deionized water for 15 min to stop demineralization.

2.5 Remineralization procedure

Forty-eight artificial WSLs enamel samples were randomized to four groups (n = 12). Group 1 (artificial saliva, NC group): Smeared with artificial saliva twice at low speed for 1 min each time. Group 2 (CPP-ACP group): Smeared with toothpaste containing CPP-ACP (5–10 wt%) twice at low speed for 1 min each time. Group 3 (PAA-ACP@aMBG group): The dry material powder was dispersed in deionized water to obtain PAA-ACP@aMBG paste (5-10 wt%), which was coated on each sample twice at low speed for 1 min each time. Group 4 (MBG group): The dry material powder was dispersed in deionized water to obtain MBG paste (5–10 wt%), which was smeared twice at low speed for 1 min each time.

All samples underwent pH cycling for 14 days and remineralization processes performed at 08:00, 14:00, and 22:00 each day (2 min each time). The samples were soaked in demineralization solution for 1 h before remineralization treatment and then placed in artificial saliva after remineralization treatment at 37°C to simulate the oral environment. The remineralization fluid was renewed daily, and a single operator handled every operation. The samples were completely rinsed in flowing water after pH cycling, and the remaining agent was then removed using an ultrasonic rinse in flowing water for 5 min.

2.6 Surface microhardness measurement

Ten samples were randomly selected from each group, and their hardness was evaluated pre-demineralization, following demineralization, and following remineralization. The SMH values of all samples was determined with a microhardness tester (HV-1000A, China). The samples were loaded with a pressure of 50 g for 15 s, and the testing device automatically measured the SMH value. Five indentations were measured on each sample, with each indentation separated by at least 100 μm. The average of the five values was taken to yield one hardness value for each sample to determine the Vickers microhardness (VHN) of the sample. SMH0 denotes the enamel sample's surface microhardness before demineralization. SMH1 denotes the enamel sample's surface microhardness after demineralization. SMH2 denotes the enamel sample's surface microhardness after remineralization treatment.

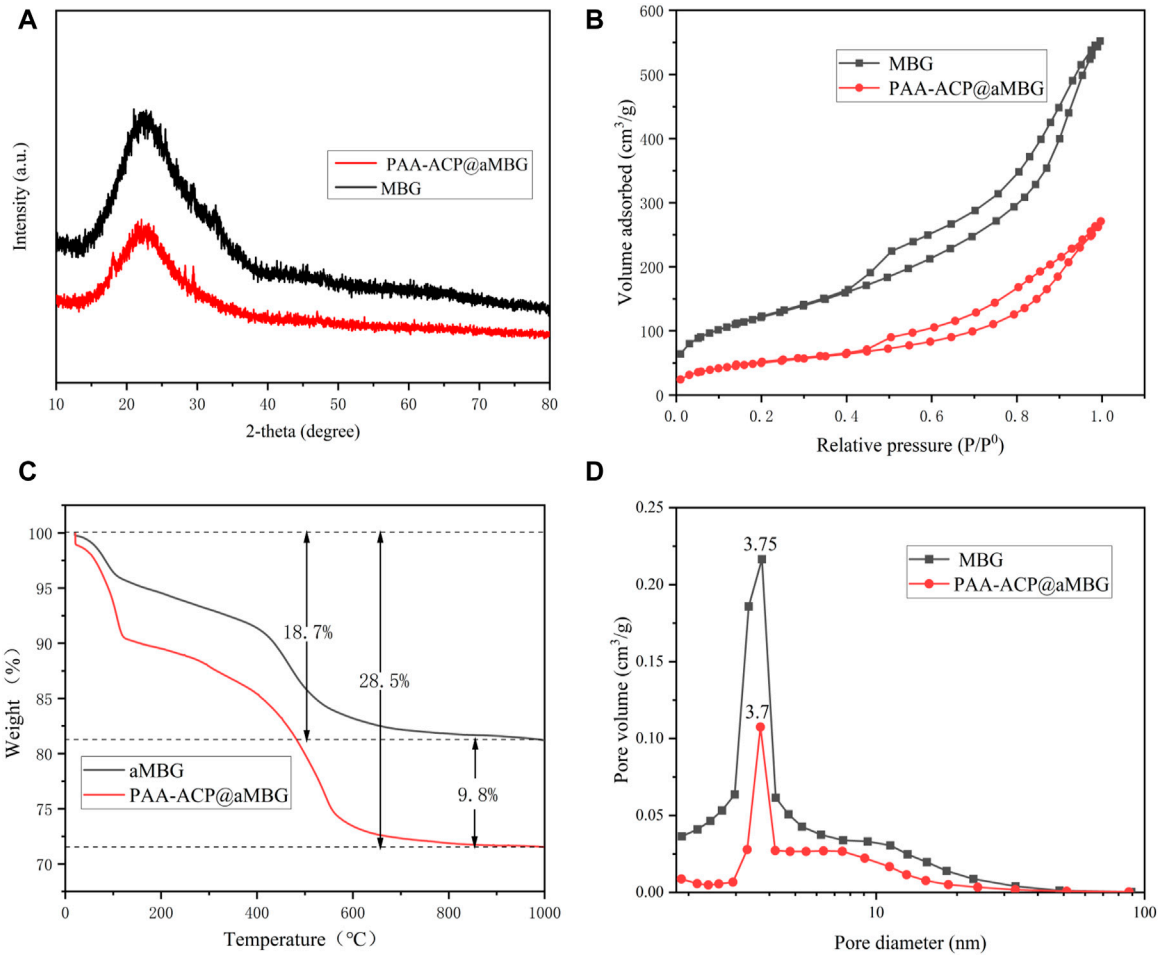

FIGURE 1
Characterization of MBG/aMBG/PAA-ACP@aMBG. **(A)** X-ray diffraction patterns of MBG and PAA-ACP@aMBG. **(B)** Nitrogen adsorption-desorption analysis of MBG and PAA-ACP@aMBG. **(C)** Thermogravimetric analysis of aMBG and PAA-ACP@aMBG. **(D)** Pore size distributions of MBG and PAA-ACP@aMBG.

TABLE 1 Specific surface areas and pore volumes of MBG and PAA-ACP@aMBG.

Samples	S_{BET} (m^2/g)	V_P (cm^3/g)
MBG	442	.85
PAA-ACP@aMBG	184	.42

S_{BET}: Specific surface area; V_P: Average pore volume.

The enamel sample's surface microhardness recovery rate (SMHRR) was calculated using the specific formula (Lv et al., 2015): $SMHRR = \frac{(SMH2-SMH1)}{(SMH0-SMH1)} \times 100\%$.

2.7 Surface color change measurement

After microhardness measurements the enamel surface color of the samples was observed using an advanced clinical portable dental spectrophotometer (VITA Easyshade® V, VITA Zahnfabrik, Bad Sackingen, Germany) and quantified by applying the CIE L*, a*, and b* values. The L* indicates the brightness from black (0) to white (100), the a* indicates red to green, and the b* indicates yellow to blue. The same lighting was used for all tests. The same operator assessed L*, a*, and b* 3 times for each sample pre- and post-demineralization and subsequent remineralization, and the mean values were recorded. Before each measurement, a white reflectance standard plate was utilized for calibration. After acquiring the L*, a*, and b* values, the color changes (ΔE1 and ΔE2) before demineralization, after demineralization, and after remineralization were calculated according to the mathematical equation $\Delta E = [(\Delta L)^2 + (\Delta a)^2 + (\Delta b)^2]^{1/2}$. Then, the formula; $CRR = \frac{\Delta E1}{\Delta E0} \times 100\%$ was used to calculate the enamel surface color recovery rate (CRR) (technology and Color, 2006).

2.8 FM measurements

Four samples from each group were randomly selected and sectioned vertically along the surface. The cross-sections were stained with 0.1 mM rhodamine B solution (Aldrich Chem.) for 1 h and rinsed three times under running water. Each set of samples was analyzed by fluorescence microscopy (Olympus BX53, Tokyo, Japan).

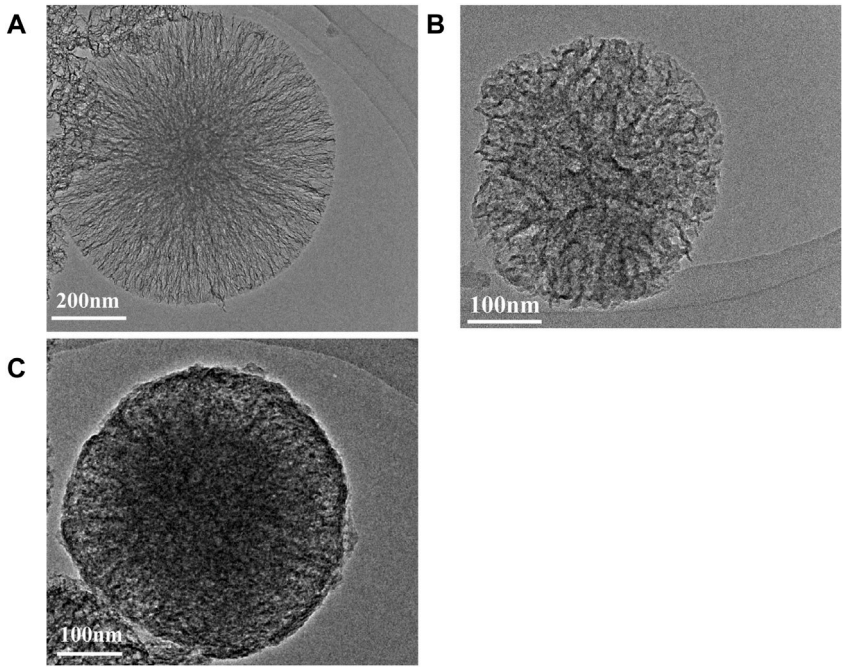

FIGURE 2
TEM images. **(A)** Bioactive glasses. **(B)** Aminated mesoporous Bioactive glasses. **(C)** PAA-ACP@aMBG.

The same laser power settings were used for all images. The remineralization depth (H) was then quantified by applying OLYMPUS cellSens software, and the data were averaged after three measurements by the same person.

2.9 XRD measurement

Four randomly selected samples from each group were scanned four times using an X-ray diffractometer (D8 ADVANCE A25, Germany) in the 2θ range to determine the crystal structure of the examined enamel surfaces.

2.10 SEM measurement

The remaining samples from each group were analyzed by SEM (JCM-7900F, Japan) after dehydration and gold coating.

2.11 Statistical analysis

The surface microhardness recovery and color recovery measurements values were tested by one-way ANOVA, and multiple comparisons were performed using the Student–Newman–Keuls test. The remineralization depth measurements by FM were tested by Kruskal–Wallis H-test. All data are expressed as the mean ± standard deviation (SD), and standard statistical analysis was performed using R version 3.5.3, $p < 0.05$ was considered as significant.

3 Results

3.1 Material characterization

3.1.1 Characterization of MBG/aMBG/PAA-ACP@aMBG

Figure 1A displays the XRD patterns of MBG and PAA-ACP@aMBG. It was determined that MBG and PAA-ACP@aMBG are typical amorphous silicate glass materials, and the loading of amorphous calcium phosphate didn't change the amorphous structure of the bioactive glass.

Figure 1C displays the thermogravimetric analysis plots of aMBG and PAA-ACP@aMBG. The total weight loss of aMBG was 18.7 wt% and that of PAA-ACP@aMBG was 28.5 wt%. The observed increase in weight loss of 9.8 wt% may be a result of PAA degradation in PAA-ACP@aMBG. This indicates that more than 9.8 wt% PAA-ACP has been absorbed onto aMBG. Nitrogen adsorption-desorption analysis (Figure 1B) showed that MBG and PAA-ACP@aMBG exhibited type IV isotherms, indicating the presence of typical mesoporous structures, with the former exhibiting H3-type hysteresis loops and the latter exhibiting H4-type hysteresis loops. The pore size, specific surface area, and pore volume decreased after MBG was loaded with amino groups and PAA-ACP (Figure 1D; Table 1).

3.1.2 TEM evaluation of PAA-ACP@aMBG

Figure 2 displays the TEM images of MBG, aMBG, and PAA-ACP@aMBG. In Figures 2A, B, it can be seen that the mesoporous bioactive glasses and the amino acid mesoporous bioactive glasses have uniform spherical structures with an average diameter of approximately 425 nm. The mesoporous structure was relatively

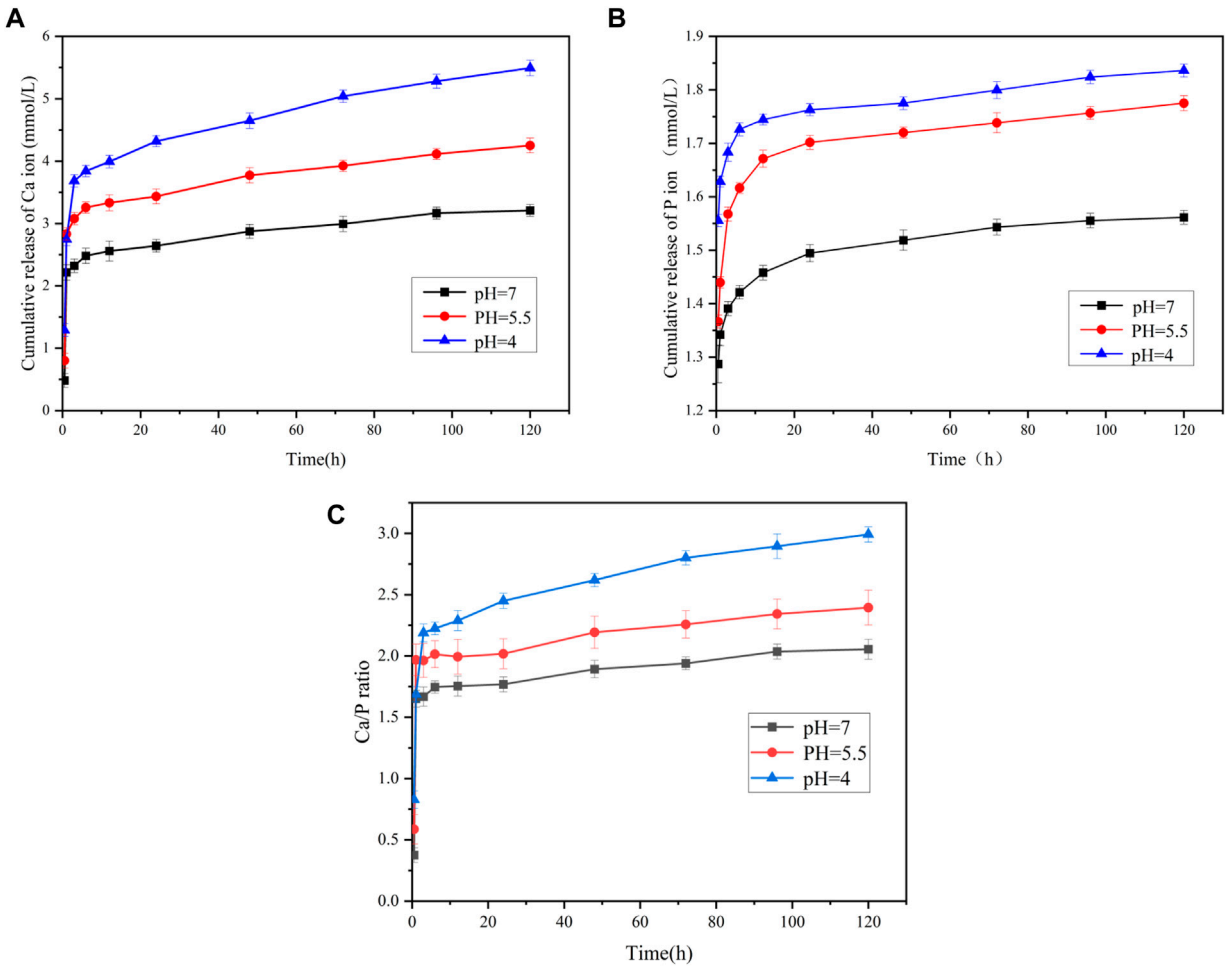

FIGURE 3
The ion release of the PAA-ACP@aMBG by ICP-OES. **(A)** Calcium ion release from PAA-ACP@aMBG. **(B)** Phosphorus ion release from PAA-ACP@aMBG under different pH conditions. **(C)** Ratio of the release of calcium and phosphorus ion from PAA-ACP@aMBG.

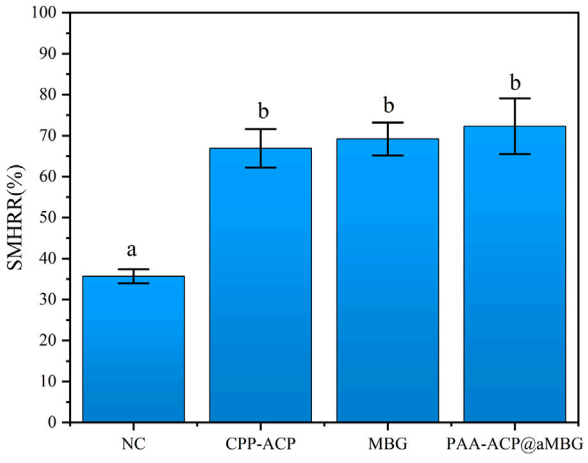

FIGURE 4
The surface microhardness recovery rates (SMHRR values) of the four groups. Identical letters indicate non-significant differences ($p > 0.05$).

fluffy and ran throughout the whole mesoporous particle with an obvious hollow structure (Figure 2A). The TEM images of the mesoporous bioactive glass materials after amination showed no significant difference in their basic morphology from the mesoporous bioactive glasses, indicating that amino functionalization didn't alter the basic structure of the materials.

After loading the PAA-ACP complex, the density of PAA-ACP@aMBG was significantly higher than that of aMBG, and the mesopores became blurred and irregular, which may be caused by blockage of the pore by PAA-ACP entry into the pore (Figures 2B, C). There were some fuzzy adsorption images on the surface of PAA-ACP@aMBG (Figure 2C), which may be caused by some PAA-ACP precursors gathering on the surface of aMBG without penetrating the interior of the mesoporous pores.

3.1.3 ICP–OES evaluation of PAA-ACP@aMBG

The release of calcium and phosphorus ions from PAA-ACP@aMBG and their ratio are shown in Figure 3. The release curves of both calcium and phosphorus ions are relatively steep at the early stage, indicating that both have a rapid release period at the early stage and then reach a smooth release period (Figures 3A, B). It is clear from the

TABLE 2 SMH values (mean ± SD, VHN) and SMH recovery rates (mean ± SD, %) of the four groups at different time points (n = 10).

Group	Baseline	Before remineralization	After remineralization	SMH recovery ratio (%)
PAA-ACP@aMBG	385.66 ± 25.53	218.5 ± 30.25	339.42 ± 25.69	72.3 ± 6.8^{b}
CPP-ACP	386.66 ± 18.64	224.83 ± 26.99	333.33 ± 13.83	66.9 ± 4.7^{b}
NC	380.33 ± 13.03	227.27 ± 17.38	281.87 ± 18.55	35.7 ± 1.7^{a}
MBG	379.3 ± 32.6	233.52 ± 27.90	334.32 ± 25.31	69.2 ± 4.0^{b}

The same letter in SMH recovery ratio (%) indicates no significant difference between groups (p > 0.05).

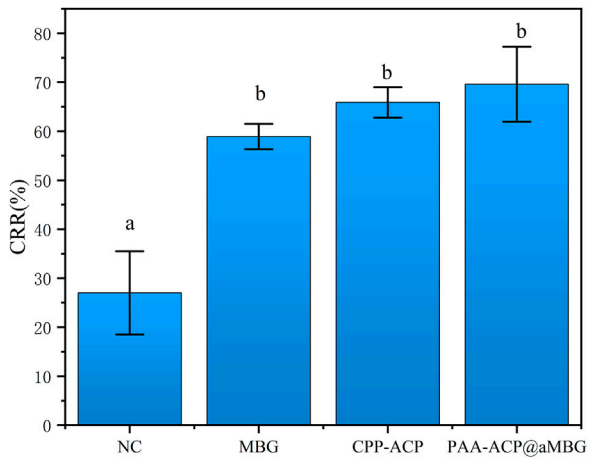

FIGURE 5
Color recovery rate (CRR) in the four groups. The same letter indicates that the difference wasn't significant (p > 0.05).

TABLE 3 Absolute values of color changes (mean ± SD) and color recovery rates (mean ± SD, %) for the four groups (n = 10).

Group	ΔE0	ΔE1	Color recovery rate (%)
PAA-ACP@aMBG	6.88 ± 1.07	4.79 ± 1.26	69.6 ± 7.6^{b}
CPP-ACP	10.03 ± 2.05	6.62 ± 1.66	65.9 ± 3.1^{b}
NC	8.73 ± 1.18	2.36 ± 1.02	27.0 ± 8.5^{a}
MBG	9.44 ± 2.57	5.57 ± 1.77	58.9 ± 2.6^{b}

The same letter in Color recovery rate (%) indicates no significant difference between groups (p > 0.05).

ICP–OES figures that there is a significant difference in the release of calcium and phosphorus ions from PAA-ACP@aMBG in the same solution with different pH values. The results demonstrate that the lower the environmental pH value is, the greater the release of calcium and phosphorus ions is, and the higher the environmental Ca/P ratio is, (Figure 3C) the better the tooth hard tissues can be protected from the effects of demineralization.

3.2 Surface microhardness measurement

Figure 4 and Table 2 display the percentage surface microhardness recovery rate (SMHRR) results. Between CPP-ACP (66.9 ± 4.7), PAA-ACP@aMBG (72.3 ± 6.8), and MBG (69.2 ± 4), there were no significant differences (p > .05). However, their SMHRR values were significantly higher than that of the NC group (35.7 ± 1.7; p < .001 for all three groups).

3.3 Surface color change measurement

Figure 5 and Table 3 display the findings of the percentage of enamel surface color recovery rate (CRR). CRR was significantly higher in the CPP-ACP (65.9 ± 3.1), PAA-ACP@aMBG (69.6 ± 7.6) and MBG groups (58.9 ± 2.6) than in the NC group (27 ± 8.5, p < .001). The MBG, CPP-ACP and PAA-ACP@aMBG groups didn't differ significantly from one another (p > .05).

3.4 FM measurement

Representative FM images are shown in Figure 6. These images reflect the fact that the fluorescent dye adsorbs to the dense remineralized enamel in the cross-section aren't easily washed away by deionized water, whereas the fluorescent dye adsorbed on the sparse demineralized enamel in the cross-section are easily washed away by flowing water (Lena Sezici et al., 2021). So, the red remineralized fluorescence band formed in the surface layer of the enamel after remineralization represents the depth of remineralization (H). Moreover, the remineralized fluorescence band in the PAA-ACP@aMBG group (Figure 6A) was wider than that in the CPP-ACP group (Figure 6B), MBG group (Figure 6D) and deionized water group (Figure 6C), which was closer to the natural enamel group (Figure 6F). The quantitative analysis results of mineralization depth (Table 4) show that the mineralization depth of PAA-ACP@aMBG group is 62.56 ± 4.98 μm, which is significantly higher than that of other groups (p < 0.001).

3.5 XRD measurement

The X-ray diffraction results are shown in Figure 7. The diffractograms of the samples in the four experimental groups were identical to those of normal enamel, indicating that the minerals deposited in the four experimental groups had the same crystal structure as normal enamel. Moreover, the diffraction peaks at 25.9° (002), 28.1° (210), 31.8° (211), 32.1° (300), 34.0° (202), 49.5° (213), 53.1° (004), 61.7° (214), and 64.1° (323/304) for all four groups of samples matched the standard hydroxyapatite X-ray diffraction spectrum (JCPDS 09-0432), indicating that the sediments are mainly hydroxyapatite.

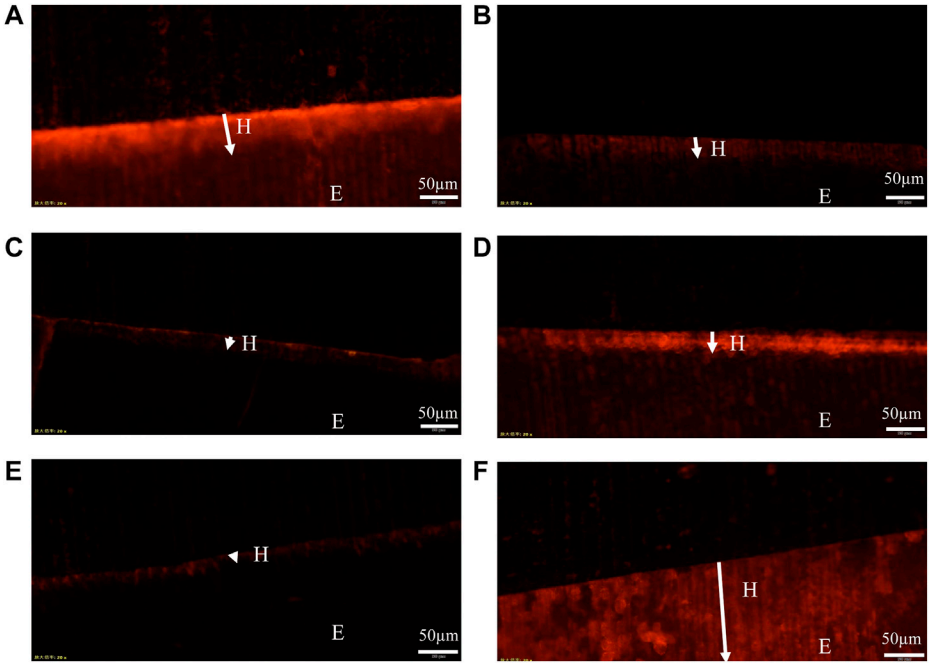

FIGURE 6
Representative FM images. **(A)**: PAA-ACP@aMBG group sample. **(B)**: CPP-ACP group sample. **(C)**: NC group sample. **(D)**: MBG group sample. **(E)**: demineralized enamel. **(F)**: normal enamel. The arrow in the figure indicates the remineralization depth (H); E represents the enamel layer.

TABLE 4 The depth of the enamel remineralization zone in the four groups of samples (n = 4).

Group	Depth (μm)
PAA-ACP@aMBG	62.56 ± 4.98[a]
CPP-ACP	46.15 ± 6.11[b]
NC	19.21 ± 1.57[c]
MBG	35.62 ± 3.76[d]

The different letter in Depth (μm) indicates significant difference between groups ($p < 0.01$).

3.6 SEM measurement

Micrographs of the enamel surface are shown in Figure 8. The pictures of the normal enamel show a flat and polished surface with obvious polishing scratches (Figure 8A). Images collected following the demineralization procedure showed interprismatic gaps caused by demineralization on the enamel surface (Figure 8B). The enamel prism impressions were still visible in the NC group pictures (Figure 8C). However, in the MBG, CPP-ACP, and PAA-ACP@aMBG groups, the enamel surfaces were quite smooth, and prismatic impressions were no longer evident, showing that significant mineral deposition covered the previously visible enamel prisms and filled the interprismatic gaps (Figures 8D–F).

4 Discussion

Enamel WSLs are an unresolved challenge in the dental field (Sampson and Sampson, 2020). Since WSLs damage is caused by

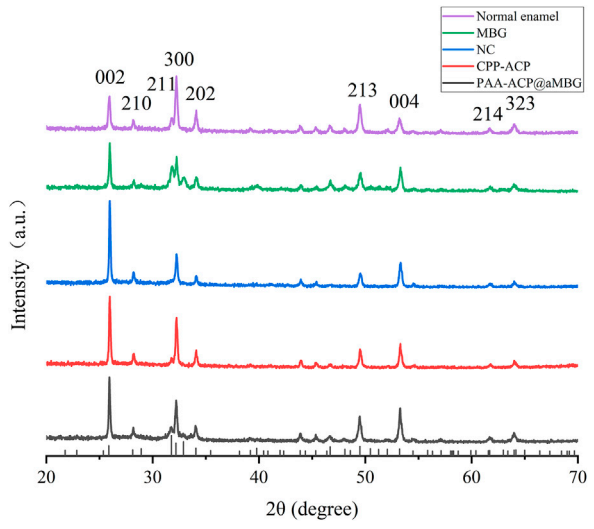

FIGURE 7
X-ray diffraction analysis of the samples. At the bottom is a standard X-ray diffraction image of hydroxyapatite (JCPDS 09-0432).

demineralization stimulated by the acidic environment of plaque biofilms, many efforts have been made to treat WSLs (Marin et al., 2022). CPP (casein phosphopeptide) is a bioactive polypeptide that can stabilize calcium and phosphorus ions in nanocomposites, thus improving the solubility and bioavailability of calcium phosphate. Therefore, CPP-ACP nanocomposites can promote remineralization by releasing these particles in response to acid attack or ion concentration changes (Philip et al., 2019). However, the distribution of CPP-ACP remineralized deposits is not uniform, and demineralized pores are still

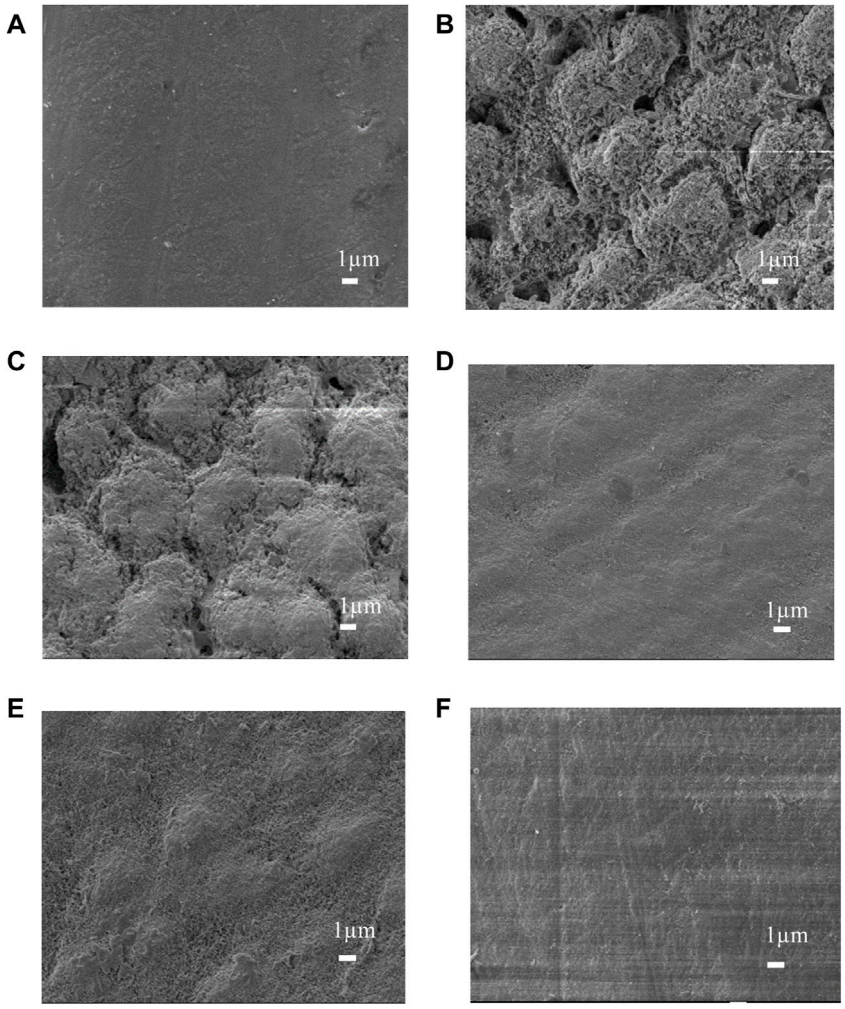

FIGURE 8
SEM images of the enamel surfaces of the four treatment groups. Images before demineralization **(A)**. Images after artificial demineralization **(B)**. Images of the nc group **(C)**. Images of the mbg **(D)**, cpp-acp **(E)** and paa-acp@ambg **(F)** groups.

visible, which may be caused by the rapid and uneven release rate of CPP-ACP, as this material dissolves and is converted into apatite microcrystals before reaching the surface of demineralized enamel (Fernández-Ferrer et al., 2018). Comparable to CPP, PAA is a bionic analog that stabilizes ACP precursors and induces them to remineralize enamel. To achieve more homogeneous stabilization and periodic replenishment of PAA-ACP, mesoporous bioactive glasses (MBGs) would be highly desirable delivery vehicles (Feito et al., 2021). We used amino groups to functionalize MBG into aMBG, making it positively charged so that it could combine with negatively charged PAA-ACP more efficiently. In this investigation, we evaluated the synergistic remineralization ability of PAA-ACP@aMBG with deionized water as the negative control and MBG and CPP-ACP as the positive controls. Artificial demineralized enamel samples were created by immersing human premolar teeth in demineralization solutions, which is similar to procedures in previous studies (Bakry and Abbassy, 2018).

In addition, the degree of remineralization of each sample was measured by two different methods, the Vickers microhardness test and FM. The surface microhardness test has been widely used to evaluate tooth hard tissue remineralization. If the hardness increases compared to that post-demineralization, it indicates enamel remineralization and improvement in the enamel crystal structure. Moreover, FM can be used to visualize the remineralization of demineralized areas by applying rhodamine B to the demineralized areas in the cross-section. The chalky enamel caused by enamel demineralization is another major feature of WSLs, so aesthetic restoration of the demineralized areas is also necessary. The values of L*, a*, and b* utilized in this study are based on the color quantification index system established by the International Commission on Illumination (CIE) in 1976, and they are the most commonly used color system in dentistry. In this system, L* indicates the degree of light and shade, a* indicates the degree of red and green, and b * indicates the degree of yellow and blue (technology and Color, 2006). In addition, more morphological details can be obtained by observing the surface of the enamel by scanning electron microscopy. The results of the surface microhardness and surface color change tests showed that the hardness and color recovery rate in the CPP-ACP and PAA-ACP@aMBG groups were significantly higher than those in the NC group, but there was no significant difference between them (Figures 4, 5; Tables 2, 3). Our observation with the scanning electron microscope validated these findings. In the negative control group (NC), enamel imprinting and prismatic gaps were still evident, while in the CPP-ACP and PAA-ACP@aMBG pictures, these interstitial

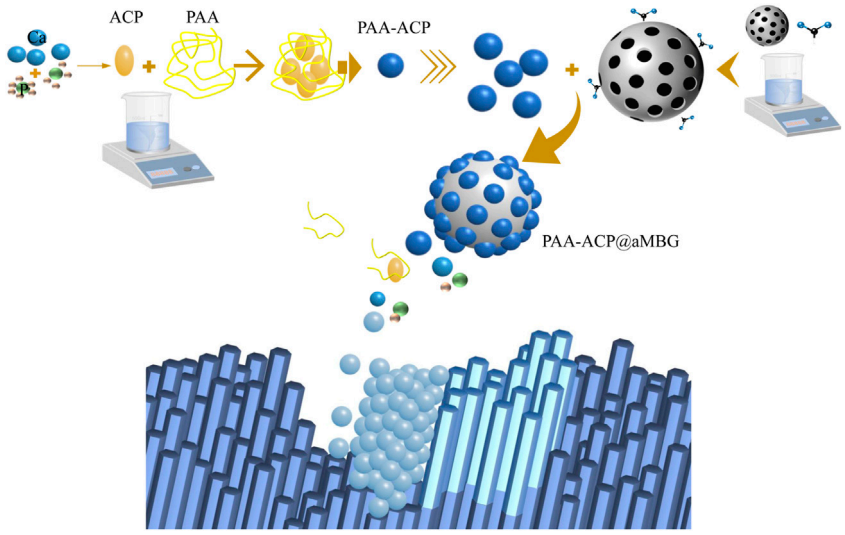

FIGURE 9
Schematic diagram.

structures weren't observed, as they were coated by precipitated minerals (Figure 8). In contrast, the FM results showed that PAA-ACP@aMBG treatment was superior to and significantly different from the CPP-ACP and MBG groups, which is strong evidence for the existence of synergistic effects between PAA-ACP and MBG.

In addition, the crystal structure of the precipitate was analyzed by X-ray diffraction. X-ray diffraction analysis is a common experimental method for identifying the crystal structures of enamel and hydroxyapatite. In this experiment, the X-ray diffraction results showed that the remineralized deposits in the four groups displayed a diffraction pattern similar to that of normal enamel, indicating that they shared a similar crystal structure (Figure 7). Moreover, comparing the diffraction peaks at 25.9°, 28.1°, 31.8°, 32.1°, 34.0°, 49.5°, 53.1°, 61.7°, and 64.1° with the standard X-ray diffraction pattern of HA (JCPDS 09-0432), these peaks were assigned to the (002), (210), (211), (300), (202), (213), (004), (214), and (323) crystallographic planes. This further indicates that the sedimentary minerals are mainly hydroxyapatite.

The periodic release of PAA-ACP from MBG can be due to the competitive replacement of physically adsorbed PAA-ACP by amphoteric ions and the gradual dissolution of MBG in body fluids (Cooper et al., 2013). The possible remineralization mechanism is shown in Figure 9 described as follows. PAA-ACP particles are periodically liberated from MBG by competitive replacement of amphoteric ions and then leave under the driving force of electrostatic interactions or capillary interactions (Nudelman et al., 2010). Demineralization enamel flaws and gaps may serve as calcium and phosphorus nucleation sites, which contribute to the attachment of PAA-ACP and the subsequent release of calcium and phosphorus (Iafisco et al., 2018). Therefore, PAA-ACP can contact the surface of demineralized enamel and dissolve with MBG to liberate calcium and phosphorus. After that, these calcium and phosphorus ions can be converted into hydroxyapatite in the gap at the top of the enamel prism. Through the periodic release of calcium and phosphorus ions, complete deposition of hydroxyapatite occurs, and finally, the surface of demineralized enamel is remineralized. Although there is no significant difference between PAA-ACP@aMBG and CPP-ACP in hardness and color recovery, PAA-ACP@aMBG nanocomposites have other advantages. First, MBG has excellent mechanical properties and can be used as a nanofiller in adhesive resins with promising applications (Balbinot et al., 2020). Second, while loading PAA-ACP, aMBG can also adsorb additional nanoparticles, including antibacterial metal cations or protein repellents, thus making the delivery system multifunctional (Jiménez-Holguín et al., 2020). Moreover, after testing, it was found that PAA-ACP@aMBG could respond to pH changes in the environment and increase the release of calcium and phosphorus ions as the simulated intraoral pH decreased, predicting that PAA-ACP@aMBG would be a very suitable remineralization material for the intraoral environment.

5 Conclusion

In this study, PAA-ACP@aMBG nanocomposites were successfully prepared. The experimental results show that the nanocomposite can effectively remineralize enamel WSLs *in vitro* and has good color recovery performance. It has thus been shown that this material provides a new strategy for the prevention and treatment of WSLs.

Data availability statement

The original contributions presented in the study are included in the article/Supplementary material, further inquiries can be directed to the corresponding authors.

Ethics statement

The studies involving human participants were reviewed and approved by Ethics Committee of The School of Stomatology of Shanxi Medical University. The patients/participants provided their written informed consent to participate in this study.

Author contributions

JuR: Concept, methodology, and writing. JiR: Concept, methodology, and writing. HW: Methodology, analysis. WH: investigation, analysis. JF: investigation, analysis. DW: investigation, analysis. WB: Concept, reviewing and editing. BZ: Reviewing and editing. XW: Reviewing and editing.

Funding

This work was supported by the Health Commission of Shanxi Province, China (project number: 2019017).

Conflict of interest

The authors declare that the research was conducted in the absence of any commercial or financial relationships that could be construed as a potential conflict of interest.

Publisher's note

All claims expressed in this article are solely those of the authors and do not necessarily represent those of their affiliated organizations, or those of the publisher, the editors and the reviewers. Any product that may be evaluated in this article, or claim that may be made by its manufacturer, is not guaranteed or endorsed by the publisher.

References

Bakry, A., and Abbassy, M. J. (2018). Increasing the efficiency of CPP-ACP to remineralize enamel white spot lesions. *J. Dent.* 76, 52–57. doi:10.1016/j.jdent.2018.06.006

Balbinot, G., Collares, F., Herpich, T., Visioli, F., Samuel, S., and Leitune, V. J. D. (2020). Niobium containing bioactive glasses as remineralizing filler for adhesive resins. *Dent. Mater* 36 (2), 221–228. doi:10.1016/j.dental.2019.11.014

Bansal, K., Balhara, N., and Marwaha, M. (2014). Remineralizing efficacy of Calcarea Fluorica tablets on the artificial carious enamel lesions using scanning electron microscope and surface microhardness testing: In vivostudy. *Indian J. Dent. Res.* 25, 777. doi:10.4103/0970-9290.152204

Chapman, J. A., Roberts, W. E., Eckert, G. J., Kula, K. S., and González-Cabezas, C. (2010). Risk factors for incidence and severity of white spot lesions during treatment with fixed orthodontic appliances. *Am. J. Orthod. Dentofac. Orthop.* 138 (2), 188–194. doi:10.1016/j.ajodo.2008.10.019

Chen, J., Zeng, L., Chen, X., Liao, T., and Zheng, J. J. B. (2018). Preparation and characterization of bioactive glass tablets and evaluation of bioactivity and cytotoxicity *in vitro*. *Bioact. Mater* 3 (3), 315–321. doi:10.1016/j.bioactmat.2017.11.004

Cölfen, H. J. N. (2010). Biomineralization: A crystal-clear view. *Nat. Mater* 9 (12), 960–961. doi:10.1038/nmat2911

Cooper, C. L., Cosgrove, T., Van Duijneveldt, J., Murray, M., and Prescott, S. W. (2013). Competition between polymers for adsorption on silica: A solvent relaxation NMR and small-angle neutron scattering study. *Langmuir* 29 (41), 12670–12678. doi:10.1021/la402556g

Dai, L., Mei, M., Chu, C., and Lo, E. J. M. (2019). Mechanisms of bioactive glass on caries management: A review. *Mater. (Basel)* 12 (24), 4183. doi:10.3390/ma12244183

Feito, M. J., Casarrubios, L., Oñaderra, M., Gómez-Duro, M., Arribas, P., Polo-Montalvo, A., et al. (2021). Response of raw 264.7 and J774A.1 macrophages to particles and nanoparticles of a mesoporous bioactive glass: A comparative study. *Colloids Surf. B Biointerfaces* 208, 112110. doi:10.1016/j.colsurfb.2021.112110

Fernández-Ferrer, L., Vicente-Ruíz, M., García-Sanz, V., Montiel-Company, J., Paredes-Gallardo, V., Almerich-Silla, J., et al. (2018). Enamel remineralization therapies for treating postorthodontic white-spot lesions: A systematic review. *J. Am. Dent. Assoc.* 149 (9), 778778–778786. doi:10.1016/j.adaj.2018.05.010

Gonçalves, F., Delbem, A., Gomes, L., Emerenciano, N., Pessan, J., Romero, G., et al. (2021). Effect of fluoride, casein phosphopeptide-amorphous calcium phosphate and sodium trimetaphosphate combination treatment on the remineralization of caries lesions: An *in vitro* study. *Arch. Oral Biol.* 122, 105001. doi:10.1016/j.archoralbio.2020.105001

Höchli, D., Hersberger-Zurfluh, M., Papageorgiou, S., and Eliades, T. J. E. (2017). Interventions for orthodontically induced white spot lesions: A systematic review and meta-analysis. *Eur. J. Orthod.* 39 (2), 122–133. doi:10.1093/ejo/cjw065

Hu, H., Feng, C., Jiang, Z., Wang, L., Shrestha, S., Yan, J., et al. (2020). Effectiveness of remineralizing agents in the prevention and reversal of orthodontically induced white spot lesions: A systematic review and network meta-analysis. *Clin. Oral Investig.* 24, 4153–4167. doi:10.1007/s00784-020-03610-z

Hua, F., Yan, J., Zhao, S., Yang, H., and He, H. J. C. (2020). *In vitro* remineralization of enamel white spot lesions with a carrier-based amorphous calcium phosphate delivery system. *Clin. Oral Investig.* 24 (6), 2079–2089. doi:10.1007/s00784-019-03073-x

Iafisco, M., Degli Esposti, L., Ramírez-Rodríguez, G., Carella, F., Gómez-Morales, J., Ionescu, A., et al. (2018). Fluoride-doped amorphous calcium phosphate nanoparticles as a promising biomimetic material for dental remineralization. *Sci. Rep.* 8 (1), 17016. doi:10.1038/s41598-018-35258-x

Jiménez-Holguín, J., Sánchez-Salcedo, S., Vallet-Regí, M., Salinas, A. J. M., and Association, I. Z. (2020). Development and evaluation of copper-containing mesoporous bioactive glasses for bone defects therapy. *Microporous Mesoporous Mater* 308, 110454. doi:10.1016/j.micromeso.2020.110454

Lena Sezici, Y., Yetkiner, E., Aykut Yetkiner, A., Eden, E., and Attin, R. (2021). Comparative evaluation of fluoride varnishes, self-assembling peptide-based remineralization agent, and enamel matrix protein derivative on artificial enamel remineralization *in vitro*. *Prog. Orthod.* 22, 4. doi:10.1186/s40510-020-00345-1

Lv, X., Yang, Y., Han, S., Li, D., Tu, H., Li, W., et al. (2015). Potential of an amelogenin based peptide in promoting reminerlization of initial enamel caries. *Arch. Oral Biol.* 60 (10), 1482–1487. doi:10.1016/j.archoralbio.2015.07.010

Marin, L. M., Xiao, Y., Cury, J. A., and Siqueira, W. L. (2022). Engineered salivary peptides reduce enamel demineralization provoked by cariogenic S. Mutans biofilm. *Microorganisms* 10, 742. doi:10.3390/microorganisms10040742

Miller, M. J., Bernstein, S., Colaiacovo, S. L., Nicolay, O., and Cisneros, G. J. (2016). Demineralized white spot lesions: An unmet challenge for orthodontists. *Seminars Orthod.* 22 (3), 193–204. doi:10.1053/j.sodo.2016.05.006

Mohabatpour, F., Chen, X., Papagerakis, S., and Papagerakis, P. J. B. (2022). Novel trends, challenges and new perspectives for enamel repair and regeneration to treat dental defects. *Biomater. Sci.* 10 (12), 3062–3087. doi:10.1039/d2bm00072e

Nudelman, F., Pieterse, K., George, A., Bomans, P., Friedrich, H., Brylka, L., et al. (2010). The role of collagen in bone apatite formation in the presence of hydroxyapatite nucleation inhibitors. *Nat. Mater* 9 (12), 1004–1009. doi:10.1038/nmat2875

Peng, S., Sang, T., Wang, H., Guan, Y., Deng, Y., Wang, P., et al. (2022). Bioinspired anti-demineralization enamel coating for orthodontics. *J. Dent. Res.* 101 (13), 1620–1627. doi:10.1177/00220345221129806

Philip, N., Leishman, S. J., Bandara, H. M. H. N., and Walsh, L. J. (2019). Casein phosphopeptide-amorphous calcium phosphate attenuates virulence and modulates microbial ecology of saliva-derived polymicrobial biofilms. *Caries Res.* 53, 643–649. doi:10.1159/000499869

Qi, C., Lin, J., Fu, L., and Huang, P. J. C. S. (2018). Calcium-based biomaterials for diagnosis, treatment, and theranostics. *Chem. Soc. Rev.* 47 (2), 357–403. doi:10.1039/c6cs00746e

Qi, C., Musetti, S., Fu, L., Zhu, Y., and Huang, L. J. C. S. (2019). Biomolecule-assisted green synthesis of nanostructured calcium phosphates and their biomedical applications. *Chem. Soc. Rev.* 48 (10), 2698–2737. doi:10.1039/c8cs00489g

Sampson, V., and Sampson, A. (2020). Diagnosis and treatment options for anterior white spot lesions. *Br. Dent. J.* 229, 348–352. doi:10.1038/s41415-020-2057-x

Shuai, C., Xu, Y., Feng, P., Wang, G., Xiong, S., and Peng, S. (2019). Antibacterial polymer scaffold based on mesoporous bioactive glass loaded with *in situ* grown silver. *Chem. Eng. J.* 374, 304–315. doi:10.1016/j.cej.2019.03.273

Song, J., Li, T., Gao, J., Li, C., Jiang, S., and Zhang, X. J. J. (2021). Building an aprismatic enamel-like layer on a demineralized enamel surface by using carboxymethyl chitosan and lysozyme-encapsulated amorphous calcium phosphate nanogels. *J. Dent.* 107, 103599. doi:10.1016/j.jdent.2021.103599

Technology, C., and Colour (2006). Billmeyer and saltzman's principles of colour technology. *Pigment Resin Technol.* 35 (5), 31–105. doi:10.1108/prt.2006.12935eac.008

Thula, T. T., Svedlund, F., Rodriguez, D. E., Podschun, J., Pendi, L., and Gower, L. B. (2010). Mimicking the nanostructure of bone: Comparison of polymeric process-directing agents. *Polymers* 3, 10–35. doi:10.3390/polym3010010

Vallet-Regi, M., and Salinas, A. J. M. (2021). Mesoporous bioactive glasses for regenerative medicine. *Mater Today Bio* 11, 100121. doi:10.1016/j.mtbio.2021.100121

Wang, Y., Van Manh, N., Wang, H., Zhong, X., Zhang, X., and Li, C. J. I. (2016). Synergistic intrafibrillar/extrafibrillar mineralization of collagen scaffolds based on a biomimetic strategy to promote the regeneration of bone defects. *Int. J. Nanomedicine* 11, 2053–2067. doi:10.2147/ijn.S102844

Xiao, Z., Que, K., Wang, H., An, R., Chen, Z., Qiu, Z., et al. (2017). Rapid biomimetic remineralization of the demineralized enamel surface using nano-particles of amorphous calcium phosphate guided by chimaeric peptides. *Dent. Mater* 33 (11), 1217–1228. doi:10.1016/j.dental.2017.07.015

Ye, B., Luo, X., Li, Z., Zhuang, C., Li, L., Lu, L., et al. (2016). Rapid biomimetic mineralization of collagen fibrils and combining with human umbilical cord mesenchymal stem cells for bone defects healing. *Mater Sci. Eng. C Mater Biol. Appl.* 68, 43–51. doi:10.1016/j.msec.2016.05.104

frontiers | Frontiers in Bioengineering and Biotechnology

TYPE Review
PUBLISHED 20 January 2023
DOI 10.3389/fbioe.2023.1100155

OPEN ACCESS

EDITED BY
Xing Wang,
Shanxi Medical University, China

REVIEWED BY
Yunfeng Liu,
Zhejiang University of Technology, China
Ting Jiao,
Shanghai Jiao Tong University, China

*CORRESPONDENCE
Hongbo Wei,
weihongbo101@126.com
Dehua Li,
lidehua@fmmu.edu.cn

SPECIALTY SECTION
This article was submitted to Biomaterials, a section of the journal Frontiers in Bioengineering and Biotechnology

RECEIVED 16 November 2022
ACCEPTED 11 January 2023
PUBLISHED 20 January 2023

CITATION
Huang S, Wei H and Li D (2023), Additive manufacturing technologies in the oral implant clinic: A review of current applications and progress.
Front. Bioeng. Biotechnol. 11:1100155.
doi: 10.3389/fbioe.2023.1100155

Additive manufacturing technologies in the oral implant clinic: A review of current applications and progress

Shitou Huang, Hongbo Wei* and Dehua Li*

State Key Laboratory of Military Stomatology, National Clinical Research Center for Oral Diseases, Shaanxi Engineering Research Center for Dental Materials and Advanced Manufacture, Department of Oral Implants, School of Stomatology, The Fourth Military Medical University, Xi'an, Shaanxi, China

Additive manufacturing (AM) technologies can enable the direct fabrication of customized physical objects with complex shapes, based on computer-aided design models. This technology is changing the digital manufacturing industry and has become a subject of considerable interest in digital implant dentistry. Personalized dentistry implant treatments for individual patients can be achieved through Additive manufacturing. Herein, we review the applications of Additive manufacturing technologies in oral implantology, including implant surgery, and implant and restoration products, such as surgical guides for implantation, custom titanium meshes for bone augmentation, personalized or non-personalized dental implants, custom trays, implant casts, and implant-support frameworks, among others. In addition, this review also focuses on Additive manufacturing technologies commonly used in oral implantology. Stereolithography, digital light processing, and fused deposition modeling are often used to construct surgical guides and implant casts, whereas direct metal laser sintering, selective laser melting, and electron beam melting can be applied to fabricate dental implants, personalized titanium meshes, and denture frameworks. Moreover, it is sometimes required to combine Additive manufacturing technology with milling and other cutting and finishing techniques to ensure that the product is suitable for its final application.

KEYWORDS

additive manufacturing technologies, 3D printing, oral implantology, surgical guides, customized titanium meshes, dental implants, custom trays, implant models

1 Introduction

In recent years, digital technologies, such as computer-aided design/computer-aided manufacture (CAD/CAM), digital intraoral scanners, and additive manufacturing (AM) technologies, have been successfully applied in implant dentistry (Dawood et al., 2015), providing new clinical and technical methods for surgical oral implant operations and restoration manufacture. Digitalization shows a steady development trend in the field of dentistry. As a typical digital manufacturing technology, AM can connect disease diagnosis, treatment planning, and production processes through data flow, forming a fully digital process for dental product processing (Salmi, 2021). Digital workflows not only greatly improve the safety of implant placement and the convenience of manufacturing restoration, but also reduce labor intensity for dentists and provide a satisfactory medical experience for patients (Barazanchi et al., 2017).

Additive manufacturing (AM) technologies, also known as three-dimensional (3D) printing technologies, are rapid prototyping technologies that have gradually become alternative

methods for generating products from CAD files in dentistry (Abduo et al., 2014). Previously, numerical control processing technology (NC technology, also known as subtractive machining technology) was typically used. In the industry, NC refers to the use of turning, milling, grinding, and other approaches to remove material from a specific solid object to form a desired shape. As the processed objects in stomatology NC machining are specific oral materials, milling and grinding techniques are often adopted according to the characteristics of the material used and precision manufacturing requirements (Abduo et al., 2014). NC is a mature processing technology that achieves high precision using a wide range of materials and can be used to directly process almost all commonly used stomatological materials. In addition, NC is the first choice for batch fabrication (Petrick and Simpson, 2015); however, the disadvantages of NC include the material waste associated with this technology, which leads to high production costs. Moreover, particularly complex dental auxiliary therapy devices (such as root-analogue implants, personalized titanium meshes, etc.) are difficult to achieve using NC (Dawood et al., 2015).

AM is a processing technology based on discrete stacking forms. The underlying principle involves transformation of a 3D digital model into continuous superposition of a two-dimensional sheet model through a discrete process, where a computer program controls the stacking of materials in order, layer by layer. The most remarkable features of AM are that it overcomes the limitations of subtractive machining technology and can be used to mass produce a variety of products with complex morphology in a short time. In addition, in principle, AM consumes a minimum amount of raw materials, and unformed raw materials (resin liquid, metal powder, etc.) can be reused, which greatly reduces costs (Kessler et al., 2020; Tian et al., 2021).

Overall, these two manufacturing methods (NC and AM) each have advantages and disadvantages, and AM is not conclusively superior to subtractive manufacturing; in most cases, the techniques present complementary advantages (Alammar et al., 2022). In implant dentistry, applications of and research into AM are becoming increasingly extensive, ranging from fabrication of surgical guides and dental implants to dental casts and implant frameworks, among other items. The use of AM has led to a progression of implant dentistry applications from traditional, purely empirical methods to more accurate digital medicine (Schweiger et al., 2021; Huang et al., 2022).

Several reviews on the applications of AM in dentistry have been published (Barazanchi et al., 2017; Revilla-Leon and Ozcan, 2019; Tian et al., 2021); however, few have focused on the application of this technology in oral implantology. Moreover, the materials reviewed have been limited to polymers, and the types of applications covered were not comprehensive (Revilla-León et al., 2020). In this review, we discuss the AM technologies commonly used in oral implantology and their applications. In addition, we compare the accuracy of different AM technologies and describe the clinical applications of products fabricated by AM.

The aim of this review is to provide readers with information on recent progress in the application of AM in oral implantology. As a result, we focus on the following questions: Which AM technologies are commonly used in implant dentistry? What are the applications of AM technologies in implant dentistry? What are the benefits of the application of AM technologies in implant dentistry?

2 Additive manufacturing technologies commonly used in implant dentistry

AM refers to a class of manufacturing processes in which parts are built by stacking layers of material on one another. There are seven 3D printing categories in the American Society for Testing and Materials classification standard: vat photopolymerization (VPP), powder bed fusion (PBF), material jetting, binder jetting, material extrusion (MEX), sheet lamination, and directed energy deposition. Although there are various AM processes, not all of them are used in implant dentistry. Technologies frequently adopted in implant dentistry practice include VPP [stereolithography (SLA), digital light processing (DLP), etc.], PBF [selective laser melting (SLM), selective laser sintering (SLS), etc.], and MEX (fused deposition modeling, etc.) (Schweiger et al., 2021). Parts are built directly from digital 3D models created using CAD software. CAD models are converted into many thin layers, and the fabrication facility uses this geometric data to build each layer in turn until the part is completed (Bozkurt and Karayel, 2021). Given this approach, AM is often referred to as layered manufacturing, direct digital manufacturing, or physical free-form manufacturing (Turkyilmaz and Wilkins, 2021).

Each 3D printing technology is based on the principle of the "additive" method, with the main differences among them being the molding methods and materials used. Appropriate 3D printing technologies should be selected according to the application purpose (Figure 1) (Jawahar and Maragathavalli, 2019; Schweiger et al., 2021).

2.1 Vat photopolymerization

2.1.1 Stereolithography

SLA is a well-known 3D printing technology that has been used for almost 30 years (Turkyilmaz and Wilkins, 2021), and is primarily applied to print surgical guides, dental model replicas, custom trays, and provisional restorations (Anadioti et al., 2018; Khorsandi et al., 2021; Schweiger et al., 2021). SLA uses a high-intensity ultraviolet light source, which applies the wavelength and heat of light to polymerize and selectively solidify liquid resin for lamination. In this process, to better integrate new layers with previous layers, the polymerization reaction of each layer is usually not fully completed under the direct light source, but further light processing is rather performed after the printing is completed (Pagac et al., 2021). Finally, the support structures added automatically by the printer require manual removal (Revilla-León et al., 2020).

2.1.2 Digital light processing

DLP, as a VPP technology, has attracted wide attention. A major area of DLP printer application is the digital manufacture of dental models (Park et al., 2021). Differences between DLP and SLA include the type of light source and the way the light source is controlled to selectively illuminate and cure the resin. In SLA, the light source is a laser, while DLP uses a projector, similar to a movie projection device, that illuminates the entire shape of the printed object at the surface of the liquid (Pagac et al., 2021; Son et al., 2021). In theory, DLP printing of an object takes less time, because each layer does not require a step-by-step laser scan; however, most DLP devices do not have the high resolution that SLA laser beams can provide (Revilla-León et al., 2020).

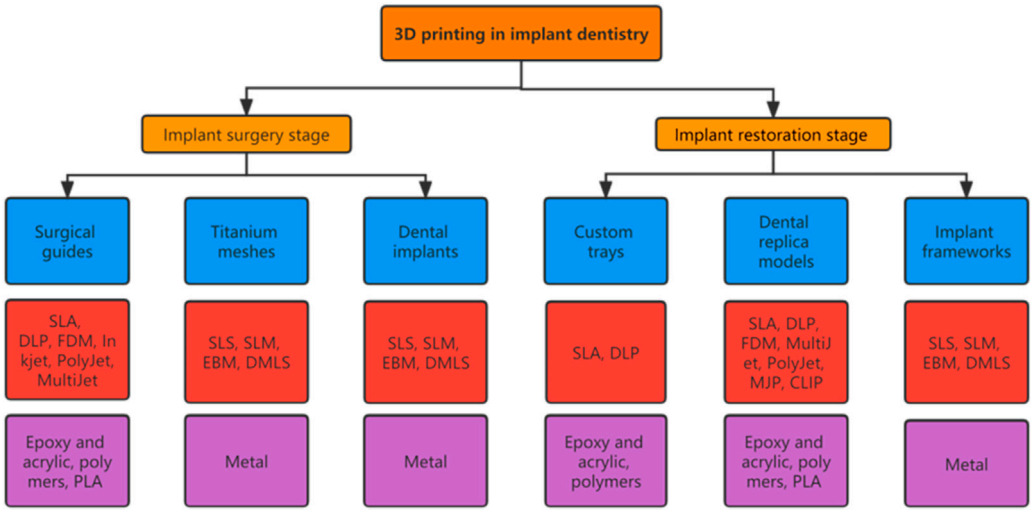

FIGURE 1
Applications of 3D printing technologies commonly used in implant dentistry. Chart showing the applications (blue boxes), primary 3D printing technologies (red boxes), and materials needed (purple boxes) (Dawood et al., 2015; Khorsandi et al., 2021; Tian et al., 2021).

Therefore, DLP is advantageous for rapid printing of larger parts with fewer details, while SLA is superior for printing accurate parts with intricate details (Huang et al., 2022).

2.1.3 Continuous liquid interface production (CLIP)

CLIP is a variant of DLP considered to be a vat-polymerization technology (Alammar et al., 2022), conducted using a liquid resin cylinder, a bottom-up construction platform, an ultraviolet lamp, an oxygen-permeable window, and a projector. The projector displays a continuous, extremely thin cross section of an object, using ultraviolet light from below (Pagac et al., 2021). Ultraviolet rays harden the liquid in cross section in a cylinder of liquid resin. Simultaneously, a lift pulls the formed objects out of the resin tank (Alammar et al., 2022). The key to CLIP printing is the presence of a window for oxygen and ultraviolet light to pass through at the bottom of the resin cylinder. As oxygen hinders the curing process, resin at the bottom of the cylinder continuously forms a "dead zone" that does not cure. This "dead zone" is very thin, such that ultraviolet light can pass through and solidify the resin above, which does not come into contact with oxygen. As there is no resin stuck to the bottom of the cylinder, the printing speed is very fast, because printing does not occur in the air but in the resin (printing in the air reduces curing speed, due to the presence of oxygen) (Alammar et al., 2022).

2.2 Powder bed fusion

PBF is the metal-printing technology most commonly used in dentistry. Ti and Cr-Co alloys are preferred metal materials in biomedical applications, primarily because of their mechanical properties, biocompatibility, thermal, magnetic, and electrical conductivity, and general high temperature resistance (Revilla-León et al., 2017). PBF includes SLS, direct metal laser sintering (DMLS), SLM, and electron beam melting (EBM). These techniques typically use high-powered lasers or electron beams to melt small particles, such as plastics, metals, ceramics, or glass, in powder form (Velasquez-Garcia and Kornbluth, 2021). The powder is usually preheated to a temperature below the melting point of the material before printing begins. The energy source is then controlled by the printer, enabling it to selectively melt powder on the surface of the powder bed. After melting one layer, the powder bed reduces by the height of one layer, and a new powder layer is then laid on top with a roller, subsequently completing printing of the new layer (Revilla-Leon et al., 2019a).

Most non-metallic materials printed by PBF do not require support structures, because the model is always fully wrapped and supported by green powder; however, metallic materials may require support structures to assist in rapidly transferring heat away from the part while reducing expansion during printing. PBF printers can build three-dimensional geometries, such as fine lattices, which are valuable for making prostheses to promote bone ingrowth; hence, PBF technology is widely used in medical fields, including orthopedics and for dental implants, among other applications (Mangano et al., 2014a). In addition, personalized titanium mesh and implant frameworks can be fabricated using this technology (Sumida et al., 2015; Barbin et al., 2020).

The main speed-limiting steps of PBF are the thermal cycle of the machine and post-processing of parts (Attarilar et al., 2021). Most PBF machines need to be warmed up to a certain temperature to start printing, and after printing, cooling is required before the printed parts can be removed from the machine. The post-processing procedures required are also highly dependent on the type of technology and materials used. For example, metal materials require processes such as thermal hardening and residual stress relaxation (Sing et al., 2016). Metal-printed parts may also require subsequent milling with a computer numerical control (CNC) lathe, to achieve a smooth finish, after they have been removed from the printer platform (Bordin et al., 2017).

At present, in the PBF category, SLM makes comprehensive use of cutting-edge technologies, such as new material, laser, and computer technologies, which have great potential for further future development (Ansari et al., 2019). Dental implants printed by SLM have higher density and strength, as well as sufficient dimensional accuracy (Chen et al., 2014), which can be attributed to the SLM forming principle. SLS

FIGURE 2
Applications of 3D printing technologies in implant dentistry clinical practice. **(A)** 3D printed surgical guide. **(B)** Personalized titanium mesh. **(C)** Standard implant. **(D)** Customized root-analogue implant. **(E)** Custom tray. **(F)** Implant models. **(G)** Implant framework. Adopted from (Mangano et al., 2012b; Revilla-Leon et al., 2017; Revilla-Leon et al., 2018a; Westover, 2019; Olea Vielba et al., 2020; Cucchi et al., 2021; Herschdorfer et al., 2021).

binds metal or non-metallic powders with high melting points by melting a metal or binder with a low melting point (Jawahar and Maragathavalli, 2019), while SLM uses a high power laser with a small spot to melt metal powder rapidly and completely, and requires higher laser power density than that used for SLS (Revilla-León et al., 2017). In addition, although SLM parts have good mechanical strength, they may have high internal stresses caused by the thermal gradients induced during processing, necessitating additional heat treatment.

EBM is also a powder bed melting technology. The principles of fabrication using EBM and SLM are similar, but the heat sources differ (Velasquez-Garcia and Kornbluth, 2021). Compared with technologies that use lasers as the energy source, EBM has many advantages, such as high energy utilization, no reflection, high power density, and convenient focusing, which can be used to make implants (Raheem et al., 2021).

2.3 Material extrusion

The MEX process is also termed fused filament fabrication (FFF) (Bozkurt and Karayel, 2021). The MEX family process, fused deposition modeling (FDM), is the most common type of printing used in medical or dental equipment; however, its printing resolution is inferior to that of SLA (Huang et al., 2017; Oberoi et al., 2018). FDM can handle a variety of materials, such as foundry wax, polyamide (commonly known as nylon), acrylonitrile butadiene styrene plastic, polylactic acid (PLA) plastic, low melting point metals, and ceramics (Lin et al., 2019). In FDM, the thermoplastic material is heated, melted, and extruded uniformly from a nozzle to generate filaments. Simultaneously, the nozzle moves along a specific path, operated by an NC system according to the continuous thin layer data planned by the slicing software, for filling. After cooling, the filamentous material is bonded layer by layer to form a thin cross-section, and finally the layers are superimposed to form a three-dimensional entity (Torabi et al., 2015).

2.4 Material jetting

In 2000, Objet (Israel) applied for a patent for PolyJet technology (now owned by Stratasys). PolyJet sprays a liquid photopolymer layer onto the construction tray and immediately solidifies it using ultraviolet light. Compared with SLA, the PolyJet laser spot diameter is 0.06–0.10 mm, allowing much higher printing accuracy than that achieved by SLA, and facilitating fabrication of smooth and precision parts. In addition, due to its high-speed raster construction process, PolyJet can achieve fast printing, and does not require secondary curing. It has been demonstrated that implant guides made using PolyJet are more accurate than those fabricated using SLA technology (Tappa and Jammalamadaka, 2018; Patpatiya et al., 2022).

3 Research status on additive manufacturing applications in implant dentistry

The accuracy of surgical implant placement is greatly improved by surgical guides constructed by 3D printing technology. Customized

titanium mesh improves the accuracy of bone augmentation, and 3D printing technology can even be used to prepare personalized implants to meet individual patient needs (Revilla-León et al., 2020). During implant restoration, 3D printing technologies can replace certain manual operations, such as the manufacture of custom trays, working casts, etc., helping to reduce human error. Suitable tray and accurate dental models are key to restoration. There is evidence that 3D printed custom trays and models are sufficiently accurate, which significantly impacts the success of the final restoration. Additionally, implant-supported frameworks generated by CNC cutting are very popular, but this process results in a waste of materials, whereas implant frameworks fabricated by 3D printing effectively avoid this problem. The emergence of 3D printing has undeniably aroused the interest of many dentists and accelerated the clinical development of implantology. Some examples of the application of 3D printing technologies in dentistry are presented in Figure 2.

3.1 Applications of additive manufacturing in the surgical stage of implant treatment

3.1.1 Surgical guides

3D printed surgical guides have been used for more than 10 years, and the digital workflow of the guides is as follows. Virtual planning and design is conducted using computer software and digital workflows for planning and manufacturing, based on data obtained from 3D imaging, and these plans are then transmitted through 3D printed surgical guides (Rouzé L'Alzit et al., 2022; Unsal et al., 2020; Zhang et al., 2020). At present, SLA is the most widely used approach, due its economical nature and speed. Some newer technologies, such as PolyJet, can also be used to prepare guides (Henprasert et al., 2020). The guide manufacturing process is illustrated in Figure 3, taking tooth-supported guides as an example (Sedov et al., 2021).

The production of guides involves multiple, closely-linked steps, including data collection and integration, design of the implanting plan and guide structure, and manufacturing, and errors in previous steps will accumulate in the final guides (Putra et al., 2022; Rouzé L'Alzit et al., 2022). Factors influencing template accuracy can be roughly divided into three categories: 1) System error: that is, errors generated during CBCT scanning and data conversion, which cannot be controlled by humans; 2) Manufacturing error: related to the type of 3D printer (Zhang et al., 2022) (Table 1), selection of printing materials, use of supporting structures, slicing method and software types (Cho et al., 2021; Elliott et al., 2022; D. D; Rubayo, et al., 2021); and 3) Other factors.

To reduce surgical complications caused by problems with 3D printed surgical guide production, it is vital to understand the limitations of 3D printing technology. Research has demonstrated that 50 μm layer printing provides better overall guide dimensions than 100 μm layer printing (Dalal et al., 2020). Further, printing angulation can influence the intaglio surface, as well as tube deviations (Dalal et al., 2020). Rubayo et al. showed that 0- and 45-degree build angles produced the most accurate surgical templates, while a 90-degree build angle generated the least accurate surgical templates (D. D. Rubayo, et al., 2021). Tahir et al. evaluated the effect of different printing directions on the placement accuracy of implant surgical templates made by DLP. The results showed that the horizontally printed templates showed excellent accuracy (Tahir and Abduo, 2022).

Regarding other factors that influence template accuracy, Zhou et al. (Zhou et al., 2018) conducted a comprehensive comparison of various clinical factors and concluded that guide accuracy may be affected by guide position (maxilla or mandible), guide fixation (fixation screw or not) (Pessoa et al., 2022), type of guide (total or partial) (Mangano et al., 2018; Lou et al., 2021; Fotopoulos et al., 2022; Gargallo-Albiol et al., 2022), flap approach (open flap or flapless), differences in implant system (Zhu et al., 2021), high temperature sterilization (Marei et al., 2019; Kirschner et al., 2022) and support mode (tooth-supported, mucosa-supported or mixed-supported) (Pan et al., 2022). In addition, Henprasert et al. concluded that there was no significant difference in accuracy between 3D-printed and milled guides, but found that the former had the advantages of high efficiency and reduced material waste (Henprasert et al., 2020). Mukai et al. compared the repeatability and accuracy of two surgical guides obtained using 3D printing and milling methods (Mukai et al., 2021) by overlaying images and the results revealed no significant differences in average mismatch between the two groups in terms of trueness ($p = 0.529$) or precision ($p = 0.3021$), indicating that both milling and printing manufacturing methods are suitable for guided surgery.

3.1.2 Customized titanium mesh

The development of customized titanium mesh generated by 3D printing technology, with the aim of solving the shortcomings of traditional titanium mesh, has become a focus in GBR research and application (Xie et al., 2020). Based on patient CBCT three-dimensional jaw data, the ideal alveolar bone is virtually designed using CAD software, according to the shape of the dental arch and the expected implant position (Manzano Romero et al., 2021). Then, the matching customized titanium mesh is designed directly on the reconstructed alveolar bone model. Finally, customized titanium mesh is manufactured using SLM or EBM (Figure 4) (Xie et al., 2020; Cucchi et al., 2019; Seiler et al., 2018).

There are many advantages of 3D printed customized titanium mesh (Seiler et al., 2018; Hartmann et al., 2019), as follows.

- The cell structure, pore size, and thickness of 3D printed titanium mesh can be adjusted according to requirements (Jung et al., 2014).
- The scope of 3D printed titanium mesh is limited to the area of the bone defect rather than extending into areas with sufficient bone mass, avoiding overstretching of soft tissue. In the second stage of surgery, the doctor only needs to remove the titanium mesh through the alveolar crest incision, avoiding the need to turn the flap again.
- The use of customized titanium mesh can reduce the operation time, thus shortening exposure to general anesthesia, decreasing blood loss, decreasing wound exposure time, and simplifying the surgical procedure.
- Personalized titanium mesh has lower exposure rates, as confirmed by a meta-analysis conducted by Zhou et al. (Zhou et al., 2021). Titanium mesh avoids nerves and blood vessels in the initial design, which is of great significance in improving the accuracy of GBR.

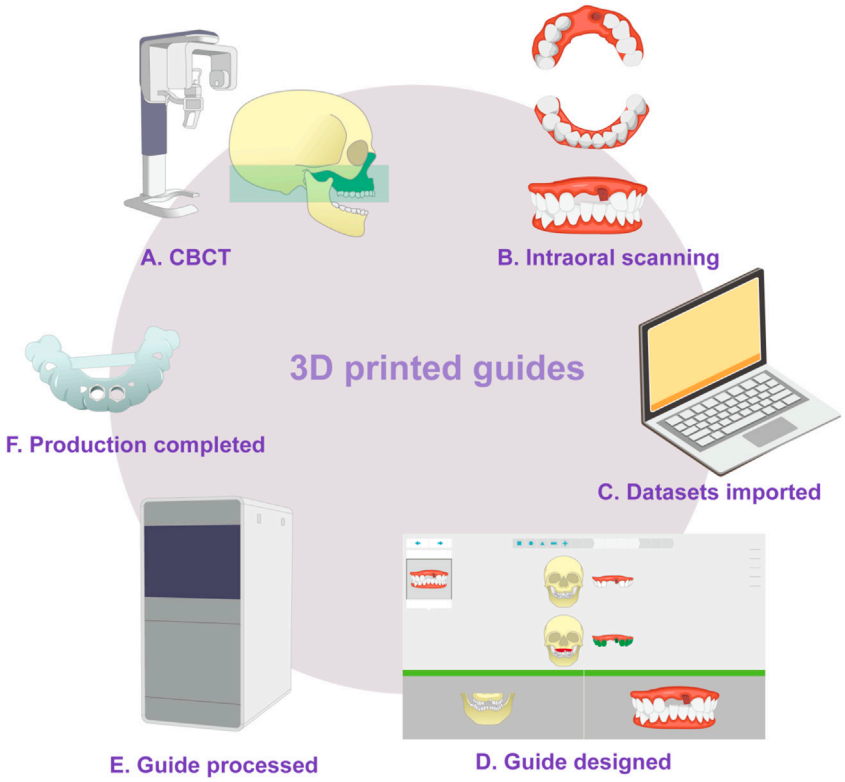

FIGURE 3
Schematic diagram of guide production. **(A)** Cone-beam computed tomography is used to generate 3D data from the teeth and jaws. **(B)** Three-dimensional information from the teeth and surrounding soft tissue is obtained by intraoral optical impression or scanned from a traditional plaster model. **(C)** In the guide design software, the two datasets are imported in turn and then matched, checked, and confirmed. **(D)** The guide is designed. **(E)** 3D printing is used to fabricate the guide. **(F)** The final guide is completed.

Guidelines for designing 3D printed customized titanium meshes have been published (Sagheb et al., 2017; Hartmann and Seiler, 2020; Li L et al., 2021) and include.

- The bone mass around the implant, the shape of alveolar bone, and the condition of soft tissues are factors that should be considered in the design.
- The distance between the boundary of the titanium mesh and adjacent teeth, nerves, blood vessels and other important structures should be ≥2 mm.
- The position and number of nail holes should be determined according to the retention needs. Nail hole diameter can be designed according to that of the titanium nail to be used.

In terms of the accuracy of 3D printed titanium mesh, Sumida et al. (Sumida et al., 2015) confirmed that the maximum error between customized titanium mesh and CAD data is <300 μm, indicating that it has sufficient accuracy for GBR. Regarding mechanical properties, the average tensile strength and test stress of titanium mesh with a thickness of 0.5 mm and a pore size of 1 mm printed by SLM are 627 ± 41 and 541 ± 26 MPa, respectively, while the average elongation strength and micro-Vickers hardness are 7.2% ± 2.8% and 203 ± 5 HV, respectively, demonstrating that titanium mesh has good mechanical properties. Otawa et al. (Otawa et al., 2015) tested the accuracy of SLM titanium mesh. The results show that dimensional accuracy, pore structure accuracy and the error between CAD design and the scanned real product by overlapped images are tolerable, and the maximum error and average error are 292 μm and 139 μm, respectively.

In term of indications, customized CAD/CAM titanium mesh can be used in bone augmentation surgery for horizontal and vertical bone defects, particularly for cases with large area, complex, combined horizontal and vertical bone defects. Some clinical studies have focused on the bone augmentation effect of CAD/CAM titanium mesh as shown in Table 2. It is worth noting that many clinical studies have shown that customized titanium mesh cannot completely avoid the problem of titanium mesh exposure, but exposure does not necessarily affect the final bone augmentation effect (Zhou et al., 2021; Ciocca et al., 2018a; Hartmann and Seiler, 2020). From the perspective of design, some scholars have demonstrated this by optimizing the design of customized titanium mesh thickness and pore size and other parameters and making the shape of customized titanium mesh smooth, so as to reduce the possibility of exposure. In addition, some scholars suggest using fibrin rich in platelets or collagen membrane to cover titanium mesh to reduce the exposure rate (Cucchi et al., 2021; Sagheb et al., 2017).

In fact, there is another way AM can help GBR, as used by Li et al. (Li S et al., 2021). By collecting intraoral scanning and DICOM (digital imaging and communications in medicine) data from patients, the implant position can be digitally designed, and the alveolar bone digitally augmented around the ideal implant position. This process provides superior precision and efficiency relative to traditional GBR

TABLE 1 Accuracy of different 3D printing techniques for fabrication of surgical guides for use in dental implantology.

References	Printing techniques used	Main conclusions
Rouzé L'Alzit et al. (2022)	SLA, DLP, FDM, and SLS, Inkjet	1. Regardless of the 3D-printer technology used, small-extent surgical guides are more accurate than large-extent guides
		2. SLA and DLP produced similar results
		3. FDM was the least accurate
Henprasert et al. (2020)	SLA, PolyJet, and MultiJet	1. Planned and final implant positions are not influenced by the additive manufacturing technologies tested
		2. The additive manufacturing technologies tested allowed for accurate implant placement
Chen et al. (2019)	SLA, PolyJet, and DMP	1. PolyJet 3D printing is more accurate and reproducible than SLA 3D printing
		2. Printed Co-Cr metal surgical templates produced using the DMP 3D printer retain their initial accuracy and reproducibility after 1 month of storage
Gjelvold et al. (2019)	SLA and DLP	1. The tested desktop 3D printers can produce surgical guides with similar deviations to those generated by definitive implant position
		2. DLP printing was more accurate concerning deviations at the entry point and vertical implant position
Abduo and Lau, (2020)	DLP and FFF	1. Although the two printers generally have similar accuracy, the guides produced by DLP printers are more accurate than those generated by FFF.
Sommacal et al. (2018)	FFF and DLP	1. There is a statistically significant difference between templates printed with a professional DLP printer and those printed with a consumer FFF3D printer
		2. Consumer FFF 3D printers are not suitable for creating templates for implant-guided surgery
Pieralli et al. (2020)	SLA and FDM	1. The accuracy of surgical guides made by FDM is similar to SLA.
Sun et al. (2019)	SLA and FDM	1. Using an FDM-printed surgical template for implant implantation is as accurate as using an SLA template for single dental space indications
Koch et al. (2019)	SLA, MultiJet and PolyJet	1. The SLA guides have the smallest deviation, followed by PolyJet and MultiJet.
		2. The average 3D deviation of two printers of the same brand and model is significantly different
Sun Y et al. (2022)	SLA and FDM	1. The placement accuracy of the FDM guide is the same as that of the SLA guide for single posterior edentulous spaces
Wegmüller et al. (2021)	MJ, SLA, FFF, and DLP	1. The accuracy of MJ guides is higher than that of FFF and DLP guides ($p < 0.01$)

DLP, digital light processing; FDM, fused deposition modeling; FFF, fused filament fabrication; SLA, stereolithography; SLS, selective laser sintering; MJ, Material Jetting.

procedures, as reflected in the preoperative virtual bone augmentation design, with an increment of 0.5 mm beyond the contour of the labial bone arch to compensate for possible bone resorption during bone healing. After 3D printing of the reconstructed alveolar bone model, the titanium mesh was trimmed and prefabricated on the alveolar bone model. The preformed personalized titanium mesh has lower technical sensitivity and better plasticity than 3D printed titanium mesh (Xie et al., 2020). Indeed, the customized titanium mesh made by both methods increases the possibility of customized bone regeneration (Seiler et al., 2018).

3.1.3 Dental implants

Interconnected pore structures are conducive to the transport of nutrients and increase surface roughness, which facilitates new bone formation and osseointegration (Chen et al., 2020; Yu et al., 2020). Moreover, porous structures reduce implant stiffness and generate an implant elastic modulus similar to that of the human jaw, thereby reducing stress shielding effects and allowing implants to be retained and function in the jaw for long periods of time (Wally et al., 2019). Titanium implants with uniform micron-scale porous structure can be produced by 3D printing (Mangano et al., 2014b). SLM and EBM are typically used to prepare dental implants, and implant materials are mainly titanium and titanium alloys, although some scholars have attempted to use zirconia (Pillai et al., 2021). Further, some researchers have proposed the use of titanium for the root portion and zirconium in the abutment portion to form one-piece implants that can achieve optimal osseointegration and ideal soft tissue attachment (Westover, 2019).

Using the characteristics of the complex geometric components formed by 3D printing, implants simulating the natural root can be customized. Personalized implants can be completely consistent with the shape of the patient's extraction socket. In immediate implant application, this approach can achieve high initial stability and reproduce the perfect gingival profile of natural teeth (Figliuzzi et al., 2012). In addition, personalized implants have similar stress conduction and distribution characteristics to natural teeth (Moin et al., 2013).

To obtain personalized implants, teeth and jaw data are collected by computed tomography or CBCT before surgery, and a three-dimensional model of the teeth reconstructed using software. Then, a CAD model of the implant is generated, exported to an STL file, and transferred to specialist reverse software. The surface of the model is smoothed to generate a regular surface, and then transferred to CAD

TABLE 2 Different studies used 3D printing titanium mesh to obtain the effect of bone augmentation.

References	Bone graft material	Design of customized titanium mesh	Printing techniques used	Whether to use other barrier membranes	Main conclusions
Sagheb et al. (2017)	Particulate autogenous bone mixed with deproteinized bovine bone mineral	-	-	A resorbable collagen membrane or a resorbable collagen membrane, followed by platelet-rich fibrin (PRF) membranes	Six months after operation, CBCT showed an average increase of 6.5 ± 1.7 mm in vertical bone mass and 5.5 ± 1.9 mm in the horizontal direction, compared with that before surgery
Ciocca et al. (2018a)	Autologous bone and anorganic bovine bone in a 1:1 ratio	The mesh was calibrated at a 0.3-mm thickness, and holes in the mesh were calibrated at 1-mm diameter	DMLS	No	Six to 8 months after surgery, cone beam CT showed an average increase of 1.72–4.1 mm (average 3.83 mm) in the mandibular arch and 2.14–6.88 mm (average 3.95 mm) in the maxilla
Cucchi et al. (2021)	A mix 50:50 of autogenous bone and bone xenograft	The meshes were usually less than 0.5 mm in thickness	SLM	Patients requiring bone augmentation procedures were randomly divided into two groups: group A received only custom-made meshes (Mesh-) and group B received custom-made meshes with collagen membrane (Mesh+)	Although group B had superior outcomes to group A in regenerated bone volume, the use of custom-made meshes alone did not seem to be inferior to custom-made meshes covered with cross-linked collagen membrane, in terms of healing complication and regeneration rates
Li L et al. (2021)	Particulate autogenous bone chips, deproteinized bovine bone mineral, and platelet-rich-fibrin (i-PRF)	The thickness of the model is 0.3 mm, and the aperture is 2.0 mm. The edge of the mesh should avoid damage to the adjacent teeth, nerves, blood vessels and other important structures, and stay away from these structures at least 2 mm	DMLS	Dual layer of resorbable collagen membrane and concentrated growth factor matrix	According to the post-implantation CBCT evaluation, the patient-based average vertical bone gain was 3.55 ± 3.74 mm, and the horizontal average bone gain at 0, 2, and 4 mm below the implant platform was 4.06 ± 2.37, 5.58 ± 2.65, 5.26 ± 2.33 mm, respectively
Cucchi et al. (2020)	Autogenous bone and bone xenograft	The meshes were usually less than 0.5 mm in thickness	SLM	No	Measurements showed an average VBG of 4.5 ± 1.8 mm at surgical re-entry. Surgical and healing complications occurred in 30% and 10% of cases, respectively. Mean values of PBV, LBV, and RBV were 984, 92, and 892 mm^3, respectively. The average RR achieved was 89%

VBG, vertical bone gain; PBV, planned bone volume; LBV, lacking bone volume; RBV, regenerated bone volume; RR, average regeneration rate.

software for abutment design. After completion, an STL file of the implant and abutment is obtained and imported into the printer for processing and manufacture (F. G. Mangano F. G. et al., 2013; Westover, 2019). Due to deviations in precision, some researchers have incremented implant CAD models by dimension percentages (0%, 5%, and 10%) for clinical applications (F. G. Mangano F. G. et al., 2013). Another technique involves laser scanning of the root to construct the final implant after extraction, and design of macro-retainers on the implant surface to increase its stability following placement (Dantas et al., 2021).

Another class of implants, referred to as patient-matched implants, are less personalized than 3D printed root-analogue implants; for example, some scholars have used 3D printing to generate narrow-diameter implants for patients with insufficient alveolar bone width (F. Mangano et al., 2013b). In addition, 3D printing is also used in the manufacture of non-customized dental implants (similar to current commercial implants). The Italian "Tixos" implant, which is similar to a traditional implant, is produced by DMLS technology and has a variety of sizes to choose from (Mangano et al., 2012a). Furthermore, implants produced by DMLS have high fatigue strength and good corrosion resistance (Yang et al., 2020). Gehrke et al. confirmed that the mean fracture strength of DMLS implants with diameter 3.5 mm and length 16 mm can reach >1200 N (Gehrke et al., 2018): However, for two-stage dental implants, it is difficult to achieve a tight connection between a 3D printed implant and the abutment due to a lack of surface accuracy, but a tight connection can be achieved by machining of the connection structure in the 3D printing implant platform (Tunchel et al., 2016). The predicted survival rates of 3D printed implants confirmed in clinical studies are presented in Table 3.

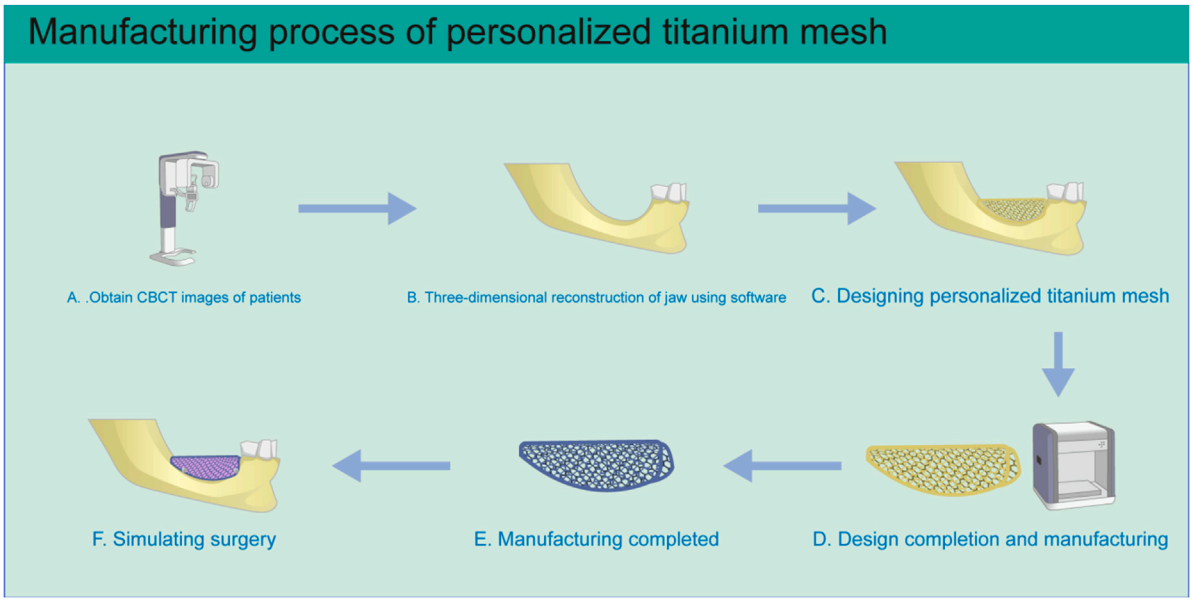

FIGURE 4
Schematic diagram of personalized titanium mesh production. **(A)** Three-dimensional CBCT image data of the patient's jaws is obtained. **(B)** The three-dimensional jaw structure is reconstructed. **(C)** Personalized titanium mesh is designed according to the condition of alveolar bone defect. **(D)** After the design is completed, the file is imported into the 3D printer for manufacturing. **(E)** After printing is completed, the titanium mesh is treated by ultrasonic cleaning, sandblasting, and acid etching. **(F)** The situation is simulated during the operation.

Poly ether ether ketone (PEEK) 3D printed implants have also attracted attention (Basgul et al., 2021b; Sun C et al., 2022). PEEK is an aromatic polymer with characteristics of corrosion resistance, high temperature resistance, non-cytotoxicity, X-ray transmission, chemical stability, and good biological safety (Najeeb et al., 2016; Panayotov et al., 2016; Basgul et al., 2021a). Compared with titanium alloy, the elastic coefficient of PEEK is relatively low and closer to that of human cortical bone, which helps to reduce stress shielding effects at the bone-implant interface, thereby minimizing implant loosening and peri-implant bone loss (Han et al., 2022). Although it has many advantages, the main challenge for PEEK as a dental implant material is that it is a bioinert material with low surface energy; Therefore, appropriate strategies should be developed to improve the biological activity of PEEK and realize its potential benefits (Jung et al., 2019; Basgul et al., 2021b).

FDM and SLS 3D printing technologies can be used to print PEEK implants, and the former is most commonly used (Schmidt et al., 2007; Baek et al., 2022; Basgul & Spece et al., 2021). The molecular structure of PEEK does not change at high temperature; thus, no toxic substances are produced in the printing process (Prechtel et al., 2020; Shilov et al., 2022). Further, 3D printed PEEK implants have many advantages, including free design, interconnected porous structures and specific surface topography (Shishkovsky et al., 2013; Torstrick et al., 2018; Yuan et al., 2018). Han et al. systematically analyzed the biological activity of PEEK implants printed by FDM, including surface roughness, wettability, cell adhesion, metabolic activity, and proliferation (Han et al., 2019a). They found that, compared with the sandblasted surface of traditional molded or milled PEEK implants, the special surface morphology and porous structure of 3D printed PEEK implants played an important role in stimulating bioactive potential.

In addition, to improve the bioactivity of 3D printed PEEK implants, Han et al. used plasma surface treatment technology to introduce Ar or O_2 functional groups into the surface of 3D printed PEEK, which significantly improved surface hydrophilicity and changed surface morphology and roughness (Han et al., 2022). Plasma-treated PEEK induced adhesion, metabolic activity, proliferation, and osteogenic differentiation of SAOS-2 cells *in vitro*. Su et al. developed a sulfonation strategy to create uniform micropores on PEEK lattice scaffolds fabricated by FFF (Su et al., 2020). The suitable lattice structure sulfonation time was 30–45 s, and the mean size of formed micropores was 0.19 ± 0.07 μm. Compared with the untreated PEEK scaffold, the micropore structure on the FFF printed PEEK lattice scaffold significantly improved cell attachment, spreading, proliferation, and bone-specific differentiation of MC3T3-E1 cells. More importantly, the existence of micropores on the lattice scaffold promoted the attachment of new soft tissue to PEEK implants.

In addition to biocompatibility studies, other investigations have been dedicated to improving the mechanical strength of PEEK (Chen et al., 2022). Numerous factors can influence the biomechanical qualities of 3D printed PEEK implants, including the size/shape of the test sample, printing temperature, printing speed, layer thickness, component orientation, nozzle diameter, and raster angle (Arif et al., 2018; Basgul & Spece et al., 2021;Basgul & Thieringer et al., 2021; Prechtel et al., 2020; Moby et al., 2022). PEEK formed by FFF has sufficient tensile, bending, and fracture strength (Arif et al., 2018), but the fatigue properties of these implants require further evaluation (Fabris et al., 2022). Sonaye et al. studied the printing parameter set of PEEK implants produced by FFF technology (Sonaye et al., 2022) and showed that the best printing parameters for PEEK implants are: nozzle temperature, 450°C; bedplate temperature, 150°C; chamber

TABLE 3 Clinical studies of 3D printed titanium implant.

References	Manufacturing method	Material	Implant features	Clinical applications	Main findings
Mangano et al. (2013a)	DMLS	Ti-6Al-4V	Root-analogue implants	Root-analogue implants were implanted in the sockets and restored with a single crown for 15 patients	1. At 1-year follow-up, implant survival rate was 100%
					2. Mean DIB was 0.7 (±0.2) mm
Mangano, et al. (2012b)	DMLS	Ti-6Al-4V	Standard implants	Implants were inserted in the edentulous mandible for 24 patients	1. After a 1-year loading time, implant survival rate was 98.9%
					2. DIB was 0.28–0.30 mm (95% CI, 0.24–0.32)
Mangano et al. (2015)	DMLS	Ti-6Al-4V	Standard implants	Implants inserted in the mandible to support ball attachment-retained mandibular overdentures for 24 patients	1. After 4 years of loading, overall cumulative survival rate was 96.9%
					2. DIB values were 0.38–0.25 and 0.62–0.20 mm at 1- and 4-year follow-up examinations, respectively
Mangano et al. (2012b)	DLMF	Ti-6Al-4V	Standard implants	201 implants (106 maxilla, 95 mandible) were inserted in 62 patients	1. Overall implant survival rate was 99.5%
					2. Mean DIB was 0.4 ± 0.2 mm
Mangano et al. (2013b)	SLS	Ti-6Al-4V	Standard implants	Implants placed in the posterior jaw for 16 patients	1. At 2-year follow-up, implant survival rate was 100%
					2. Implant success rate was 94.6%
					3. DIB was 0.4 ± 0.3 mm
Mangano et al. (2014b)	DMLS	Ti-6Al-4V	Standard implants	Implants used to support bar-retained maxillary overdentures for 30 patients	1. 3-year implant survival rates were 97.4% (implant-based) and 92.9% (patient-based)
					2. Biological complication incidence rates were 3.5% (implant-based) and 7.1% (patient-based)
					3. The incidence of prosthetic complication was 17.8% (patient-based)
Tunchel et al. (2016)	DMLS	Ti-6Al-4V	Standard implants	Eighty-two patients (44 male, 38 female; age range 26–67 years) were enrolled. A total of 110 3DP/AM titanium dental implants (65 maxilla, 45 mandible) were installed: 75 in healed alveolar ridges and 35 in post-extraction sockets. Prosthetic restorations included 110 single crowns	1. After 3 years of loading, six implants failed, for an overall implant survival rate of 94.5%
					2. Among the 104 surviving implant-supported restorations, 6 showed complications and were therefore considered unsuccessful, for an implant-crown success rate of 94.3%
					3. Mean DIB values were 0.75 (±0.32) mm and 0.89 (±0.45) mm after 1 and 3 years of loading, respectively

DIB, distance from the implant shoulder to the first visible bone-to-implant contact; DMLS, direct metal laser sintering; SLS, selective laser sintering.

temperature, 90°C; layer thickness, 0.1 mm; and printing speed, 30 mm/s. The use of optimized process parameters resulted in implants with excellent fatigue performance. Further, reinforcement of PEEK with various materials, such as glass fiber, carbon fiber, and silicate based bioceramics, improves its mechanical strength to a certain extent (Han et al., 2019b; Petersmann et al., 2020; Taymour et al., 2022).

In summary, the excellent overall properties of PEEK mean that it has considerable prospects for application as dental implant material. Combined with 3D printing, customized and graded porous PEEK implants can be manufactured quickly, resulting in implants with better performance than those generated by traditional manufacturing processes. However, 3D printing of PEEK implants is mostly at the laboratory research stage, and wide application of PEEK implants in the clinic requires more supportive evidence from basic research and clinical trials.

3.2 Applications of additive manufacturing in the restoration stage of implant therapy

3.2.1 Custom trays

Three-dimensional printing technology has been applied to fabricate custom trays for implants (Kim et al., 2019b). Revilla-León et al. and Piedra et al. described an implant impression technique for a complete arch, digitally designing metal splint structured and custom trays, which were generated using DMLS and DLP technology, respectively (Revilla-León and Özcan, 2017; Piedra and Revilla-Leon, 2018). Good matching between the metal splint structure and the impression copings makes it simple to locate in the patient's mouth. Compared with manual individual trays, 3D printed custom trays have many advantages: First, custom trays have sufficient extension range and more uniform 3D impression material space between the splinting structure and the custom tray (Sun et al.,

2017), providing more accurate oral tissue records; and second, they reduce the time required to fix the impression rod using materials such as resin, shorten clinical operation duration, and avoid the inaccuracies in definitive models caused by resin polymerization shrinkage (Kim et al., 2019a; Revilla-Leon and Ozcan, 2019).

Research confirms that 3D printed custom trays are stronger than traditional custom trays (Liu et al., 2019), which can be attributed to the parameters set in the manufacturing process. With increasing printing layer thickness, the tensile bond strength of trays first increases and then decreases, reaching a peak at 0.4 mm thickness, and printing time decreases sharply. Although bending and tensile strength decrease, dimensional printing accuracy remains constant from 0.1 to 0.4 mm, and then decreases at 0.5 mm, demonstrating that moderate layer thickness provides the best performance for 3D printing of custom trays (Liu et al., 2021).

To meet clinical requirements, tray materials should have both sufficient rigidity and dimensional stability and provide sufficient retention of impression materials. Xu et al. evaluated the bonding strength between three 3D printed custom tray materials (SLA, DLP, and FFF) and three elastomeric impression/adhesive systems [vinyl siloxane ether (VSXE), vinyl polysiloxane (VPS), and polyether (PE)] using the peel test (Xu et al., 2020). The results showed that the three 3D printing tray materials have good chemical compatibility with adhesives such as VSXE, VPS, and PE, and that 3D printing tray materials can provide sufficient clinical bonding strength with elastic impression/adhesive systems; when severe impression removal resistance is detected, it is recommended to use both PLA and VPS.

The studies described above confirmed that 3D printed custom trays have sufficient strength, hardness, and bonding strength with impression materials. Hence, 3D printing implant impression techniques could provide alternatives to conventional impression techniques for implant restoration.

3.2.2 Implant models

Materializing digital impressions is among the earliest applications of 3D printing in dentistry (Revilla-Leon and Ozcan, 2019). The definitive implant model must ensure accurate implant location and relationship with adjacent teeth. Compared with traditional plaster models, 3D printed models have the advantages of being lightweight, resistant to damage, and having high finish, good wear resistance, and avoiding the inaccurate position of the analogue, which may be caused by artificial fixation of the implant analogue on the impression (Monaco et al., 2018; Tian et al., 2021). Moreover, 3D printed models overcome the disadvantages of digital models, as the physical model facilitates simple evaluation of the occlusal condition and interproximal contact (Buda et al., 2018).

Printed model inaccuracy results from accumulation of distortions caused by the acquisition method, parameters determined by the design software, and the printing process (Tian et al., 2021), which may be affected by many factors, such as scanner selection and the digitization process, among others. Papaspyridakos et al. (Papaspyridakos et al., 2020) proposed that the deviation of a printed model for use in implant restoration should ideally be <100 μm and should not exceed 150 μm.

Maria et al. (Maria et al., 2021) measured the physical positions of implants in a master model and analogs in printed resin models using a coordinate measuring machine. Three analog implant systems for 3D printed resin models [Straumann (ST), Core3DCentres (CD) and Medentika (MD)] were tested. Mean 3D linear distortion for ST (−155.7 ± 60.6 μm), CD (124.9 ± 65.0 μm), and MD (−92.9 ± 48.0 μm) differed significantly ($p < 0.01$), confirming that the implant analog system has a significant effect on the accuracy of analogs in 3D printed models. Mean absolute angular distortion did not differ significantly between ST (0.57° ± 0.48°) and CD (0.41° ± 0.27°), while both differed significantly from MD (2.11° ± 1.14°). Print orientation had a significant effect on 3D linear distortion, but no discernible trend could be found. Michelinakis et al. pointed out that, when choosing a semi-digital method, the cumulative deviation of the model in the 3D printing process may lead to a deviation in the position of the implant analogue, which depends on the printing technique and materials used (Table 4) (Michelinakis et al., 2021). In addition, Yousef et al. (Yousef et al., 2021) suggested that restoration be conducted as soon as possible after the model is printed, as the 3D printed model will deform during long-term storage.

3.2.3 Implant frameworks

CAD/CAM technologies are widely used to design and manufacture frameworks for implant-supported prostheses (Kapos and Evans, 2014). After completing CAD of implant-supported frameworks, the virtual design is transformed into a physical object by addition or subtraction manufacturing (Revilla-Leon et al., 2019b). Compared with traditional casting technology, subtractive technologies reduce some clinical steps and eliminate certain human errors, but result in waste of materials and may fail to reflect the finer details of frameworks (Svanborg et al., 2018). Metal AM processes, such as SLM or EBM, are also used to fabricate implant frameworks, and effectively reduce material waste (Barbin et al., 2020). The mechanical properties of 3D printed implant frameworks can be comparable to, or even better than, those of traditional casting (Revilla-Leon et al., 2021). In addition, the shape of retainers on frameworks can be freely designed to increase the adhesion between the framework and the resin material.

The accuracy of the fit between implant frameworks and the underlying structures is an extremely important factor in avoiding biological and technical complications (Svanborg et al., 2018), which affect the long-term clinical success of implant-supported restorations. In an *in vitro* study, Revilla-Leon et al. evaluated discrepancies in the manufacture of titanium frameworks for implant-supported complete-arch prostheses manufactured using SLM and EBM(Revilla-Leon et al., 2018a). First, titanium frameworks for implant-supported complete-arch prostheses were designed using dental software. Then, frameworks were fabricated using SLM or EBM technology. The manufactured titanium frameworks and framework STL files were fitted and superimposed using a coordinate measuring machine. The results showed that there were no significant differences between SLM and EBM in the *x* and *y*-axes of implant frameworks, while the *z*-axis varied. The 3D discrepancies of all comparisons ranged from 60 ± 18 μm to 69 ± 30 μm, and the differences were not statistically significant. The discrepancy in the *y*-axis was largest (37–56 μm), followed by the x (16–44 μm) and z (6–11 μm) axes. Revilla-Leon et al. also compared the discrepancy at the implant abutment-prosthesis interface of complete-arch cobalt-chromium implant frameworks fabricated by additive and subtractive technologies before and after ceramic veneering in a separate study (Revilla-Leon et al., 2021). No significant differences were detected between the CNC and AM groups, except that the AM group presented a significantly higher discrepancy on the *x*-axis compared with the CNC group. Abu and Onoral. (2021) fabricated

TABLE 4 Accuracy of different 3D printing techniques for fabrication of implant models for use in dental implantology.

References	Printing techniques used	Main conclusions
Olea Vielba et al. (2020)	MultiJet	1. There was no significant difference in x-, y-, and z-linear, or XZ angular discrepancy between the conventional and additive manufacturing groups
		2. The AM group had a significantly higher median YZ angular discrepancy than the CNV group ($p = 0.007$)
Buda et al. (2018)	PolyJet and SLA	1. Significant differences in accuracy among the implant analog cast fabrication systems
		2. The PolyJet industrial printing system was more accurate than the conventional gypsum implant analog cast
Revilla-Leon et al. (2018a)	MJP1, SLA, MJP2, DLP	1. Regardless of the cast system, *x*-axes showed more distortion (42.6 μm) than y- (34.6 μm) and z- (35.97 μm) axes
		2. Among additive manufacturing technologies, MJP2 presented the highest (64.3 ± 83.6 μm), and MJP1 (21.57 ± 16.3 μm) and DLP (27.07 ± 20.23 μm) the lowest distortion, which did not differ significantly from that of conventional dental stone (32.3 ± 22.73 μm)
Rungrojwittayakul et al. (2020)	CLIP and DLP	1. All 3D printed models generated using CLIP and DLP printers had clinically acceptable levels of trueness
		2. Models produced using the CLIP printer exhibited significantly greater trueness, relative to the reference model, although the difference was small
Kim et al. (2018)	SLA, DLP, FFF, PolyJet	1. The PolyJet and DLP techniques were more precise than the FFF and SLA methods, with PolyJet exhibiting the highest accuracy for 3D model printing
Hazeveld et al. (2014)	DLP, 3DP, MJP	1. All replicas were sufficiently accurate and could be used interchangeably with plaster models

3DP, 3-dimensional printing; CLIP, continuous liquid interface production; DLP, digital light processing; FFF, fused filament fabrication; SLA, stereolithography.

3-unit Co-Cr frameworks with three indirect (conventional technique, polymethyl methacrylate milling, SLA) and two direct (SLM and soft alloy milling) methods. The mean vertical marginal discrepancy value of the SLM group (74.2 ± 20.5 μm) was significantly lower than those of all other groups ($p < 0.05$), demonstrating superior fitting accuracy. Barbin et al. (2020) evaluated the influence of milling, SLM, and EBM on full-arch fixed dental prostheses (FAFDPs) manufacture, in terms of marginal FAFDP misfits, prosthetic screw stability, and strain and stress on implant-supported systems, among other parameters. Compared with SLM and EBM frameworks, milled frameworks had the highest average marginal match, but the deviation of the former was within a clinically acceptable range. Ceramic veneer had no significant effect on the average marginal misfit values of any manufacturing process, while spark erosion reduced mean marginal misfit values for SLM and EBM titanium frameworks. On screw stability analysis, milled frameworks showed higher mean screw-loosening values, but after chewing simulations, none of the frameworks exhibited screw loosening.

In a recent systematic review (Thakur et al., 2021), the marginal fit and accuracy of complete-arch implant-supported frameworks, implant-retained fixed partial dentures, single implant crowns, and interim implant-retained restorations fabricated using AM and subtractive manufacturing methods were compared. The results showed that there was no significant difference in the marginal fit of single implant crowns or complete-arch implant frameworks between the two fabrication methods. For implant-supported fixed partial dentures, AM was superior to subtractive milling, but both digital fabrication methods produced implant-supported superstructures with clinically acceptable marginal fit.

The characteristic superficial texture of the layer-by-layer buildup in AM technologies results in a rough metal surface. A strong correlation between the roughness values on mating surfaces and implant-prosthodontic discrepancy has been reported. To achieve acceptable implant prosthodontic discrepancy, some scholars have combined 3D printing technologies and subtractive processing, electropolishing, sandblasting, or other post-processing techniques (Revilla-Leon et al., 2019b; Revilla-Leon et al., 2021). Ciocca et al. (2018b) compared the trueness and precision of frameworks manufactured with an SLM/milling hybrid technique (SLM/m) and conventional milling. The maximum misfit for the milled group was 20–35 μm, while there was no significant difference between SLM and SLM/m, with errors of 8–16 μm and 9–22 μm, respectively. Moreover, irrespective of the manufacture method, the trueness of titanium framework misfit was affected by framework span.

4 Discussion

The focus of this review was to provide an overview of AM technologies commonly used in implant dentistry and their application in the surgical and restoration stages of implant therapy. In addition, the accuracy of different 3D printing techniques for fabrication of printed parts is summarized in Table 2 and Table 4. The growing interest in 3D printing technologies clearly shows their potential impact on the future of implant dentistry (Nikoyan and Patel, 2020). With their advantages of high material utilization, ability to form complex geometric structures, and production of personalized products, 3D printing technologies have become an alternative method to generate components from CAD files. The various materials used in implant dentistry require the application of different AM techniques. Metal materials, such as personalized titanium meshes and titanium dental implants, can be manufactured using DMLS/SLM/EBM, whereas polymer materials, such as surgical guides and implant models, are fabricated using SLA, DLP, and PolyJet techniques.

Resin material products (surgical guides and implant models, etc.) produced by VPP technology have been widely studied and applied; however, there are specific areas that warrant further investigation. In

particular, the numbers of patients and observation time in clinical studies of personalized titanium mesh generated by 3D printing have been limited to date; hence, the therapeutic effects of this approach require further study and verification. In future research, to ensure mechanical strength, continued optimization of personalized titanium mesh parameters, such as thickness, pore diameter, and shape, is required. In addition, the effects of combining personalized titanium mesh with absorbable collagen membrane, concentrated growth factor membrane, or other bone augmentation techniques warrant further exploration. Furthermore, 3D printing to manufacture dental implants has only recently been introduced; thus, more research and clinical studies are needed to understand the long-term safety and clinical efficacy of 3D printed implants. Future work will include study of the mechanical properties and structural characteristics, as well as printing process optimization of 3D printed dental implants, to achieve improved accuracy and performance (Oliveira and Reis, 2019). Finally, although it may seem that all oral implant medical devices can be made using 3D printers, a single technology may not be able to meet all patient needs. For some applications, 3D printing technology needs to be combined with milling or other cutting/finishing techniques, to generate a product that can achieve the final application goal (de Oliveira Campos et al., 2020).

Author contributions

SH and HW were involved in study design, literature research, data analysis, and writing the manuscript. HW was also involved in project administration, writing-review and editing, and conceptualization. DL was involved in conceptualization, study design, supervision, submission of the manuscript, and obtaining funding.

Funding

This work was supported by grants from The National Key Research and Development Program of China (2017YFB1104100).

Conflict of interest

The authors declare that the research was conducted in the absence of any commercial or financial relationships that could be construed as a potential conflict of interest.

Publisher's note

All claims expressed in this article are solely those of the authors and do not necessarily represent those of their affiliated organizations, or those of the publisher, the editors and the reviewers. Any product that may be evaluated in this article, or claim that may be made by its manufacturer, is not guaranteed or endorsed by the publisher.

References

Abduo, J., and Lau, D. (2020). Effect of manufacturing technique on the accuracy of surgical guides for static Computer-Aided implant surgery. *Int. J. Oral Maxillofac. Implants* 35 (5), 931–938. doi:10.11607/jomi.8186

Abduo, J., Lyons, K., and Bennamoun, M. (2014). Trends in computer-aided manufacturing in prosthodontics: A review of the available streams. *Int. J. Dent.* 2014, 1–15. doi:10.1155/2014/783948

Abu, G. A., and Onoral, O. (2021). An assessment of the passivity of the fit of multiunit screw-retained implant frameworks manufactured by using additive and subtractive technologies. *J. Prosthet. Dent.* [Epub ahead of print]. doi:10.1016/j.prosdent.2021.06.022

Alammar, A., Kois, J. C., Revilla León, M., and Att, W. (2022). Additive manufacturing technologies: Current status and future perspectives. *J. Prosthodont.* 31, 4–12. doi:10.1111/jopr.13477

Anadioti, E., Kane, B., and Soulas, E. (2018). Current and emerging applications of 3D printing in restorative dentistry. *Curr. Oral Health Rep.* 5 (2), 133–139. doi:10.1007/s40496-018-0181-3

Ansari, M. J., Nguyen, D., and Park, H. S. (2019). Investigation of SLM process in terms of temperature distribution and melting pool size: Modeling and experimental approaches. *Materials* 12 (8), 1272. doi:10.3390/ma12081272

Arif, M. F., Kumar, S., Varadarajan, K. M., and Cantwell, W. J. (2018). Performance of biocompatible PEEK processed by fused deposition additive manufacturing. *Mater. Des.* 146, 249–259. doi:10.1016/j.matdes.2018.03.015

Attarilar, S., Ebrahimi, M., Djavanroodi, F., Fu, Y., Wang, L., and Yang, J. (2021). 3D printing technologies in metallic implants: A thematic review on the techniques and procedures. *Int. J. Bioprint* 7 (1), 306. doi:10.18063/ijb.v7i1.306

Baek, I., Kwon, O., Lim, C., Park, K. Y., and Bae, C. (2022). 3D PEEK objects fabricated by fused filament fabrication (FFF). *Materials* 15 (3), 898. doi:10.3390/ma15030898

Barazanchi, A., Li, K. C., Al-Amleh, B., Lyons, K., and Waddell, J. N. (2017). Additive technology: Update on current materials and applications in dentistry. *J. Prosthodont.* 26 (2), 156–163. doi:10.1111/jopr.12510

Barbin, T., Velôso, D. V., Del Rio Silva, L., Borges, G. A., Presotto, A. G. C., Barão, V. A. R., et al. (2020). 3D metal printing in dentistry: An *in vitro* biomechanical comparative study of two additive manufacturing technologies for full-arch implant-supported prostheses. *J. Mech. Behav. Biomed.* 108, 103821. doi:10.1016/j.jmbbm.2020.103821

Basgul, C., Spece, H., Sharma, N., Thieringer, F. M., and Kurtz, S. M. (2021a). Structure, properties, and bioactivity of3D printedPAEKs for implant applications: A systematic review. *J. Biomed. Mater. Res. Part B Appl. Biomaterials* 109 (11), 1924–1941. doi:10.1002/jbm.b.34845

Basgul, C., Thieringer, F. M., and Kurtz, S. M. (2021b). Heat transfer-based non-isothermal healing model for the interfacial bonding strength of fused filament fabricated polyetheretherketone. *Addit. Manuf.* 46, 102097. doi:10.1016/j.addma.2021.102097

Bordin, A., Sartori, S., Bruschi, S., and Ghiotti, A. (2017). Experimental investigation on the feasibility of dry and cryogenic machining as sustainable strategies when turning Ti6Al4V produced by Additive Manufacturing. *J. Clean. Prod.* 142, 4142–4151. doi:10.1016/j.jclepro.2016.09.209

Bozkurt, Y., and Karayel, E. (2021). 3D printing technology; Methods, biomedical applications, future opportunities and trends. *J. Mater. Res. Technol.* 14, 1430–1450. doi:10.1016/j.jmrt.2021.07.050

Buda, M., Bratos, M., and Sorensen, J. A. (2018). Accuracy of 3-dimensional computer-aided manufactured single-tooth implant definitive casts. *J. Prosthet. Dent.* 120 (6), 913–918. doi:10.1016/j.prosdent.2018.02.011

Chen, J., Xiao, Z., Yangpeng, S., Deng, F., and Zhiguang, Z. (2020). Production of inter-connective porous dental implants by computer-aided design and metal three-dimensional printing. *J. Biomater. Appl.* 34 (9), 1227–1238. doi:10.1177/0885328219899523

Chen, J., Zhang, Z., Chen, X., Zhang, C., Zhang, G., and Xu, Z. (2014). Design and manufacture of customized dental implants by using reverse engineering and selective laser melting technology. *J. Prosthet. Dent.* 112 (5), 1088–1095.e1. doi:10.1016/j.prosdent.2014.04.026

Chen, L., Lin, W., Polido, W. D., Eckert, G. J., and Morton, D. (2019). Accuracy, reproducibility, and dimensional stability of additively manufactured surgical templates. *J. Prosthet. Dent.* 122 (3), 309–314. doi:10.1016/j.prosdent.2019.02.007

Chen, W., Zhang, X., Tan, D., Xu, P., Yang, B., Shi, K., et al. (2022). Improvement in mechanical properties of 3D-printed PEEK structure by nonsolvent vapor annealing. *Macromol. Rapid Comm.* 43 (7), 2100874. doi:10.1002/marc.202100874

Cho, J. Y., Kim, S. B., and Ryu, J. (2021). The accuracy of a partially guided system using an in-office 3D-printed surgical guide for implant placement. *Int. J. Comput. Dent.* 24 (1), 19–27.

Ciocca, L., Lizio, G., Baldissara, P., Sambuco, A., Scotti, R., and Corinaldesi, G. (2018a). Prosthetically CAD-CAM-Guided bone augmentation of atrophic jaws using customized titanium mesh: Preliminary results of an open prospective study. *J. Oral Implantol.* 44 (2), 131–137. doi:10.1563/aaid-joi-D-17-00125

Ciocca, L., Meneghello, R., Savio, G., Scheda, L., Monaco, C., Gatto, M. R., et al. (2018b). Manufacturing of metal frameworks for full-arch dental restoration on implants: A comparison between milling and a novel hybrid technology. *J. Prosthodont.* 28 (5), 556–563. doi:10.1111/jopr.13067

Cucchi, A., Bianchi, A., Calamai, P., Rinaldi, L., Mangano, F., Vignudelli, E., et al. (2020). Clinical and volumetric outcomes after vertical ridge augmentation using computer-aided-design/computer-aided manufacturing (CAD/CAM) customized titanium meshes: A pilot study. *BMC Oral Health* 20 (1), 219. doi:10.1186/s12903-020-01205-4

Cucchi, A., Giavatto, M. A., Giannatiempo, J., Lizio, G., and Corinaldesi, G. (2019). Custom-Made titanium mesh for maxillary bone augmentation with immediate implants and delayed loading. *J. oral Implant.* 45 (1), 59–64. doi:10.1563/aaid-joi-D-18-00141

Cucchi, A., Vignudelli, E., Franceschi, D., Randellini, E., Lizio, G., Fiorino, A., et al. (2021). Vertical and horizontal ridge augmentation using customized CAD/CAM titanium mesh with versus without resorbable membranes. A randomized clinical trial. *Clin. Oral Implan. Res.* 32 (12), 1411–1424. doi:10.1111/clr.13841

Dalal, N., Ammoun, R., Abdulmajeed, A. A., Deeb, G. R., and Bencharit, S. (2020). Intaglio surface dimension and guide tube deviations of implant surgical guides influenced by printing layer thickness and angulation setting. *J. Prosthodont.* 29 (2), 161–165. doi:10.1111/jopr.13138

Dantas, T., Madeira, S., Gasik, M., Vaz, P., and Silva, F. (2021). Customized root-analogue implants: A review on outcomes from clinical trials and case reports. *Materials* 14 (9), 2296. doi:10.3390/ma14092296

Dawood, A., Marti, B. M., Sauret-Jackson, V., and Darwood, A. (2015). 3D printing in dentistry. *Brit. Dent. J.* 219 (11), 521–529. doi:10.1038/sj.bdj.2015.914

de Oliveira Campos, F., Araujo, A. C., Jardini Munhoz, A. L., and Kapoor, S. G. (2020). The influence of additive manufacturing on the micromilling machinability of Ti6Al4V: A comparison of SLM and commercial workpieces. *J. Manuf. Process.* 60, 299–307. doi:10.1016/j.jmapro.2020.10.006

Elliott, T., Hamilton, A., Griseto, N., and Gallucci, G. O. (2022). Additively manufactured surgical implant guides: A review. *J. Prosthodont.* 31 (S1), 38–46. doi:10.1111/jopr.13476

Fabris, D., Moura, J. P. A., Fredel, M. C., Souza, J. C. M., Silva, F. S., and Henriques, B. (2022). Biomechanical analyses of one-piece dental implants composed of titanium, zirconia,PEEK,CFR-PEEK, orGFR-PEEK: Stresses, strains, and bone remodeling prediction by the finite element method. *J. Biomed. Mater. Res. Part B Appl. Biomaterials* 110 (1), 79–88. doi:10.1002/jbm.b.34890

Figliuzzi, M., Mangano, F., and Mangano, C. (2012). A novel root analogue dental implant using CT scan and CAD/CAM: Selective laser melting technology. *Int. J. Oral Max. Surg.* 41 (7), 858–862. doi:10.1016/j.ijom.2012.01.014

Fotopoulos, I., Lillis, T., Panagiotidou, E., Kapagiannidis, I., Nazaroglou, I., and Dabarakis, N. (2022). Accuracy of dental implant placement with 3D-printed surgical templates by using Implant Studio and MGUIDE. An observational study. *Int. J. Comput. Dent.* 25 (3), 249–256. doi:10.3290/j.ijcd.b2599735

Gargallo-Albiol, J., Zilleruelo-Pozo, M. J., Lucas-Taulé, E., Muñoz-Peñalver, J., Paternostro-Betancourt, D., and Hernandez-Alfaro, F. (2022). Accuracy of static fully guided implant placement in the posterior area of partially edentulous jaws: A cohort prospective study. *Clin. Oral Invest.* 26 (3), 2783–2791. doi:10.1007/s00784-021-04254-3

Gehrke, S. A., Pérez-Díaz, L., and Dedavid, B. A. (2018). Quasi-static strength and fractography analysis of two dental implants manufactured by direct metal laser sintering. *Clin. Implant Dent. R.* 20 (3), 368–374. doi:10.1111/cid.12590

Gjelvold, B., Mahmood, D., and Wennerberg, A. (2019). Accuracy of surgical guides from 2 different desktop 3D printers for computed tomography-guided surgery. *J. Prosthet. Dent.* 121 (3), 498–503. doi:10.1016/j.prosdent.2018.08.009

Han, X., Sharma, N., Spintzyk, S., Zhou, Y., Xu, Z., Thieringer, F. M., et al. (2022). Tailoring the biologic responses of 3D printed PEEK medical implants by plasma functionalization. *Dent. Mat.* 38 (7), 1083–1098. doi:10.1016/j.dental.2022.04.026

Han, X., Sharma, N., Xu, Z., Scheideler, L., Geis-Gerstorfer, J., Rupp, F., et al. (2019a). An *in vitro* study of osteoblast response on Fused-Filament fabrication 3D printed PEEK for dental and Cranio-Maxillofacial implants. *J. Clin. Med.* 8 (6), 771. doi:10.3390/jcm8060771

Han, X., Yang, D., Yang, C., Spintzyk, S., Scheideler, L., Li, P., et al. (2019b). Carbon fiber reinforced PEEK composites based on 3D-Printing technology for orthopedic and dental applications. *J. Clin. Med.* 8 (2), 240. doi:10.3390/jcm8020240

Hartmann, A., Hildebrandt, H., Schmohl, J. U., and Kämmerer, P. W. (2019). Evaluation of risk parameters in bone regeneration using a customized titanium mesh: Results of a clinical study. *Implant Dent.* 28, 543–550. Publish Ahead of Print. doi:10.1097/ID.0000000000000933

Hartmann, A., and Seiler, M. (2020). Minimizing risk of customized titanium mesh exposures – A retrospective analysis. *BMC Oral Health* 20 (1), 36. doi:10.1186/s12903-020-1023-y

Hazeveld, A., Huddleston Slater, J. J. R., and Ren, Y. (2014). Accuracy and reproducibility of dental replica models reconstructed by different rapid prototyping techniques. *Am. J. Orthod. Dentofac.* 145 (1), 108–115. doi:10.1016/j.ajodo.2013.05.011

Henprasert, P., Dawson, D. V., El Kerdani, T., Song, X., Couso Queiruga, E., and Holloway, J. A. (2020). Comparison of the accuracy of implant position using surgical guides fabricated by additive and subtractive techniques. *J. Prosthodont.* 29 (6), 534–541. doi:10.1111/jopr.13161

Herschdorfer, L., Negreiros, W. M., Gallucci, G. O., and Hamilton, A. (2021). Comparison of the accuracy of implants placed with CAD-CAM surgical templates manufactured with various 3D printers: An *in vitro* study. *J. Prosthet. Dent.* 125 (6), 905–910. doi:10.1016/j.prosdent.2020.03.017

Huang, G., Wu, L., Hu, J., Zhou, X., He, F., Wan, L., et al. (2022). Main applications and recent research progresses of additive manufacturing in dentistry. *Biomed. Res. Int.* 2022, 1–26. doi:10.1155/2022/5530188

Huang, Y., Zhang, X., Gao, G., Yonezawa, T., and Cui, X. (2017). 3D bioprinting and the current applications in tissue engineering. *Biotechnol. J.* 12 (8), 1600734. doi:10.1002/biot.201600734

Jawahar, A., and Maragathavalli, G. (2019). Applications of 3D printing in dentistry – A review. *J. Pharm. Sci. Res.* 11 (5), 1670–1675.

Jung, G., Jeon, J., Hwang, K., and Park, C. (2014). Preliminary evaluation of a three-dimensional, customized, and preformed titanium mesh in peri-implant alveolar bone regeneration. *J. Korean Assoc. Oral Maxillofac. Surg.* 40 (4), 181. doi:10.5125/jkaoms.2014.40.4.181

Jung, H., Jang, T., Lee, J. E., Park, S. J., Son, Y., and Park, S. (2019). Enhanced bioactivity of titanium-coated polyetheretherketone implants created by a high-temperature 3D printing process. *Biofabrication* 11 (4), 045014. doi:10.1088/1758-5090/ab376b

Kapos, T., and Evans, C. (2014). CAD/CAM technology for implant abutments, crowns, and superstructures. *Int. J. oral Maxillofac. implants* 29, 117–136. doi:10.11607/jomi.2014suppl.g2.3

Kessler, A., Hickel, R., and Reymus, M. (2020). 3D printing in dentistry—State of the art. *Oper. Dent.* 45 (1), 30–40. doi:10.2341/18-229-L

Khorsandi, D., Fahimipour, A., Abasian, P., Saber, S. S., Seyedi, M., Ghanavati, S., et al. (2021). 3D and 4D printing in dentistry and maxillofacial surgery: Printing techniques, materials, and applications. *Acta Biomater.* 122, 26–49. doi:10.1016/j.actbio.2020.12.044

Kim, J. E., Kwon, D. H., Kim, J. H., and Shim, J. S. (2019a). A digital implant custom tray fabrication method using the design process for simulating the position of the impression copings and 3D printing technology. *J. Prosthet. Dent.* 121 (4), 566–570. doi:10.1016/j.prosdent.2018.07.005

Kim, J. E., Park, J. H., Kim, J. H., and Shim, J. S. (2019b). Computer-based implant planning involving a prefabricated custom tray with alumina landmark structures. *J. Prosthet. Dent.* 121 (3), 373–377. doi:10.1016/j.prosdent.2018.06.002

Kim, S., Shin, Y., Jung, H., Hwang, C., Baik, H., and Cha, J. (2018). Precision and trueness of dental models manufactured with different 3-dimensional printing techniques. *Am. J. Orthod. Dentofac.* 153 (1), 144–153. doi:10.1016/j.ajodo.2017.05.025

Kirschner, A., David, S., Brunello, G., Keilig, L., Drescher, D., Bourauel, C., et al. (2022). Impact of steam autoclaving on the mechanical properties of 3D-Printed resins used for insertion guides in orthodontics and implant dentistry. *Appl. Sci.* 12 (12), 6195. doi:10.3390/app12126195

Koch, G. K., James, B., Gallucci, G. O., and Hamilton, A. (2019). Surgical template fabrication using Cost-Effective 3D printers. *Int. J. Prosthodont.* 32 (1), 97–100. doi:10.11607/ijp.5975

Li, L., Wang, C., Li, X., Fu, G., Chen, D., and Huang, Y. (2021). Research on the dimensional accuracy of customized bone augmentation combined with3D -printing individualized titanium mesh: A retrospective case series study. *Clin. Implant Dent. R.* 23 (1), 5–18. doi:10.1111/cid.12966

Li, S., Zhang, T., Zhou, M., Zhang, X., Gao, Y., and Cai, X. (2021). A novel digital and visualized guided bone regeneration procedure and digital precise bone augmentation: A case series. *Clin. Implant Dent. R.* 23 (1), 19–30. doi:10.1111/cid.12959

Lin, L., Fang, Y., Liao, Y., Chen, G., Gao, C., and Zhu, P. (2019). 3D printing and digital processing techniques in dentistry: A review of literature. *Adv. Eng. Mat.* 21 (6), 1801013. doi:10.1002/adem.201801013

Liu, Y., Bai, W., Cheng, X., Tian, J., Wei, D., Sun, Y., et al. (2021). Effects of printing layer thickness on mechanical properties of 3D-printed custom trays. *J. Prosthet. Dent.* 126 (5), 671.e1–671.e7. doi:10.1016/j.prosdent.2020.08.025

Liu, Y., Di, P., Zhao, Y., Hao, Q., Tian, J., and Cui, H. (2019). Accuracy of multi-implant impressions using 3D-printing custom trays and splinting versus conventional techniques for complete arches. *Int. J. Oral Maxillofac. Implants* 34 (4), 1007–1014. doi:10.11607/jomi.7049

Lou, F., Rao, P., Zhang, M., Luo, S., Lu, S., and Xiao, J. (2021). Accuracy evaluation of partially guided and fully guided templates applied to implant surgery of anterior teeth: A randomized controlled trial. *Clin. Implant Dent. R.* 23 (1), 117–130. doi:10.1111/cid.12980

Mangano, C., Mangano, F. G., Shibli, J. A., Ricci, M., Perrotti, V., D'Avila, S., et al. (2012a). Immediate loading of mandibular overdentures supported by unsplinted direct laser Metal-Forming implants: Results from a 1-Year prospective study. *J. Periodontol.* 83 (1), 70–78. doi:10.1902/jop.2011.110079

Mangano, C., Mangano, F., Shibli, J. A., Luongo, G., De Franco, M., Briguglio, F., et al. (2012b). Prospective clinical evaluation of 201 direct laser metal forming implants: Results from a 1-year multicenter study. *Laser. Med. Sci.* 27 (1), 181–189. doi:10.1007/s10103-011-0904-3

Mangano, F., Chambrone, L., van Noort, R., Miller, C., Hatton, P., and Mangano, C. (2014a2014). Direct metal laser sintering titanium dental implants: A review of the current literature. *Int. J. Biomaterials* 2014, 1–11. doi:10.1155/2014/461534

Mangano, F. G., Caprioglio, A., Levrini, L., Farronato, D., Zecca, P. A., and Mangano, C. (2015). Immediate loading of mandibular overdentures supported by one-piece, direct metal laser sintering mini-implants: A short-term prospective clinical study. *J. Periodontol.* 86 (2), 192–200. doi:10.1902/jop.2014.140343

Mangano, F. G., De Franco, M., Caprioglio, A., Macchi, A., Piattelli, A., and Mangano, C. (2013a). Immediate, non-submerged, root-analogue direct laser metal sintering (dlms) implants: A 1-year prospective study on 15 patients. *Laser. Med. Sci.* 29, 1321–1328. doi:10.1007/s10103-013-1299-0

Mangano, F., Hauschild, U., and Admakin, O. (2018). Full in-office guided surgery with open selective tooth-supported templates: A prospective clinical study on 20 patients. *Int. J. Env. Res. Pub. He.* 15 (11), 2361. doi:10.3390/ijerph15112361

Mangano, F., Luongo, F., Shibli, J. A., Anil, S., and Mangano, C. (2014b). Maxillary overdentures supported by four splinted direct metal laser sintering implants: A 3-year prospective clinical study. *Int. J. Dent.* 2014, 1–9. doi:10.1155/2014/252343

Mangano, F., Pozzi-Taubert, S., Zecca, P. A., Luongo, G., Sammons, R. L., and Mangano, C. (2013b). Immediate restoration of fixed partial prostheses supported by One-Piece Narrow-Diameter selective laser sintering implants. *Implant Dent.* 22 (4), 388–393. doi:10.1097/ID.0b013e31829afa9d

Manzano Romero, P., Vellone, V., Maffia, F., and Cicero, G. (2021). Customized surgical protocols for guided bone regeneration using 3D printing technology: A retrospective clinical trial. *J. Craniofac. Surg.* 32 (2), e198–e202. doi:10.1097/SCS.0000000000007081

Marei, H. F., Alshaia, A., Alarifi, S., Almasoud, N., and Abdelhady, A. (2019). Effect of steam heat sterilization on the accuracy of 3D printed surgical guides. *Implant Dent.* 28 (4), 372–377. doi:10.1097/ID.0000000000000908

Maria, R., Tan, M. Y., Wong, K. M., Lee, B. C. H., Chia, V. A. P., and Tan, K. B. C. (2021). Accuracy of implant analogs in 3D printed resin models. *J. Prosthodont.* 30 (1), 57–64. doi:10.1111/jopr.13217

Michelinakis, G., Apostolakis, D., Kamposiora, P., Papavasiliou, G., and Özcan, M. (2021). The direct digital workflow in fixed implant prosthodontics: A narrative review. *BMC Oral Health* 21 (1), 37. doi:10.1186/s12903-021-01398-2

Moby, V., Dupagne, L., Fouquet, V., Attal, J., François, P., and Dursun, E. (2022). Mechanical properties of fused deposition modeling of polyetheretherketone (PEEK) and interest for dental restorations: A systematic review. *Materials* 15 (19), 6801. doi:10.3390/ma15196801

Moin, D. A., Hassan, B., Mercelis, P., and Wismeijer, D. (2013). Designing a novel dental root analogue implant using cone beam computed tomography and CAD/CAM technology. *Clin. Oral Implan. Res.* 24, 25–27. doi:10.1111/j.1600-0501.2011.02359.x

Monaco, C., Scheda, L., Ciocca, L., and Zucchelli, G. (2018). The prototype concept in a full digital implant workflow. *J. Am. Dent. Assoc.* 149 (10), 918–923. doi:10.1016/j.adaj.2018.04.026

Mukai, S., Mukai, E., Santos-Junior, J. A., Shibli, J. A., Faveri, M., and Giro, G. (2021). Assessment of the reproducibility and precision of milling and 3D printing surgical guides. *BMC Oral Health* 21 (1), 1. doi:10.1186/s12903-020-01362-6

Najeeb, S., Zafar, M. S., Khurshid, Z., and Siddiqui, F. (2016). Applications of polyetheretherketone (PEEK) in oral implantology and prosthodontics. *J. Prosthodont. Res.* 60 (1), 12–19. doi:10.1016/j.jpor.2015.10.001

Nikoyan, L., and Patel, R. (2020). Intraoral scanner, Three-Dimensional imaging, and Three-Dimensional printing in the dental office. *Dent. Clin. N. Am.* 64 (2), 365–378. doi:10.1016/j.cden.2019.12.004

Oberoi, G., Nitsch, S., Edelmayer, M., Janjić, K., Müller, A. S., and Agis, H. (2018). 3D printing—Encompassing the facets of dentistry. *Front. Bioeng. Biotechnol.* 6, 172. doi:10.3389/fbioe.2018.00172

Olea Vielba, M., Jareño García, D., Methani, M. M., Martinez Klemm, I., and Revilla León, M. (2020). Accuracy of the implant replica positions on the complete edentulous additive manufactured cast. *J. Prosthodont.* 29 (9), 780–786. doi:10.1111/jopr.13179

Oliveira, T. T., and Reis, A. C. (2019). Fabrication of dental implants by the additive manufacturing method: A systematic review. *J. Prosthet. Dent.* 122 (3), 270–274. doi:10.1016/j.prosdent.2019.01.018

Otawa, N., Sumida, T., Kitagaki, H., Sasaki, K., Fujibayashi, S., Takemoto, M., et al. (2015). Custom-made titanium devices as membranes for bone augmentation in implant treatment: Modeling accuracy of titanium products constructed with selective laser melting. *J. Craniomaxillofac Surg.* 43 (7), 1289–1295. doi:10.1016/j.jcms.2015.05.006

Pagac, M., Hajnys, J., Ma, Q., Jancar, L., Jansa, J., Stefek, P., et al. (2021). A review of vat photopolymerization technology: Materials, applications, challenges, and future trends of 3D printing. *Polymers-Basel.* 13 (4), 598. doi:10.3390/polym13040598

Pan, Y., Tu, Y., Wang, T., Liang, J., and Lin, H. (2022). Clinical study of precision analysis and deviation control of a domestic guide plate-assisted edentulous implant surgery. *J. Stomatol. Oral Maxillofac. Surg.* 2022, 101328. doi:10.1016/j.jormas.2022.11.004

Panayotov, I. V., Orti, V., Cuisinier, F., and Yachouh, J. (2016). Polyetheretherketone (PEEK) for medical applications. *J. Mater. Sci. Mater. Med.* 27 (7), 118. doi:10.1007/s10856-016-5731-4

Papaspyridakos, P., Chen, Y. W., Alshawaf, B., Kang, K., Finkelman, M., Chronopoulos, V., et al. (2020). Digital workflow: *In vitro* accuracy of 3D printed casts generated from complete-arch digital implant scans. *J. Prosthet. Dent.* 124 (5), 589–593. doi:10.1016/j.prosdent.2019.10.029

Park, J. M., Jeon, J., Koak, J. Y., Kim, S. K., and Heo, S. J. (2021). Dimensional accuracy and surface characteristics of 3D-printed dental casts. *J. Prosthet. Dent.* 126 (3), 427–437. doi:10.1016/j.prosdent.2020.07.008

Patpatiya, P., Chaudhary, K., Shastri, A., and Sharma, S. (2022). A review on polyjet 3D printing of polymers and multi-material structures. *Proc. Institution Mech. Eng. Part C J. Mech. Eng. Sci.* 236 (14), 7899–7926. doi:10.1177/09544062221079506

Pessoa, R., Siqueira, R., Li, J., Saleh, I., Meneghetti, P., Bezerra, F., et al. (2022). The impact of surgical guide fixation and implant location on accuracy of static computer-assisted implant surgery. *J. Prosthodont.* 31 (2), 155–164. doi:10.1111/jopr.13371

Petersmann, S., Spoerk, M., Van De Steene, W., Üçal, M., Wiener, J., Pinter, G., et al. (2020). Mechanical properties of polymeric implant materials produced by extrusion-based additive manufacturing. *J. Mech. Behav. Biomed.* 104, 103611. doi:10.1016/j.jmbbm.2019.103611

Petrick, I. J., and Simpson, T. W. (2015). 3D printing disrupts manufacturing: How economies of one create new rules of competition. *Res. Technol. Manage.* 56 (6), 12–16. doi:10.5437/08956308X5606193

Piedra, C. W., and Revilla-Leon, M. (2018). Digital workflow for the design and additively manufacture of a splinted framework and custom tray for the impression of multiple implants: A dental technique. *J. Prosthet. Dent.* 120 (6), 805–811. doi:10.1016/j.prosdent.2018.02.003

Pieralli, S., Spies, B. C., Hromadnik, V., Nicic, R., Beuer, F., and Wesemann, C. (2020). How accurate is oral implant installation using surgical guides printed from a degradable and Steam-Sterilized biopolymer? *J. Clin. Med.* 9 (8), 2322. doi:10.3390/jcm9082322

Pillai, S., Upadhyay, A., Khayambashi, P., Farooq, I., Sabri, H., Tarar, M., et al. (2021). Dental 3D-printing: Transferring art from the laboratories to the clinics. *Polymers-Basel* 13 (1), 157. doi:10.3390/polym13010157

Prechtel, A., Reymus, M., Edelhoff, D., Hickel, R., and Stawarczyk, B. (2020). Comparison of various 3D printed and milled PAEK materials: Effect of printing direction and artificial aging on Martens parameters. *Dent. Mat.* 36 (2), 197–209. doi:10.1016/j.dental.2019.11.017

Putra, R. H., Yoda, N., Astuti, E. R., and Sasaki, K. (2022). The accuracy of implant placement with computer-guided surgery in partially edentulous patients and possible influencing factors: A systematic review and meta-analysis. *J. Prosthodont. Res.* 66 (1), 29–39. doi:10.2186/jpr.JPR_D_20_00184

Raheem, A. A., Hameed, P., Whenish, R., Elsen, R. S., Aswin, G., Jaiswal, A. K., et al. (2021). A review on development of bio-inspired implants using 3D printing. *Biomimetics* 6 (4), 65. doi:10.3390/biomimetics6040065

Revilla-Leon, M., Ceballos, L., Martinez-Klemm, I., and Ozcan, M. (2018a). Discrepancy of complete-arch titanium frameworks manufactured using selective laser melting and electron beam melting additive manufacturing technologies. *J. Prosthet. Dent.* 120 (6), 942–947. doi:10.1016/j.prosdent.2018.02.010

Revilla-Leon, M., Ceballos, L., and Ozcan, M. (2019a). Implant-prosthodontic discrepancy of complete-arch cobalt-chromium implant frameworks manufactured through selective laser melting additive manufacturing technology using a coordinate measuring machine. *Int. J. Oral Maxillofac. Implants* 34 (3), 698–707. doi:10.11607/jomi.6739

Revilla-Leon, M., Gonzalez-Martin, O., Perez, L. J., Sanchez-Rubio, J. L., and Ozcan, M. (2018b). Position accuracy of implant analogs on 3D printed polymer versus conventional dental stone casts measured using a coordinate measuring machine. *J. Prosthodont.* 27 (6), 560–567. doi:10.1111/jopr.12708

Revilla-Leon, M., Meyer, M. J., and Ozcan, M. (2019b). Metal additive manufacturing technologies: Literature review of current status and prosthodontic applications. *Int. J. Comput. Dent.* 22 (1), 55–67.

Revilla-León, M., and Özcan, M. (2017). Additive manufacturing technologies used for 3D metal printing in dentistry. *Curr. Oral Health Rep.* 4 (3), 201–208. doi:10.1007/s40496-017-0152-0

Revilla-Leon, M., and Ozcan, M. (2019). Additive manufacturing technologies used for processing polymers: Current status and potential application in prosthetic dentistry. *J. Prosthodont.* 28 (2), 146–158. doi:10.1111/jopr.12801

Revilla-León, M., Sadeghpour, M., and Özcan, M. (2020). An update on applications of 3D printing technologies used for processing polymers used in implant dentistry. *Odontology* 108 (3), 331–338. doi:10.1007/s10266-019-00441-7

Revilla-Leon, M., Sanchez-Rubio, J. L., Oteo-Calatayud, J., and Ozcan, M. (2017). Impression technique for a complete-arch prosthesis with multiple implants using additive manufacturing technologies. *J. Prosthet. Dent.* 117 (6), 714–720. doi:10.1016/j.prosdent.2016.08.036

Revilla-Leon, M., Sanchez-Rubio, J. L., Perez-Lopez, J., Rubenstein, J., and Ozcan, M. (2021). Discrepancy at the implant abutment-prosthesis interface of complete-arch cobalt-chromium implant frameworks fabricated by additive and subtractive technologies before and after ceramic veneering. *J. Prosthet. Dent.* 125 (5), 795–803. doi:10.1016/j.prosdent.2020.03.018

Rouzé L'Alzit, F., Cade, R., Naveau, A., Babilotte, J., Meglioli, M., and Catros, S. (2022). Accuracy of commercial 3D printers for the fabrication of surgical guides in dental implantology. *J. Dent.* 117, 103909. doi:10.1016/j.jdent.2021.103909

Rubayo, D. D., Phasuk, K., Vickery, J. M., Morton, D., and Lin, W. S. (2021). Influences of build angle on the accuracy, printing time, and material consumption of additively manufactured surgical templates. *J. Prosthet. Dent.* 126 (5), 658–663. doi:10.1016/j.prosdent.2020.09.012

Rungrojwittayakul, O., Kan, J. Y., Shiozaki, K., Swamidass, R. S., Goodacre, B. J., Goodacre, C. J., et al. (2020). Accuracy of 3D printed models created by two technologies of printers with different designs of model base. *J. Prosthodont.* 29 (2), 124–128. doi:10.1111/jopr.13107

Sagheb, K., Schiegnitz, E., Moergel, M., Walter, C., Al-Nawas, B., and Wagner, W. (2017). Clinical outcome of alveolar ridge augmentation with individualized CAD-CAM-produced titanium mesh. *Int. J. Implant Dent.* 3 (1), 36. doi:10.1186/s40729-017-0097-z

Salmi, M. (2021). Additive manufacturing processes in medical applications. *Materials* 14 (1), 191. doi:10.3390/ma14010191

Schmidt, M., Pohle, D., and Rechtenwald, T. (2007). Selective laser sintering of PEEK. *CIRP Ann.* 56 (1), 205–208. doi:10.1016/j.cirp.2007.05.097

Schweiger, J., Edelhoff, D., and Güth, J. (2021). 3D printing in digital prosthetic dentistry: An overview of recent developments in additive manufacturing. *J. Clin. Med.* 10 (9), 2010. doi:10.3390/jcm10092010

Sedov, Y. G., Avanesov, A. M., Saleev, R. A., Saleeva, G. T., and Yarulina, Z. I. (2021). A classification of surgical guides application for dental implantation. *Stomatologiya* 100 (1), 84. doi:10.17116/stomat202110001184

Seiler, M., Kammerer, P. W., Peetz, M., and Hartmann, A. (2018). Customized lattice structure in reconstruction of three-dimensional alveolar defects. *Int. J. Comput. Dent.* 21 (3), 261–267.

Shilov, S. Y., Rozhkova, Y. A., Markova, L. N., Tashkinov, M. A., Vindokurov, I. V., and Silberschmidt, V. V. (2022). Biocompatibility of 3D-Printed PLA, PEEK and PETG: Adhesion of bone marrow and peritoneal lavage cells. *Polymers-Basel* 14 (19), 3958. doi:10.3390/polym14193958

Shishkovsky, I., Volchkov, S., Veiko, V. P., and Vartanyan, T. A. (2013). "Influence of the laser assisted fabricated 3D porous scaffolds from bioceramoplasts of micron and nano sizes on culture of MMSC," in Proc. SPIE 9065, Fundamentals of Laser-Assisted Micro- and Nanotechnologies 2013, St. Petersburg. Russia, June 24-28. 2013. Paper presented at the.

Sing, S. L., An, J., Yeong, W. Y., and Wiria, F. E. (2016). Laser and electron-beam powder-bed additive manufacturing of metallic implants: A review on processes, materials and designs. *J. Orthop. Res.* 34 (3), 369–385. doi:10.1002/jor.23075

Sommacal, B., Savic, M., Filippi, A., Kühl, S., and Thieringer, F. M. (2018). Evaluation of two 3D printers for guided implant surgery. *Int. J. oral Maxillofac. implants* 33 (4), 743–746. doi:10.11607/jomi.6074

Son, K., Lee, J., and Lee, K. (2021). Comparison of intaglio surface trueness of interim dental crowns fabricated with SLA 3D printing, DLP 3D printing, and milling technologies. *Healthcare* 9 (8), 983. doi:10.3390/healthcare9080983

Sonaye, S. Y., Bokam, V. K., Saini, A., Nayak, V. V., Witek, L., Coelho, P. G., et al. (2022). Patient-specific 3D printed Poly-ether-ether-ketone (PEEK) dental implant system. *J. Mech. Behav. Biomed.* 136, 105510. doi:10.1016/j.jmbbm.2022.105510

Su, Y., He, J., Jiang, N., Zhang, H., Wang, L., Liu, X., et al. (2020). Additively-manufactured poly-ether-ether-ketone (PEEK) lattice scaffolds with uniform microporous architectures for enhanced cellular response and soft tissue adhesion. *Mater. Des.* 191, 108671. doi:10.1016/j.matdes.2020.108671

Sumida, T., Otawa, N., Kamata, Y. U., Kamakura, S., Mtsushita, T., Kitagaki, H., et al. (2015). Custom-made titanium devices as membranes for bone augmentation in implant treatment: Clinical application and the comparison with conventional titanium mesh. *J. Cranio Maxill. Surg.* 43 (10), 2183–2188. doi:10.1016/j.jcms.2015.10.020

Sun, C., Kang, J., Yang, C., Zheng, J., Su, Y., Dong, E., et al. (2022). Additive manufactured polyether-ether-ketone implants for orthopaedic applications: A narrative review. *Biomater. Transl.* 3 (2), 116–133. doi:10.12336/biomatertransl.2022.02.001

Sun, Y., Chen, H., Li, H., Deng, K., Zhao, T., Wang, Y., et al. (2017). Clinical evaluation of final impressions from three-dimensional printed custom trays. *Sci. Rep.-UK* 7 (1), 14958. doi:10.1038/s41598-017-14005-8

Sun, Y., Ding, Q., Tang, L., Zhang, L., Sun, Y. C., and Xie, Q. F. (2019). Accuracy of a chairside fused deposition modeling 3D-printed single-tooth surgical template for implant placement: An *in vitro* comparison with a light cured template. *J. Cranio Maxill. Surg.* 47 (8), 1216–1221. doi:10.1016/j.jcms.2019.03.019

Sun, Y., Ding, Q., Yuan, F., Zhang, L., Sun, Y., and Xie, Q. (2022). Accuracy of a chairside, fused deposition modeling three-dimensional-printed, single tooth surgical guide for implant placement: A randomized controlled clinical trial. *Clin. Oral Implan. Res.* 33 (10), 1000–1009. doi:10.1111/clr.13981

Svanborg, P., Eliasson, A., Stenport, V., Sahlgrenska, A., Göteborgs, U., Gothenburg, U., et al. (2018). Additively manufactured titanium and Cobalt-Chromium implant frameworks: Fit and effect of ceramic veneering. *Int. J. oral Maxillofac. implants* 33 (3), 590–596. doi:10.11607/jomi.6028

Tahir, N., and Abduo, J. (2022). An *in vitro* evaluation of the effect of 3D printing orientation on the accuracy of implant surgical templates fabricated by desktop printer. *J. Prosthodont.* 31, 791–798. doi:10.1111/jopr.13485

Tappa, K., and Jammalamadaka, U. (2018). Novel biomaterials used in medical 3D printing techniques. *J. Funct. Biomaterials* 9 (1), 17. doi:10.3390/jfb9010017

Taymour, N., Fahmy, A. E., Gepreel, M. A. H., Kandil, S., and El-Fattah, A. A. (2022). Improved mechanical properties and bioactivity of silicate based bioceramics reinforced poly(ether-ether-ketone) nanocomposites for prosthetic dental implantology. *Polymers-Basel.* 14 (8), 1632. doi:10.3390/polym14081632

Thakur, J., Parlani, S., Shivakumar, S., and Jajoo, K. (2021). Accuracy of marginal fit of an implant-supported framework fabricated by 3D printing versus subtractive manufacturing technique: A systematic review and meta-analysis. *J. Prosthet. Dent.* [Epub ahead of print]. doi:10.1016/j.prosdent.2021.05.010

Tian, Y., Chen, C., Xu, X., Wang, J., Hou, X., Li, K., et al. (2021). A review of 3D printing in dentistry: Technologies, affecting factors, and applications. *Scanning* 2021, 1–19. doi:10.1155/2021/9950131

Torabi, K., Farjood, E., and Hamedani, S. (2015). Rapid prototyping technologies and their applications in prosthodontics, a review of literature. *J. Dent. (Shiraz).* 16 (1), 1–9.

Torstrick, F. B., Lin, A. S. P., Potter, D., Safranski, D. L., Sulchek, T. A., Gall, K., et al. (2018). Porous PEEK improves the bone-implant interface compared to plasma-sprayed titanium coating on PEEK. *Biomaterials* 185, 106–116. doi:10.1016/j.biomaterials.2018.09.009

Tunchel, S., Blay, A., Kolerman, R., Mijiritsky, E., and Shibli, J. A. (2016). 3D printing/additive manufacturing single titanium dental implants: A prospective multicenter study with 3 years of follow-up. *Int. J. Dent.* 2016, 1–9. doi:10.1155/2016/8590971

Turkyilmaz, I., and Wilkins, G. N. (2021). 3D printing in dentistry – exploring the new horizons. *J. Dent. Sci.* 16 (3), 1037–1038. doi:10.1016/j.jds.2021.04.004

Unsal, G., Turkyilmaz, I., and Lakhia, S. (2020). Advantages and limitations of implant surgery with CAD/CAM surgical guides: A literature review. *J. Clin. Exp. Dent.* 12, e409–e417. doi:10.4317/jced.55871

Velasquez-Garcia, L. F., and Kornbluth, Y. (2021). Biomedical applications of metal 3D printing. *Annu. Rev. Biomed. Eng.* 23, 307–338. doi:10.1146/annurev-bioeng-082020-032402

Wally, Z. J., Haque, A. M., Feteira, A., Claeyssens, F., Goodall, R., and Reilly, G. C. (2019). Selective laser melting processed Ti6Al4V lattices with graded porosities for dental applications. *J. Mech. Behav. Biomed.* 90, 20–29. doi:10.1016/j.jmbbm.2018.08.047

Wegmüller, L., Halbeisen, F., Sharma, N., Kühl, S., and Thieringer, F. M. (2021). Consumer vs. High-end 3D printers for guided implant surgery—An *in vitro* accuracy assessment study of different 3D printing technologies. *J. Clin. Med.* 10 (21), 4894. doi:10.3390/jcm10214894

Westover, B. (2019). Three-Dimensional Custom-Root replicate tooth dental implants. *Oral Maxil. Surg. Clin.* 31 (3), 489–496. doi:10.1016/j.coms.2019.03.010

Xie, Y., Li, S., Zhang, T., Wang, C., and Cai, X. (2020). Titanium mesh for bone augmentation in oral implantology: Current application and progress. *Int. J. Oral Sci.* 12 (1), 37. doi:10.1038/s41368-020-00107-z

Xu, Y., Huettig, F., Schille, C., Schweizer, E., Geis-Gerstorfer, J., and Spintzyk, S. (2020). Peel bond strength between 3D printing tray materials and elastomeric impression/adhesive systems: A laboratory study. *Dent. Mat.* 36 (7), e241–e254. doi:10.1016/j.dental.2020.04.015

Yang, Z., Xu, Y., Sisson, R. D., and Liang, J. (2020). Factors influencing the corrosion behavior of direct metal laser sintered Ti-6Al-4V for biomedical applications. *J. Mat. Eng. Perform.* 29 (6), 3831–3839. doi:10.1007/s11665-020-04904-9

Yousef, H., Harris, B. T., Elathamna, E. N., Morton, D., and Lin, W. S. (2021). Effect of additive manufacturing process and storage condition on the dimensional accuracy and stability of 3D-printed dental casts. *J. Prosthet. Dent.* 128, 1041–1046. doi:10.1016/j.prosdent.2021.02.028

Yu, T., Gao, H., Liu, T., Huang, Y., and Wang, C. (2020). Effects of immediately static loading on osteointegration and osteogenesis around 3D-printed porous implant: A histological and biomechanical study. *Mater. Sci. Eng. C* 108, 110406. doi:10.1016/j.msec.2019.110406

Yuan, B., Cheng, Q., Zhao, R., Zhu, X., Yang, X., Yang, X., et al. (2018). Comparison of osteointegration property between PEKK and PEEK: Effects of surface structure and chemistry. *Biomaterials* 170, 116–126. doi:10.1016/j.biomaterials.2018.04.014

Zhang, C., Yuan, Y., and Chen, J. (2022). Material extrusion based fabrication of surgical implant template and accuracy analysis. *Materials* 15 (5), 1738. doi:10.3390/ma15051738

Zhang, F., Gao, X., Ye, Z. Y., Xu, D. Q., and Ding, X. (2020). The clinical accuracy of the implant digital surgical guide: A meta-analysis. *Am. J. Dent.* 33 (6), 296–304.

Zhou, L., Su, Y., Wang, J., Wang, J., Wang, X., and Liu, Q. (2021). Effect of exposure rates with customized versus conventional titanium mesh on guided bone regeneration: Systematic review and meta-analysis. *J. Oral Implantol.* 48, 339–346. doi:10.1563/aaid-joi-D-20-00200

Zhou, W., Liu, Z., Song, L., Kuo, C. L., and Shafer, D. M. (2018). Clinical factors affecting the accuracy of guided implant Surgery-A systematic review and meta-analysis. *J. Evid. Based Dent. Pract.* 18 (1), 28–40. doi:10.1016/j.jebdp.2017.07.007

Zhu, F., Mao, M., Zhu, H., Chen, Y., You, J., and Pan, H. (2021). Comparison of positioning accuracy between 2 different implant systems using mucosa-supported surgical templates: A retrospective clinical study. *J. oral Implant.* 48, 15–20. doi:10.1563/aaid-joi-D-19-00283

frontiers | Frontiers in Bioengineering and Biotechnology

TYPE Original Research
PUBLISHED 24 January 2023
DOI 10.3389/fbioe.2023.1105248

OPEN ACCESS

EDITED BY
Jianyun Zhang,
Peking University Hospital of Stomatology, China

REVIEWED BY
Dejian Li,
Fudan University Pudong Medical Center, China
Xian Liu,
Sichuan University, China

*CORRESPONDENCE
Zhiyu Chen,
kqxfchen@163.com

SPECIALTY SECTION
This article was submitted to Biomaterials, a section of the journal Frontiers in Bioengineering and Biotechnology

RECEIVED 22 November 2022
ACCEPTED 13 January 2023
PUBLISHED 24 January 2023

CITATION
Li S, Xiaowen Y, Yang Y, Liu L, Sun Y, Liu Y, Yin L and Chen Z (2023), Osteogenic and anti-inflammatory effect of the multifunctional bionic hydrogel scaffold loaded with aspirin and nano-hydroxyapatite.
Front. Bioeng. Biotechnol. 11:1105248.
doi: 10.3389/fbioe.2023.1105248

Osteogenic and anti-inflammatory effect of the multifunctional bionic hydrogel scaffold loaded with aspirin and nano-hydroxyapatite

Shaoping Li[1], Yundeng Xiaowen[1], Yuqing Yang[1], Libo Liu[2], Yifan Sun[2], Ying Liu[2], Lulu Yin[2] and Zhiyu Chen[1]*

[1]Key Laboratory of Stomatology in Hebei Province, Hospital of Stomatology Hebei Medical University, Shijiazhuang, China, [2]College of Dentistry, Hebei Medical University, Shijiazhuang, China

Although tissue engineering offered new approaches to repair bone defects, it remains a great challenge to create a bone-friendly microenvironment and rebuild bone tissue rapidly by a scaffold with a bionic structure. In this study, a multifunctional structurally optimized hydrogel scaffold was designed by integrating polyvinyl alcohol (PVA), gelatin (Gel), and sodium alginate (SA) with aspirin (ASA) and nano-hydroxyapatite (nHAP). The fabrication procedure is through a dual-crosslinking process. The chemical constitution, crystal structure, microstructure, porosity, mechanical strength, swelling and degradation property, and drug-release behavior of the hydrogel scaffold were analyzed. Multi-hydrogen bonds, electrostatic interactions, and strong "egg-shell" structure contributed to the multi-network microstructure, bone tissue-matched properties, and desirable drug-release function of the hydrogel scaffold. The excellent performance in improving cell viability, promoting cell osteogenic differentiation, and regulating the inflammatory microenvironment of the prepared hydrogel scaffold was verified using mouse pre-osteoblasts (MC3T3-E1) cells. And the synergistic osteogenic and anti-inflammatory functions of aspirin and nano-hydroxyapatite were also verified. This study provided valuable insights into the design, fabrication, and biological potential of multifunctional bone tissue engineering materials with the premise of constructing a bone-friendly microenvironment.

KEYWORDS

aspirin, multifunctional hydrogel scaffold, sustained release, tissue engineering, nano-hydroxyapatite

1 Introduction

The implant denture is a superior method to restore lost teeth, oral function, and aesthetics. In clinic, severe and large-sized jaw and alveolar bone defects are often secondary to trauma, periodontal disease, tumors, etc., (Esposito et al., 2006). Bone augmentation surgery is indispensable to ensure adequate and stable implant osseointegration in this situation (Schmitz and Hollinger, 1986; Hegde et al., 2016). In the bone tissue engineering field, increasing experimental evidence has confirmed that the application of bioactive synthetic materials is superior to several conventional methods (e.g autologous bone, allogeneic bone, and artificial bone meal filling), for eliminating the restraint of limited sources of donors, secondary trauma, pathogen transmission, and immune rejection (Li et al., 2018). Recent studies have reported that inflammatory and reconstructive microenvironment resulting from microtrauma and the body's physiological adaptation instincts can lead to the decline of osteoblast function

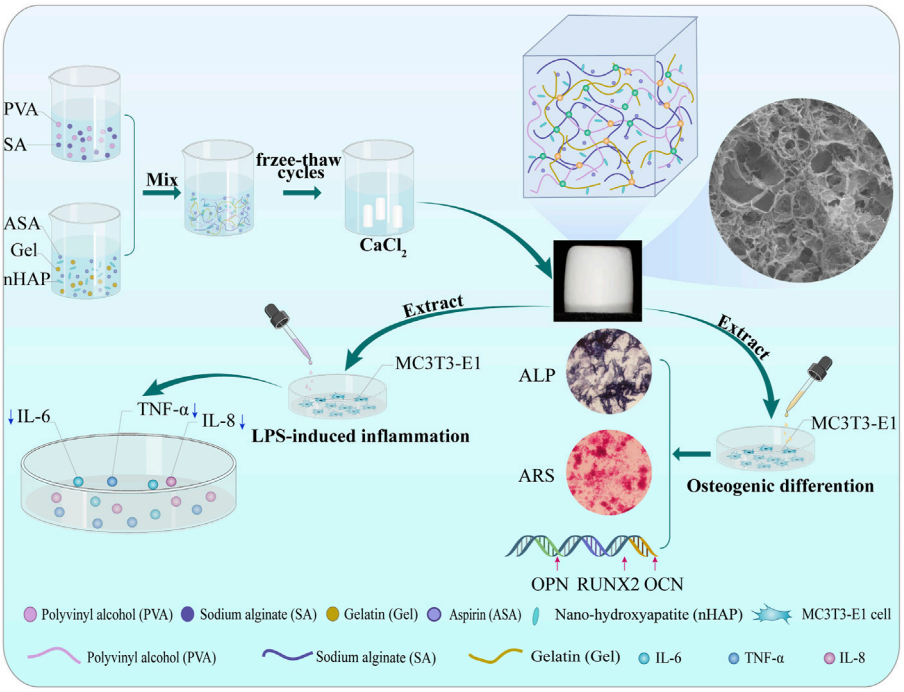

SCHEME 1
Schematic illustration of the procedures of the dual-crosslinking hydrogel scaffolds. Effects on MC3T3-E1 cells bioactivity, osteogenic differentiation, and anti-inflammatory capacity.

(Fasolino et al., 2019). Several studies have suggested that bone-friendly bioactive materials may accelerate bone regeneration, but it remains a challenge (Zhang et al., 2022). Hence, it is of great clinical and scientific value to develop a high-quality bone tissue engineering material that can outperform currently available protocols.

Hydrogels have been widely applied to facilitate functional and constructive tissue repair in many clinical applications. Invaluable qualities such as interconnected porous morphology and architecture similar to extracellular matrix (ECM), irreplaceable water retention capacity, drugs and growth factors delivery effect, and biodegradability enable hydrogel to adapt to specific physical and soft tissue regeneration environment (Han et al., 2021; Sreekumaran et al., 2021; Sun et al., 2022). Furthermore, some attention has been fortunately drawn to the roles of the non-steroidal anti-inflammatory drug (NSAIDs) of aspirin, since it is used to alleviate the inflammation and activate osteoblasts in the surgical site within the concentration range of 50–300 μg/mL (Fattahi et al., 2022). Studies have confirmed that an appropriate dose of aspirin can improve trabecular bone structure, bone mineral density, and bone mechanical strength (Tao et al., 2020). Low-dose aspirin can promote bone marrow mesenchymal stem cells to change into osteoblasts and accelerate bone regeneration (Xie et al., 2019). Previous literature has reported that local injection of aspirin also can reduce Interferon γ (IFN-γ) and tumor necrosis cytokines (TNF-α) in the bone defect area (Liu et al., 2018). However, to maintain effective concentration and efficacy in the defect area, systemic high doses drug application is inevitably required because of the short half-life of aspirin (Bliden et al., 2016; Tao et al., 2019), which may lead to adverse effects such as liver and kidney damage and gastrointestinal bleeding (CAVAGNI et al., 2016). It is a viable option that the application of hydrogel scaffolds as a platform to release aspirin. So far, many efforts have been taken to explore an ideal hydrogel for bone tissue engineering. Yet, the current structure and properties are still unsatisfactory, whether prepared by a single component or single cross-linking method.

Gelatin (Gel) is temperature-sensitive, and is a partial hydrolysis product of native collagen. Sodium alginate (SA) is a natural polysaccharide derived from brown seaweed that has been extensively applied in tissue engineering to deliver drugs and growth factors (Fang et al., 2022; Tan et al., 2022). Moreover, SA can be chemically cross-linked by Ca^{2+} (Wang et al., 2019). There is a strong electrostatic interaction between Gel and SA when they are mixed and cross-linked (Xu et al., 2019). Additionally, polyvinyl alcohol (PVA) stands out from synthetic organic compounds due to its excellent water solubility and stable chemical properties (Ahmed et al., 2021). Since there are a large number of free hydroxyl groups, the PVA is tightly connected through hydrogen bonds when treated by cyclic freeze-thaw (Ahmed et al., 2021).

To warrant optimal behavior, especially the mechanical strength and bone repair capacity, the desired quality of the bone tissue engineering scaffold involves adding inorganic bioceramic components (Patel et al., 2019). Nano-hydroxyapatite (nHAP) is a reasonable choice as it has similar chemical compositions to natural bone. And it is regarded as a promising material due to its outstanding osteoconductivity, osteoinductivity, drug-loading property, and suitable cell adhesion property (Raina et al., 2020; Jiang et al., 2021). Furthermore, the incorporation of hydroxyapatite nanoparticles into a hydrogel may also provide a possibility to

TABLE 1 Primer sequences of target genes for qRT-PCR.

Gene description	Forward primer	Reverse primer
GAPDH	GGTGAAGGTCGGTGTGAACG	CTCGCTCCTGGAAGATGGTG
RUNX2	GACTGTGGTTACCGTCATGGC	ACTTGGTTTTTCATAACAGCGGA
OPN	AGCAAGAAACTCTTCCAAGCAA	GTGAGATTCGTCAGATTCATCCG
OCN	CTGACCTCACAGATCCCAAGC	TGGTCTGATAGCTCGTCAAAG

overcome its disadvantages of high brittleness, morphological instability, and slow degradation (Pina et al., 2015; Chocholata et al., 2020), simultaneously, improving the mechanical strength and characterizations of the hydrogel (Wang et al., 2020; Karimipour-Fard et al., 2021). Yet, the impact of aspirin and nano-hydroxyapatite on hydrogel scaffolds, and whether they have a synergistic function, is still unclear.

This study proposed a novel strategy for preparing a multifunctional and highly biomimetic hydrogel scaffold. A hydrogel scaffold by a combination of PVA, SA, and Gel with the addition of aspirin and nano-hydroxyapatite was successfully constructed by cyclic freeze-thawing and soaking in calcium chloride ($CaCl_2$) solutions. This method is practical, economical, and efficient. Subsequently, the hydrogel scaffold was characterized by Fourier Transform Infrared Spectroscopy (FTIR), X-ray Diffraction (XRD), and Scanning Electron Microscope (SEM) to confirm the chemical constitution, crystal structure, and microstructure. The porosity, mechanical property, swelling, degradation and drug release behavior of the hydrogel scaffold were investigated *in vitro*. The biocompatibility such as cytotoxicity, cell proliferation, cell adhesion behavior, and the osteogenic differentiation ability of alkaline phosphatase (ALP) activity, the expression of calcium nodules and osteogenesis-related genes, as well as the anti-inflammatory effect of the prepared hydrogel scaffold was evaluated using mouse preosteoblasts (MC3T3-E1) cells (Scheme 1).

2 Materials and methods

2.1 Materials

Polyvinyl alcohol (PVA-124) was purchased from GHTECH (Guangdong, China). Aspirin (ASA), gelatin (Gel, type B), sodium alginate (SA), and anhydrous calcium chloride ($CaCl_2$) were obtained from Aladdin (Shanghai, China); nano-hydroxyapatite particle (nHAP, size = 20 nm) was purchased from EMPEROR NANO (Nanjing, China). Phosphate buffer (PBS) and penicillin and streptomycin mixture (100×) were acquired from Solarbio (Beijing, China); fetal bovine serum (FBS) and α-MEM medium were purchased from Biological Industries (Israel). ELISA kits were purchased from Inova (Wuhan, China). Other reagents and solvents were commercially obtained and used as received.

2.2 Preparation of the hydrogel scaffold

All solutions were prepared in ultrapure water. Briefly, 1 g of PVA powder was dissolved in 30 mL ultrapure water and constantly agitated at 95°C until completely dissolved to acquire PVA solution. To prepare the PVA-SA solution, when the PVA solution reached a temperature of 37°C, 1 g of SA powder was added and mixed. Meanwhile, 2 g of Gel, 200 μg of aspirin, and 5 g of nano-hydroxyapatite were mixed in 20 mL of ultrapure water to prepare Gel-ASA, Gel-nHAP, and Gel-ASA-nHAP solutions, respectively. Next, various solutions were thoroughly mixed. Air bubbles and the undissolved nano-hydroxyapatite in the hydrogel solutions were removed and shattered with an ultrasonic cleaner for 30 min. Each group of the hydrogel solutions was charged into moulds, frozen at −20°C for 18 h, and then thawed at room temperature for 4 h. The chemical cross-link was carried out after three freeze-thaw cycles, which involved submerging them in 2% $CaCl_2$ for 24 h. The hydrogel scaffolds were rinsed with ultrapure water for three times, irradiated, and sterilized at ^{60}Co to produce ASA/PVA/Gel/SA, nHAP/PVA/Gel/SA, and ASA-nHAP/PVA/Gel/SA hydrogel scaffolds, named ASA group, nHAP group, and ASA-nHAP group, respectively.

2.3 Chemical constitution and crystal structure

2.3.1 FTIR

An IS 50 Fourier Transform Infrared Spectroscopy (FTIR: Thermo, United States) with a resolution of 4 cm^{-1} was used to evaluate the chemical constitution and functional groups in the hydrogel scaffold. At room temperature, the raw materials and freeze-dried hydrogel scaffolds were pulverized and mixed completely with the proper amount of KBr, respectively, before being compacted into tablets. The data of the FTIR spectra were obtained in the range of 4,000–400 cm^{-1} with 32-times scan and then analyzed by Origin 2021 ware.

2.3.2 XRD

The hydrogel scaffolds were compressed as described in 2.3.1 and scanned using a Bruker D8 X-ray Diffractometer (XRD: Advance, Germany). A speed of 2°/min between 10° and 70° was set to acquire the data. The physical phase of the raw materials and hydrogel scaffolds were analyzed by X'Pert High Score software and Origin 2021 ware.

2.4 Microstructure

To observe the 3D porous structure of the hydrogel scaffolds, before gold-sputtered, the freeze-dried hydrogel scaffolds were cut in liquid nitrogen. The S-4800 Scanning Electron Microscope (SEM: Hitachi, Japan) was used to observe the microstructure of the hydrogel

10.3389/fbioe.2023.1105248

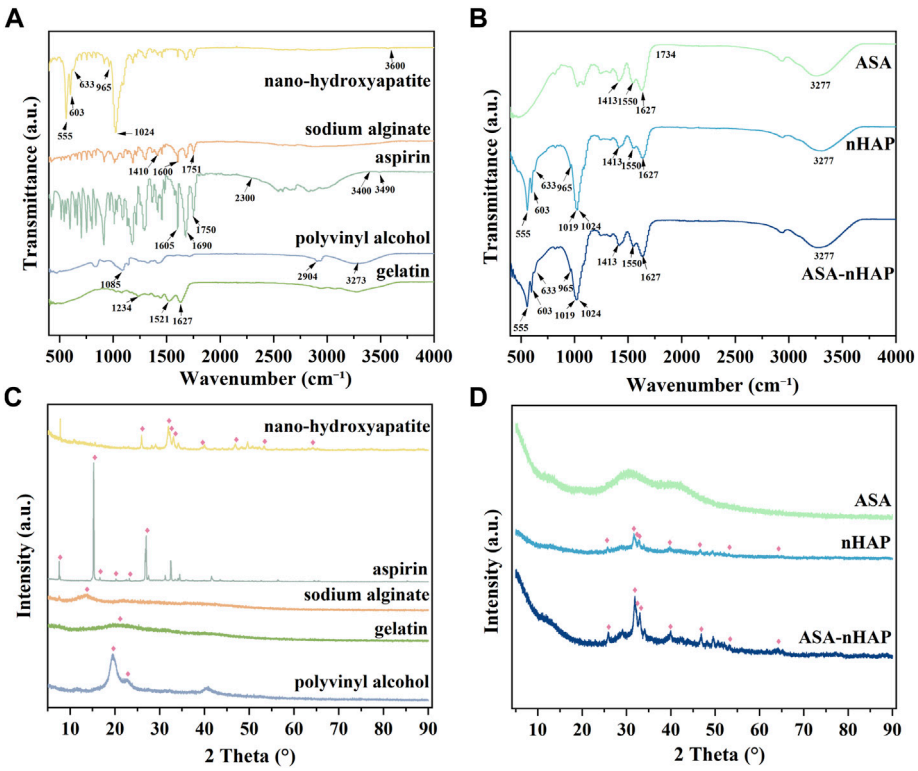

FIGURE 1
Chemical constitution and crystal structure analysis of the raw powders and the composited hydrogel scaffolds. **(A)** The FTIR spectra of nanohydroxyapatite, aspirin, sodium alginate (SA), gelatin (Gel), and polyvinyl alcohol (PVA). **(B)** The FTIR spectra of ASA/PVA/Gel/SA (ASA group), nHAP/PVA/Gel/SA (nHAP group), and ASA-nHAP/PVA/Gel/SA (ASA-nHAP group) hydrogel scaffold. **(C)** The XRD pattern of nanohydroxyapatite, aspirin, sodium alginate (SA), gelatin (Gel), and polyvinyl alcohol (PVA). **(D)** The XRD pattern of ASA/PVA/Gel/SA (ASA group), nHAP/PVA/Gel/SA (nHAP group), and ASA-nHAP/PVA/Gel/SA (ASA-nHAP group) hydrogel scaffold.

scaffolds. The imposed accelerating voltage was 15 kV, and the different pore sizes were analyzed.

2.5 Characterization of the hydrogel scaffold

2.5.1 Porosity

The porosity was calculated by the liquid displacement method. Briefly, the hydrogel scaffolds (15 mm in diameter, 2 mm in thickness, n = 3) were completely immersed in a volume V1 of anhydrous ethanol. After 48 h, the volume V2 was recorded when the hydrogel scaffolds should be completely immersed in anhydrous ethanol, and the liquid surface was free of air bubbles. Subsequently, the hydrogel scaffolds were removed, and the remaining anhydrous ethanol volume V3 was recorded. Porosity was calculated using the following formula: P (%) = (V1–V3)/(V2–V3) × 100%.

2.5.2 Mechanical property

The maximum compression strength and compression modulus of the hydrogel scaffolds (8 mm in diameter, 10 mm in height, n = 3) were tested by an RGM-2100 Universal Mechanical Testing Machine (Rigel, Guangzhou, China). The compression test was carried out with a 10 mm diameter flat probe at a speed of 5 mm/min. Compression tests were performed along the long axis of the hydrogel scaffolds at room temperature and 52% relative humidity. When the deformation reached 100%, the compression test was stopped. Then the stress-strain curve and the maximum compression strength were obtained. The compression modulus was calculated as the slope of the linear region of the stress-strain curve.

2.5.3 Swelling property

The swelling performance was examined by calculating the water absorption rate in PBS. Initially, the freeze-dried hydrogel scaffolds (15 mm in diameter, 2 mm in height, n = 3) were weighed of W0. Subsequently, the hydrogel scaffolds were immersed in 3 mL of PH = 7.4 PBS at 37°C. The hydrogel scaffolds were removed at different time points, and the surface water was gently wiped. And then they were weighed again of W1 until they reached swelling equilibrium. The swelling property was measured using the formula: swelling rate (%) = W1-W0/W0×100%.

2.5.4 *In vitro* degradation property

To study the *in vitro* degradation property, the freeze-dried hydrogel scaffolds (8 mm in diameter, 10 mm in height, n = 3) with the initial weight of W0 were immersed in 4 mL of PBS. Then, the hydrogel scaffolds were placed at 37°C. After 7, 14, 21, and 28 days, they were removed and weighted again of W1 after being freeze-dried. The PBS was changed every 2 days. The degradation rate

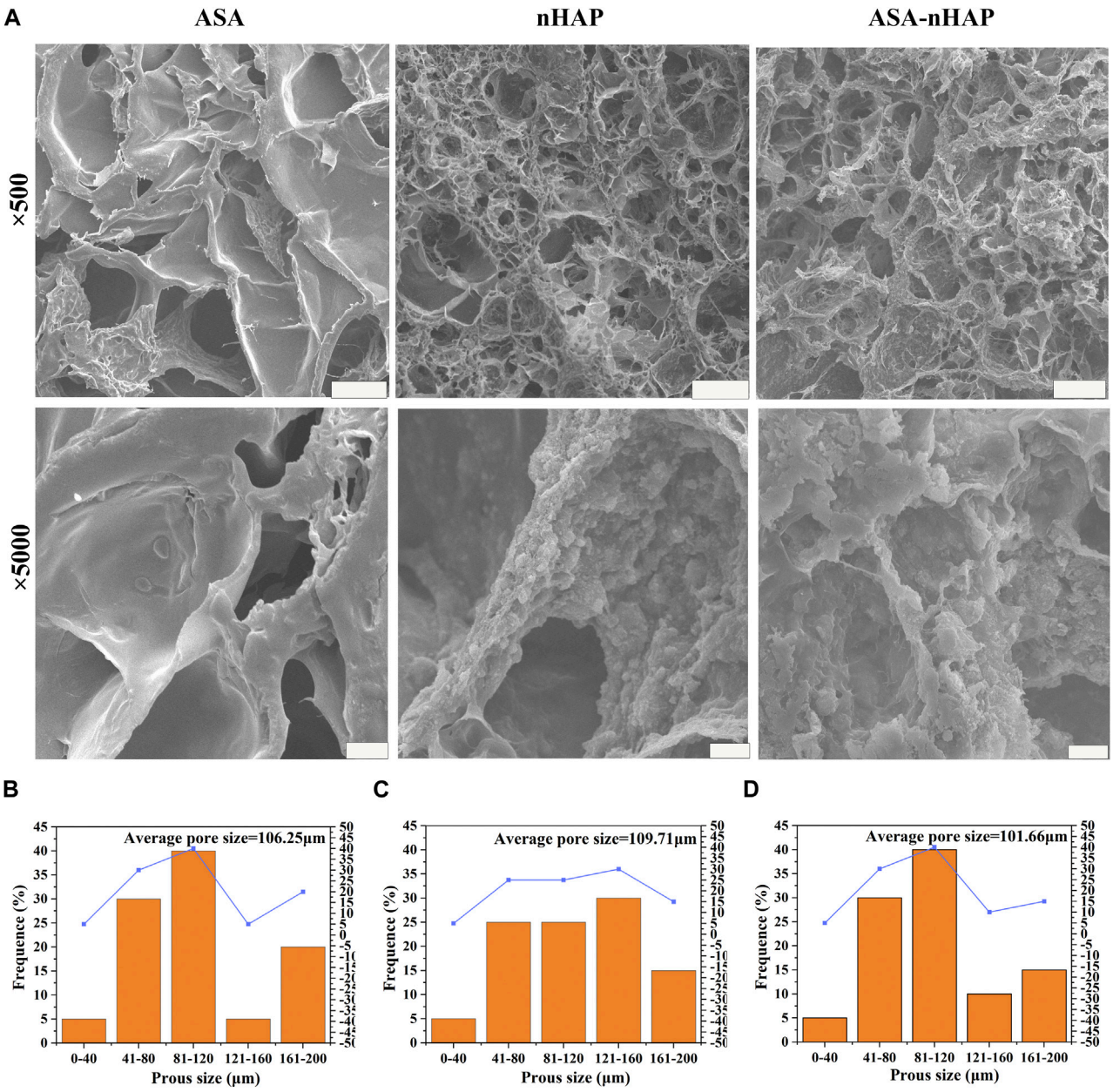

FIGURE 2
Microstructure of hydrogel scaffolds. **(A)** SEM images of the ASA group, nHAP group, and ASA-nHAP group. The scale bar for low-magnification images is 100 μm; the scale bar for high-magnification images is 10 μm. **(B–D)** Pore size distribution pattern of the ASA group, nHAP group, and ASA-nHAP group.

was evaluated by calculating its weight loss rate with the following formula: degradation rate (%) = (W0-W1)/W0×100%.

2.5.5 *In vitro* aspirin release property

The *in vitro* release of aspirin from the hydrogel scaffolds was estimated. Firstly, the absorbance of aspirin standard working solutions was measured at 274 nm using a TU-1950 Double-beam UV Spectrophotometer (Persee, Beijing, China) for 0, 12.5, 25, 50, 100, 200, and 400 (μg/mL). Next, the standard curve of aspirin was plotted, and the regression equation was calculated (Supplementary Figure S1). Subsequently, the hydrogel scaffolds (n = 3) were immersed in 10 mL of PBS at 37°C. Then, 3 mL of liquid was aspirated and centrifuged at corresponding time points respectively. Consequently, 2 mL of supernatant was used to measure the absorbance at 274 nm. Finally, it was replenished with fresh PBS to 10 mL. The cumulative release property of aspirin from the hydrogel scaffold was analyzed by Origin 2021 ware.

2.6 Cell growth study

The MC3T3-E1 cells obtained from puonuosai (Wuhan, China) were cultured with a complete medium (CM, containing 10% FBS, and 1% penicillin and streptomycin) in a humidified atmosphere containing at 37°C. All cells were cultured up to the third generation for the subsequent experiments. It was crucial to obtain extraction solutions of

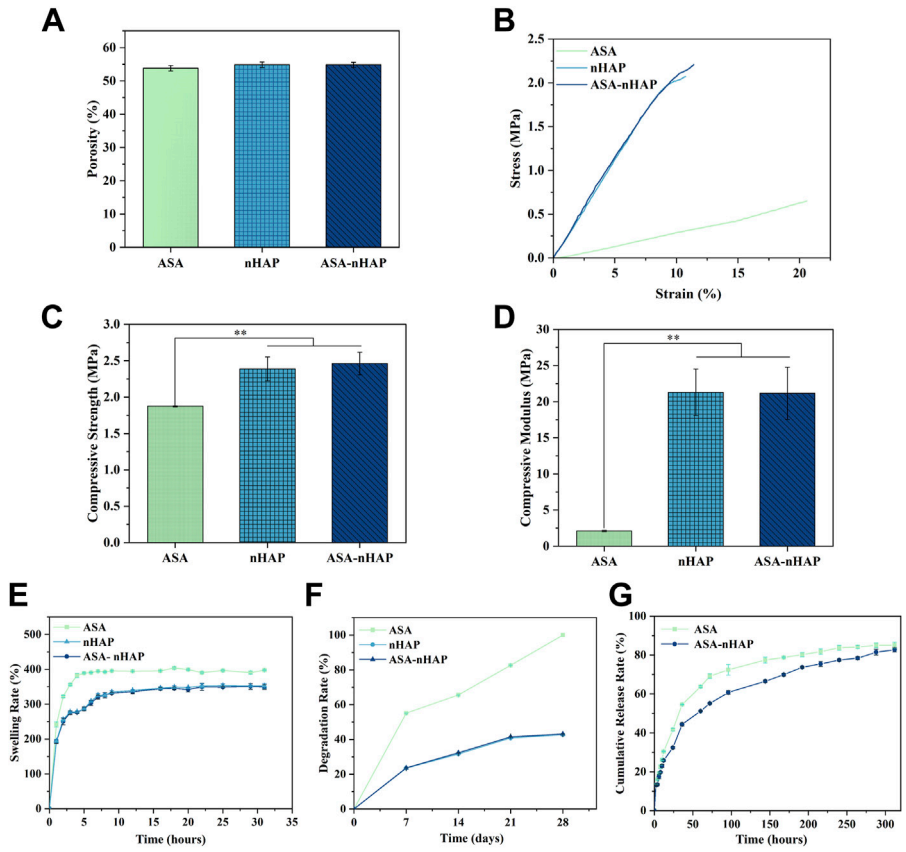

FIGURE 3
Characterization of hydrogel scaffolds. **(A)** The porosity of hydrogel scaffolds. **(B)** The stress-strain curve of hydrogel scaffold. **(C)** The compressive strength of hydrogel scaffold. **(D)** The compressive modulus of hydrogel scaffold. **(E)** The swelling performance of hydrogel scaffolds. **(F)** The degradation performance of hydrogel scaffolds. **(G)** The drug release performance of hydrogel scaffolds. (**$p < 0.01$).

the hydrogel scaffolds. Briefly, the ASA, nHAP, and ASA-nHAP group were immersed in CM at a ratio of 10 mg/mL for 24 h. Subsequently, the extractions were filtered by a 0.22 μm filter and stored at 4°C for the next use. For the cytotoxicity and cell proliferation assay, the CM group was used as a control, and the ASA, nHAP, and ASA-nHAP group were regarded as the experiment groups.

2.6.1 Cell viability assay

The cytotoxicity was assessed with a Live/dead Staining Kit (Solarbio, Beijing, China). The MC3T3-E1 cells were seeded in a 96-well plate at a density of 3,000 per well ($n = 3$). After 24 h, the original CM was replaced by 100 μL fresh CM, and the extractions of ASA, nHAP, and ASA-nHAP group for further incubation. The original CM and extractions were replaced with 100 μL of live/dead cell staining reagent after 1, 3, and 5 days and stained for 30 min. The stained cells were observed and imaged by a X171 Inverted Fluorescence Microscope (Olympus, Japan), and then analyzed cell viability.

2.6.2 Cell proliferation assay

A Cell Proliferation Kit (CCK-8, Solarbio, Beijing, China) was applied according to the manufacturer's instructions. The cells were cultured as described in 2.4.1. After 1, 3, and 5 days, the medium was aspirated. And the cells were mixed with 10 μL of CCK-8 and 100 μL fresh CM. After 1 h of incubation, the optical density (OD) value was detected at a wavelength of 450 nm with a SpectraMax M2 Enzyme Marker (Molecular Devices, United States). The cell proliferation effect was evaluated by comparing the OD value.

2.6.3 Cell adhesion assay

The nucleus and cytoskeleton of MC3T3-E1 cells were observed by the FV1200MPE Laser Confocal Microscopy (CLSM, Olympus, Japan) to evaluate the morphology and adhesion behavior of the MC3T3-E1 cells on the ASA, nHAP, and ASA-nHAP group. The hydrogel scaffolds were incubated with CM for 1 day. Next, the cells were seeded on hydrogel scaffolds at a density of 5×10^4. Two days later, the hydrogel scaffolds were rinsed once with PBS. Then, the cells were fixed with 4% paraformaldehyde for 10 min, and permeabilized with 2% Triton X-100 for 30 min, respectively. The cells were then stained by FITC Phalloidim and 4′, 6-diamantine-2-phenylindole (DAPI), (Solarbio, Beijing, China) at 37°C in dark. Finally, the adhesion behavior of MC3T3-E1 cells was observed by CLSM, and the fluorescence staining area was semi-quantitatively analyzed using Image-Pro Plus 6.0.

2.7 Cell osteogenic differentiation study

For the osteogenic differentiation assay, the MC3T3-E1 cells were cultured with osteogenic induction medium (ODM), and the hydrogel scaffold extractions of ASA, nHAP, and ASA-nHAP group, which contains 50 M ascorbic acid, 100 M

10.3389/fbioe.2023.1105248

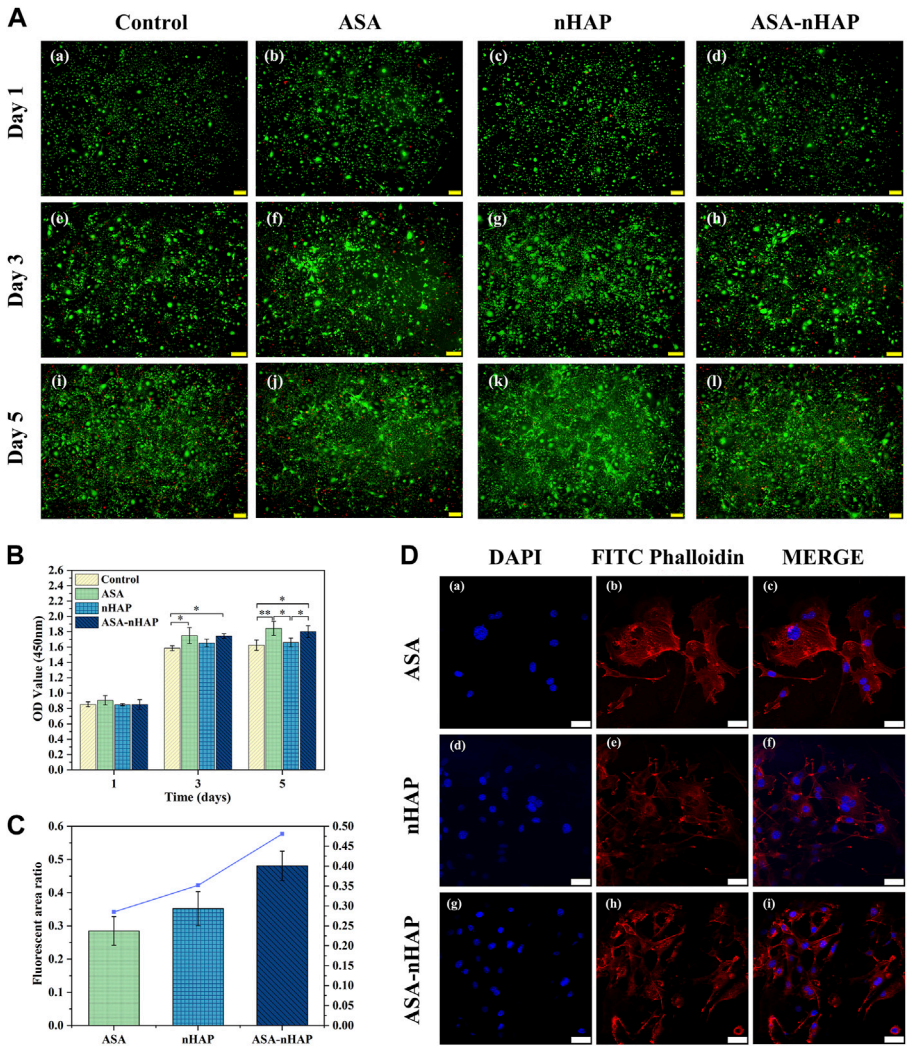

FIGURE 4
Growth ability of MC3T3-E1 cells cultured *in vitro*. **(A)** Live/dead staining images of MC3T3-E1 cells cultured with the hydrogel extractions for 1, 3, and 5 d. **(B)** The OD value of the control group, ASA group, nHAP group, and ASA-nHAP group from the CCK-8 assay (*$p < 0.05$, **$p < 0.01$). **(C, D)** Semi-quantitative analysis and laser confocal images of MC3T3-E1 cells on the ASA group, nHAP group, and ASA-nHAP group. Blue represents the nucleus stained by DAPI and red represents the cytoskeleton stained by FITC phalloidin at a scale bar of 40 μm.

dexamethasones (Solarbio, Beijing, China) and 10 mM β-sodium glycerophosphate (Sigma-Aldrich, United States). And the solution was changed every 3 days. The ODM group was used as a control, and the ASA, nHAP, and ASA-nHAP group was regarded as the experiment groups.

2.7.1 ALP activity assay

ALP, whose expression was assessed according to the protocol of the 5-Bromo-4-Chloro-3-Indolyl phosphate/Nitro Blue Tetrazolium Kit (BCIP/NBT, Beyotime, Shanghai, China), is an early marker of osteogenic differentiation. The MC3T3-E1 cells were inoculated at a density of 5×10^4 per well in 12-well plates ($n = 3$), and the CM was replaced by ODM of the control group, ASA, nHAP, and ASA-nHAP group when their confluence reached 80%. After 2, 7, and 14 days of culture, the cells were fixed with 4% paraformaldehyde (Solarbio, Beijing, China) for 10 min at room temperature. Then the cells were stained with BCIP/NBT ALP staining solutions in dark for 30 min, and finally terminated the reaction with distilled water. The staining intensity and area were observed and photographed by an Inverted Microscope (Olympus, Japan) to evaluate the ALP activity.

2.7.2 Calcium nodule expression assay

The late osteogenic marker was calcium nodules. It was examined according to the instructions of Alizarin Red Staining solution (Beyotime, Shanghai, China). The cells were cultured as described in 2.5.1 for 7, 14, and 21 days. They were fixed with 95% ethanol for 10 min, and the washed by PBS for three times. The staining procedure was terminated with distilled water after adding appropriate Alizarin Red Staining solution for 30 min. Calcium nodules were observed with a XI71 Inverted Microscope (Olympus, Japan). A semi-quantitative analysis of the expression levels of calcium nodules was also carried out. Briefly, 500 μL of 10% Hexadecane-pyridinium Chloride solution (Solarbio, Beijing, China) was added to the plates containing calcium nodules. The liquid was added to 96 wells at 100 ul per well after 15 min ($n = 3$). The OD value was read at 506 nm, and the semi-quantitative calcium nodules in each group were evaluated.

10.3389/fbioe.2023.1105248

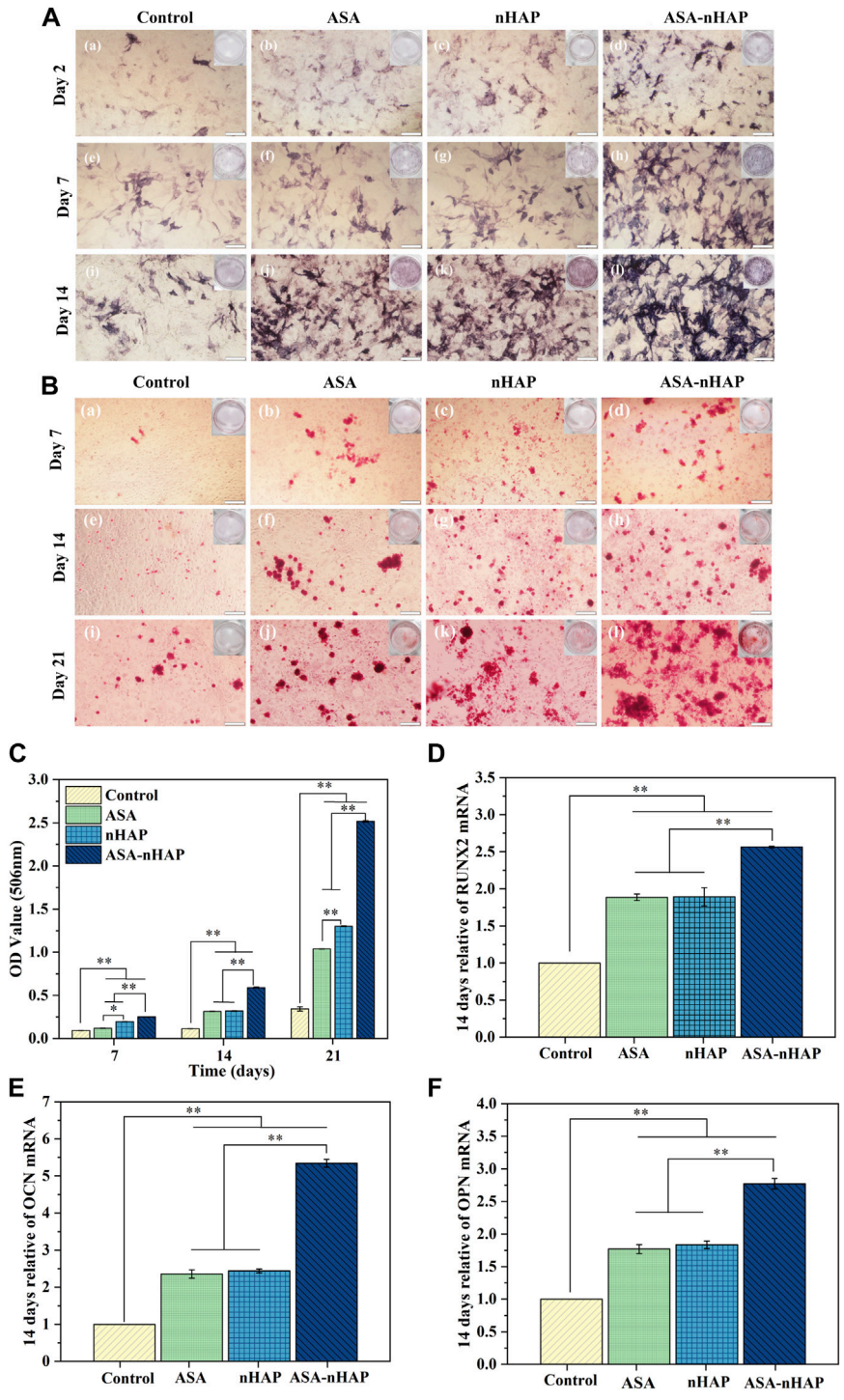

FIGURE 5
Osteogenic differentiation ability of MC3T3-E1 cells cultured *in vitro*. **(A)** Digital and microscopic images of MC3T3-E1 cells in the control group, ASA group, nHAP group, and ASA-nHAP group after 2, 7, and 14 days to assess ALP activity, the scale bar is 200 μm. **(B)** Digital and microscopic images of MC3T3-E1 cells in the control group, ASA group, nHAP group, and ASA-nHAP group after 7, 14, and 21 days to assess the expression of calcium nodules, scale bar is 200 μm. **(C)** Semi-quantitative analysis of the expression of calcium nodules in the control group, ASA group, nHAP group, and ASA-nHAP group after 7, 14, and 21 days (**$p < 0.01$). **(D–F)** Expression of osteogenic genes of RUNX2, OCN, and OPN after 14 days (**$p < 0.01$).

2.7.3 Osteogenesis-related gene expression assay

The expressions of RUNX2 family transcription factor (RUNX2), osteopontin (OPN), and osteocalcin (OCN) were evaluated by qRT-PCR assay. MC3T3-E1 cells were cultured in a 6-well plate at a density of 1×10^5 per well and cultured as before for 14 days. The total RNA was extracted following the manufacturer's instructions (ZHONGSHI TONTRU, Tianjin, China), and the concentration was calculated by NanoDrop 2000C (Thermal Fisher Scientific, United States). RNA was reversely transcribed to cDNA by the Reverse Transcription Kit (ZHONGSHI TONTRU, Tianjin, China). Then, an ABI Prism

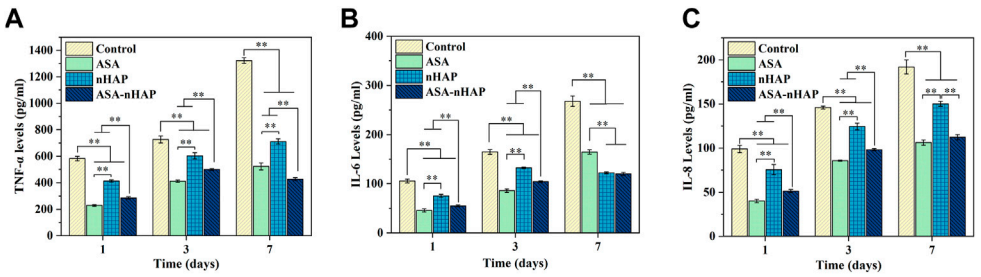

FIGURE 6
Expression of the inflammatory mediators of MC3T3-E1 cells in the inflammatory environment after 1, 3, and 7 d **(A)** TNF-α. **(B)** IL-6. **(C)** IL-8. (**$p < 0.01$).

7,500 Real-Time PCR system (Applied Biosystem, United States) was used after the Mix was added according to the instructions of the Fluorescence Quantitative PCR Kit (ZHONGSHI TONTRU, Tianjin, China). GAPDH was a normalized gene, and the control group was set as 1. The relative expression levels of RUNX2, OCN, and OPN were evaluated ($n = 3$) by the $2^{-\triangle\triangle CT}$ method. Thermo Fisher synthesized the primers, and the sequence is shown in Table 1.

2.8 Anti-inflammatory property study

The anti-inflammatory ability of the hydrogel scaffolds was evaluated by the expression of inflammatory cytokines of MC3T3-E1 cells cultured in a lipopolysaccharide (LPS)-induced (Solarbio, Beijing, China) inflammatory environment. MC3T3-E1 cells were cultured in 6-well plate at a density of 2×10^5, and the medium was replaced with fresh CM, ASA group, nHAP group, and ASA-nHAP group extractions after 24 h. After 30 min, LPS was added to each well at 10 μg/mL. The supernatants of each group were collected after being cultured for 1, 3, and 7 days. And the expression levels of tumour necrosis cytokines (TNF-α), interleukin 6 (IL-6), and interleukin 8 (IL-8) were examined according to the recommended procedure of ELISA Kits (Inova, Wuhan, China). The OD value was measured at 450 nm by the RT-6100 Enzyme Marker (Rayto, Shanghai, China). The concentration of inflammatory cytokines was proportional to the OD value.

2.9 Statistical analysis

SPSS, version 22 (IBM), was used for statistical analysis, and the results were compared by the one-way analysis of variance (ANOVA). The data were expressed as mean ± standard deviation. Data were considered to be different when *$p < 0.05$, and significantly different when **$p < 0.01$. Origin 2021 was used for plotting.

3 Results

3.1 Chemical constitution and crystal structure analysis

3.1.1 FTIR analysis

FTIR was used to obtain information on the chemical constitution and related changes of the original powders in hydrogel scaffolds. Figures 1A,B shows the FTIR spectra of the raw material powders and hydrogel scaffolds. As for Gel, its strong absorption peaks amide I band (C=O stretching vibration peak), amide II band (N-H bending vibration peak), and amide III band (C-N stretching vibration peak) located at 1,627 cm^{-1}, 1,521 cm^{-1}, and 1,234 cm^{-1}, respectively. The spectra of PVA showed that the peak at 3,273 cm^{-1}, 2,904 cm^{-1}, and 1,085 cm^{-1} belonged to the stretching vibration of O-H, C-O, and C-H, respectively. In aspirin, the stretching vibration peaks of -OH presented at 3,490 cm^{-1}. The other short peaks in the zone of 2,300–3,400 cm^{-1} were related to -COOH. In addition, the typical peaks of C=O and C=C appeared at 1,690 cm^{-1}, 1750 cm^{-1}, and 1,605 cm^{-1}. The stretching vibration peak of C=O at 1751 cm^{-1}. The anti-symmetric and symmetric contraction of -COO- at 1,600 cm^{-1} and 1,410 cm^{-1} were from SA. The prominent peaks of nano-hydroxyapatite posited at 1,024 cm^{-1}, 965 cm^{-1}, 603 cm^{-1}, and 555 cm^{-1} were attributed to the stretching vibration and deformation vibration of PO_4^{3-}. The stretching and bending vibration peaks of -OH were observed at 3,600 cm^{-1} and 633 cm^{-1}.

In Figure 1B, the FTIR spectra of the three synthesized hydrogel scaffolds showed the common broad peak at 3,277 cm^{-1}, which may correspond to the change and shift of -OH when compared with the raw materials. The amide I bond was significantly broadened at 1,627 cm^{-1}, and the amide II band blue-shifted to 1,550 cm^{-1}. The weak peaks of aspirin and SA in the fingerprint region also disappeared in the composite hydrogel scaffolds. Another point to notice was that the small peak at 1734 cm^{-1} was related to the shift of C=O, which belonged to SA. These changes in the hydrogel scaffolds proved the formation of hydrogen bonds and strong electrostatic interaction between PVA, SA, Gel, and aspirin (Yang et al., 2020; Zhang et al., 2021). In line with previous studies, the peak at 1,413 cm^{-1} was the "egg-shell" structure formed by the -COO- of SA and Ca^{2+} of the $CaCl_2$ (Zhang et al., 2021). The pattern of the nHAP group and ASA-nHAP group showed characteristic peaks at 603 cm^{-1} and 555 cm^{-1}. But compared with nano-hydroxyapatite, the peak at 965 cm^{-1} disappeared, and the peak at 1,024 cm^{-1} red-shifted to 1,019 cm^{-1}. The reason could be rooted in the formation of hydrogen bonds between PO_4^{3-} and the raw materials, especially the PVA (Liu et al., 2011; Tohamy et al., 2018). In addition, the difference in intensity of some peaks among the nHAP group and ASA-nHAP group may relate to the presence of aspirin. These results indicated that the physical and chemical cross-linking method was feasible and effective.

3.1.2 XRD analysis

XRD was employed to acquire information on crystalline structure and relevant changes in the hydrogel scaffolds and raw organic

powders. The XRD patterns are shown in Figures 1C,D. The characteristic crystalline peaks at 2θ = 19.69° and 2θ = 22° were related to the three-dimensional (3D) porous network in the micro-crystalline regions of the PVA. The Gel and SA were known in the non-crystalline state, their diffuse and broad diffraction peaks at 2θ = 20° and 2θ = 15°, respectively (Yang et al., 2020). Aspirin exhibited some characteristic crystalline peaks at 2θ = 14.37°, 17.3°, 20.0°, 23.5°, and 26.4°. In hydrogel scaffolds, the characteristic diffraction peaks of PVA and aspirin disappeared. And the large and broad diffraction peaks appeared at 2θ = 22.5°–50°, indicating that the organic components interacted with each other during the cross-linking process. Nano-hydroxyapatite displayed some characteristic diffraction peaks at 2θ = 25°, 31.8°, 32.1°, 33°, 39.4°, 46.2°, 53.1°, and 64.1°, which was in agreement with the standard card for nHAP (JCPDS-09–0,432). Peaks of nano-hydroxyapatite in the nHAP group and ASA-nHAP group appeared one by one, indicating that nano-hydroxyapatite was successfully connected to the raw materials. In addition, the intensity of some peaks in the ASA-nHAP group was more obvious than in the nHAP group. A possible explanation was that aspirin successfully attached to nano-hydroxyapatite in the ASA-nHAP group, thus exhibiting stronger diffraction. These results indicated that neither the activity of organic materials nor the crystalline structure of nano-hydroxyapatite was disrupted in the hydrogel scaffolds.

3.2 Microstructure analysis

The microstructure of the hydrogel scaffolds was examined by SEM. As shown in Figure 2A, the images showed a uniform and interconnected distribution of pores in the ASA group. Additionally, smooth pore walls also could be observed. As for the nHAP group and ASA-nHAP group, a pronounced hierarchical multi-network structure appeared when the hydroxyapatite nanoparticles were uniformly and closely attached to the surface of the pore. Compared with the ASA group, the sidewall's thickness and roughness were increased. Additionally, Figure 2B illustrates the regularities of distribution of the pore sizes of the ASA, nHAP, and ASA-nHAP group. The average pore size was about 106.25 μm, 109.71 μm, and 101.66 μm, respectively. The results showed that aspirin had no significant impact, while nano-hydroxyapatite provided a more reliable microstructure and the application potential of the hydrogel scaffold in bone tissue engineering. Furthermore, it verified that the dual-crosslinking method made a tight association between organic materials and nano-hydroxyapatite.

3.3 Characterization analysis

3.3.1 Porosity analysis

Figure 3A shows the porosity of different hydrogel scaffolds. The porosity was similar, and about 53.8 ± 0.82%, 54.87 ± 0.76%, and 54.83 ± 0.84% for the ASA, nHAP, and ASA-nHAP group, respectively ($p > 0.05$). This provided evidence neither aspirin nor nanohydroxyapatite adversely affected the porosity of the hydrogel scaffold. And it was also confirmed that nano-hydroxyapatite adhered tightly to the porous surface.

3.3.2 Mechanical strength analysis

The hydrogel scaffold's compression strength and compression modulus were evaluated in depth. As shown in Figure 3B, the stress-strain curve of the ASA group had the lowest slope. As for the nHAP and ASA-nHAP group, they were higher and extremely similar. By comparison, with the same test condition, the ASA group exhibited worse mechanical strength. As shown in Figure 3C, the compressive strength of the ASA group, nHAP group, and ASA-nHAP group was about 1.88 ± 0.01 MPa, 2.39 ± 0.16 MPa, and 2.46 ± 0.15 MPa, respectively. Additionally, Figure 3D shows the results of the compression modulus by further analysis of the stress-strain curve. Compared with 2.11 ± 0.08 MPa of the ASA group ($p < 0.01$), the compression modulus of the nHAP and ASA-nHAP group was positively enhanced to 21.16 ± 3.23 MPa and 21.28 ± 3.62 MPa ($p > 0.05$), respectively. These findings hinted that they could withstand compression without breaking. Moreover, the addition of nano-hydroxyapatite could significantly improve the mechanical properties of hydrogels composed by pure organic materials.

3.3.3 Swelling property analysis

As shown in Figure 3E, the ASA group, nHAP group, and ASA-nHAP group had similar swelling profiles and suitable swelling rates in PBS. Conspicuously, the ASA group reached swelling equilibrium as early as 6 h, with a swelling rate of 397.71 ± 1.28%. The ASA group had the highest swelling rate compared to the nHAP and ASA-nHAP group ($p < 0.01$). Also, the swelling rate of the nHAP and ASA-nHAP group was not significantly different, which decreased to 349.18 ± 6.34% and 352.30 ± 6.92% ($p > 0.05$), respectively. Meanwhile, the time to swelling equilibrium was significantly prolonged to 16 h, which suggested they were equipped with more appropriate swelling behavior. The results showed that nano-hydroxyapatite with smaller hydrophilic could reduce the swelling behavior, resulting in a better release of aspirin.

3.3.4 *In vitro* degradation property analysis

The *in vitro* degradation capacity of the hydrogel scaffold was evaluated according to the weight reduction rate when immersed in PBS for a certain period. As shown in Figure 3F, the ASA group degraded more rapidly than the nHAP group and ASA-nHAP group, with a degradation rate of 100% after 28 days ($p < 0.01$). The final degradation rate of the nHAP group and the ASA-nHAP group was significantly lower than the ASA group, and was about 42.72 ± 0.01% and 43.11 ± 0.02%, respectively ($p > 0.05$). The results indicated that the nHAP group and ASA-nHAP group had a more trustworthy stability. Another point according to Figure 3F was that the degradation speed was higher at the first 7 days for the three groups, but then the speed became slower until 28 days, especially the nHAP group and ASA-nHAP group.

3.3.5 *In vitro* drug release property analysis

The drug release property of the hydrogel scaffolds was investigated *in vitro* at 37°C. The drug release rate and profile of the ASA group and ASA-nHAP group are presented in Figure 3G. The ASA group and ASA-nHAP group had excellent drug loading efficiency for their cumulative release rate of 85.13% and 82.75%, respectively. As we can see, a burst release of aspirin happened in the first 48 h in all groups, and the ASA group had a more obvious burst release rate. The burst release presumably resulted from the exchange

of water molecules and the breakage of organic polymerization chains. After 48 h, the release speed was gradually reduced and sustained until 312 h, suggesting that the fabricated hydrogel scaffold kept a long time of releasing aspirin. The aspirin release profile of the ASA-nHAP group was flatter after 48 h, which indicated that the ASA-nHAP group had a better-sustained release capacity. This also confirmed the drug-loaded capacity of nano-hydroxyapatite.

3.4 Cell growth properties

3.4.1 Cell viability analysis

The ability to maintain cell viability is a primary prerequisite for further functional studies and clinical applications of the hydrogel scaffold. Figure 4A shows the viability of MC3T3-E1 cells with live/dead staining after 1, 3, and 5 days. Green fluorescence represented viable cells, and red fluorescence represented dead cells. The cells cultured with different experimental groups exhibited higher viability and growth trend than the control group over time. Furthermore, the images showed a uniform distribution of cells with a polygonal morphology. This proved that the hydrogel scaffolds was no cytotoxicity.

3.4.2 Cell proliferation analysis

The results of the CCK-8 experiment are shown in Figure 4B. The OD value was proportional to cell proliferation. Although there was no significant difference in OD value among all groups on the first day, the OD value increased over time. And the higher OD value in the experimental groups emerged at the 3 days and 5 days. It also could be found that among the three experimental groups, the ASA group had a more significant cell proliferation effect, and the nHAP group had a slightly lower cell proliferation effect. The results indicated that the hydrogel scaffold could promote cell proliferation over time, which was consistent with the results of cytotoxicity experiments.

3.4.3 Cell adhesion analysis

The semi-quantitative and staining results are shown in Figures 4C,D. The actin filament was stained red by FITC Phalloidin, and the nucleus was stained blue by DAPI in CLSM. Interestingly, in different groups, MC3T3-E1 cells strongly attached to the surface, regularly distributed, and formed cell bridges, which suggested that the biocompatibility and the 3D porous structure of the hydrogel scaffold facilitated cell interaction and cell adhesion. A slightly larger number of MC3T3-E1 cells were observed in the nHAP and ASA-nHAP group than in the ASA group. The connection of cell pseudopods was also more intimate, especially in the ASA-nHAP group. These results indicated that the prepared ASA-nHAP group may provide a more bone-friendly microenvironment for the growth of MC3T3-E1 cells.

3.5 Cell osteogenic differentiation property

3.5.1 ALP activity analysis

Figure 5A shows the ALP activity of each group. The expression of ALP occurs in the early phase of bone regeneration. ALP activity was evaluated according to the color intensity. The results showed that the ALP activity increased over time in all groups. In contrast to the control group, a significantly visible purple color emerged in the experimental groups at 2, 7, and 14 days. Similar color intensity could be seen in the ASA and nHAP group at all time points. Interestingly, the ASA-nHAP group exhibited the most augmented color intensity. It could be concluded that the hydrogel scaffolds promoted MC3T3-E1 cell's osteogenic differentiation in the early stage, especially the ASA-nHAP group.

3.5.2 Calcium nodule expression analysis

To further investigate the mineralization effect, the expression of calcium nodules was also detected. Figures 5B,C shows ARS staining and semi-quantitative results after 7, 14, and 21 days. What was obvious was that the more and larger red calcium nodules in the experimental groups, *versus* the control group. Clusters of calcium nodules even appeared in the ASA-nHAP group at 21 days. Also, no significant difference could be observed between the ASA group and the nHAP group. Consistent with the staining results, the analysis of the semi-quantitative results displayed significantly higher OD values of the experimental groups than the control group. It could be found that the most notable OD value is in the ASA-nHAP group. The mineralization of the extracellular matrix demonstrated that hydrogel scaffolds promoted late osteogenic markers' expression.

3.5.3 Osteogenesis-related gene expression analysis

To further verify the superiority of hydrogel scaffolds on osteogenic differentiation of MC3T3-E1 cells, the expression of osteogenesis-related genes such as RUNX2, OCN, and OPN were assessed, whose high expression was the primary condition for maturation and mineralization of osteoblasts. As shown in Figures 5D–F, the relative expression of RUNX2, OCN, and OPN of the experimental groups were higher than the control group ($p < 0.05$, $p < 0.01$) at 14 days. The ASA-nHAP group exhibited the highest gene expression. In detail, there was about a 2.5-times higher expression level of RUNX2 in the ASA-nHAP group when compared with the control group. As for OCN and OPN, it was remarkably increased in the ASA-nHAP group by offering a 5.3-times and 2.7-times than the control group, respectively. These results supported that the fabricated hydrogel scaffolds could reinforce the expression of the osteogenesis-related genes, especially for the ASA-nHAP group.

3.6 Anti-inflammatory property analysis

ELISA was used to detect the anti-inflammatory level of the hydrogel scaffolds. As shown in Figures 6A–C, compared with the control group, the expression of TNF-α, IL-6, and IL-8 in experimental groups were lower ($p < 0.01$) at every time point. The expression of inflammatory cytokines in the control group increased over time. The increase in quantity in experiment groups was much smaller than in the control group ($p < 0.01$). Further analysis revealed that among the three experiment groups, the nHAP group had a higher level of inflammatory cytokines expression ($p < 0.01$). In the ASA group, the expression of inflammatory cytokines was significantly lower. These results indicated that the addition of aspirin and nano-hydroxyapatite gave the hydrogel scaffold an excellent anti-inflammatory effect.

4 Discussion

It is a superior protocol and also a great challenge that fill bone defects and promote osteoblasts' function with bone tissue engineering

materials in a special microenvironment. The design and preparation of bionic hydrogel scaffolds not only should optimize the physical, chemical, and mechanical characterization, but also improve the biological functions. To meet the need of multifunctional bionic materials, aspirin and nano-hydroxyapatite were introduced into PVA/Gel/SA hydrogel solution. Based on previous work, a dual cross-linking approach with cyclic freeze-thaw and $CaCl_2$ immersion was adopted (Xu et al., 2019). The results of drug release properties, cell growth, osteogenic differentiation, and anti-inflammatory properties suggested that both aspirin and nano-hydroxyapatite are essential for the biological function of hydrogel scaffolds. Meanwhile, the synergistic biological functions to promote cell osteogenic differentiation and reduce the expression of inflammatory mediators of aspirin and nanohydroxyapatite were verified.

The interaction between molecules from different components can form new chemical structures or cause the movement of chemical bonds during the cross-linking process. FTIR analysis showed that in the hydrogel scaffold, the characteristic peaks appeared at 3,277 cm^{-1}, 1734 cm^{-1}, 1,627 cm^{-1}, 1,550 cm^{-1}, 1,024 cm^{-1}, and 1,019 cm^{-1} were due to electrostatic interactions and the formation of new hydrogen bonds among raw materials during cyclic freeze-thaw (Yang et al., 2020; Zhang et al., 2021). The addition of nano-hydroxyapatite created the potential to improve the cross-link density, and the physical crosslinking made full preparation for the ideal structure of the hydrogel scaffold. The chemical cross-linking method formed a firm "egg-shell" structure, which made the molecules bound more tightly, and further enriched the 3D structure. The biological activity of the scaffolds is related to the crystal structure of the organic components. Based on XRD analysis, the results verified that the ordered arrangement of the original molecular chains and oxygen functional groups of PVA and aspirin changed, so their crystalline state disappeared in hydrogel scaffolds (Zhang et al., 2019; Maneewattanapinyo et al., 2020). The crystalline structure of nano-hydroxyapatite was not affected, which in favour to improve the mechanical strength of the hydrogel scaffold. Meanwhile, the more obvious crystalline strength of the ASA-nHAP group verified the drug-loaded ability of nano-hydroxyapatite. Some studies have reported SA, Gel, and PVA were preferred materials for the preparation of drug-loaded hydrogel scaffolds, but the bioactivity of PVA/Gel/SA hydrogel scaffold mixed with aspirin and nano-hydroxyapatite is unclear. In this study, the promoting vitality and proliferation results may be linked to the thermosensitive Gel, which is morphologically reversible during the extract process at 37°C and rich in amino acids (Zhang et al., 2021). The excellent biocompatibility of SA and PVA is also certified (Xu et al., 2019). Among the three experiment groups, the lower OD value of the nHAP group could be explained by the weakened cell viability after they devoured the nano-hydroxyapatite particles. The aspirin-loaded hydrogel could promote cell proliferation (Zhang et al., 2022). The more remarkable proliferative impact of the ASA group implied that the positive effect of aspirin compensated for the negative effect caused by nano-hydroxyapatite (Ren et al., 2018; Zhang et al., 2018). Taken together, these findings indicated that hydrogel scaffolds could effectively activate MC3T3-E1 cells and promote cell growth, which rationalized the feasibility of further studies.

During bone regeneration, not only the nutrient transport and metabolite removal, but also bio-mechanical support are influenced by the microstructure and porosity of the hydrogel scaffold (Patel et al., 2019). The graded multi-network microstructure is more suitable for cells, tissues, blood vessel ingrown and new bone formation (Zhao et al., 2022). Extensive experimental evidence demonstrated that the suitable pore size for cell adhesion and survival is 100–500 μm. The ideal porosity is 50%–90%. Moreover, smaller pore size and penetrated channel facilitate signal transduction between cells (Murphy et al., 2010; Perez and Mestres, 2016). In this study, the ideal multi-network pore structure, morphology, size, and varied orientation of the hydrogel scaffold were acquired and superior to the results of previous studies (Xu et al., 2020; Sreekumaran et al., 2021). Meanwhile, the cell-scaffold and cell-cell interaction are affected by the microstructure, surface roughness, and structural stability of the hydrogel (Schaap-Oziemlak et al., 2014; Xia et al., 2020). The compressive strength of cancellous bone was reported in the range of 0.2–4 MPa, and the compression modulus is between 20–400 Mpa (Bobbert et al., 2017). The tested compression strength of the ASA-nHAP group was 2.39 ± 0.16 MPa, and the compression modulus was 21.28 ± 3.62 MPa. They were matched to the bone tissue according to the previous literature (Goto et al., 2021). The ideal mechanical strength could be attributed to the following two reasons. Firstly, the nano-hydroxyapatite with high specific surface energy not only increased the thickness of the porous wall, but also reduced the brittleness of the nano-hydroxyapatite (Rezwan et al., 2006; Pina et al., 2015). Secondly, the Ca^{2+} released from nano-hydroxyapatite increased the cross-linking degree of SA and the formation of hydrogen-bond (Liu et al., 2020a; Suvarnapathaki et al., 2020). More importantly, it is reported that the hydrogel scaffold with excellent mechanical performance can satisfy the support demand against external stress and speed up bone formation with the stress change in the microenvironment (Chaudhuri et al., 2016). In this study, the microstructure and mechanical strength of the prepared hydrogel scaffolds provided the possibility for the growth of MC3T3-E1. The observations of the cell adhesion assay proved that the fabricated hydrogel scaffold created a favourable environment for cell proliferation. Compared with the ASA group and the nHAP group, the ASA-nHAP group attracted more cells and increased the connection between cells and cells, or the cells and their surroundings. Compared with the smooth pore wall, the rough crystal structures of nano-hydroxyapatite and the loaded aspirin could provide a focal point for the pseudopods of the MC3T3-E1 cells, which was more favourable for cell growth and crawl along the surface of the hydrogel scaffold (Hao et al., 2021). These results indicated that the hydrogel scaffold coated with nano-hydroxyapatite could provide a rougher surface and a bone-friendly environment for cell growth.

The degree of cross-linking between raw materials and the compactness of the structure are key considerations (Ozeki and Tabata, 2005), which can affect the swelling and degradation behavior of the hydrogel scaffold. During the swelling and degradation process, the hydrogel scaffold can promote cell adherence and proliferation, and perform an osteogenic function in the inflammatory environment (Akhlaq et al., 2021; Shaabani et al., 2021). Eventually, the scaffold is gradually replaced by neogenetic bones. The water-induced swelling and degradation process is linked to the breakage of polymeric chains within the biopolymer. Hence, it is critical to take the type, proportion, and cross-linking method of raw materials into consideration (Ji et al., 2020). The swelling performance of gelatin hydrogel can reach up to 1,000%, however, its stability is too poor to meet the needs of bone tissue regeneration (Zhang et al., 2019). Despite the outstanding hydrophilic properties of SA, Gel, and PVA,

the suitable swelling rate of 397.71% of the ASA group manifested that the design and fabrication of the hydrogel scaffold in this study were rational. As for the nHAP and ASA-nHAP group, the dense microstructure also reduced the space where water molecules could pass, therefore, acquiring a slightly decreased swelling rate of 349.18% and 352.30%, which were consistent with the reported research (Shuai et al., 2021). Excessive swelling rate may even damage the soft tissue, increasing the risk of exposure and failure of bone healing. The internal spatial structure of hydrogel scaffolds will also change during the swelling process. Too small swelling rate makes the hydrogel scaffolds unable to absorb enough blood and provide more adequate space. Moreover, the appropriate swelling property would make the hydrogel scaffold readily adjust to the shape and volume of the bone defect area, filling the defect as soon as possible. According to the result of *in vitro* degradation rate of the nHAP and ASA-nHAP group, they could meet the requirements of bone regeneration and the osseointegration of the implant (Esposito et al., 2006). This also verified that the homogeneously dispersed nano-hydroxyapatite was tightly connected to the sites from organic components with hydrogen bonds and increased the stability of the microstructure (Uemura et al., 2019). Although the degradation rate in all groups was faster in the first 7 days, it may facilitate the release of aspirin and maintain the effective drug concentration (Tao et al., 2020). These findings fully validated that a dual-crosslinked hydrogel scaffold incorporated with aspirin and nano-hydroxyapatite made it possible to fabricate a more stable and robust material.

To regulate the inflammatory microenvironment and ensure the osteoblasts' viability, it is advisable to use a hydrogel scaffold with a porous structure and drug binding sites as sustained release systems, and exert multi-function at different bone regeneration stages (Mauri et al., 2016). Compared to the ASA group, the current results of the continued release time of the ASA-nHAP group was 312 h. The cumulative drug release rate was 82.75%. The results were similar to the porous aspirin-loaded nanocomposite films reported in a previous study, and indicated that the hydrogel scaffold was able to retain the drug molecules without excessive loss of aspirin during the preparation process (Ji et al., 2016). As the FTIR results showed, aspirin was immobilized *via* the physical method in a 3D network structure, and nano-hydroxyapatite increased this wrapping efficiency. This not only ensures a stable chemical structure, but also significantly improves the drug release kinetics. As a result, we obtain smaller drug burst release rates and smoother release profiles. Notably, the special particle size, morphology, and crystalline state of nano-hydroxyapatite particles gave the hydrogel scaffold the potential to absorb and bind drug molecules without changing pharmacokinetic structure (Raina et al., 2020; Liu et al., 2022). When analyzed from the microstructure level, the dense and complicated polymeric chains formed by the nano-hydroxyapatite also could improve drug release behavior. In conclusion, the present results indicated that the incorporation of nano-hydroxyapatite can significantly improve the characterization of the hydrogel scaffold. Although the effect of aspirin on the structure of hydrogel scaffold was not significant, it was of great value in improving bioactivity.

Since bone repair is a complex process, it involves not only the reconstructive microenvironment, but also the inflammatory microenvironment caused by the body's immunity and surgical microtrauma. Inflammation can stimulate the body's immune system and promote the clearance of foreign body, but may destroy microenvironmental homeostasis. However, in the early period after biomaterial implantation, excessive inflammatory mediators produced by the foreign body rejection can disrupt osteoblast function, leading to unsatisfactory bone regeneration effect or even failure. Aspirin, bioactive nanoparticles, and Ca^{2+} released from the hydrogel scaffold can serve as major elements to promote MC3T3-E1 cells' osteogenic differentiation. Aspirin could exert an osteogenic effect by activating the Wnt/β-catenin pathway, and increasing telomerase activity (Yamaza et al., 2008). On the surface of contained-aspirin titanium, MC3T3-E1 cells had a more pronounced osteogenic differentiation effect (Ren et al., 2018). Moreover, animal study has also demonstrated that aspirin-loaded titanium implants could treat aseptic loosening and promote osseointegration (Wei et al., 2020). Similar to the previous studies, the ASA and ASA-nHAP group showed excellent ALP activity and expression of calcium nodules. Bone tissue regeneration materials containing nano-hydroxyapatite have had comprehensive applications according to previous studies (Liao et al., 2021). The Ca^{2+} and PO_4^{3-} released from nano-hydroxyapatite are the favorite elements for osteoblasts, which can regulate the proliferation, migration, and differentiation of osteoblasts (Kargozar et al., 2019). Therefore, the excellent results of the nHAP group and ASA-nHAP group may be explained by the hypothesis that Ca^{2+} and PO_4^{3-} provided a suitable osteogenic differentiation microenvironment for MC3T3-E1 cells (González Ocampo et al., 2019). The qRT-PCR assay further confirmed the osteogenic differentiation effect of hydrogel scaffolds and the synergistic function of aspirin and nano-hydroxyapatite. RUNX2 reportedly is particularly important in early osteogenesis, as it is the central control gene of the osteoblast phenotype (Maji et al., 2020). OCN and OPN are the representative genes in the later osteogenic differentiation (Maji et al., 2020). The increased expression levels of related genes in the experiment groups, especially the ASA-nHAP group, demonstrated that scaffold loaded with nano-hydroxyapatite and aspirin presented excellent osteogenic differentiation capacity. Inflammatory mediators such as TNF-α, IL-6, and IL-8 can cause fever and participate in the body's inflammatory response and immune response, which are involved in the bone destruction process (Fong et al., 2008; Gazivoda et al., 2009). The lower expression of inflammatory cytokines of experiment groups was related to the release of aspirin, Ca^{2+} and nano-hydroxyapatite. Previous literature has demonstrated that aspirin can reduce the expression of TNF-α and IFN-γ, and block the adverse effect of the NF-κB signaling pathway on osteogenesis (Clària and Serhan, 1995). The formation and resorption of bone are associated with the presence of inflammatory LPS. The Ca^{2+} can decrease the stability and amphiphilic of LPS. The ELISA results of the nHAP group and ASA-nHAP can be explained by structural modifications of LPS due to the interaction of nano-hydroxyapatite and its molecular components, inhibiting the formation of links with reactive groups of LPS and its inflammatory activity (Martínez-Sanmiguel et al., 2019). This study supports evidence of previous observations that aspirin can prevent apoptosis and inhibit inflammation (Kang et al., 2021; Yu et al., 2021), and create a friendly microenvironment (Liu et al., 2020b). Studies have confirmed that small amounts of inflammatory mediators not only maintain osteoblast viability, but also stimulate the body's osteogenic mechanisms and accelerate bone formation (Tang et al., 2014). Thus, it is imperative to promote bone repair by regulating the expression of inflammatory cytokines and the function of the osteoblast through hydrogel scaffolds. What must be emphasized is that the ASA-nHAP hydrogel scaffold prepared in this study has excellent bionic characterization, biocompatibility, osteogenic potential, and anti-inflammatory property.

Although the multifunctional biomimetic hydrogel scaffold loaded with aspirin and nano-hydroxyapatite prepared in this study can provide

a bone-friendly microenvironment and improve osteoblast activity, there are still some shortcomings. The synergistic osteogenic mechanism of aspirin and nano-hydroxyapatite is lacking, which will be benefit to further *in vivo* studies and clinical translation. However, we also made some meaningful contributions. We suggest that the design of future bioactive biomaterials should focus on a bone-friendly microenvironment which involves the regulation of the microenvironment and the improvement of the osteoblast activity and differentiation functionton to accelerate bone regeneration. It is important to consider not only the bionic structure, but also that can modulate biological processes, which involve overcoming early inflammatory responses and safely transitioning to regeneration.

5 Conclusion

In this work, a novel multifunctional-bionic hydrogel scaffold was designed and fabricated with a dual-crosslinking approach combined with aspirin and nano-hydroxyapatite to provide a promising osteogenic and anti-inflammatory treatment strategy for bone tissue regeneration. The characterization of hydrogel scaffolds, and their effects on cytotoxicity, osteogenic differentiation, and anti-inflammatory property were evaluated. The cyclic freeze-thawing approach created firm hydrogen bonds and electrostatic interaction among raw materials, following a secondary chemical cross-linking to form a stronger "egg-shell" structure. This method sustained the physical and biological characteristics of the raw materials, creating a bionic structure. The ASA-nHAP group preserved or even optimized the mircostructure, porosity, mechanical strength, swelling property, degradation property, and drug-release property to some extent. The ASA-nHAP group performed best in promoting MC3T3-E1 cell proliferation, adhesion, osteogenic differentiation, and anti-inflammation *in vitro* investigation. In conclusion, the simultaneous incorporation of aspirin and nano-hydroxyapatite into a hydrogel scaffold is a promising strategy for the preparation of multifunctional bone tissue engineering materials.

Data availability statement

The original contributions presented in the study are included in the article/Supplementary Material, further inquiries can be directed to the corresponding author.

Author contributions

SL contributed to experiment implement, data curation, writing-Original Draft, writing-review and editing, project administration. YX assissted with software, visualization, writing-review and editing. YY helped with writing-review and editing, supervision. LL assissted with software. YS contributed to data curation, supervision. YL helped with experiment implement. LY helped with experiment implement. ZC contributed to conceptualization, methodology, writing-review and editing, supervision, Funding acquisition.

Funding

This work was supported by the Hebei Province "333 Talent Project" funded project (Grant no: A202102010); Hebei Provincial Government funded project of training excellent talents in clinical medicine: (Grant no:361029).

Conflict of interest

The authors declare that the research was conducted in the absence of any commercial or financial relationships that could be construed as a potential conflict of interest.

Publisher's note

Supplementary material

The Supplementary Material for this article can be found online at: https://www.frontiersin.org/articles/10.3389/fbioe.2023.1105248/full#supplementary-material

References

Ahmed, R., Afreen, A., Tariq, M., Zahid, A. A., Masoud, M. S., Ahmed, M., et al. (2021). Bone marrow mesenchymal stem cells preconditioned with nitric-oxide-releasing chitosan/PVA hydrogel accelerate diabetic wound healing in rabbits. *Biomed. Mat.* 16, 035014. doi:10.1088/1748-605X/abc28b

Akhlaq, M., Azad, A. K., Ullah, I., Nawaz, A., Safdar, M., Bhattacharya, T., et al. (2021). Methotrexate-loaded gelatin and polyvinyl alcohol (gel/PVA) hydrogel as a pH-sensitive matrix. *Polymers* 13, 2300. doi:10.3390/polym13142300

Bliden, K. P., Patrick, J., Pennell, A. T., Tantry, U. S., and Gurbel, P. A. (2016). Drug delivery and therapeutic impact of extended-release acetylsalicylic acid. *Futur. Cardiol.* 12, 45–58. doi:10.2217/fca.15.60

Bobbert, F. S. L., Lietaert, K., Eftekhari, A. A., Pouran, B., Ahmadi, S. M., Weinans, H., et al. (2017). Additively manufactured metallic porous biomaterials based on minimal surfaces: A unique combination of topological, mechanical, and mass transport properties. *Acta Biomater.* 53, 572–584. doi:10.1016/j.actbio.2017.02.024

Cavagni, J., Muniz, F. W. M. G., and Rösing, C. K. (2016). The effect of inflammatory response modulator agents on gingivitis and periodontitis. *RGO, Rev. Gaúch. Odontol.* 64, 312–319. doi:10.1590/1981-86372016000300000112165

Chaudhuri, O., Gu, L., Klumpers, D., Darnell, M., Bencherif, S. A., Weaver, J. C., et al. (2016). Hydrogels with tunable stress relaxation regulate stem cell fate and activity. *Nat. Mat.* 15, 326–334. doi:10.1038/nmat4489

Chocholata, P., Kulda, V., Dvorakova, J., Kolaja Dobra, J., and Babuska, V. (2020). Biological evaluation of polyvinyl alcohol hydrogels enriched by hyaluronic acid and hydroxyapatite. *Int. J. Mol. Sci.* 21, 5719. doi:10.3390/ijms21165719

Clària, J., and Serhan, C. N. (1995). Aspirin triggers previously undescribed bioactive eicosanoids by human endothelial cell-leukocyte interactions. *Proc. Natl. Acad. Sci. U.S.A.* 92, 9475–9479. doi:10.1073/pnas.92.21.9475

Esposito, M., Grusovin, M., Worthington, H., Coulthard, P., and Ryan, P. C. (2006). Interventions for replacing missing teeth: Bone augmentation techniques for dental implant treatment. *Aust. Dent. J.* 51, 96–97. doi:10.1111/j.1834-7819.2006.tb00409.x

Fang, Y., Li, H., Chen, J., Xiong, Y., Li, X., Zhou, J., et al. (2022). Highly water-absorptive and antibacterial hydrogel dressings for rapid postoperative detumescence. *Front. Bioeng. Biotechnol.* 10, 845345. doi:10.3389/fbioe.2022.845345

Fasolino, I., Raucci, M. G., Soriente, A., Demitri, C., Madaghiele, M., Sannino, A., et al. (2019). Osteoinductive and anti-inflammatory properties of chitosan-based scaffolds for bone regeneration. *Mat. Sci. Eng. C* 105, 110046. doi:10.1016/j.msec.2019.110046

Fattahi, R., mohebichamkhorami, F., Khani, M. M., Soleimani, M., and Hosseinzadeh, S. (2022). Aspirin effect on bone remodeling and skeletal regeneration: Review article. *Tissue Cell* 76, 101753. doi:10.1016/j.tice.2022.101753

Fong, Y.-C., Maa, M.-C., Tsai, F.-J., Chen, W.-C., Lin, J.-G., Jeng, L.-B., et al. (2008). Osteoblast-derived TGF-β1 stimulates IL-8 release through AP-1 and NF-κB in human cancer cells. *J. Bone Min. Res.* 23, 961–970. doi:10.1359/jbmr.080206

Gazivoda, D., Dzopalic, T., Bozic, B., Tatomirovic, Z., Brkic, Z., and Colic, M. (2009). Production of proinflammatory and immunoregulatory cytokines by inflammatory cells from periapical lesions in culture. *J. Oral Pathol. Med.* 38, 605–611. doi:10.1111/j.1600-0714.2009.00788.x

González Ocampo, J. I., Machado de Paula, M. M., Bassous, N. J., Lobo, A. O., Ossa Orozco, C. P., and Webster, T. J. (2019). Osteoblast responses to injectable bone substitutes of kappa-carrageenan and nano hydroxyapatite. *Acta Biomater.* 83, 425–434. doi:10.1016/j.actbio.2018.10.023

Goto, R., Nishida, E., Kobayashi, S., Aino, M., Ohno, T., Iwamura, Y., et al. (2021). Gelatin methacryloyl–riboflavin (GelMA–RF) hydrogels for bone regeneration. *Int. J. Mol. Sci.* 22, 1635. doi:10.3390/ijms22041635

Han, Y., Yang, J., Zhao, W., Wang, H., Sun, Y., Chen, Y., et al. (2021). Biomimetic injectable hydrogel microspheres with enhanced lubrication and controllable drug release for the treatment of osteoarthritis. *Bioact. Mat.* 6, 3596–3607. doi:10.1016/j.bioactmat.2021.03.022

Hao, M., Zhang, Z., Liu, C., Tian, Y., Duan, J., He, J., et al. (2021). Hydroxyapatite nanorods function as safe and effective growth factors regulating neural differentiation and neuron development. *Adv. Mat.* 33, 2100895. doi:10.1002/adma.202100895

Hegde, R., Prasad, K., and Shroff, K. (2016). Maxillary sinus augmentation using sinus membrane elevation without grafts - a Systematic Review. *J. Indian Prosthodont.* 16, 317. doi:10.4103/0972-4052.191289

Ji, M., Li, H., Guo, H., Xie, A., Wang, S., Huang, F., et al. (2016). A novel porous aspirin-loaded (GO/CTS-HA) n nanocomposite films: Synthesis and multifunction for bone tissue engineering. *Carbohydr. Polym.* 153, 124–132. doi:10.1016/j.carbpol.2016.07.078

Ji, X., Yuan, X., Ma, L., Bi, B., Zhu, H., Lei, Z., et al. (2020). Mesenchymal stem cell-loaded thermosensitive hydroxypropyl chitin hydrogel combined with a three-dimensional-printed poly(ε-caprolactone)/nano-hydroxyapatite scaffold to repair bone defects via osteogenesis, angiogenesis and immunomodulation. *Theranostics* 10, 725–740. doi:10.7150/thno.39167

Jiang, Y., Pan, X., Yao, M., Han, L., Zhang, X., Jia, Z., et al. (2021). Bioinspired adhesive and tumor microenvironment responsive nanoMOFs assembled 3D-printed scaffold for anti-tumor therapy and bone regeneration. *Nano Today* 39, 101182. doi:10.1016/j.nantod.2021.101182

Kang, M., Lee, C.-S., and Lee, M. (2021). Bioactive scaffolds integrated with liposomal or extracellular vesicles for bone regeneration. *Bioengineering* 8, 137. doi:10.3390/bioengineering8100137

Kargozar, S., Ramakrishna, S., and Mozafari, M. (2019). Chemistry of biomaterials: Future prospects. *Curr. Opin. Biomed. Eng.* 10, 181–190. doi:10.1016/j.cobme.2019.07.003

Karimipour-Fard, P., Jeffrey, M. P., JonesTaggart, H., Pop-Iliev, R., and Rizvi, G. (2021). Development, processing and characterization of Polycaprolactone/Nano-Hydroxyapatite/Chitin-Nano-Whisker nanocomposite filaments for additive manufacturing of bone tissue scaffolds. *J. Mech. Behav. Biomed. Mat.* 120, 104583. doi:10.1016/j.jmbbm.2021.104583

Li, J. J., Ebied, M., Xu, J., and Zreiqat, H. (2018). Current approaches to bone tissue engineering: The interface between biology and engineering. *Adv. Healthc. Mat.* 7, 1701061. doi:10.1002/adhm.201701061

Liao, J., Shi, K., Jia, Y., Wu, Y., and Qian, Z. (2021). Gold nanorods and nanohydroxyapatite hybrid hydrogel for preventing bone tumor recurrence via postoperative photothermal therapy and bone regeneration promotion. *Bioact. Mat.* 6, 2221–2230. doi:10.1016/j.bioactmat.2021.01.006

Liu, S., Huang, D., Hu, Y., Zhang, J., Chen, B., Zhang, H., et al. (2020a). Sodium alginate/collagen composite multiscale porous scaffolds containing poly(ε-caprolactone) microspheres fabricated based on additive manufacturing technology. *RSC Adv.* 10, 39241–39250. doi:10.1039/D0RA04581K

Liu, S., Zheng, Y., Wu, Z., Hu, J., and Liu, R. (2020b). Preparation and characterization of aspirin-loaded polylactic acid/graphene oxide biomimetic nanofibrous scaffolds. *Polymer* 211, 123093. doi:10.1016/j.polymer.2020.123093

Liu, Y., Wang, L., Kikuiri, T., Akiyama, K., Chen, C., Xu, X., et al. (2011). Mesenchymal stem cell–based tissue regeneration is governed by recipient T lymphocytes via IFN-γ and TNF-α. *Nat. Med.* 17, 1594–1601. doi:10.1038/nm.2542

Liu, Y., Wei, H., Wang, Z., Li, Q., and Tian, N. (2018). Simultaneous enhancement of strength and toughness of PLA induced by miscibility variation with PVA. *Polymers* 10, 1178. doi:10.3390/polym10101178

Liu, Y., Zhang, Y., Zheng, Z., Zhong, W., Wang, H., Lin, Z., et al. (2022). Incorporation of NGR1 promotes bone regeneration of injectable HA/nHAp hydrogels by anti-inflammation regulation via a MAPK/ERK signaling pathway. *Front. Bioeng. Biotechnol.* 10, 992961. doi:10.3389/fbioe.2022.992961

Maji, K., Dasgupta, S., Bhaskar, R., and Gupta, M. K. (2020). Photo-crosslinked alginate nano-hydroxyapatite paste for bone tissue engineering. *Biomed. Mat.* 15, 055019. doi:10.1088/1748-605X/ab9551

Maneewattanapinyo, P., Yeesamun, A., Watthana, F., Panrat, K., Pichayakorn, W., and Suksaeree, J. (2020). Transdermal patches of lidocaine/aspirin ionic liquid drug-loaded gelatin/polyvinyl alcohol composite film prepared by freeze-thawed procedure. *An. Acad. Bras. Cienc.* 92, e20191073. doi:10.1590/0001-3765202020191073

Martínez-Sanmiguel, J. J., G Zarate-Triviño, D., Hernandez-Delgadillo, R., Giraldo-Betancur, A. L., Pineda-Aguilar, N., Galindo-Rodríguez, S. A., et al. (2019). Anti-inflammatory and antimicrobial activity of bioactive hydroxyapatite/silver nanocomposites. *J. Biomater. Appl.* 33, 1314–1326. doi:10.1177/0885328219835995

Mauri, E., Rossi, F., and Sacchetti, A. (2016). Tunable drug delivery using chemoselective functionalization of hydrogels. *Mat. Sci. Eng. C* 61, 851–857. doi:10.1016/j.msec.2016.01.022

Murphy, C. M., Haugh, M. G., and O'Brien, F. J. (2010). The effect of mean pore size on cell attachment, proliferation and migration in collagen–glycosaminoglycan scaffolds for bone tissue engineering. *Biomaterials* 31, 461–466. doi:10.1016/j.biomaterials.2009.09.063

Ozeki, M., and Tabata, Y. (2005). *In vivo* degradability of hydrogels prepared from different gelatins by various cross-linking methods. *J. Biomater. Sci.-Polym* 16, 549–561. doi:10.1163/156856205378373116

Patel, P. P., Buckley, C., Taylor, B. L., Sahyoun, C. C., Patel, S. D., Mont, A. J., et al. (2019). Mechanical and biological evaluation of a hydroxyapatite-reinforced scaffold for bone regeneration. *J. Biomed. Mater Res. A* 107, 732–741. doi:10.1002/jbm.a.36588

Perez, R. A., and Mestres, G. (2016). Role of pore size and morphology in musculo-skeletal tissue regeneration. *Mat. Sci. Eng. C* 61, 922–939. doi:10.1016/j.msec.2015.12.087

Pina, S., Oliveira, J. M., and Reis, R. L. (2015). Natural-Based nanocomposites for bone tissue engineering and regenerative medicine: A review. *Adv. Mat.* 27, 1143–1169. doi:10.1002/adma.201403354

Raina, D. B., Liu, Y., Isaksson, H., Tägil, M., and Lidgren, L. (2020). Synthetic hydroxyapatite: A recruiting platform for biologically active molecules. *Acta Orthop.* 91, 126–132. doi:10.1080/17453674.2019.1686865

Ren, L., Pan, S., Li, H., Li, Y., He, L., Zhang, S., et al. (2018). Effects of aspirin-loaded graphene oxide coating of a titanium surface on proliferation and osteogenic differentiation of MC3T3-E1 cells. *Sci. Rep.* 8, 15143. doi:10.1038/s41598-018-33353-7

Rezwan, K., Chen, Q. Z., Blaker, J. J., and Boccaccini, A. R. (2006). Biodegradable and bioactive porous polymer/inorganic composite scaffolds for bone tissue engineering. *Biomaterials* 27, 3413–3431. doi:10.1016/j.biomaterials.2006.01.039

Schaap-Oziemlak, A. M., Kühn, P. T., van Kooten, T. G., and van Rijn, P. (2014). Biomaterial–stem cell interactions and their impact on stem cell response. *RSC Adv.* 4, 53307–53320. doi:10.1039/C4RA07915A

Schmitz, J. P., and Hollinger, J. O. (1986). The critical size defect as an experimental model for craniomandibulofacial nonunions. *Clin. Orthop. Rel. Res.* 205, 299–308. doi:10.1097/00003086-198604000-00036

Shaabani, A., Sedghi, R., Motasadizadeh, H., and Dinarvand, R. (2021). Self-healable conductive polyurethane with the body temperature-responsive shape memory for bone tissue engineering. *Chem. Eng. J.* 411, 128449. doi:10.1016/j.cej.2021.128449

Shuai, C., Yang, W., Feng, P., Peng, S., and Pan, H. (2021). Accelerated degradation of HAP/PLLA bone scaffold by PGA blending facilitates bioactivity and osteoconductivity. *Bioact. Mat.* 6, 490–502. doi:10.1016/j.bioactmat.2020.09.001

Sreekumaran, S., Radhakrishnan, A., Rauf, A. A., and Kurup, G. M. (2021). Nanohydroxyapatite incorporated photocrosslinked gelatin methacryloyl/poly (ethylene glycol)diacrylate hydrogel for bone tissue engineering. *Prog. Biomater.* 10, 43–51. doi:10.1007/s40204-021-00150-x

Sun, M., Cheng, L., Xu, Z., Chen, L., Liu, Y., Xu, Y., et al. (2022). Preparation and characterization of vancomycin hydrochloride-loaded mesoporous silica composite hydrogels. *Front. Bioeng. Biotechnol.* 10, 826971. doi:10.3389/fbioe.2022.826971

Suvarnapathaki, S., Wu, X., Lantigua, D., Nguyen, M. A., and Camci-Unal, G. (2020). Hydroxyapatite-incorporated composite gels improve mechanical properties and bioactivity of bone scaffolds. *Macromol. Biosci.* 20, 2000176. doi:10.1002/mabi.202000176

Tan, G., Chen, R., Tu, X., Guo, L., Guo, L., Xu, J., et al. (2022). Research on the osteogenesis and biosafety of ECM–loaded 3D–printed gel/SA/58sBG scaffolds. *Front. Bioeng. Biotechnol.* 10, 973886. doi:10.3389/fbioe.2022.973886

Tang, J., Xiong, J., Wu, T., Tang, Z., Ding, G., Zhang, C., et al. (2014). Aspirin treatment improved mesenchymal stem cell immunomodulatory properties via the 15d-PGJ_2/PPARγ/TGF-β1 pathway. *Stem Cells Dev.* 23, 2093–2103. doi:10.1089/scd.2014.0081

Tao, Z.-S., Wu, X.-J., Zhou, W.-S., Wu, X., Liao, W., Yang, M., et al. (2019). Local administration of aspirin with β-tricalcium phosphate/poly-lactic-co-glycolic acid (β-TCP/PLGA) could enhance osteoporotic bone regeneration. *J. Bone Min. Metab.* 37, 1026–1035. doi:10.1007/s00774-019-01008-w

Tao, Z.-S., Zhou, W.-S., Xu, H.-G., and Yang, M. (2020). Aspirin modified strontium-doped β-tricalcium phosphate can accelerate the healing of femoral metaphyseal defects in ovariectomized rats. *Biomed. Pharmacother.* 132, 110911. doi:10.1016/j.biopha.2020.110911

Tohamy, K. M., Mabrouk, M., Soliman, I. E., Beherei, H. H., and Aboelnasr, M. A. (2018). Novel alginate/hydroxyethyl cellulose/hydroxyapatite composite scaffold for bone regeneration: *In vitro* cell viability and proliferation of human mesenchymal stem cells. *Int. J. Biol. Macromol.* 112, 448–460. doi:10.1016/j.ijbiomac.2018.01.181

Uemura, A., Ogawa, S., Isono, Y., and Tanaka, R. (2019). Elucidation of the time-dependent degradation process in insoluble hyaluronic acid formulations with a controlled degradation rate. *J. Tissue Eng.* 10, 204173141988503. doi:10.1177/2041731419885032

Wang, B., Wan, Y., Zheng, Y., Lee, X., Liu, T., Yu, Z., et al. (2019). Alginate-based composites for environmental applications: A critical review. *Crit. Rev. Environ. Sci. Technol.* 49, 318–356. doi:10.1080/10643389.2018.1547621

Wang, L., Pathak, J. L., Liang, D., Zhong, N., Guan, H., Wan, M., et al. (2020). Fabrication and characterization of strontium-hydroxyapatite/silk fibroin biocomposite nanospheres for bone-tissue engineering applications. *Int. J. Biol. Macromol.* 142, 366–375. doi:10.1016/j.ijbiomac.2019.09.107

Wei, Y., Liu, Z., Zhu, X., Jiang, L., Shi, W., Wang, Y., et al. (2020). Dual directions to address the problem of aseptic loosening via electrospun PLGA @ aspirin nanofiber coatings on titanium. *Biomaterials* 257, 120237. doi:10.1016/j.biomaterials.2020.120237

Xia, J., Yuan, Y., Wu, H., Huang, Y., and Weitz, D. A. (2020). Decoupling the effects of nanopore size and surface roughness on the attachment, spreading and differentiation of bone marrow-derived stem cells. *Biomaterials* 248, 120014. doi:10.1016/j.biomaterials.2020.120014

Xie, Y., Pan, M., Gao, Y., Zhang, L., Ge, W., and Tang, P. (2019). Dose-dependent roles of aspirin and other non-steroidal anti-inflammatory drugs in abnormal bone remodeling and skeletal regeneration. *Cell Biosci.* 9, 103. doi:10.1186/s13578-019-0369-9

Xu, M., Qin, M., Zhang, X., Zhang, X., Li, J., Hu, Y., et al. (2020). Porous PVA/SA/HA hydrogels fabricated by dual-crosslinking method for bone tissue engineering. *J. Biomater. Sci.-Polym* 31, 816–831. doi:10.1080/09205063.2020.172015531

Xu, X., Gu, Z., Chen, X., Shi, C., Liu, C., Liu, M., et al. (2019). An injectable and thermosensitive hydrogel: Promoting periodontal regeneration by controlled-release of aspirin and erythropoietin. *Acta Biomater.* 86, 235–246. doi:10.1016/j.actbio.2019.01.001

Yamaza, T., Miura, Y., Bi, Y., Liu, Y., Akiyama, K., Sonoyama, W., et al. (2008). Pharmacologic stem cell based intervention as a new approach to osteoporosis treatment in rodents. *PLoS ONE* 3, e2615. doi:10.1371/journal.pone.0002615

Yang, L., Yang, J., Qin, X., Kan, J., Zeng, F., and Zhong, J. (2020). Ternary composite films with simultaneously enhanced strength and ductility: Effects of sodium alginate-gelatin weight ratio and graphene oxide content. *Int. J. Biol. Macromol.* 156, 494–503. doi:10.1016/j.ijbiomac.2020.04.057

Yu, Y., Xie, K., Xie, L., and Deng, Y. (2021). Endowing polyetheretherketone with anti-inflammatory ability and improved osteogenic ability. *J. Biomater. Sci.-Polym. Ed.* 32, 42–59. doi:10.1080/09205063.2020.1815634

Zhang, S., Han, D., Ding, Z., Wang, X., Zhao, D., Hu, Y., et al. (2019). Fabrication and characterization of one interpenetrating network hydrogel based on sodium alginate and polyvinyl alcohol. *J. Wuhan. Univ. Technol.-Mat. Sci. Ed.* 34, 744–751. doi:10.1007/s11595-019-2112-0

Zhang, X., Miao, F., Niu, L., Wei, Y., Hu, Y., Lian, X., et al. (2021). Berberine carried gelatin/sodium alginate hydrogels with antibacterial and EDTA-induced detachment performances. *Int. J. Biol. Macromol.* 181, 1039–1046. doi:10.1016/j.ijbiomac.2021.04.114

Zhang, Y., Dou, X., Zhang, L., Wang, H., Zhang, T., Bai, R., et al. (2022). Facile fabrication of a biocompatible composite gel with sustained release of aspirin for bone regeneration. *Bioact. Mat.* 11, 130–139. doi:10.1016/j.bioactmat.2021.09.033

Zhang, Y., Xiong, Y., Chen, X., Chen, C., Zhu, Z., and Li, L. (2018). Therapeutic effect of bone marrow mesenchymal stem cells pretreated with acetylsalicylic acid on experimental periodontitis in rats. *Int. Immunopharmacol.* 54, 320–328. doi:10.1016/j.intimp.2017.11.028

Zhao, Q., Wu, J., Li, Y., Xu, R., Zhu, X., Jiao, Y., et al. (2022). Promotion of bone formation and antibacterial properties of titanium coated with porous Si/Ag-doped titanium dioxide. *Front. Bioeng. Biotechnol.* 10, 1001514. doi:10.3389/fbioe.2022.1001514

frontiers | Frontiers in Bioengineering and Biotechnology

TYPE Original Research
PUBLISHED 25 January 2023
DOI 10.3389/fbioe.2023.1113367

OPEN ACCESS

EDITED BY
Jianyun Zhang,
Peking University Hospital of Stomatology, China

REVIEWED BY
Cheng Hu,
Sichuan University, China
Rongbing Tang,
Lanzhou University, China

*CORRESPONDENCE
Sheng Yang,
ysdentist@hospital.cqmu.edu.cn

†These authors have contributed equally to this work

SPECIALTY SECTION
This article was submitted to Biomaterials, a section of the journal Frontiers in Bioengineering and Biotechnology

RECEIVED 01 December 2022
ACCEPTED 13 January 2023
PUBLISHED 25 January 2023

CITATION
Deng Y, Ren M, He P, Liu F, Wang X, Zhou C, Li Y and Yang S (2023), Genetically engineered cell membrane-coated nanoparticles for antibacterial and immunoregulatory dual-function treatment of ligature-induced periodontitis.
Front. Bioeng. Biotechnol. 11:1113367.
doi: 10.3389/fbioe.2023.1113367

Genetically engineered cell membrane-coated nanoparticles for antibacterial and immunoregulatory dual-function treatment of ligature-induced periodontitis

Yangjia Deng[1,2,3†], Mingxing Ren[1,2,3†], Ping He[1,2,3†], Fengyi Liu[1,2,3], Xu Wang[1,2,3], Chongjing Zhou[1,2,3], Yuzhou Li[1,2,3] and Sheng Yang[1,2,3*]

[1]College of Stomatology, Chongqing Medical University, Chongqing, China, [2]Chongqing Key Laboratory of Oral Diseases and Biomedical Sciences, Chongqing, China, [3]Chongqing Municipal Key Laboratory of Oral Biomedical Engineering of Higher Education, Chongqing, China

Purpose: In order to overcome the problem that conventional pharmacological treatments of periodontitis cannot effectively synergizing antimicrobial and immunomodulation, inspired by the critical role of toll-like receptor 4 (TLR4) in bacterial recognition and immune activation, we demonstrated a combined antibacterial-immunoregulatory strategy based on biomimetic nanoparticles.

Methods: Functioned cell membranes and silk fibroin nanoparticles (SNs) loaded with minocycline hydrochloride (Mino) were used to prepare a biomimetic nanoparticle (MSNCs). SNs and MSNCs were characterized by Scanning Electron Microscope, size, zeta potential, dispersion index. At the same time, SNs were characterized by cell counting kit-8 and real-time Polymerase Chain Reaction (RT-PCR). TLR4-expressing cell membranes were characterized by RT-PCR and western blot (WB). Cell membrane coating was characterized by Transmission Electron Microscope (TEM), the Bradford staining and WB. Then, Laser confocal, flow cytometry and agar plate coating were evaluated in vitro with antibacterial effects, RT-PCR was simultaneously evaluated with immunoregulatory effects. Finally, Anti-inflammatory treatment of MSNCs was evaluated in a ligature-induced periodontitis (LIP) mouse model.

Results: Successfully prepared cell membranes overexpressing TLR4 and constructed MSNCs. *In vitro* studies had shown that MSNCs effectively targeted bacteria via TLR4 and acted as molecular decoys to competitively neutralize lipopolysaccharide (LPS) in the microenvironment as well as inhibit inflammatory activation of macrophages. *In vivo*, MSNCs effectively attenuated periodontal tissue inflammation and alveolar bone loss in a LIP mouse model.

Conclusion: MSNCs have good targeted antibacterial and immunoregulatory effects, and provide a new and effective strategy for the treatment of periodontitis and have good potential for application in various types of pathogenic bacterial infections.

KEYWORDS

cell membrane coating, biomimetic nanoparticles, periodontitis, antibacterial therapy, immune regulation, TLR4

1 Introduction

The high prevalence of periodontitis is not only a major cause of tooth loss, but also a potential risk factor for diseases such as rheumatoid arthritis, cardiovascular disease and gastric cancer (Kinane et al., 2017; Hoare et al., 2019; Chen et al., 2021). The pathological features of periodontitis are mainly characterized by bacterial infection and local immune disorders, therefore antimicrobial therapy and regional immunomodulation are important tools in the treatment of periodontitis (Teng et al., 2000). However, the conventional mechanical treatment-based modalities still suffer from the problem of easy reattachment of plaque after treatment, which affects the therapeutic effectiveness (Slot et al., 2020). Therefore, basic treatment followed by adjuvant pharmacotherapy is increasingly considered to be the key to better treatment of periodontitis. Nevertheless, the current pharmacological treatment regimens for periodontitis still suffer from incomplete elimination of pathogenic bacteria and lack of improvement in immune dysfunction (Szulc et al., 2018). Consequently, the development of therapeutic regimens with both antibacterial and local immunoregulatory functions for the specific pathological microenvironment of periodontitis would help to solve the current dilemma.

It is well known that innate immunity, as the first line of defense against bacterial invasion, relies heavily on pattern recognition receptors (PRRs) (Zhou et al., 2018). In particular, recognition of pathogenic bacteria by neutrophils, macrophages and dendritic cells through toll-like receptors (TLR) is a key pathway for activating innate immunity (Federico et al., 2020). Numerous studies have found that LPS is one of the most important components of bacterial immune stimulation in periodontitis and is a key factor in periodontitis triggering systemic inflammation and sepsis (Rathinam et al., 2019). TLR4, as the predominant bacterial endotoxin receptor that recognizes innate immunity, plays a vital role in the activation of the immune response in periodontitis (Gu and Han, 2020). Innate immune cells recognize LPS released by bacteria in the microenvironment through TLR4 and activate inflammatory signaling pathways. In addition, they can also recognize and capture bacteria through TLR4 binding to LPS on the bacterial surface (Tsukamoto et al., 2018; Wang et al., 2018). Therefore, TLR4 in immune activation wound provide innovative thinking for the treatment of periodontitis. However, synergistic TLR4-based therapeutic approaches for precise antibacterial and immunoregulatory remain to be developed.

Nanodelivery systems are an important means to achieve targeted drug delivery and local immunomodulation (Sahu et al., 2021). Targeted drug delivery using nanoparticles is usually functionally modified using cationic groups (Hu et al., 2017; Huang et al., 2017), peptides (Huang et al., 2017), antibodies (Lambert and Berkenblit, 2018), *etc.* Surface membrane biomimetic modification of nanoparticles is a novel and efficient way. The cell membrane is coated around the nanoparticle surface by physical extrusion, ultrasonic or electroporation methods, which gives the nanoparticles bionic properties and preserves the protein function of the source cell membrane (Ai et al., 2020; Zou et al., 2020). For example, erythrocyte membranes (Zhang L. et al., 2018), leukocyte membranes (Parodi et al., 2013), platelet membranes (Li et al., 2018), and bacterial membranes (Gao et al., 2015) have been successfully used to prepare membrane-coated nanoparticles and provide an effective targeting delivery platform for antimicrobial and antitumor therapies. Additionally, the innovative applications of genetic engineering technologies can overexpress or newly express desired target proteins on cell membrane, highlighting and amplifying the functions of the key proteins (Ai et al., 2020), which also provides more expansion possibilities for the application of cell membrane bionanotechnology in targeted drug delivery and immune microenvironment modulation.

Herein, inspired by the critical role of TLR4 in the recognition of pathogenic bacteria invasion and activation of inflammatory responses, we have innovatively developed a TLR4-expressing nanoplatform with cell membrane bionic effects. The nanoplatform was genetically engineered to construct TLR4-expressing RAW264.7 macrophages and extract their cell membranes, and then the functionalized cell membranes were physically extruded to coat the surface of SNs loaded with the antimicrobial agent MINO to prepare nanodelivery systems MSNCs. With this novel dual-functional construction strategy, nanoparticles with both targeted bactericidal and immunomodulatory functions were successfully synthesized. *In vitro* experiments demonstrated that MSNCs had good targeting to *Escherichia coli* (*E. coli*) and can release antibacterial drugs to kill bacteria efficiently. Moreover, they effectively inhibited the inflammatory activation of macrophages by neutralizing LPS in the microenvironment. *In vivo* studies showed that MSNCs effectively suppressed periodontal inflammation and reduced alveolar bone resorption in a ligature-induced periodontitis (LIP) mouse model (Figure 1).

2 Materials and methods

2.1 Reagents and materials

Bombyx mori (B.mori) cocoons were donated from Southwest University (Chongqing, China); TLR4 lentivirus was purchased from Genechem Co. (Shanghai, China); FITC and LPS were purchased from Sigma-Aldrich (St. Louis, MO, United States); Cell counting kit-8 was purchased from MCE (New Jersey, United States); Sodium carbonate, lithium bromide, paraformaldehyde and hematoxylin, and eosin staining kit were purchased from Solarbio Science and Technology Co. (Beijing, China); acetone was purchased from CHUANDONG CHEMICAL (Chongqing, China); Membrane and Cytosol Protein Extraction Kit, Dil, BCA Protein Assay Kit and DAPI were purchased from Beyotime Biotechnology (Shanghai, China).

2.2 Cell and bacterial culture

RAW264.7 cells is a macrophage cell line (American Type Culture Collection, ATCC) that was established from a tumor in a male mouse induced with the Abelson murine leukemia virus. And the cell line was used for macrophage membranes collection in the current study. RAW264.7 cells cultured in Dulbecco's modified Eagle's medium (H-DMEM, Sigma) supplemented with 10% fetal bovine serum (FBS, Excell Bio) and 1% penicillin-streptomycin (HyClone, United States) at 37°C in a 5% CO_2 atmosphere. Gram-negative bacteria *E. coli* (ATCC 43888) was grown in LB medium at 37°C in an aerobic environment, and bacteria used in all experiments were in the mid-exponential growth period. The bacterial suspension was

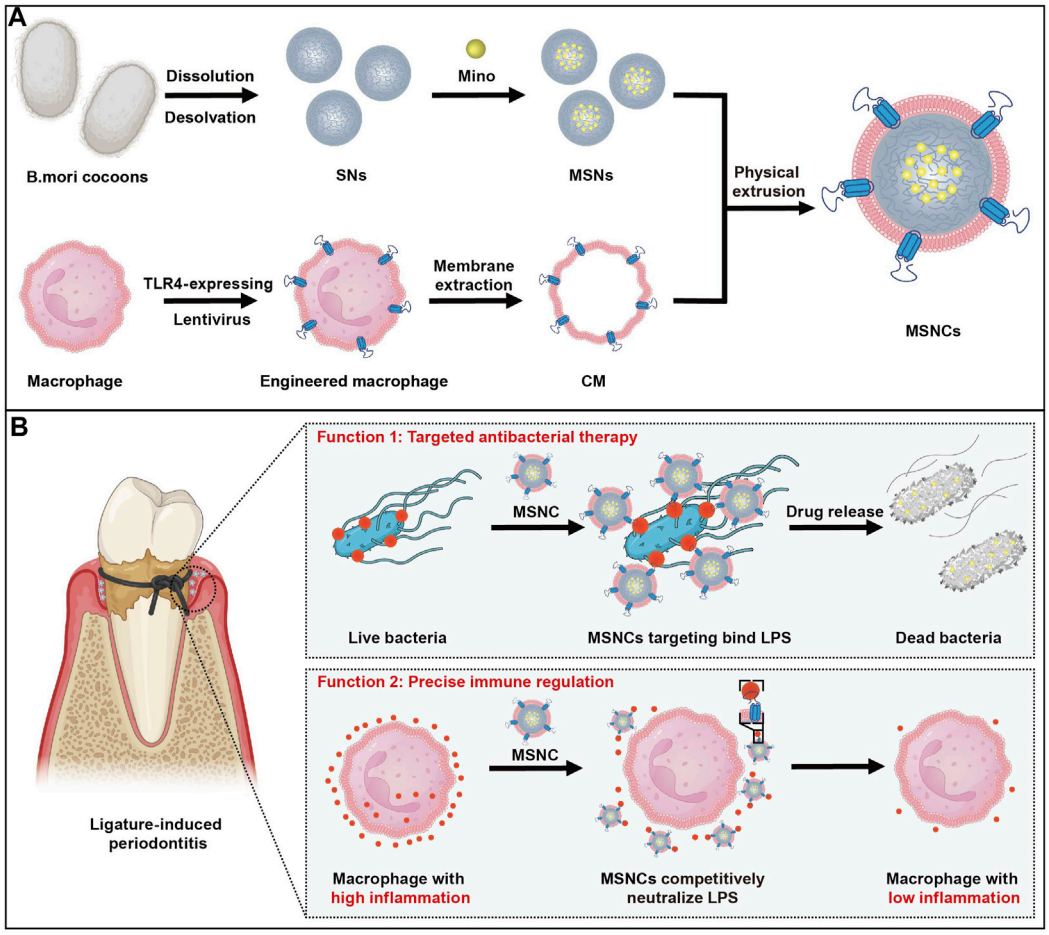

FIGURE 1
The fabrication and application of functioned cell membrane coated silk fibroin nanoparticles loaded with minocycline hydrochloride. **(A)** MSNCs are fabricated by coating engineered macrophage membranes onto SNs. **(B)** Application of MSNCs with targeted antimicrobial and precise immune regulation through topical administration of periodontitis.

diluted to $1*10^6$ colony forming units (CFU per mL) for experimental use after measuring the optical density at 600 nm using a microplate reader (ELX800, Gene Company Limited, China).

2.3 Preparation and characterization of SNs

Silk fibroin solution was prepared as previously described (Xiang et al., 2022). Briefly, B.mori cocoons were cut into pieces and then boiled in 0.02 M sodium carbonate for 60 min and then completely rinsed and dried in the convection oven at 37°C for 24 h. Next, the degummed silk fibroin was dissolved using 9.3 M lithium bromide at 60°C for 4 h and dialyzed in double-distilled water for 72 h. Then, the silk fibroin solution was purified by centrifugation at 5,000 rpm. As reported in the literature (Wongpinyochit et al., 2016), 5% silk fibroin solution was added dropwise to acetone, and nanoparticles were precipitated using a high-speed centrifuge at 32,000 g for 2 h at 4°C. The supernatant was removed and resuspended in double-distilled water, the nanoparticles were dispersed by vortex and ultrasound probe, and repeated twice. Finally, the nanoparticles were resuspended using double-distilled water and stored at 4°C until used. The morphology of SNs was observed by scanning electron microscopy (Hitachi SU8010, Japan). Mean particle size and potential were detected by a dynamic light scattering (DLS) detector (Brookhaven NanoBrook Omni, United States). Cytotoxicity assay was verified by cell counting kit-8. Biocompatibility was confirmed by real-time polymerase chain reaction (Bio-Rad, United States).

2.4 Mino loading assay of SNs

Add the corresponding mass of Mino in SNs suspension at different mass ratios (Mino: SNs = 0.125, 0.375, 0.5) and stir away from light overnight at room temperature. The supernatant was centrifuged at 32,000 g for 30 min, and the double-distilled water was resuspended and repeatedly washed twice before being stored at 4°C, protected from light. The supernatant was collected and used to calculate the encapsulation efficiency and drug loading efficiency. The equations of drug loading and encapsulation efficiency were described as follows:

$$\text{Drug loading efficiency} = \frac{\text{Weight of feeded drug} - \text{Drug amount in supernatant}}{\text{Weight of dry NPs}} \times 100\,\%$$

$$\text{Encapsulation efficiency} = \frac{\text{Weight of feeded drug} - \text{Drug amount in supernatant}}{\text{Weight of feeded drug}} \times 100\,\%$$

TABLE 1 The prime sequences of all genes used in RT-PCR.

Gene	Forward primer (5′–3′)	Reverse primer (5′–3′)
TLR4	TTCACCTCTGCCTTCACTACA	GGGACTTCTCAACCTTCTCAA
IL-1β	TTGAAGTTGACGGACCCCA	GAGTGATACTGCCTGCCT GAAG
IL-6	GTTGCCTTCTTGGGACTGATG	TTGGGAGTGGTATCCTCT GTGA
GAPDH	GCACCGTCAAGGCTGAGAAC	TGGTGAAGACGCCAGTGGA

2.5 Genetic engineering of RAW264.7

Lentiviral transfection of RAW264.7 cells was performed according to the product instructions. Briefly, RAW264.7 cells (50 000/well) were incubated for 12 h, then appropriate H-DMEM, TLR4 lentivirus (MOI = 50), and empty lentivirus were added separately to the culture medium for 10 h. After 48 h of incubation, the cells were harvested for the TLR4 mRNA levels by RT-PCR. Among them, the medium-treated group served as the control group for the experiment, the blank vector lentivirus group served as the negative control (NC) group, and the TLR4 lentivirus-treated group served as the TLR4 group. The sequences of the primers (Takara, Japan) were shown in Table 1. Cells were selected by adding 4 μg/mL puromycin in serum-containing medium for 2 days after passaging and continued to transfect the cell line with 2 μg/mL puromycin to maintain steadily for 1 w. An antibody against TLR4 (sc-293072, Santa) was used to detect markers in cell homogenization by Western blot.

2.6 Preparation and characterization of SNCs

CMs extraction was performed according to Membrane and Cytosol Protein Extraction Kit. Briefly, functionalized macrophages were repeatedly rinsed with PBS after collection and cell counting. The cells were resuspended with Membrane Protein Extraction Reagent A containing PMSF. After 10 min of an ice bath, the cell suspension was homogenized using an ultrasonic disruptor and centrifugated at 700 g for 10 min, then the supernatant was collected and centrifugated at 14,000 g for 30 min, and resuspended the precipitate with PBS. Eventually, the concentration of CMs suspension was determined by the BCA method, and the suspension was stored at −80°C for use. The extracted CMs and SNs were mixed in a 1:1 mass ratio and repeatedly extruded through a polycarbonate membrane with the aid of a liposome extruder to obtain MSNCs. The morphology and structure of MSNCs were separately observed by scanning electron microscopy and transmission electron microscopy (JEOL JEM-1400PLUS, Japan). Mean particle size and potential were detected by DLS. Finally, the Bradford method and WB were used to verify the successful coating of the CMs. After preparation of MSNCs, two equal groups of MSNCs were added into dialysis bags with appropriate amount of *E. coli* in one group. The dialysis bags were completely submerged in PBS (PH = 7.4) and drug release was monitored at a constant temperature of 37°C for 0, 1, 4, 8, 12, 24, and 48 h.

2.7 Targeting binding of MSNCs to bacteria *in vitro*

The red fluorescent dye Dil and the green fluorescent dye FITC were used to label CMs and SNs, respectively. Dil -SNCs were prepared by a liposome extruder after mixing Dil with CMs for 2 h at room temperature; FITC-SNs were prepared by mixing SNs with FITC overnight away from light and purified by dialysis. *E. coli* suspension was fixed with paraformaldehyde and washed twice with PBS. Dil-SNCs were added to the experimental group, incubated at 37°C for 1 h, stained with DAPI for 3 min, and resuspended after centrifugation to obtain the suspension. The suspension was dropped on slides for sample preparation and then images were acquired by laser confocal microscopy (Leica TCS SP8, Germany). Meanwhile, after paraformaldehyde fixation of *E. coli*, the experimental groups were incubated with FITC-SNs and FITC-SNC individually for 1 h at 37°C and washed for flow cytometry detection (BD Bioscience, United States).

2.8 Antibacterial effects of MSNCs

E. coli were inoculated on 24-well plates, and SNCs and MSNCs were added to the experimental groups, respectively, and incubated for 24 h in a 37°C bacterial incubator. The incubated mixture was serially diluted and coated on nutrient agar plates, incubated for 24 h in a 37°C bacterial incubator, and photographed to observe the growth of colonies in the plates.

2.9 LPS neutralization of SNCs *in vitro*

RAW264.7 cells were used to detect SNCs biocompatibility and LPS neutralization. Cells were inoculated with a complete Medium in the control group and 40, 80, 120, 160, and 200 μg/mL of SNCs H-DMEM medium suspension in the experimental group, and cell viability was detected using the CCK-8 kit after 24 h of incubation. In addition, the experimental groups were incubated with LPS, LPS + SNs, and LPS + SNCs for 12 h, after being incubated in the cell incubator for 24 h. RT-PCR was performed as before.

2.10 The biological role of MSNCs *in vivo*

6-week-old male C57 mice were provided by the laboratory Animal Center of Chongqing Medical University. Periodontitis molds were completed by ligating the cervical portions of the bilateral maxillary first and second M of C57 mice for 1 week using 5–0 silk wire. To study the diffusion of MSNCs at the site of inflammation, we prepared FITC-labeled MSNCs and injected FITC-MSNCs into the palatal gingiva of mice with ligature-induced periodontitis, collected at 0, 4, and 24 h, and observed their diffusion in the periodontium by fluorescence distribution under a stereomicroscope. Then, all mice were divided into four groups, no treatment in the control group, no treatment in the periodontitis group after completion of periodontal ligation, and the rest of the experimental groups were administered with the effective drug concentration of 0.5 mg/ml in MSNs and MSNCs suspension respectively at the ligated tooth position by drops of 5 μl on each

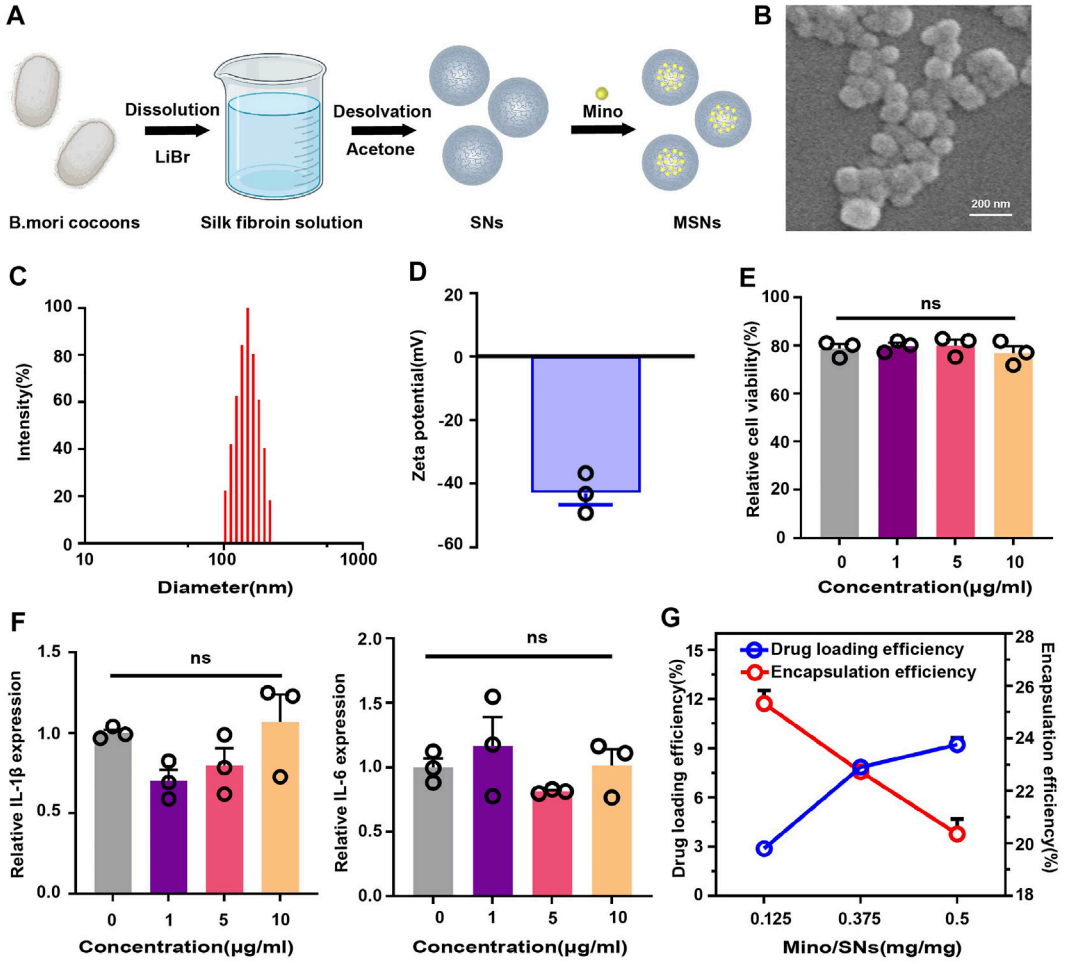

FIGURE 2
Characterization of silk fibroin nanoparticles. **(A)** Schematic illustration of the synthesis of drug-loaded SNs. **(B)** Scanning electron microscopy of SNs. **(C)** Particle size distribution of SNs. **(D)** Zeta potential diagram of SNs. **(E)** CCK-8 of SNs. **(F)** RT-PCR of SNs at different concentrations. **(G)** Drug loading and encapsulation efficiency for different mass ratios of Mino and SNs. Data are presented as means ± SEM, ns $p > 0.5$; by one-way analysis of variance (ANOVA) with Tukey's *post hoc* test **(E** and **F)**.

side for 1 week. Mice were anesthetized and executed after 1 week, and periodontal tissues were taken from bilateral ligated tooth sites for RT-PCR, WB, and Hematoxylin Eosin (HE) staining to detect the inflammatory changes. An antibody against IL-1β (ab9722, Abcam) was used to detect markers in cell homogenization by WB. Animal handling and surgical procedures were performed following the protocol approved by the Ethics Committee of the Affiliated Stomatological Hospital of Chongqing Medical University (2022 (No. 062)).

2.11 Statistical analysis

All experimental data are presented as the mean ± standard error of the mean (SEM), and the results were analyzed using a one-way analysis of variance (ANOVA) among groups followed by Tukey's *post hoc* test. A value of $p < 0.05$ was considered statistically significant ($^{*}p < 0.05$, $^{**}p < 0.01$, $^{***}p < 0.001$, $^{****}p < 0.0001$).

3 Results

3.1 Preparation and characterization of SNs

SNs were prepared by the desolvation method and loaded with Mino (Figure 2A). Scanning electron microscopy showed that the nanoparticles were spherical together with a clear boundary, and the diameter was about 150 nm (Figure 2B). DLS showed that the size of SNs was 114.63 ± 4.55 nm (Figure 2C), zeta surface potential was −39.70 ± 2.77 mV (Figure 2D), and polydispersity index (PDI) was 0.31 ± 0.02. The CCK-8 assay indicated that the viability of RAW264.7 cells had no significant difference ($p > 0.05$) to the increased concentration of SNs (Figure 2E). The gene expression of both IL-1β and IL-6 in RAW264.7 cells was of no meaningful difference ($p > 0.05$) to the increased concentration of SNs (Figure 2F). There different mass ratios of Mino: SNs (Mino: SNs = 0.125, 0.375, 0.5) were examined, and the drug loading efficiency and encapsulation efficiency of Mino were determined, as shown in Figure 2G. When the ratio increased from

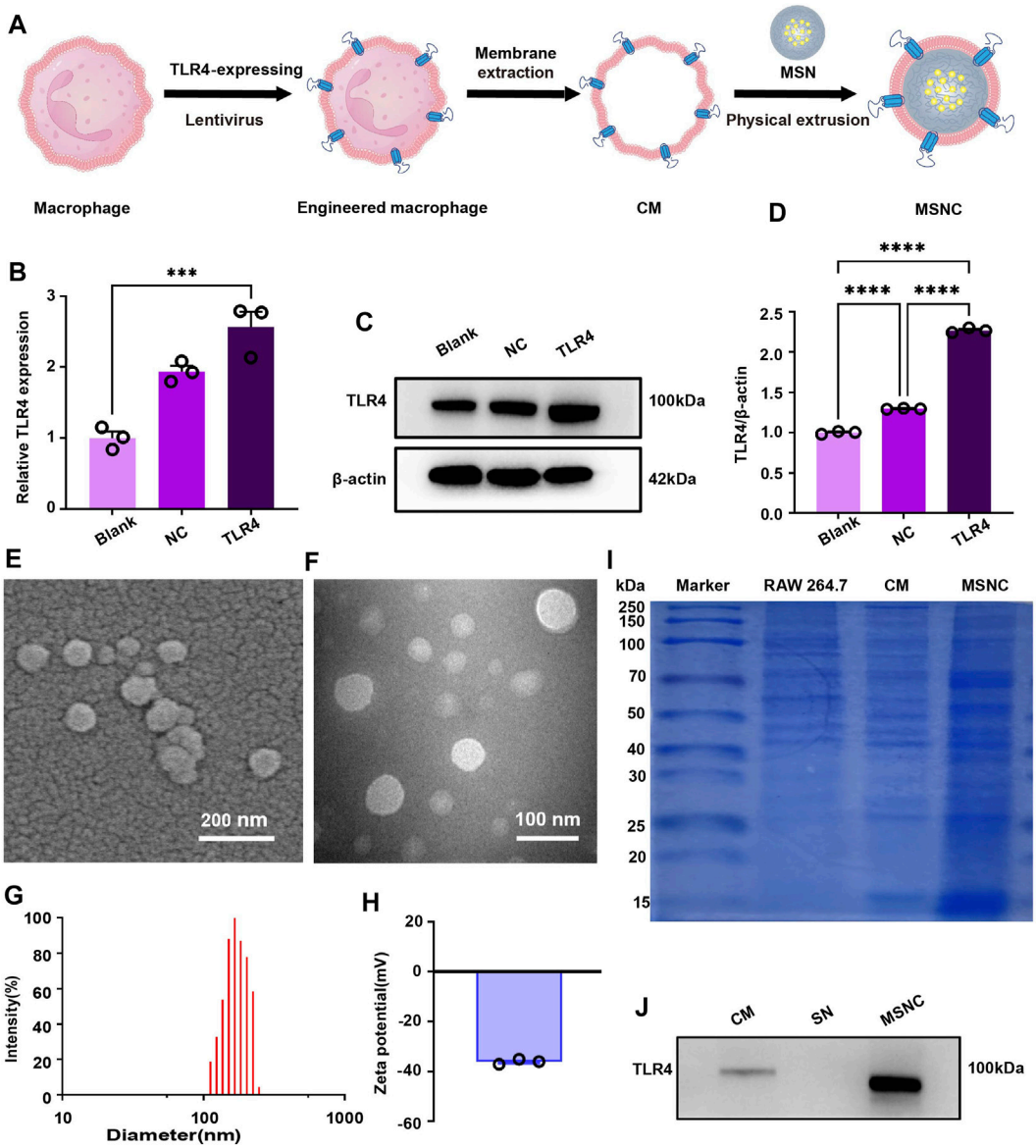

FIGURE 3
Characterization of functioned cell membrane coated silk fibroin nanoparticles loaded with minocycline hydrochloride. **(A)** Schematic illustration of MSNCs. **(B)** TLR4-expressing in RAW264.7 cells by RT-PCR. **(C)** TLR4-expressing in RAW264.7 cells by WB. **(D)** Quantitative analysis of the WB. **(E)** Scanning electron microscopy of MSNCs. **(F)** TEM of MSNCs. **(G)** Particle size distribution of MSNCs. **(H)** Zeta potential diagram of MSNCs. **(I)** The protein composition of MSNCs was verified by SDS-PAGE followed by the Bradford staining. **(J)** The successful translocation of CMs proteins was verified by WB. Data are presented as means ± SEM, ***$p < 0.001$, and ****$p < 0.0001$; by one-way analysis of variance (ANOVA) with Tukey's *post hoc* test **(B,D)**.

0.125 to 0.375, the drug loading efficiency of Mino increased from 2.89% to 7.86%. However, when the ratio increased to 0.5, the drug loading efficiency increased slightly to 9.24%. And the encapsulation decreased all the time from 25.34% to 20.36%. Therefore, Mino and SNs with a mass ratio of 0.375 were chosen for the follow-up experiment owing to their most suitable drug loading rate and encapsulation rate.

3.2 Preparation and characterization of MSNCs

TLR4-expressing RAW264.7 cells were constructed by lentivirus, RT-PCR, and WB assays showed that the TLR4 gene and protein expression had increased in TLR4 treatment, compared control group (Figures 3B–D). After the preparation of MSNCs (Figure 3A), scanning electron microscopy showed that the surface of MSNCs was covered with an unsmooth film structure (Figure 3E), and TEM showed that MSNCs had a ring-like structure, the density of the ring layer was the highest, the density inside the ring was the second highest, and the density outside the ring was the lowest (Figure 3F). The DLS results showed that the MSNCs size was 134.04 ± 1.50 nm (Figure 3G), the zeta potential was −36.09 ± 0.98 mV, and PDI was 0.37 ± 0.98 (Figure 3H). Therefore, the size of MSNCs increased by about 20 nm compared with the size of SNs. Above all, the results of DLS and TEM tentatively proved the successful preparation of MSNCs. As shown in Supplementary

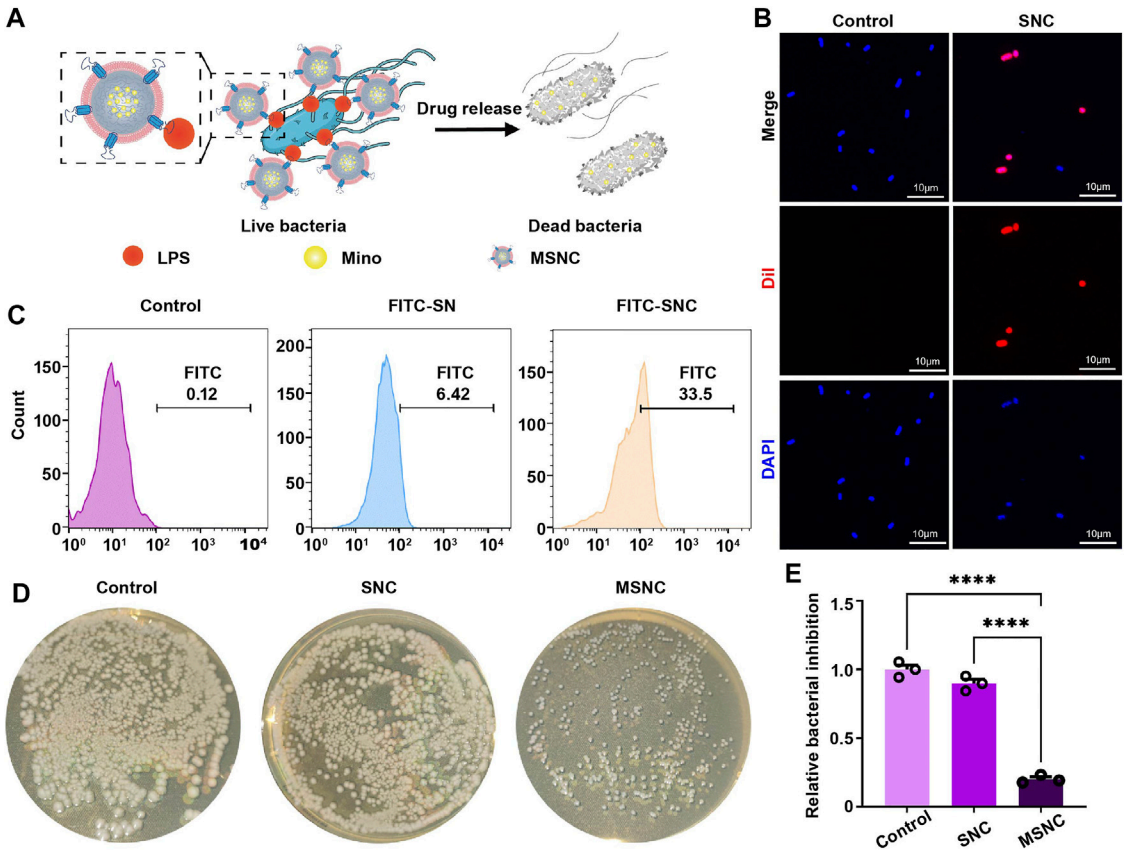

FIGURE 4
Targeting antibacterial effect of functioned cell membrane coated silk fibroin nanoparticles loaded with minocycline hydrochloride. **(A)** Schematic illustration of MSNCs targeting antibacterial effects. **(B)** Probing bacterial targeting using Dil-labeled cell membranes of SNCs with DAPI-labeled bacteria by laser confocal microscopy. **(C)** Probing bacterial targeting using FITC-labeling of SNCs by flow cytometry. **(D)** The antibacterial effect of MSNCs on *E. coli* in agar plates. **(E)** Quantitative analysis of the number of bacteria on agar plates. Data are presented as means ± SEM, ***$p < 0.001$, and ****$p < 0.0001$; by one-way analysis of variance (ANOVA) with Tukey's *post hoc* test **(E)**.

Figure S1, the combination with bacteria does not affect the continuous release of the drug and helps to slow down the initial slow release of the drug, and the later release of the drug is the same as usual.

3.3 Verification of cell membrane coat to MSNCs

The results of protein bands after Bradford staining showed that the three groups of protein bands of cell homogenate, CMs, and MSNCs were similar, indicating that the membrane components were similar, and the protein bands of MSNCs and CMs groups were highly overlapping (Figure 3I). It represented the successful coat of CMs on the surface of MSNCs. Moreover, TLR4 protein was present in both the CMs and MSNCs groups, but no TLR4 protein was expressed in the SNs group, indicating successful translocation of CMs proteins on the MSNCs surface (Figure 3J).

3.4 Targeting binding of SNCs to *E. coli*

To investigate the adherence of SNCs to *E. coli* (Figure 4A), Dil and FITC were used to mark CMs and SNs respectively, and then the adherence to *E. coli* was evaluated by laser scanning confocal microscopy and flow cytometry. Under the microscope, bacteria were marked in blue, CMs were marked in red. It would show a pink morphology when SNCs and *E. coli* co-localized (Figure 4B). In addition, the result of flow cytometry show that a low binding rate (6.42%) was found between SNs and *E. coli*. However, SNCs containing macrophage membranes presented a higher binding rate (33.5%), demonstrating that macrophage membrane camouflaging could improve the adherence to *E. coli* and achieve precise delivery of Mino (Figure 4C). In addition, the results of nutrient agar plate coating showed a good antibacterial effect on MSNCs, while the unloaded SNCs did not have an antibacterial effect (Figures 4D,E). It was suggested that Mino was successfully loaded into SNCs and effectively released within 24 h to exert antibacterial effects.

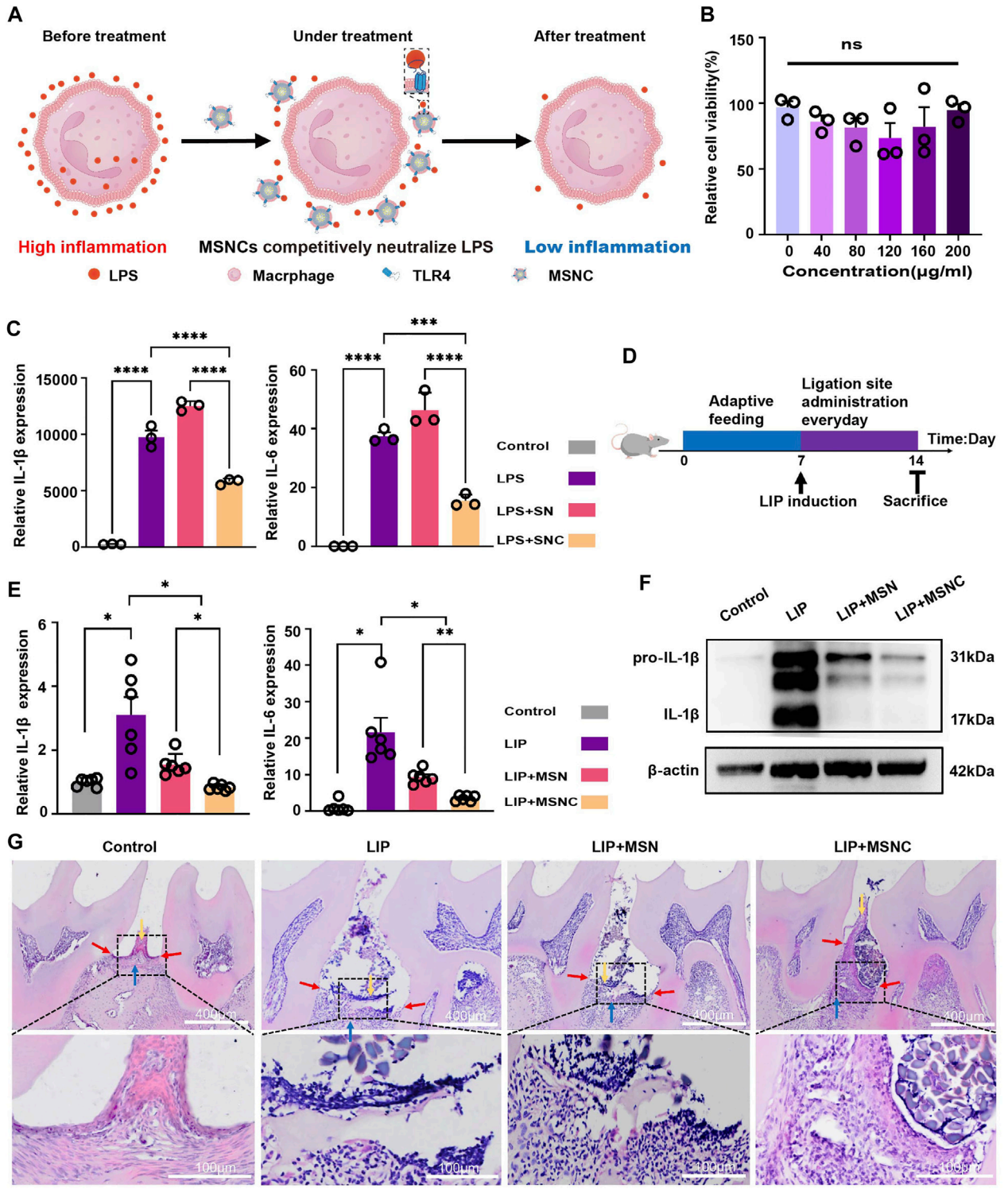

FIGURE 5
Anti-inflammatory effects of functioned cell membrane coated silk fibroin nanoparticles loaded with minocycline hydrochloride *in vitro* and vivo. **(A)** Schematic illustration of MSNCs immunoregulatory effects *in vitro*. **(B)** CCK-8 of SNCs. **(C)** RT-PCR for SNCs neutralization of LPS. **(D)** Schematic illustration of animal experiments. **(E)** RT-PCR of MSNCS with reducing periodontal tissue inflammation. **(F)** WB of MSNCs with reducing periodontal tissue inflammation. **(G)** HE staining of MSNCs with reducing periodontal tissue inflammation. The yellow arrow represents the position of the gingival epithelial peg, the red arrow represents the position of the junctional epithelium and the blue arrow represents the position of the alveolar bone. Data are presented as means ± SEM, ns $p > 0.5$, *$p < 0.05$, **$p < 0.01$, ***$p < 0.001$, and ****$p < 0.0001$; by one-way analysis of variance (ANOVA) with Tukey's *post hoc* test **(B,C, E)**.

3.5 Immunoregulatory effects of SNCs

The TLR4 receptor on the surface of macrophage membranes might neutralize LPS and modulate the local immune microenvironment (Figure 5A). The CCK-8 assay indicated that the viability of RAW264.7 cells had no significant difference ($p > 0.05$) to the increased concentration of SNCs (Figure 5B). However, the gene expression of both IL-1β and IL-6 in RAW264.7 cells was markedly downregulated in SNCs groups ($p < 0.001$), indicating that SNCs competitively neutralized LPS in the microenvironment and effectively inhibited the activation of pro-inflammatory macrophages (Figure 5C).

3.6 Biological effects of MSNCs *in vivo*

A mouse model of ligature-induced periodontitis was constructed to evaluate the *in vivo* biological effects of MSNCs (Figure 5D). Significant diffusion was observed after FITC-MSNCs were injected into the tissue (Supplementary Figure S2). at 0 h, obvious green fluorescence was visible at the injection site with bright fluorescence and comparatively aggregated location; at 4 h, the fluorescence at the injection site attenuated and obvious green fluorescence diffusion was visible around; at 24h, the fluorescence at the injection site diminished significantly and the fluorescence range was larger, and obvious green fluorescence was visible at the periodontitis site. Moreover, RT-PCR assay showed that IL-1β and IL-6 gene expression had prominently decreased in the MSNCs group ($p < 0.05$), and WB assay suggested that IL-1β protein expression had significantly decreased in MSNCs (Figures 5E,F). Furthermore, HE staining showed that the gingival epithelial pegs proliferated (yellow arrows), the junctional epithelium receded toward the root (red arrows) and the alveolar bone height decreased (blue arrows) in the periodontitis group; Nevertheless, with the treatment of MSNCs, gingival epithelial peg proliferation combined with epithelial recession and alveolar bone loss improved significantly (Figure 5G).

4 Discussion

In this study, we constructed cell membrane-coated silk fibroin nanoparticles (MSNCs) overexpressing TLR4 by genetic engineering and proposed a new antibacterial and immunoregulatory synergistic therapy for periodontitis. The TLR4 was used to achieve precise targeted drug delivery and killing of pathogens, while nanoparticles with TLR4 acted as ideal decoys for LPS to reduce the activation of immune cells. The synergistic therapy based on MSNCs made up for the defects of the current treatment and realized the effective control of periodontal inflammation.

Nanoparticles are an effective platform to achieve precise drug delivery and cellular regulation (Wang et al., 2019; Mitchell et al., 2021). Nanoparticles can not only overcome the limitations of free drug therapeutic approaches, but also overcome the heterogeneity among different patients and diseases through targeted therapy (Tiwari et al., 2012; Wilczewska et al., 2012; Ren et al., 2021). In addition, the effects of nanoparticles on cellular viability and polarity have been widely researched to improve the disease microenvironment. Considering the effect of nanoparticles on cytotoxicity, natural polymers are often chosen as raw materials for the preparation of nanoparticles due to their good biocompatibility and degradability (Idrees et al., 2020; Wang et al., 2022; Yu et al., 2022). They are used for the pharmacotherapy of small molecule drugs, proteins, and nucleic acids, which are widely studied in the fields of tumor therapy, tissue engineering, and regenerative medicine (Balazs et al., 2006; Malafaya et al., 2007; Pina et al., 2015; Chen et al., 2019). In the present study, we prepared nanoparticles with a natural polymeric silk fibroin. The scanning electron microscopy results showed that the SNs had a circular morphology. The DLS results showed that the size and zeta potential were respectively about 114.63 nm and −39.70 mV, which were similar to the study by Shuang, Q. Gou (Gou et al., 2019). We demonstrated that SNs had no significant cytotoxicity against RAW264.7 and did not cause significant inflammatory responses, indicating the good biocompatibility of the silk fibroin nanoparticles, which were similar to the findings of Mercedes G. Montalbán (Montalbán et al., 2018), Alessandra Mari Bossi (Bossi et al., 2021) et al. Moreover, we investigated the drug-loading properties of SNs, and the results showed that SNs have good drug-loading performance, and the loaded SNs have good antibacterial effects. However, the loading rate and encapsulation rate still have room for further improvement, and it is difficult to achieve precision therapy with unfunctionally modified SNs.

To achieve functions including precise drug delivery and immune escape, nanoparticles often require complex functionalization modifications (Guerrini et al., 2018). As an emerging technology, cell membrane bionanotechnology is considered to have great potential for application because of its advantages of improving the biocompatibility of nanoparticles, prolonging the retention time in blood circulation, achieving immune escape and homologous targeting (Zou et al., 2020; Oroojalian et al., 2021). Recent studies have shown that immune cell membrane-mimetic nanoparticles can well target the inflamed endothelium due to the expression of adhesion receptors and that antigenic membrane proteins facilitate their diffusion at the site of inflammation (Park et al., 2021). For example, macrophage membrane-mimetic nanoparticles have been shown to diffuse to sites of systemic inflammation and are used in the management of sepsis (Thamphiwatana et al., 2017); Neutrophil membrane-encapsulated nanoparticles are well aggregated in inflamed osteoarthritic sites and show better tissue penetration than erythrocyte membrane-mimetic particles (Zhang Q. et al., 2018). Moreover, genetic engineering techniques have been innovatively applied to enhance cell membrane functions, greatly increasing the potential of cell membrane bionanotechnology applications. Genetic engineering is a versatile platform to achieve the expression of specific target ligands on cell membranes without disturbing membrane proteins and with significantly lower technical difficulty than chemical modifications (Ai et al., 2020; Park et al., 2021). In this study, we genetically engineered TLR4-expressing RAW264.7 cells and extracted functionalized cell membranes to physically extrude with drug-loaded SNs to successfully prepare MSNCs. Scanning electron microscopy results showed that the surface of MSNCs was not smooth and differed significantly from the smooth surface of SNs. The TEM results demonstrated the distinct shell-core structure of MSNCs, which showed a high-density image of drug-loaded SNs in the middle and a lower-density cell membrane image closely surrounding the outer layer. The DLS results showed that the particle size and zeta potential of MSNCs became larger compared to SNs, indicating the successful coating of CMs, and the change of the surface charge of the particles after coating. The Bradford staining results showed that the cell membrane surface proteins were well preserved during the extraction of cell membranes as well as the preparation of bionanoparticles, indicating that MSNCs could inherit the relevant

functions of the source cell surface proteins. What's more, the western blot results showed that the surface of MSNCs still contained a large number of TLR4, further proving the successful preparation of MSNCs. it can be seen that the drug release rate increased continuously with the increasing time, it indicates that more drug was released; and when *E. coli* combined with MSNCs, the initial release rate of the drug slowed down significantly, but this effect diminished significantly after 8 h. And similar to Gou's study (Gou et al., 2019), the drug release rate of MSNCs was up to 20% within 48 h in PBS solution with neutral PH. Thus, MSNCs maintained a sustained drug release after binding to bacteria.

We still verified that SNCs have good biocompatibility. We next verified that MSNCs have good antibacterial effects based on their targeted drug-release properties. On the one hand, the functionalized cell membrane on the surface of the nanoparticles could bind specifically to the LPS on bacterial due to TLR4, which made them have significant bacterial binding ability; on the other hand, MSNCs could release antibacterial drugs in a short period of time to kill *E. coli* precisely (Thamphiwatana et al., 2017; Wu et al., 2021). LPS activates TLR4 and leads to the activation and overexpression of MyD88, which in turn activates the NF-κB pathway, leading to NF-κB phosphorylation and translocation from the cytoplasm to the nucleus, promoting the expression of pro-inflammatory cytokines such as IL-1β and IL-6 (Lu et al., 2008; Thamphiwatana et al., 2017; Zhuang et al., 2020). The RT-PCR results showed that the inflammatory gene expression level was significantly increased after LPS stimulation, and the inflammatory gene expression level remained unchanged significantly after treatment with SNs, which further indicated that SNs have good biocompatibility. However, the inflammatory gene expression level was significantly reduced in the SNCs-treated group, suggesting the immunoregulatory ability of SNCs. Based on the properties of cell membranes overexpressing TLR4, we hypothesized that SNCs inhibited inflammatory responses by neutralizing LPS in the microenvironment and effectively reducing the activation of macrophages by LPS. These results suggest that MSNCs possess both precise antibacterial and immunoregulatory properties.

To verify the inhibitory effect of MSNCs on inflammation in periodontal tissues, a LIP mouse model was constructed in this study, and its therapeutic effect was evaluated after the topical administration of treatment. MSNCs have good local storage capacity and tissue penetration and can selectively diffuse to the periodontal inflammation site with good target diffusion of inflammation. The results showed that the level of inflammation in periodontal tissues was significantly lower and tissue destruction was significantly reduced in the MSNCs group compared with the no-treatment and MSNs groups, suggesting that MSNCs effectively reduced inflammation and inhibited bone loss in periodontitis.

5 Conclusion

In summary, we constructed an engineered cell membrane-encapsulated nanosystem MSNCs for precise targeting and inhibition of bacteria, and to neutralize LPS in the microenvironment to inhibit inflammatory cell activation. MSNCs effectively inhibited periodontal inflammation and bone loss through dual regulation of antibacterial and immunity. Based on this nanoplatform, genetically engineered modifications with different ligand-receptor patterns can be constructed to respond to immune diseases infected by different pathogens. In addition, this system still has some potential for improvement, such as the drug loading rate can be further optimized and the therapeutic effect can be evaluated over a longer period of time. In conclusion, MSNCs provide a new therapeutic platform for periodontitis, and the dual functional design of antibacterial and immunoregulation provides additional consideration for the treatment of inflammatory diseases with bacterial infections.

Data availability statement

The original contributions presented in the study are included in the article/Supplementary Material, further inquiries can be directed to the corresponding author.

Ethics statement

The animal study was reviewed and approved by The Affiliated Stomatological Hospital of Chongqing Medical University.

Author contributions

SY designed the study. YD did the experiments, performed the analysis and wrote the manuscript. MR and PH helped to write the manuscript and the data acquisition. FL, XW and CZ assisted in the statistical analysis and manuscript validation. YL offered resources and project administration. SY provided funding support, supervised the study, and critically revised the manuscript.

Funding

This work was supported by the National Natural Science Foundation of China (Grant No. 82171010), the Natural Science Foundation of Chongqing (Grant No. cstc2021jcyj-jqX0028), Chongqing Science and Health Joint Project (Grant No. 2020GDRC015), Program for Youth Innovation in Future Medicine, Chongqing Medical University (No. W0079).

Acknowledgments

Thanks to Biorender for providing the elements for the article drawing.

Conflict of interest

The authors declare that the research was conducted in the absence of any commercial or financial relationships that could be construed as a potential conflict of interest.

Publisher's note

Supplementary material

The Supplementary Material for this article can be found online at: https://www.frontiersin.org/articles/10.3389/fbioe.2023.1113367/full#supplementary-material

SUPPLEMENTARY FIGURE S1
Drug release profiles of MSNCs and E. coli-treated MSNCs from 0 h to 48 h.

SUPPLEMENTARY FIGURE S2
Diffusion of MSNCs in vivo. The white curved line indicates the mouse molar; the red arrow and red curved line indicate the main green fluorescence.

References

Ai, X., Wang, S., Duan, Y., Zhang, Q., Chen, M. S., Gao, W., et al. (2020). Emerging approaches to functionalizing cell membrane-coated nanoparticles. *Biochemistry* 60 (13), 941–955. doi:10.1021/acs.biochem.0c00343

Balazs, A. C., Emrick, T., and Russell, T. P. (2006). Nanoparticle polymer composites: Where two small worlds meet. *Science* 314 (5802), 1107–1110. doi:10.1126/science.1130557

Bossi, A. M., Bucciarelli, A., and Maniglio, D. (2021). Molecularly imprinted silk fibroin nanoparticles. *ACS Appl. Mater. Interfaces* 13 (27), 31431–31439. doi:10.1021/acsami.1c05405

Chen, P., Ma, Y., Zheng, Z., Wu, C., Wang, Y., and Liang, G. (2019). Facile syntheses of conjugated polymers for photothermal tumour therapy. *Nat. Commun.* 10 (1), 1–10. doi:10.1038/s41467-019-09226-6

Chen, Y., Yang, Q., Lv, C., Chen, Y., Zhao, W., Li, W., et al. (2021). NLRP3 regulates alveolar bone loss in ligature-induced periodontitis by promoting osteoclastic differentiation. *Cell Prolif.* 54 (2), e12973. doi:10.1111/cpr.12973

Federico, S., Pozzetti, L., Papa, A., Carullo, G., Gemma, S., Butini, S., et al. (2020). Modulation of the innate immune response by targeting toll-like receptors: A perspective on their agonists and antagonists. *J. Med. Chem.* 63 (22), 13466–13513. doi:10.1021/acs.jmedchem.0c01049

Gao, W., Fang, R. H., Thamphiwatana, S., Luk, B. T., Li, J., Angsantikul, P., et al. (2015). Modulating antibacterial immunity via bacterial membrane-coated nanoparticles. *Nano Lett.* 15 (2), 1403–1409. doi:10.1021/nl504798g

Gou, S., Huang, Y., Wan, Y., Ma, Y., Zhou, X., Tong, X., et al. (2019). Multi-bioresponsive silk fibroin-based nanoparticles with on-demand cytoplasmic drug release capacity for CD44-targeted alleviation of ulcerative colitis. *Biomaterials* 212, 39–54. doi:10.1016/j.biomaterials.2019.05.012

Gu, Y., and Han, X. (2020). Toll-like receptor signaling and immune regulatory lymphocytes in periodontal disease. *Int. J. Mol. Sci.* 21 (9), 3329. doi:10.3390/ijms21093329

Guerrini, L., Alvarez-Puebla, R. A., and Pazos-Perez, N. (2018). Surface modifications of nanoparticles for stability in biological fluids. *Materials* 11 (7), 1154. doi:10.3390/ma11071154

Hoare, A., Soto, C., Rojas-Celis, V., and Bravo, D. (2019). Chronic inflammation as a link between periodontitis and carcinogenesis. *Mediat. Inflamm.* 2019, 1029857. doi:10.1155/2019/1029857

Hu, D., Li, H., Wang, B., Ye, Z., Lei, W., Jia, F., et al. (2017). Surface-adaptive gold nanoparticles with effective adherence and enhanced photothermal ablation of methicillin-resistant *Staphylococcus aureus* biofilm. *ACS Nano* 11 (9), 9330–9339. doi:10.1021/acsnano.7b04731

Huang, N., Chen, X., Zhu, X., Xu, M., and Liu, J. (2017). Ruthenium complexes/polypeptide self-assembled nanoparticles for identification of bacterial infection and targeted antibacterial research. *Biomaterials* 141, 296–313. doi:10.1016/j.biomaterials.2017.07.005

Idrees, H., Zaidi, S. Z. J., Sabir, A., Khan, R. U., Zhang, X., and Hassan, S.-u. (2020). A review of biodegradable natural polymer-based nanoparticles for drug delivery applications. *Nanomaterials* 10 (10), 1970. doi:10.3390/nano10101970

Kinane, D. F., Stathopoulou, P. G., and Papapanou, P. N. (2017). Periodontal diseases. *Nat. Rev. Dis. Prim.* 3, 17038. doi:10.1038/nrdp.2017.38

Lambert, J. M., and Berkenblit, A. (2018). Antibody–drug conjugates for cancer treatment. *Annu. Rev. Med.* 69, 191–207. doi:10.1146/annurev-med-061516-121357

Li, J., Angsantikul, P., Liu, W., Esteban-Fernández de Ávila, B., Chang, X., Sandraz, E., et al. (2018). Biomimetic platelet-camouflaged nanorobots for binding and isolation of biological threats. *Adv. Mater* 30 (2), 1704800. doi:10.1002/adma.201704800

Lu, Y.-C., Yeh, W.-C., and Ohashi, P. S. (2008). LPS/TLR4 signal transduction pathway. *Cytokine* 42 (2), 145–151. doi:10.1016/j.cyto.2008.01.006

Malafaya, P. B., Silva, G. A., and Reis, R. L. (2007). Natural-origin polymers as carriers and scaffolds for biomolecules and cell delivery in tissue engineering applications. *Adv. Drug Deliv. Rev.* 59 (4-5), 207–233. doi:10.1016/j.addr.2007.03.012

Mitchell, M. J., Billingsley, M. M., Haley, R. M., Wechsler, M. E., Peppas, N. A., and Langer, R. (2021). Engineering precision nanoparticles for drug delivery. *Nat. Rev. Drug Discov.* 20 (2), 101–124. doi:10.1038/s41573-020-0090-8

Montalbán, M. G., Coburn, J. M., Lozano-Pérez, A. A., Cenis, J. L., Víllora, G., and Kaplan, D. L. (2018). Production of curcumin-loaded silk fibroin nanoparticles for cancer therapy. *Nanomaterials* 8 (2), 126. doi:10.3390/nano8020126

Oroojalian, F., Beygi, M., Baradaran, B., Mokhtarzadeh, A., and Shahbazi, M. A. (2021). Immune cell Membrane-Coated biomimetic nanoparticles for targeted cancer therapy. *Small* 17 (12), 2006484. doi:10.1002/smll.202006484

Park, J. H., Jiang, Y., Zhou, J., Gong, H., Mohapatra, A., Heo, J., et al. (2021). Genetically engineered cell membrane–coated nanoparticles for targeted delivery of dexamethasone to inflamed lungs. *Sci. Adv.* 7 (25), eabf7820. doi:10.1126/sciadv.abf7820

Parodi, A., Quattrocchi, N., van de Ven, A. L., Chiappini, C., Evangelopoulos, M., Martinez, J. O., et al. (2013). Synthetic nanoparticles functionalized with biomimetic leukocyte membranes possess cell-like functions. *Nat. Nanotechnol.* 8 (1), 61–68. doi:10.1038/nnano.2012.212

Pina, S., Oliveira, J. M., and Reis, R. L. (2015). Natural-based nanocomposites for bone tissue engineering and regenerative medicine: A review. *Adv. Mater.* 27 (7), 1143–1169. doi:10.1002/adma.201403354

Rathinam, V. A., Zhao, Y., and Shao, F. (2019). Innate immunity to intracellular LPS. *Nat. Immunol.* 20 (5), 527–533. doi:10.1038/s41590-019-0368-3

Ren, M., Li, Y., Zhang, H., Li, L., He, P., Ji, P., et al. (2021). An oligopeptide/aptamer-conjugated dendrimer-based nanocarrier for dual-targeting delivery to bone. *J. Mater. Chem. B* 9 (12), 2831–2844. doi:10.1039/d0tb02926b

Sahu, T., Ratre, Y. K., Chauhan, S., Bhaskar, L., Nair, M. P., and Verma, H. K. (2021). Nanotechnology based drug delivery system: Current strategies and emerging therapeutic potential for medical science. *J. Drug Deliv. Sci. Technol.* 63, 102487. doi:10.1016/j.jddst.2021.102487

Slot, D. E., Valkenburg, C., and Van der Weijden, G. (2020). Mechanical plaque removal of periodontal maintenance patients: A systematic review and network meta-analysis. *J. Clin. Periodontology* 47, 107–124. doi:10.1111/jcpe.13275

Szulc, M., Zakrzewska, A., and Zborowski, J. (2018). Local drug delivery in periodontitis treatment: A review of contemporary literature. *Dent. Med. problems* 55 (3), 333–342. doi:10.17219/dmp/94890

Teng, Y. T., Nguyen, H., Gao, X., Kong, Y. Y., Gorczynski, R. M., Singh, B., et al. (2000). Functional human T-cell immunity and osteoprotegerin ligand control alveolar bone destruction in periodontal infection. *J. Clin. investigation* 106 (6), R59–R67. doi:10.1172/jci10763

Thamphiwatana, S., Angsantikul, P., Escajadillo, T., Zhang, Q., Olson, J., Luk, B. T., et al. (2017). Macrophage-like nanoparticles concurrently absorbing endotoxins and proinflammatory cytokines for sepsis management. *Proc. Natl. Acad. Sci.* 114 (43), 11488–11493. doi:10.1073/pnas.1714267114

Tiwari, G., Tiwari, R., Sriwastawa, B., Bhati, L., Pandey, S., Pandey, P., et al. (2012). Drug delivery systems: An updated review. *Int. J. Pharm. investigation* 2 (1), 2. doi:10.4103/2230-973x.96920

Tsukamoto, H., Takeuchi, S., Kubota, K., Kobayashi, Y., Kozakai, S., Ukai, I., et al. (2018). Lipopolysaccharide (LPS)-binding protein stimulates CD14-dependent Toll-like receptor 4 internalization and LPS-induced TBK1–IKKε–IRF3 axis activation. *J. Biol. Chem.* 293 (26), 10186–10201. doi:10.1074/jbc.m117.796631

Wang, C., Wang, Y., Zhang, L., Miron, R. J., Liang, J., Shi, M., et al. (2018). Pretreated macrophage-membrane-coated gold nanocages for precise drug delivery for treatment of bacterial infections. *Adv. Mater* 30 (46), e1804023. doi:10.1002/adma.201804023

Wang, J., Yu, Y.-D., Zhang, Z.-G., Wu, W.-C., Sun, P.-L., Cai, M., et al. (2022). Formation of sweet potato starch nanoparticles by ultrasonic—Assisted nanoprecipitation: Effect of cold plasma treatment. *Front. Bioeng. Biotechnol.* 10, 986033. doi:10.3389/fbioe.2022.986033

Wang, Y., Feng, L., and Wang, S. (2019). Conjugated polymer nanoparticles for imaging, cell activity regulation, and therapy. *Adv. Funct. Mater.* 29 (5), 1806818. doi:10.1002/adfm.201806818

Wilczewska, A. Z., Niemirowicz, K., Markiewicz, K. H., and Car, H. (2012). Nanoparticles as drug delivery systems. *Pharmacol. Rep.* 64 (5), 1020–1037. doi:10.1016/s1734-1140(12)70901-5

Wongpinyochit, T., Johnston, B. F., and Seib, F. P. (2016). Manufacture and drug delivery applications of silk nanoparticles. *J. Vis. Exp.* 116, 54669. doi:10.3791/54669

Wu, S., Huang, Y., Yan, J., Li, Y., Wang, J., Yang, Y. Y., et al. (2021). Bacterial outer membrane-coated mesoporous silica nanoparticles for targeted delivery of antibiotic rifampicin against Gram-negative bacterial infection *in vivo*. *Adv. Funct. Mater.* 31 (35), 2103442. doi:10.1002/adfm.202103442

Xiang, J., Li, Y., Ren, M., He, P., Liu, F., Jing, Z., et al. (2022). Sandwich-like nanocomposite electrospun silk fibroin membrane to promote osteogenesis and antibacterial activities. *Appl. Mater. Today* 26, 101273. doi:10.1016/j.apmt.2021.101273

Yu, H., Wu, M., Chen, S., Song, M., and Yue, Y. (2022). Biomimetic nanoparticles for tumor immunotherapy. *Front. Bioeng. Biotechnol.* 10, 989881. doi:10.3389/fbioe.2022.989881

Zhang, L., Wang, Z., Zhang, Y., Cao, F., Dong, K., Ren, J., et al. (2018). Erythrocyte membrane cloaked metal–organic framework nanoparticle as biomimetic nanoreactor for starvation-activated colon cancer therapy. *ACS Nano* 12 (10), 10201–10211. doi:10.1021/acsnano.8b05200

Zhang, Q., Dehaini, D., Zhang, Y., Zhou, J., Chen, X., Zhang, L., et al. (2018). Neutrophil membrane-coated nanoparticles inhibit synovial inflammation and alleviate joint damage in inflammatory arthritis. *Nat. Nanotechnol.* 13 (12), 1182–1190. doi:10.1038/s41565-018-0254-4

Zhou, P., She, Y., Dong, N., Li, P., He, H., Borio, A., et al. (2018). Alpha-kinase 1 is a cytosolic innate immune receptor for bacterial ADP-heptose. *Nature* 561 (7721), 122–126. doi:10.1038/s41586-018-0433-3

Zhuang, C., Liu, G., Barkema, H. W., Zhou, M., Xu, S., ur Rahman, S., et al. (2020). Selenomethionine suppressed TLR4/NF-κB pathway by activating selenoprotein S to alleviate ESBL Escherichia coli-induced inflammation in bovine mammary epithelial cells and macrophages. *Front. Microbiol.* 11, 1461. doi:10.3389/fmicb.2020.01461

Zou, S., Wang, B., Wang, C., Wang, Q., and Zhang, L. (2020). Cell membrane-coated nanoparticles: Research advances. *Nanomedicine* 15 (06), 625–641. doi:10.2217/nnm-2019-0388

frontiers | Frontiers in Bioengineering and Biotechnology

TYPE Original Research
PUBLISHED 03 February 2023
DOI 10.3389/fbioe.2023.1070117

OPEN ACCESS

EDITED BY
Xing Wang,
Shanxi Medical University, China

REVIEWED BY
Jing Zhou,
Zhejiang University, China
Lu Wang,
Shanxi Medical University, China
Takeshi Kikuchi,
Aichi Gakuin University, Japan

*CORRESPONDENCE
Jian Yu,
13688611282@163.com
Hongrui Liu,
yf1blhr@126.com

†These contributed have equally to this work

SPECIALTY SECTION
This article was submitted to Biomaterials, a section of the journal Frontiers in Bioengineering and Biotechnology

RECEIVED 14 October 2022
ACCEPTED 24 January 2023
PUBLISHED 03 February 2023

CITATION
Gao R, Zhang W, Jiang Y, Zhai J, Yu J, Liu H and Li M (2023), Eldecalcitol effectively prevents alveolar bone loss by partially improving Th17/Treg cell balance in diabetes-associated periodontitis. *Front. Bioeng. Biotechnol.* 11:1070117. doi: 10.3389/fbioe.2023.1070117

Eldecalcitol effectively prevents alveolar bone loss by partially improving Th17/Treg cell balance in diabetes-associated periodontitis

Ruihan Gao[1,2†], Weidong Zhang[1,2†], Yujun Jiang[1,2], Junzhe Zhai[2], Jian Yu[3*], Hongrui Liu[1,2*] and Minqi Li[1,2]

[1]Department of Bone Metabolism, School and Hospital of Stomatology, Cheeloo College of Medicine, Shandong University & Shandong Key Laboratory of Oral Tissue Regeneration & Shandong Engineering Laboratory for Dental Materials and Oral Tissue Regeneration & Shandong Provincial Clinical Research Center for Oral Diseases, Jinan, China, [2]Center of Osteoporosis and Bone Mineral Research, Shandong University, Jinan, China, [3]Department of Radiology, School and Hospital of Stomatology, Cheeloo College of Medicine, Shandong University & Shandong Key Laboratory of Oral Tissue Regeneration & Shandong Engineering Laboratory for Dental Materials and Oral Tissue Regeneration, Jinan, China

Background: Diabetes-associated periodontitis (DPD) is an inflammatory and destructive disease of periodontal tissues in the diabetic population. The disease is manifested as more severe periodontal destruction and is more difficult to treat when compared with periodontitis (PD). Eldecalcitol (ELD) is a novel active vitamin D3 analog; however, little clinical evidence is available on its role on improving PD and DPD, and its specific mechanisms remain unclear. In this study, we evaluated the preventative effects of ELD toward PD and DPD and explored its underlying molecular mechanisms.

Methods: Experimental PD and DPD mouse models were established by ligation combined with lipopolysaccharide (LPS) from *Porphyromonas gingivalis* injection in C57BL/6J and C57BLKS/J Iar- + Leprdb/+Leprdb (db/db) mice, respectively. Simultaneously, ELD (0.25 μg/kg) was orally administered to mice *via* an intragastric method. Micro-computed tomography (CT), hematoxylin-eosin (HE) staining, immunohistochemistry (IHC), and tartrate-resistant acid phosphatase (TRAP) staining were used to evaluate alveolar bone alterations *in vivo*. Flow cytometry, immunofluorescence, and real-time polymerase chain reaction (qRT-PCR) were also used to examine gene expression and probe systemic and local changes in Treg and Th17 cell numbers. Additionally, western blotting and immunofluorescence staining were used to examine changes in STAT3/STAT5 signaling.

Results: Micro-CT and HE staining showed that the DPD group had higher alveolar bone loss when compared with the PD group. After applying ELD, alveolar bone loss decreased significantly in both PD and DPD groups, and particularly evident in the DPD group. IHC and TRAP staining also showed that ELD promoted osteoblast activity while inhibiting the number of osteoclasts, and after ELD treatment, the receptor activator of nuclear factor-κB ligand (RANKL) to osteoprotegerin (OPG) ratio decreased. More importantly, this decreasing trend was more obvious in the DPD group. Flow cytometry and qRT-PCR also showed that the systemic Th17/Treg imbalance in PD and DPD groups was partially resolved when animals were supplemented with ELD, while immunofluorescence staining and qRT-PCR data showed the Th17/Treg imbalance was partially resolved in the alveolar bone of both ELD supplemented groups. Western blotting and immunofluorescence staining showed increased p-STAT5 and decreased p-STAT3 levels after ELD application.

Conclusion: ELD exerted preventative effects toward PD and DPD by partially rectifying Th17/Treg cell imbalance *via* STAT3/STAT5 signaling. More importantly, given the severity of DPD, we found ELD was more advantageous in preventing DPD.

KEYWORDS

diabetes-associated periodontitis, periodontitis, Th17/Treg balance, eldecalcitol, STAT3/STAT5 signaling

1 Introduction

Periodontitis (PD) is a chronic infectious disease in teeth-supporting tissue and is characterized by microbially-associated and host-mediated inflammation that causes periodontal attachment loss (Tonetti et al., 2018). Thanks to greater insights from periodontal medicine research, correlations between periodontitis and systemic diseases have been proposed (Cecoro et al., 2020). Several studies have confirmed a mutual relationship between periodontitis and diabetes: diabetes is an important risk factor of periodontitis, and persistent periodontal infection can increase difficulties controlling blood glucose (Barutta et al., 2022). A recent meta-analysis reported that the prevalence of periodontitis in diabetic patients was twice that of non-diabetic patients (Zheng et al., 2021). Furthermore, studies have listed periodontitis as the sixth complication of diabetes, known as diabetes-associated periodontitis (DPD) (Löe, 1993). When compared with PD, DPD has more complex systemic factors, increased rapid alveolar bone resorption rates, greater reduced periodontal tissue repair capabilities, and less satisfactory clinical treatment outcomes (Barutta et al., 2022). Therefore, it is vital to explore DPD pathogenesis and identify preventative measures.

In recent years, DPD pathogenesis has attracted considerable research attention, with multiple reported mechanisms, including microbial factors, immune homeostasis imbalance, and oxidative stress (Polak and Shapira, 2018). It is accepted that the initiating factors for PD are dental plaque biofilms (Valm, 2019). Furthermore, accumulating evidence now suggests that the cause of accelerated periodontal destruction in diabetes mellitus is not solely related to changes in microbial pathogenicity but more to imbalanced host immune responses (Bosshardt, 2018). Moreover, it was reported that PD and diabetes shared common immune characteristics, e.g., chronic inflammation and imbalanced immune homeostasis (Zou et al., 2022). Consequently, these factors are critical for the mutual promotion of diabetes and PD and exploring imbalanced immune homeostasis is important to fully characterize DPD pathogenesis (Luong et al., 2021).

$CD4^+$ T helper cell ($CD4^+$ T cell)-mediated cellular immune responses have important roles in immune homeostasis (Zhu and Zhu, 2020). $CD4^+$ T cells comprise significant cell subsets which respond to different immune environments, including Th1, Th2, Th17, and Treg (T regulatory), and Tfh (follicular T helper) cells. In recent years, Th17 and Treg cell functions have aroused particular concerns (Lee, 2018). Th17 cells exert pro-inflammatory effects by secreting interleukin-17 (IL-17), which has multiple cell sources, such as Th17 cells (main sources), γδT cells, LTi cells, epithelial cells and so on (Gu et al., 2013). Alternatively, Treg cells have important roles in immunological self-tolerance, and prevent excessive damage by the immune system. Clinical and animal model studies have indicated that Th17/Treg cell imbalance, i.e., increased Th17 cell and decreased Treg cell proportions, is a common immune mechanism in periodontitis and diabetes (Kou et al., 2021; Li et al., 2022). More importantly, this imbalance has a vital role in the reciprocal relationship between diabetes and periodontitis; periodontitis exacerbates insulin resistance and blood glucose control by imbalancing Th17/Treg cell levels (Tao et al., 2019). Conversely, diabetes-mediated Th17/Treg cell imbalance massively activates and releases inflammatory factors, such as IL-17, thereby destroying periodontal tissue (Huang et al., 2020a). Hence, correcting the imbalance of Th17/Treg may be an important strategy preventing and treating DPD.

The active form of vitamin D is metabolized by the kidney and liver and has classical biological functions in regulating calcium and phosphorus metabolism and improving osteoporosis (Ringe, 2020). In recent years, active vitamin D function in regulating the immune system has attracted much research attention (Ribeiro et al., 2022). It was reported that active vitamin D reduced $CD4^+$ T cell differentiation into Th17 cell subsets, and altered them to Treg cells, thereby providing protective effects toward Th17/Treg cell imbalance (Ji et al., 2019). Eldecalcitol (ELD) is a novel active vitamin D analog with anti-osteoporosis properties (Liu et al., 2022). Since ELD was used in clinical treatment of osteoporosis in 2011, it has achieved great clinical evaluation, which can effectively increase bone mineral density (BMD) and promote bone mineralization (Matsumoto et al., 2011). Compared with the original active vitamin D, its half-life in the blood is longer, so that the bioavailability is greatly improved; in addition, it makes up for the defect of calcium-phosphate imbalance caused by the original active vitamin D, and achieves the optimization of medicinal property (Saito et al., 2017). Studies have also shown that ELD can effectively regulate calcium homeostasis (Jiang et al., 2019), inhibit bone resorption (Han et al., 2017), and induce unique "mini-modeling" bone formation (de Freitas et al., 2011). Our group has systematically studied the effects and mechanisms underpinning ELD, and observed good hypoglycemic effects (Lu et al., 2022). Additionally, we confirmed ELD protective effects toward gingival fibroblasts, thereby providing a theoretical basis for preventing PD (Huang et al., 2020b). However, the beneficial effects of ELD toward DPD remain largely unreported.

Given the regulatory effects of active vitamin D on Th17/Treg cell imbalance and the aforementioned ELD effects, we explored the effects of ELD on DPD and analyzed its underlying mechanisms to provide a theoretical basis for a better understanding of DPD pathogenesis. Also, using ELD in such situations provides new ideas for preventing and treating DPD.

2 Materials and methods

2.1 Animal and tissue preparation

Eighteen male C57BL/6J mice, weighing 25–30 g and aged 8 weeks, were purchased from the animal center of Shandong

University. Additionally, twelve male C57BLKS/J Iar- + Lepr^{db}/+Lepr^{db} mice (db/db), weighing 33–45 g and aged 8 weeks, were purchased from SPF Biotechnology [SPF (Beijing) Biotechnology Co., Ltd. China] as a diabetic mouse model. Mice were fed under standard laboratory conditions and subjected to light and dark condition for 12 h at 20°C. The study protocol was approved by the Experimental Animal Medicine Ethics Committee of Shandong University School of Stomatology (No. 20211211).

C57BL/6J mice were randomly assigned to three groups (n = 6): control (Control), experimental periodontitis (PD), and experimental periodontitis fed ELD (PD + ELD). Additionally, db/db mice were randomly divided into two groups (n = 6): experimental periodontitis (DPD) and experimental periodontitis fed ELD (DPD + ELD). The experimental periodontitis model was established according to a previous method (Teramachi et al., 2017). After mice were anesthetized by the intraperitoneal injection of 1% pentobarbital (50 mg/1000 g body weight), a silk thread (No. 5-0) ligation was performed bilaterally on the maxillary second molar cervical area. Every other day for 2 weeks, 1.0 mg/mL lipopolysaccharide (LPS) from *Porphyromonas gingivalis* (InvivoGen, United States) in 10 μL was injected into the gingival tissue near the upper second molar (Li et al., 2020). Mice in the control group were injected with the same volume of phosphate buffer saline (PBS) (pH 7.4) for 2 weeks without ligating the corresponding area. In addition to establishing an experimental periodontitis model, mice in PD + ELD and DPD + ELD groups were orally treated three times a week for 2 weeks with 0.25 μg/kg ELD (Chugai Pharmaceutical Co., Ltd. Japan) (Hirota et al., 2018). During drug intervention procedures, mice were deprived of water and food for 8 h every 3 days, the tail vein punctured, and fasting blood glucose levels measured using a blood glucose meter (Yuwell Medical Equipment Co., Ltd. China). After 2 weeks, animals were humanely euthanized *via* anesthetic overdose (intraperitoneal injection of 1% pentobarbital at 100 mg/1000 g body weight). Spleens were removed under sterile conditions for flow cytometry studies and RNA extraction. Maxilla were dissected and some components stored at −80°C. The remaining samples were immersed in 4% paraformaldehyde for 24 h and analyzed using a micro-computed tomography (CT) system to assess alveolar bone loss. The remaining samples were demineralized in 10% EDTA-2Na at 4°C for 1 month, dehydrated in ethanol, embedded in paraffin using standard procedures, and prepared as 5-μm sections for histological analyses.

2.2 Micro-CT assessments

Three maxilla samples from each group were randomly selected for scanning (SCANCO Medical AG, Switzerland). Voltage = 70 kV, current = 200 μA, and layer thickness = 10 μM. Scanning was performed from the proximal edge of the first molar to the distal edge of the third molar along the long maxilla axis, and the bone tissue of the proximal and distal alveolar bone of the maxillary second molar was used to analyze alveolar bone alterations. All samples were reconstructed and analyzed using a micro-CT analysis system (SCANCO Medical AG). The distance (mm) from the lingual alveolar bone of the maxillary second molar to the cementoenamel junction (CEJ) was measured using Image Pro Plus 6.2 software (Media Cybernetics, Inc. United States).

2.3 Splenic lymphocyte isolation and flow cytometry

Spleens were removed under aseptic conditions and dissected on a 70-μm cell sieve. Splenic cell suspensions were collected, and after isolating mononuclear cells using mouse Lymphocyte Isolation Solution (Dakewe Biotech Co., Ltd. China), single cells were suspended in RPMI 1640 medium (Biological Industries, Göttingen, Germany) plus 10% fetal bovine serum (FBS). Cells were stained with fluorescein isothiocyanate-conjugated anti-CD4 antibody (100,406, BioLegend, Inc. CA, United States) for 30 min on ice. After permeabilization and fixation in eBioscience™ FOXP3/transcription factor staining buffer set (Thermo Fisher Scientific, Waltham, MA, United States), cells were incubated with phycoerythrin-conjugated anti- FOXP3 antibody (563,101, BD Biosciences, United States) and allophycocyanin-conjugated anti-IL-17A antibody (506,916, BioLegend) for 1 h at 4°C. Finally, 0.2 mL PBS was added and cells resuspended. Labeled cells were detected by flow cytometry (BD Accuri C6 Plus, United States), and Treg ($CD4^+$ $FOXP3^+$) and Th17 ($CD4^+$ $IL\text{-}17A^+$) cell percentages determined. Data were analyzed using FlowJo™ v10.8 Software (BD Life Sciences, United States). All experiments were independently performed three times.

2.4 Hematoxylin-eosin (HE) staining

Alveolar bone sections were dewaxed and rehydrated for HE staining. Sections were immersed in hematoxylin for 15 min, washed twice in distilled water, and stained with eosin for 7 min. After dehydration and mounting, stained sections were observed under optical microscopy (BX-53; Olympus Corp. Japan), and digital images captured at original magnifications of ×100. The distance from the alveolar bone of the maxillary second molar to the CEJ was measured using Image Pro Plus 6.2 software (Media Cybernetics). Specifically, three tissue sections were selected to quantitative mean histological values.

2.5 Immunohistochemistry (IHC) and tartrate-resistant acid phosphatase (TRAP) staining

Sections underwent IHC staining to examine alkaline phosphatase (ALP), receptor activator of nuclear factor-κB ligand (RANKL), and osteoprotegerin (OPG) expression. After dewaxing and rehydration, tissue sections were immersed in PBS plus 0.3% hydrogen peroxide (H_2O_2) for 30 min to inhibit endogenous peroxidase, followed by blocking in 1% bovine serum albumin (BSA) in PBS (1% BSA-PBS) for 20 min to prevent non-specific staining. Sections were then incubated overnight at 4°C with: (Tonetti et al., 2018) anti-ALP antibody (1:50; ab65834, Abcam, United Kingdom), (Cecoro et al., 2020) anti-RANKL antibody (1:75; ab216484, Abcam), or (Barutta et al., 2022) anti-OPG antibody (1:100; ab9986, Abcam). After rinsing in PBS, sections were incubated with goat anti-rabbit IgG H&L antibody (1:200, ab6721, Abcam) for 1 h. Immunoreactivity was observed using diaminobenzidine (Sigma-Aldrich, Germany). Sections were washed in double-distilled water and immersed in a TRAP staining solution (Li et al., 2013). All sections were then re-stained in methyl green,

sealed, observed under optical microscopy (Olympus Corp), and digital images captured.

For statistical analysis, three sections were selected for quantitative histological measurements, and average values calculated. Furthermore, serial sections were selected and a consistent field recorded for different markers. TRAP-positive osteoclasts were counted at an original magnification of ×200, while at × 400, the mean optical density of ALP, RANKL, and OPG levels were determined in three randomly selected non-overlapping microscopic fields using Image-Pro Plus 6.2 software (Media Cybernetics). Using this approach, regions of interest were manually selected in a color cube.

2.6 Immunofluorescence staining

For immunofluorescence staining, paraffin-embedded sections were immersed in 0.3% H_2O_2 for 30 min and blocked in 1% BSA-PBS for 20 min. Double immunofluorescence staining was performed on sections to localize Treg cells, Th17 cells, p-STAT3$^+$IL-17A$^+$ cells and p-STAT5$^+$FOXP3$^+$ cells. Sections were incubated overnight at 4°C with the following mixed antibodies: (Tonetti et al., 2018) anti-IL-17A antibody (1:100; ab189377, Abcam) and anti-CD4 antibody (1:300; ab183685, Abcam), (Cecoro et al., 2020) anti-FOXP3 antibody (1:100; ab253297, Abcam) and anti-CD4 antibody (1:300; ab183685, Abcam), (Barutta et al., 2022) anti-IL-17A antibody (1:100; ab189377, Abcam) and anti-p-STAT3 (1:100; ab76315, Abcam), (Zheng et al., 2021) anti-FOXP3 antibody (1:100; ab253297, Abcam) and anti-p-STAT5 antibodies (1:100, AF3304, Affinity Biosciences, United States). Sections were incubated with mixed green fluorescent goat anti-rabbit IgG H&L (Alexa Fluor 647) (1:200; ab150081, Abcam) and red fluorescent goat anti-mouse IgG H&L (Alexa Fluor 488) (1:200; ab150119, Abcam) antibodies at room temperature in the dark for 1 h. After washing three times in PBS, samples were nuclear stained with 4′,6-diamidino-2-phenylindole (ab104139, Abcam) for 5 min. Images were obtained under inverted fluorescence microscopy (DMi8 S; Leica, Germany) and the periodontal membrane near the root of the maxillary second molar was selected as the area of interest. All cells were counted at × 400 magnification of the original magnification in immunofluorescence images.

2.7 Real-time polymerase chain reaction (qRT-PCR) analysis

To extract RNA from bone, liquid nitrogen was continuously and rapidly added to grind down alveolar bone until a powder was generated. Also, spleens were removed under sterile conditions and lymphocytes isolated to extract RNA. Total RNA was extracted from bone and cell samples using Trizol reagent (AG21102, Accurate Biotechnology Co., Ltd. China). cDNAs were synthesized using the Evo M-MLV RT Reverse Transcription kit II (AG11711, Accurate Biotechnology Co., Ltd.) according to manufacturer's instructions. Using qRT-PCR instrumentation (LightCycler® 96 SW 1.1; Roche Ltd., Switzerland), qRT-PCR was performed using the SYBR Green Pro Taq HS premixed qRT-PCR kit (AG11701, Accurate Biotechnology). Treg cell-related factors (transforming Growth Factor-β (TGF-β) and FOXP3) and Th17 cell-related factors (retinoic acid-related orphan receptor γ (ROR-γt) and IL-17A) were analyzed. Glyceraldehyde 3-phosphate dehydrogenase (GAPDH) was used as an internal control, and results were presented as relative gene expression. Fold-change in gene expression was calculated relative to controls using the $2^{-\Delta\Delta Cq}$ method in GraphPad Prism software (GraphPad Inc. United States). Primer sequences are shown (Table 1).

2.8 Western blotting

As described, alveolar bone was ground to a powder and RIPA lysis buffer (Lot 02408/60412, CwBio Biotechnology Co., Ltd. China) used to extract proteins. Protein concentrations were determined using a bicinchoninic acid protein assay detection kit (P0012S, BeyoTime Biotechnology, China). Samples were mixed with a 1/4 volume of 5× sodium dodecyl sulfate loading buffer and heated to 95°C for 5 min. Proteins then underwent sodium dodecyl sulfate-polyacrylamide gel electrophoresis, were transferred to polyvinylidene fluoride membranes, and blocked in 5% BSA in Tris buffered saline with Tween-20 (TBST) (5% BSA-TBST) at room temperature for 1 h. Membranes were incubated overnight at 4°C with the following: (Tonetti et al., 2018) anti-p-STAT3 (1:1000; ab76315, Abcam), (Cecoro et al., 2020) anti-p-STAT5 antibodies (1:1000, AF3304, Affinity Biosciences), (Barutta et al., 2022) anti- STAT3 (1:1000; ab68153, Abcam), (Zheng et al., 2021) anti- STAT5 (1:1000; ab32043, Abcam) and followed by incubation with a horseradish peroxidase-conjugated goat anti-rabbit IgG antibody (1:1000, ab6721, Abcam) for 1 h. Immunoreactive bands were detected using enhanced chemiluminescence reagent (B500024, Proteintech, United States) and a gel imaging system (Amersham Imager 600; General Electric Company, United States) to capture images. Image-Pro Plus 6.2 software (Media Cybernetics) was used to analyze and quantify grayscale values normalized to GAPDH levels. Experiments were repeated at least three times.

2.9 Statistical analysis

Statistical analysis was performed in GraphPad Prism software (GraphPad Inc., abcamLa Jolla, San Diego, CA, United States). Differences between three or more groups were tested using one-way analysis of variance. All values were expressed as the mean ± standard deviation. $p < 0.05$ was considered statistically significant.

3 Results

3.1 Aggravated alveolar bone loss in DPD mice when compared with PD mice

As shown in 3-dimesnional (3D) micro-CT images, in the control group, the alveolar ridge crest (ARC) was near the CEJ. The ARC location was lower in the PD group when compared with the control group, and had a lower location was observed in the DPD group (Figures 1A). Quantitative analyses showed that alveolar bone loss in PD and DPD groups increased when compared with control animals (Figure 1A). In the control group, HE staining showed intact gingival morphology with abundant bone matrix. The periodontal ligament was arranged regularly and alveolar bone around maxillary

10.3389/fbioe.2023.1070117

TABLE 1 Specific primers for control and target genes.

Gene	Forward	Reverse
FOXP3	5′-AGTGCCTGTGTCCTCAATGGTC-3′	5′-GGTGAAGGTCGGTGTGAACG-3
TGF-β	5′-TACGGCAGTGGCTGAACCAA-3′	5′-AGGGCCAGCATAGGTGCAAG-3′
IL-17A	5′-TCAGACTACCTCAACCGTTCCA-3′	5′-CGGTTCATGTCATGGATGGTG-3′
ROR-γt	5′-GCTCCATATTTGACTTTTCCCACT-3′	5′-GATGTTCCACTCTCCTCTTCTCTTG-3′
GAPDH	5′-CTCGCTCCTGGAAGA TGGTG-3	5′-GGTGAAGGTCGGTGTGAACG-3

https://www.jianguoyun.com/p/DUv82SwQ-ZWHCxjUkt8EIAA.

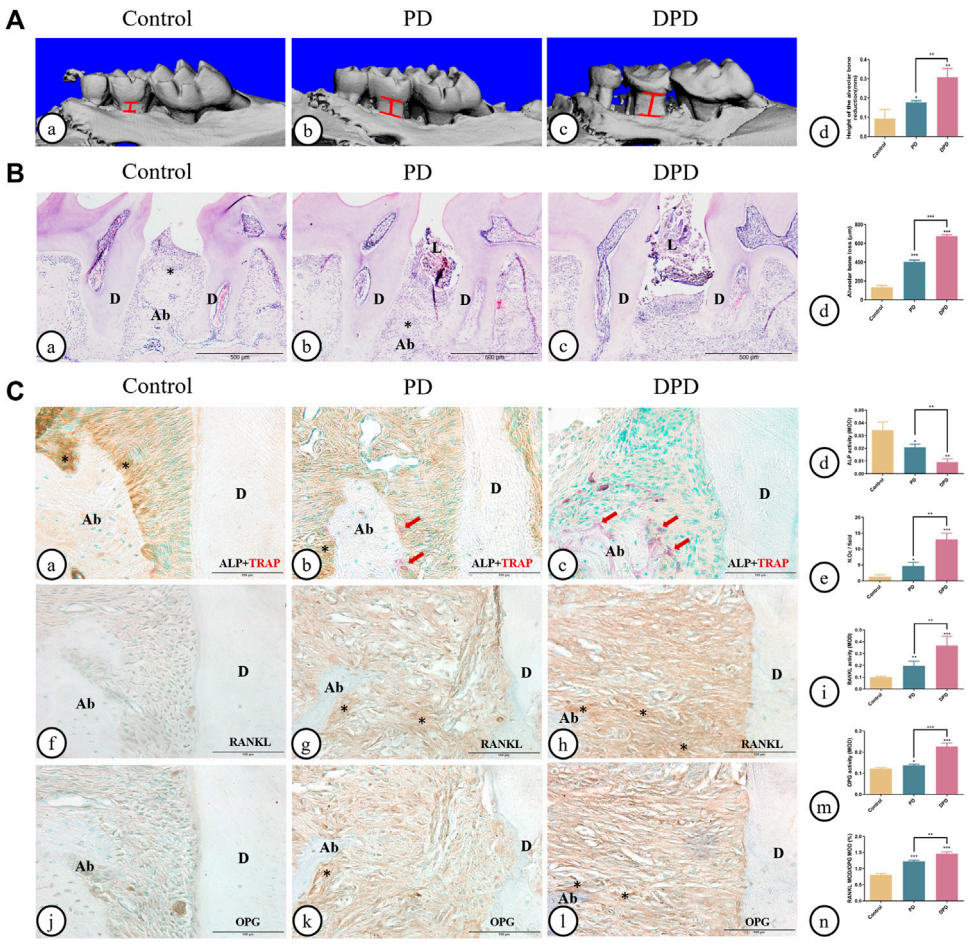

FIGURE 1
Micro-CT analysis and histological alterations in the maxillary alveolar bone. **(A)** 3D images of micro-CT in the **(A)** control, **(B)** PD and **(C)** DPD groups. (d) Statistical analysis of alveolar bone loss. **(B)** Low magnification of histological images of the alveolar bone in the **(A)** control, **(B)** PD and **(C)** DPD groups. (d) Statistical analysis of alveolar bone loss. "*", the alveolar ridge crest. **(C)** Double staining for ALP (brown) and TRAP (red) in the alveolar bone of the **(A)** control, **(B)** PD and **(C)** DPD groups. (d) Statistical analyses of ALP positive. (e) TRAP positive osteoclast count. Immunostaining of RANKL in the (f) control, (g) PD and (h) DPD groups. (i) Statistical analysis of the activity of RANKL. Immunostaining of OPG in the (j) control, (k) PD and (l) DPD groups. (m) Statistical analysis of the activity of OPG. (n) The ratio of RANKL/OPG. Positive staining has been marked with arrows or "*" in the figures. Data were shown as mean ± SD (*$p < 0.05$. **$p < 0.01$. ***$p < 0.001$ https://www.frontiersin.org/register. Ab, alveolar bone; D, dentin; L, ligature.

second molars was intact. However, in PD animals, gingival atrophy and gingival papillae destruction were evident, with only a few bone islands and a deranged periodontal ligament structure distribution. These changes were more pronounced in DPD animals (Figures 1A). Statistical analyses showed that alveolar bone loss increased in PD and DPD groups when compared with the control group, but this loss was more significant in DPD animals (Figure 1B).

The control group exhibited higher ALP-positive osteoblasts on alveolar bone surfaces and periodontal ligaments. In the PD group, ALP-positive osteoblasts decreased and some TRAP-positive

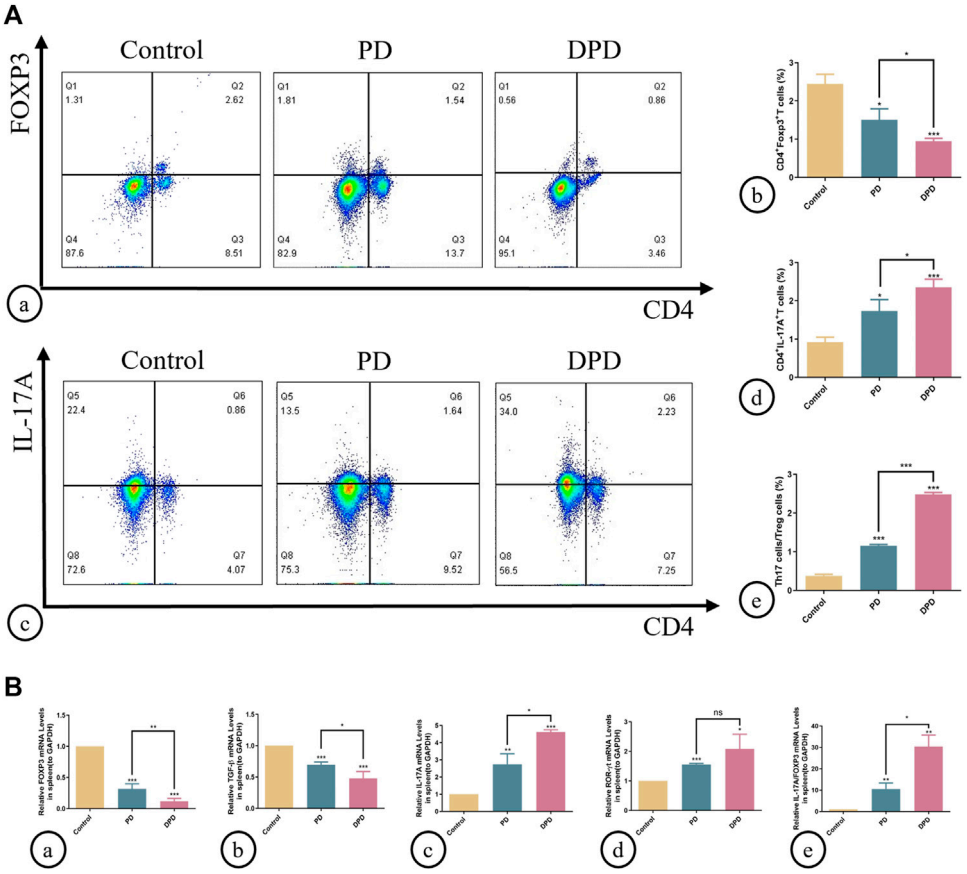

FIGURE 2
Flow cytometry and qRT-PCR analysis of Th17 and Treg cells in spleen lymphocytes. **(A) (A)** Flow cytometry analysis of $CD4^+$ $FOXP3^+$ T cells (in the upper right quadrant) in the spleen lymphocytes in the control, PD and DPD groups. (b) Statistical analysis of $CD4^+$ $FOXP3^+$ T cells in the spleen lymphocytes. (c) Flow cytometry analysis of $CD4^+$ IL-$17A^+$ T cells (in the upper right quadrant) in the spleen lymphocytes in the control, PD and DPD groups. (d) Statistical analysis of $CD4^+$ IL-$17A^+$ T cells in the spleen lymphocytes. (e) The ratio of Th17/Treg cells. **(B)** Relative mRNA expression level of **(A)** FOXP3, (b) TGF-β, (c) IL-17A, (d) ROR-γt, and (e) the ratio of IL-17A/FOXP3 in the control, PD and DPD groups. Data were shown as mean ± SD (*$p < 0.05$. **$p < 0.01$. ***$p < 0.001$).

osteoclasts were observed around the alveolar bone. When compared with this group, more TRAP-positive osteoclasts and lower ALP-positive osteoblasts were observed in DPD animals (Figures 1A). Statistical analyses also confirmed lower ALP-positive osteoblasts and more TRAP-positive osteoclasts in PD and DPD groups when compared with the control group, while DPD group changes were more significant when compared with the PD group (Figures 1). Relatively weak RANKL expression levels were observed in the control group, but the PD group exhibited increased levels when compared with this group. RANKL expression in the DPD group was the highest of all groups (Figures 1). OPG expression trends were similar (Figures 1J–L). These analyses confirmed our observations, with the RANKL to OPG ratio showing an upward trend (Figures 1). Thus, aggravated alveolar bone loss occurred in DPD when compared with PD.

3.2 Higher unbalanced Th17/Treg ratios in DPD when compared with PD mice

As indicated (Figure 2), circulating Treg cells decreased more significantly in DPD mice than in PD mice when compared with control animals (Figures 2A, B). Conversely, circulating Th17 cell percentages increased in PD mice when compared with control animals, whereas levels increased markedly in the DPD group (Figures 2A, C, D). Further evaluations showed that Th17/Treg ratios in PD and DPD groups increased when compared with control animals, particularly in the DPD group, and suggested that Th17/Treg cell proportions in PD and DPD mice were unbalanced when compared with controls. Also, the imbalance in the DPD group was more serious (Figure 2A).

We used qRT-PCR to analyze the expression of Treg (FOXP3 and TGF-β) and Th17 cell-related cytokines (IL-17A and ROR-γt) in the spleen. As shown (Figure 2), higher decreases in FOXP3 and TGF-β expression were observed in the DPD group than in the PD group when compared with the control group, while the expression of Th17 cell-related cytokines increased significantly (Figure 2). Further evaluations showed that IL-17A/FOXP3 mRNA expression ratios increased in the DPD group (Figure 2B). Thus, imbalanced Th17/Treg cell were more severe in the DPD group when compared with the PD group.

Additionally, we determined Th17/Treg cell proportions in periodontal tissue. Both immunofluorescence staining and statistical analyses showed that Treg cell numbers labeled with both $CD4^+$ (green) and $FOXP3^+$ (red) fluorescence increased in PD and

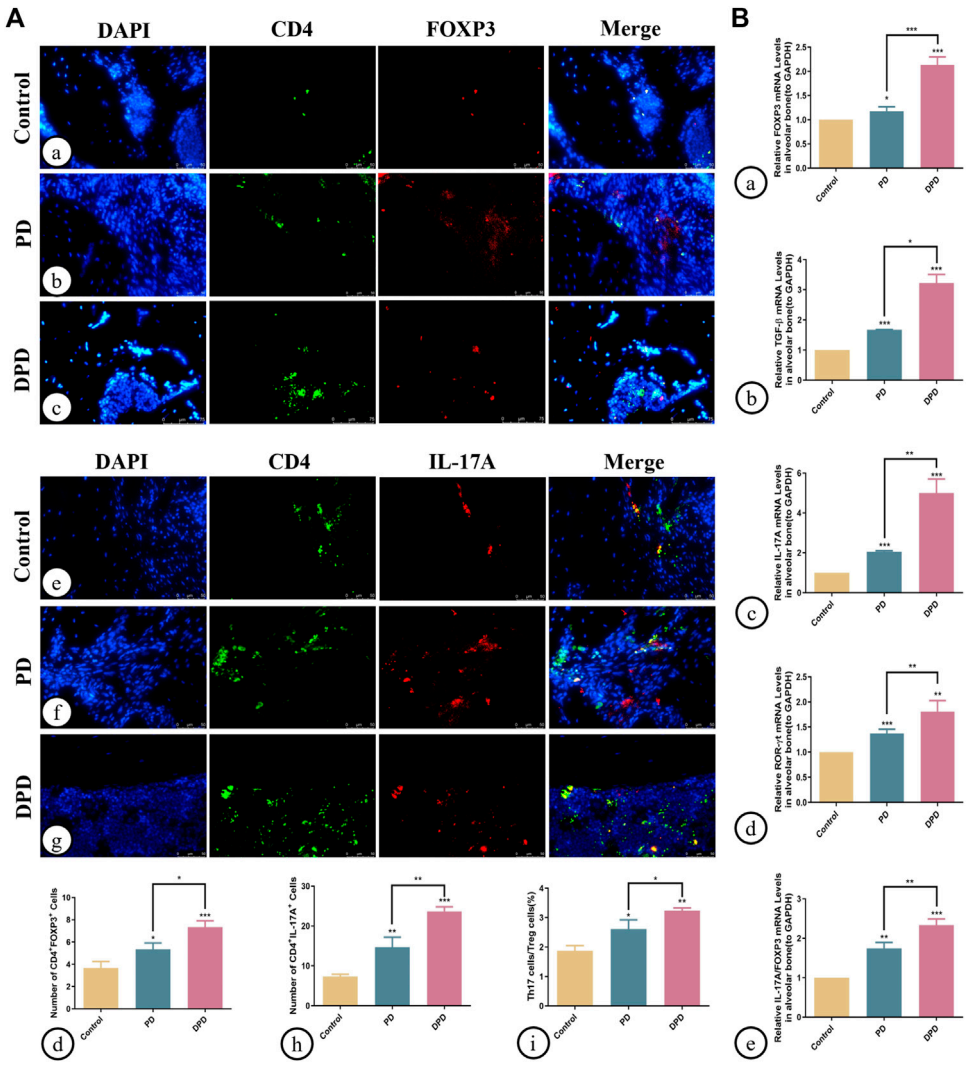

FIGURE 3
Immunofluorescence and qRT-PCR analysis of Th17 and Treg cells in the maxillary alveolar bone. **(A)** The representative immunofluorescence staining images of $CD4^+$ $FOXP3^+$ T cells in the (a) control, (b) PD and (c) DPD groups. (d) The statistical analysis of $CD4^+FOXP3^+$ T cell counts. The representative immunofluorescence staining images of $CD4^+$ $IL\text{-}17A^+$ T cells in the (e) control, (f) PD and (g) DPD groups. (h) The statistical analysis of $CD4^+$ $IL\text{-}17A^+$ T cell counts. (i) The ratio of Th17/Treg cells. **(B)** Relative mRNA expression level of (a) FOXP3, (b) TGF-β, (c) IL-17A, (d) ROR-γt, and (e) the ratio of IL-17A/FOXP3 in the control, PD and DPD groups. Data were shown as mean ± SD (*$p < 0.05$. **$p < 0.01$. ***$p < 0.001$).

DPD groups (Figure 3A). Similarly, Th17 cell numbers labeled with both $CD4^+$ (green) and $IL\text{-}17A^+$ (red) fluorescence increased in PD and DPD groups. More strikingly, the DPD group had higher Th17 cell numbers when compared with the PD group (Figure 3A). Further statistical analyses showed that Th17/Treg cell ratios increased in PD and DPD groups when compared with control animals, particularly in the DPD group, suggesting that Th17/Treg cell proportions in alveolar bone was imbalanced in PD and DPD mice, but more severe in DPD animals (Figure 3A).

We also determined Treg and Th17 cell-related cytokine expression in alveolar bone. As shown (Figure 3), increased FOXP3, TGF-β, IL-17A, and ROR-γt mRNA expression was observed in PD and DPD groups when compared with control animals, particularly in DPD mice (Figure 3B). Further evaluations showed that IL-17A/FOXP3 mRNA expression ratios increased in PD and DPD groups (Figure 3B). Thus, circulating and local Th17/Treg cell levels were imbalanced in PD and DPD animals, but the imbalance was more severe in DPD mice.

3.3 ELD was more advantageous in preventing DPD

Micro-CT and 3D image data showed that ELD reduced alveolar bone loss in PD and DPD mice. Interestingly, alveolar bone loss height in PD + ELD and DPD + ELD groups was similar. Since alveolar bone resorption was more severe in DPD when compared with PD mice, and ELD restored levels, these findings suggested that ELD was more advantageous in preventing DPD-induced alveolar bone loss when compared with PD (Figure 4A).

HE staining showed that alveolar bone destruction decreased significantly in PD + ELD and DPD + ELD groups when

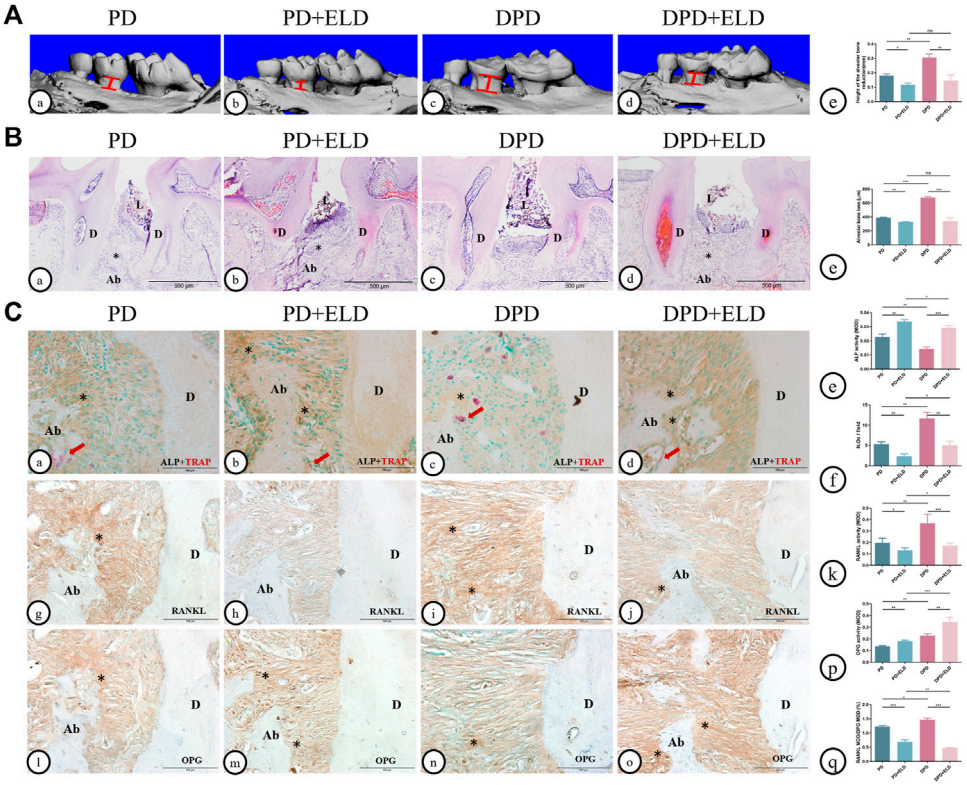

FIGURE 4
Micro-CT analysis and histological alterations in the maxillary alveolar bone with ELD treatment. **(A)** 3D images of micro-CT in the (a) PD, **(B)** PD + ELD, (c) DPD and (d)DPD + ELD groups. (e) Statistical analysis of the data from micro-CT for alveolar bone loss. **(B)** Low magnification of histological images of the alveolar bone in the (a) PD, **(B)** PD + ELD, (c) DPD and (d) DPD + ELD groups. (e) Statistical analysis of the data from HE staining for alveolar bone loss. "*", the alveolar ridge crest. **(C)** Double staining for ALP (brown) and TRAP (red) in the alveolar bone of the (a) PD, (b) PD + ELD, (c) DPD and (d) DPD + ELD groups. Statistical analysis of (e) ALP positive and (f) TRAP positive osteoclast counts. Immunostaining of RANKL in the **(G)** PD, (h) PD + ELD, (i) DPD and (j) DPD + ELD groups. (k) Statistical analysis of the activity of RANKL. Immunostaining of OPG in the (l) PD, (m) PD + ELD, (n) DPD and (o) DPD + ELD groups. (*p*) Statistical analysis of the activity of OPG. (q) The ratio of RANKL/OPG. Positive staining has been marked with arrows or "*" in the figures. Data were shown as mean ± SD (*$p < 0.05$. **$p < 0.01$. ***$p < 0.001$). Ab, alveolar bone; D, dentin; L, ligature.

compared with PD and DPD groups, respectively (Figure 4B). Statistical analyses revealed that alveolar bone loss height in PD + ELD and DPD + ELD groups was similar (Figure 4B).

Also, PD + ELD and DPD + ELD groups exhibited increased ALP-positive osteoblasts and fewer TRAP-positive osteoclasts when compared with PD and DPD groups, respectively (Figure 4C). Additionally, RANKL expression had decreased and OPG expression had increased after ELD treatment (Figure 4C). Also, PD + ELD and DPD + ELD groups exhibited decreased RANKL/OPG ratios when compared with PD and DPD groups, respectively and this decreasing trend was more obvious in the DPD group (Figure 4C). These findings suggested that ELD was more advantageous in preventing DPD.

3.4 The preventative effect of ELD was achieved by ameliorating Th17/Treg imbalance

To determine if ELD prevented alveolar bone loss by preventing Th17/Treg cell imbalance, we examined circulating and local Th17/Treg cell ratios. Flow cytometry showed that spleen Treg cell proportions increased in PD + ELD and DPD + ELD groups when compared with PD and DPD groups, respectively (Figure 5A). But these proportions did not return to control group levels. Moreover, reduced Th17 cell proportions were observed in PD + ELD and DPD + ELD groups. Consistent with Treg cells, Th17 cell proportions in PD + ELD and DPD + ELD groups were still higher when compared with control animals (Figure 5A). Further evaluations showed that Th17/Treg cell ratios decreased in PD + ELD and DPD + ELD groups when compared with PD and DPD groups, suggesting that ELD prevented Th17/Treg cell imbalance. Though Th17/Treg cell ratios in PD + ELD and DPD + ELD groups were still unbalanced, the improvement of Th17/Treg cell imbalance in DPD + ELD group was more obvious than that in PD + ELD group (Figure 5A).

Similarly, Treg and Th17 cell-related cytokine expression was investigated in the spleen. The mRNA expression of FOXP3 and TGF-β increased in PD + ELD and DPD + ELD groups when compared with PD and DPD groups, respectively (Figure 5B). Conversely, the mRNA expression of IL-17A and ROR-γt decreased after ELD treatment in PD and DPD group (Figure 5B). Also, IL-17A/FOXP3 mRNA expression ratios decreased in PD + ELD and DPD + ELD groups (Figure 5B). Therefore, ELD exerted preventative effects on Th17/Treg cell imbalance.

Additionally, Th17/Treg cell ratios in alveolar bone were measured by immunofluorescence. As indicated (Figure 6),

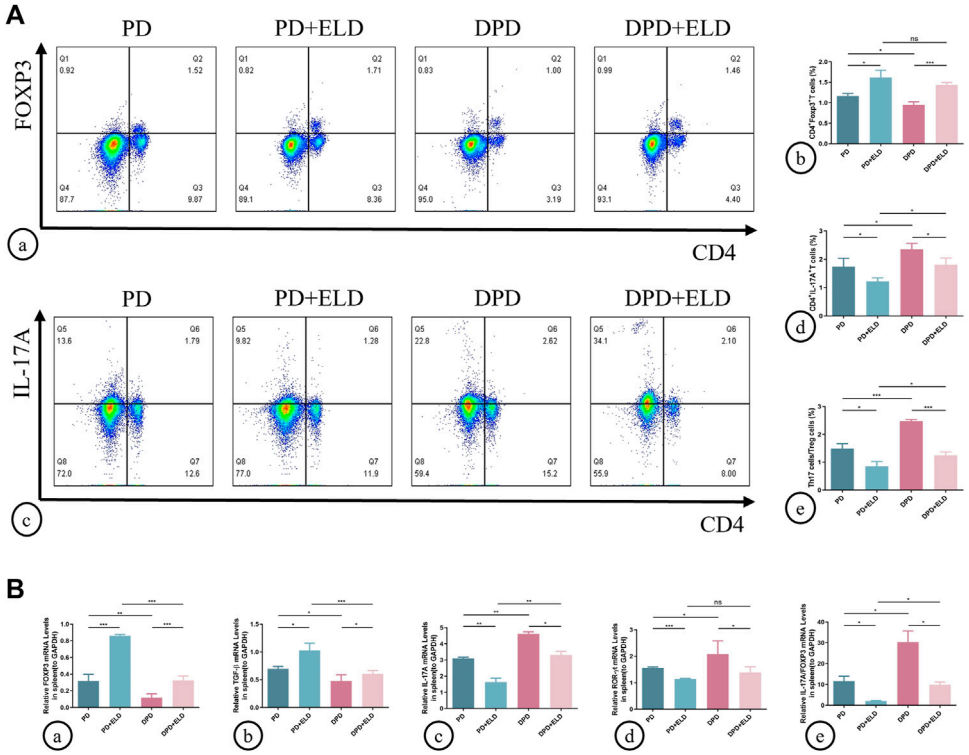

FIGURE 5
Flow cytometry and qRT-PCR analysis of Th17 and Treg cells with ELD treatment in spleen lymphocytes. **(A)** (a) Flow cytometry analysis of $CD4^+$ $FOXP3^+$ T cells (in the upper right quadrant) in the spleen lymphocytes in the PD, PD + ELD, DPD and DPD + ELD groups. (b) Statistical analysis of $CD4^+$ $FOXP3^+$ T cells in the spleen lymphocytes. (c) Flow cytometry analysis of $CD4^+$ $IL\text{-}17A^+$ T cells (in the upper right quadrant) in the spleen lymphocytes in the PD, PD + ELD, DPD and DPD + ELD groups. (d) Statistical analysis of $CD4^+$ $IL\text{-}17A^+$ T cells in the spleen lymphocytes. (e) The ratio of Th17/Treg cells. **(B)** Relative mRNA expression levels of (a) FOXP3, (b) TGF-β, (c) IL-17A, (d) ROR-γt and (e) the ratio of IL-17A/FOXP3 in the PD, PD + ELD, DPD and DPD + ELD groups. Data were shown as mean ± SD (*$p < 0.05$. **$p < 0.01$. ***$p < 0.001$).

increased Treg and decreased Th17 cell numbers were identified in PD + ELD and DPD + ELD groups when compared with PD and DPD groups (Figure 6A. Further statistical analyses showed that Th17/Treg cell ratios decreased in PD + ELD and DPD + ELD groups when compared with PD and DPD groups (Figure 6A). Additionally, the detection of Treg and Th17 cell-related cytokines by qRT-PCR also confirmed that ELD have the preventative effect on the imbalance of Th17/Treg (Figure 6B). These findings suggested that ELD has an effective preventive effect on local Th17/Treg cell imbalance.

3.5 The preventative effects of ELD on Th17/Treg cells imbalance *via* STAT3/STAT5 signaling

To further clarify the molecular mechanisms underpinning ELD-induced preventative effects on Th17/Treg imbalance, western blotting and immunofluorescence were performed to evaluate STAT3/STAT5 signaling. P-STAT3 and p-STAT5 were used to detect active phosphorylated protein forms. Western blotting showed higher p-STAT5/STAT5 and lower p-STAT3/STAT3 expression levels in PD + ELD and DPD + ELD groups when compared with PD and DPD groups (Figure 7A). Statistical analyses confirmed our observations (Figure 7A), and further evaluations showed that p-STAT3/p-STAT5 expression level ratios decreased more significantly in the DPD + ELD groups (Figure 7A).

Additionally, immunofluorescence showed that $p\text{-}STAT5^+FOXP3^+$ expression was significantly enhanced in the periodontal tissue cells from PD + ELD and DPD + ELD groups when compared with PD and DPD groups. (Figure 7B). Moreover, $p\text{-}STAT3^+IL\text{-}17A^+$ expression in PD + ELD and DPD + ELD groups decreased significantly (Figure 7B). Further statistical analyses showed that the cell ratios decreased in PD + ELD and DPD + ELD groups when compared with PD and DPD groups (Figure 7B). These findings suggested that ELD exerted preventative effects on Th17/Treg cell imbalance *via* STAT3/STAT5 signaling.

4 Discussion

In this study, the DPD group showed significant alveolar bone loss when compared with the control group and the PD group. Moreover, a circulating and local Th17/Treg cell imbalance was observed in PD and DPD groups by detecting Th17/Treg cell ratios in the spleen and alveolar bone; in particular, the DPD group had a more serious imbalance. Surprisingly, ELD was more advantageous in preventing alveolar bone loss in the DPD group, and further investigations showed that ELD exerted preventative effects on Th17/Treg cell

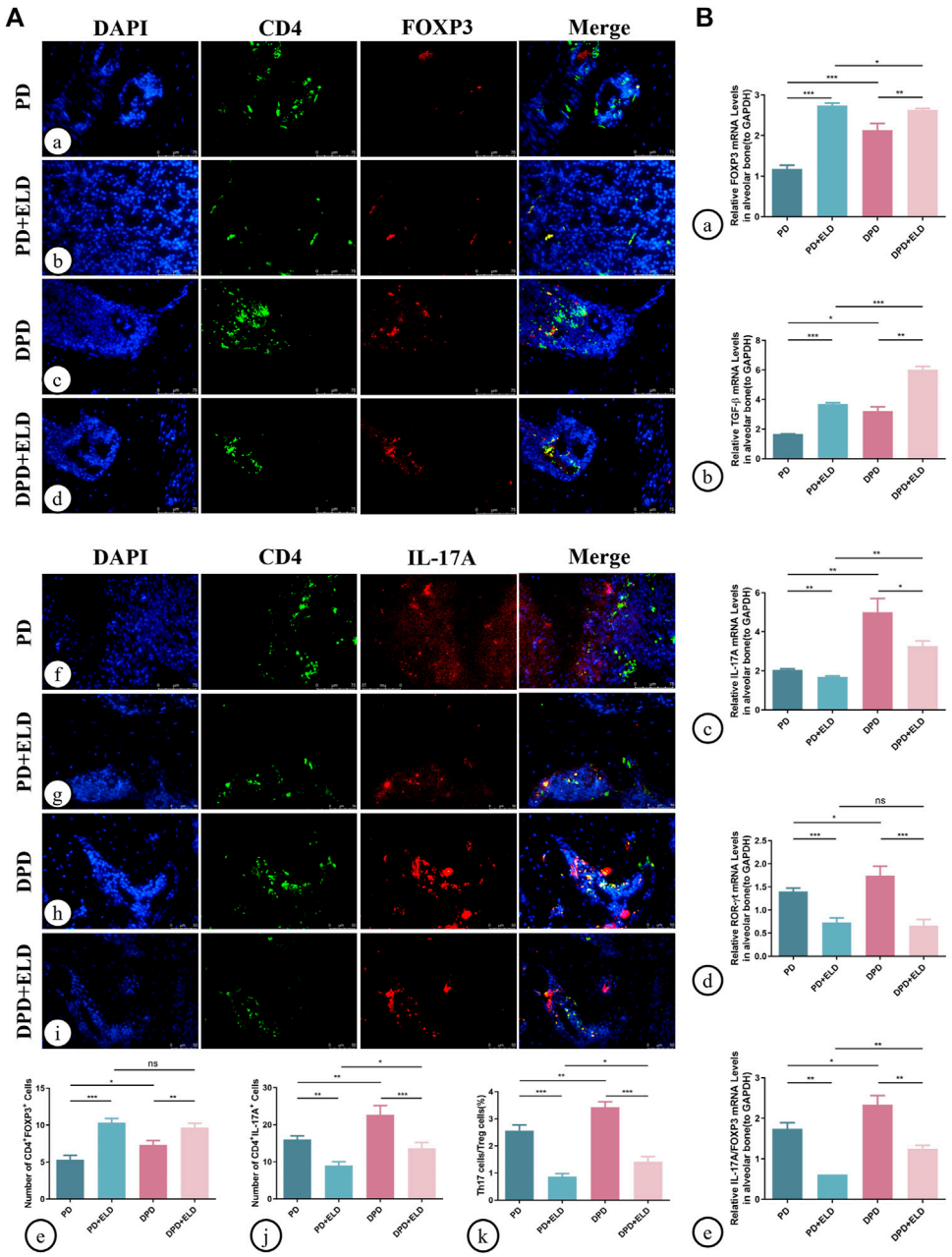

FIGURE 6
Immunofluorescence and qRT-PCR analysis of Th17 and Treg cells in the maxillary alveolar bone with ELD treatment. **(A)** The representative immunofluorescence staining images of $CD4^+$ $FOXP3^+$ T cells in the (a) PD, (b) PD + ELD, (c) DPD and (d) DPD + ELD groups. (e) The statistical analysis of $CD4^+$ $FOXP3^+$ T cell counts. The representative immunofluorescence staining images of $CD4^+$ IL-$17A^+$ T cells in the (f) PD, (g) PD + ELD, (h) DPD and (i) DPD + ELD groups. (j) The statistical analysis of the number of $CD4^+$ IL-$17A^+$ T cells. (k) The ratio of Th17/Treg cells. **(B)** Relative mRNA expression levels of **(A)** FOXP3, (b) TGF-β, (c) IL-17A, (d) ROR-γt and (e) the ratio of IL-17A/FOXP3 in the PD, PD + ELD, DPD and DPD + ELD groups. Data were shown as mean ± SD (*$p < 0.05$. **$p < 0.01$. ***$p < 0.001$).

imbalance. Although ELD showed a good preventive effect in the DPD group, Th17/Treg cell ratios did not return to normal levels in PD + ELD and DPD + ELD groups.

In previous studies, db/db mice have been widely used to simulate diabetes (Suriano et al., 2021). In our study, ligation combined with Pg-LPS injection was used to establish an experimental periodontitis model. Micro-CT and HE staining showed obvious alveolar bone loss in PD and DPD models, indicating that our approach successfully induced periodontitis and diabetes-associated periodontitis. Compared with the control and PD group, micro-CT and histomorphological examinations showed more serious periodontal destruction in the DPD group, manifested by more alveolar bone loss and fewer bone islands. Physiologically, alveolar bone undergoes an orderly process of bone remodeling, including bone resorption and bone formation (Li et al., 2021). Periodontitis is essentially an imbalance in bone remodeling homeostasis which is induced by inflammation and immune responses, ultimately resulting in alveolar bone loss (Becerra-Ruiz et al., 2022). We identified

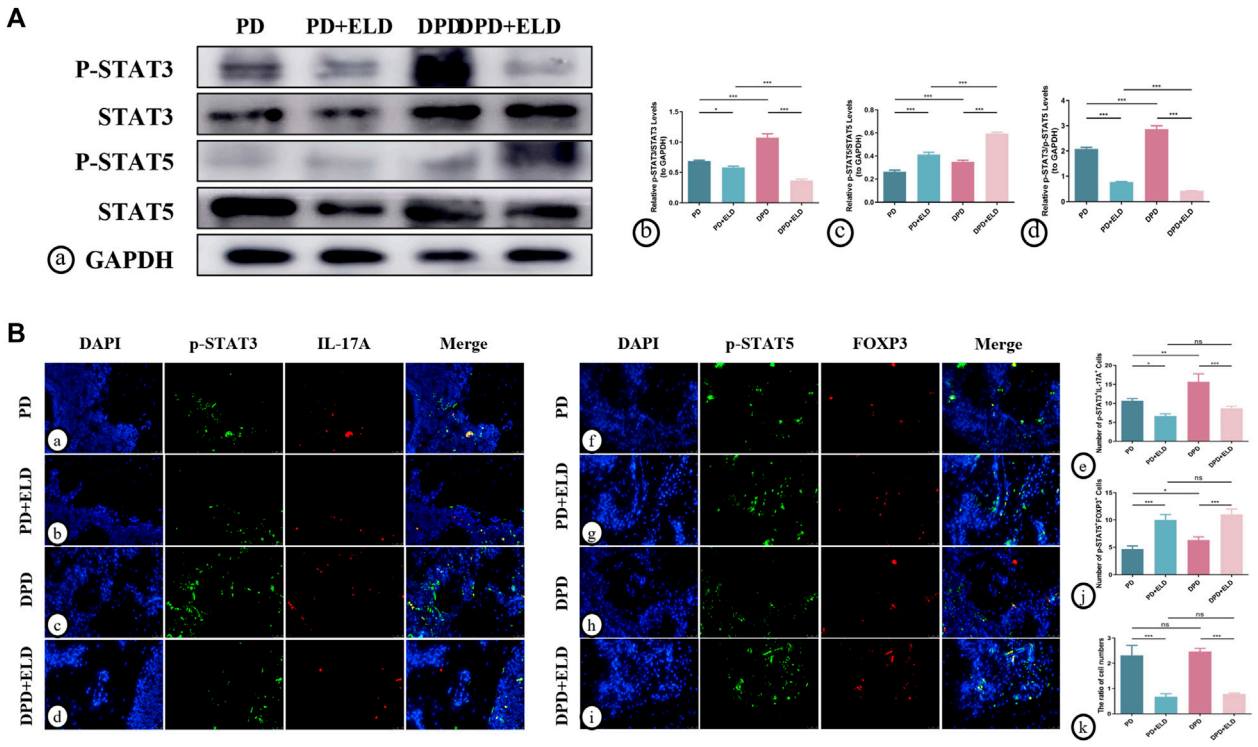

FIGURE 7
ELD regulated Th17/Treg cells through the STAT3/STAT5 signal. **(A)** (a) The protein expression of p-STAT3, STAT3, p-STAT5, STAT5 and GAPDH detected by western blotting in the PD, PD + ELD, DPD and DPD + ELD groups. The statistical analysis of (b) p-STAT3/STAT3, (c) p-STAT5/STAT5 and (d) the ratio of p-STAT3/p-STAT5 in western blotting. **(B)** The representative immunofluorescence staining images of p-STAT3$^+$IL-17A$^+$ cells in the (a) PD, (b) PD + ELD, (c) DPD and (d) DPD + ELD groups. (e) The statistical analysis of p-STAT3$^+$IL-17A$^+$ cell counts. The representative immunofluorescence staining images of p-STAT5$^+$FOXP3$^+$ cells in the (f) PD, (g) PD + ELD, (h) DPD and (i) DPD + ELD groups. (j) The statistical analysis of p-STAT5$^+$FOXP3$^+$ cell counts. (k) The ratio of p-STAT3$^+$IL-17A$^+$/p-STAT5$^+$FOXP3$^+$ cells. Data were shown as mean ± SD (*p < 0.05. **p < 0.01. ***p < 0.001).

decreased osteoblastic bone formation capacity (ALP-positive) and increased osteoclastic bone resorption capacity (TRAP-positive) in DPD group when compared with control and PD group, suggesting a more severe bone remodeling imbalance which showed less bone formation and more bone resorption. To further explore osteoclast activity, we investigated RANKL and OPG expression. It is accepted that the RANKL/RANK/OPG system has important roles in osteoclast function and bone remodeling (Tobeiha et al., 2020). RANKL increases osteoclast formation and enhances activity by interacting with RANK (homotrimeric transmembrane receptor from the tumor necrosis factor family). In contrast, OPG, a soluble RANKL decoy receptor, inhibits RANKL-RANK interactions, preventing osteoclast formation, and osteoclastic bone resorption (Udagawa et al., 2021). We found that RANKL to OPG expression ratios increased in PD and DPD mice but was more pronounced in DPD animals. Therefore, to a certain extent, changes in osteoclast activity were involved in alveolar bone loss in PD and DPD groups, which may be related to immune imbalance.

Th17 and Treg cells are specific CD4$^+$ T-lymphocyte subsets with important roles maintaining immune homeostasis (Lee, 2018). In local and circulating PD and DPD group studies, we observed relatively elevated Th17/Treg ratios when compared with the control group, consistent with clinical data showing Th17/Treg cell imbalance in patients with periodontitis (Zheng et al., 2019). Furthermore, our statistical analyses showed that relative Treg cell numbers were elevated at the local microenvironment but decreased in the systemic environment. This difference may have been due to the fact that immune cells, especially T cells, are substantially elevated in local inflammation environments (Dutzan et al., 2016). In recent years, studies have indicated that Th17 and Treg cells have important roles in bone remodeling homeostasis (Cafferata et al., 2021). Th17 lymphocytes produce pro-inflammatory cytokines, such as IL-6, IL-17A, IL-23, and RANKL, to promote osteoclast differentiation (Huang et al., 2022). However, Treg cells secrete anti-inflammatory cytokines, such as IL-10 and TGF-β1 which inhibit osteoclast differentiation (Zhu et al., 2020). Hence, we hypothesize that Th17/Treg cell imbalance has important roles in PD and DPD development. We also observed that the Th17/Treg cell imbalance was more pronounced in DPD when compared with PD animals. Furthermore, it was previously reported that Th17/Treg cell imbalance was involved in insulin resistance and led to hyperglycemia (Tao et al., 2019). In turn, hyperglycemia converts Treg cells to Th1 or Th17 cells, thereby exacerbating this imbalance (Zhang et al., 2021a) and impairing defense systems in periodontal tissue *via* the release of inflammatory factors, such as IL-17, to significantly increase periodontitis risk and severity (Huang et al., 2020a). This evidence suggests that Th17/Treg cell imbalance is not only a common immune mechanism in periodontitis and diabetes, but is key to their relationship in DPD pathogenesis. Hence, based on these observations, correcting the Th17/Treg cell imbalance may be an

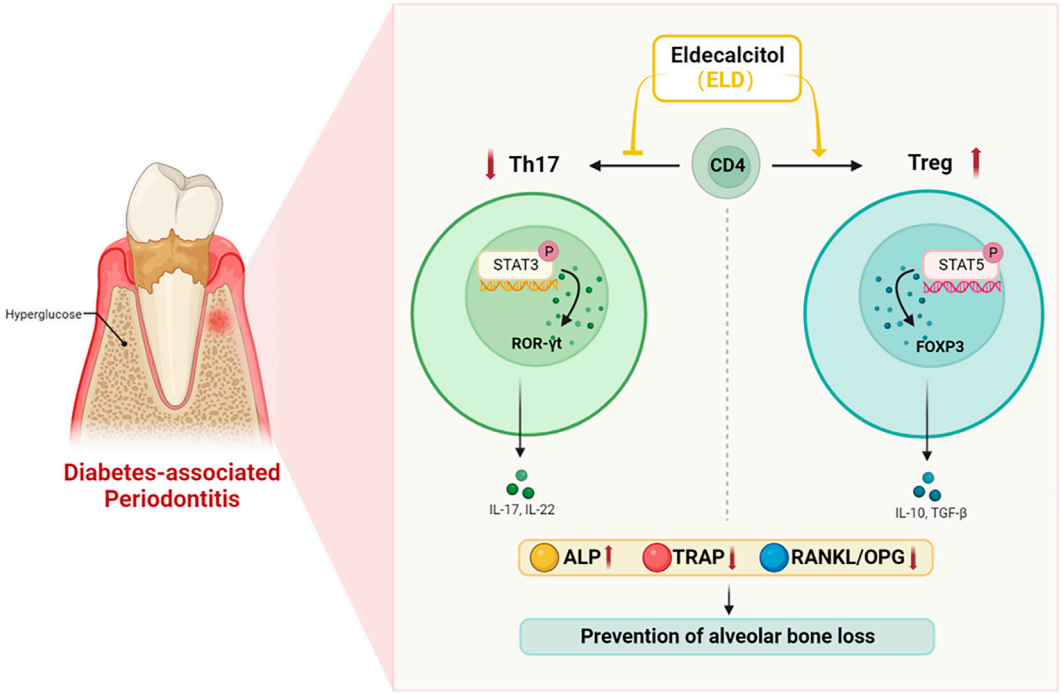

FIGURE 8
ELD effectively prevented alveolar bone loss by partially correcting the imbalance in Th17/Treg cells in DPD *via* the STAT3/STAT5 signal. ELD prevented alveolar bone loss in DPD by partially correcting the imbalance in Th17/Treg cells. One possible action mechanism may be that ELD corrected the imbalance in Th17/Treg cells by the STAT3/STAT5 signal.

effective treatment modality for PD and DPD, particularly DPD. Clinical and experimental data indicated that vitamin D supplementation benefited periodontal health (Han et al., 2019; Meghil et al., 2019). In our study, for the first time, we explored the preventative effects of ELD toward PD and DPD. Micro-CT and histomorphological examinations identified less alveolar bone loss in PD + ELD and DPD + ELD groups when compared with PD and DPD groups, respectively, suggesting ELD exerted preventative effects on alveolar bone loss caused by periodontitis. More interestingly, this bone loss in PD + ELD and DPD + ELD groups was broadly similar. Since alveolar bone resorption was more severe in DPD than in PD groups, and the final alveolar bone loss height was similar in both groups, our findings suggest that ELD was more advantageous in preventing DPD-induced alveolar bone loss when compared with PD. In addition, in this study, we found ELD has a hypoglycemic effect and it just presented in DPD mice but not in PD group (Supplementary Fig. 1). It was well known that impairment in glucose has an unfavorable effect on bone remodeling by the accumulation of AGEs and directly affecting the activity of osteoblast and osteoclast (Lecka-Czernik, 2017). It may be part of the reason why ELD has an advantage in preventing alveolar bone loss in DPD group.

Further, we compared the regulatory effects of ELD on Th17/Treg cell imbalance in DPD and PD groups. Our results showed that ELD did partially prevent Th17/Treg cell imbalance in PD and DPD animals, but we do not have enough evidence to prove the better preventive effect of ELD on Th17/Treg balance in the DPD group. This observation suggested that the preventive effect of ELD on DPD was not solely dependent on preventing Th17/Treg cell imbalance. Our previous studies have shown that ELD can improve the state of diabetic osteoporosis through promoting M2 macrophage polarization, which is accompanied by a decrease in blood glucose (Lu et al., 2022). Because of the immune imbalance in diabetes, the control of blood glucose is beneficial to inhibit the secretion of inflammatory factors by pro-inflammatory immune cells, promote the immunosuppressive effect of anti-inflammatory immune cells, thus indirectly regulate the balance of bone metabolism (Zhang et al., 2021b). In addition, we also found that after ELD treatment, $CD4^-$ $IL\text{-}17^+$ cells increased in DPD group, whereas reduced in PD group (Figures 5A, B). This may because that there are a variety of $CD4^-IL\text{-}17A^+$ cells in spleen lymphocytes, such as γδ T cells, LTi cells, some $CD8^+$ T cells and B cells and so on (Gu et al., 2013), and active vitamin D may have a complex regulatory effect on immune cells under different conditions (Baeke et al., 2010). Therefore, ELD may play a role in bone remodeling through multiple pathways, and its specific mechanism needs to be further explored.

As ELD significantly improved Th17/Treg cell imbalance *in vivo*, a comprehensive exploration of its molecular mechanisms was warranted. We focused on classical STAT3/STAT5 signaling and observed that ELD not only inhibited STAT3 signaling but also activated STAT5 signaling. Additionally, $p\text{-}STAT3^+IL\text{-}17A^+$/$p\text{-}STAT5^+FOXP3^+$ cell ratios decreased significantly *via* ELD actions, indicating an association between ELD and STAT3/STAT5 signaling. From previous studies, STAT3 signaling appeared to promote Th17 differentiation, while STAT5 signaling promoted Treg differentiation, with a balance observed between signaling (Zhao et al., 2018). Thus, in PD and DPD, low STAT3 and high

STAT5 activities were vital to prevent Th17/Treg cell imbalance. These findings supported our hypothesis that ELD exerted its preventative effects on PD and DPD *via* STAT3/STAT5 signaling. At present, there are few studies on how active vitamin D affects STAT3 and STAT5, but the research on JAK/STAT (Zhou et al., 2022), SOCS3/STAT (Wang et al., 2020) signaling pathway has entered the public view. Therefore, we hypothesized that ELD may regulate the phosphorylation of STAT3 and STAT5 through some regulatory factors. As latent cytoplasmic transcription factors, STATs can convey signals from the cell surface to the nucleus. This process requires the activation by cytokines and growth factors so that STATs undergo phosphorylation, involved in diverse biological functions (Abroun et al., 2015). Therefore, ELD may regulate the phosphorylation of STAT3 and STAT5 through cytokines and growth factors, and play an indirect rather than direct role, but the underling mechanism may need further exploration. In addition, though we used alveolar bone as a source of protein for western blotting, which not only contained $CD4^{+}$T cells but also comprised other cells such as bone cells and may affect the results of western blotting. But fluorescent double staining partially can reflect the changes of STAT3 and STAT5 in Th17 and Treg cells. Identifying definitive signaling mechanisms may make us better understand ELD actions and provide new concepts for future ELD applications.

In this study, we administered ELD to the whole body *via* gavage and focused on its preventative rather than therapeutic effects toward DPD. Therefore, a study limitation may be that in an already inflamed microenvironment, high protease, low pH, and increased angiogenesis levels existed (Leblebicioglu et al., 1996; Oikonomopoulou et al., 2018; Wei et al., 2021), and therefore, altering Treg/Th17 cell ratios by applying drugs to locally induce cell differentiation may not have been as effective. Considering alveolar bone loss in DPD, which is difficult to recover from, preventing DPD may be a better approach. However, when considering alveolar bone loss, further investigations are required to determine if ELD can reverse inflammation and generate periodontal regeneration. Additionally, we observed that ELD displayed some advantages in improving DPD. Considering the status of DPD treatment, simple local basic treatments may be ineffective. Therefore, ELD has the potential to become an important systemic adjuvant drug based on immune regulation, and combined applications with local basic therapies may enhance its efficacy. However, further studies are required to address this hypothesis. We also identified some study limitations related to experimental design and our data. One study limitation was that our conclusions were mainly based on animal experiments, without *in vitro* cell validation studies. *In vivo* studies were only conducted using single-time detection, without detecting Th17/Treg changes at multiple time intervals. In future investigations, we will focus on *in vitro* studies to determine if a high glucose environment affects Th17/Treg cell imbalance and if ELD improves this high glucose-mediated imbalance.

In summary, ELD was more advantageous in preventing alveolar bone loss by partially correcting Th17/Treg cell imbalance in DPD. As a recently launched drug in China, ELD provides a promising adjuvant therapeutic against bone loss in DPD patients (Figure 8).

Data availability statement

The raw data supporting the conclusion of this article will be made available by the authors, without undue reservation.

Ethics statement

The animal study was reviewed and approved by Experimental Animal Medicine Ethics Committee of Shandong University School of Stomatology.

Author contributions

Conceptualization: HL, ML, and JY; methodology: HL, YJ, and JZ; formal analysis and investigation: HL, YJ, and JZ; writing—original draft preparation: WZ and HL; writing—review and editing: WZ, HL; data curation: HL, YJ, and JZ; funding acquisition: HL and ML; resources: HL and ML; supervision: HL and ML; project administration: ML; Software: HG and JY; validation: HL and JY; visualization: HL and WZ.

Funding

This study was partially supported by the National Natural Science Foundation of China (No. 81972072) to ML, the National Natural Science Foundation of China (No. 81800982) and the Construction Engineering Special Fund of "Taishan Young Scholars" of Shandong Province (No. tsqn202103177) to HL.

Conflict of interest

The authors declare that the research was conducted in the absence of any commercial or financial relationships that could be construed as a potential conflict of interest.

Publisher's note

All claims expressed in this article are solely those of the authors and do not necessarily represent those of their affiliated organizations, or those of the publisher, the editors and the reviewers. Any product that may be evaluated in this article, or claim that may be made by its manufacturer, is not guaranteed or endorsed by the publisher.

Supplementary material

The Supplementary Material for this article can be found online at: https://www.frontiersin.org/articles/10.3389/fbioe.2023.1070117/full#supplementary-material

References

Abroun, S., Saki, N., Ahmadvand, M., Asghari, F., Salari, F., and Rahim, F. (2015). STATs: An old story, yet mesmerizing. *Cell J.* 17 (3), 395–411. doi:10.22074/cellj.2015.1

Baeke, F., Takiishi, T., Korf, H., Gysemans, C., and Mathieu, C. (2010). Vitamin D: Modulator of the immune system. *Curr. Opin. Pharmacol.* 10 (4), 482–496. doi:10.1016/j.coph.2010.04.001

Barutta, F., Bellini, S., Durazzo, M., and Gruden, G. (2022). Novel insight into the mechanisms of the bidirectional relationship between diabetes and periodontitis. *Biomedicines* 10 (1), 178. doi:10.3390/biomedicines10010178

Becerra-Ruiz, J. S., Guerrero-Velázquez, C., Martínez-Esquivias, F., Martínez-Pérez, L. A., and Guzmán-Flores, J. M. (2022). Innate and adaptive immunity of periodontal disease. From etiology to alveolar bone loss. *Oral Dis.* 28 (6), 1441–1447. doi:10.1111/odi.13884

Bosshardt, D. D. (2018). The periodontal pocket: Pathogenesis, histopathology and consequences. *Periodontol. 2000* 76 (1), 43–50. doi:10.1111/prd.12153

Cafferata, E. A., Castro-Saavedra, S., Fuentes-Barros, G., Melgar-Rodríguez, S., Rivera, F., Carvajal, P., et al. (2021). Boldine inhibits the alveolar bone resorption during ligature-induced periodontitis by modulating the Th17/Treg imbalance. *J. Periodontol.* 92 (1), 123–136. doi:10.1002/jper.20-0055

Cecoro, G., Annunziata, M., Iuorio, M. T., Nastri, L., and Guida, L. (2020). Periodontitis, low-grade inflammation and systemic health: A scoping review. *Med. Kaunas.* 56 (6), 272. doi:10.3390/medicina56060272

de Freitas, P. H., Hasegawa, T., Takeda, S., Sasaki, M., Tabata, C., Oda, K., et al. (2011). Eldecalcitol, a second-generation vitamin D analog, drives bone minimodeling and reduces osteoclastic number in trabecular bone of ovariectomized rats. *Bone* 49 (3), 335–342. doi:10.1016/j.bone.2011.05.022

Dutzan, N., Konkel, J. E., Greenwell-Wild, T., and Moutsopoulos, N. M. (2016). Characterization of the human immune cell network at the gingival barrier. *Mucosal Immunol.* 9 (5), 1163–1172. doi:10.1038/mi.2015.136

Gu, C., Wu, L., and Li, X. (2013). IL-17 family: Cytokines, receptors and signaling. *Cytokine* 64 (2), 477–485. doi:10.1016/j.cyto.2013.07.022

Han, J., Cheng, C., Zhu, Z., Lin, M., Zhang, D-X., Wang, Z-M., et al. (2019). Vitamin D reduces the serum levels of inflammatory cytokines in rat models of periodontitis and chronic obstructive pulmonary disease. *J. Oral Sci.* 61 (1), 53–60. doi:10.2334/josnusd.17-0357

Han, X., Du, J., Liu, D., Liu, H., Amizuka, N., and Li, M. (2017). Histochemical examination of systemic administration of eldecalcitol combined with guided bone regeneration for bone defect restoration in rats. *J. Mol. Histol.* 48 (1), 41–51. doi:10.1007/s10735-016-9705-0

Hirota, Y., Nakagawa, K., Isomoto, K., Sakaki, T., Kubodera, N., Kamao, M., et al. (2018). Eldecalcitol is more effective in promoting osteogenesis than alfacalcidol in Cyp27b1-knockout mice. *PLoS One* 13 (10), e0199856. doi:10.1371/journal.pone.0199856

Huang, C., Zhang, C., Yang, P., Chao, R., Yue, Z., Li, C., et al. (2020). <p>Eldecalcitol inhibits LPS-induced NLRP3 inflammasome-dependent pyroptosis in human gingival fibroblasts by activating the Nrf2/HO-1 signaling pathway</p>. *Drug Des. Devel Ther.* 14, 4901–4913. doi:10.2147/dddt.s269223

Huang, F., Wong, P., Li, J., Lv, Z., Xu, L., Zhu, G., et al. (2022). Osteoimmunology: The correlation between osteoclasts and the Th17/Treg balance in osteoporosis. *J. Cell Mol. Med.* 26 (13), 3591–3597. doi:10.1111/jcmm.17399

Huang, Z., Pei, X., and Graves, D. T. (2020). The interrelationship between diabetes, IL-17 and bone loss. *Curr. Osteoporos. Rep.* 18 (1), 23–31. doi:10.1007/s11914-020-00559-6

Ji, J., Zhai, H., Zhou, H., Song, S., Mor, G., and Liao, A. (2019). The role and mechanism of vitamin D-mediated regulation of Treg/Th17 balance in recurrent pregnancy loss. *Am. J. Reprod. Immunol.* 81 (6), e13112. doi:10.1111/aji.13112

Jiang, Y., Tang, H., Ma, X., Cheng, Q., Lin, H., Jin, X., et al. (2019). Eldecalcitol increases bone mineral density in Chinese osteoporotic patients without vitamin D or calcium supplementation. *J. Bone Min. Metab.* 37 (6), 1036–1047. doi:10.1007/s00774-019-01009-9

Kou, Y., Jiang, Y., Liu, S., Yang, P., Lu, Y., Liu, H., et al. (2021). Regulatory T cells showed characteristics of T helper-17(Th17) cells in mice periodontitis model. *Oral Dis.* 2021. doi:10.1111/odi.14072

Leblebicioglu, B., Lim, J. S., Cario, A. C., Beck, F. M., and Walters, J. D. (1996). pH changes observed in the inflamed gingival crevice modulate human polymorphonuclear leukocyte activation *in vitro*. *J. Periodontol.* 67 (5), 472–477. doi:10.1902/jop.1996.67.5.472

Lecka-Czernik, B. (2017). Diabetes, bone and glucose-lowering agents: Basic biology. *Diabetologia* 60 (7), 1163–1169. doi:10.1007/s00125-017-4269-4

Lee, G. R. (2018). The balance of Th17 versus Treg cells in autoimmunity. *Int. J. Mol. Sci.* 19 (3), 730. doi:10.3390/ijms19030730

Li, J., Wang, J., Song, X., Li, Z., Zhang, Y., Lu, H., et al. (2022). Effect of type 2 diabetes mellitus and periodontitis on the Th1/Th2 and Th17/Treg paradigm. *Am. J. Dent.* 35 (1), 55–60.

Li, M., Hasegawa, T., Hogo, H., Tatsumi, S., Liu, Z., Guo, Y., et al. (2013). Histological examination on osteoblastic activities in the alveolar bone of transgenic mice with induced ablation of osteocytes. *Histol. Histopathol.* 28 (3), 327–335. doi:10.14670/HH-28.327

Li, Y., Ling, J., and Jiang, Q. (2021). Inflammasomes in alveolar bone loss. *Front. Immunol.* 12, 691013. doi:10.3389/fimmu.2021.691013

Li, Y., Lu, Z., Zhang, L., Kirkwood, K. L., Lopes-Virella, M. F., and Huang, Y. (2020). Acid sphingomyelinase deficiency exacerbates LPS-induced experimental periodontitis. *Oral Dis.* 26 (3), 637–646. doi:10.1111/odi.13268

Liu, H., Wang, G., Wu, T., Mu, Y., and Gu, W. (2022). Efficacy and safety of eldecalcitol for osteoporosis: A meta-analysis of randomized controlled trials. *Front. Endocrinol. (Lausanne)* 13, 854439. doi:10.3389/fendo.2022.854439

Löe, H. (1993). Periodontal disease. The sixth complication of diabetes mellitus. *Diabetes Care* 16 (1), 329–334. doi:10.2337/diacare.16.1.329

Lu, Y., Liu, S., Yang, P., Kou, Y., Li, C., Liu, H., et al. (2022). Exendin-4 and eldecalcitol synergistically promote osteogenic differentiation of bone marrow mesenchymal stem cells through M2 macrophages polarization via PI3K/AKT pathway. *Stem Cell Res. Ther.* 13 (1), 113. doi:10.1186/s13287-022-02800-8

Luong, A., Tawfik, A. N., Islamoglu, H., Gobriel, H. S., Ali, N., Ansari, P., et al. (2021). Periodontitis and diabetes mellitus co-morbidity: A molecular dialogue. *J. Oral Biosci.* 63 (4), 360–369. doi:10.1016/j.job.2021.10.006

Matsumoto, T., Ito, M., Hayashi, Y., Hirota, T., Tanigawara, Y., Sone, T., et al. (2011). A new active vitamin D3 analog, eldecalcitol, prevents the risk of osteoporotic fractures-a randomized, active comparator, double-blind study. *Bone* 49 (4), 605–612. doi:10.1016/j.bone.2011.07.011

Meghil, M. M., Hutchens, L., Raed, A., Multani, N. A., Rajendran, M., Zhu, H., et al. (2019). The influence of vitamin D supplementation on local and systemic inflammatory markers in periodontitis patients: A pilot study. *Oral Dis.* 25 (5), 1403–1413. doi:10.1111/odi.13097

Oikonomopoulou, K., Diamandis, E. P., Hollenberg, M. D., and Chandran, V. (2018). Proteinases and their receptors in inflammatory arthritis: An overview. *Nat. Rev. Rheumatol.* 14 (3), 170–180. doi:10.1038/nrrheum.2018.17

Polak, D., and Shapira, L. (2018). An update on the evidence for pathogenic mechanisms that may link periodontitis and diabetes. *J. Clin. Periodontol.* 45 (2), 150–166. doi:10.1111/jcpe.12803

Ribeiro, V. R., Romao-Veiga, M., Nunes, P. R., de Oliveira, L. R. C., Romagnoli, G. G., Peracoli, J. C., et al. (2022). Immunomodulatory effect of vitamin D on the STATs and transcription factors of CD4+ T cell subsets in pregnant women with preeclampsia. *Clin. Immunol.* 234, 108917. doi:10.1016/j.clim.2021.108917

Ringe, J. D. (2020). Plain vitamin D or active vitamin D in the treatment of osteoporosis: Where do we stand today? *Arch. Osteoporos.* 15 (1), 182. doi:10.1007/s11657-020-00842-0

Saito, H., Kakihata, H., Nishida, Y., Yatomi, S., Nihojima, S., Kobayashi, Y., et al. (2017). The safety and effectiveness profile of eldecalcitol in a prospective, post-marketing observational study in Japanese patients with osteoporosis: Interim report. *J. Bone Min. Metab.* 35 (4), 456–463. doi:10.1007/s00774-016-0779-2

Suriano, F., Vieira-Silva, S., Falony, G., Roumain, M., Paquot, A., Pelicaen, R., et al. (2021). Novel insights into the genetically obese (ob/ob) and diabetic (db/db) mice: Two sides of the same coin. *Microbiome* 9 (1), 147. doi:10.1186/s40168-021-01097-8

Tao, L., Liu, H., and Gong, Y. (2019). Role and mechanism of the Th17/Treg cell balance in the development and progression of insulin resistance. *Mol. Cell Biochem.* 459 (1-2), 183–188. doi:10.1007/s11010-019-03561-4

Teramachi, J., Inagaki, Y., Shinohara, H., Okamura, H., Yang, D., Ochiai, K., et al. (2017). PKR regulates LPS-induced osteoclast formation and bone destruction *in vitro* and *in vivo*. *Oral Dis.* 23 (2), 181–188. doi:10.1111/odi.12592

Tobeiha, M., Moghadasian, M. H., Amin, N., and Jafarnejad, S. (2020). RANKL/RANK/OPG pathway: A mechanism involved in exercise-induced bone remodeling. *Biomed. Res. Int.* 2020, 1–11. doi:10.1155/2020/6910312

Tonetti, M. S., Greenwell, H., and Kornman, K. S. (2018). Staging and grading of periodontitis: Framework and proposal of a new classification and case definition. *J. Clin. Periodontol.* 45 (20), S149–S161. doi:10.1111/jcpe.12945

Udagawa, N., Koide, M., Nakamura, M., Nakamichi, Y., Yamashita, T., Uehara, S., et al. (2021). Osteoclast differentiation by RANKL and OPG signaling pathways. *J. Bone Min. Metab.* 39 (1), 19–26. doi:10.1007/s00774-020-01162-6

Valm, A. M. (2019). The structure of dental plaque microbial communities in the transition from health to dental caries and periodontal disease. *J. Mol. Biol.* 431 (16), 2957–2969. doi:10.1016/j.jmb.2019.05.016

Wang, Q., Zhou, X., Zhang, P., Zhao, P., Nie, L., Ji, N., et al. (2020). 25-Hydroxyvitamin D(3) positively regulates periodontal inflammaging via SOCS3/STAT signaling in diabetic mice. *Steroids* 156, 108570. doi:10.1016/j.steroids.2019.108570

Wei, K., Nguyen, H. N., and Brenner, M. B. (2021). Fibroblast pathology in inflammatory diseases. *J. Clin. Invest* 131 (20), e149538. doi:10.1172/JCI149538

Zhang, B., Yang, Y., Yi, J., Zhao, Z., and Ye, R. (2021). Hyperglycemia modulates M1/M2 macrophage polarization via reactive oxygen species overproduction in ligature-induced periodontitis. *J. Periodontal Res.* 56 (5), 991–1005. doi:10.1111/jre.12912

Zhang, P., Yang, C-L., Du, T., Liu, Y-D., Ge, M-R., Li, H., et al. (2021). Diabetes mellitus exacerbates experimental autoimmune myasthenia gravis via modulating both adaptive and innate immunity. *J. Neuroinflammation* 18 (1), 244. doi:10.1186/s12974-021-02298-6

Zhao, P., Li, J., Tian, Y., Mao, J., Liu, X., Feng, S., et al. (2018). Restoring Th17/Treg balance via modulation of STAT3 and STAT5 activation contributes to the amelioration of chronic obstructive pulmonary disease by Bufei Yishen formula. *J. Ethnopharmacol.* 217, 152–162. doi:10.1016/j.jep.2018.02.023

Zheng, M., Wang, C., Ali, A., Shih, Y. A., Xie, Q., and Guo, C. (2021). Prevalence of periodontitis in people clinically diagnosed with diabetes mellitus: A meta-analysis of epidemiologic studies. *Acta Diabetol.* 58 (10), 1307–1327. doi:10.1007/s00592-021-01738-2

Zheng, Y., Dong, C., Yang, J., Jin, Y., Zheng, W., Zhou, Q., et al. (2019). Exosomal microRNA-155-5p from PDLSCs regulated Th17/Treg balance by targeting sirtuin-1 in chronic periodontitis. *J. Cell Physiol.* 234 (11), 20662–20674. doi:10.1002/jcp.28671

Zhou, W., Wang, W., Yuan, X. J., Xiao, C. C., Xing, Y., Ye, S. D., et al. (2022). The effects of RBP4 and vitamin D on the proliferation and migration of vascular smooth muscle cells via the JAK2/STAT3 signaling pathway. *Oxid. Med. Cell Longev.* 2022, 1–23. doi:10.1155/2022/3046777

Zhu, L., Hua, F., Ding, W., Ding, K., Zhang, Y., and Xu, C. (2020). The correlation between the Th17/Treg cell balance and bone health. *Immun. Ageing* 17, 30. doi:10.1186/s12979-020-00202-z

Zhu, X., and Zhu, J. (2020). CD4 T helper cell subsets and related human immunological disorders. *Int. J. Mol. Sci.* 21 (21), 8011. doi:10.3390/ijms21218011

Zou, H., Zhou, N., Huang, Y., Luo, A., and Sun, J. (2022). Phenotypes, roles, and modulation of regulatory lymphocytes in periodontitis and its associated systemic diseases. *J. Leukoc. Biol.* 111 (2), 451–467. doi:10.1002/jlb.3vmr0321-027rrr

frontiers | Frontiers in Bioengineering and Biotechnology

TYPE Original Research
PUBLISHED 16 February 2023
DOI 10.3389/fbioe.2023.1135655

OPEN ACCESS

EDITED BY
Xing Wang,
Shanxi Medical University, China

REVIEWED BY
Haibo Wang,
Sichuan University, China
Duoyi Zhao,
Fourth Affiliated Hospital of China Medical University, China

*CORRESPONDENCE
Hao Chen,
hchen2020@yzu.edu.cn
Jianwei Du,
doctorduyz@163.com
Huihui Wang,
wanghh56@163.com

†These authors have contributed equally to this work

SPECIALTY SECTION
This article was submitted to Biomaterials, a section of the journal Frontiers in Bioengineering and Biotechnology

RECEIVED 01 January 2023
ACCEPTED 03 February 2023
PUBLISHED 16 February 2023

CITATION
Wang X, Li G, Li K, Shi Y, Lin W, Pan C, Li D, Chen H, Du J and Wang H (2023), Controlled-release of apatinib for targeted inhibition of osteosarcoma by supramolecular nanovalve-modified mesoporous silica.
Front. Bioeng. Biotechnol. 11:1135655.
doi: 10.3389/fbioe.2023.1135655

Controlled-release of apatinib for targeted inhibition of osteosarcoma by supramolecular nanovalve-modified mesoporous silica

Xinglong Wang[1†], Gongke Li[2†], Ke Li[1], Yu Shi[1], Wenzheng Lin[1], Chun Pan[1], Dandan Li[1], Hao Chen[1*], Jianwei Du[1*] and Huihui Wang[1*]

[1]Department of Orthopedics, Affiliated Hospital of Yangzhou University, Yangzhou, Jiangsu, China, [2]Department of Critical Care Medicine, Affiliated Hospital of Yangzhou University, Yangzhou, Jiangsu, China

Targeted delivery of antitumor drugs has been recognized as a promising therapeutic modality to improve treatment efficacy, reduce the toxic side effects and inhibit tumor recurrence. In this study, based on the high biocompatibility, large specific surface area, and easy surface modification of small-sized hollow mesoporous silica nanoparticles β-cyclodextrin (β-CD)-benzimidazole (BM) supramolecular nanovalve, together with bone-targeted alendronate sodium (ALN) were constructed on the surface of small-sized HMSNs. The drug loading capacity and efficiency of apatinib (Apa) in HMSNs/BM-Apa-CD-PEG-ALN (HACA) were 65% and 25%, respectively. More importantly, HACA nanoparticles can release the antitumor drug Apa efficiently compared with non-targeted HMSNs nanoparticles in the acidic microenvironment of the tumor. *In vitro* studies showed that HACA nanoparticles exhibited the most potent cytotoxicity in osteosarcoma cells (143B cells) and significantly reduced cell proliferation, migration and invasion. Therefore, the drug-efficient release of antitumor effect of HACA nanoparticles is a promising way to treat osteosarcoma.

KEYWORDS

supramolecular nanovalves, HMSNs, Cd, AlN, APA

1 Introduction

Osteosarcoma is the most common primary malignant bone tumor, often occurring in adolescents, with a high tendency of local infiltration and distant metastasis, high recurrence rate and low survival rate (Jaffe, 2010; Freyer and Seibel, 2015; Spraker-Perlman et al., 2019). With the development of neoadjuvant chemotherapy and surgical techniques, amputation for osteosarcoma has been replaced by limb-preserving surgery and radiotherapy. The 5-year survival rate for patients has increased to about 70% (Ando et al., 2013). Unfortunately, the cure rate for osteosarcoma has not improved in the last 30 years (Liu et al., 2017). Therefore, there is an urgent need to find new treatment methods and drugs. Novel targeted therapies for osteosarcoma are currently attracting increasing interest. Apa is a novel, highly selective inhibitor of the vascular endothelial growth factor receptor 2 (VEGFR2) complex kinase that blocks downstream signaling of VEGFR2 and exerts antitumor effects in a variety of tumors

(Hicklin and Ellis, 2005). Recent studies have shown that Apa has a growth inhibitory effect on osteosarcoma cells (Liu et al., 2017). For example, Han et al. reported that Apatinib inhibits cell proliferation and migration of osteosarcoma *via* activating LINC00261/miR-620/PTEN axis (Han et al., 2021). In addition, Li et al. also revealed that overcoming therapeutic failure in osteosarcoma *via* Apatinib-encapsulated hydrophobic poly(ester amide) nanoparticles (Li et al., 2020). However, Apa, like most chemotherapy drugs, cannot target tumor cells and has multi-organ toxicity, such as cardiotoxicity, hepatotoxicity and other systemic multi-organ toxicities (Maluccio and Covey, 2012; Gan et al., 2018). Nanoparticle-mediated targeted drug delivery systems are currently considered to be an effective strategy to address this problem. In addition, research on multifunctional nanoparticles as drug delivery systems continues to increase and is expected to be a new avenue for the treatment of tumors.

In recent years, HMSNs nanoparticles have received increasing attention due to their superior water dispersibility, biocompatibility and diverse biomedical applications (Ambrogio et al., 2011; Porta et al., 2013; Shen et al., 2013; Teng et al., 2013). As a drug delivery system, HMSNs nanoparticles have many advantages such as large specific surface area, uniform mesopore distribution, relatively large pore size, easy surface modification, good biocompatibility and high drug loading efficiency (Baù et al., 2009; Gao et al., 2011; Li et al., 2019). HMSNs are synthesized in various ways, such as Kirkendall effect method (Chen et al., 2010), soft/hard template method (Zhou et al., 2014), point-couple substitution method (Skrabalak et al., 2008), and hydrothermal method (Skrabalak et al., 2008). Most HMSNs are manufactured by the soft/hard template method, which requires complex steps to remove the template after the reaction. For example, in order to create internal void spaces, it is inevitable that the template is calcined at high temperatures or solvent extracted and cleaned with strong acids or bases (Skrabalak et al., 2008). This template-assisted method is effective for producing HMSNs with relatively narrow size distributions, but removing the core template may lead to agglomeration, or mutual adhesion to form larger particles (Lin et al., 2009). In addition, these techniques usually make it difficult to prepare spheres with sizes smaller than 100 nm. This limits their effective application as nanocarriers in the biological field, as they are extremely poorly absorbed by cells during drug delivery *in vivo* and tend to accumulate in the body (Lin et al., 2009). Highly dispersed mesoporous silica spheres with intact hollow interiors and through pores on the shell were fabricated (She et al., 2015). Cui et al. reported that the TBC/HMSN/P28 scaffold can promote proliferation and osteogenic differentiation of MC3T3-E1 cells *in vitro* and new bone tissue generation *in vivo*. HMSNs with small particle size were easier to enter bone tissue (Cui et al., 2018). Moreover, the lack of tumor specificity of HMSNs, like most antitumor drugs, also severely limits the application of HMSNs nanoparticles.

HMSNs can contain drugs through a simple physical adsorption process and release them independently. More importantly, the rational design of supramolecular nano-valve can prevent the early release of drugs during blood circulation and mitigate the non-selective damage to normal organs. Supramolecular nanovalves typically respond to biological signals (e.g., pH, enzymes) through the relative motion of large rings on a functionalized linear stem (Barat et al., 2015; Qiu et al., 2015). Based on the structural characteristics of β-cyclodextrin (β-CD) and the formation of "nanovalves" with various molecules (benzimidazole, etc.), its dissociation is closely related to the environmental conditions (temperature and pH) (Ma and Zhao, 2015). For instance, the acidic nature of the tumor microenvironment (TME) (Gong et al., 2018; Barve et al., 2020) allows the dissociation and disintegration of CD-based "nanovalves". Meng et al. reported that CD nanovalves were modified on the surface of mesoporous silica spheres to achieve responsive release of the anticancer drug DOX, however, the loading of DOX by the mesoporous silica spheres was only about 2% and lacked tumor targeting ability (Meng et al., 2010). In addition, bisphosphonates have a relatively high binding affinity for hydroxyapatite compared to other calcium minerals such as calcium oxalate, calcium carbonate or calcium pyrophosphate (Zaheer et al., 2001; Lenkinski et al., 2003; Torres Martin de Rosales et al., 2009; Hyun et al., 2014). This advantage has led to the widespread use of bisphosphonates in bone targeting. Take ALN as an example, it can be used not only as a bone disease drug, but also as a bone targeting ligand (Sun et al., 2016). Guven et al. used bisphosphonic acid groups as biomineralization-inducing sites, recruiting positive ions [mainly calcium ions (Ca^{2+})] and negative ions [mainly phosphate groups (PO_4^{3-})]. Nanoparticles reach the tumor tissue and form a mineral barrier around it, effectively inhibiting the proliferation and migration of cancer cells (Guven et al., 2018). In addition, as a diphosphonate, ALN attenuates the bone destruction involved in osteosarcoma by inhibiting the activity of osteoclasts, which also contributes to delaying the possibility of pulmonary metastasis (Jiang et al., 2022).

Therefore, a supramolecular "nanovalve" - β-CD-benzimidazole (BM) - anchored on the outer surface of small-sized HMSNs was designed and loaded with Apa, then modified with bone-targeting ALN. The nanoparticles can act as a bifunctional nanosystem, which not only targets bone tissue, but also effectively releases the antitumor drug Apa in the low pH microenvironment, reducing its toxic effects on the organism. Thus, the design of this nanoparticle provides a new paradigm for the treatment of bone tumors.

2 Materials and methods

2.1 Materials

Hexadecyltrimethylammonium bromide (CTAB) was purchased from sigma (Shanghai, China); Octanol, cyclohexane, X-100 Trition, ammonia, anhydrous ethanol, acetic acid, tetraethylorthosilicate (TEOS), (3-Aminopropyltriethoxysilane (APTES), acetone, 2-benzimidazolepropionic acid (BM) were purchased from Aladdin Ltd. (Shanghai, China). NHS-PEG-COOH (PEG) was purchased from Tuo Yang Biotechnology (Shanghai, China). Alendronate sodium trihydrate (ALN), β-Cyclodextrin (CD), N-Hydroxysuccinimide-1-hydroxypyrrolidine-2,5-dione (NHS), (1- (3-Dimethylaminopropyl)-3-ethylcarbodiimide hydrochloride (EDC·HCl), Dimethyl sulfoxide (DMSO) were purchased from Beyoytime (Shanghai, China); 3-(4,5-dimethyl-2-thiazolyl)-2,5-diphenyl-2-H-tetrazolium bromide (MTT), Crystalline violet staining solution, Chlorin e6 (Ce6), 4%

Paraformaldehyde, 4,6-Diamidino-2-phenylindole dihydrochloride (DAPI), Pore polycarbonate film (pore size 8 mm), Matrigel were purchased from Solarbio (Beijing, China). All chemicals were used without further purification. Distilled and deionized water was used throughout the experiments.

2.2 Methods

2.2.1 Preparation of HACA

2.2.1.1 Preparation of HMSNs

Cyclohexane 145.2 mL, n-octanol 35.2 mL, CTAB (30 mg, 0.08 mmol) and X-100 Trition 35.76 g were mixed thoroughly in a round bottom flask and 8.8 mL of distilled water containing 20 ul of APTEs was added separately. After thorough stirring, $NH_3{\cdot}H_2O$ (1.6 mL) and TEOS (1.6 mL) were added respectively. After stirring for 24 h, the reaction was terminated by adding an appropriate amount of acetone until a flocculent substance appeared. After centrifugation, the white precipitate was obtained, and the appropriate amount of distilled water and anhydrous ethanol were added and stirred thoroughly until completely dissolved and then centrifuged, and each of such steps was operated three times. The resulting white precipitate was put into a round bottom flask with an appropriate amount of acetic acid and stirred for 4 h, then centrifuged, washed again with distilled water for 3 times, and finally dried at 60°C to obtain HMSNs for further use.

2.2.1.2 Preparation of HMSNs/BM and HMSNs/BM-Apa (HA)

BM (100 mg, 0.53 mmol), EDC (201.58 mg, 1.05 mmol) and NHS (121.01 mg, 1.05 mmol) were added to deionized water (30 mL) in turn and stirred thoroughly for 30 min, followed by the addition of the above prepared HMSNs (50 mg) and Apa (50 mg, 0.10 mmol), dissolve completely after sonication, continue to stir for 24 h and then centrifuge and dry at 60°C.

2.2.1.3 Preparation of OTs-β-CD (CD)

First, cyclodextrin (42 g, 0.037 mol) was dissolved in 300 mL distilled water. NAOH (0.333 g/mL, 12 mL) solution was added to make the solution turn yellow. Then p-toluenesulfonyl chloride (6.06 g, 0.032 mol) in 20 mL acetonitrilewas added into the above solution within 10 min. White precipitate appeared immediately. Afterwords, the solution was stirred for 2.5 h, filtered, neutralized with hydrochloric acid until slightly alkaline. After filtration, the product was recrystallized twice and dried to obtain OTs-β-CD. OTs-β-CD (1.5 g, 1.17 mmol) is added to 5 mL of ethylenediamine under nitrogen atmosphere and stirred for 24 h at 60 °C. Finally, the product is filtered in a large amount of ethanol to obtain white precipitate and dried for further use.

2.2.1.4 Preparation of CD-PEG-ALN (CA) and HACA

Firstly, CD (58.85 mg, 0.05 mmol) and PEG (100 mg, 0.05 mmol) were added to deionized water (20 mL) and stirred for 24 h. Then EDC (19.17 mg, 0.10 mmol), NHS (11.51 mg, 0.10 mmol) and ALN (27.11 mg, 0.10 mmol), stirred again for 24 h and then dialyzed overnight, and finally lyophilized to obtain CD-PEG-ALN (CA). Dissolving CD (5 mg), CD-PEG (5 mg) and CA (5 mg) in a certain amount of deuterium water (500 ul) and being analyzed by Nuclear magnetic resonance spectrometer (AVANCE 600, Germany). CD-PEG: ^{1}H NMR (400 MHz, D_2O) δ 4.88 (s, 1H), 3.72 (dt, J = 15.6, 11.0 Hz, 4H), 3.52 (s, 18H), 3.05 – 3.02 (m, 1H), 2.77 (s, 1H), 2.50 (s, 1H), 2.26 (s, 1H). CD-PEG-ALN: 1H NMR (400 MHz, d2o) δ 4.88 (d, J = 3.8 Hz, 2H), 3.80 – 3.61 (m, 5H), 3.52 (s, 31H), 3.07 – 2.82 (m, 5H), 2.69 (s, 2H), 2.56 (s, 1H), 1.82 (s, 2H), 0.89 (t, J = 7.2 Hz, 1H). Finally, CA (20 mg) was mixed with HA (20 mg) for 24 h and centrifugally dried to obtain the final product HACA. Similarly, in the preparation of HMSNs/BM-CD-PEG-ALN (HCA) and HMSNs/BM-Apa-CD-PEG (HAC), Apa and ALN are not added in the above preparation process, and the rest of the steps are obtained in the same way.

2.3 Characterization

The morphology of the synthesized HMSNs and HACA nanoparticles was observed by Tecnai 12 transmission electron microscopy (TEM, Philips Netherlands). The TEM samples were sonicated and dispersed in ethanol on a deposited porous carbon grid. Fourier transform infrared (FTIR, Nicolet 6700, Thermo Fisher, United States) spectroscopy is used to analyze changes in the biochemical composition of a sample. Following the KBr pellet method, a small quantity of the samples was grinded with KBr powder. All measurements were performed with transmittance mode and recorded in the spectral range of 4000–400 cm^{-1} for 16 scans and with a spectral resolution of 4 cm^{-1}. The UV–Vis absorption of the sample and quantitative analy-sis was performed by an UV–vis spectrophotometer (Nicolet Evolution 300, Thermo Fisher, United States). The samples were evenly dispersed in DMSO and the UV–Vis absorption spectra of the samples were measured at room temperature. The data was qualitatively and quantitatively analyzed by the standard curve method.

2.4 Cell culture

Osteosarcoma cell line 143B was purchased from Jihe Biotechnology (Shanghai, China). This cell line was cultured with DMEM medium containing 10% fetal bovine serum (FBS) and 1% penicillin/streptomycin. The culture was maintained at 37 °C and under humidified 5% CO_2. These cells were passaged every 2 days. Once the fusion state was reached, the cells were collected by trypsin (containing 0.25% EDTA) digestion for further experiments.

2.5 *In vitro* targeted uptake of nanoparticles

The affinity of ALN for bone minerals was investigated for non-targeted HA, HAC, compared with targeted HACA nanoparticles. The same masses of HA, HAC and HACA nanoparticles were taken with 5 times the mass of hydroxyapatite and centrifuged for 24 h, respectively. The precipitates were washed several times with appropriate amount of deionized water and dried in an oven for scanning electron microscopy (SEM, SIGMA 300, Germany) characterization.

2.6 Intracellular nanoparticle uptake

The intracellular behavior of HACA nanoparticles containing fluorescent Ce6 was observed by laser scanning confocal microscopy (LSCM, Leica, TCS SP5, Germany). 143B cells were inoculated in a 6-well plate with a sterile coverslip at the bottom of each well, and 1.5×10^5 cells were inoculated per well. Cells were incubated with DMEM medium containing 10% fetal bovine serum (FBS) and 1% penicillin/streptomycin in a humidified 5% CO_2 incubator at 37 °C. 200ug/mL of HMSNs/BM-Ce6-Apa-CD-PEG-ALN (HACA-Ce6) nanoparticles were added to the culture medium. After 24 h of incubation, the medium was removed and the cells were rinsed 3 times with PBS. Cells were fixed in 4% paraformaldehyde in PBS for 20 min and then gently rinsed with PBS 3 times. The fixed cells were stained with DAPI for 15 min, washed 3 times with PBS and the coverslips were fixed on glass microscope slides. Finally, the samples were observed under LSCM.

2.7 Loading and release of Apa *in vitro*

First, a certain amount of Apa was dissolved in DMSO, and mixed with an equal mass of HMSNs/BM in deionized water. The suspension was centrifuged at 10,000 r min^{-1} for 15 min at 4°C and dried to obtain HA, and the supernatant was used for further quantitative analysis. Apa was quantified by photometer absorption spectroscopy using the standard curve method. The standard curve was established by measuring the highest absorption peak at 260 nm for different concentrations of Apa. The absorbance was measured by ultramicro spectrophotometer and the fitted standard curve was: Y = 38.904X-0.2601, R^2 = 0.996. Therefore, the drug loading capacity (LC) of Apa and the Apa loading efficiency (EE) are calculated by the following equation:

$$LC\% = \frac{\text{Amount of loaded Apa}}{Total\ weight\ of\ nanoparticles} * 100\%$$

$$EE\% = \frac{\text{Amount of loaded Apa}}{Amount\ of\ \ feeding\ Apatinib} * 100\%$$

The prepared HACA solutions were transferred to dialysis bags, sealed, and immersed in PBS buffer at pH 6.0 and pH 7.4, respectively. The dialysis experiment was maintained at 37 °C with a continuous vibration of 100 rpm. The sample solutions were extracted at 0.25, 0.5, 1, 2, 4, 6, 8, 10, 12, 24, 24, 48, 72, 96 and 120 h, respectively. Replenish with equal amounts of fresh PBS. The release of Apa was quantified by standard curve method. The release profile of Apa was investigated by calculating the cumulative release rate of Apa.

2.8 Cell biocompatibility of HCA and cell viability assay of HACA

The cytotoxicity of HCA and HACA were assessed using MTT colorimetric assay. 143B cells were inoculated into 96-well plates at a density of 5×10^3 cells/well and incubated at 37 °C in a 5% CO_2 incubator for 24 h. Then, DMEM medium containing 10% FBS was configured with different concentrations of HCA and HACA (0, 50, 100, 200, 400, 600, 800, 1600, 2000 ug/mL). After 24 h, 10 ul of MTT solution was added to each well and the cells were then incubated in the dark for 4 h. Afterwards, the supernatant was aspirated and washed 3 times with PBS, DMSO (200 ul) was quickly added to each well, and then placed on a shaker for 10 min. The absorbance values were then measured at 570 nm using a multifunctional enzyme marker (TECAN Austria). The following equation is used to calculate cell viability: Cell viability (%) = (OD of experimental group - OD of blank group)/(OD of control group - OD of blank group)*100% (Du et al., 2017). Each sample was tested in triplicate.

2.9 Cell migration assay, *in vitro* transwell cell invasion assay and cell clone formation assay

Scratching experiments were performed to investigate the effect of HACA nanoparticles on the migration ability of 143B cells. The experimental groups included HMSNs, Apa, HAC, HACA and control group with the pH of the medium was set to 6.0. The 143B cells were inoculated in 6-well plates with 5×10^5 cells per well. After 24 h of incubation, the cells form a monolayer and cover approximately 80% of the bottom of the well. The cell monolayer was scraped using the pipette tip to create a scratch, and then carefully rinsed 3 times with PBS. HMSNs, Apa, HAC, and HACA nanoparticles were added, respectively, and then incubated for 24 h. The *in vitro* wound formation and its repopulation were assessed by inverted microscopy.

The *in vitro* invasive capacity of 143B cells was determined by a modified Boyden chamber system. The 24-Transwell Boyden Chamber unit (Neuroprobe, United States) is divided into two compartments with a porous polycarbonate membrane (8 mm pore size) between the upper and lower chambers. Matrigel is used to simulate the barrier of the extracellular matrix, and its coating on the membrane forms a thin layer of barrier. 143B cell suspension (2.0×10^5 cells/well, DMEM medium) was inoculated onto the gel membrane of the top chamber. The transwell was incubated for 24 h, and then the non-invasive cells were removed with a cotton swab. Migrated cells were fixed with 4% paraformaldehyde for 30 min and stained with crystal violet solution (0.1%) for 15 min. Wash the Transwell insert several times. Observe and count the invading cells under an inverted microscope using white light.

For cell colony formation assay, 143B cell suspension (500 cells/well, DMEM medium) was inoculated onto 6-well plates. After 24 h, HMSNs, Apa, HAC, and HACA materialswere added, respectively. After 5 days of incubation, the supernatant was aspirated, fixed with 4% paraformaldehyde for 15 min, and stained with crystal violet solution (0.1%) for 15 min. The proliferating cells were observed and counted under an inverted microscope using the same white light.

2.10 Statistical analysis

All data were expressed as mean ± standard deviation (Mean ± SD), and statistical analyses were performed using SPSS 19.0 software and plotted using GraphPad Prism8 software. Student's t-test was used to compare statistical differences between the two groups and One-way ANOVA was used to test

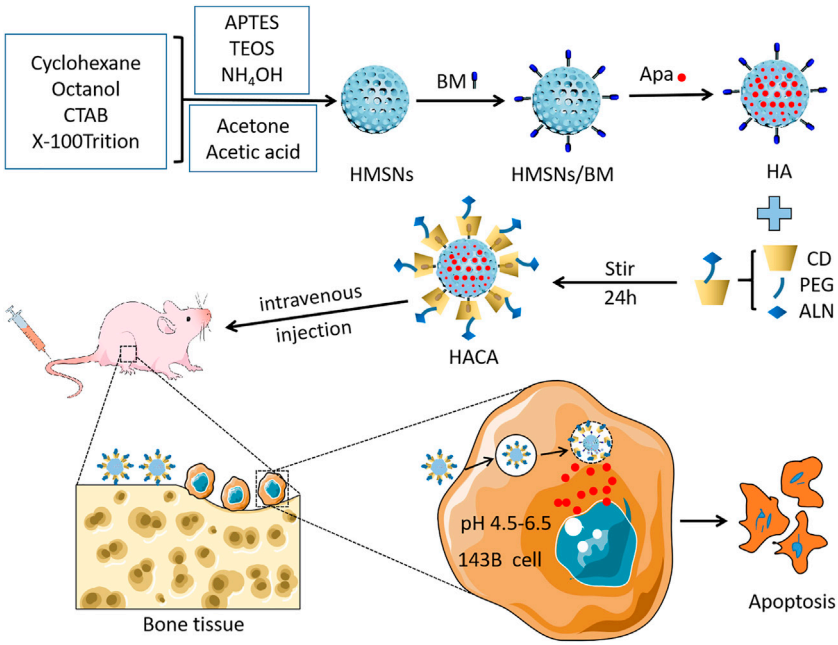

SCHEME 1
Schematic illustration of the fabrication of the HACA and their application for pH-responsive drug release after specific binding with bone tissue.

for differences between multiple groups. P< 0.05 was considered statistically different.

3 Results and discussion

3.1 Morphological characterization and analysis

Scheme 1 showed the detailed preparation of HACA. HMSNs were synthesized by the one-step method using a modified water-in-oil (W/O) reverse microemulsion system containing APTES, X-100 Triton, n-hexanol, cyclohexane and water, a well-studied system for the synthesis of silica nanoparticles with the size less than hundred nanometers. After the addition of TEOS, the polymerization was triggered with NH_4OH and continued for 24 h. Afterwards, acetone was added to terminate the reaction. The HMSNs underwent a spontaneous morphology change from solid to hollow when they were washed with ethanol and water by such a simple etching-free strategy. Finally, the CTAB template was removed by acidic ethanol extraction to obtain homogeneous HMSNs. Then, BM is affixed to the amine group on the surface of HMSNs by forming an "amide bond" and HMSNs/BM is formed. Apa, used as a model anticancer drug, was loaded into the porous structure of the HMSNs/BM shell.

ALN-modified CD with bone-targeting ability binds to a linear stem provided by the HA surface to obtain HACA (Figure 1). In addition, CD-PEG and CD-PEG-ALN (CA) were characterized by ^{1}H nuclear magnetic resonance (NMR) spectroscopy in the supporting information. The peaks at approximately 3.51 ppm were assigned to the repeating unit -O-CH_2-CH_2- on the PEG chain (Supplementary Figure S1) and the characteristic peaks at

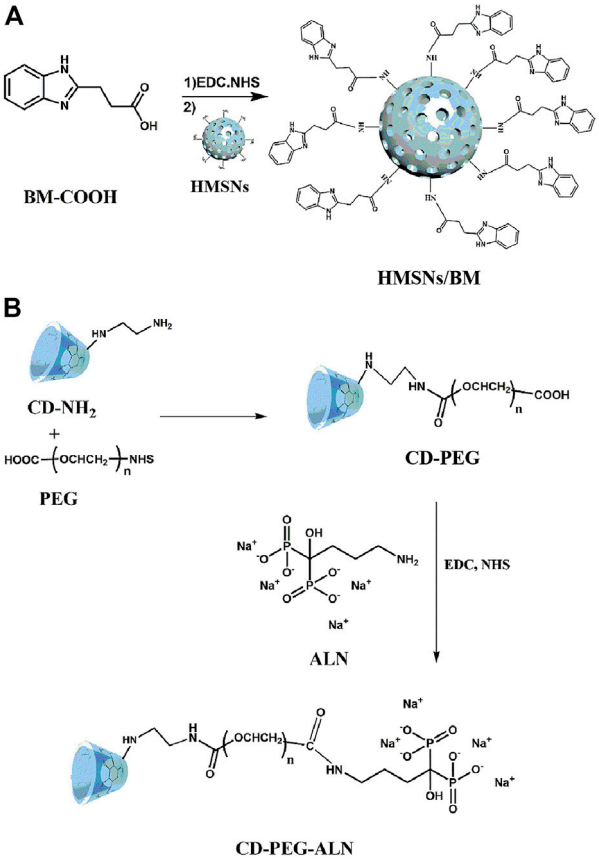

FIGURE 1
The synthesis of HMSNS/BM **(A)** and CD-PEG-ALN **(B)**.

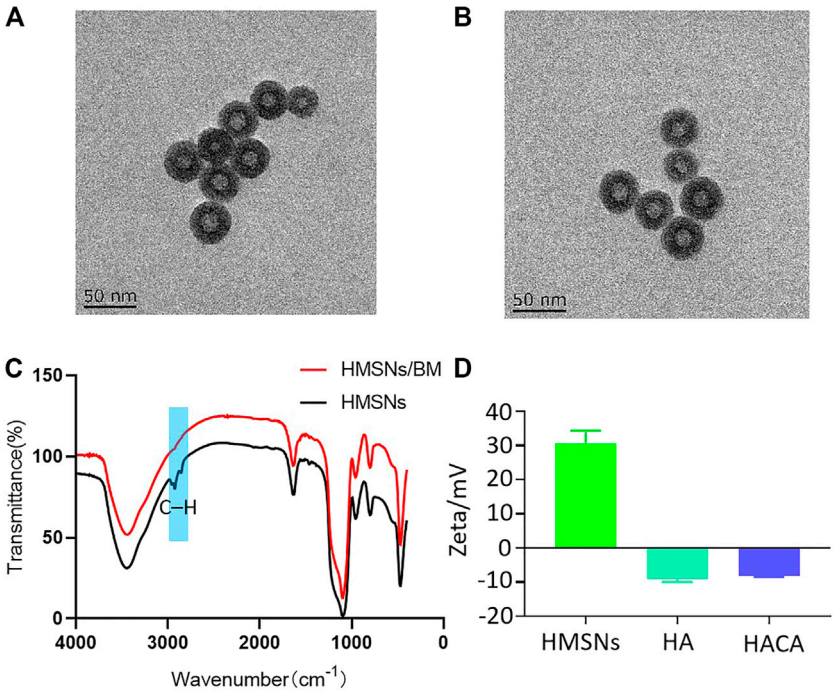

FIGURE 2
Preparation and characterization of HACA nanoparticles. **(A, B)** Transmission electron microscopy images of HMSNs and HACA, respectively. **(C)** FTIR spectroscopy of HMSNs and HMSNs/BM. **(D)** Zeta potential of HMSNs, HA and HACA. Scale bar is 50 nm.

2.68 ppm were assigned to the proton in -NH-CO- (Supplementary Figure S2), which demonstrated that the successful synthesis of CD-PEG and CD-PEG-ALN.

The morphology and structure of HMSNs and HACA nanoparticles were observed by transmission electron microscopy. As shown in Figures 2A, B, the HMSNs and HACA nanoparticles are almost spherical with uniform size distribution and the range of diameters is about 30–40 nm, while the morphological and structural changes are not obvious. The FTIR spectrum for HMSNs (Figure 2C) showed the absorption band at 2920 and 2848 cm^{-1}, belonging to C–H stretching vibrations, experienced a substantial reduction in HMSNs/BM. The two curves of the remaining parts approach each other, indicating that HMSNs-BM basically retains the structural characteristics of HMSNs. These data further demonstrate the presence of BM on the surface of the prepared HMSNs. In addition, the zeta potential analysis (Figure 2D) showed that the average potential of the positively charged HMSNs was 26 mV, while the average potential of the synthesized HA was −9 mV. Similarly, the potential of HACA was −7 mV which became smaller, further indicating the successful synthesis of ALN on the surface of HACA nanoparticles.

3.2 Cellular uptake of HACA *in vitro*

The targeting of ALN to bone tissue is an important prerequisite to ensure the effectiveness of HACA nanoparticles for clinical application. Hydroxyapatite (HAP) is the most abundant mineral component in bone tissue, which was chosen to simulate the bone microenvironment for *in vitro* experimental validation. *In vitro* targeting ability of HACA were simulated through HAP experiments. As shown in Figures 3A, B, the same concentrations of HA, HAC, HACA were co-incubated with HAP for 24 h. After scanning by electron microscopy, it was found that the HAP surface.

Was covered by a large amount of HACA. However, HA and HAC nanoparticles without ALN modification were observed with a smaller number of nanoparticles on the surface of HAP.

In addition, in order to investigate the uptake of nanoparticles by cells *in vitro*, Ce6 was operated in parallel with Apa during the synthesis process. CLSM was used to visualize the internalization and intracellular distribution of HA-Ce6、HAC-Ce6 and HACA-Ce6 in 143B cells following incubation for 24 h. As shown in Figures 3C, D, the red fluorescence strengthened with the different nanoparticles and the targeted HACA-Ce6 particles were more likely to enter tumor cells compared with non-targeted HA-Ce6 and HAC-Ce6 nanoparticles. These results suggest that ALN has a good bone targeting ability, which can make the nanoparticles target bone tissue more and enter tumor cells more effectively.

3.3 Loading and releasing of Apa *in vitro*

As an anti-tumor drug, Apa has strong tumor treatment ability, but its non-specific effect brings toxic side effects to the normal tissues, which limits the clinical application. HACA nanoparticles are mainly composed of 3 parts, including HMSNs/BM, Apa, and

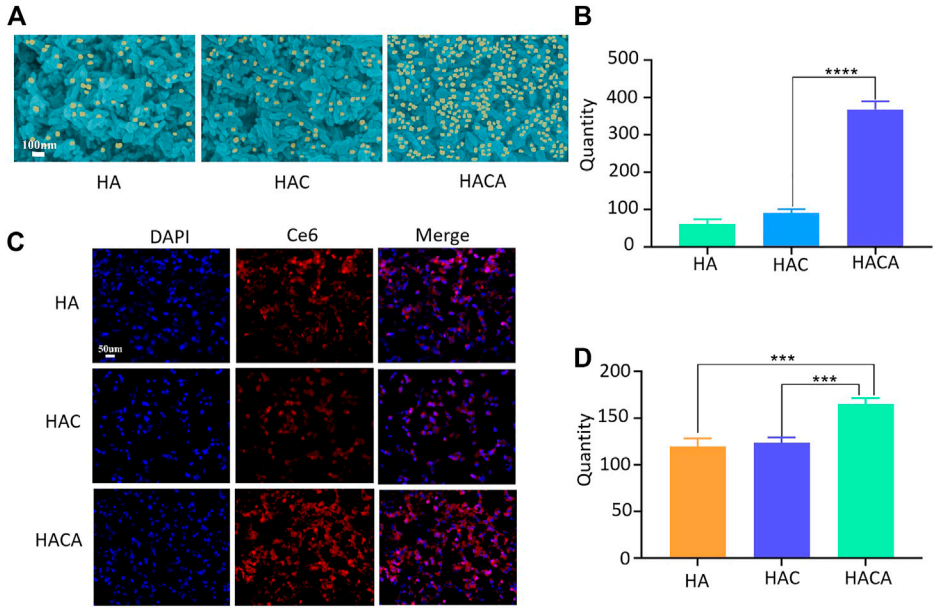

FIGURE 3
Schematic diagram of *in vitro* cellular uptake of nanoparticles. **(A)** Scanning electron microscopy images of HA, HAC and HACA bound to hydroxyapatite. **(B)** Analysis of nanoparticles numbers bound to hydroxyapatite. **(C)** Intracellular uptake of HA, HAC and HACA in 143B cells. Confocal laser scanning microscopy images of 143B cells depict intracellular uptake of Ce6-labeled HA, HAC and HACA (red), where the nuclei are stained with DAPI (blue). **(D)** Analysis of the number of 143B cells engulfed by Ce6-labeled nanoparticles. *$p < 0.05$, **$p < 0.01$ and ***$p < 0.001$ vs. blank. Scale bars are 100 μm.

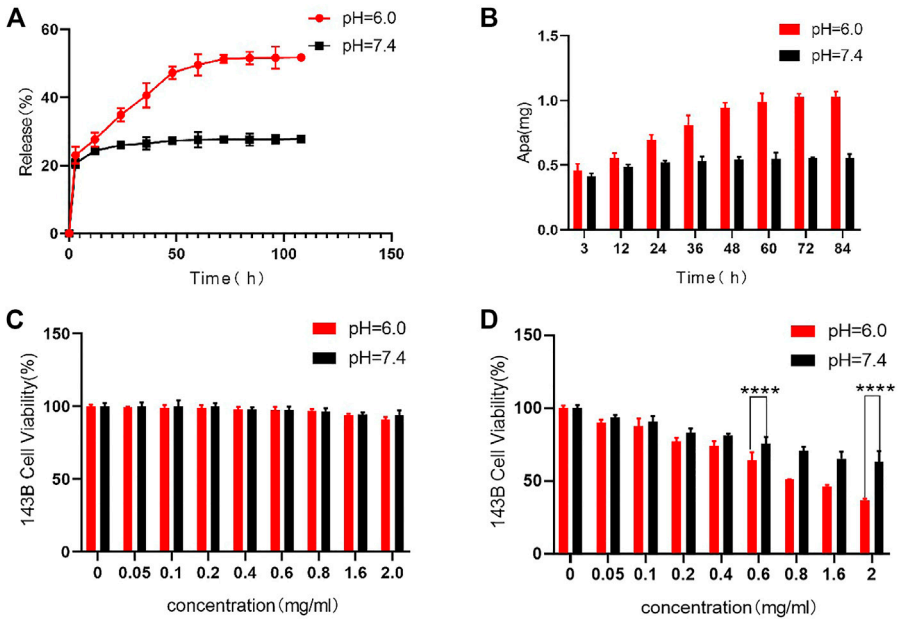

FIGURE 4
In vitro release of Apa and *in vitro* cytotoxicity to 143B cells. **(A) (B)** Release curves of Apa from HACA under different pH conditions. **(C)** Effect of HAC on 143B cell viability at different pH. **(D)** Effect of different concentrations of HACA on 143B cell viability under different pH conditions. *$p < 0.05$, **$p < 0.01$ and ***$p < 0.001$ vs. blank.

CD-PEG-ALN. HACA nanoparticles have high drug LC and drug EE of 65% and 25%, respectively. The ideal drug carrier should not only have a good drug loading rate, but also have environmentally controlled release capability. The drug release curves of Apa in Figures 4A, B were conducted by dispersing HACA in different PBS buffers (pH 6.0 and 7.4, respectively). The Apa in HACA

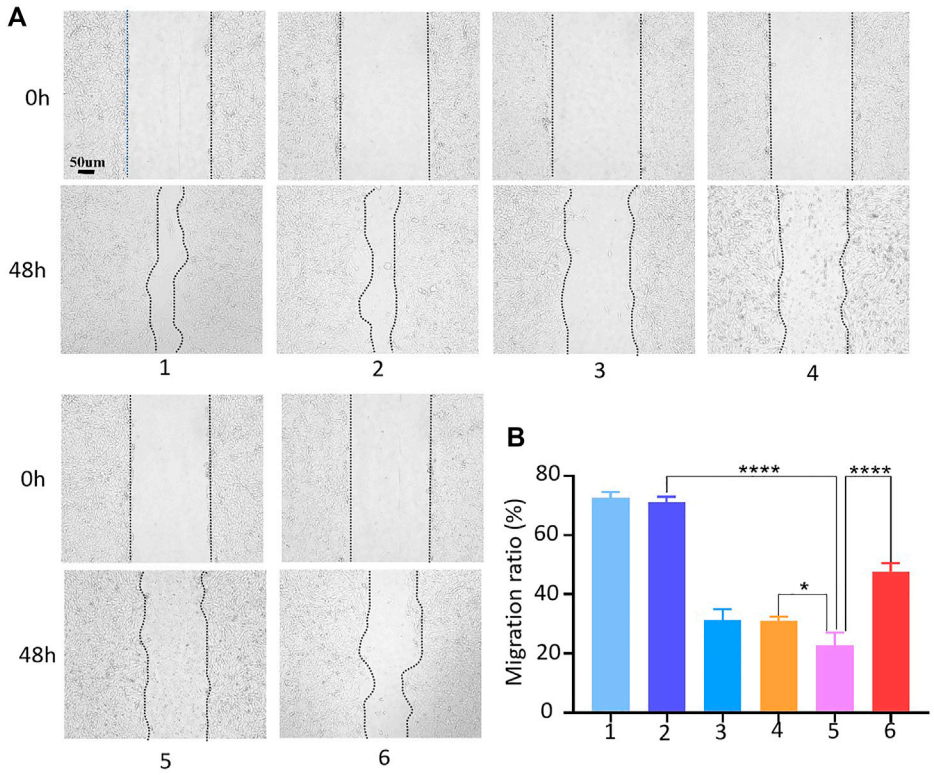

FIGURE 5
Cell migration assay. **(A)** Conditioned medium-mediated cell migration assay of 143B cells at 0–48 h. **(B)** Mobility % = $(S_0\text{-}S_{48})/S_0$*100%, where S_0 and S_{48} indicate the area of the scratch at 0h and 48h. 1, 2, 3, 4, 5 and 6 represent blank control, HMSNs, Apa, HA, HACA in medium pH = 6.0 and HACA in medium pH = 7.4, respectively. *$p < 0.05$, **$p < 0.01$ and ***$p < 0.001$ vs. blank. The scale bar is 100 μm.

nanoparticles was released more easily at pH 6.0. Almost 58% of Apa was simultaneously released from the particles. However, only 24% of the Apa in HACA was released after 48 h of immersion in the pH 7.4 environment. This is mostly attributed to the "nano-valve" made of CD disintegrating in an acidic environment, which exposes the pore channels on HMSNs and causes the release of Apa.

Was significantly lower in pH 6.0 than in pH 7.4. Since the tumor environment and other areas of inflammation tend to be more acidic than the normal physiological environment, it is expected that these areas of higher acidity would permit greater Apa release. The pH-responsive release of Apa can be utilized to achieve efficient intracellular delivery.

3.4 Cell biocompatibility and the evaluation of anti-tumor effect of HACA *in vitro*

HCA and HACA nanoparticles were incubated with 143B cells to assess their biocompatibility and tumor treatment effect. As shown in Figure 4C, cell viability measured by the MTT assay after being incubated with HCA nanoparticles for 48 h in different pH environments. When the concentration of HCA nanoparticles increased to 2 mg/mL, the cell survival rate remained above 95%. This result indicates that HCA nanoparticles have no significant toxicity on the cellular activity and can be used as ideal drug carriers for tumor treatment. While as shown in Figure 4D, when HACA nanoparticles were co-incubated with 143B cells in medium of different pH, the survival rate of 143B cells gradually decreased as the concentration of HACA nanoparticles increased. In comparison with the same concentration of HACA nanoparticles co-incubated with 143B in different pH conditions, the cell survival rate.

3.5 Effect of HACA on migration, invasion and proliferation abilities

The effects of HACA nanoparticles on migration, invasion and proliferation ability of 143B cells were also assessed. The process of scratch healing was observed with an optical microscope and the cell migration rate was calculated by ImageJ software. As shown in Figures 5A, B, compaired with the strongest migration ability in control group, HMSNs, free Apa, HA and HACA significantly inhibited the migration of 143B cells. Notably, HACA was much more effective in retarding the migration of 143B cells at pH 6.0 than that of in neutral condition. This is mainly due to that HACA nanoparticles released more Apa in the acidic tumor environment. These results showed that the HACA nanoparticles could reduce the migration ability of 143B cells, which will effectively prevent the metastasis of tumor cells.

The 143B cell suspension was spread in Transwell chambers, and HMSNs, Apa, HA, HAC, and HACA nanoparticles were added

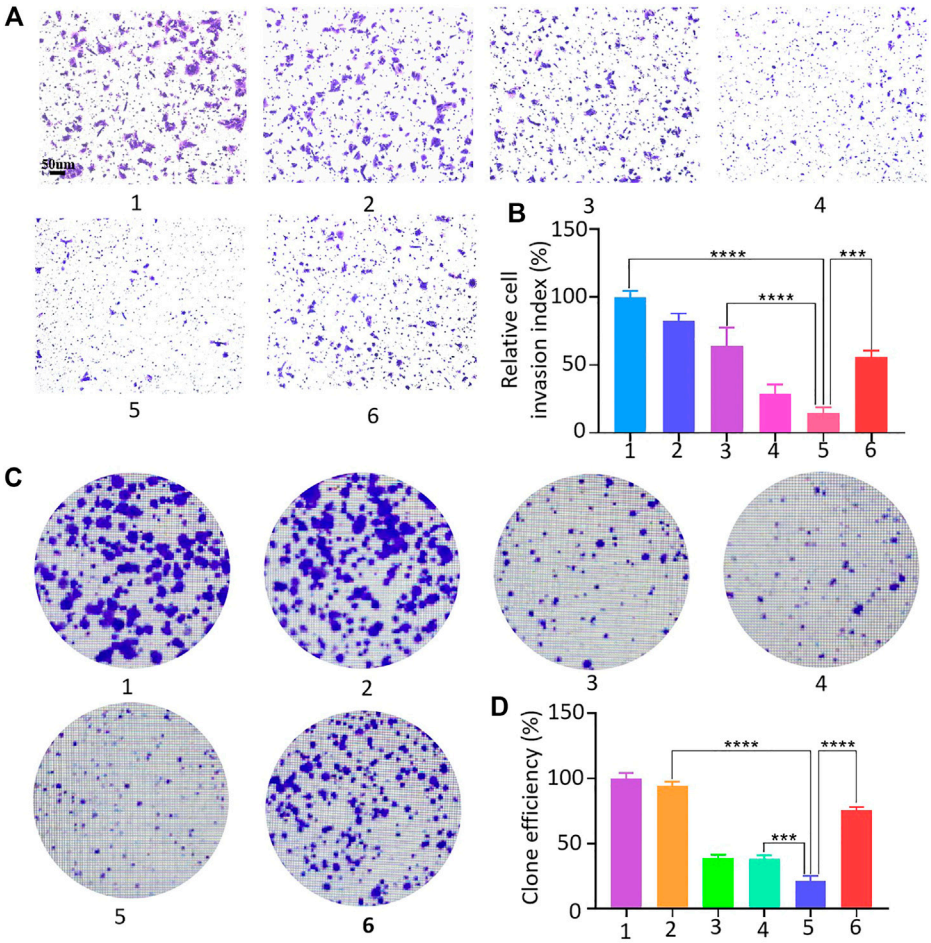

FIGURE 6
143B cell invasion assay and clone formation assay. **(A–D)** 143B cell invasion and proliferation capacity assessment: 1, 2, 3, 4, 5 and 6 represent control, HMSNs, Apa, HA, HACA in medium pH = 6.0 and HACA in medium pH = 7.4, respectively. *$p < 0.05$, **$p < 0.01$ and ***$p < 0.001$ vs. blank. Scale bars are 100 μm.

into the chamber, and PBS solution was added as the control group. The number of cells that degrade the basement membrane and pass through the polycarbonate membrane was observed under a microscope. Figures 6A, B showed that 143B cells in the control group had strong invasion ability and most cells can pass through the polycarbonate membrane after 48 h. While the invasion ability of 143B cells in the experimental groups were weakened significantly, and the 143B cells in the HACA nanoparticles group at pH 6.0 condition could barely pass through the polycarbonate membrane, so the cell invasion ability was greatly reduced.

The effect of HACA nanoparticles on the proliferative capacity of 143B cells were investigated. As shown in Figures 6C, D, similarly, free Apa, HA and HACA significantly inhibited the proliferative capacity of 143B cells, and HACA was much more effective in retarding the proliferative capacity of 143B cells. When the pH was at 6.0, the HACA nanoparticle group showed the strongest inhibition of 143B cell proliferation and significantly reduced the colony formation. These results demonstrated that HACA nanoparticles could significantly inhibit the proliferation of 143B cells.

4 Discussion and conclusion

In this report, nanoplatforms HACA was successfully constructed basing on the small-sized HMSNs as the template and CD-BM supramolecular assemblies as the valves, which can load and control the release of Apa and target bone tissue. This method is easy and economical for large-scale preparation. The HACA nanoparticles were in the size of about 30–40 nm. When incubated with different concentrations of HCA nanoparticles within 143B cells, and the cell vitality is not reduced significantly which showed the good biocompatibility of the nanocarriers. A standard curve was established according to the highest absorption peak at 260 nm of Apa solutions with different concentrations, and it was obtained that the nanoparticles had a high drug loading efficiency, up to 25%. ALN-modified nanoparticles are easier to bind to hydroxylapatite and have good bone tumor targeting capabilities. After co-incubation of HACA-Ce6 with 143B cells, the fluorescence was observed under CLSM, and the results showed that HACA-Ce6 nanoparticles were more easily

absorbed by 143B cells. The pH of tumor tissues is lower than the normal physiological environment due to the high metabolism of tumor cells, which can lead to lactic acid accumulation. Therefore, the release of Apa in HACA was examined by simulating the tumor microenvironment and normal physiological environment *in vitro*. The results showed that HACA nanoparticles released more Apa at pH = 6.0. After 48 h, the release rate of Apa from HACA was about 58%, while in normal physiological environment, the release rate of Apa from HACA was only 25%. Furthermore, tumors have the characteristics of unlimited proliferation, local invasion, and distant metastasis. Cell motility plays a crucial role in many physiological and pathological processes, including embryonic development, wound healing, and metastasis of tumor cells. To study the effect of tumor cell migration ability on tumor metastasis and recurrence, cell scratch assay is considered as a simple, effective and direct method to observe cell migration process *in vitro*. Cells at the edge of the scratch will gradually enter the blank area, allowing the "scratch" to heal, simulating the process of cell migration *in vivo* (Liang et al., 2007). *In vitro* cell invasion ability is one of the distinguishing features of tumor cell metastasis. The Transwell cell invasion assay simulates tumor cell invasion and assesses the invasive ability of tumor cells *in vitro*. The assessment of HACA nanoparticles on 143B cell migration, invasion and proliferation were performed by simulating the tumor microenvironment *in vitro*. The results showed that the HACA nanoparticles exhibited a strong ability to inhibit the proliferation, invasion, and migration of 143B cells when the pH of the microenvironment is 6.0.

In summary, the HACA nano-drug delivery system was successfully prepared and used for the treatment of osteosarcoma *in vitro*. HACA nanoparticles were spherical with an average diameter of about 30–40 nm and they have a high drug loading efficiency (25%) and pH-responsive slow-release capacity. It was shown that HCA nanoparticles had low cytotoxicity to cells, but HACA could effectively inhibit the proliferation, migration and invasion ability of 143B cells. It provides new ideas and methods for clinical oncology treatment. Although HACA nanoparticles have certain advantages and application prospects for the treatment of osteosarcoma, they also have shortcomings. For example, 1) the experiments lacks *in vivo* validation, and the complexity of the tumor microenvironment *in vivo* is much higher than that simulated *in vitro*. 2) The toxicity of HACA nanoparticles to human normal cells lacks verification. Whether it will cause toxic side effects to normal tissues and organs is unknown.

Data availability statement

The original contributions presented in the study are included in the article/Supplementary Material, further inquiries can be directed to the corresponding authors.

Author contributions

XW: Conceptualization, Methodology, Writing - original draft. GL: Writing - original draft, Data curation. KL: Formal analysis. YS: Data curation. WL: Investigation. CP: Formal analysis. HC: Funding acquisition, Supervision. JD: Writing - review and editing. HW: Writing - review and editing, Methodology.

Funding

This study was supported by National Natural Science Foundation of China (8217090346, 81802132), Natural Science Foundation of Jiangsu Province (SBK2021022619), Natural Science Fund for Colleges and Universities in Jiangsu Province (21KJB320009, 21KJB310017).

Conflict of interest

The authors declare that the research was conducted in the absence of any commercial or financial relationships that could be construed as a potential conflict of interest.

Publisher's note

Supplementary material

The Supplementary Material for this article can be found online at: https://www.frontiersin.org/articles/10.3389/fbioe.2023.1135655/full#supplementary-material

References

Ambrogio, M. W., Thomas, C. R., Zhao, Y. L., Zink, J. I., and Stoddart, J. F. (2011). Mechanized silica nanoparticles: A new frontier in theranostic nanomedicine. *Acc. Chem. Res.* 44 (10), 903–913. doi:10.1021/ar200018x

Ando, K., Heymann, M. F., Stresing, V., Mori, K., Redini, F., and Heymann, D. (2013). Current therapeutic strategies and novel approaches in osteosarcoma. *Cancers* 5 (2), 591–616. doi:10.3390/cancers5020591

Barat, R., Legigan, T., Tranoy-Opalinski, I., Renoux, B., Peraudeau, E., Clarhaut, J., et al. (2015). A mechanically interlocked molecular system programmed for the delivery of an anticancer drug. *Chem. Sci.* 6 (4), 2608–2613. doi:10.1039/c5sc00648a

Barve, A., Jain, A., Liu, H., Zhao, Z., and Cheng, K. (2020). Enzyme-responsive polymeric micelles of cabazitaxel for prostate cancer targeted therapy. *Acta Biomater.* 113, 501–511. doi:10.1016/j.actbio.2020.06.019

Baù, L., Bartova, B., Arduini, M., and Mancin, F. (2009). Surfactant-free synthesis of mesoporous and hollow silica nanoparticles with an inorganic template. *Chem. Commun. (Camb)* 2009, 7584–7586. doi:10.1039/b917561j

Chen, Y., Chen, H., Guo, L., He, Q., Chen, F., Zhou, J., et al. (2010). Hollow/rattle-type mesoporous nanostructures by a structural difference-based selective etching strategy. *ACS Nano* 4 (1), 529–539. doi:10.1021/nn901398j

Cui, W., Liu, Q., Yang, L., Wang, K., Sun, T., Ji, Y., et al. (2018). Sustained delivery of BMP-2-related peptide from the true bone ceramics/hollow mesoporous silica nanoparticles scaffold for bone tissue regeneration. *ACS Biomater. Sci. Eng.* 4 (1), 211–221. doi:10.1021/acsbiomaterials.7b00506

Du, F., Lou, J., Jiang, R., Fang, Z., Zhao, X., Niu, Y., et al. (2017). Hyaluronic acid-functionalized bismuth oxide nanoparticles for computed tomography imaging-guided radiotherapy of tumor. *Int. J. Nanomedicine* 12, 5973–5992. doi:10.2147/ijn.s130455

Freyer, D. R., and Seibel, N. L. (2015). The clinical trials gap for adolescents and young adults with cancer: Recent progress and conceptual framework for continued research. *Curr. Pediatr. Rep.* 3 (2), 137–145. doi:10.1007/s40124-015-0075-y

Gan, L., Liu, Z., and Sun, C. (2018). Obesity linking to hepatocellular carcinoma: A global view. *Biochim. Biophys. Acta Rev. Cancer* 1869 (2), 97–102. doi:10.1016/j.bbcan.2017.12.006

Gao, Y., Chen, Y., Ji, X., He, X., Yin, Q., Zhang, Z., et al. (2011). Controlled intracellular release of doxorubicin in multidrug-resistant cancer cells by tuning the shell-pore sizes of mesoporous silica nanoparticles. *ACS Nano* 5 (12), 9788–9798. doi:10.1021/nn2033105

Gong, F., Cheng, L., Yang, N., Jin, Q., Tian, L., Wang, M., et al. (2018). Bimetallic oxide MnMoO(X) nanorods for *in vivo* photoacoustic imaging of GSH and tumor-specific photothermal therapy. *Nano Lett.* 18 (9), 6037–6044. doi:10.1021/acs.nanolett.8b02933

Guven, M. N., Altuncu, M. S., Bal, T., Oran, D. C., Gulyuz, U., Kizilel, S., et al. (2018). Bisphosphonic acid-functionalized cross-linkers to tailor hydrogel properties for biomedical applications. *ACS Omega* 3 (8), 8638–8647. doi:10.1021/acsomega.8b01103

Han, G., Guo, Q., Ma, N., Bi, W., Xu, M., and Jia, J. (2021). Apatinib inhibits cell proliferation and migration of osteosarcoma via activating LINC00261/miR-620/PTEN axis. *Cell Cycle* 20 (18), 1785–1798. doi:10.1080/15384101.2021.1949132

Hicklin, D. J., and Ellis, L. M. (2005). Role of the vascular endothelial growth factor pathway in tumor growth and angiogenesis. *J. Clin. Oncol.* 23 (5), 1011–1027. doi:10.1200/jco.2005.06.081

Hyun, H., Wada, H., Bao, K., Gravier, J., Yadav, Y., Laramie, M., et al. (2014). Phosphonated near-infrared fluorophores for biomedical imaging of bone. *Angew. Chem. Int. Ed. Engl.* 53 (40), 10844–10848. doi:10.1002/ange.201404930

Jaffe, N. (2010). "Osteosarcoma: Review of the past," in *Impact on the future. The American experience. Pediatric and adolescent osteosarcoma* (Boston, MA: Springer US), 239–262.

Jiang, Z., Liu, Y., Shi, R., Feng, X., Xu, W., Zhuang, X., et al. (2022). Versatile polymer-initiating biomineralization for tumor blockade therapy. *Adv. Mater* 34 (19), e2110094. doi:10.1002/adma.202110094

Lenkinski, R. E., Ahmed, M., Zaheer, A., Frangioni, J. V., and Goldberg, S. (2003). Near-infrared fluorescence imaging of microcalcification in an animal model of breast cancer. *Acad. Radiol.* 10 (10), 1159–1164. doi:10.1016/s1076-6332(03)00253-8

Li, X., Wang, L., Wang, L., Yu, J., Lu, G., Zhao, W., et al. (2020). Overcoming therapeutic failure in osteosarcoma via Apatinib-encapsulated hydrophobic poly(ester amide) nanoparticles. *Biomater. Sci.* 8 (21), 5888–5899. doi:10.1039/d0bm01296c

Li, Z., Zhang, Y., and Feng, N. (2019). Mesoporous silica nanoparticles: Synthesis, classification, drug loading, pharmacokinetics, biocompatibility, and application in drug delivery. *Expert Opin. Drug Deliv.* 16 (3), 219–237. doi:10.1080/17425247.2019.1575806

Liang, C. C., Park, A. Y., and Guan, J. L. (2007). *In vitro* scratch assay: A convenient and inexpensive method for analysis of cell migration *in vitro*. *Nat. Protoc.* 2 (2), 329–333. doi:10.1038/nprot.2007.30

Lin, Y. S., Wu, S. H., Tseng, C. T., Hung, Y., Chang, C., and Mou, C. Y. (2009). Synthesis of hollow silica nanospheres with a microemulsion as the template. *Chem. Commun. (Camb)* 2009, 3542–3544. doi:10.1039/b902681a

Liu, K., Ren, T., Huang, Y., Sun, K., Bao, X., Wang, S., et al. (2017). Apatinib promotes autophagy and apoptosis through VEGFR2/STAT3/BCL-2 signaling in osteosarcoma. *Cell Death Dis.* 8 (8), e3015. doi:10.1038/cddis.2017.422

Ma, X., and Zhao, Y. (2015). Biomedical applications of supramolecular systems based on host-guest interactions. *Chem. Rev.* 115 (15), 7794–7839. doi:10.1021/cr500392w

Maluccio, M., and Covey, A. (2012). Recent progress in understanding, diagnosing, and treating hepatocellular carcinoma. *CA Cancer J. Clin.* 62 (6), 394–399. doi:10.3322/caac.21161

Meng, H., Xue, M., Xia, T., Zhao, Y. L., Tamanoi, F., Stoddart, J. F., et al. (2010). Autonomous *in vitro* anticancer drug release from mesoporous silica nanoparticles by pH-sensitive nanovalves. *J. Am. Chem. Soc.* 132 (36), 12690–12697. doi:10.1021/ja104501a

Porta, F., Lamers, G. E. M., Morrhayim, J., Chatzopoulou, A., Schaaf, M., den Dulk, H., et al. (2013). Folic acid-modified mesoporous silica nanoparticles for cellular and nuclear targeted drug delivery. *Adv. Healthc. Mater.* 2 (2), 281–286. doi:10.1002/adhm.201200176

Qiu, X. L., Li, Q. L., Zhou, Y., Jin, X. Y., Qi, A. D., and Yang, Y. W. (2015). Sugar and pH dual-responsive snap-top nanocarriers based on mesoporous silica-coated Fe3O4 magnetic nanoparticles for cargo delivery. *Chem. Commun. (Camb)* 51 (20), 4237–4240. doi:10.1039/c4cc10413g

She, X., Chen, L., Velleman, L., Li, C., Zhu, H., He, C., et al. (2015). Fabrication of high specificity hollow mesoporous silica nanoparticles assisted by Eudragit for targeted drug delivery. *J. Colloid Interface Sci.* 445, 151–160. doi:10.1016/j.jcis.2014.12.053

Shen, S., Tang, H., Zhang, X., Ren, J., Pang, Z., Wang, D., et al. (2013). Targeting mesoporous silica-encapsulated gold nanorods for chemo-photothermal therapy with near-infrared radiation. *Biomaterials* 34 (12), 3150–3158. doi:10.1016/j.biomaterials.2013.01.051

Skrabalak, S. E., Chen, J., Sun, Y., Lu, X., Au, L., Cobley, C. M., et al. (2008). Gold nanocages: Synthesis, properties, and applications. *Acc. Chem. Res.* 41 (12), 1587–1595. doi:10.1021/ar800018v

Spraker-Perlman, H. L., Barkauskas, D. A., Krailo, M. D., Meyers, P. A., Schwartz, C. L., Doski, J., et al. (2019). Factors influencing survival after recurrence in osteosarcoma: A report from the children's oncology group. *Pediatr. Blood Cancer* 66 (1), e27444. doi:10.1002/pbc.27444

Sun, W., Han, Y., Li, Z., Ge, K., and Zhang, J. (2016). Bone-targeted mesoporous silica nanocarrier anchored by zoledronate for cancer bone metastasis. *Langmuir* 32 (36), 9237–9244. doi:10.1021/acs.langmuir.6b02228

Teng, I. T., Chang, Y. J., Wang, L. S., Lu, H. Y., Wu, L. C., Yang, C. M., et al. (2013). Phospholipid-functionalized mesoporous silica nanocarriers for selective photodynamic therapy of cancer. *Biomaterials* 34 (30), 7462–7470. doi:10.1016/j.biomaterials.2013.06.001

Torres Martin de Rosales, R., Finucane, C., Mather, S. J., and Blower, P. J. (2009). Bifunctional bisphosphonate complexes for the diagnosis and therapy of bone metastases. *Chem. Commun. (Camb)* 2009, 4847–4849. doi:10.1039/b908652h

Zaheer, A., Lenkinski, R. E., Mahmood, A., Jones, A. G., Cantley, L. C., and Frangioni, J. V. (2001). *In vivo* near-infrared fluorescence imaging of osteoblastic activity. *Nat. Biotechnol.* 19 (12), 1148–1154. doi:10.1038/nbt1201-1148

Zhou, X., Cheng, X., Feng, W., Qiu, K., Chen, L., Nie, W., et al. (2014). Synthesis of hollow mesoporous silica nanoparticles with tunable shell thickness and pore size using amphiphilic block copolymers as core templates. *Dalton Trans.* 43 (31), 11834–11842. doi:10.1039/c4dt01138d

frontiers | Frontiers in Bioengineering and Biotechnology

TYPE Original Research
PUBLISHED 21 February 2023
DOI 10.3389/fbioe.2023.1098172

OPEN ACCESS

EDITED BY
Jianyun Zhang,
Peking University Hospital of Stomatology, China

REVIEWED BY
Roberta Tasso,
University of Genoa, Italy
Ana Claudia Oliveira Carreira,
Federal University of ABC, Brazil

*CORRESPONDENCE
Tong Zhang,
love_bama@163.com
Juan Xu,
newxj@hotmail.com
Quan Shi,
shiquan3333@sina.cn

†These authors have contributed equally to this work

SPECIALTY SECTION
This article was submitted to Biomaterials, a section of the journal Frontiers in Bioengineering and Biotechnology

RECEIVED 14 November 2022
ACCEPTED 10 February 2023
PUBLISHED 21 February 2023

CITATION
Wang S, Liu Z, Yang S, Huo N, Qiao B, Zhang T, Xu J and Shi Q (2023), Extracellular vesicles secreted by human gingival mesenchymal stem cells promote bone regeneration in rat femoral bone defects.
Front. Bioeng. Biotechnol. 11:1098172.
doi: 10.3389/fbioe.2023.1098172

Extracellular vesicles secreted by human gingival mesenchymal stem cells promote bone regeneration in rat femoral bone defects

Situo Wang[1,2†], Ziwei Liu[1,2,3†], Shuo Yang[1†], Na Huo[1], Bo Qiao[1], Tong Zhang[1*], Juan Xu[1*] and Quan Shi[1*]

[1]Department of Stomatology, The First Medical Center, Chinese PLA General Hospital, Beijing, China, [2]Orthopedic Laboratory of PLA General Hospital, Beijing, China, [3]Medical School of Chinese PLA, Beijing, China

Extracellular vesicles (EVs), important components of paracrine secretion, are involved in various pathological and physiological processes of the body. In this study, we researched the benefits of EVs secreted by human gingival mesenchymal stem cells (hGMSC-derived EVs) in promoting bone regeneration, thereby providing new ideas for EVs-based bone regeneration therapy. Here, we successfully demonstrated that hGMSC-derived EVs could enhance the osteogenic ability of rat bone marrow mesenchymal stem cells and the angiogenic capability of human umbilical vein endothelial cells. Then, femoral defect rat models were created and treated with phosphate-buffered saline, nanohydroxyapatite/collagen (nHAC), a grouping of nHAC/hGMSCs, and a grouping of nHAC/EVs. The results of our study indicated that the combination of hGMSC-derived EVs and nHAC materials could significantly promote new bone formation and neovascularization with a similar effect to that of the nHAC/hGMSCs group. Our outcomes provide new messages on the role of hGMSC-derived EVs in tissue engineering, which exhibit great potential in bone regeneration treatment.

KEYWORDS

extracellular vesicles, human gingival mesenchymal stem cells, osteogenic ability, angiogenic capability, bone regeneration

1 Introduction

The repair and regeneration of bone defects caused by tumors, trauma, and infection have always been a hot issue in the field of orthopedics and stomatology (Nguyen, et al., 2018). Autologous bone grafts are considered the "gold standard" for bone repair (Kumar, et al., 2016). However, they have some disadvantages, such as the need for a secondary operation, defects in the donor site, and unpredictable autogenous bone absorption (Valtanen, et al., 2021).

In recent years, tissue engineering strategies based on mesenchymal stem cells (MSCs) have been widely used in the field of bone regeneration. Human gingival mesenchymal stem cells (hGMSCs) are adult stem cells isolated from the gingival lamina propria with multidirectional differentiation potential and high proliferation characteristics; in addition, they have abundant sources and can be easily harvested minimal invasively

(Fawzy El-Sayed and Dörfer, 2016). Compared with bone marrow mesenchymal stem cells (BMSCs), hGMSCs have the advantages of faster proliferation and more stable morphology *in vitro* (Tomar, et al., 2010). In addition, as the majority of hGMSCs are derived from cranial neural crest cells, hGMSCs have good tissue regeneration and immunomodulation functions (Xu, et al., 2013). hGMSCs have been extensively investigated for bone regeneration and have shown good application effects (Al-Qadhi, et al., 2020; Hasani-Sadrabadi, et al., 2020). However, there are disadvantages to MSC transplantation, such as a low survival rate of transplanted cells, tumorigenic effects and immunological rejection (Eggenhofer, et al., 2014). Therefore, avoiding the risk of using MSCs or finding substitutes for MSCs to achieve cell-free therapy is one of the problems to be solved at present.

A recent basic study indicated that the tissue repair function of MSCs is mainly exerted by paracrine secretion of bioactive molecules (Liang, et al., 2014; Najar, et al., 2021; Williams et al., 2022). As an important paracrine factor, extracellular vesicles (EVs) are lipid bilayer nanovesicles secreted by living cells and their classification and nomenclature were formulated by the International Society of Extracellular Vesicles (ISEV) (Boere, et al., 2018). EVs carry a variety of bioactive molecules, such as microRNAs (miRNAs), mRNAs, lipids, and proteins, and are widely distributed in body fluids, such as breast milk, saliva, urine and bile (Trajkovic, et al., 2008; Rani, et al., 2015). After being secreted, EVs can be absorbed by receptor cells through ligand/receptor recognition, membrane fusion or phagocytosis and can regulate cell-to-cell communication by transmitting bioactive molecules (Tarasov, et al., 2021). It has been reported that MSC-derived EVs have shown remarkable therapeutic effects in many disease models, such as cardiovascular diseases, nervous system diseases and immune system diseases (Moghadasi, et al., 2021). Accumulating studies have shown that MSC-derived EVs can effectively promote the repair and regeneration of bone defects, and this effect is closely related to the regulation of osteogenesis and angiogenesis-related cells by MSC-derived EVs (Qin, et al., 2016). However, the therapeutic effect of hGMSC-derived EVs on bone defect repair and regeneration is unclear.

Therefore, in this study, we examined the effect of hGMSC-derived EVs on osteogenesis and angiogenesis by treating rat bone marrow mesenchymal stem cells (rBMSCs) and human umbilical vein endothelial cells (HUVECs) with hGMSC-derived EVs. In addition, we evaluated the bone repair capacity of nanohydroxyapatite/collagen (nHAC) scaffolds loaded with hGMSC-derived EVs on rat femoral defects. Our study showed that the combination of hGMSC-derived EVs/nHAC could promote the repair and regeneration of bone defects by accelerating new bone formation and angiogenesis, potentially providing application value for the treatment of bone defects.

2 Materials and methods

2.1 Cell isolation and culture

The methods for extraction and culture of primary hGMSCs were as previously described (Shi, et al., 2017). Gingival tissue was obtained from healthy young patients undergoing tooth crown lengthening operation, impacted third molar extraction and secondary implant surgery. Briefly, the gingival tissue was digested in 2 mg/ml dispase (Roche) at 4°C for 12 h after several rinses with phosphate-buffered saline (PBS). Then, the lamina propria was separated from the gingival tissue, minced and digested with 2 mg/ml collagenase IV (Roche) at 37 °C for 1 h. Afterward, the cell and tissue pellets were cultured in Dulbecco's modified Eagle's medium, nutrient mixture F-12 (DMEM/F12, Gibco) supplemented with 10% fetal bovine serum (FBS, Gibco), 100 U/ml penicillin, 100 μg/ml streptomycin and 0.25 μg/ml amphotericin B at 37°C with 5% CO2. hGMSCs at passages three to six were used in this experiment. The methods for extraction and culture of primary rBMSCs were as previously described (Liu, et al., 2020). Briefly, bone marrow was flushed from the femoral bones of SD suckling rats using α-minimum essential medium (α-MEM, Gibco) supplemented with 10% fetal bovine serum (FBS, Gibco), 100 U/ml penicillin, 100 μg/ml streptomycin and 0.25 μg/ml amphotericin B. The cell and tissue pellets were then cultured in α-MEM complete medium. HUVECs were purchased from PROCELL (Wuhan, China) and cultured in HUVEC special medium (Procell). All experimental procedures obtained approval from Clinical Ethics Committee of the Chinese PLA General Hospital.

2.2 Isolation and identification of hGMSC-Derived EVs

hGMSCs were cultured in exosome-free FBS medium to collect conditioned medium (Théry, et al., 2006). First, the cells were cultured in osteogenic induction medium (OM):α-MEM supplemented with 10% FBS, 0.1 μmol/L dexamethasone (Gibco), 10 mmol/L β-glycerol sodium phosphate (Gibco) and 50 μg/mL ascorbic acid (Gibco) for 3 days, then OM was replaced with α-MEM medium supplemented with 10% exosome-free FBS for culture with an additional 2 days to collect the conditioned medium. Afterward, the conditioned medium was centrifuged at 500 × g for 10 min and 1,000 × g for 30 min and then filtered through a 0.22 μm sterilized filter. The filtered medium was added to an ultrafiltration centrifuge tube (15 ml Amicon Ultra 30kD, Millipore) and centrifuged at 5000 × g for 20 min to concentrate the medium. Subsequently, the concentrated supernatant was ultracentrifuged at 100,000 × g for 60 min, and then the supernatant was replaced with PBS for the same operation for 60 min to obtain the EVs. The EVs were stored at −80°C.

The morphology of EVs was observed by transmission electron microscopy (TEM, HITACHI). Briefly, 5 μl of EVs was loaded onto a copper grid for 5 min, and the excess liquid was removed by filter paper. After staining with 2% uranyl acetate dihydrate for 1 min, the sample was detected by TEM. The particle size distribution was examined by using nanoparticle tracking analysis (NTA). In addition, Western blotting was performed according to standard protocol as previously reported (Swanson, et al., 2020) to detect the EVs marker CD9 (ab236630, Abcam), tumor susceptibility gene (Tsg) 101 (ab133586, Abcam) and heat shock protein (Hsp) 70 (ab5439, Abcam). All antibodies were diluted at a concentration ratio of 1:1,000. The protein concentrations of the EVs were measured by using the BCA Protein Assay Kit (Servicebio).

TABLE 1 Primers Used for Real-Time qPCR.

Gene	Forward (5′-3′)	Reverse (3′-5′)
ALP	TGGTACTCGGACAATGAGATGC	GCTCTTCCAAATGCTGATGAGGT
OCN	AGGGCAGTAAGGTGGTGAATAGA	GAAGCCAATGTGGTCCGCTA
RUNX2	CAGTATGAGAGTAGGTGTCCCGC	AAGAGGGGTAAGACTGGTCATAGG
GAPDH	GGCACAGTCAAGGCTGAGAATG	ATGGTGGTGAAGACGCCAGTA

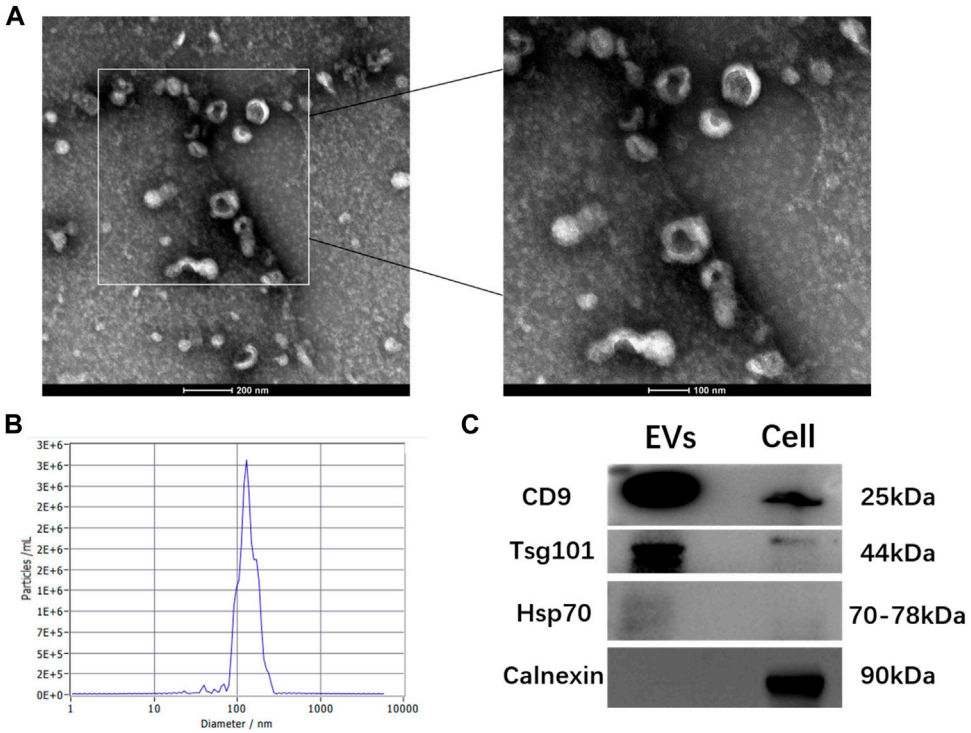

FIGURE 1
Characterization of hGMSC-derived EVs **(A)** hGMSC-derived EVs morphology observed by TEM **(B)** Particle size distribution of hGMSC-derived EVs detected by NTA **(C)** Western blotting results of the EVs surface markers CD9, Tsg101, and Hsp 70.

2.3 BMSC osteogenic differentiation assay

Four groups were established as follows: 1) OM (control), 2) OM complemented with 25 μg/ml hGMSC-derived EVs (25 μg/ml EVs), 3) OM complemented with 50 μg/ml hGMSC-derived EVs (50 μg/ml EVs), and 4) OM complemented with 100 μg/ml hGMSC-derived EVs (100 μg/ml EVs).

Alkaline phosphatase (ALP) staining (Beyotime) and an ALP assay kit (Beyotime) were used to assess ALP activity after 14 days of osteoinduction. Alizarin red staining (Solarbio) was conducted to assess mineralization following 14 days of osteoinduction. To quantify the matrix calcifications, the calcium was deposited with 10% cetylpyridinium chloride (Sigma) for 60 min and measured by the absorbance at 562 nm.

To further examine the expression of osteogenesis-related genes and proteins, real-time qPCR and Western blotting were conducted. The operation steps of real-time qPCR are briefly described as follows. Total RNA was extracted from cells by TRIzol (Servicebio) after 14 days of osteoinduction and then synthesized into cDNA by using StarScript III RT Mix (Genstar). Afterward, quantitative polymerase chain reaction was performed using StarScript III SYBR Mix (Genstar). The primers for *ALP*, osteocalcin (*OCN*) and runt-related transcription factor 2 (*RUNX2*) are presented in Table 1. In addition, total protein was isolated from cells using cell lysis buffer (Beyotime) after 14 days of osteoinduction. Western blotting was performed to detect the expression of osteogenesis-related proteins ALP (No. 60294-1-Ig, Proteintech), OCN (GTX64348, GeneTex) and RUNX2 (No. 20700-1-AP, Proteintech).

2.4 HUVEC angiogenic differentiation assay

HUVECs were cultured in HUVEC special medium with or without different concentrations of EVs (25 μg/ml, 50 μg/ml, and 100 μg/ml). Tube formation assays were performed to assess the impact of hGMSC-derived EVs on angiogenesis. HUVECs pretreated with or without EVs

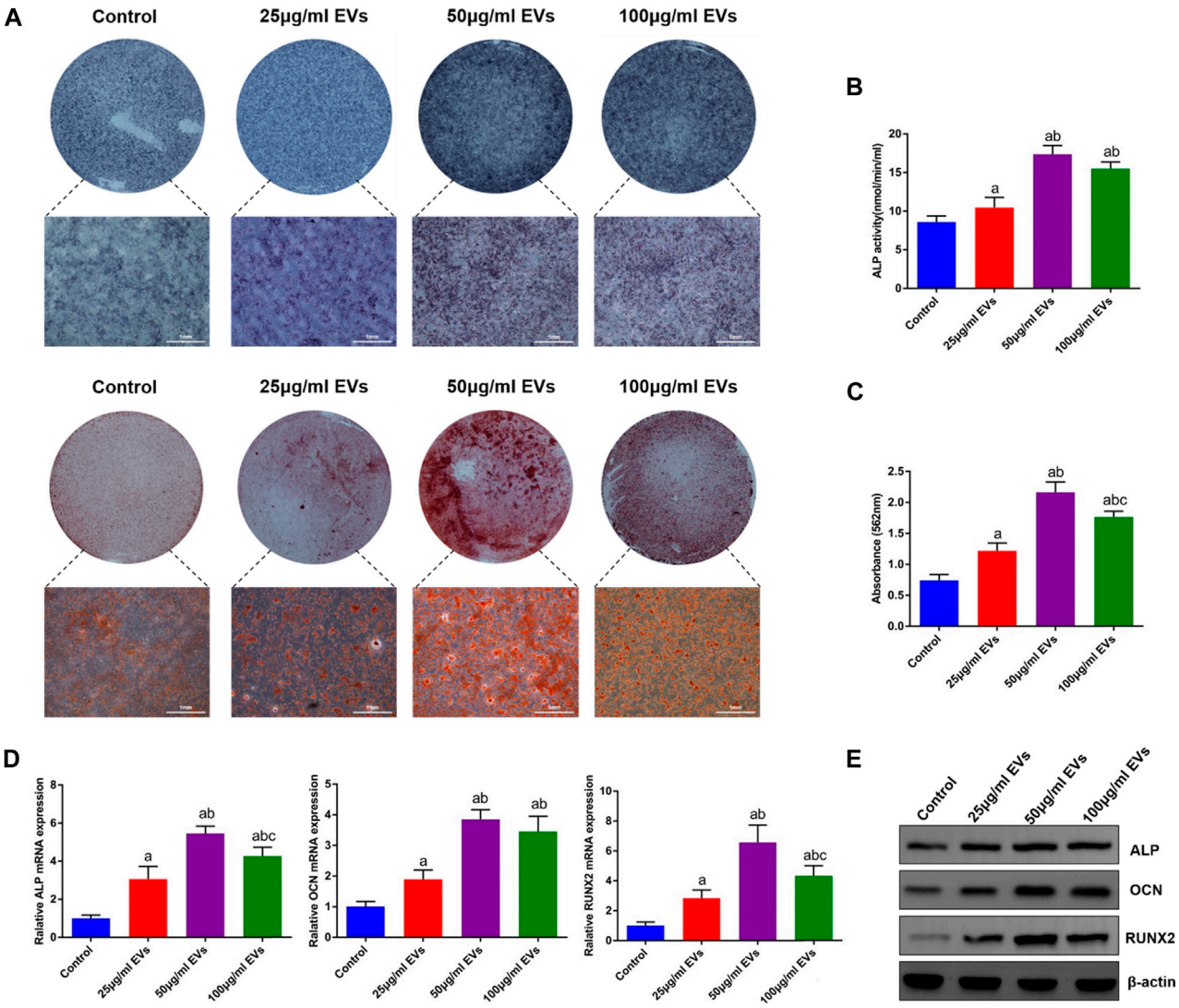

FIGURE 2
Effects of EVs on the osteogenic differentiation of rBMSCs **(A)** The observation of ALP and alizarin red staining **(B)** Quantification of ALP activity **(C)** Quantification of alizarin red staining **(D)** The expression of osteogenic genes (ALP, OCN and RUNX2) **(E)** The expression of osteogenic proteins (ALP, OCN and RUNX2). a, $p < 0.05$ compared with the control group; b, $p < 0.05$ compared with the 25 μg/ml EVs group; c, $p < 0.05$ compared with the 50 μg/ml EVs group.

were seeded into 24-well plates covered with Matrigel (BD Biosciences). Images of tube formation were obtained by microscopy after 6 h of culture. ImageJ software was used to quantitatively analyze the number and total length of tubes.

2.5 Animal experiment design

2.5.1 Preparation and characterization of nHAC-containing cells and EVs

nHAC materials with diameters of 3.5 mm, comprising collagen I and nanohydroxyapatite, were purchased from Allgens Medical Co., Ltd. (Beijing, China). Small pieces 4 mm in length were cut from the nHAC material with a scalpel as scaffolds. Each scaffold was injected with 50 μl of 4 × 106 cells/ml cell solution and then transferred to 24-well plates.

nHAC materials with hGMSCs were cultured in DMEM/F12 complete medium for 3 days. Scaffolds with or without hGMSCs were observed under a scanning electron microscope (JEOL).

Then, 100 μl of EVs at a concentration of 1 μg/μl was injected into each scaffold. To investigate the loading of EVs in the scaffold, EVs were labeled green with DIO (green) dye (Abmole) according to the manufacturer's protocol. The control group was injected with the same volume of PBS. Fluorescence expression was examined under a laser scanning confocal microscope (LSCM, ZEISS).

2.5.2 Critical-sized femoral defect model

The animal experiments in this study were approved by Animal Care and Use Committee of Chinese PLA General Hospital. A total of 60 male Sprague-Dawley rats (12 weeks old, SPF) were purchased from Sibeifu Biotechnology Co., Ltd. (Beijing, China). The rats were randomly divided into four groups as follows: 1) defects with PBS treatment (control, n =

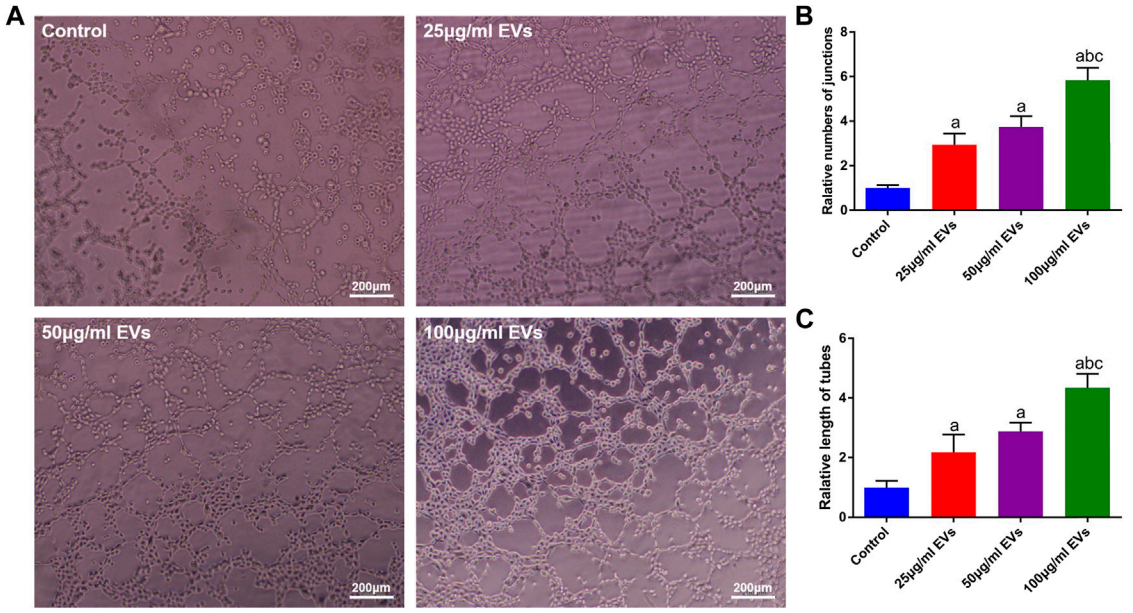

FIGURE 3
Effects of EVs on the angiogenic capacity of HUVECs **(A)** Image of the tube formation assay **(B)** Quantification analysis of tube numbers **(C)** Quantification analysis of tube length. a, $p < 0.05$ compared with the control group; b, $p < 0.05$ compared with the 25 μg/ml EVs group; c, $p < 0.05$ compared with the 50 μg/ml EVs group.

15); 2) defects treated with nHAC scaffolds (nHAC, $n = 15$); 3) defects treated with nHAC scaffolds loaded with hGMSCs (nHAC/hGMSCs, $n = 15$); and 4) defects treated with nHAC scaffolds loaded with EVs (nHAC/EVs, $n = 15$). The femoral defect model was established as previously described (Wang, et al., 2020). Briefly, the rats were anesthetized by intraperitoneal injection of 2% sodium pentobarbital solution (45 mg/kg). Then, Critical-sized defects of $4 \times 4 \times 4\ mm^3$ were created at the lateral femoral condyle. After 4, 8, and 12 weeks, five animals were sacrificed in each group. Then, the femoral condyle defect sites were obtained and fixed in 4% paraformaldehyde for 48 h.

2.5.3 Gross observation and imaging examination

The specimens were examined under a stereomicroscope (Nikon). X-ray images were then obtained by a Faxitron cabinet X-ray system to observe defect healing. The femoral condyles with defects were scanned with a micro-CT scanner (Skyscan). Three-dimensional (3D) reconstruction was performed and analyzed using 3D visualization software (Skyscan). The BMD, bone volume/tissue volume (BV/TV%), trabecular thickness (Tb. Th), and trabecular separation/spacing (Tb.Sp) were calculated.

2.5.4 Histological and immunohistochemical (IHC) analysis

After micro-CT analysis, the specimens were decalcified using 10% EDTA (pH 7.4) for 30 days, dehydrated and embedded in paraffin. Ultimately, the specimens were cut into 4-μm-thick sections. HE, Masson and Goldner staining were conducted to assess bone healing in the defect sites. To further assess new bone formation and neovascularization in femoral condyle defect sites, immunohistochemical staining for osteogenesis-related protein OCN and angiogenesis-related protein CD34 was performed. The primary antibodies anti-OCN (Servicebio) and anti-CD34 (Servicebio) were diluted 1:500 and used according to the manufacturer's instructions.

2.6 Statistical analysis

All data are presented as the mean ± standard deviation for three experiments per group. Student's t-test was used for two-group comparisons, and one-way ANOVA was used for comparisons among three or four groups. $p < 0.05$ was considered statistically significant.

3 Results

3.1 Characterization of hGMSC-derived EVs

The TEM analysis showed that hGMSC-derived EVs had a cup-shaped morphology with a bilayer membrane structure (Figure 1A). The NTA analysis revealed that the peak of the diameter distribution of these nanoparticles was approximately 120 nm, and it was 127.1 ± 37.6 nm in the quantitative analysis (Figure 1B). The Western blotting results demonstrated that hGMSC-derived EVs expressed CD9, TSG101 and HSP70 (Figure 1C).

3.2 hGMSC-derived EVs promote the osteogenic differentiation of BMSC

To investigate the effect of hGMSC-derived EVs on the osteogenic differentiation of rBMSCs, rBMSCs were cultured in OM with or without

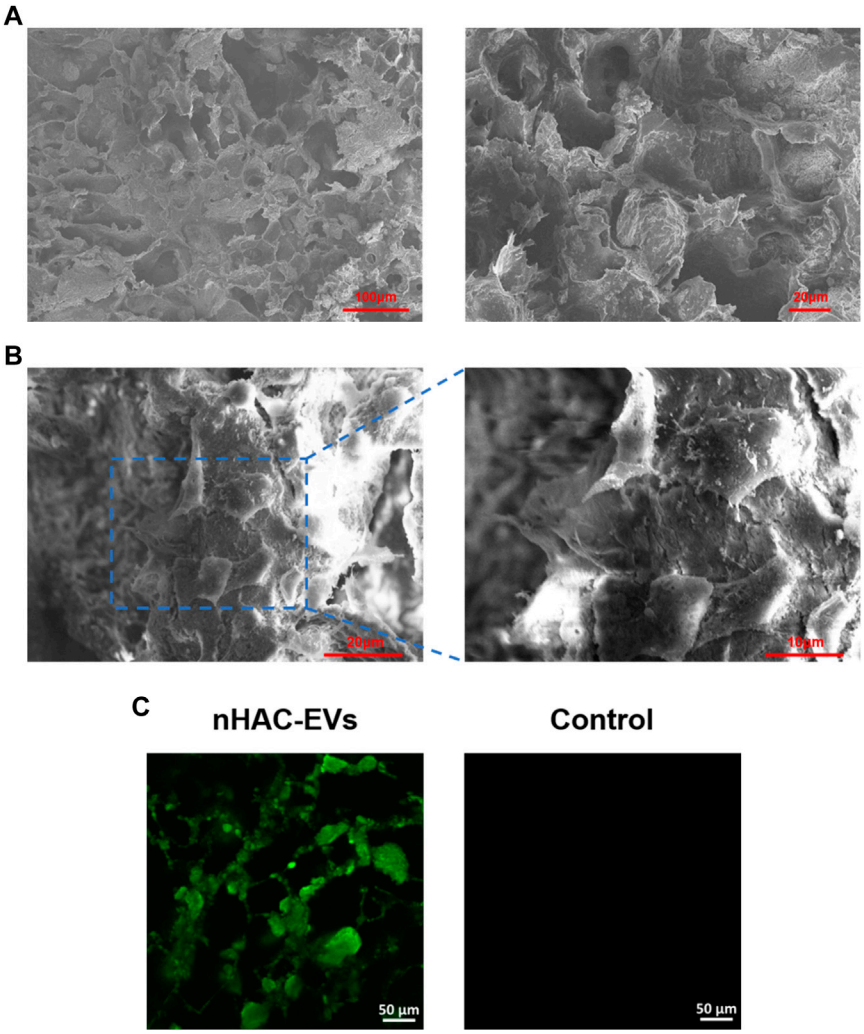

FIGURE 4
Detection of hGMSCs and EVs on the nHAC scaffold **(A)** SEM image of the nHAC scaffold (a: 200×; b: 600×) **(B)** SEM image of the nHAC scaffold with hGMSCs (a: 1100×; b: 2200×) **(C)** LSCM images of the nHAC scaffold with DiO-labeled EVs.

different concentrations of EVs (25 μg/ml, 50 μg/ml, and 100 μg/ml). Following 14 days of induction, ALP staining and ALP activity in rBMSCs were significantly increased in the EVs groups compared with the control group, among which the 50 μg/ml EVs group had the best effect (Figures 2A, B). Additionally, alizarin red staining revealed that the mineralization capacity of rBMSCs was enhanced by EVs with the best effect of 50 μg/ml (Figures 2A, C). Likewise, osteogenic mRNA and protein expression (ALP, OCN and RUNX2) was upregulated by EVs, with the highest level in the 50 μg/ml EVs group (Figures 2D, E).

3.3 hGMSC-derived EVs promote the angiogenic capacity of HUVEC

To evaluate the effect of hGMSC-derived EVs on the angiogenic ability of HUVECs, a tube formation assay was conducted. As shown in Figure 3A, the HUVECs in the EVs groups exhibited stronger angiogenic ability than those in the control group, and this ability was enhanced with increasing EVs concentration. Similarly, the quantitative analysis also showed that the number and total length of tubes were significantly higher in the EVs groups (Figures 3B, C).

3.4 hGMSC and EVs detection from the nHAC scaffold

SEM showed that the nHAC material had a porous structure with a uniform pore size of approximately 50–150 μm (Figure 4A). After 3 days of culture, hGMSCs on the nHAC scaffold grew well and adhered to the surface of the material. Moreover, secreted filamentous extracellular matrix around cells could be observed under high magnification (Figure 4B). After DIO-labeled EVs were added to the nHAC material, a large amount of green fluorescence was observed on the material by LSCM, and no fluorescence was detected in the control group (Figure 4C).

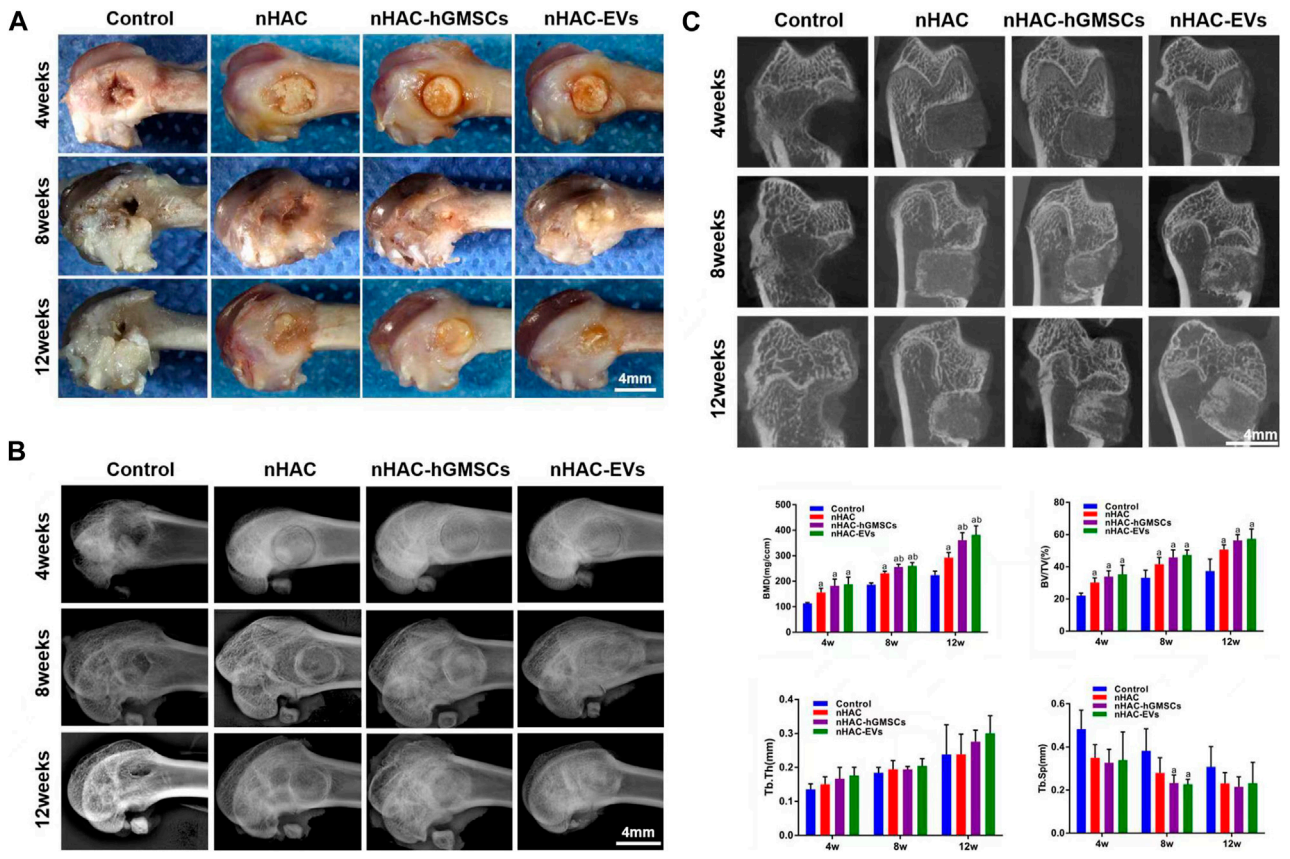

FIGURE 5
Cross observation and imaging analysis of bone regeneration **(A)** Cross observation images of bone defect sites **(B)** X-ray images of bone defect sites **(C)** Micro-CT images and analysis of bone formation using BMD, BV/TV%, Tb.Th, and Tb. Sp. a, $p < 0.05$ compared with the control group; b, $p < 0.05$ compared with the nHAC group.

3.5 Cross observation and imaging analysis of bone regeneration

A total of 60 Sprague-Dawley rats with femoral defects were divided into four groups (control, nHAC, nHAC/hGMSCs and nHAC/EVs; n = 15/group) and euthanized by dislocation of cervical vertebrae under deep anesthesia in three different times (at 4, 8, and 12 weeks). As shown in Figure 5A, defects gradually decreased with healing time, as observed under a stereomicroscope. As expected, the defects of each group implanted with nHAC healed better than those of the control group. Among them, the defect healing of the nHAC/hGMSCs group and nHAC/EVs group was better than that of the nHAC group. Moreover, the results of X-ray and micro-CT imaging also showed that the bone healing effect of the nHAC/hGMSCs group and nHAC/EVs group was better than that of the other two groups, and the defects in the nHAC group healed better (Figures 5B, C). According to 3D reconstruction analysis, the BMD, BV/TV%, Tb.Th, and Tb. Sp results further revealed that more new bone formation was discovered in the HAC/hGMSCs group and nHAC/EVs group than in the nHAC group and control group. In addition, no significant difference was found in the amount of new bone formation between the HAC/hGMSCs group and the nHAC/EVs group (Figure 5C).

3.6 Histological results of bone regeneration

The HE staining results at 4, 8, and 12 weeks are shown in Figure 6. The regenerative bone mass in the femoral defect area increased over time in each group, although it was higher in groups implanted with nHAC, among which the nHAC/hGMSCs group and nHAC/EVs group were better. The Masson and Goldner staining results indicated that the nHAC/hGMSCs group and nHAC/EVs group at each time point had more collagen deposition and new bone formation than the other two groups (Figures 7, 8).

3.7 Immunohistochemical staining results of bone regeneration

As an important indicator for evaluating osteogenic ability, OCN-positive areas can be stained dark brown by immunohistochemical staining. IHC staining indicated that the expression levels of OCN in groups implanted with nHAC at each time point were higher than those in the control group. Moreover, the nHAC/hGMSCs group and nHAC/EVs group had the highest OCN expression with no significant

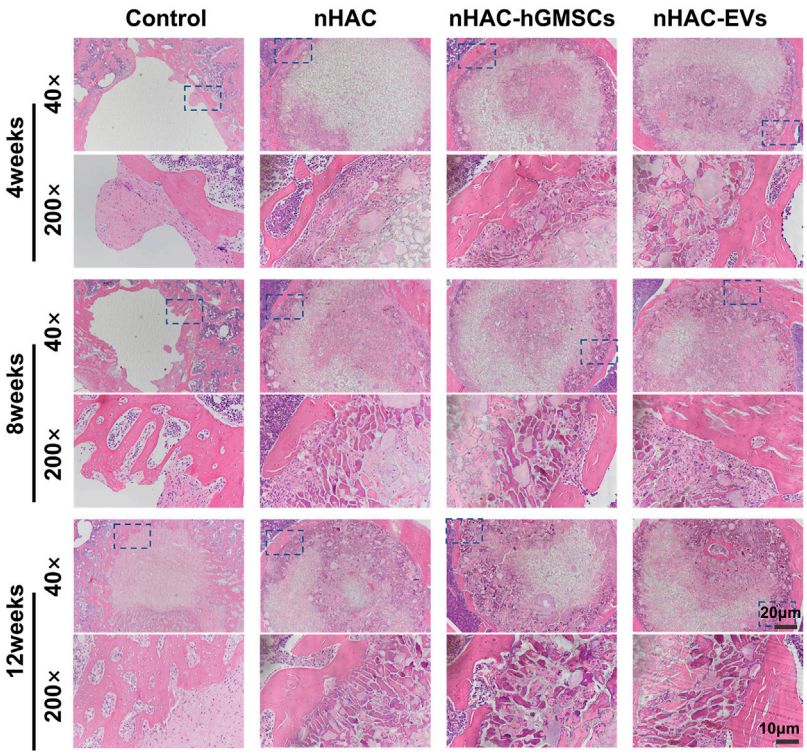

FIGURE 6
Representative images of HE staining of the bone defect area. The 200× image is an enlargement in the dashed box of the 40× image.

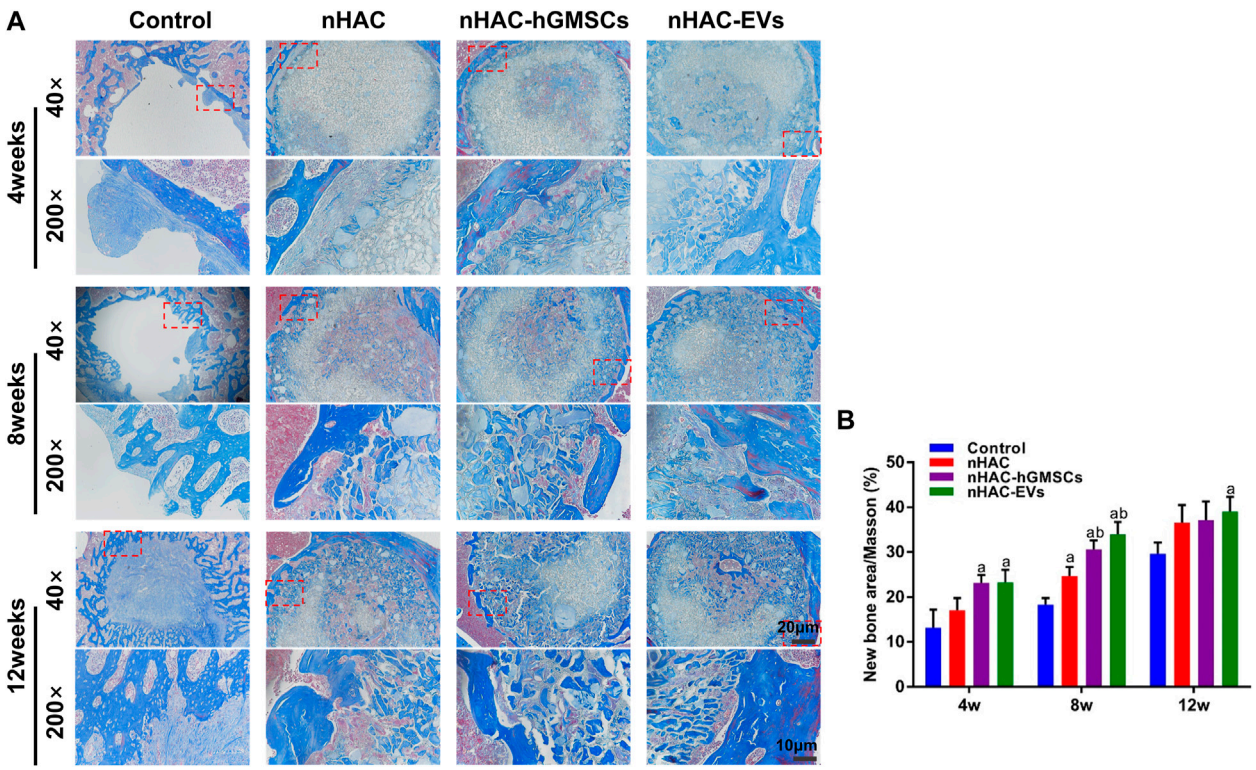

FIGURE 7
Masson staining results of bone regeneration **(A)** Representative images of Masson staining of the bone defect area. The 200× image is an enlargement in the dashed box of the 40× image **(B)** Quantitative analysis of new bone. a, $p < 0.05$ compared with the control group; b, $p < 0.05$ compared with the nHAC group.

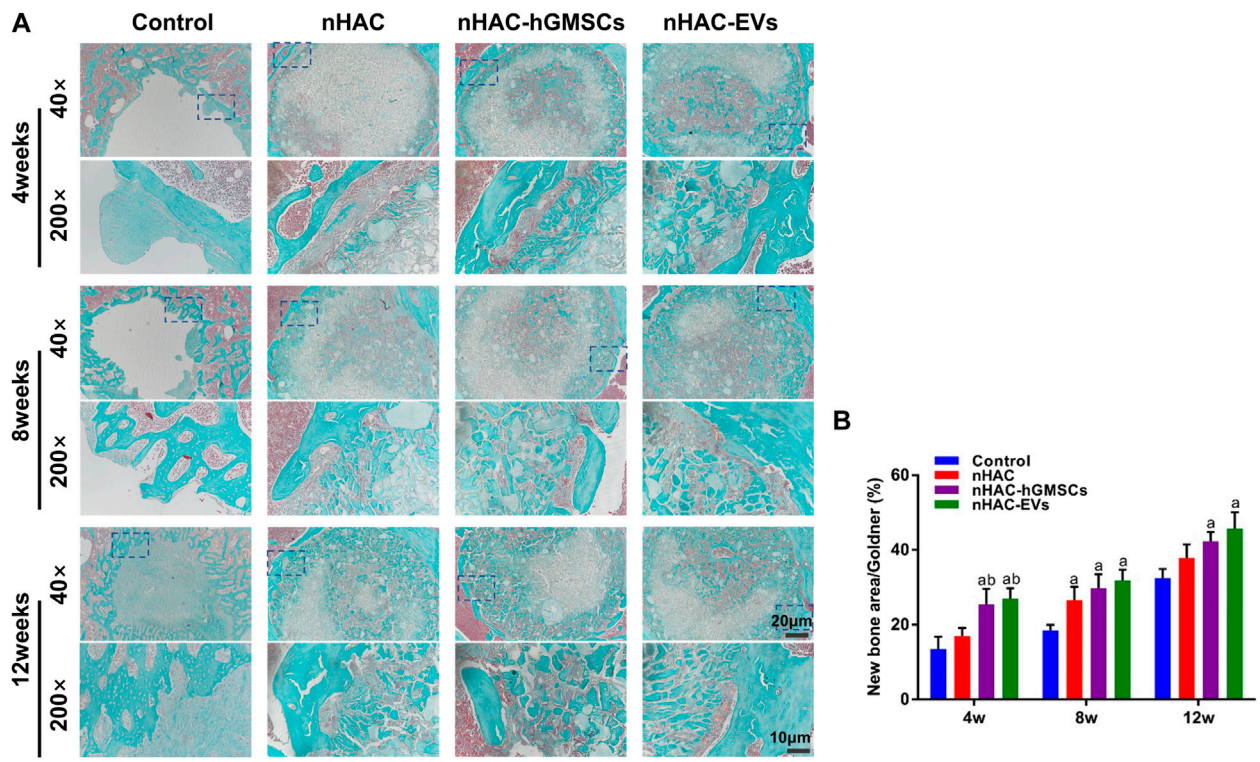

FIGURE 8
Goldner staining results of bone regeneration **(A)** Representative images of Goldner staining of the bone defect area. The 200× image is an enlargement in the dashed box of the 40× image **(B)** Quantitative analysis of new bone. a, $p < 0.05$ compared with the control group; b, $p < 0.05$ compared with the nHAC group.

difference (Figures 9A, B). Additionally, more angiogenesis-related protein CD34 was observed in the nHAC/hGMSCs group and nHAC/EVs group than in the other two groups, suggesting that more new blood vessels were formed in the nHAC/hGMSCs group and nHAC/EVs group (Figures 9C, D).

4 Discussion

In general, bone tissue shows good tissue repair function after trauma, but the repair of large-scale bone defects is still a difficult problem in clinical therapy. Bone regeneration is a complex process involving many aspects, such as angiogenesis, osteogenesis, and anti-inflammation (Dimitriou, et al., 2011). Although MSC transplantation therapy has shown good application effects for the repair of bone defects, recent studies have shown that its specific mechanism is mainly accomplished by paracrine effects of MSCs (Rani, et al., 2015; Reis, et al., 2018). As critical paracrine factors secreted by cells, EVs can mediate intercellular communication by delivering proteins, mRNAs, miRNAs and other substances to recipient cells, thereby regulating the biological functions of target cells (Hu, et al., 2021; Tarasov, et al., 2021).

hGMSCs are a kind of MSC with multiple differentiation potential and strong self-renewal ability isolated from the human gingival lamina propria (Fawzy El-Sayed and Dörfer, 2016). The special tissue living environment of the gingiva also makes hGMSCs different from other MSCs. Compared with other MSCs, hGMSCs are easy to obtain, rich in sources, and have good biological properties, showing good application prospects in cell therapy and regenerative medicine (Fawzy El-Sayed and Dörfer, 2016). Several *in vivo* studies have shown that hGMSCs can promote bone regeneration (Xu, et al., 2014; Al-Qadhi, et al., 2020; Hasani-Sadrabadi, et al., 2020). Xu et al. (Xu, et al., 2014) found that hGMSCs could promote the repair of mandibular defects in mice by intravenous injection of hGMSCs applied to the defect. In addition, Al-Qadhi et al. (Al-Qadhi, et al., 2020) indicated that hGMSCs had osteogenic ability similar to that of BMSCs in a tibial defect animal model. However, few studies have reported on bone tissue engineering with hGMSC-derived EVs. A study performed by Jiang et al. (2020) demonstrated that hGMSC-derived EVs could promote the migration and osteogenic differentiation of preosteoblasts. However, the effect of hGMSC-derived EVs on bone defect repair *in vivo* has not been reported. Therefore, the study was conducted *in vitro* and *in vivo* to deeply explore the bone repair effect of hGMSC-derived EVs.

With the deepening of research, it was found that the osteogenic effect of MSC-derived EVs without osteogenic induction is not obvious (Zhang, et al., 2019). Moreover, Liu et al. (Liu, et al., 2020) indicated that the osteogenic differentiation capacity of MSCs could be enhanced by osteogenic induction and that the enhancement effect was

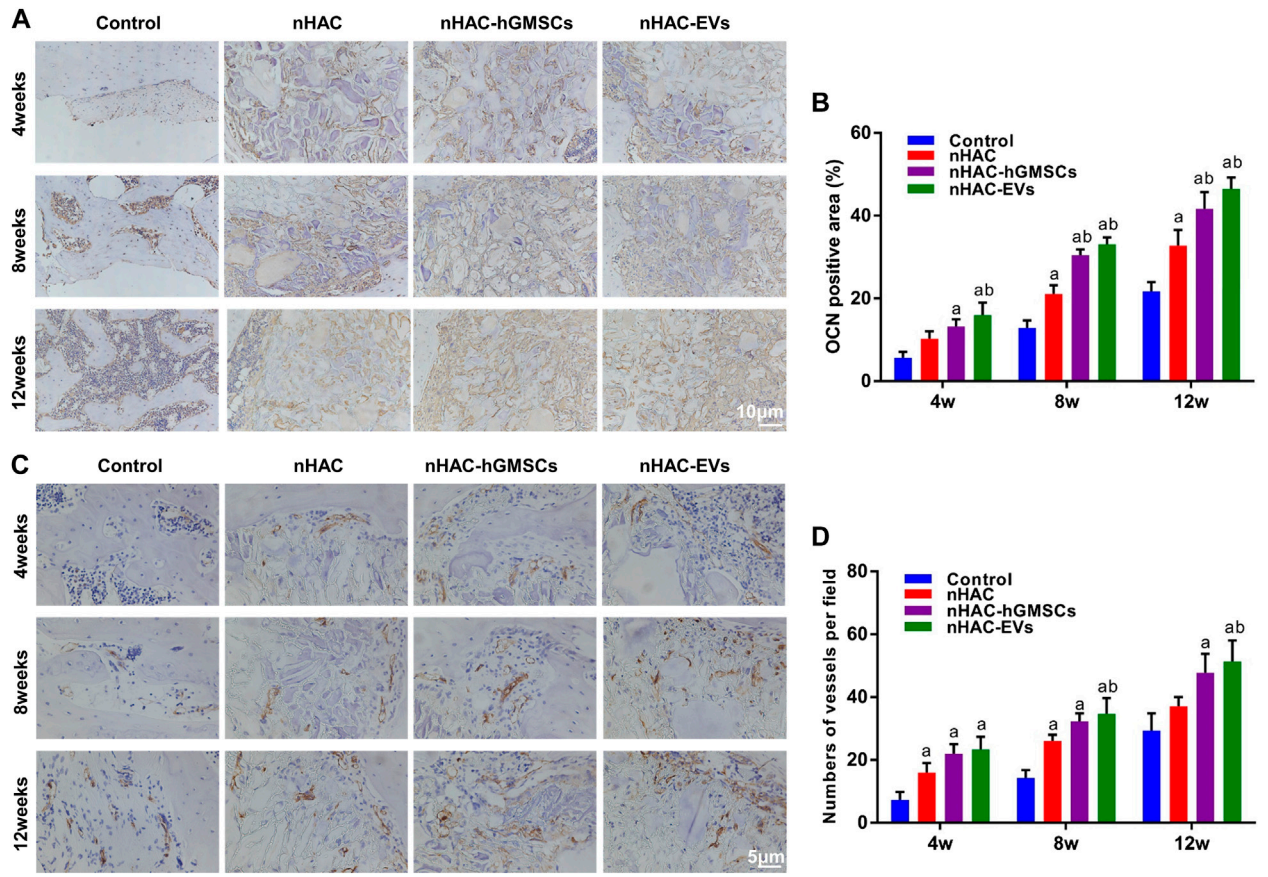

FIGURE 9
Immunohistochemical staining results of bone regeneration **(A)** Representative images of OCN staining **(B)** Quantitative analysis of OCN expression **(C)** Representative images of CD34 staining **(D)** Quantitative analysis of CD34 expression. a, $p < 0.05$ compared with the control group; b, $p < 0.05$ compared with the nHAC group.

related to the time of osteogenic induction of MSCs. This study further showed that the osteogenic effect of EVs after 3 days and 14 days of induction was better (Liu, et al., 2020). However, the stemness and paracrine capacity of MSCs were reduced as the induction time increased (Yeo, et al., 2013). Therefore, in this study, we chose EVs derived from hGMSCs after 3 days of osteogenic induction.

Bone regeneration involves the participation of a variety of cells, and bone-related cells and blood vessel-related cells play an important role (Dimitriou, et al., 2011; Sun, et al., 2022). BMSCs are adult stem cells present in the bone marrow stroma that are activated and mobilized upon injury and serve as the main repair cell type in bone regeneration (Deschaseaux, et al., 2009).

Endothelial cells (ECs) are the first cells to enter the bone marrow after bone tissue injury and coordinate tissue development, maintenance, and regeneration by secreting beneficial vascular secretory signals (Kenswil, et al., 2021). When bone defects occur, BMSCs and ECs can synergistically regulate the bone microenvironment of the defect site and promote bone regeneration by accelerating angiogenesis (Cheng, et al., 2022). Therefore, in this study, we selected rat bone marrow mesenchymal stem cells (rBMSCs) and human umbilical vein endothelial cells (HUVECs) to evaluate the effects of hGMSC-derived EVs on the osteogenic ability of osteoblasts and the angiogenic capability of endothelial cells *in vitro*.

In this study, we found that hGMSC-derived EVs could promote osteogenic differentiation and upregulate the expression of ALP, OCN and RUNX2 osteogenic genes and proteins in rBMSCs. To evaluate the effect of different concentrations of EVs on the osteogenic ability of rBMSCs, we treated rBMSCs with 25 μg/ml, 50 μg/ml and 100 μg/ml EVs. The results showed that 50 μg/ml EVs had the strongest osteogenic ability. In addition, we also demonstrated that hGMSC-derived EVs could enhance the angiogenic ability of HUVECs *in vitro* such that the higher the EVs concentration was, the better the enhancement effect. MSC-derived EVs could promote the osteogenesis of BMSCs and the angiogenesis of HUVECs, which may contribute to the repair of bone defects. Wu et al. (Wu, et al., 2019) found that EVs derived from stem cells from human exfoliated deciduous teeth could enhance the repair of alveolar bone defects through the regulation of osteogenesis of BMSCs and angiogenesis of HUVECs. Moreover, Zhang et al. (Zhang, et al., 2020) also found that BMSC-derived EVs could accelerate fracture healing of non-union through the promotion of osteogenesis and angiogenesis. In this study, hGMSC-derived

EVs enhanced the osteogenic ability of rBMSCs and the angiogenic capability of HUVECs. Therefore, we speculated that hGMSC-derived EVs could be an effective approach for bone regeneration *in vivo*.

In animal models of femoral defects, nanohydroxyapatite/collagen was selected as scaffolding material to carry EVs to the site of defects to verify the repair effect of hGMSC-derived EVs on bone defects. In addition, we set up an nHAC/hGMSC group to better evaluate the role of hGMSC-derived EVs. Our data showed that nHAC materials were biocompatible and could be used as application vectors for cells and EVs. At 4, 8 and 12 weeks postsurgery, the bone repair effect of the nHAC/hGMSCs group and the nHAC/EVs group was better than that of the nHAC group and the control group, while the bone repair effect of the nHAC/hGMSCs group and the nHAC/EVs group was not significantly different. Moreover, HE staining, Masson staining, Goldner staining, and immunohistochemical staining for OCN and CD34 showed that more new bone and new blood vessels were produced after treatment with hGMSC-derived EVs, with effects comparable with those of transplanted hGMSCs. In bone tissue engineering, the combination of bone repair materials and bioactive molecules that induce osteogenesis could enhance the function of biomaterials and promote the aggregation and differentiation of osteoblasts, thereby accelerating the repair and regeneration of bone defects (Zuo, et al., 2022). At present, nHAC materials have been widely used in the repair of bone defects, and it is a feasible application strategy to combine them with nanoactive molecular EVs that have good bone induction ability and proangiogenic ability. In this study, hGMSC-derived EVs were able to stimulate osteogenesis of rBMSCs and angiogenesis of HUVECs *in vitro*. In addition, OCN and CD34 were highly expressed in the bone defect areas of the EVs treatment group. Therefore, hGMSC-derived EVs may promote osteogenesis and angiogenesis in bone defect areas by influencing the biological function of endogenous cells, such as BMSCs and ECs. Our findings suggested that the combination of hGMSC-derived EVs with nHAC scaffolds was a reliable method for bone defect repair.

However, this study has some limitations. First, this study did not explore in depth the possible mechanisms of hGMSC-derived EVs in osteogenic differentiation and bone repair at the molecular level. Second, bone regeneration is achieved through bone formation and bone resorption with the participation of osteoblasts and osteoclasts. This study explored the effect of hGMSC-derived EVs on the osteogenic differentiation of osteoblasts, but there is a lack of studies on the biological characteristics of osteoclasts. Finally, in this study, the femoral defect of ordinary rats was selected as the model, and whether it is suitable for femoral defects in osteoporotic rats is not known.

5 Conclusion

In this study, we successfully extracted EVs derived from hGMSCs and combined the EVs with a nanohydroxyapatite/collagen scaffold for bone defect repair. Our results demonstrated that the combination of hGMSC-derived EVs and nHAC could significantly promote bone regeneration by advancing osteogenesis and angiogenesis. Therefore, this strategy could serve as a clinical therapy for bone regeneration.

Data availability statement

The original contributions presented in the study are included in the article/supplementary material, further inquiries can be directed to the corresponding authors.

Ethics statement

The studies involving human participants were reviewed and approved by Clinical Ethics Committee of the Chinese PLA General Hospital. The patients/participants provided their written informed consent to participate in this study. The animal study was reviewed and approved by Animal Care and Use Committee of Chinese PLA General Hospital.

Author contributions

QS, JX, and TZ conceived of the study and designed the experiments jointly. SW, ZL, SY, NH, and BQ carried out the experiments and analyzed the experimental results. SW, ZL, and SY summarized the literature and wrote the manuscript. All authors approved the final manuscript.

Funding

This study was supported by the National Natural Science Foundation of China (81901034), Beijing Municipal Natural Science Foundation (7212091), Military Healthcare Special Project (19BJZ22)and Military Medical Science Foundation (21QNPY104).

Conflict of interest

The authors declare that the research was conducted in the absence of any commercial or financial relationships that could be construed as a potential conflict of interest.

Publisher's note

References

Al-Qadhi, G., Soliman, M., Abou-Shady, I., and Rashed, L. (2020). Gingival mesenchymal stem cells as an alternative source to bone marrow mesenchymal stem cells in regeneration of bone defects: *In vivo* study. *Tissue Cell* 63, 101325. doi:10.1016/j.tice.2019.101325

Boere, J., Malda, J., van de Lest, C., van Weeren, P. R., and Wauben, M. (2018). Extracellular vesicles in joint disease and therapy. Front. Immunol. 9, 2575. doi:10.3389/fimmu.2018.02575

Cheng, P., Cao, T., Zhao, X., Lu, W., Miao, S., Ning, F., et al. (2022). Nidogen1-enriched extracellular vesicles accelerate angiogenesis and bone regeneration by targeting Myosin-10 to regulate endothelial cell adhesion. *Bioact. Mater* 12, 185–197. doi:10.1016/j.bioactmat.2021.10.021

Deschaseaux, F., Sensébé, L., and Heymann, D. (2009). Mechanisms of bone repair and regeneration. *Trends Mol. Med.* 15 (9), 417–429. doi:10.1016/j.molmed.2009.07.002

Dimitriou, R., Jones, E., McGonagle, D., and Giannoudis, P. V. (2011). Bone regeneration: Current concepts and future directions. *BMC Med.* 9, 66. doi:10.1186/1741-7015-9-66

Eggenhofer, E., Luk, F., Dahlke, M. H., and Hoogduijn, M. J. (2014). The life and fate of mesenchymal stem cells. *Front. Immunol.* 5, 148. doi:10.3389/fimmu.2014.00148

Fawzy El-Sayed, K. M., and Dörfer, C. E. (2016). Gingival mesenchymal stem/progenitor cells: A unique tissue engineering gem. *Stem Cells Int.* 2016, 1–16. doi:10.1155/2016/7154327

Hasani-Sadrabadi, M. M., Sarrion, P., Pouraghaei, S., Chau, Y., Ansari, S., Li, S., et al. (2020). An engineered cell-laden adhesive hydrogel promotes craniofacial bone tissue regeneration in rats. *Sci. Transl. Med.* 12 (534), eaay6853. doi:10.1126/scitranslmed.aay6853

Hu, Y., Wang, Y., Chen, T., Hao, Z., Cai, L., and Li, J. (2021). Exosome: Function and application in inflammatory bone diseases. *Oxid. Med. Cell Longev.* 2021, 1–17. doi:10.1155/2021/632491210.1155/2021/6324912

Jiang, S., and Xu, L. (2020). Exosomes from gingival mesenchymal stem cells enhance migration and osteogenic differentiation of pre-osteoblasts. *Pharmazie* 75 (11), 576–580. doi:10.1691/ph.2020.0652

Kenswil, K., Pisterzi, P., Sánchez-Duffhues, G., van Dijk, C., Lolli, A., Knuth, C., et al. (2021). Endothelium-derived stromal cells contribute to hematopoietic bone marrow niche formation. *Cell Stem Cell* 28 (4), 653–670.e11. doi:10.1016/j.stem.2021.01.006

Kumar, B. P., Venkatesh, V., Kumar, K. A., Yadav, B. Y., and Mohan, S. R. (2016). Mandibular reconstruction: Overview. *J. Maxillofac. Oral Surg.* 15 (4), 425–441. doi:10.1007/s12663-015-0766-5

Liang, X., Ding, Y., Zhang, Y., Tse, H. F., and Lian, Q. (2014). Paracrine mechanisms of mesenchymal stem cell-based therapy: Current status and perspectives. *Cell Transpl.* 23 (9), 1045–1059. doi:10.3727/096368913X667709

Liu, T., Hu, W., Zou, X., Xu, J., He, S., Chang, L., et al. (2020). Human periodontal ligament stem cell-derived exosomes promote bone regeneration by altering MicroRNA profiles. *Stem Cells Int.* 2020, 1–13. doi:10.1155/2020/8852307

Moghadasi, S., Elveny, M., Rahman, H. S., Suksatan, W., Jalil, A. T., Abdelbasset, W. K., et al. (2021). A paradigm shift in cell-free approach: The emerging role of MSCs-derived exosomes in regenerative medicine. *J. Transl. Med.* 19 (1), 302. doi:10.1186/s12967-021-02980-6

Najar, M., Melki, R., Khalife, F., Lagneaux, L., Bouhtit, F., Moussa Agha, D., et al. (2021). Therapeutic mesenchymal stem/stromal cells: Value, challenges and optimization. *Front. Cell Dev. Biol.* 9, 716853. doi:10.3389/fcell.2021.716853

Nguyen, M. K., Jeon, O., Dang, P. N., Huynh, C. T., Varghai, D., Riazi, H., et al. (2018). RNA interfering molecule delivery from *in situ* forming biodegradable hydrogels for enhancement of bone formation in rat calvarial bone defects. *Acta Biomater.* 75, 105–114. doi:10.1016/j.actbio.2018.06.007

Qin, Y., Sun, R., Wu, C., Wang, L., and Zhang, C. (2016). Exosome: A novel approach to stimulate bone regeneration through regulation of osteogenesis and angiogenesis. *Int. J. Mol. Sci.* 17 (5), 712. doi:10.3390/ijms17050712

Rani, S., Ryan, A. E., Griffin, M. D., and Ritter, T. (2015). Mesenchymal stem cell-derived extracellular vesicles: Toward cell-free therapeutic applications. *Mol. Ther.* 23 (5), 812–823. doi:10.1038/mt.2015.44

Reis, M., Mavin, E., Nicholson, L., Green, K., Dickinson, A. M., and Wang, X. N. (2018). Mesenchymal stromal cell-derived extracellular vesicles attenuate dendritic cell maturation and function. *Front. Immunol.* 9, 2538. doi:10.3389/fimmu.2018.02538

Shi, Q., Qian, Z., Liu, D., Sun, J., Wang, X., Liu, H., et al. (2017). GMSC-derived exosomes combined with a chitosan/silk hydrogel sponge accelerates wound healing in a diabetic rat skin defect model. *Front. Physiol.* 8, 904. doi:10.3389/fphys.2017.00904

Sun, Y., Wan, B., Wang, R., Zhang, B., Luo, P., Wang, D., et al. (2022). Mechanical stimulation on mesenchymal stem cells and surrounding microenvironments in bone regeneration: Regulations and applications. *Front. Cell Dev. Biol.* 10, 808303. doi:10.3389/fcell.2022.808303

Swanson, W. B., Zhang, Z., Xiu, K., Gong, T., Eberle, M., Wang, Z., et al. (2020). Scaffolds with controlled release of pro-mineralization exosomes to promote craniofacial bone healing without cell transplantation. *Acta Biomater.* 118, 215–232. doi:10.1016/j.actbio.2020.09.052

Tarasov, V. V., Svistunov, A. A., Chubarev, V. N., Dostdar, S. A., Sokolov, A. V., Brzecka, A., et al. (2021). Extracellular vesicles in cancer nanomedicine. *Semin. Cancer Biol.* 69, 212–225. doi:10.1016/j.semcancer.2019.08.017

Théry, C., Amigorena, S., Raposo, G., and Clayton, A. (2006). Isolation and characterization of exosomes from cell culture supernatants and biological fluids. *Curr. Protoc. Cell Biol.* 30, Unit 3.22. doi:10.1002/0471143030.cb0322s30

Tomar, G. B., Srivastava, R. K., Gupta, N., Barhanpurkar, A. P., Pote, S. T., Jhaveri, H. M., et al. (2010). Human gingiva-derived mesenchymal stem cells are superior to bone marrow-derived mesenchymal stem cells for cell therapy in regenerative medicine. *Biochem. Biophys. Res. Commun.* 393 (3), 377–383. doi:10.1016/j.bbrc.2010.01.126

Trajkovic, K., Hsu, C., Chiantia, S., Rajendran, L., Wenzel, D., Wieland, F., et al. (2008). Ceramide triggers budding of exosome vesicles into multivesicular endosomes. *Science* 319 (5867), 1244–1247. doi:10.1126/science.1153124

Valtanen, R. S., Yang, Y. P., Gurtner, G. C., Maloney, W. J., and Lowenberg, D. W. (2021). Synthetic and Bone tissue engineering graft substitutes: What is the future. *Injury* 52 (2), S72–S77. doi:10.1016/j.injury.2020.07.040

Wang, L., Wang, J., Zhou, X., Sun, J., Zhu, B., Duan, C., et al. (2020). A new self-healing hydrogel containing hucMSC-derived exosomes promotes bone regeneration. *Front. Bioeng. Biotechnol.* 8, 564731. doi:10.3389/fbioe.2020.564731

Williams, T., Salmanian, G., Burns, M., Maldonado, V., Smith, E., Porter, R. M., et al. (2022). Versatility of mesenchymal stem cell-derived extracellular vesicles in tissue repair and regenerative applications. *Biochimie* 207, 33–48. doi:10.1016/j.biochi.2022.11.011

Wu, J., Chen, L., Wang, R., Song, Z., Shen, Z., Zhao, Y., et al. (2019). Exosomes secreted by stem cells from human exfoliated deciduous teeth promote alveolar bone defect repair through the regulation of angiogenesis and osteogenesis. *ACS Biomater. Sci. Eng.* 5 (7), 3561–3571. doi:10.1021/acsbiomaterials.9b00607

Xu, Q. C., Wang, Z. G., Ji, Q. X., Yu, X. B., Xu, X. Y., Yuan, C. Q., et al. (2014). Systemically transplanted human gingiva-derived mesenchymal stem cells contributing to bone tissue regeneration. *Int. J. Clin. Exp. Pathol.* 7 (8), 4922–4929.

Xu, X., Chen, C., Akiyama, K., Chai, Y., Le, A., Wang, Z., et al. (2013). Gingivae contain neural-crest- and mesoderm-derived mesenchymal stem cells. *J. Dent. Res.* 92 (9), 825–832. doi:10.1177/0022034513497961

Yeo, R. W., Lai, R. C., Zhang, B., Tan, S. S., Yin, Y., Teh, B. J., et al. (2013). Mesenchymal stem cell: An efficient mass producer of exosomes for drug delivery. *Adv. Drug Deliv. Rev.* 65 (3), 336–341. doi:10.1016/j.addr.2012.07.001

Zhang, L., Jiao, G., Ren, S., Zhang, X., Li, C., Wu, W., et al. (2020). Exosomes from bone marrow mesenchymal stem cells enhance fracture healing through the promotion of osteogenesis and angiogenesis in a rat model of nonunion. *Stem Cell Res. Ther.* 11 (1), 38. doi:10.1186/s13287-020-1562-9

Zhang, Y., Hao, Z., Wang, P., Xia, Y., Wu, J., Xia, D., et al. (2019). Exosomes from human umbilical cord mesenchymal stem cells enhance fracture healing through HIF-1α-mediated promotion of angiogenesis in a rat model of stabilized fracture. *Cell Prolif.* 52 (2), e12570. doi:10.1111/cpr.12570

Zuo, Y., Li, Q., Xiong, Q., Li, J., Tang, C., Zhang, Y., et al. (2022). Naringin release from a nano-hydroxyapatite/collagen scaffold promotes osteogenesis and bone tissue reconstruction. *Polym. (Basel)* 14 (16), 3260. doi:10.3390/polym14163260

Frontiers in
Bioengineering and Biotechnology

Accelerates the development of therapies, devices, and technologies to improve our lives

A multidisciplinary journal that accelerates the development of biological therapies, devices, processes and technologies to improve our lives by bridging the gap between discoveries and their application.

Discover the latest Research Topics

See more →

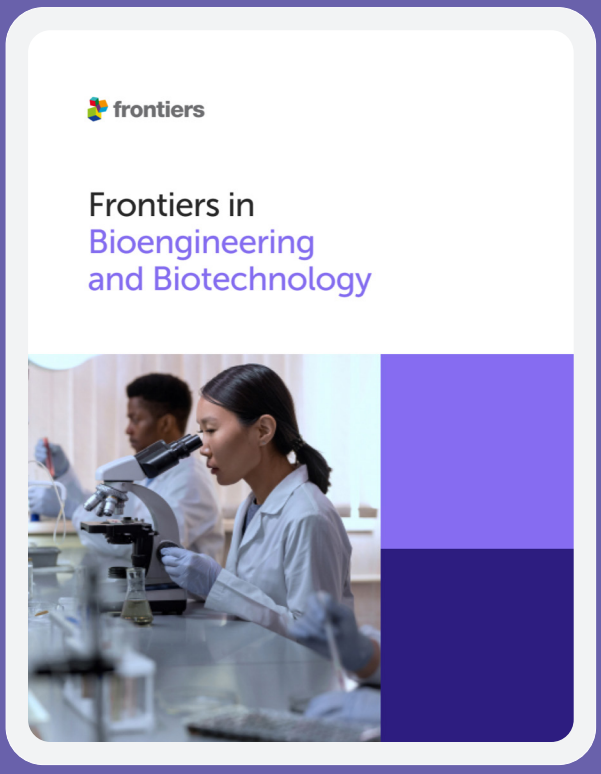

Frontiers

Avenue du Tribunal-Fédéral 34
1005 Lausanne, Switzerland
frontiersin.org

Contact us

+41 (0)21 510 17 00
frontiersin.org/about/contact